UNIVERSITÀ DEGLI STUDI DI TRIESTE

e

UNIVERSITÀ CA' FOSCARI DI VENEZIA

XXXI CICLO DEL DOTTORATO DI RICERCA IN

CHIMICA

Zn(II)-porphyrin metallacycles: versatile building units for the self-assembling of discrete 3D multi-component systems with tuned geometries and properties

Settore scientifico-disciplinare: **CHIM 03**

DOTTORANDA

AGNESE AMATI

COORDINATORE

PROF. BARBARA MILANI

SUPERVISORE DI TESI

PROF. ELISABETTA IENGO

Abstract

The research carried out during this PhD project and reported in this Thesis is focused on the design, preparation, and characterization of multi-component supramolecular 3D architectures obtained by appropriate paneling multitopic pyridyl ligands with flat Zn-porphyrin metallacycles. The versatility of the synthetic approach pursued, allowed to efficiently construct libraries of elaborated 3D structures, tuning the shape and dimension of the target systems, modulating the inter-component photo-induced properties and/or introducing new functions deriving from the geometrical organization of a precise number of active metal centers, by cleverly tailoring the molecular building blocks.

In Chapter 1, a general introduction on the key role of porphyrins as functional and structural building unit for the assembly of artificial discrete supramolecular structures is presented, together with the main designing concepts of the metal-mediated self-assembling synthetic strategy. Few examples of elegant multiporphyrin architectures and their application are reported. Finally, the modular synthetic approach pursued during this research project is described.

In Chapter 2, a thorough investigation on the possibility to produce new hetero-multimetallic ordered discrete structures, by self-assembling of a zinc-porphyrin metallacycle (**1Zn**) with dipyridyl clathrochelate metalloligands (provided by the group of Prof. K. Severin, EPFL, Lausanne, CH), is discussed. In particular, linear Fe^{II} metal containing ligands with terminal 4-pyridyl groups, length between 1.5 and 3.2 nm, and containing either one or two clathrochelate cores were chosen. The final aim is the easy access, by a modular approach, to higher order functional systems comprising defined numbers and spatial organizations of metal-active centers (*e.g.* magnetically, redox or catalytically active).

Chapter 3 reports on the metal-mediated assembling of a linear dipyridyl diazadioxa[8]circulene (**Circ**, provided by the group of Prof. M. Pittelkow, University of Copenhagen, DK) with either **1Zn** and a *cis*-protected diphosphines Pt^{II} complex. **Circ** is a flat and conjugated compound presenting a central antiaromatic cyclooctatetraene core. The designing idea was to endow the ligand in structures, enforcing conformations which could enable to find experimental evidence of the antiaromaticity, by observation of deshielding effect due to the paratropic ring current of the COT core. Discussion of their structural analysis in solution and in the solid state is described.

The work described in Chapter 4 focused on the synthesis of giant 3D discrete supramolecular architectures, with tuned dimensions, geometry and a varied number of porphyrin units, obtained by simple mixing different (metallo)porphyrin modules. By appropriate tailoring of the *meso*-4'pyridylporphyrin connectors, i.e. increasing the number of basic donor sites and/or playing on their relative disposition, larger molecular architectures become easily available. Cleverly designed molecular building units, in terms of lability/inertness and hard/soft metal-to-ligand discriminations, quantitatively self-connect by the formation of mutual coordination bonds. The obtained discrete multi-porphyrin structures constitute a spatially-ordered lattice of chromophores featuring photoinduced antenna-effect and charge transfer processes.

In Chapter 5, is reported the work performed during a six-month internship in the laboratories of Dr. Romain Ruppert, University of Strasbourg (FR). The research was devoted at investigating and tackling the possibility to employ a Pd^{II}-linked Zn(II)-porphyrin dimer (**ZnPdZn**), as alternative photo-active platforms for the assembling of discrete supramolecular sandwich structures. From a photo-physical view-point, **ZnPdZn** differs markedly from **1Zn** in that strong electronic communication between the two porphyrin macrocycles is observed to occur, mediated by the exocyclic coordination connection. On the other hand, from a supramolecular assembling view-point, dimer **ZnPdZn**, preserves the required features already offered by **1Zn**: two Zn^{II} anchoring points, a good inertness of the exocyclic metal coordination bonds and sufficiently coplanar and rigid disposition of the zinc-porphyrin components.

Finally, a publication on a side project is attached. A conjugate triad, featuring two L-tyrosinato residues axially coordinated to the tin centre of a Sn(IV)-tetraphenylporphyrin, is reported as the first example of a supramolecular dyad for photochemical proton-coupled electron-transfer (PCET). It is noteworthy that the excitation of the conjugate in the presence of a suitable base is followed by photoinduced PCET leading to a radical pair state with a surprisingly long lifetime.

Chapter 1

Nature has employed porphyrins in a wide range of biological systems and for a broad range of purposes, rising both from their functional and structural properties. Most biological roles require porphyrins to be monomeric but, in some cases, as for light-harvesting antenna complexes (Fig. 1a), these macrocycles must be finely organized into elegant, symmetric arrays in order to accomplish their unique function. Taking inspiration by Nature, with the purpose to better understand the structure-function correlations, various attempts have been made to construct artificial simple but realistic mimics of complex biological systems involving porphyrins, such as antenna systems or heme-proteins. [1]

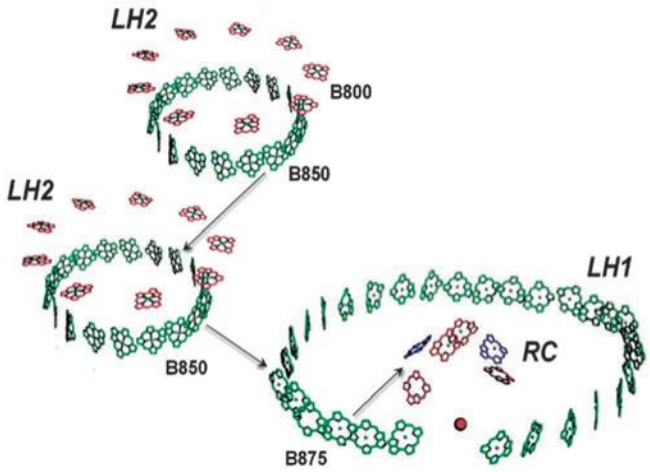

Figure 1.1. Schematic representation of the two light-harvesting antenna systems (LH) and reaction centre (RC) arrangement in purple bacteria; adapted from ref. 1d.

The classic covalent approach led to a plethora of porphyrin arrays. Yet, the multi-step synthesis of such complex structures is time-consuming and, most of the time, limited by final unsatisfactory product yields. After the 1987 Nobel Prize, recognizing (and maybe foreseeing) the enormous, revolutionary potentialities of Supramolecular Chemistry, chemists fascinated by this ‘‘new’’ field have been challenged by the noncovalent syntheses of functional mimics. Nature itself makes use of a variety of weak, noncovalent interactions such as hydrogen bonding, charge-charge, donor-acceptor, π-π, van der Waals, and hydrophilic and hydrophobic, etc., interactions to achieve these highly complex and often symmetrical architectures.

The non-covalent approach looks apparently easier; at first sight, it resembles a lego-game in which pre-organized simpler pieces are self-assembled by one-pot mixing. Indeed, the spontaneous self-assembly of molecules leading to a designed, complex architecture is still a source of wonder. The supramolecular noncovalent approach is unique because it requires a full, rational exploitation of the entire landscape of chemistry: from thermodynamics to kinetics, from organic to inorganic chemistry. In 1994 M. C. Drain and J.-M. Lehn published their pioneering work[2] presenting a quick, one-pot noncovalent synthesis (in organic solvent) of various porphyrin arrays – from dimers to tetramers (Scheme 1.1) – with controlled stoichiometry and geometry. The *cis*- and *trans*-coordination of the labile benzonitrile ligands in the starting (inert) dichloride complex $[MCl_2(NCPh)_2]$ (with M = Pt(II) or Pd(II)) was used in combination of complementary porphyrin units to metal-mediate and geometrically control the formation of porphyrin cyclic dimers or tetramers.

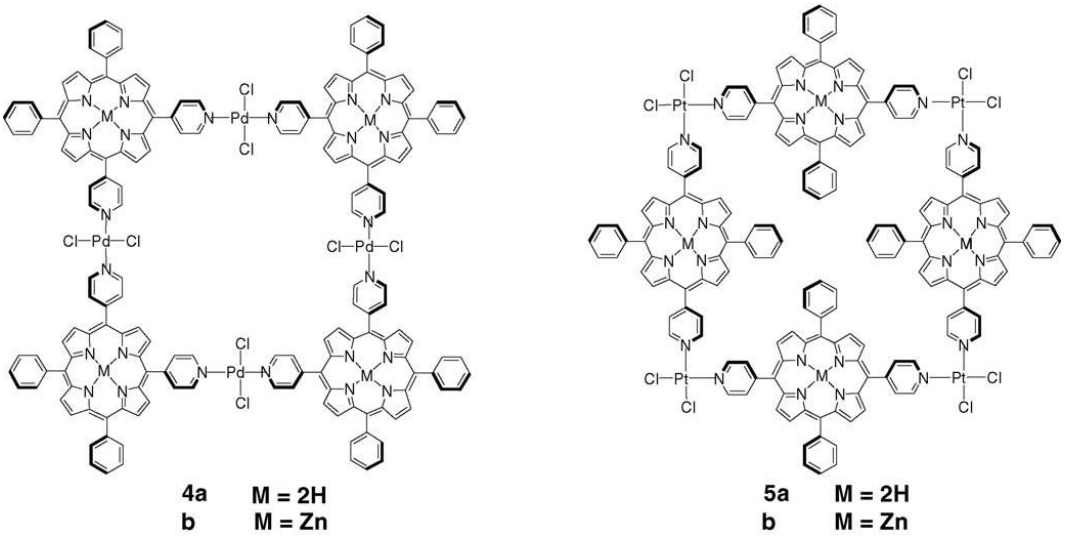

Scheme 1.1. Square porphyrin tetramers, reproduced from Ref. 2.

Another relevant achievement of this approach is that the yield of these syntheses is very close to 100%. From a chemist's point of view, the work presented by Lehn and Drain is complete: thermodynamics, kinetics, and coordination chemistry are at work simultaneously and in a convergent mode. Starting from this early examples, a wide variety of two-dimensional (2D) cyclic porphyrinic systems (rhomboids, squares, rectangles, triangles, etc.) have been reported along the years, with synergic contributions by several groups —Stang,[3] Raymond,[4] Fujita,[5] and others[6]— and quick evolution of this synthetic strategy, soon afforded more complex 3D architectures (trigonal pyramids, trigonal prisms, cubes, cuboctahedra, double squares, adamantanoids, dodecahedra, and a variety of other cages) with well-defined shapes and sizes.[7] These kinds of artificial discrete assemblies of porphyrins, thanks to the multiple and tunable properties of these chromophores, find interesting applications in various fields, like artificial photosynthesis,[8] molecular electronics,[9] molecular machines,[10] catalysis,[11] therapy,[12] and surface engineering.[13]

1.1 Synthetic Strategy

Self-assembly is an equilibrium between two or more molecular components to create a more complex entity with a structure that depends only on the intrinsic information contained within the starting materials, termed *building blocks*. Among the different approaches that can be exploited to guide the self-assembling process, the metal-mediated directional-bonding has emerged over the years as a general, high yielding synthetic strategy that gives access to a variety of 2D (rhomboids, squares, rectangles, triangles, etc.) and 3D (trigonal pyramids and prisms, cubes, cuboctahedra, double squares, adamantanoids, dodecahedra, and a variety of other cages) supramolecular ensembles.[3c,d,14] One of the most attractive characteristics of this approach is that the design of supramolecular structures can be guided by geometrical considerations relaying on the highly directional and predictable nature of the metal coordination sphere and of the geometry of the donor sites of rigid organic fragments. Transition metals, with their preferred coordination geometries, have

served as Lewis-acidic acceptor units, both as naked ions or as metal fragments (*i.e.* bearing some inert ancillary ligands in their coordination sphere, with various rigid or flexible Lewis-basic donors to self-assemble larger and predictable architectures, based on the geometrical codifications of the acceptor and donor units (Figure 1.2).

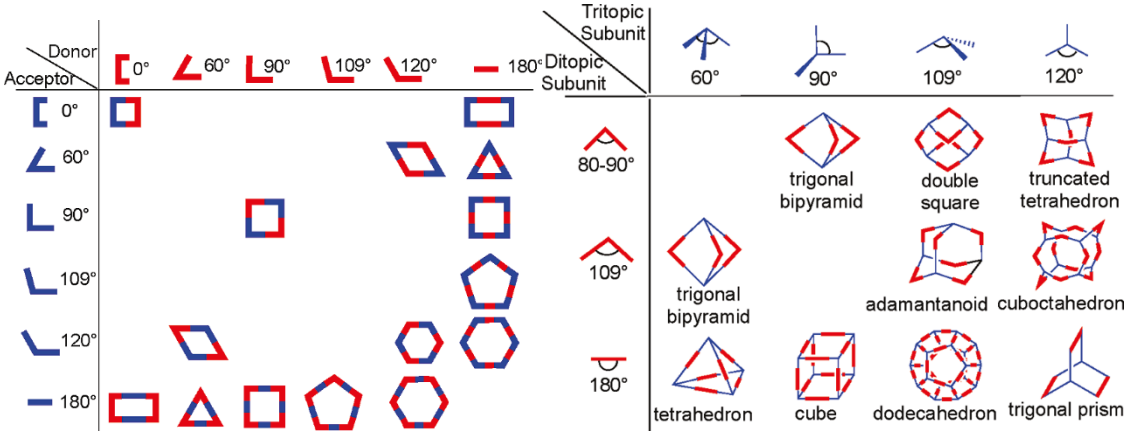

Figure 1.2. Combination of various complementary metal acceptor/donor building blocks, schematized in function of the number and geometry of their reactive sites, for the clever design and metal-mediated assembling of 2D polyhedra (on the left), and 3D architectures, from Ref. 3c.

If the assembling process occurs under thermodynamic control (i.e. reversible equilibria), and this mostly depends on the nature of the metal and provided that the intended supramolecular structure effectively represent the most stable thermodynamic product, then initial intermediates and/or less stable products self-correct in time and final high conversion to a unique stable product occurs.

1.2 Porphyrins as Building Blocks in the Construction of Supramolecular Assemblies

Porphyrins are a unique and versatile precursor for metal-mediated assemblies since they are able to perform at the same time a structural (acting as donor, acceptor, or both) and a functional role.

The large and flat aromatic surface of these macrocycles is ideal for the construction of 3D cage structures. The arrangement of a defined number of these molecules within a single discrete system, usually results in unexpected novel properties. The choice of the porphyrin macrocycle peripheral substituents and that of the inner metal, permit to vary and modulate their inherent properties to a large extent, while allowing at the same time to introduce, in a controlled fashion, a variety of useful reactive or connecting groups.

In fact, porphyrins present a rigid and planar aromatic surface providing very peculiar electronic properties: intense absorption and emission spectra in the UV-visible region together with accessible redox potentials. Interestingly, their solubility and physical properties can be fine-tuned by functionalization of the *meso* or the β-pyrrolic positions (Figure 1.3). For example, perfluorinated phenyl rings in the *meso* positions increase the electron acceptor properties of a (metallo)porphyrins, while aliphatic chains in the *beta* positions increase the range of solubility in organic solvents, while bulky groups prevent stacking in solution.

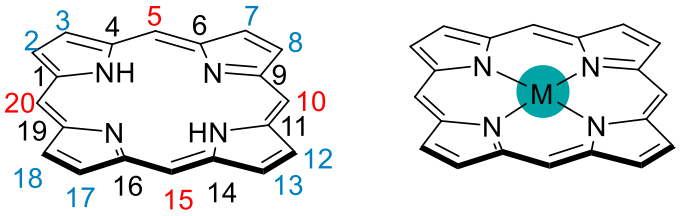

Figure 1.3. Left: schematic general structure of a porphyrin with indicated the α (black), β (blue) and *meso* (red) positions. Right: schematic general structure of a metalloporphyrin, with M that can range between a variety of metal cations, *e.g.* Zn(II), Ru(II), Al(III), Sn(IV), Co(II).

A suitable choice and insertion of a metal center in the pyrrolic core have also a high impact at modulating the porphyrin properties, with particular reference to the redox and catalytic features. From a building block view point, metalloporphyrin are very peculiar and can be considered as acceptor metalloligands: presence of donor groups at the *meso* peripheral positions may serve as Lewis base binding sites (offering from one up to four controlled topologies), while the inner metal center may function as Lewis acceptor (enabling axial coordination of one or two ligands), while. Aditionally, the nature can provide ligands selection by means of hard/soft discriminations.[15] For example, *hard* metal centers in high-oxidation states, like Sn(IV), preferentially coordinate apical moieties via oxygen, thus carboxylic or hydroxyl functions are the most suited complemental donor groups, establishes relatively inert bonds, with kinetics in the time scale of minutes, and has a octahedral coordination sphere, and thus accommodate two apical ligands. *Soft* low-oxidation state metals, like Zn(II), are instead selective toward N– or P–ligands and form five-coordinate square pyramidal complexes. They are by far the most popular ones in self-assembly because the Zn–N axial bond is highly directional (perpendicular to the porphyrin plane with tolerated deviation up to 10°), and the metal labile nature usually guarantee that assembling processes *via* axial Zn–N bond formation occurs under thermodynamic control (ligand-exchange rates in the order of the μs) and typically with single bond binding constants of about 10^3–10^4 M^{-1}.[16]

Particularly interesting porphyrin arrays are those based on *Meso*-pyridyl/phenyl (PyPs), i.e. porphyrins carrying a number (*n* = 1–4) of pyridyl substituents at the *meso* positions (with the remaining 4-*n* positions occupied by aryl groups). A great variety of metal-bridged arrays have been obtained by coordination of pyridylporphyrins to appropriate metal complex fragments.[6e,17]. The peripheral N atom(s) of PyPs can be either in the 4' or 3' position. PyPs can provide geometrically well-defined connections to as many as four metal centers by coordination of the pyridyl groups. With 4'-PyPs, the exocyclic coordination bonds are established in the plane of the porphyrin, along the *meso* C–*C* bond axes; with 3'-PyPs instead, since the pyridyl rings lay perpendicular to the macrocycle plane, the coordination bonds are directed out of this plane. For instance, simple self-coordination of Zn-PyPs was used to obtain 3D arrays (Figure 1.4).

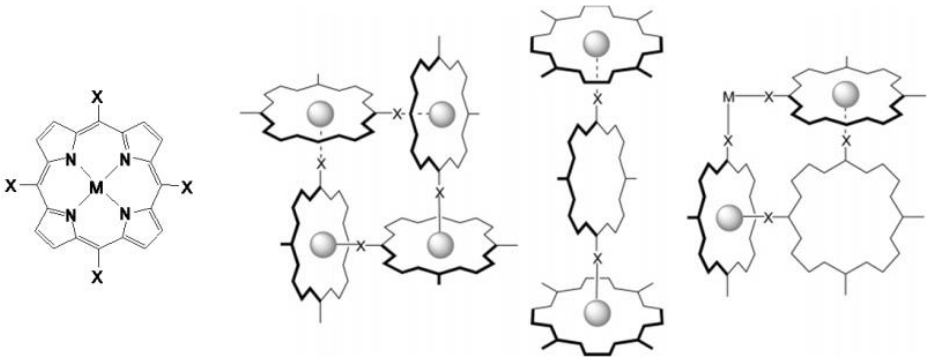

Figure 1.4. Schematic examples of discrete side-to-face Zn-4'-PyPs self-assembled arrays. X = 4'-Py, M = Zn(II).

1.3. 3D Multiporphyrin Discrete Assemblies

The design of molecular 3D systems including porphyrins as host structural units are indeed very attractive: porphyrin, as a large structural element, will delineate the molecular cavity, and usually produce a considerably hydrophobic inner environment; the large π-delocalized surface may establish constructive interactions with other π-conjugated guest molecules or with protons of aliphatic chains of guests.[18] A metalloporphyrin structural units may use the inner metals as guest binders and as catalyst for the transformation of bound substrates.

In 2001, Fujita and co-workers introduced the concept of molecular panelling, i.e. the use of flat molecules with multiple peripheral donor atoms that are connected to one another through external metal clips. A multiporphyrinic trigonal prism featuring several interesting properties was assembled from 1 equiv of zinc(II) 5,10,15,20-tetra(3'-pyridyl)porphyrin (**Zn-TMPYP**) and 2 eq. of [Pd(en)(NO_3)$_2$] (en = ethylenediamine) (Figure 1.5).[19] The assembly process performed at 80 °C in a mixture of water and acetonitrile led to desired product in 96% yield. Because of the high positive charge of the assembly (12+), the system is soluble in water. The X-ray diffraction analysis confirmed the D3h symmetry of the molecular cage in which the Pd centers occupy the apical positions of the prism. The nitrate ion, originally trapped inside the hollow framework, could be expelled by the inclusion of pyrene or other large aromatic guests like perylene or triphenylene, added in excess in CD_3OD/D_2O (1/1). Short peptide fragments, involving Ala-Ala-Ala sequence, were also efficiently encapsulated[20] and the hydrophobic cavity favored oligopeptide folding, through CH–π interactions.

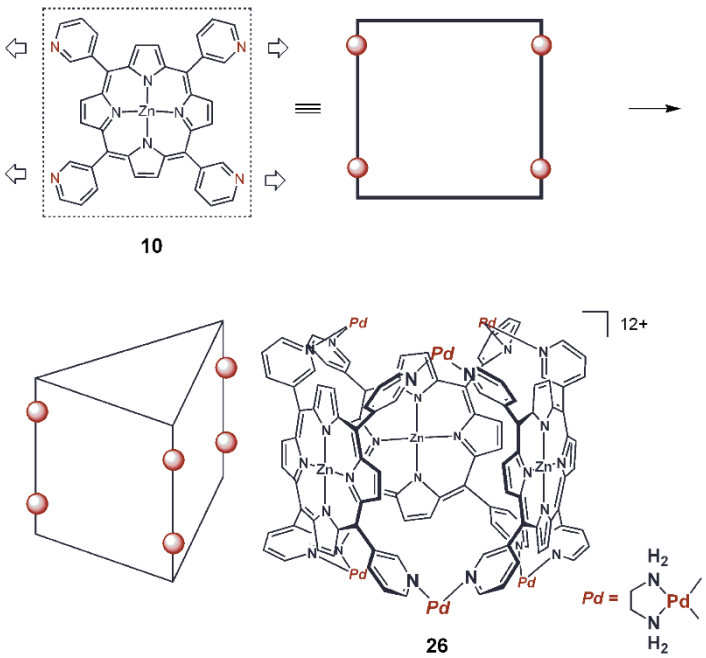

Figure 1.5. Schematic representation of molecular paneling of Zn-TMPYP, from Ref 17a.

The presence of multiple metal sites within the molecular architecture also has the potential to introduce unique characteristics such as magnetic, photochemical or electrochemical properties and metal-centered chirality. In 2011, a new class of closed-face coordination cubic hosts was developed by Nitschke and co-workers through an efficient templated subcomponent self-assembly approach.[21] The reaction of nickel(II) tetrakis(4′-aminophenyl)porphyrin with iron(II) complex $Fe(OTf)_2$ and 2-formylpyridine in a 6:8:24 ratio resulted in the quantitative formation of a cubic structure, with 8 low spin Fe(II) ions on the corners and 6 porphyrins on the faces (Figure 1.6). In this elegant synthesis, Fe(II) both templated the formation of the imino-pyridine chelates and organized the cage assembly. was obtained. From the X-ray structure of the Ni-porphyrin cage, an internal cavity of approximately 1340 $Å^3$ and a Ni−Ni face-to-face distance of 15 Å, appropriate to incorporate large aromatic guest molecules, were determined. Indeed, the addition of excess coronene to the cage in DMF led to host−guest complexes incorporating precisely three coronene molecules.

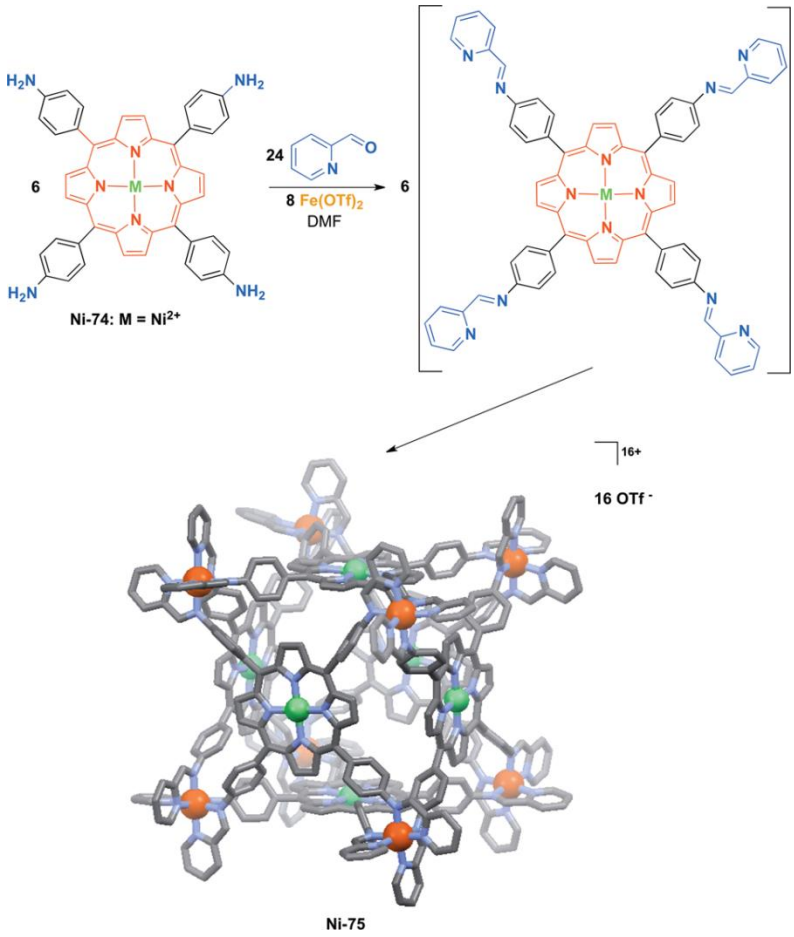

Figure 1.6. X-ray structure of the closed-face coordination cube obtained from Ni-porphyrin *via* a subcomponent self-assembly approach, from Ref. 7. Color code: Ni(II) green sphere, Fe(II) orange sphere.

Solution studies also evidenced a higher affinity of Ni-cage for C_{70} over C_{60}, the less spherical shape of the former being suitable to engage more π–π interactions with the porphyrinic faces. Furthermore, these cubic hosts are chiral, with either (Λ)8 or (Δ)8 configurations at the iron vertices, so that interesting chiral guest discrimination applications can be foreseen. Following this established procedure, more recently an analogous cubic cage flexible and compatible with aqueous media was synthesized from the self-assembly of Fe^{II} and a zinc-porphyrin-containing ligand.[22] Its selectivity of encapsulation is driven by the coordination of guest functional groups to the zinc porphyrins. This new host thus specifically encapsulates guests incorporating imidazole and thiazole moieties, including drugs and peptides. Once encapsulated, the reactivity of a peptide is dramatically altered: encapsulated peptides are protected from trypsin hydrolysis, whereas physicochemically similar peptides that do not bind are cleaved.

Indeed, if correctly played, the metal-mediated self-assembling approach allows to easily and efficiently synthesize large highly symmetric molecular structures (trigonal pyramids, trigonal prisms, cubes, etc.). The preparation of less-symmetric multi-component supramolecular assemblies is indeed synthetically more demanding, as very selective and simultaneous recognition events between the building units have to occur. In this contest, the control over the self-assembly process can be possibly achieved by the concerted use of two or more different metal ions having different

coordination preferences: employing metal to ligand hard/soft discrimination or either taking advantage of metal ions forming coordination bonds with a distinct degree of inertness, in a precise stepwise manner.

An impressive work, in terms of both the number, the diversity of the self-assembled multiporphyrinic compounds, and the properties displayed by these architectures, was realized by Hupp and co-workers in 2008.[23a] They took advantage of the larger affinities of Zn(II) and Sn(IV) for nitrogen and oxygen Lewis bases, respectively, to build new molecular boxes. As an example, four butadiyne-linked zinc(II) porphyrin trimers (T and T') were elegantly combined with two meso-substituted *trans*-di(4'-pyridyl) Sn(IV) porphyrin dimers (A), to generate a symmetrical 16-porphyrin box structure (AAT_4 in Figure 1.7). Binding sterically crowded carboxylate ligands to Sn(IV) centers of the porphyrin dimers forces the trans pyridine ligands in A and C to bind selectively to the external Zn(II)porphyrins of trimer T in the assembly. This box featured a large cavity 22 × 14 × 10 Å, from computational calculations, in which catalytically active manganese porphyrin dimer M was coordinated to the central zinc porphyrin of the trimer T, to yield a supramolecular catalyst ($AMAT_4$ in Figure 1.7).[21b]

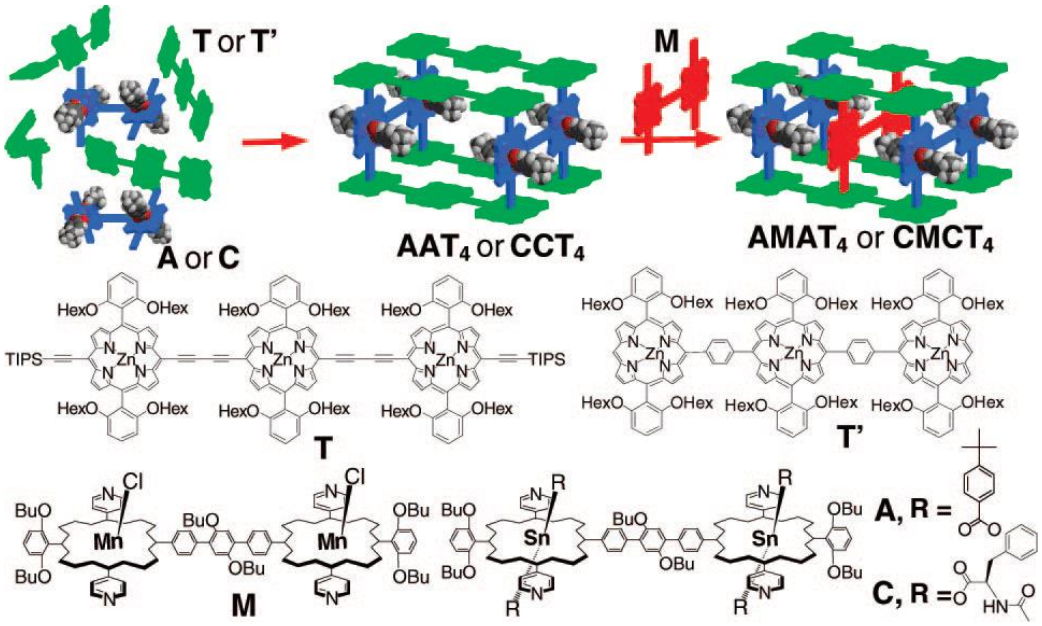

Figure 1.7. Schematic representation of the steric-self-sorting assembly of supramolecular catalytic boxes, $AMAT_4$ and $CMCT_4$, from Ref. 21b.

Various metallated porphyrins (Zn^{II}, Sn^{IV}, and Mn^{III}) have a well-established function in the supramolecular box: Zn(II) porphyrins and Sn(IV) porphyrins act as structural elements of the container; Sn(IV) porphyrins limit the aperture of the box and the hollow space, thanks to their axial coordinated ligands; and Mn(III) porphyrins function as catalysts and perform the reaction inside the cavity. In $AMAT_4$, the manganese porphyrin dimer divided the cavity into two separate inner spaces. This supramolecular catalyst, tested in olefin epoxidation reaction, proved to be effective. The restrictive cavity was responsible for the selectivity of the reaction against a sterically hindered olefin. In addition, when a chiral carboxylate (N-acetyl-(D)-phenylalanine) was bound to the Sn(IV) porphyrins of the dimer C at the periphery of the box $CMCT_4$, enantioselective sulfoxidation, with an enantiomeric excess of 12%, was demonstrated.

1.4 Modular Self-Assembling Approach for the Synthesis of Multiporphyrin Structures

The group in which the present project was developed, introduced a modular strategy for the obtainment of multiporphyrin 3D discrete systems, built on the Ru(II)-based metallacycle of zinc-porphyrins [*trans,cis,cis*-$RuCl_2(CO)_2$(Zn·4'-*cis*DPyP)]$_2$ (**1Zn**) (Scheme 1.3), bearing two embedded Zn^{II} cations as metal acceptor sites.[17l,24] The intermediate precursor of this derivative, [*trans,cis,cis*-$RuCl_2(CO)_2$(4'-*cis*DPyP)]$_2$ (**1**), is obtained in *ca.* 50% yield by treatment of the octahedral Ru(II) complex [*trans,cis,cis*-$RuCl_2(CO)_2$(dmso-O)$_2$], bearing in *cis* position two labile dmso coordinated *via* oxygen, with equimolar amounts of a *cis*-4'-dipyridylphenylporphyrin (4'-*cis*DPyP) at room temperature for 48h, followed by chromatography purification (Scheme 1.2).[24a]

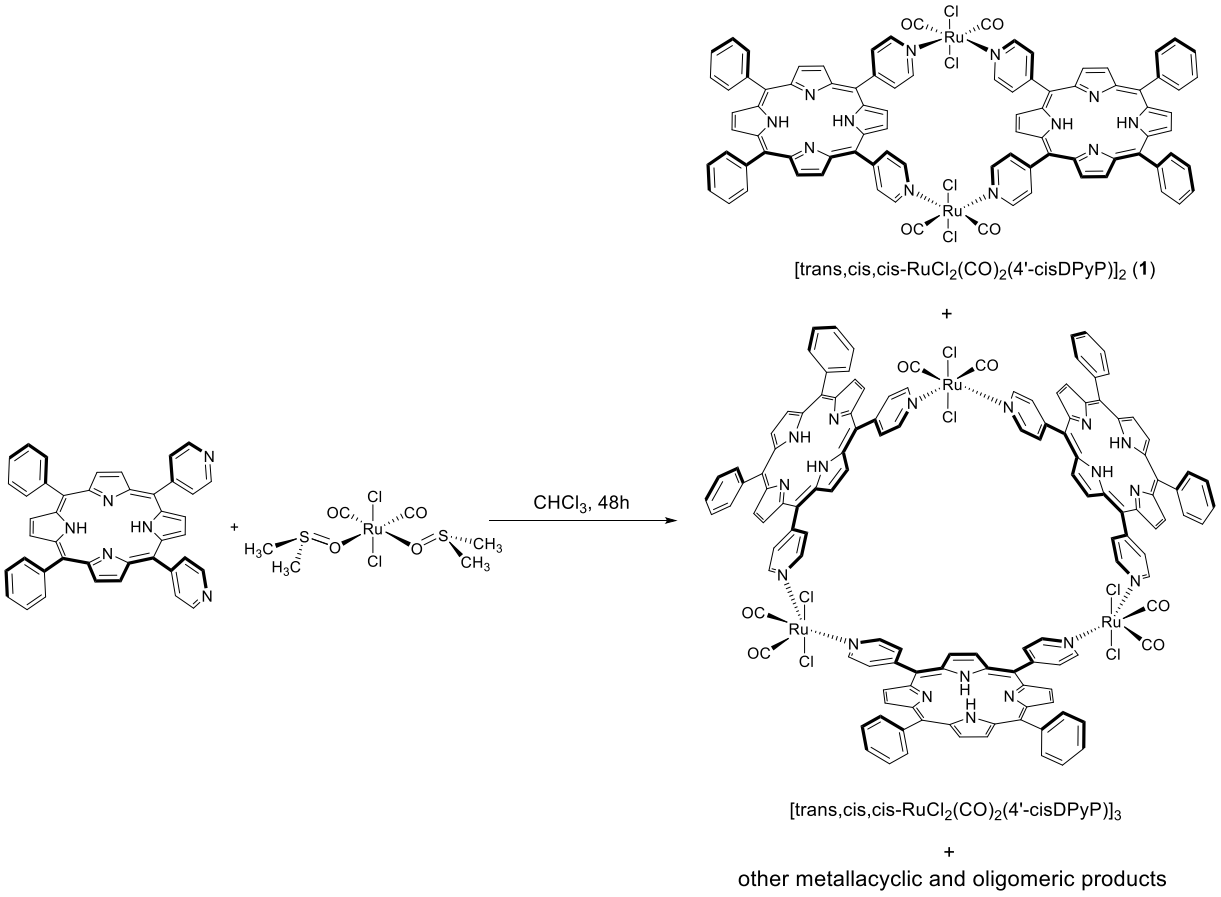

Scheme 1.2. Synthesis of the [*trans,cis,cis*-$RuCl_2(CO)_2$(4'-*cis*DPyP)]$_2$ (**1**) from 4'-*cis*DPyP and [*trans,cis,cis*-$RuCl_2(CO)_2$(dmso-O)$_2$] in ratio 1:1.

Despite the geometrical directional constraints provided by the high convergence of the acceptor and donor sites of the building blocks, the reaction leads to the concomitant formations of other metallacyclic species. In fact, the second most abundant cyclic product is the metallacycle [*trans,cis,cis*-$RuCl_2(CO)_2$(4'-*cis*DPyP)]$_3$, in which three 4'-*cis*DPyP are held together in a not coplanar mutual and strained disposition by three [*trans,cis,cis*-$RuCl_2(CO)_2$] fragments. The metallacyclic products, isolated *via* column chromatography, are perfectly symmetrical, rigid, kinetically inert, and thermodynamically stable, allowing for a subsequent tailoring in order to construct higher order porphyrin assemblies (see below). Further treatment of [*trans,cis,cis*-$RuCl_2(CO)_2$(4'-*cis*DPyP)]$_2$ with

excess of zinc acetate leads to the desired platform **1Zn** (Scheme 1.3). The inertness of the Ru–N bonds prevents the pyridyl groups to scramble between the two different metal ions.

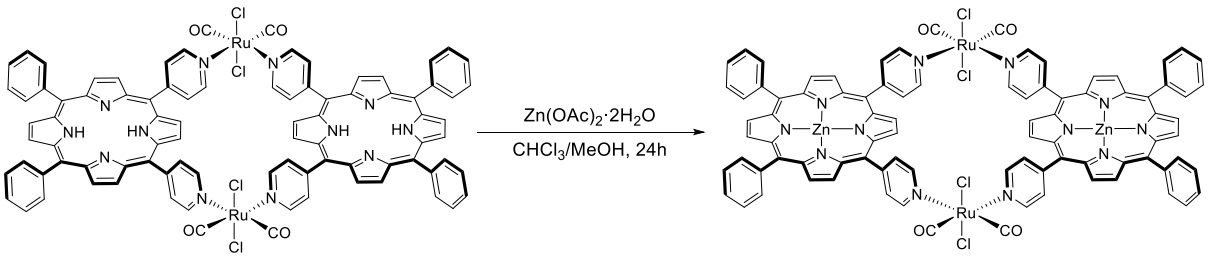

Scheme 1.3. Synthesis of the [*t,c,c*-$RuCl_2(CO)_2$(Zn·4'-*cis*DPyP)]$_2$ (**1Zn**).

Single crystal X-ray analysis of [*trans,cis,cis*-$RuCl_2(CO)_2$(Zn·4'-*cis*DPyP)]$_2$ revealed an almost perfect flat disposition of the two zinc-porphyrin components, with Ru-Ru and Zn-Zn distances of 14.01 Å and 14.03 Å, respectively. In the structure, the coordination sphere of the Zn(II) ions (that are usually found surrounded by five ligands, and normally show a strong preference for N-based groups) is saturated by a molecule of EtOH driving from the crystallization process (Figure 1.8).[17l]

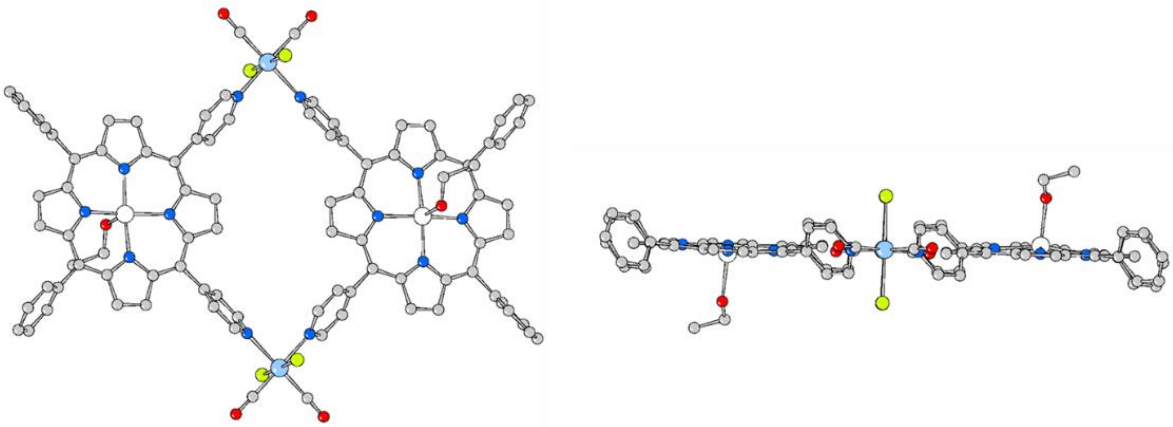

Figure 1.8. Two different views of the crystal structure of **1Zn**, one apical molecule of EtOH for each Zn(II) center. Colour code: C, grey; Cl, green; O, red; N, blue; Ru, cyan; Zn, white.

The [*t,c,c*-$RuCl_2(CO)_2$(Zn·4'-*cis*DPyP)]$_2$ metallacycle **1Zn** can be therefore conveniently described as a flat panel with two embedded metal connectors (the two zinc atoms). Combining platform **1Zn** with appropriate different polytopic nitrogen-ligands allows to very efficiently and quantitatively produce a wide variety of multiporphyrin 3D discrete structures, consisting of two up to four porphyrin metallacycles connected face-to-face through the bridging ligand, axially bound to the zinc centers.

As unambiguously evidenced by NMR spectroscopy, titration of **1Zn** in $CDCl_3$ solution with one equivalent of a linear ditopic N-ligand (**L**) leads rapidly to the quantitative assembling of sandwich-like 2:2 supramolecular adducts of formula **[1Zn·L]$_2$** (**L** = 4,4'-bipyridine; **L** = 5,15-bis(4'-pyridyl)-2,8,12,18-tetra-*n*-propyl-3,7,-13,17-tetramethylporphyrin); **L** = 5,15-(4'-pyridyl)-10,20-phenylporphyrin (***trans*DPyP**)), formed by two parallel metallacycles connected by two bridging

ligands which are axially bound to the zinc-porphyrins (Scheme 1.4).[23a] This type of modular assembling is made possible by virtue of the thermodynamic and kinetic stability of the Ru–pyridyl bonds (as noted above), which allows for the further ligation of other N ligands (to the zinc centers), while metallacycle **1Zn** remains intact.

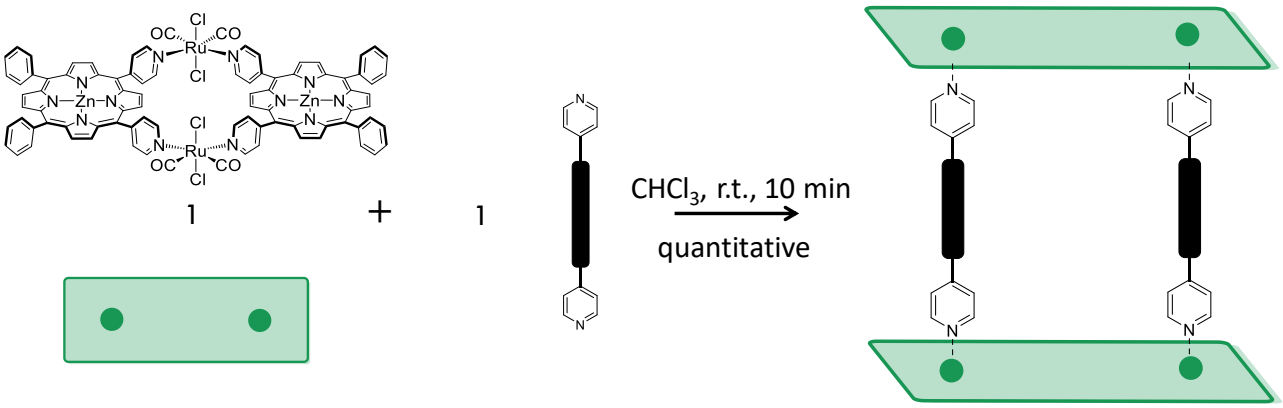

Scheme 1.4. Self-assembly reaction between **1Zn** and a generic linear dipyridyl ligand.

Addition of less than stoichiometric amounts of **L** to a $CDCl_3$ solution of **1Zn** induces the appearance of some relatively broad signals, which sharpen upon lowering the temperature. Below -20 °C, two sets of resonances are detected, one relative to **1Zn** and the other assigned to the 2:2 supramolecular adduct **[1Zn·L]$_2$**. No signals relative to uncoordinated **L** or to reaction intermediates are observed. When the stoichiometric ratio between **1Zn** and **L** is reached, only one set of resonances is observed, corresponding to the complete formation of **[1Zn·L]$_2$**. In general, these systems present common peculiar spectral features which unambiguously establish the geometry of the adducts. Herein, the system built on **1Zn** and ***trans*DPyP** will be described in more details.

At room temperature, the spectrum of **[1Zn·*trans*DPyP]$_2$** (Figure 1.9) presents a set of relatively broad signals that sharpen upon lowering the temperature down to –20°C**.** The main spectral characteristics are the following: (i) relative integration of ***trans*DPyP** and of **1Zn** signals indicates that there is one molecule of bridging ligand every two Zn-porphyrin units; (ii) the two ligands give rise to two equally intense resonances only, implying that they are equivalent to each other and symmetrically coordinated; (iii) axial coordination of the pyridyl moieties is unequivocally indicated by the large upfield shift of $H_{2,6}$ and $H_{3,5}$ resonances, due to the combined ring currents of both porphyrins. All the Zn-porphyrin platforms are equivalent and give only one set of signals which are slightly upfield shifted as compared to those of **1Zn**: this is consistent with a cofacial disposition of the two molecular squares which induce a mutual shielding of the porphyrin cores. Each resonance of the *meso* aryl substituents of **1Zn**, is split into two sharp signals of equal intensity: since the *meso* pyridyl and phenyl rings are on average normal to the porphyrin plane due to steric interactions with the pyrrole protons, their protons (with the exception of the phenyl para protons) experience two different magnetic environments, depending whether they are oriented toward the inside (endo) or the outside (exo) of the assembly. In agreement with this, in the 2D EXSY spectrum of the assembly, each pair of resonances of endo and exo aromatic protons is connected by an exchange cross-peak. By lowering the temperature down to – 40°C the resonance of the internal pyrrolic protons of ***trans*DPyP**, upfield shift of *ca.* –0.25 ppm, in agreement with the previous reported temperature dependence of

analogous porphyrin spectra.[25] At this temperature, due to the slow tautomeric exchange rate of the internal -NH protons,[26] an extra-splitting of the β resonances of ***trans*DPyP** unit is observed, due to the no longer equivalence of the pyrrolic units (see spectrum d in Figure 1.9).

Interestingly, the inner pyrrolic protons in **[1Zn·*trans*DPyP]$_2$** resonate more than 0.2 ppm farther upfield compared to the same protons in the corresponding model compounds featuring two Zn-*tetra*phenylporphyrin axially coordinated to ***trans*DPyP**. This extra shielding was attributed to a mutual ring current effect of the two macrocycles assuming that, as an average, in solution they preferentially maintain the cofacial orientation found in the solid state (see below).

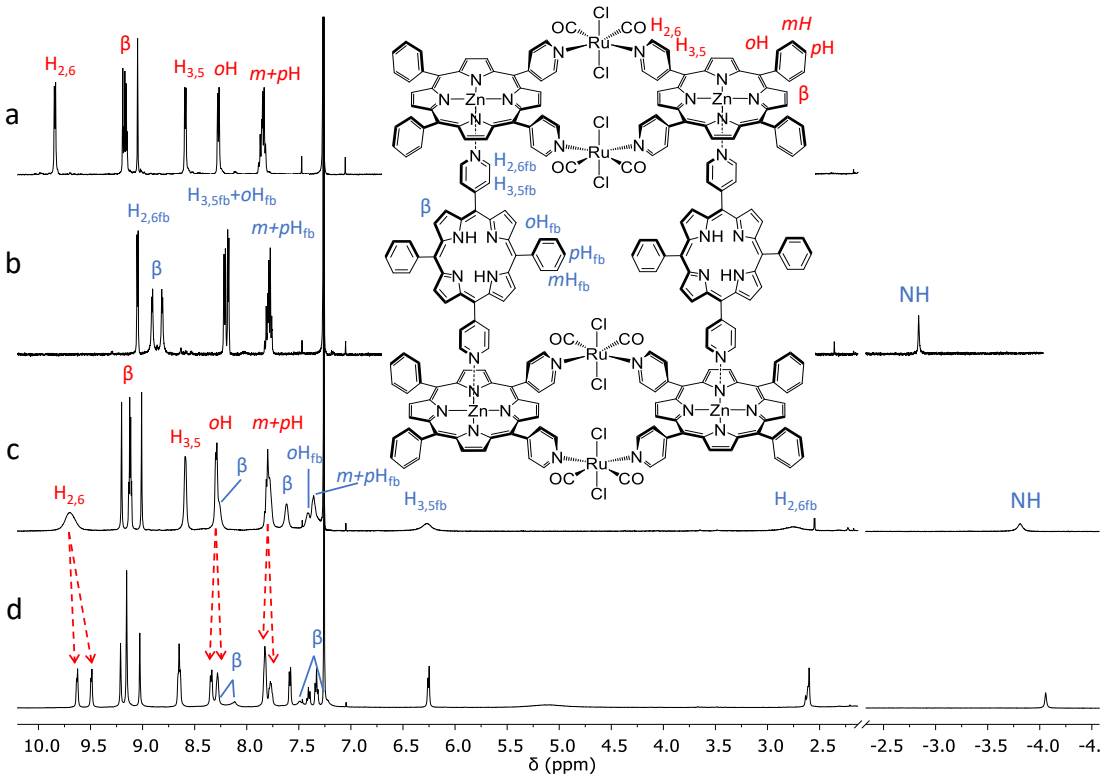

Figure 1.9. ^{1}H-NMR spectra ($CDCl_3$) of a) **1Zn**, b) ***trans*DPyP**, c) **[1Zn·*trans*DPyP]$_2$** (25°C) and d) **[1Zn·*trans*DPyP]$_2$** (-40°C). Highlighted in red are the labels belonging to **1Zn**, in light blue the ***trans*DPyP** ones.

The overall NMR features indicate that, at ambient temperature, the dynamic equilibrium between **1Zn** and **L** to yield **[1Zn·L]$_2$** has an intermediate fast to slow rate on the NMR time scale (by going from room T down to –20°C) and is totally shifted toward the 2:2 product (all or nothing process), suggesting that there must be considerable cooperativity between the coordination of the first and the second bridging ligands. Formation constants higher than 10^{18} M^{-3} were estimated in chloroform and the NMR spectra of $CDCl_3$ solutions, diluted to the limit of detection, showed the resonances of the intact assemblies exclusively. The high stability of the adducts was attributed to cooperativity in the stepwise coordination of the two bridging ligands and to entropy considerations: owing to the rigidity of the fragments, formation of the sandwich molecules requires limited conformational changes (see also Paragraph 1.5).

The solid-state X-ray structure of **[1Zn·*trans*DPyP]$_2$** revealed a distance between the two facing metallacycles of ca. 19.5 Å, and the two perpendicular bridging porphyrins in a mutual cofacial disposition at a distance of ca. 11.4 Å (Figure 1.10).

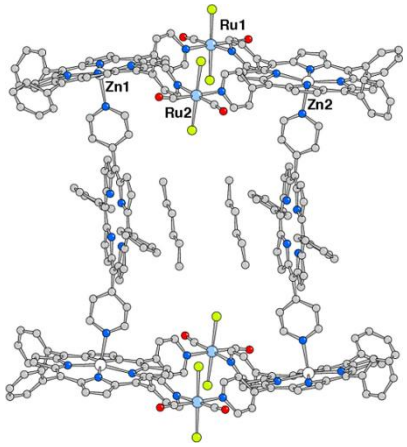

Figure 1.10. Single crystal X-ray structure of **[1Zn·*trans*DPyP]$_2$**.

In **[1Zn·*trans*DPyP]$_2$**, the zinc–porphyrin fluorescence is strongly quenched (this feature allows also to determine a value of 7 x 10^{-5} M as the lower limit concentration at which the assembly is still intact). This quenching is accompanied by a sensitization of the free-base porphyrin emission, indicating the occurrence of singlet energy transfer from the metallated porphyrin to the free-base ones. In other words, the light energy harvested by the outer zinc–porphyrin units of the two metallacycles is funneled into the central connecting porphyrin ligands (with a rate constant of *ca.* 32 ps).

Focusing on the tuning of the nature and efficiency of the photoinduced intercomponent properties, the flexibility of this synthetic modular approach was conveniently applied for the assembling of a multichromophore supramolecular adduct, in which the connecting axial ligand is trans-di-(4-pyridyl)-perylene-bisimide dyes.[24b] Given the peculiar photophysical properties of the perylene unit, the photoexcitation is followed by a fast electron transfer process from the Zn-porphyrin unit to the perylene one, leading to the formation of the charge-separated state with a lifetime of ca. 440 ps (as inferred from ultra-fast time-resolved spectroscopic techniques). Again, the emission spectra reveal remarkable stability of the assembly in chlorinated solvents (6 x 10^{-5} M as value for the lower limit concentration in dichloromethane).

Finally, three new multiporphyrin supramolecular cages, with tuned shapes and sizes, were obtained by combining metallacyle **1Zn** with nitrogen polytopic ligands.[24c] The nature of the polytopic linker varies from the tri-topic trigonal planar 2,4,6-tris (4-pyridyl)-triazine (**tpt**), to the tetra-topic 5,15,10,20-tetra- (4-pyridyl)-porphyrin (**TPyP**) or 5,15,10,20-tetra-(4-pyridylphenyl)- porphyrin (**TPhPyP**), yielding to the deriving assemblies **[(1Zn)$_3$(tpt)$_2$]**, **[(1Zn)$_4$(TPyP)$_2$]** and **[(1Zn)$_4$(TPhPyP)$_2$]**, respectively (Chart 1.1).

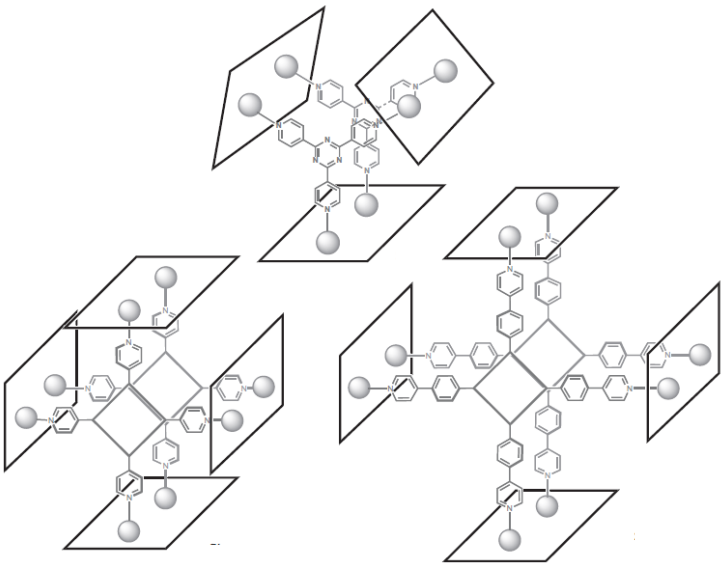

Chart 1.1. (from Ref. 23c)

The resulting cages feature either three or four peripheral metallacycles **1Zn**, depending on the numbers of nitrogen donors embedded in the polytopic connecting ligand. **$[(1Zn)_3(tpt)_2]$** possesses a trigonal prismatic structure, while **$[(1Zn)_4(TPyP)_2]$** and **$[(1Zn)_4(TPhPyP)_2]$** have a cubic-shaped architecture. For **$[(1Zn)_3(tpt)_2]$** the X-ray structure was also determined (Figure 1.11). The three outer metallacycles **1Zn** occupy the side-walls of an almost equilateral trigonal prism, with an inner volume of ca. 280 Å, considering the two triazines and the six zinc centers as delimiting lids and vertexes, respectively.

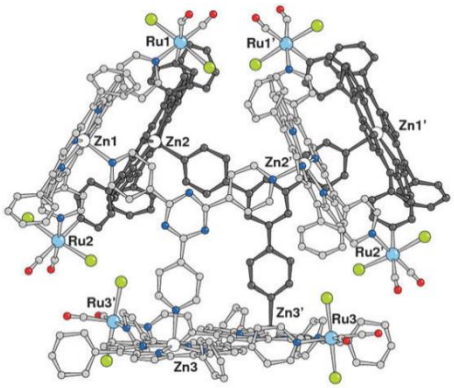

Figure 1.11. X-ray structure of **$[(1Zn)_3(tpt)_2]$**, perspective view (the back half is in dark grey), from Ref. 23c.

It is to be expected that for steric reasons the two **TPyP** ligands in **$[(1Zn)_4(TPyP)_2]$** are not eclipsed but staggered (Chart 1.2). This implies that the four metallacycles have an oblique - rather than orthogonal - orientation with respect to the **TPyP** units and that **$[(1Zn)_4(TPyP)_2]$** presents a D4 symmetry (most likely in solution there is a dynamic equilibrium between opposite - and enantiomeric - staggered conformers). The NMR spectrum of **$[(1Zn)_4(TPyP)_2]$** is consistent with this lower symmetry (compared to the D4h symmetry of a cubic molecule in which the two **TPyP** are eclipsed): in fact, whereas the four metallacycles give a single set of resonances, the connecting **TPyP** give two well-resolved resonances for the β-pyrrolic protons (labelled *a* and *b* in Chart 1.2).

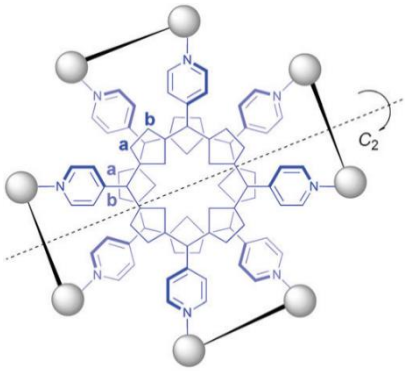

Chart 1.2.

Attempts performed to study the encapsulation properties of large aromatic guests, resulted ineffective. The low solubility of these supramolecular boxes, restricted to chlorinated organic solvents, indeed prevents the systems from benefitting of the energetic advantage given by the hydrophobic effect contribution to the encapsulation driving force, limiting the application of these molecular containers in host-guest chemistry.

1.5 Cooperative Self-Assembly of Sandwich-like Structures.

A system built on a collection of identical interactions displays cooperativity when its stability is higher than what expected based on the sum of the contributions from the single independent binding interactions. Recently, three types of cooperativity, namely allosteric, chelate and interannular, have been delineated (Figure 1.12).[27]

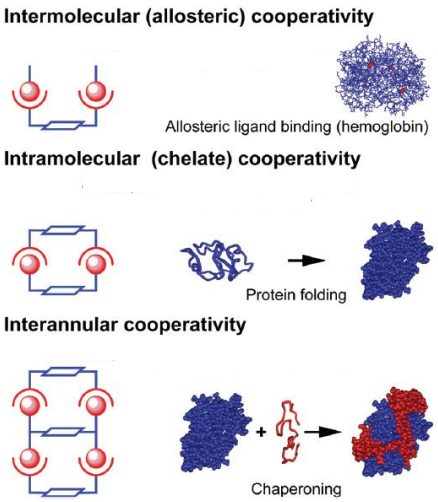

Figure 1.12. Schematic depiction of the three types of cooperativity in discrete supramolecular complexes.

The first phenomenon arises from the interplay of two or more intermolecular binding interactions, as exemplified by the binding of oxygen to hemoglobin. The second can manifest in the presence of multibinding (or multivalency), described as an assembling process from (at least) ditopic acceptor and donor building units, and comprises the classical “chelate effect”. The third type arises from the

interplay of two or more chelating interactions on one multivalent component and is related to the entropy loss and the preorganization occurring after the first binding event (e.g. a first divalent component binds to a tetravalent one and preorganizes the other binding sites in a way that enhances or diminishes the binding strength of the second divalent component).

Allosteric, chelate and interannular cooperativity may occur separately, as well as take place simultaneously, yielding more complex cooperativity effects. To meaningfully address chelate cooperativity, the following three-step procedure appears mandatory:

- evaluation of the single binding interaction (the reference);
- development of a model (the noncooperative model) for which there is a separate contribution of every interaction, equal to that displayed by the reference;
- Evaluating the stability of the actual system and draw a comparison with the stability outcome predicted by a noncooperative model: any deviation, positive or negative, is by definition the unambiguous mark of cooperativity taking place in the actual system.

As anticipated, in the formation of the sandwich-like assemblies **[1Zn·L]$_2$**, from structurally alike rigid linear bipyridyl ligands **L** (divalent *bb* unit) axially coordinating to platform **1Zn** (divalent conformationally rigid *aa* unit), there must be considerable chelate cooperativity contributions in the overall stability of the final assemblies. Given the above premises, an appropriate experimental study of the relevant thermodynamic cycle of equilibria, and parallel titration experiments on reference systems (e.g. Zn-porphyrin + monopyridyl ligand model, metallacycle **1Zn** + monopyridyl ligand model and Zn-porphyrin + dipyridyl ligand and on...) by means of UV-vis and/or ITC analysis, should be performed in order to discriminate over possible different contributions to cooperativity. Still, some considerations can be done on the basis of the overall NMR, UV-visible and X-ray data collected and by comparison with other similar reported systems.

The absence of any electronic communication between the two porphyrin units, the structural rigidity and the distance spanned by the Zn(II) cations (ca 13 Å), suggest that the two binding events in **1Zn** can be considered independent to each other. The same should stand for the pyridyl donor sites of ***trans*DPyP** and the other dipyridyl ligands previously employed in combination with platform **1Zn**. However, given the lateral extension of ***trans*DPyP** an allosteric negative contribution to the coordination of the second pyridyl ligand to platform **1Zn** cannot be excluded (the phenyl groups of parallel bridging porphyrin might sterically hinder each other).

The NMR features of the sandwich-like assemblies described above indicate that, at room temperature, the equilibrium between **1Zn** and **L** to yield **[1Zn·L]$_2$** has an intermediate fast to slow rate on the NMR time scale (relatively broad signals for **L**) and is totally shifted toward the 2:2 product with no observation of any intermediate species (such as **[(1Zn)$_2$·L]** or **[1Zn·(L)$_2$]**), In line with the presence of the so-called all-or-nothing process. This was previously observed and well documented for 2:2 discrete multiporphyrin ladder architectures by Anderson and co-workers,[28] featuring two rather flexible zinc porphyrin dimer axially connected by two bridging linear and rigid ligands (e.g. DABCO or 4,4'-bipy, see Chart 1.3). Subsequent accurate investigations (by ^{1}H-NMR and UV/visible and ITC titrations) over the formation and stability of such type of double stranded arrays, the authors

concluded that ladder formation and dissociation exhibit, in most cases, a contribution of positive chelate cooperativity (of which the all-or-nothing two-state situation between the building units, observed by NMR, is already a reliable indication).

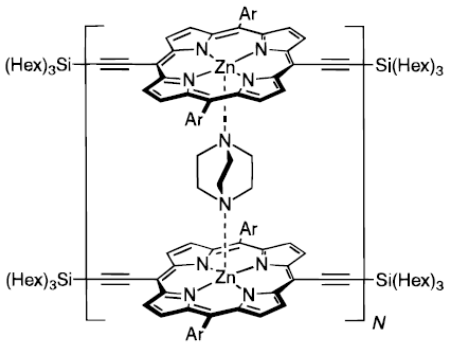

Chart 1.3.

In particular, it was observed that by gradual addition of excess bridging ligand to solutions of fully assembled ladders a progressive broadening of the ligand NMR signals occurred, as consequence of the establishment of a fast exchange between **[1Zn·L]$_2$**, the open species **[1Zn·(L)$_2$]** (which bears monocoordinated **L**), and uncoordinated **L**. This observation was later on defined as typical for systems stabilized by positive chelate cooperative effects.[26b] It must be noted that while the zinc porphyrin dimers reported by Anderson are flexible and can undergo conformational rearrangements when forming the ladders, in the present case, the **1Zn** platform is rigid, thus entropy considerations (no global conformational changes required) should be more in favor to the assembling process. In other words, the chelate effect of a rigid dimer such as **1Zn**, after binding the first bidentate ligand, is expected to be larger than that of a flexible dimer.

Reek and co-workers studied the self-assembly of supramolecular sandwich-like structures based on a rigid bis-Zn^{II}–salphen building block and various linear bipyridine ligands.[29] The Zn^{II} center in the salphen complexes has a higher Lewis acid character (compared to a Zn(II)-porphyrin), which result in stronger axial coordination (i.e. higher association constant for the single binding), also macroscopically reflected in the slow exchange regime observed (at room T) in the ^{1}H NMR of the derived supramolecular assemblies. However, the conformation rigidity and the poor communication between the Zn(II) centers of the salphen complex make this divalent acceptor (*aa*) unit a more appropriate comparative system for platform **1Zn**. The features of the 2:2 box assemblies built on the bis-Zn^{II}-salphen were investigated in detail by (variable temperature) NMR spectroscopy, UV-visible spectroscopy, NMR titrations, and X-ray crystallographic studies. Also for these systems, titration curves monitored by UV-visible showed a chelate cooperative effect between the two bipyridine ligands upon complexation to the bis-Zn^{II} template, leading to the formation of 2:2 complexes through an all-ot-nothing process. From a thorough investigation of the binding of linear dipyridyl ligands (*bb*) to the divalent Zn-salphen complex they also concluded that, when rigid building blocks are used, the distance between the two nitrogen donor atoms has no influence on determining whether polymers or discrete species are formed. On the other hand, the distance between the acceptor Zn(II) cations represents a key factor.[29b]

1.6 Aim of the Thesis

The research carried out during this PhD project and reported in this Thesis is focused on the design, preparation, and characterization of multi-component supramolecular 3D architectures obtained by appropriate paneling multitopic pyridyl ligands with flat Zn-porphyrin metallacycles. The modular approach pursued, allowed to efficiently construct libraries of elaborated 3D structures, tuning the shape and dimension of the target systems, modulating the inter-component photo-induced properties and/or introducing new functions deriving from the geometrical organization of a precise number of active metal centers, by simply cleverly tailoring the nature of the molecular building blocks. A summary of the various systems and the properties investigated is given in the Abstract.

1.7 References

[1] a) J. Otsuki, *J. Mater. Chem. A* 2018, *6*, 6710; b) Y. Zeng, J. Chen, T. Yu, G. Yang, Y. Li, *ACS Energy Lett.* 2017, *2*, 357; c) S. Kundu, A. Patra, *Chem. Rev.* 2017, *117*, 712; d) J. Yang, M.-C. Yoon, H. Yoo, P. Kim and D. Kim, Chem. Soc. Rev. 2012, *41*, 4808.

[2] C. M. Drain, J.-M. Lehn, *J. Chem. Soc., Chem. Commun.,* 1994, 2313.

[3] a) P. J. Stang, D.H. Cao, *J. Am. Chem. Soc.* 1994, *116*, 4981; b) S.-S. Li, B. H. Northrop, Q.-H. Yuan, L.-J. Wan, P.J. Stang, *Acc. Chem. Res.* 2008, *42*, 249; c) T. R. Cook, Y.-R. Zheng, P. J. Stang *Chem. Rev.* 2013, *113*, 734; d) T. R. Cook, P. J. Stang *Chem. Rev.* 2015, *115*, 7001.

[4] a) D.L. Caulder, K.N. Raymond, *J. Chem. Soc., Dalton Trans.* 1999, 1185; b) D.L. Caulder, K.N. Raymond, *Acc. Chem. Res.* 1999, *32*, 975; c) D. L. Caulder, C. Brückner, R.E. Powers, S. König, T.N. Parac, J.A. Leary, K.N. Raymond, *J. Am. Chem. Soc.* 2001, *123*, 8923; d) M. D. Pluth, R.G. Bergman, K.N. Raymond, *Acc. Chem. Res.* 2009, *42*, 1650.

[5] a) M. Fujita, M. Tominaga, A. Hori, B. Therrien, *Acc. Chem. Res*. 2005, *38*, 371.

[6] a) S. De, K. Mahata, M. Schmittel, *Chem. Soc. Rev.* 2010, *39*, 1555. b) J.R. Nitschke, *Acc. Chem. Res.* 2007, *40*, 103. c) M.M. Safont-Sempere, G. Fernández, F. Würthner, *Chem. Rev.* 2011, *111 (9)*, 5784; d) S. J. Lee, J. T. Hupp. *Coord. Chem. Rev.* 2006, *250*, 1710; e) E. Iengo, P. Cavigli, D. Milano, P. Tecilla, *Inorg. Chim. Acta* 2014, *417*, 59.

[7] S. Durot, J. Taesch, V. Heitz, *Chem. Rev.* 2014, *114,* 8542.

[8] a) A. Takai, M. Chkounda, A. Eggenspiller, C.P. Gros, M. Lachkar, J.-M. Barbe, S. Fukuzumi, *J. Am. Chem. Soc.* 2010, *132*, 4477; b) F.-L. Jiang, D. Fortin, P.D. Harvey, *Inorg. Chem*. 2010, *49*, 2614. c) Y. Pellegrin, F. Odobel, *Coord. Chem. Rev.* 2011, *255*, 2578; d) H. Imahori, T. Umeyama, K. Kurotobi, Y. Takano, *Chem. Commun.* 2012, *48*, 4032; e) E. Iengo, G. Dan Pantosx, J. K. M. Sanders, M. Orlandi, C. Chiorboli, S. Fracassoc, F. Scandola, *Chem. Sci*., 2011, *2*, 676; f) A. Amati, P. Cavigli, A. Kahnt, M. T. Indelli, E. Iengo *J. Phys. Chem. A* 2017, *121*, 4242; g) C. Colomban, C. Fuertes-Espinosa, S. Goeb, M. Sall, M. Costas, L. Blancafort, X. Ribas *Chem. Eur. J.* 2018, *24*, 4371; h) J. Otsuki *J. Mater. Chem. A*, 2018, *6*, 6710.

[9] a) B. K. Kang, N. Aratani, J.K. Lim, D. Kim, A. Osuka, K.-H. Yoo, *Mater. Sci. Eng. C*, 2006, *26*, 1023; b) M. Hoffmann, C.J. Wilson, B. Odell, H.L. Anderson, *Angew. Chem., Int. Ed*. 2007, *46*, 3122; c) M. Jurow, A.E. Schuckman, J.D. Batteas, C.M. Drain, *Coord. Chem. Rev.* 2010, *254*, 2297; d) J. Karnbratt, M. Hammarson, S.M. Li, H.L. Anderson, B. Albinsson, J. Andreasson, *Angew. Chem., Int. Ed*. 2010, *49*, 1854; e) M.J. Latter, S.J. Langford, *Int. J. Mol. Sci*. 2010, *11*, 1878; f) J.S. Lindsey, D.F. Bocian, *Acc. Chem. Res.* 2011, *44*, 638.

[10] a) J. Frey, C. Tock, J.-P. Collin, V. Heitz, J.-P. Sauvage, *J. Am. Chem. Soc.* 2008, *130*, 4592; b) J.-P. Collin, F. Durola, J. Frey, V. Heitz, F. Reviriego, J.-P. Sauvage, Y. Trolez, K. Rissanen, *J. Am. Chem. Soc*. 2010, *132*, 6840; c) T. Lang, E. Graf, N. Kyritsakas, M.W. Hosseini, *Dalton Trans*. 2011, *40*, 5244; d) S. Shinkai, M. Ikeda, A. Sugasaki, M. Takeuchi, *Acc. Chem. Res*. 2001, *34*, 494; e) S. Ogi, T. Ikeda, R. Wakabayashi, S. Shinkai, M. Takeuchi, *Chem.- Eur. J.* 2010, *16*, 8285; f) J.S. Marois, K. Cantin, A. Desmarais, J.F. Morin, *Org. Lett*. 2008, *10*, 33; g) S. Saha, A.H. Flood, J.F. Stoddart, S. Impellizzeri, S. Silvi, M. Venturi, A. Credi, *J. Am. Chem. Soc.* 2007, *129*, 12159; h) T. Muraoka, K. Kinbara, T. Aida, *Nature* 2006, *440*, 512; i) H. Kai, S. Nara, K. Kinbara, T. Aida, *J. Am. Chem. Soc*. 2008, *130*, 6725.

[11] a) C.M. Che, V.K.Y. Lo, C.Y. Zhou, J.S. Huang, *Chem. Soc. Rev*. 2011, *40*, 1950; b) D. Intrieri, A. Caselli, E. Gallo, *Eur. J. Inorg. Chem*. 2011, 5071; c) A. Takai, B. Habermeyer, S. Fukuzumi, *Chem. Commun*. 2011, *47*, 6804; d) V. Pradines, G. Pratviel, *Angew. Chem., Int. Ed*. 2013, *52*, 2185; e) W.-P. To, Y. Liu, T.-C. Lau, C.-M. Che, *Chem.-Eur. J.* 2013, *19*, 5654.

[12] a) J.F. Lovell, T.W.B. Liu, J. Chen, G. Zheng, *Chem. Rev.* 2010, *110*, 2839; b) M. Ethirajan, Y.H. Chen, P. Joshi, R.K. Pandey, *Chem. Soc. Rev.* 2011, *40*, 340; c) C.M. Lemon, P.J. Brothers, B. Boitrel, *Dalton Trans*. 2011, *40*, 6591; d) B. Therrien, *Chemistry of Nanocontainers. In Topics in Current Chemistry*; Albrecht, M., Hahn, E., Eds.; Springer: Berlin, Heidelberg, 2012; Vol. *319*, pp 35−55.

[13] a) L. Grill, M. Dyer, L. Lafferentz, M. Persson, M.V. Peters, S. Hecht, *Nat. Nanotechnol*. 2007, *2*, 687; b) M. Koepf, J.A. Wytko, J.-P. Bucher, J. Weiss, *J. Am. Chem. Soc*. 2008, *130*, 9994, c) C.M. Drain, A. Varotto, I. Radivojevic, *Chem. Rev.* 2009, *109*, 1630; d) S. Mohnani, D. Bonifazi, *Coord. Chem. Rev.* 2010, *254*, 2342; e) J. Otsuki, *Coord. Chem. Rev*. 2010, *254*, 2311; f) D. Heim, D. Écija, K. Seufert, W. Auwärter, C. Aurisicchio, C. Fabbro, D. Bonifazi, J.V. Barth, *J. Am. Chem. Soc.* 2010, *132*, 6783; g) D. Écija, W. Auwärter, S. Vijayaraghavan, K. Seufert, F. Bischoff, K. Tashiro, J.V. Barth, *Angew. Chem., Int. Ed.* 2011, *50*, 3872; h) M. Koepf, F. Chérioux, J.A. Wytko, J. Weiss, *Coord. Chem. Rev.* 2012, *256,* 2872.

[14] a) X. Jing, C. He, L. Zhao, C. Duan, *Acc. Chem. Res.*, 2019, *52*, 100; b) S. Saha, I. Regeni, G. Clever, *Coord. Chem. Rev.* 2018, *374*, 1; c) Y.-Y. Zhang, W.-X. Gao, L. Lin, G.-X. Jin, *Coord. Chem. Rev.* 2017, *344*, 323; d) M. M. J. Smulders, I. A. Riddell, C. Browne, J. R. Nitschke, *Chem. Soc. Rev.,* 2013, *42*, 1728.

[15] J. K. M. Sanders, N. Bampos, Z. Clyde-Watson, S. L. Darling, J. C.Hawley, H.-J.Kim, C. C. Mak, S. J.Webb, in *The Porphyirin Handbook* (Eds.: K. M. Kadish, K. M. Smith, R. Guillard), Academic Press, San Diego, CA, USA, 2000, vol. 3, chapter 1.

[16] A. Satake, Y. Kobuke, *Tetrahedron* 2005, *61*, 13.

[17] a) J.-C. Chambron, V. Heitz, J.-P. Sauvage, K.M. Kadish, K.M. Smith, R. Guillard, *The Porphyrin Handbook*, 2000, *6*, Chapter 40; b) J. Wojaczynski, L. Latos-Grazynsky, *Coord. Chem. Rev.*, 2000, *204*, 113. (c) T. Imamura, K. Fukushima, *Coord. Chem. Rev.*, 2000, *198*, 133. (d) P.J. Stang, J. Fan, B. Olenyuk, *Chem. Commun.* ,1997, 1453. (f) C.M. Drain, F. Nifiatis, A. Vasenko, J.D. Batteas, *Angew. Chem. Int. Ed. Engl.* 1998, *37*, 2344. (g) J. Fan, J.A. Whiteford, B. Olenyuk, M.D. Levin, P.J. Stang, E.B. Fleischer, *J. Am. Chem. Soc.* 1999, *121*, 2741. (h) E. Iengo, B. Milani, E. Zangrando, S. Geremia, E. Alessio, *Angew.Chem. Int. Ed.* 2000, *39*, 1096. (i) K.E. Splan, M. Keefe, A.M. Massari, K.A. Walters, J.T. Hupp, *Inorg. Chem.* 2002, *41*, 619. (l) E. Iengo, E. Zangrando, M. Bellini, E. Alessio, A. Prodi, C. Chiorboli, F. Scandola, *Inorg. Chem.* 2005, *44*, 9752. (m) F. Scandola, C. Chiorboli, A. Prodi, E. Iengo, E. Alessio *Coord. Chem. Rev.* 2006, *250*, 1471 (n) M. Boccalon, E. Iengo, P. Tecilla, *J. Am. Chem. Soc.* 2012, *134*, 20310.

[18] R. Dev Mukhopadhyay, Y. Kim, J. Koo, K. Kim, *Acc. Chem. Res.* 2018, *51*, 2730.

[19] (a) N. Fujita, K. Biradha, M. Fujita, S. Sakamoto, K. Yamaguchi, *Angew. Chem., Int. Ed.* 2001, *40*, 1718; (b) M. Fujita, K. Umemoto, M. Yoshizawa, N. Fujita, T. Kusukawa, K. Biradha, *Chem. Commun*. 2001, 509.

[20] (a) S. Tashiro, M. Kobayashi, M. Fujita, *J. Am. Chem. Soc.* 2006, *128*, 9280; (b) Y. Hatakeyama, T. Sawada, M. Kawano, M. Fujita, *Angew. Chem., Int. Ed.* 2009, *48*, 8695.

[21] (a) W.J. Meng, B. Breiner, K. Rissanen, J.D. Thoburn, J.K. Clegg, J.R. Nitschke, *Angew. Chem., Int. Ed.* 2011, *50*, 3479; (b) T.K. Ronson, S. Zarra, S.P. Black, J.R. Nitschke, *Chem. Commun.* 2013, *49*, 2476.

[22] J. Mosquera, B. Szyszko, S.K.Y. Ho, J.R. Nitschke, *Nature Comm.* 2017, *8*, 14882.

[23] (a) S. J. Lee, K. L. Mulfort, X. Zuo, A. J. Goshe, P. J. Wesson, S. T. Nguyen, J. T. Hupp, D. M. Tiede, *J. AM. CHEM. SOC.* 2008, *130*, 836; (b) S. J. Lee, S. H. Cho, K. L. Mulfort, D. M. Tiede, J. T. Hupp, S. T. Nguyen, *J. Am. Chem. Soc.* 2008, *130*, 16828.

[24] (a) E. Iengo, E. Zangrando, R. Minatel, E. Alessio, *J. Am. Chem. Soc.* 2002, 124, 1003; (b) M.T. Indelli, C. Chiorboli, F. Scandola, E. Iengo. P. Osswald, F. Würthner, *J. Phys. Chem. B* 2010, *114,* 14495; (c) E. Alessio, M. Casanova, E. Zangrando, E. Iengo, *Chem. Commun*. 2012, 48, 5112; (d) E. Iengo, P. Cavigli, D. Milano, P. Tecilla, *Inorganica Chim. Acta,* 2014, 417, 59.

[25] M. J. Webb, N. Bampos, *Chem. Sci.* 2012, *3*, 2351.

[26] R.J. Abrahma, G.E. Hawkes, X.H. Baith, *Tetrahedron Letters* 1974, *16*, 1483

[27] (a)L.K.S. von Krbek, C. Schalley, P. Thordarson, *Chem. Soc. Rev.* 2017, *46*, 2622, and references therein; (b) G. Ercolani, L. Schiaffino, *Angew. Chem. Int. Ed.* 2011, 50, 1762; (c) C.A. Hunter, H.L. Anderson, *Angew. Chem. Int. Ed.* 2009, *48*, 7488.

[28] (a) K.L. Anderson, *Inorg. Chem.* 1994, *33*, 972; (b) G.S. Wilson, H.L. Anderson, *Chem. Commun.* 1999, 1539; (c) P.N. Taylor, H.L. Anderson, *J. Am. Chem. Soc.* 1999, *121*, 11538.]

[29] (a) A.W. Kleij, M. Kuil, D.M. Tooke, M. Lutz, A. L. Spek, J.N.H. Reek, *Chem. Eur. J.* 2005, *11*, 4743; (b) M. Kuil, I.M. Puijk, A.W. Kleij, DM. Tooke, A.L. Spek, J.N.H. Reek, *Chem. Asian J.* 2009, *4*, 50]

Chapter 2

*The work presented in this Chapter was done in collaboration with Prof. K. Severin, École Polytechnique Fédérale de Lausanne (EPFL), Lausanne (CH). The X-ray analysis was performed in collaboration with Dr. N. Demitri, Elettra – Synchrotron Light Source –Trieste (IT), and Prof. E. Zangrando, University of Trieste (IT).

Metalloligands (also termed as *metal containing ligands*) are metal complexes with free donor groups at their periphery, available for coordination to other metal ions, that find extensive application as building blocks in supramolecular chemistry.[1a] They are of great interest because they allow to prepare heterometallic architectures, which contain a number of different metal centers in defined geometries. Compared to homometallic derivatives, heterometallic discrete assemblies and materials can possess additional functionalities and new potentials for a number of applications (such as catalysis and molecular magnetism).[1,2] The utilization of metalloligands can also be interesting from a structural view-point, as unusual geometries, difficult to obtain with organic scaffolds, may become available.[1,3] Finally, the synthetic access to metalloligands may be easier if assisted by a metal templating effect.[1]

2.1 Fe(II) Clathrochelate Linear Metalloligands

The group of Prof. K. Severin has widely reported on the preparation, and further employment in the metal-mediated assembling of supramolecular structures, of linear and rigid dipyridyl clathrochelate mononuclear metal containing ligands, that are macrobicyclic iron(II) tris(dioxime) complexes, capped by pyridyl boronate esters (Scheme 2.1).[4] This class of compounds can be obtained in high yields by a one-pot metal-templated condensation reaction of a dioxime, an aryl boronic acid and the $FeCl_2$ salt (Scheme 2.1, left). By variation of the dioxime starting material, it is possible to modify the lateral size of these clathrochelates (and their solubility to a certain extent), while the nature of the peripheral functional groups (*i.e.* 4- or 3-pyridyl) can be tuned by appropriate choice of the aryl boronic acid.[4,5] Notably, donor groups such as pyridine or carboxylic acids can be employed without compromising the metal-templated reaction.

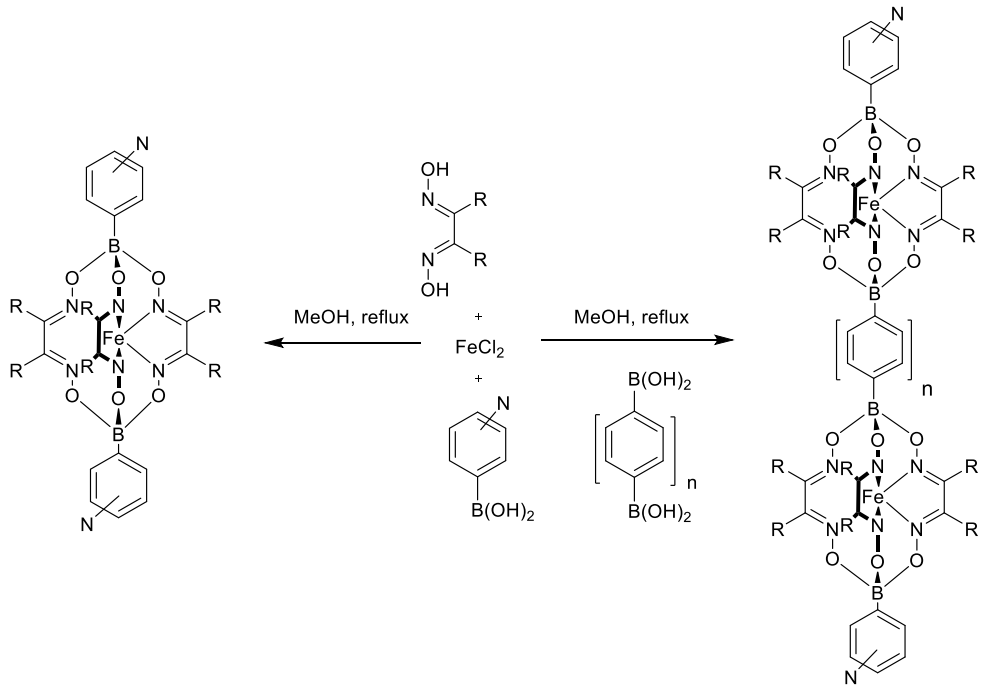

Scheme 2.1. One pot synthesis mono- (left) and di-nuclear (right) Fe(II) clathrochelate metal containing ligands terminally capped by either two 4-pyridyl, or two 3-pyridyl functional groups.

Ditopic linear metalloligands with extended lengths and multiple clathrochelate cores were prepared by two strategies: *i)* introduction of a diboronic acid as third component of the one-pot condensation reaction, with formation of a statistical mixture of two products featuring either one or two metal cores (Scheme 2.1, right); *ii)* Sonogashira coupling reactions between either two preformed asymmetric clathrochelate (in a 1:1 ratio) with partner reactive terminals at one end, or one asymmetric complex and one aryl fragment (in a 2:1 ratio) with two symmetric reactive terminals.[4c,h] These strategies enabled the straightforward preparation of a set of rigid, rod-shaped bipyridyl ligands with lengths ranging from 1.5 nm to 5.4 nm (some examples are shown in Figure 2.1)[4h] Notably, the preparation of purely organic dipyridyl ligands spanning these lengths would require substantial synthetic effort.

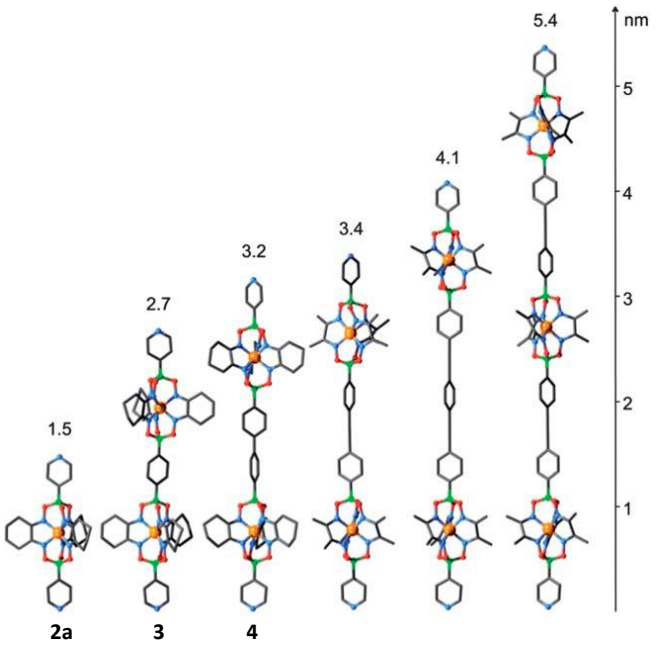

Figure 2.1. X-ray structures (dipyridyl clathrochelates **2a** and **3**) and molecular modeled structures (**4** and more extended versions) with the pyridyl-nitrogen distance values in nanometers, from Ref. 4h). Colour code: N, blue; O, red; B, green; C, grey; Fe, orange.

Successively, clathrochelate ligands with tuned number and orientation of appended pyridyl groups were also obtained, *via* Pd-catalyzed cross-coupling reactions (Figure 2.2).[4i] The use of phenoldioximes, in place of simple 1,2-dioximes, afforded dinuclear mono-anionic M^{II}/M^{II} ($M^{II} = Mn^{2+}$, Fe^{2+}, Co^{2+}, or Zn^{2+}) or neutral paramagnetic Fe^{II}/Fe^{III} complexes.

This class of metalloligands are in general very stable: the boronate ester groups are not susceptible to hydrolysis, and ligand exchange reactions are only observed under very drastic conditions; it is worth mentioning that the Fe^{II} containing ligands are not air and moisture sensitive.

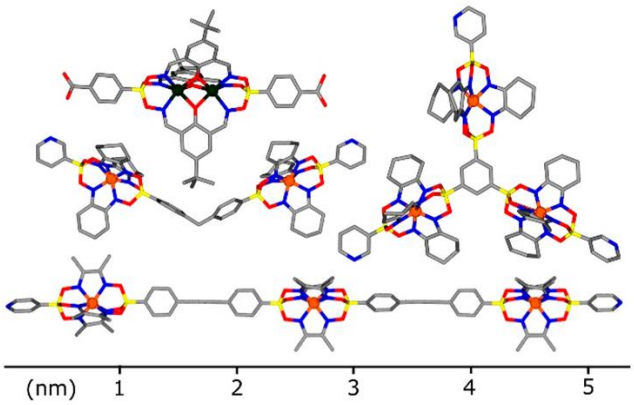

Figure 2.2. Few examples of clathrochelate ligands with tuned shape, dimension, nature, and number of the metal cores, from Ref 4i.

The 3-pyridyl Fe(II) containing ligands, that function as bent connectors, were successfully used in combination with Pd(II) naked ions for the preparation of a variety of coordination cages.[4a-g] Investigations on the influence of the dioxime lateral substituents steric hindrance over the geometries of the resulting cationic supramolecular cages demonstrated that entropically disfavored octahedral cages are selectively formed, in place of the expected tetrahedra, when the steric bulk of the substituents is increased (Figure 2.3).[4d]

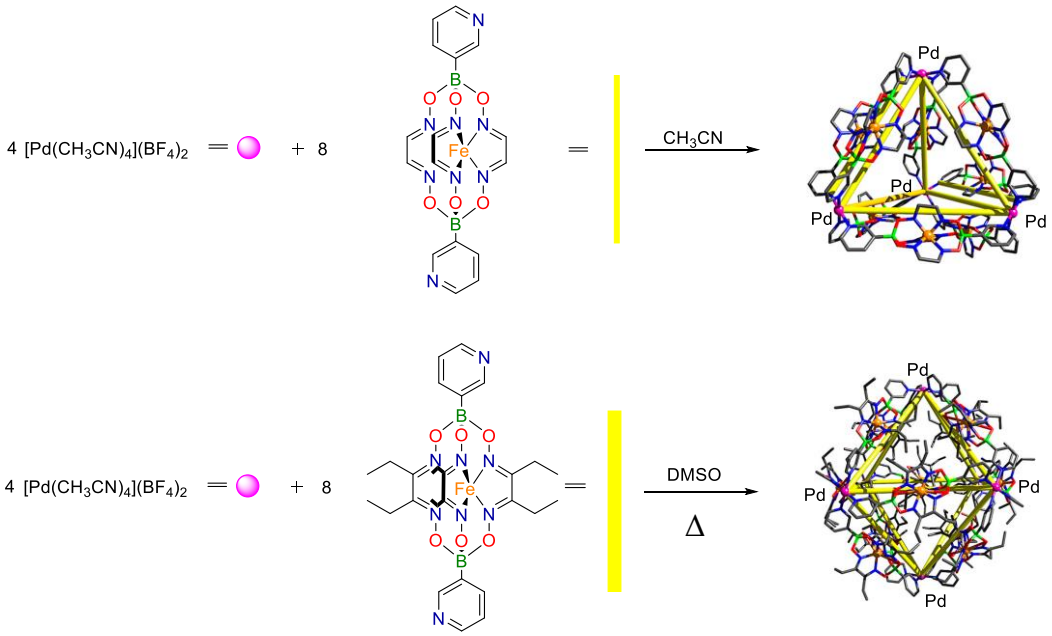

Figure 2.3. Different coordination cages (X-ray structures are shown on the right side) obtained by 1:2 combinations of $[Pd(CH_3CN)_4](BF_4)_2$ and dipyridyl Fe(II) clathrochelate ligands differing from the dioxime lateral substitution pattern (from Ref. 4d). Hydrogen atoms and counteranions omitted for clarity. Color code: C, grey; N, dark blue; B, green; O, red; Pd, pink; Fe, orange.

So far, the use of linear ditopic 4-pyridyl iron(II) clathrochelate metalloligands was limited to the preparation of Cr_7Ni-ring nanomagnets,[4f] and for the assembling of either Re^{I}- or Ir^{III}- based hetero-metallacycles.[4h,3c] For the latter case, different spacing between two parallel Fe^{II}-clathrochelate

connectors was controlled by varying the length of a di-[Cp*Iridium] pincer unit (Fe^{II}- Fe^{II} distances of either 10.9 ˚A or 15.2 ˚A were determined by X-ray analysis Figure 2.4).[3c]

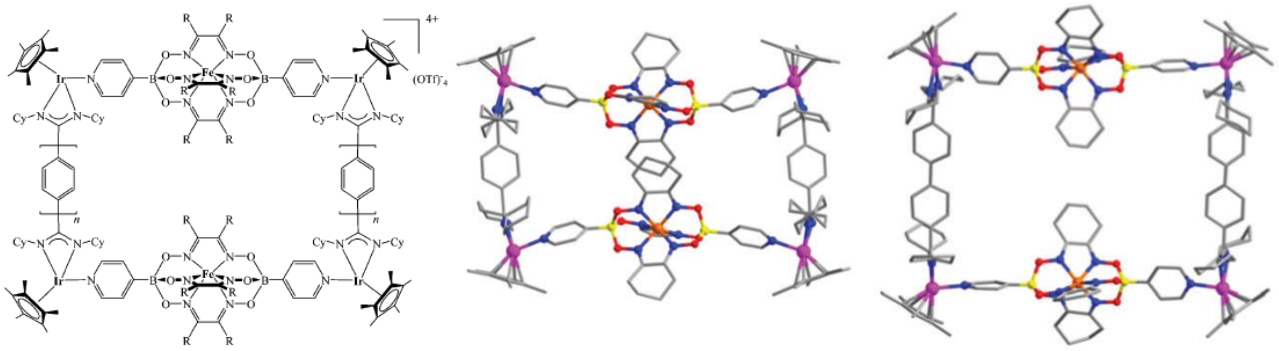

Figure 2.4. Schematic depiction (left) and X-ray structures (right, hydrogens and counterions omitted) of the hetero-metallacycles $[(Cp^*Ir)_4(L_1)_2(\mathbf{2a})_2][OTf]_4$, from Ref. 3c. Color code: B, yellow; C, grey; N, blue; O, red; Fe, violet;Ir, violet.

In parallel, it must be noted that so far the discrete supramolecular assemblies derived from the **1Zn** zinc-porphyrin platform all featured purely organic pyridyl connecting units (see previous Chapter).[6-8] In the work here described, a thorough investigation on the possibility to produce new hetero-multimetallic sandwich-like structures, by self-assembling of **1Zn** with ditopic 4-pyridyl metalloligands (provided by the group of Prof. K. Severin, EPFL, Lausanne, CH), is discussed (Scheme 2.2).

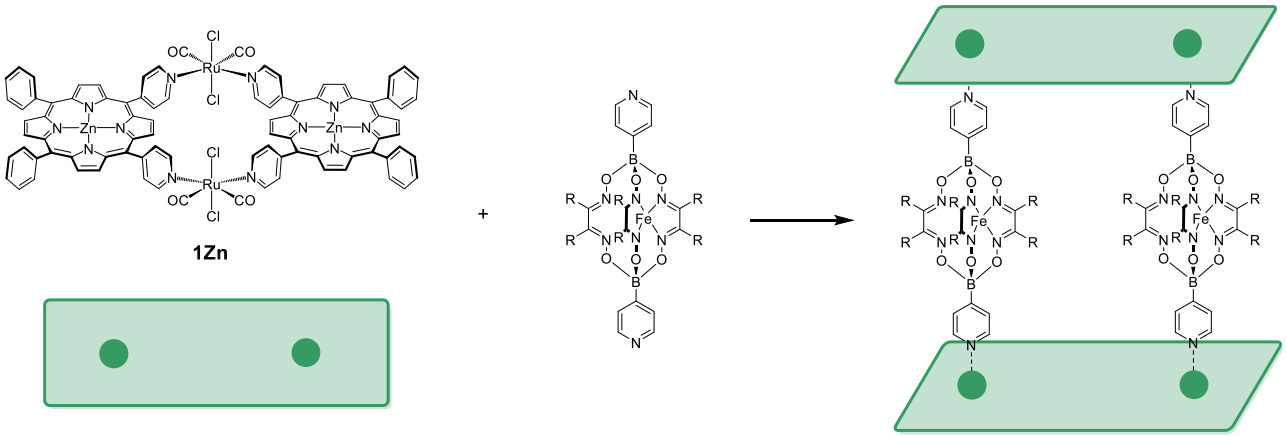

Scheme 2.2. Self-assembling of **1Zn** with a ditopic 4-pyridyl metalloligand.

The initial choice of this pioneering study was that of employing the remarkedly stable and diamagnetic iron(II) complexes. In fact, these features, combined with the availability of a wide range of skeleton variations, are useful to gather detailed information. In particular, linear metal containing ligands with terminal 4-pyridyl groups, lengths between 1.5 and 3.2 nm, and containing either one or two clathrochelate Fe^{II} cores, were selected (Chart 2.1).

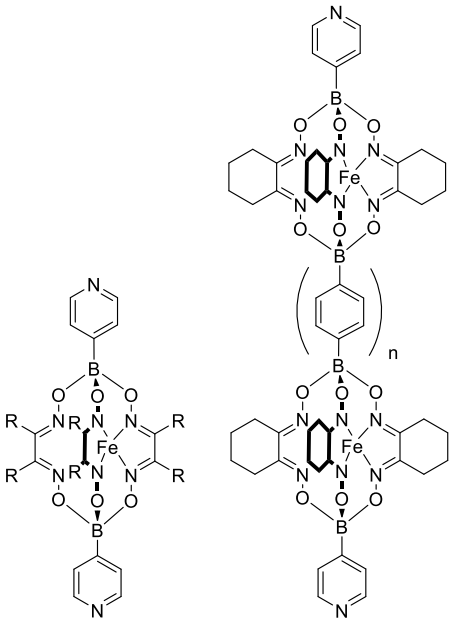

Chart 2.1.

The shorter mono-clathrochelates **2a**-**2c** bear varied dioxime lateral substituents, while the more extended bis-clathrochelates **3** and **4** present the same cyclohexyl lateral substituents, but different Fe(II)-Fe(II) distances (see also Figure 2.1 for the corresponding X-ray and modelled structures). The main goals of the present systematic study are those of verifying: i) the efficacy of the previously established assembling approach in the presence of rigid but substantially more extended ligands; ii) the degree of control, exerted by the mutual preorganizations of **1Zn** and the metalloligands partners, over the spatial distribution of the various metal centers. The future perspective may be that of translating a reliable modular approach to more appealing, *albeit* less trivial to handle, metallo-ligands (e.g. paramagnetic metal analogues), and get access to functional systems, featuring defined numbers of organized metal-active centers (*e.g.* magnetically, redox or catalytically active). The presence of peripheral antenna/photosensitizer units (the zinc-porphyrins) may increase the potentials of these hetero-multimetallic supramolecular systems.

2.2 Results and Discussion

2.2.1 Synthesis and Characterization of Sandwich-like Heterometallic Assemblies

Treatment of **1Zn** in chloroform solution at room temperature with 1 eq. of ligands **2a/b/c** (at mM concentrations) results in the formation of systems **5a/b/c** in quantitative yield (Scheme 2.3). The occurrence of the self-assembling process of the building blocks was qualitatively observed by an instantaneous colour change of the solution from the initial dark violet to purple with green-blue shades. By slow diffusion of *n*-hexane on the corresponding $CHCl_3$ solutions, all the products were isolated as pure microcrystalline solids. ^{1}H NMR spectroscopy, together with conventional 2D NMR experiments (HH-COSY,-NOESY, and-ROESY), revealed the formation of sandwich-like supramolecular

assemblies, with mostly identical spectroscopic features, that will therefore be presented more in detail for **5a**, while a comparison between the various systems will be limited to few relevant points.

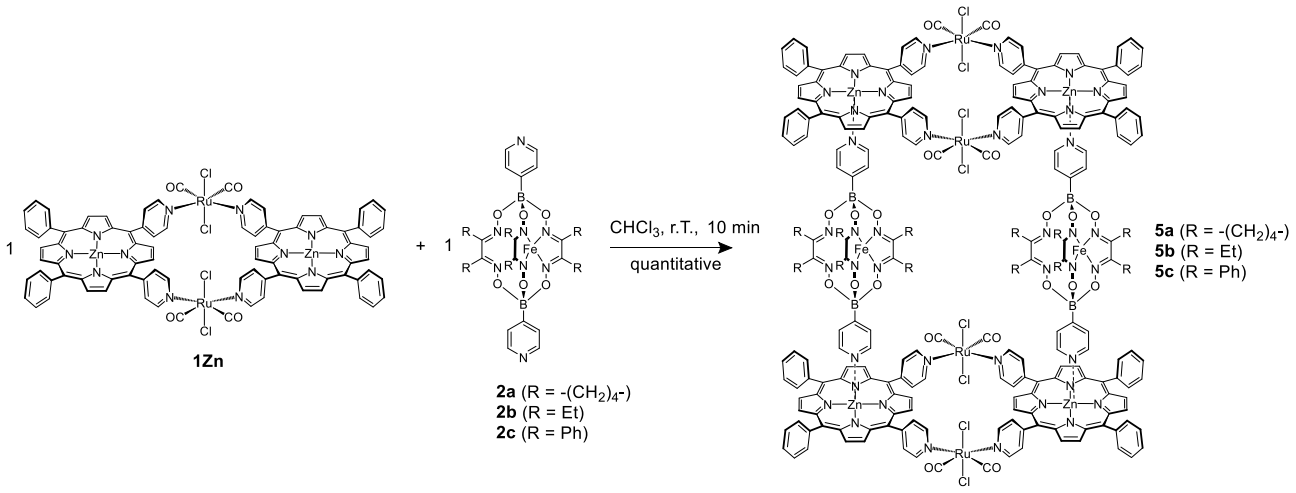

Scheme 2.3. Synthesis of the assemblies **5a-c**.

At room temperature, the ^{1}H NMR spectra ($CDCl_3$) of **5a-c**, all present one set of sharp and well-resolved resonances (Figures 2.5), in agreement with the high symmetry of the derivatives, and highlighting a distinct kinetic inertness and higher thermodynamic stability with respect to the reference system **[1Zn·*trans*DPyP]$_2$** earlier reported (i.e. slow exchange assembling regime as compared to intermediate slow-to-fast regime, see previous Chapter and below).[6,7]

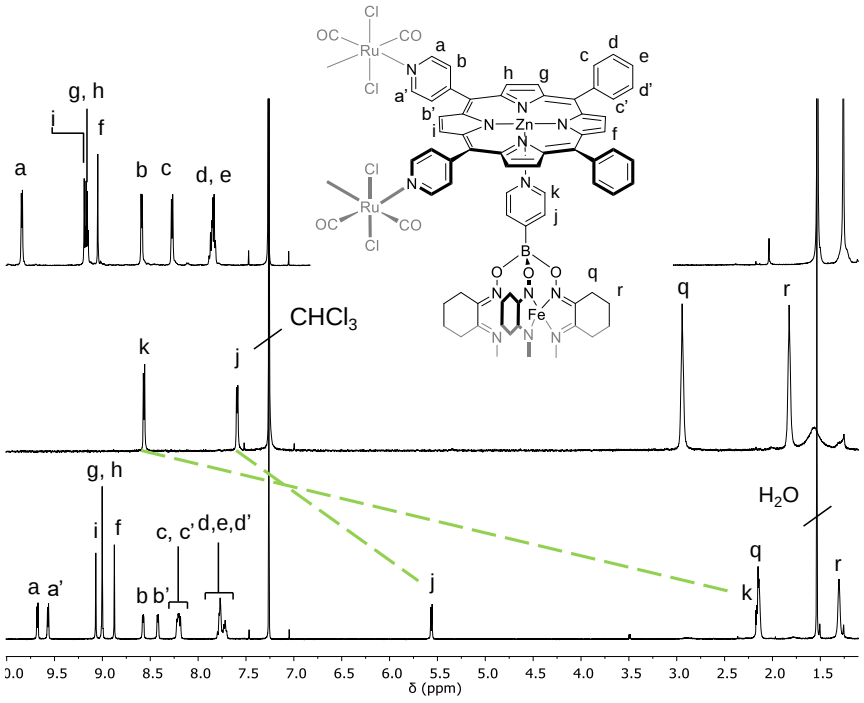

Figure 2.5. ^{1}H NMR spectra ($CDCl_3$) of complex **1Zn** (top), **2a** (middle) and of assembly **5a** (bottom), with proton labeling scheme.

VT ^{1}H NMR experiments (ΔT = +50 ÷ –20°C) do not show any appreciable changes, indicating that the systems maintain the slow exchange kinetics in the whole temperature interval explored.

This novel distinct feature resulted extremely valuable at disclosing/addressing a variety of aspects: clear evidence of the "*all or nothing*" self-assembling process was made possible (see also below); detailed solution NMR characterization, especially in terms of comparative spectroscopic structure-related features, (*e.g.*, discrimination/elucidation of different but concomitant intramolecular dynamic processes, analogies/discrepancy arising from subtle or substantial metalloligand variations); high degree of control over the purity of the samples; ^{1}H DOSY complete and careful analysis; access to self-sorting preliminary surveys (see below).

In general, all the ^{1}H resonances have been assigned by means of 2D H–H and H–C experiments and present correct relative intensities. As previously observed in related systems, the coordination of the linear dipyridyl connectors to the Zn(II) centers of the platform causes a general upfield shift of the connector proton resonances, due to magnetic shielding of the combined porphyrin ring currents of the two facing **1Zn** metallacycles. This effect decreases gradually with the distance of the protons from the zinc porphyrin planes (in the ^{1}H NMR spectrum of **5a**: $\Delta\delta = -6.42$ (Hk), $\Delta\delta = -2.00$ (Hj), $\Delta\delta = -0.80$ (Hq) and $\Delta\delta = -0.51$ (Hr)). The presence of two distinct magnetic environments on the two sides of each **1Zn** metallacycles (i.e. increased magnetic shielding about the inside region of the assembly), is evidenced by the concomitant split in two doublets of equal intensity observed for the Ha/Hb pyridyl and Hc/Hd phenyl protons of **1Zn**. The doublets of each proton sets are connected by exchange peaks in the ^{1}H ROESY experiments (Figure 2.6), in agreement with the slow rotation of the aryl porphyrin rings along the C*meso*–C*ring* at room T, and the perpendicular average disposition of these rings with respect to the porphyrin planes.

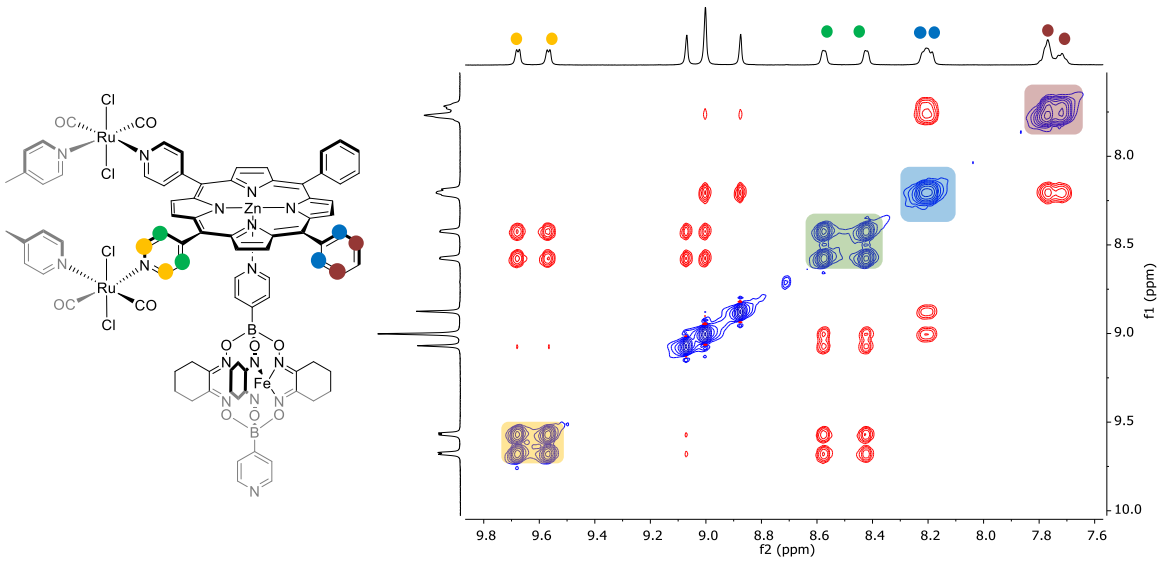

Figure 2.6. Aromatic region of the ^{1}H ROESY spectrum ($CDCl_3$) of **5a**, exchange cross peaks between pair of pyridyl and phenyl split resonances are evidenced with a schematic color code.

A comparison between the patterns of ^{1}H resonances of the bridging metalloligands for **5a-c**, clearly suggests that the two Zn^{II} centers within each facing platform offer enough space to accommodate pairs of metalloligands with varied steric hindrance (see also self-sorting experiments below). Moreover, free motion of the two connecting ligands is generally observed, even upon lowering the Temperature. These observations are valid also for derivative **5c**, for which the steric demand of six

phenyl side arms at each of the two clathrochelate cores was expected to cause physical restraints of some sort.

To further insight the stability of these systems, the model trimeric compound [(ZnTPP)$_2$(**2a**)] (**8**) (TPP = 5,10,15,20-phenylporphyrin), featuring a Fe(II)-clathrochelate ligand axially bound to two Zn-porphyrins, was also investigated. By NMR titration of a $CDCl_3$ solution of **2a** with weighted aliquots of ZnTPP, an association constant of about 10^7 M^{-2} was obtained. This value is one order higher compared to the 10^{-6} M^{-2} constant calculated by NMR titration of a *trans*-dipyridylporphyrin with ZnTPP.[6a] Indeed, a more reliable association constant should be determined by spectrophotometric experiments; however, the obtained value clearly hints increased stability compared to the purely organic ligand.

Analogously, systems **6** and **7** were obtained by self-assembly of the distinct building blocks. The NMR data provided clear evidence for the formation of defined assemblies (**6** and **7**; Scheme 2.4).

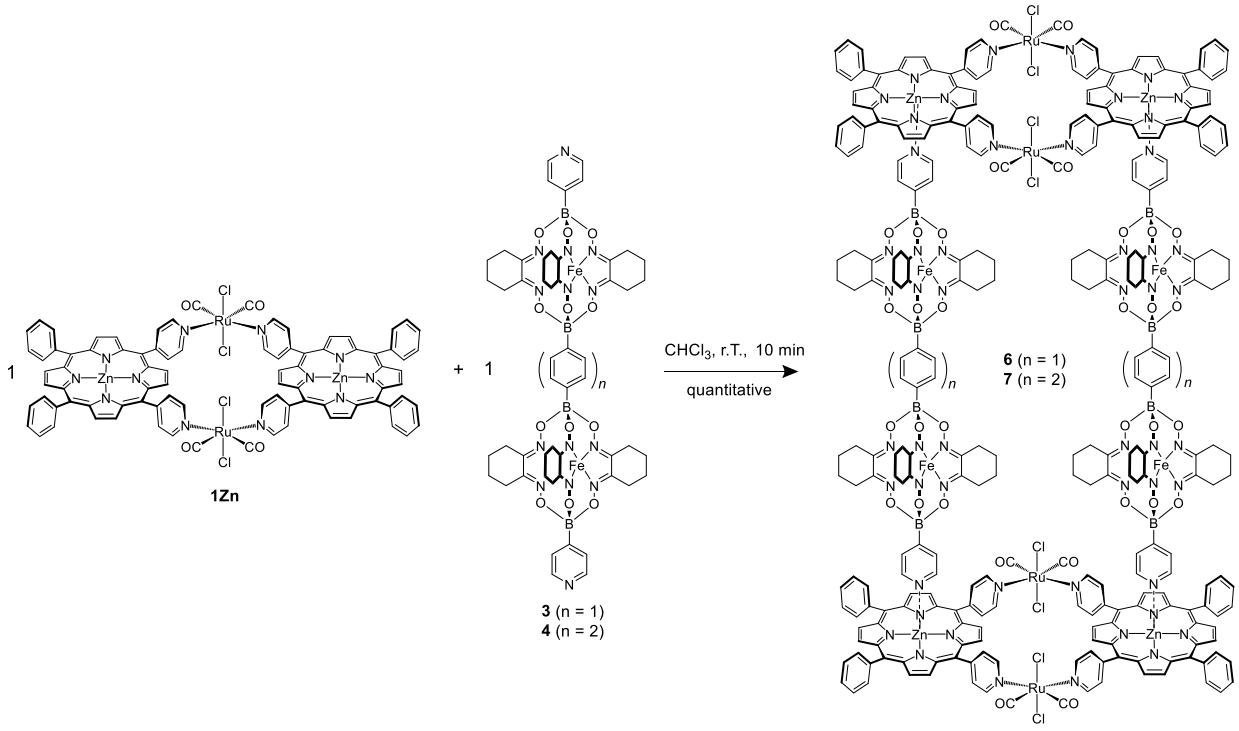

Scheme 2.4. Synthesis of the assemblies **6** and **7**.

As in the case of **5**, at room temperature, the proton spectra show a unique and well-resolved set of signals, strong high field shifts for the pyridyl protons of the metalloligands, along with the typical splitting of the pyridyl and phenyl protons signals of platform **1Zn** (Figure 2.7).

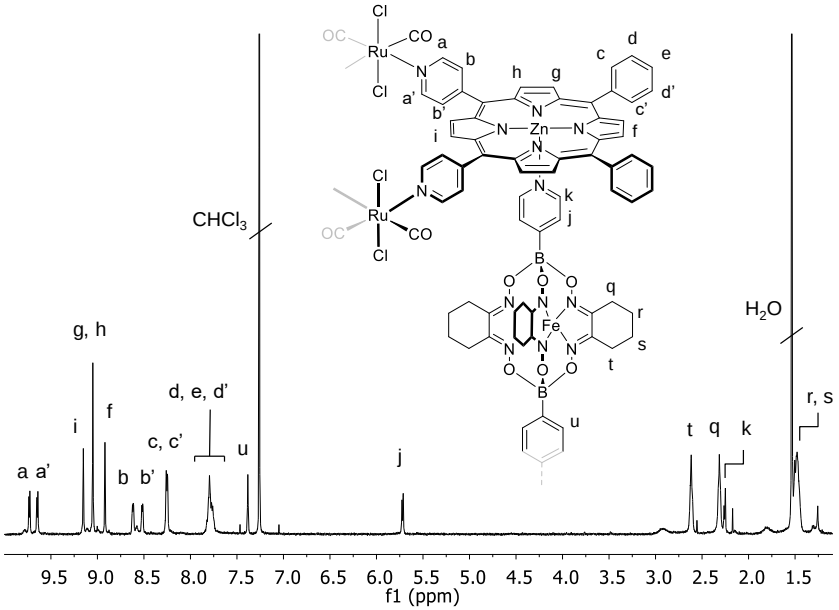

Figure 2.7. ^{1}H NMR spectrum ($CDCl_3$) of **6**.

These observations indicate that the modular self-assembling approach applied remain efficient also when the connecting linear metal-containing ligands span a considerable length between the two basic pyridyl donor sites.

To gather additional information over the size of the assemblies, Diffusion-Ordered Spectroscopy (DOSY) experiments were performed. In recent years, DOSY has become a widespread analytical tool for the solution characterization of supramolecular systems.[9] This unique technique allows to virtually separate species present in solution on the base of their diffusion coefficient (*Dt*), which is directly correlated to the hydrodynamic volume (V_H), i.e. to the dimension and shape of the diffusing species.[10] In Figure 2.8 the 2D DOSY map (processed with the Bayesian DOSY Transform of the MestreNova software) of **5a** overlapped with those of the molecular building units **2a** and **1Zn**, is reported. From this superimposition, the differences in *Dt* values are clearly appreciable, also with respect to the smaller, faster diffusing, solvent molecules. Moreover, the building units and the relative assembled species are correctly ordered top to bottom following decreasing coefficient values, which well correlate to the relative dimension trend.

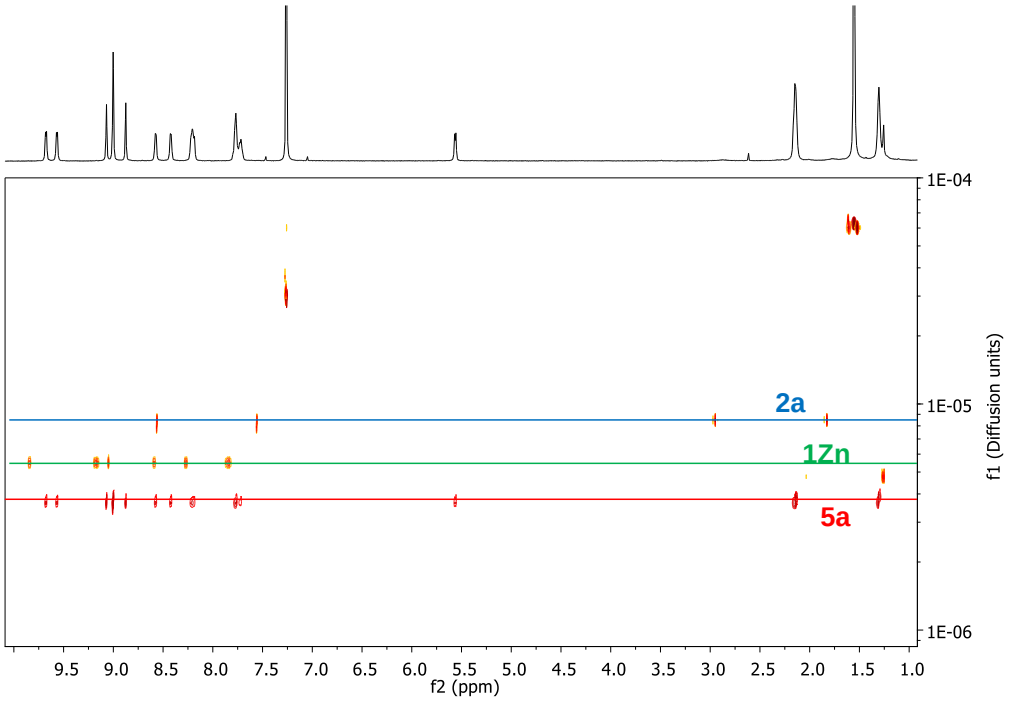

Figure 2.8. Overlay of the 2D ^{1}H-DOSY spectra ($CDCl_3$, Bayesian DOSY Transform) of **5a** (red), **1Zn** (green) and **2a** (blue); only the ^{1}H trace of **5a** is reported in the horizontal axis.

More accurate *Dt* values were obtained by the analysis of the experimental signal decay (see Appendix 1). In Table 2.1, the values of the self-diffusion coefficient, hydrodynamic radius, and volume, calculated for each assembly **5a/b/c**, **6** and **7** and the single molecular building units, are summarized. The hydrodynamic radius for each compound was calculated through the Stokes-Einstein equation for linear diffusion: $D_t = \frac{k_B T}{6\pi\eta r_H}$

where: k_B is the Boltzmann constant, T is the absolute temperature, η is the fluid viscosity, dependent from solvent and temperature. The equation practically assesses that a species with a diffusion coefficient *Dt* diffuses in a given solvent with the same rate of a sphere of radius r_H, which can be considered the hydrodynamic radius of the molecule if its shape fits the spherical approximation.

Table 2.1. Experimental diffusion coefficient values D_t determined from the DOSY experiments. Hydrodynamic radius r_H and hydrodynamic volume V_H calculated from Stokes-Einstein equation.

	D_t[a]	r_H (Å)[b]	V_H (Å^3)[c]
2a	8.41 ± 0.03	4.8	463
2b	8.44 ± 0.06	4.8	463
2c	6.41 ± 0.08	6.3	1047
3	6.17 ± 0.04	6.6	1204
4	5.58 ± 0.08	7.3	1630

1Zn	5.58 ± 0.03	7.3	1630
5a	3.70 ± 0.03	11	5575
5b	3.67 ± 0.07	11.1	5729
5c	3.71 ± 0.08	11	5575
6	3.36 ± 0.03	12.1	7420
7	3.13 ± 0.04	13	9200

[a] $D_t / 10^{-10}$ m^2 s^{-1}. [b] calculated from Stokes-Einstein ($\eta_{chloroform}$ = 5.37 x10^{-4} N m^{-2} s, at 25 °C). [c] $V_H = {}^4/_3 \pi r_H^3$.

The hydrodynamic radius gives qualitative information over the size of the assemblies and conclusions can be formulated by a general comparison of the values obtained for the assemblies and the building blocks.

In general, clathrochelate ligands with the same length (defined by the N···N distance between the peripheral pyridyl groups) afford assemblies with comparable sizes (and therefore comparable self-diffusion coefficients), despite the presence of different lateral substituents. In fact, in the assembled systems, the ligand skeletons are buried within the space defined by the two facing zinc-porphyrin platforms. On the other hand, the DOSY analysis of the free clathrochelate ligands affords hydrodynamic radii of decreasing values ongoing for **5c** to **5a** and **5b** (6.2, 4.8 and 4.6 Å, respectively), in good agreement with the diminished steric hindrance of the lateral substituent series (phenyl-cyclohexyl-hexyl groups).

Notably, the trends in the values of both self-diffusion coefficients and hydrodynamic radii for **5a**, **6** and **7** (11, 12.1 and 13 Å, respectively), are nicely consistent with the formation of assemblies with progressively larger dimensions. A congruent trend is also observed by comparing the values derived for the three Fe(II)-clathrochelate ligands on their own.

The UV-Vis absorption spectrum ($CHCl_3$) of **5a/b/c** very well matches the sum of the absorption spectra of the building units, presenting both the porphyrin absorption bands (the intense -Soret at 420 nm, and the Q bands around 500-650 nm) and the ligand MLCT band (around 430-500 nm, depending on the lateral substituents). The Fe(II) clathrochelate ligands are not emitting, therefore only the typical fluorescence spectrum of the zinc-porphyrin units, with maxima at 635 and 670 nm, is observed. As expected (given the redox-inactive nature of these iron(II) ligands), no quenching of then zinc-porphyrin emission is observed. The effect of the coordination of the pyridyl ligands is a bathochromic shift of few nanometres of both the absorption and emission spectra, as compared to free **1Zn**, as already reported for previous related systems. Integrity of the systems is observed for concentrations ≥ 1×10^{-5} M, by fluorescence dilution experiments (Figure 2.9), in line with a general increase of the stability of these derivatives with respect to the reference system **[1Zn·*trans*DPyP]$_2$** earlier reported (for which a limit concentration of ≥ 7x10^{-5} M was found).[7c]

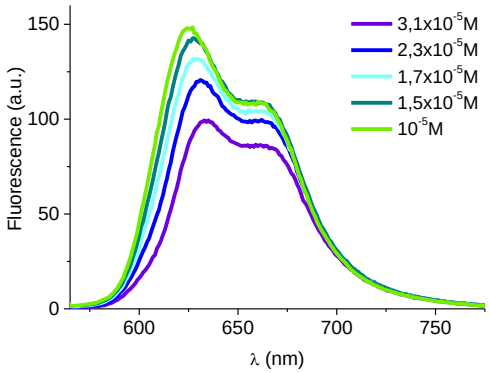

Figure 2.9. Emission spectra ($CHCl_3$, λ_{ex} = 550 nm) of **5c** registered at different concentrations.

Single crystals for all the series of five assemblies and of the reference system **8**, were obtained and analyzed by means of the XR1 beamline of Elettra synchrotron facility (Trieste, IT). The derived structures are fully consistent with the solution data, and present the envisaged sandwich-like architecture made of two parallel and roughly aligned clathrochelate ligands axially bound at their periphery to the Zn(II) centres of two parallel **1Zn** platforms (Figure 2.10), in analogy with the reference system **[1Zn·*trans*DPyP]$_2$**.[6a] For assembly **5a** two different triclinic crystal forms (**5a** and **5a'** in Figure 2.10) were obtained from very similar crystallization conditions. These differ essentially for the conformation adopted by the bridging ligands (see below). In all the structures, the asymmetric unit consists of the (longitudinal) half of the assembly, that gets fully generated by an inversion center located at the barycenter of the construct. This fact allowed to perform a meaningful comparative analysis over several geometrical parameters (see also Table 2.2 below), and parallel some of the solid state and solution data. Discussion of the salient points will be here presented.

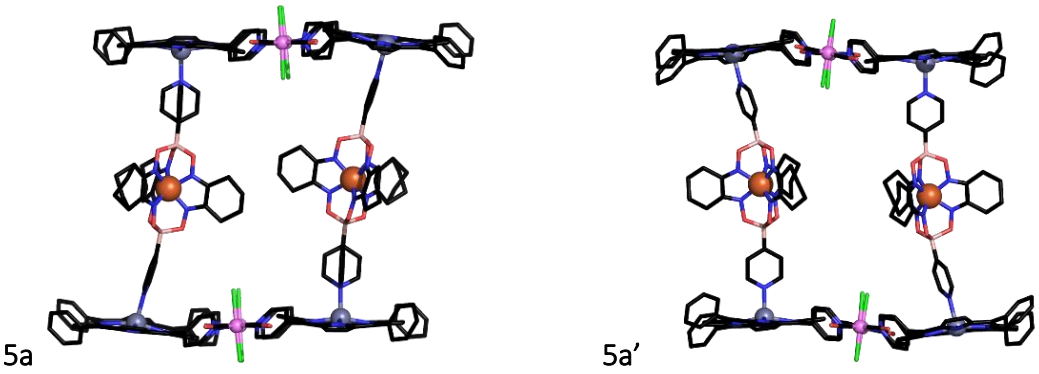

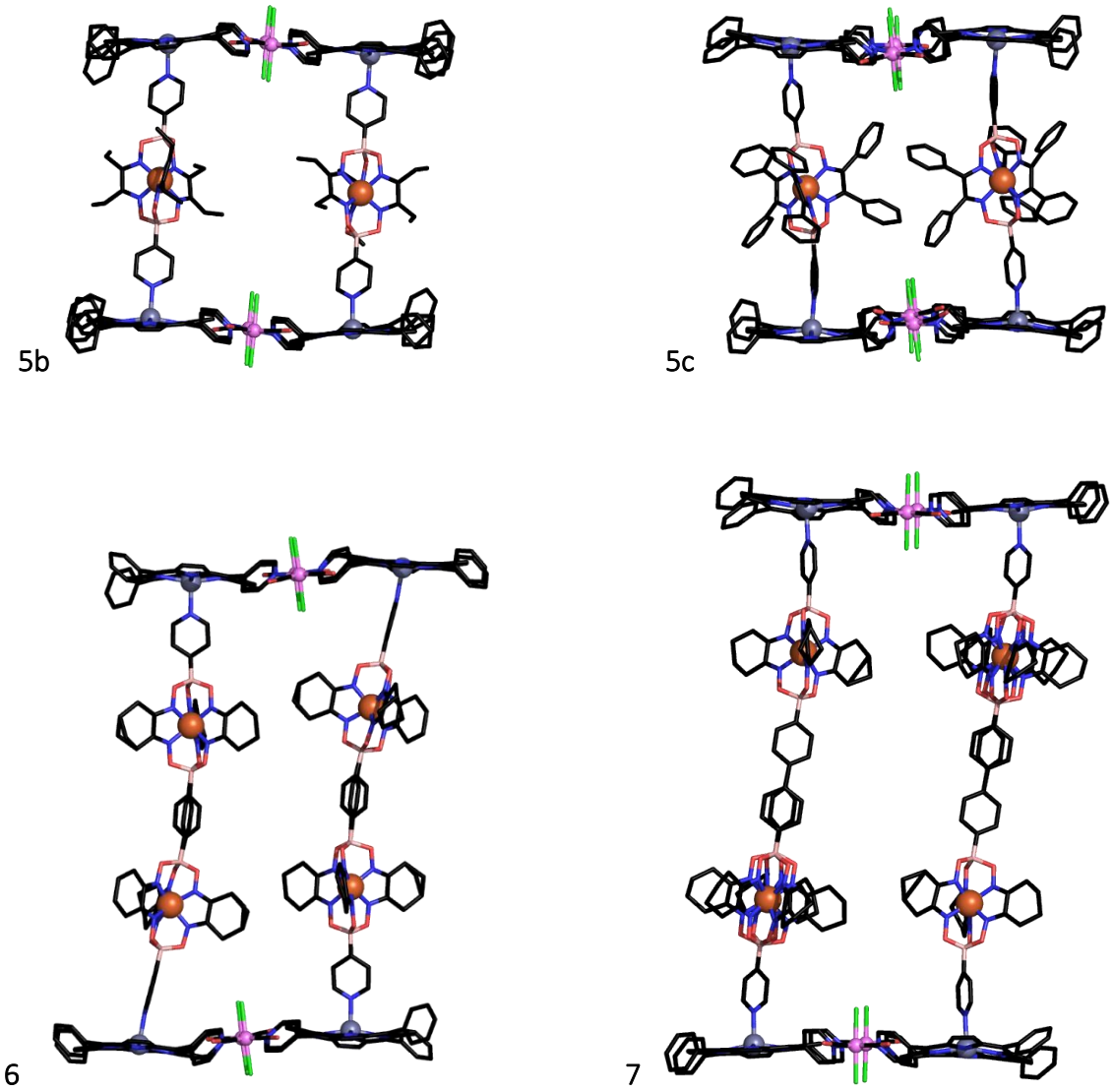

Figure 2.10. X-ray structures of the assemblies **5a**, **5a'**, **5b**, **5c**, **6** and **7**. Solvent molecules and hydrogen atoms are omitted for clarity. Color coding: black sticks for C, blue for N, red for O, pink for B, violet for Ru, orange for Fe, purple for Zn, green for Cl.

In all the assemblies, the **1Zn** two porphyrin macrocycles present modest distortions, producing only minor deviations (the porphyrin main planes form an average angle of ca. 4.3°) from the almost perfect coplanarity found for free **1Zn**.[6b] The distances between the two Zn(II) and two Ru(II) atoms within the same **1Zn** platform are quite comparable ($Zn\cdots Zn_{short}$ in between 13.6 and 14.1 Å, and $Ru\cdots Ru_{short}$ in between 13.9 and 14.1 Å, respectively). The two parallel and facing **1Zn** platforms are found mostly aligned and eclipsing one another (with some discrepancies found for **5a** and **5b**, see also Appendix).

Table 2.2. Selected distances [Å] for assemblies **5a**, **5a'**, **8**, **5b**, **5c**, **6**, **7**, and the references **1Zn** and **[1Zn·*trans*DPyP]$_2$** .

	Zn•••Zn$_{long}$[a]	Zn•••Zn$_{short}$[b]	Fe•••Fe[c]	N•••N[d]	Ru•••Ru$_{short}$[e]
5a	18.950(5)	13.899(8)	12.572(7)	14.74(1)	13.924(4)
5a'	18.838(8)	13.568(7)	11.932(8)	14.67(3)	14.079(6)
8	19,125(6)	N.A.	N.A.	14.89(1)	N.A.
5b	19.026(5)	13.756(4)	13.683(4)	14.75(2)	14.131(4)
5c	18.92(1)	13.714(3)	13.063(3)	14.700(8)	14.050(5)
6	31.05(1)	14.072(4)	12.062(4) [12.091(4)][f]	26.80(2) [26.82(1)][f]	13.885(5)
7	35.24(1)	13.811(4)	13.141(7) [13.070(4)]*	31.00(2)	14.103(6)
1Zn[g]		14.028(3)			14.009(3)
[1Zn·*trans*DPyP]$_2$[h]	19.463(7)	13.532(5)	[11.455(2)]*	15.18(2)	14.454(5)

(a) Distance between two Zn atoms connected by a (metallo)ligand. (b) Distance between the two Zn atoms of the **1Zn** platform. (c) Inter-ligand distance between two aligned Fe atoms. (d) distance between the terminal N atoms of the metalloligand. (e) Distance between the two Ru atoms of the **1Zn** porphyrin platform. (f) Values from Ref. 4h. (g) Values from Ref. 6b. (h) Values from Ref. 6a.

The distance between two zinc centers connected by one bridging ligand (Zn···Zn$_{long}$ in Table 2.2) spans from ~19 Å for the assemblies built on mononuclear clathrochelate ligands, up to 35 Å for assembly **7**, featuring the most extended dinuclear metalloligand. These lengths describe the longitudinal dimensions of each assembly and are substantially determined by the ligand respective lengths plus the minor additional contribution of the N–Zn bonds. In all the assemblies the Fe(II)···Fe(II) distance between the two iron atoms of the bridging ligands is shorter than the Zn···Zn$_{short}$ distance of **1Zn**, as a consequence of slight distortions of the ligands, which are bent towards the centre of the structure. This is appreciable also by the comparison between the structures of **2a** and **3** in the assemblies **5a** and **6** respectively, and those of the free ligands previously published[4h] (see Figure A2.30 in the Appendix).

In **5a** each ligand features one cyclohexyl group pointing toward the inner part of the assembly and the other two toward the outside of the structure. For **5a'** the orientation of lateral groups is reverted (Figure A2.34 in the Appendix). These observations highlight the possibility for the metalloligands to assume different mutual disposition. Given that in solution a single pattern of resonances is found for the sidechains within each of the assemblies, and the exchange between the fully assembled and free components is slow, it is reasonable to conclude that in solution the two bridging units are in free and fast rotation along their coordination axes.

In the structure of **5c**, π···π stacking interaction is found to occur between two lateral phenyl substituents of the pillar clathrochelates of a same assembly. The flexible and less bulky lateral ethyl chains of ligand **2b** allow assembly **5b** to adopt a skewed conformation, where the clathrochelates slope of 79° respect to the planes defined by the **1Zn** platforms (Figure A2.33).

In general, no marked differences are found in the structure of the sandwich-like assembly, by replacement of the organic ***trans*DPyP** connector with the Fe(II) clathrochelate ligands. Also, the $N_{pyridine}$-Zn bond distances (see Table A2.1 in the Appendix) in all the assemblies present comparable values with those found for **[1Zn·*trans*DPyP]$_2$** (shorter bond lengths could have suggested a stronger bind of the clathrochelate pyridyl groups to the Zn(II) cations, supporting the increased stability shown by assemblies **5**-**7**).

Collection of single crystal X-ray data for the whole series evidenced the possibility to tune and extend the longitudinal length of the sandwich-like assemblies with minimal structural distortion of the building units, affording a high degree of geometrical control over the number and spatial disposition of the various metal fragments. This maybe pictorially visualized considering the pattern defined by the porphyrin Zn^{II} centers and the Fe^{II} centers of the metalloligands: discrete 2D rectangular grids made of two aligned equal rugs of the type Zn···(Fe)···Zn (Scheme 2.5). The metalloligands encodes the characteristics of the rug (span, number and relative position of iron centers), while the zinc-porphyrin metallacycle duplicates the rug at a fixed distance on the other dimension (platforms with tuned Zn-Zn distances may be easily accessible). Quite impressively, negligible, and comparable, deviations from this strict geometrical control are found, even upon increasing the longitudinal length of the assembly up to 35 Å.

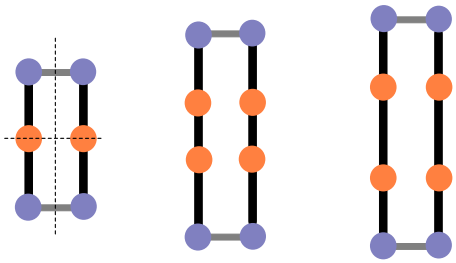

Scheme 2.5. Pictorial view of the metal grids described by the heterometallic assemblies **5**-**7**. Colour code: orange for Fe, purple for Zn.

2.2.2 Self-Sorting Behaviour of Building Blocks

The self-sorting behaviour of a mixture of the mononuclear and dinuclear Fe(II)-clathrochelates **2a** and **3** in combination with the platform **1Zn** was investigated, by mixing the three components in a 1:1:2 ratio, at mM concentrations. in order to observe if the two assemblies or a more complex entity, indicated as mixed assembly, form from the mixture of building blocks and, once formed, if the products are equally favoured (Scheme 2.6). This constitutes a very simplified study since only two way of self-sorting can manifest: a social *nonintegrative* self-sorting by formation of two assemblies with a single type of metalloligand each, or a social *integrative* self-sorting with formation of the

assembly with mixed ligands. A total inefficient self-sorting behaviour would lead to a statistical mixture of all the possible assemblies. Clearly, given the rigidity of the building components and the marked length difference of the chosen clathrochelates (respectively 1.8 and 2.7 nm for **2a** and **3**), and the distance between the Zn atoms in **1Zn**, an *integrative* self-sorting is expected to be highly disfavoured, if not impossible.

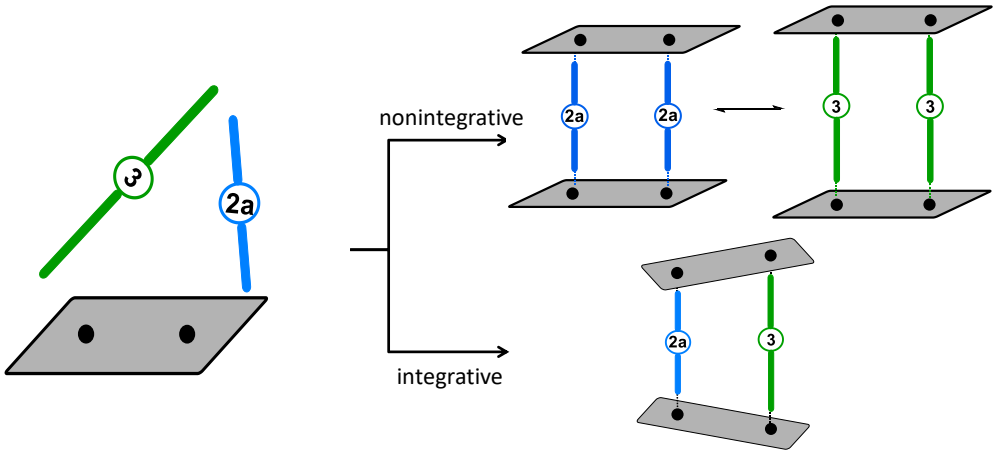

Scheme 2.6. Schematic depiction of the possible equilibrating mixtures formed by combination, in a 2:1:1 ratio, of **1Zn**, **2a** and **3** (ca. 10^{-3} M) in $CHCl_3$ at room Temperature.

First, the clathrochelate ligands were dissolved together in $CDCl_3$ (0.7 ml) and stirred for 15 minutes. After the stoichiometric ratio (1:1) between the two ligands was confirmed by ^{1}H NMR spectroscopy, 2 eq of **1Zn** were added. The formation of one or more assemblies can be qualitatively observed from the characteristic purple colour of the solution with green-blue reflections. The reaction mixture was characterized and investigated by NMR spectroscopy in $CDCl_3$ at room temperature (1D ^{1}H NMR, 2D H-H COSY, HSQC, and H-H ROESY). The NMR analysis confirmed that a self-sorting behaviour takes place. The ^{1}H NMR spectrum (Figure 2.11) reveals the presence of two patterns of resonances attributed to the two hetero metallic assemblies **5a** and **6** in the correct stoichiometric ratio (1:1). No evidence of the mixed assembly or polymeric structures was observed.

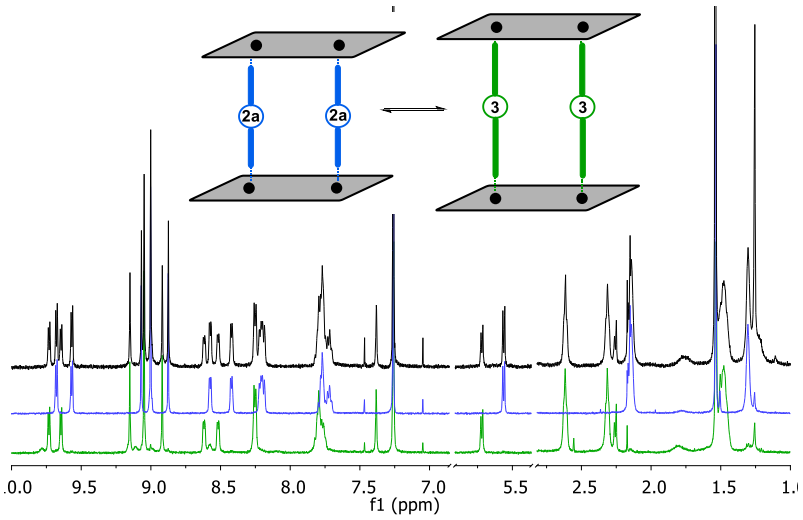

Figure 2.11. Overlay of the ^{1}H NMR spectra (selected region, $CDCl_3$) of a 2:1:1 mixture of **1Zn**, **2a** and **3** (black); **5a** (blue) and **6** (green).

The assignments of the resonances are consistent with the previous NMR spectroscopic analysis (see above). A second experiment was performed by mixing all the building blocks as powders that were simultaneously dissolved in the solvent ($CDCl_3$, 0.7 ml). The mixture was then stirred for 10 minutes at 30°C and the building blocks self-sorted, as seen in the previous case. A further experiment was performed by mixing together the two assemblies **5a** and **6**, once formed, in the same concentration of the earlier experiments. In all the three cases studied, the two assemblies **5a** and **6** formed in ratio 1:1 and no presence of the mixed assembly was observed in solution. The H-H ROESY spectrum of the self-sorting mixture revealed the correlations along the diagonals (blue phase) of all the **1Zn** resonances in the two different assemblies, indicating an intermolecular exchange of the two species in solution at the thermodynamic equilibrium, which is slow at the NMR scale (Figure 2.12). On the other hand, no coupling was observed for the resonances of the clathrochelates ligand in the ROESY spectrum.

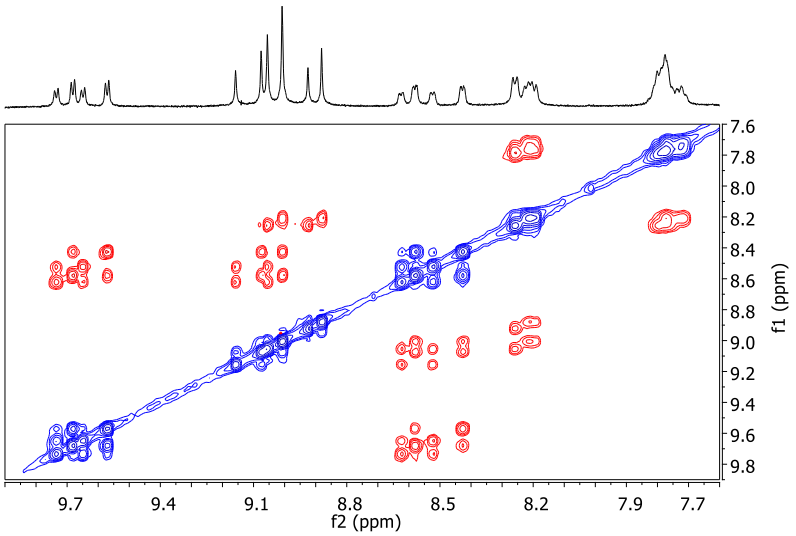

Figure 2.12. Aromatic region of H-H ROESY spectrum ($CDCl_3$) of a 2:1:1 mixture of **1Zn**, **2a** and **3.**

To further investigate the self-sorting behaviour, additional experiments were performed by combination of the platform **1Zn** with two mononuclear Fe(II)-clathrochelate ligands of the same length, such as **2a** and **2c**. The two clathrochelate ligands **2a** and **2c** present respectively one cyclohexyl and two phenyl groups as lateral substituents on the dioxime, the same N – N distance and characteristic patterns of signals. In this case, the formation of the mixed assembly, is more probable than the previous case due to the same length of the clathrochelate ligands. The proton spectrum of a 2:1:1 mixture of **1Zn**, **2a** and **2c**, evidenced the statistical formation of the two homonuclear assemblies and of the mixed one (Figure 2.13).

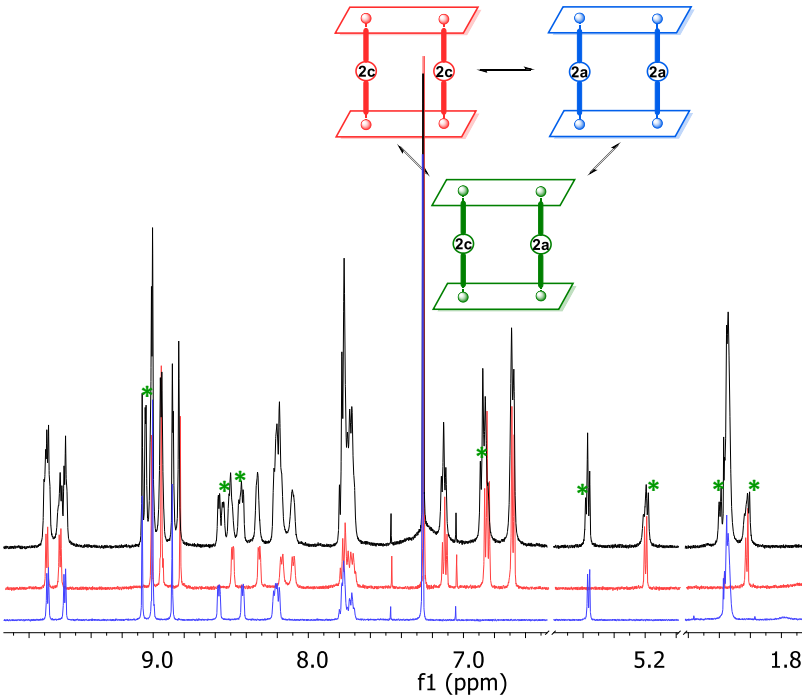

Figure 2.13. Overlay of the ^{1}H NMR spectra (selected region, $CDCl_3$) of a 2:1:1 mixture of **1Zn**, **2a** and **2c** (black), **5c** (red), and **5a** (blue). Some of the peaks of the hetero-ligand assembly are labelled with a green asterisk.

This indicates that the nature of the later substituents does not affect the coordination of the ligands to the zinc porphyrin platform and that in each assembly the two pillar units are independent one to the other (i.e. no secondary inter-ligand interactions occur, may they be simple steric hindrance or of other nature).

2.3 General Conclusions

In this Thesis work, a library of new 3D hetero tri-metallic supramolecular systems with extended dimensions and increased number of metallic cores was assembled by the separate combination of the Zn(II)-porphyrin metallacycle **1Zn** with the dipyridyl Fe(II)-clathrochelate ligands **2**-**4**. The deriving assemblies, **5**-**7** present a sandwich-like structure with two platforms **1Zn** axially connected through two bridging clathrochelate ligands. These new systems were fully characterized in solution by means of 1D and 2D NMR spectroscopy. For all the systems the single crystal X-ray analysis, by means of Synchrotron radiation, confirmed the sandwich-like structure observed in solution. Moreover, the comparative DOSY analysis was proved to be a reliable method for the estimation of the size trend of the assemblies in solution, in addition of the solid-state characterization.

One of the most important distinct characteristics from previous 2:2 assemblies built on organic ligands, is the remarked structural rigidity of the rod-shaped dipyridyl metalloligands, satisfying the preorganization of the zinc-porphyrin metallacycle. The variable lengths of the metalloligands, in combination with their substantial preservation of the structural rigidity, allows to extend

impressively the distance between the chromophore platforms, in a controlled fashion, without perturbing the selectivity towards the discrete 2:2 assembly.

The slow-rate assembling regime, with respect to room temperature NMR timescale, as compared to the slow-to-fast regime previously observed for the reference parent **[1Zn·*trans*DPyP]$_2$**, is an unambiguous indication of the general higher stability (also confirmed by emission dilution experiments). At present we don't have additional experimental evidences: the $\Delta\delta$ measured for the pyridyl protons Hk upon binding are quite comparable and the same stands for the $N_{pyridine}$-Zn distances found in the solid state. The comparison between the association constants for the models cannot be considered conclusive as the values are above/around the limit of the NMR technique (aside the fact that we are assuming that the two binding events are independent, while this should be checked). Given that the parent original assemblies and the present share a common "all or nothing" self-assembling process, the same divalent conformationally rigid *aa* unit, and very alike divalent *bb* (dipyridyl linear fragments, i.e. same statistical factors and likely similar entropy compensations), only an appropriate experimental study of the relevant thermodynamic cycle of equilibria, and parallel titration experiments on reference systems (e.g. metallacycle + monopyridyl ligand model and Zn-porphyrin + monopyridyl ligand model and Zn-porphyrin + dipyridyl ligand and on..) by means of UV-vis and/or ITC analysis, is the way to derive quantitative stability data. This investigation should also afford a deeper understanding of the energetic rationale behind the differences observed - higher stability related to multi-binding (sum of the single association larger for the present system) and/or different contributions of the cooperative effect. However, even though a relatively moderate increase in the stability may be enough to slow down the kinetics, with respect to the NMR timescale, this novel distinct feature has a dramatic impact over a series of valuable aspects: clean evidence of the "all or nothing" self-assembling process; detailed solution NMR characterization with concomitant direct reliable comparison of spectroscopic structural-related features; high degree of control over the purity of the samples.

The future perspective may be that of translating a reliable modular approach to more appealing, *albeit* less trivial to handle, metallo-ligands (e.g. paramagnetic metal analogues), and get access to functional systems, featuring defined numbers of organized metal-active centers (*e.g.* magnetically, redox or catalytically active). The presence of peripheral antenna/photosensitizer units (the zinc-porphyrins) capable of absorbing visible light, and to form long-lived excited states, may also play a crucial role in these multi-component supramolecular hetero-metallic systems.

2.4 Experimental Section

Instrumentations and experimental procedures

NMR. 1D and 2D NMR (1D ^{1}H,^{13}C, ^{1}H DOSY and 2D HH–COSY, HSQC, HH–ROESY) experiments were recorded on a Varian Innova 500 (operating at 500 MHz for ^{1}H and 125 MHz for ^{13}C) or a Bruker Avance III spectrometer (operating at 400 MHz for ^{1}H and for 101 ^{13}C). All spectra were recorded at 298K and the ^{1}H chemical shifts were referenced to the peak of residual non deuterated solvents for ^{1}H: $CDCl_3$, δ = 7.26 ppm and for ^{13}C: $CDCl_3$, δ = 77.16 ppm. For 2D DOSY the *Bipolar Pulse Pair Stimulated Echo* with *convection compensation sequence* (bppste_cc) of VnmrJ software was implemented on the Varian spectrometer. For the DOSY analysis, the Bayesian DOSY transform from MestreNova was employed.

IR Spectroscopy. Infrared spectra were recorded on a Perkin Elmer Spectrum One Golden Gate FT/IR spectrometer in the transmission mode.

UV-Vis Absorption Spectroscopy. Absorption spectra were recorded in 1 cm path length quartz cell with an Agilent Cary 60 spectrophotometer.

Emission Spectroscopy. Emission spectra were recorded at 25 °C in 1 cm path length quartz cell with a Varian Cary Eclipse Fluorescence Spectrophotometer equipped with a Varian Cary Single Cell Peltier SPVF-1X0 temperature controller.

X-ray Analysis. Data collections were performed at the X-ray diffraction beamline (XRD1) of the Elettra Synchrotron, Trieste (Italy).[11] The crystals were dipped in NHV oil (Jena Bioscience, Jena, Germany) and mounted on the goniometer head with a nylon loop. Complete datasets were collected at 100 K (nitrogen stream supplied through an Oxford Cryostream 700 - Oxford Cryosystems Ltd., Oxford, United Kingdom) through the rotating crystal method. Data were acquired using a monochromatic wavelength of 0.700 Å, on a Pilatus 2M hybrid-pixel area detector (DECTRIS Ltd., Baden-Daettwil, Switzerland). The diffraction data were indexed and integrated using XDS.[12] Scaling have been done using CCP4-Aimless code.[13] Complete datasets for all the triclinic crystal forms of the molecules of interest have been obtained merging data collected from two different random orientations of one or two crystals. The structures were solved by the dual space algorithm implemented in the SHELXT code.[14] Fourier analysis and refinement were performed by the full-matrix least-squares methods based on F^2 implemented in SHELXL (Version 2017/1).[15] The Coot program was used for modeling.[16] Anisotropic thermal motion refinement have been used for all atoms with full occupancy. Geometric and thermal motion parameters restrains (DFIX, DANG, SIMU or DELU) have been applied on disordered and poorly defined fragments. Hydrogen atoms were included at calculated positions with isotropic $U_{factors} = 1.2 \cdot U_{eq}$ or $U_{factors} = 1.5 \cdot U_{eq}$ for hydroxyl and methyl groups (U_{eq} being the equivalent isotropic thermal factor of the bonded non hydrogen atom). All the structures contain relevant amount of solvent (in ~40% of cell volume), only partially ordered. Disordered solvent contributions that couldn't be modeled have been removed with Platon SQUEEZE routine[17] (the number of electrons squeezed and the cell volume voids are reported in Table 1S).

Geometrical assembly parameters have been calculated using Diamond software[18] and are reported in Tables 2.2 and 2.3. Essential crystal and refinement data are reported below in Table 1S. Pictures were prepared using either Ortep3 or Pymol software.[19]

Materials and Methods

All reagents were purchased from Sigma-Aldrich and used without further purification unless otherwise stated. [*trans*,*cis*,*cis*-$RuCl_2(CO)_2(Zn{\cdot}4'\text{-}cis\text{-DPyP})]_2$ (**1Zn**),[6] and Zinc(II)-meso-*tetra*phenylporphyrin (**ZnTPP**) were prepared as described earlier.[20]

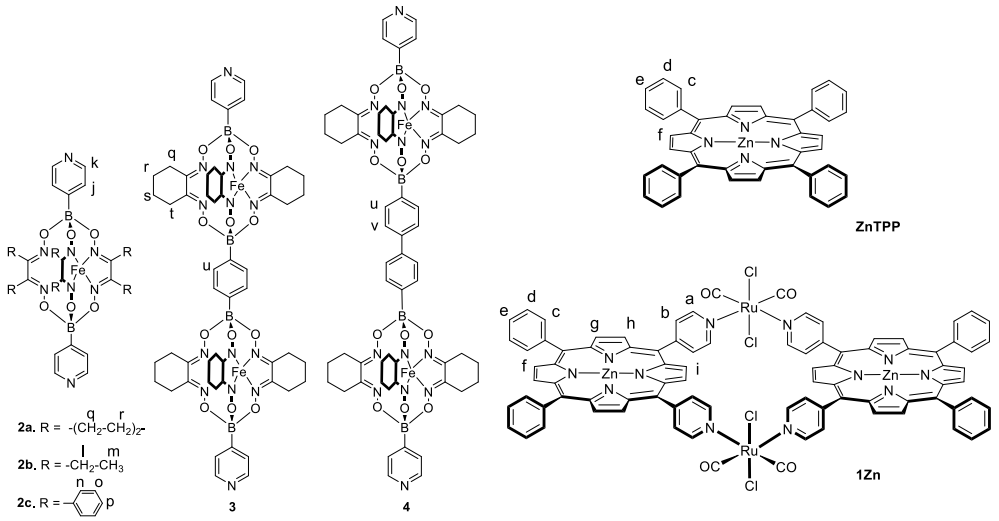

Schematic depiction with labeling of the building blocks: **ZnTPP**, **1Zn**, and 4'-dipyridyl-FeII(clathrochelate) ligands **2**-**4**.

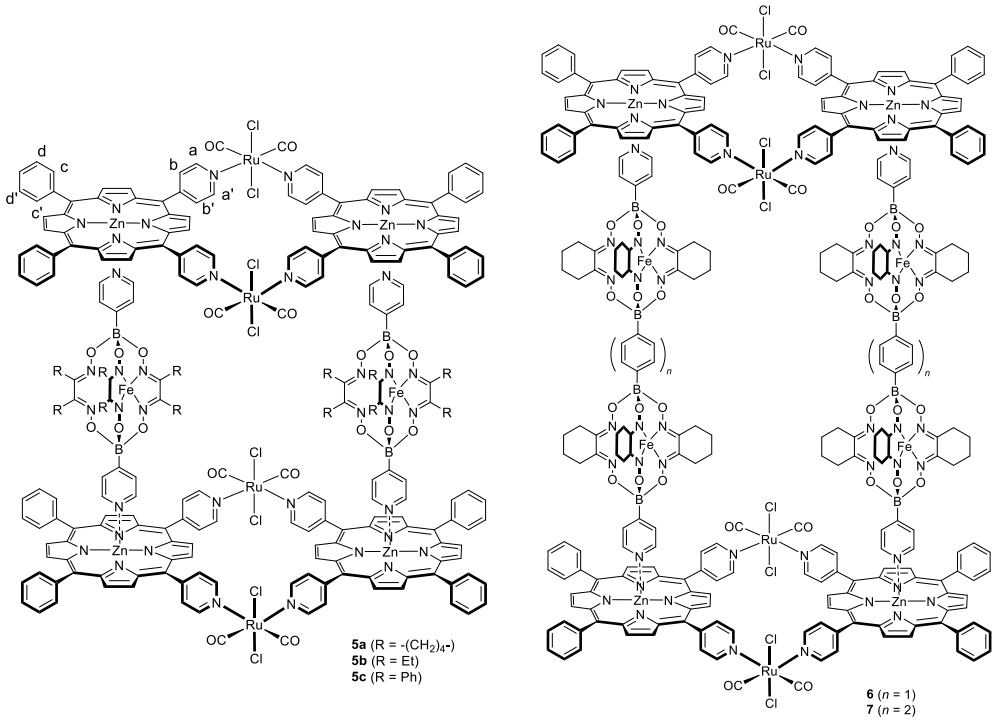

Schematic depiction of the supramolecular assemblies **5**-**7**.

Preparation of the assemblies {[*trans*,*cis*,*cis*-$RuCl_2(CO)_2$(Zn•4′-*cis*-DPyP)]$_2$}$_2${4′-dipyridyl-Fe^{II}(clathrochelate)]}$_2$ (**5-7**) and of the model compound (**8**) followed a common procedure here described for **5a**.

5a: 25.0 mg of **1Zn** (0.013 mmol) were dissolved in 10 mL of $CHCl_3$ and 8.7 mg of **2a** (0.013 mmol) were then added. The colour of the solution turned immediately from purple to deep violet. The homogeneous system was kept under stirring at room temperature for fifteen minutes. Diffusion of *n*-hexane over the deep red solution induced the precipitation of the pure product as a purple microcrystalline solid that was collected by filtration, washed with *n*-hexane, and vacuum-dried. Yield: 30.1 mg (94%).

^{1}H NMR (500 MHz, $CDCl_3$, 25°C) δ (ppm): 9.68 (d, *J* = 5.3 Hz, 8H; H_a), 9.57 (d, *J* = 5.3 Hz, 8H; $H_{a'}$), 8.98 (m, 32H; H_i, H_g, H_h, H_f), 8.57 (d, *J* = 5.4 Hz, 8H; H_b), 8.42 (d, *J* = 5.4 Hz, 8H; $H_{b'}$), 8.19 (m, 16H; H_c), 7.78 (m, 24H; H_d, H_e), 5.56 (d, *J* = 6.3 Hz, 8H; H_k), 2.14 (bs, 32H; H_j, H_q), 1.31 (2, 24H; H_r).

^{13}C NMR (125 MHz, $CDCl_3$, 25°C, from HSQC) δ (ppm): 150.60 (C_a), 150.21 ($C_{a'}$), 142.38 (C_j), 135.58 (C_c), 132.12 (C_b), 132.74 (C_f, C_g, C_h, C_i), 127.34 (C_k), 127.28 (C_d, C_e), 26.02 (C_q), 20.37 (C_r).

IR (KBr, selected bands): $\tilde{\upsilon}$ = 2065, 1999 (C=O), 1611 (C=N) cm^{-1}.

UV/Vis (chloroform): λ_{max} (ε, $M^{-1}cm^{-1}$) = 440, 570 ($7x10^4$), 610 nm.

Red needle-shaped single crystals have been obtained by slow diffusion of *n*-hexane over a chloroform solution of **5a** at room temperature.

5b: The same synthetic procedure described for **5a** was followed starting from 25.0 mg of **1Zn** (0.013 mmol) and 8.8 mg of **2b** (0.013 mmol). Yield: 29.7 mg (92%).

^{1}H NMR (500 MHz, $CDCl_3$, 25°C) δ (ppm): 9.69 (d, *J* = 5.4 Hz, 8H; H_a), 9.58 (d, *J* = 5.4 Hz, 8H; $H_{a'}$), 9.09 (s, 8H; H_i), 9.03 (s, 16H; H_g, H_h), 8.89 (s, 8H; H_f), 8.57 (d, *J* = 5.3 Hz, 8H; H_b), 8.48 (d, *J* = 5.3 Hz, 8H; $H_{b'}$), 8.23 (m, 16H; H_c, $H_{c'}$), 7.78 (m, 24H; H_d, H_e, $H_{d'}$), 5.59 (d, *J* = 6.4 Hz, 8H; H_j), 2.22 (d, *J* = 6.4 Hz, 8H; H_k), 2.10 (q, *J* = 7.5 Hz, 24H; H_l), 0.52 (t, *J* = 7.5 Hz, 36H; H_m).

^{13}C NMR (125 MHz, $CDCl_3$, 25°C, from HSQC) δ (ppm): 150.32 (C_a), 149.80 ($C_{a'}$), 141.11 (C_k), 134.61 (C_c, $C_{c'}$), 133.47 (C_g), 132.48 (C_f), 132.34 ($C_{b'}$), 132.14 (C_b), 130.90 (C_i), 130.86 (C_h), 127.59 (C_e), 126.55 (C_d), 126.25 ($C_{d'}$), 125.14 (C_j), 19.19 (C_l), 10.74 (C_m).

IR (KBr, selected bands): $\tilde{\upsilon}$ = 2065, 1999 (C=O), 1611 (C=N) cm^{-1}.

UV/Vis (chloroform): λ_{max} (ε, $M^{-1}cm^{-1}$) = 441, 570 ($7x10^4$), 611 nm.

Red needle-shaped single crystals have been obtained by slow diffusion of *n*-hexane over a chloroform solution of **5b** at room temperature.

5c: The same synthetic procedure described for **5a** was followed starting from 25.0 mg of **1Zn** (0.013 mmol) and 12.6 mg of **2c** (0.013 mmol). Yield: 33.2 mg (92%).

^{1}H NMR (500 MHz, $CDCl_3$, 25°C) δ (ppm): 9.70 (d, *J* = 5.4 Hz, 8H; H_a), 9.61 (d, *J* = 5.4 Hz, 8H; $H_{a'}$), 9.01 (s, 8H; H_i), 8.95 (s, 16H; H_g, H_h), 8.83 (s, 8H; H_f), 8.50 (d, *J* = 5.3 Hz, 8H; H_b), 8.33 (d, *J* = 5.3 Hz, 8H: $H_{b'}$), 8.18 (d, *J* = 6.3 Hz, 8H; H_c), 8.11 (d, *J* = 6.4 Hz, 8H; $H_{c'}$), 7.76 (m, 24H; H_d, H_e, $H_{d'}$), 7.13 (t, *J* = 7.4 Hz, 12H; H_p), 6.86 (t, *J* = 7.7 Hz, 24H; H_o), 6.69 (d, *J* = 7.5 Hz, 24H; H_n), 5.22 (d, *J* = 7.0 Hz, 8H; H_j), 2.03 (d, *J* = 7.0 Hz, 8H; H_k).

^{13}C NMR (125 MHz, $CDCl_3$, 25°C, from HSQC) δ (ppm): 150.26 (C_a), 149.52 ($C_{a'}$), 140.79 (C_k), 134.49 ($C_{c'}$), 134.47 (C_c), 133.33 (C_g), 132.41 (C_f), 132.89 ($C_{b'}$), 131.91 (C_b), 130.79 (C_h), 130.48 (C_i), 129.96 (C_n), 129.71 (C_p), 127.45 (C_e), 127.34 (C_o), 126.49 (C_d), 126.13 ($C_{d'}$), 125.19 (C_j).

IR (KBr, selected bands): $\tilde{\upsilon}$ = 2065, 1999 (C=O), 1611 (C=N) cm^{-1}.

UV/Vis (chloroform): λ_{max} (ε, $M^{-1}cm^{-1}$) = 440, 492, 569 ($7x10^4$), 610 nm.

Red needle-shaped single crystals have been obtained by slow diffusion of *n*-hexane over a chloroform solution of **5c** at room temperature.

6: The same synthetic procedure described for **5a** was followed starting from 25.0 mg of **1Zn** (0.013 mmol) and 16.3 mg of **2** (0.013 mmol). Yield: 36.9 mg (93%).

^{1}H NMR (500 MHz, $CDCl_3$, 25°C) δ (ppm): 9.74 (d, *J* = 5.6 Hz, 8H; H_a), 9.66 (d, *J* = 5.6 Hz, 8H; $H_{a'}$), 9.06 (m, 32H; H_f, H_g, H_h, H_i), 8.62 (d, *J* = 5.5 Hz, 8H; H_b), 8.53 (d, *J* = 5.6 Hz, 8H; $H_{b'}$), 8.26 (m, 16H; H_c), 7.79 (m, 24H: H_d, H_e), 7.38 (s, 8H; H_u), 5.72 (d, *J* = 6.0 Hz, 8H; H_k), 2.61 (s, 12H; H_i, H_q), 2.31 (s, 12H; H_t), 2.23 (d, *J* = 6.0 Hz, 8H; H_j), 1.48 (s, 24H; H_r, H_s).

^{13}C NMR (125 MHz, $CDCl_3$, 25°C, from HSQC) δ (ppm): 151.32 (C_a), 150.10 ($C_{a'}$), 142.60 (C_j), 134.24 (C_f, C_g, C_h, C_i), 133.84 (C_c), 133.34 ($C_{b'}$), 132.80 (C_b), 130.80 (C_u), 128.10 (C_k), 127.40 (C_d, C_e), 28.10 (C_q), 27.60 (C_t), 20.80 (C_r, C_s).

IR (KBr, selected bands): $\tilde{\upsilon}$ = 2065, 1999 (C=O), 1611 (C=N) cm^{-1}.

UV/Vis (chloroform): λ_{max} (ε, $M^{-1}cm^{-1}$) = 438, 568, ($7x10^4$), 609 nm.

Red needle-shaped single crystals have been obtained by slow diffusion of *n*-hexane over a chloroform solution of **6** at 4 °C.

7: the same synthetic procedure described for **5a** was followed starting from 25.0 mg of **1Zn** (0.013 mmol) and 17.3 mg of **3** (0.013 mmol). Yield: 37.5 mg (92%).

^{1}H NMR (500 MHz, $CDCl_3$, 25°C) δ (ppm): 9.73 (d, *J* = 5.5 Hz, 8H, H_a), 9.66 (d, *J* = 5.5 Hz, 8H, $H_{a'}$), 9.05 (m, 32H; H_f, H_g, H_h, H_i), 8.62 (d, *J* = 5.4 Hz, 8H; H_b), 8.54 (d, *J* = 5.5 Hz, 8H; $H_{b'}$), 8.26 (m, 16H; H_c), 7.80 (m, 24H, H_d, H_e), 7.51 (d, *J* = 8.8 Hz, 8H; H_u), 7.40 (d, *J* = 8.8 Hz, 8H; H_v), 5.74 (d, *J* = 6.4 Hz, 8H; H_k), 2.68 (s, 12H; H_q), 2.34 (s, 12H; H_t), 2.27 (d, *J* = 6.3 Hz, 8H; H_j), 1.51 (s, 24H, H_r, H_s).

^{13}C NMR (125 MHz, $CDCl_3$, 25°C, from HSQC) δ (ppm): 151.67 (C_a), 151.10 ($C_{a'}$), 143.69 (C_j), 134.70 (C_b), 134.24 (C_f, C_g, C_h, C_i), 133.80 (C_c), 133.67 (C_u), 133.10 ($C_{b'}$), 128.32 (C_d, C_e), 127.29 (C_v, C_k), 27.07 (C_q), 26.13 (C_t), 20.77 (C_r, C_s).

IR (KBr, selected bands): $\tilde{\upsilon}$ = 2065, 1999 (C=O), 1611 (C=N) cm^{-1}.

UV/Vis (chloroform): λ^{max} (ε, $M^{-1}cm^{-1}$) = 438, 568, ($7x10^4$), 609 nm.

Red needle-shaped single crystals have been obtained by slow diffusion of *n*-hexane over a chloroform solution of **7** at 4 °C.

8: the same synthetic procedure described for **5a** was followed starting from 3.2 mg of **2a** (0.005 mmol) and 6.6 mg of **ZnTPP** (0.009 mmol). Yield: 8.9 mg (91%).

^{1}H NMR (400 MHz, $CDCl_3$, 25°C) δ (ppm): 8.83 (s, 16H; H_f), 8.19 (d, J(H,H) = 6.8 Hz, 16H; H_c), 7.69 (m, 24H; H_d, H_e), 5.77 (s, 4H, H_j), 2.84 (s, 4H; H_k), 2.29 (s, 12H; H_q) 1.43 (s, 12H; H_r).

^{13}C NMR (100 MHz, $CDCl_3$, 25°C, from HSQC) δ (ppm): 134.66 (C_c), 131.52 (C_f), 126.45 (C_d, C_e), 125.18 (C_j), 25.72 (C_q), 21.20 (C_r).

UV/Vis (chloroform): λ^{max} = 424, 553, 594 nm.

Red needle-shaped single crystals have been obtained by slow diffusion of ether vapour over a dichloromethane solution of **8** at room temperature.

Spectrofluorimetric dilution titration. The spectrofluorimetric dilution titration experiment was performed recording emission spectra (λ_{ex} = 550 nm, 1 cm path length quartz cuvette) of progressive diluted chloroform solutions of **5c**, starting from a $5x10^{-5}$ M stock solution. The concentration was checked by absorption spectroscopy.

Self-sorting experiments. The study on mixtures of **1Zn**, **2a** and **3** followed three parallel procedures, by keeping the **1Zn**/**2a**/**3** ratio fixed at 2/1/1:

1) 0.52 mg of **2a** ($0.8x10^{-3}$ mmol) and 0.98 mg of **3** ($0.8x10^{-3}$ mmol) were dissolved in 0.7 mL of $CDCl_3$ and the ligand stoichiometric ratio was checked by ^{1}H NMR; 3 mg of **1Zn** ($1.6x10^{-3}$ mmol) were then added. The resulting homogeneous solution was monitored over time by ^{1}H NMR spectroscopy.
2) 3.50 mg of **5a** ($7.1x10^{-4}$ mmol) and 4.31 mg of **6** ($7.1x10^{-4}$ mmol) were dissolved in 1 mL of $CDCl_3$ and the resulting homogeneous solution was monitored over time by ^{1}H NMR spectroscopy.
3) 3.51 mg of **1Zn** ($1.8x10^{-3}$ mmol), 0.61 mg of **2a** ($0.9x10^{-3}$ mmol) and 1.15 mg of **3** ($0.9x10^{-3}$ mmol) were dissolved in 0.7 mL of $CDCl_3$ and the resulting homogeneous solution was monitored over time by ^{1}H NMR spectroscopy.

The study on mixtures of **1Zn**, **2a** and **2c** was performed by following a single procedure: 0.52 mg of **2a** ($0.8x10^{-3}$ mmol) and 0.76 mg of **2c** ($0.8x10^{-3}$ mmol) were in 0.7 mL of $CDCl_3$ and the ligand

stoichiometric ratio was checked by ^{1}H NMR; 3 mg of **1Zn** ($1.6x10^{-3}$ mmol) were then added and the resulting homogeneous solution was monitored over time by ^{1}H NMR spectroscopy.

NMR titration experiment. To a $CDCl_3$ solution (ca. 5 mM) of **2a**, were added weighed amounts of **ZnTPP** (0.2 eq for each addition), and the ^{1}H NMR spectra were recorded. **ZnTPP** was added until the chemical shifts of the adduct did not change. The apparent *K*f value at room temperature (ca. 10^7 M^{-2}) was obtained by nonlinear regression analyses of the chemical shifts data (for Hk and Hq) versus concentration of **ZnTPP**. The data fit was made using a 1:2 binding model of the software package BindFit (www.supramolecular.org).

Table 1S. Crystallographic data and refinement details for **5a**, **5a'**, **6** and **7**.

	5a·8$CHCl_3$·14C_6H_{14} [$C_{232}H_{168}B_4Cl_8Fe_2N_{40}O_{20}Ru_4Zn_4$·8$CHCl_3$·14$C_6H_{14}$]	**5a'**·10$CHCl_3$·2.5C_6H_{14} [$C_{232}H_{168}B_4Cl_8Fe_2N_{40}O_{20}Ru_4Zn_4$·10$CHCl_3$·2.5$C_6H_{14}$]	**6**·10$CHCl_3$·19C_6H_{14} [$C_{280}H_{224}B_8Cl_8Fe_4N_{52}O_{32}Ru_4Zn_4$·10$CHCl_3$·19$C_6H_{14}$]	**7**·30$CHCl_3$·6C_6H_{14} [$C_{292}H_{232}B_8Cl_8Fe_4N_{52}O_{32}Ru_4Zn_4$·30$CHCl_3$·6$C_6H_{14}$]
Chemical Formula	$C_{324}H_{372}B_4Cl_{32}Fe_2N_{40}O_{20}Ru_4Zn_4$	$C_{257}H_{213}B_4Cl_{38}Fe_2N_{40}O_{20}Ru_4Zn_4$	$C_{404}H_{500}B_8Cl_{38}Fe_4N_{52}O_{32}Ru_4Zn_4$	$C_{358}H_{346}B_8Cl_{98}Fe_4N_{52}O_{32}Ru_4Zn_4$
Formula weight (g/mol)	7101.69	6349.46	8919.27	10338.59
Temperature (K)	100(2)	100(2)	100(2)	100(2)
Wavelength (Å)	0.700	0.700	0.700	0.700
Crystal system	Triclinic	Triclinic	Triclinic	Triclinic
Space Group	*P* -1	*P* -1	*P* -1	*P* -1
Unit cell dimensions	*a* = 20.066(4) Å	*a* = 19.346(4) Å	*a* = 21.169(4) Å	*a* = 18.739(4) Å
	b = 23.667(5) Å	*b* = 20.732(4) Å	*b* = 24.320(5) Å	*b* = 22.432(4) Å
	c = 24.049(5) Å	*c* = 20.762(4) Å	*c* = 25.085(5) Å	*c* = 34.773(7) Å
	α = 65.22(3) °	α = 95.56(3)°	α = 71.92(3)°	α = 93.97(3)°
	β = 85.10(3) °	β = 96.28(3)°	β = 78.09(3)°	β = 98.48(3)°
	γ = 65.02(3) °	γ = 115.68(3)°	γ = 78.51(3)°	γ = 113.24(3)°
Volume (Å^3)	9341(4)	7363(3)	11885(5)	13152(5)
Z	1	1	1	1
Density (calculated) (g·cm^{-3})	1.263	1.432	1.246	1.305
Absorption coefficient (mm^{-1})	0.734	0.972	0.679	0.901
F(000)	3668	3209	4630	5220
Crystal size (mm^3)	0.03 x 0.03 x 0.01	0.03 x 0.01 x 0.01	0.03 x 0.03 x 0.01	0.03 x 0.03 x 0.01
Crystal habit	Red thin plates	Red thin needles	Red thin plates	Red thin plates
Theta range for data collection	0.92° to 24.01°	1.09° to 15.38°	0.85° to 22.36°	1.22° to 20.07°
Resolution (Å)	0.86	1.3	0.92	1.02
Index ranges	-23 ≤ h ≤ 23 -24 ≤ k ≤ 27 0 ≤ l ≤ 27	-14 ≤ h ≤ 14 -15 ≤ k ≤ 15 -15 ≤ l ≤ 15	-23 ≤ h ≤ 22 -26 ≤ k ≤ 26 -26 ≤ l ≤ 27	-18 ≤ h ≤ 18 -21 ≤ k ≤ 21 -34 ≤ l ≤ 34
Reflections collected	86606	25024	91167	93481
Independent reflections (data with I>2σ(I))	30121 (18002)	6691 (4229)	30935 (15321)	25660 (12973)

Data multiplicity (max resltn)	2.82 (2.81)	3.73 (3.72)	2.86 (2.12)	3.61 (3.57)
I/σ(I) (max resltn)	10.48 (3.27)	3.14 (2.53)	6.97 (1.43)	4.58 (1.40)
R_{merge} (max resltn)	0.1087 (0.4891)	0.1563 (0.2758)	0.0857 (0.5018)	0.1173 (0.5347)
Data completeness (max resltn)	98.1% (97.5%)	99.9% (99.9%)	96.9% (92.9%)	99.0% (98.9%)
Refinement method	Full-matrix least-squares on F^2	Full-matrix least-squares on F^2	Full-matrix least-squares on F^2	Full-matrix least-squares on F^2
Data / restraints / parameters	30121 / 177 / 1652	6691 / 97 / 1061	30935 / 197 / 2004	25660 / 515 / 2032
Goodness-of-fit on F^2	1.011	1.120	1.043	0.944
Δ/σ_{max}	0.014	0.009	0.024	0.027
Final R indices [I>2σ(I)]	R_1 = 0.0919, wR_2 = 0.2529	R_1 = 0.1286, wR_2 = 0.3036	R_1 = 0.1190, wR_2 = 0.2867	R_1 = 0.1309, wR_2 = 0.2796
R indices (all data)	R_1 = 0.1436, wR_2 = 0.2993	R_1 = 0.1791, wR_2 = 0.3538	R_1 = 0.1897, wR_2 = 0.3302	R_1 = 0.1973, wR_2 = 0.3253
Largest diff. peak and hole (eÅ^{-3})	0.951 and -0.948	0.874 and -0.457	1.060 and -0.746	1.118 and -0.851
R.M.S. deviation from mean (eÅ^{-3})	0.121	0.120	0.110	0.105
Squeezed electrons (e/cell)	616	42	866	1160
Squeezed Voids Volume (Å^3/cell) (%)	2429 (26.0%)	296 (4.0%)	3229 (27.2%)	3893 (29.6%)
Total Solvent Voids Volume (Å^3/cell) (%)	4798 (51.4%)	2879 (39.1%)	6237 (52.5%)	3903 (29.7%)

$$R_1 = \Sigma \; ||Fo|-|Fc|| \; / \; \Sigma \; |Fo|; \; wR_2 = \{\Sigma \; [w(Fo^2 - Fc^2)^2] \; / \; \Sigma \; [w(Fo^2)^2]\}^{½}$$

Table 2S (cont.). Crystallographic data and refinement details for **5b**, **5c** and **8**.

	5b·6CHCl$_3$·2C$_6$H$_{14}$ [C$_{232}$H$_{180}$B$_4$Cl$_8$Fe$_2$N$_{40}$O$_{20}$Ru$_4$Zn$_4$·8CHCl$_3$·14C$_6$H$_{14}$]	**5c**·17CHCl$_3$·8C$_6$H$_{14}$ [C$_{280}$H$_{180}$B$_4$Cl$_8$Fe$_2$N$_{40}$O$_{20}$Ru$_4$Zn$_4$·17CHCl$_3$·8C$_6$H$_{14}$]	**8**·6C$_6$H$_{14}$ [C$_{116}$H$_{88}$B$_2$FeN$_{16}$O$_6$Zn$_2$·6C$_6$H$_{14}$]
Chemical Formula	C$_{324}$H$_{384}$B$_4$Cl$_{32}$Fe$_2$N$_{40}$O$_{20}$Ru$_4$Zn$_4$	C$_{345}$H$_{309}$B$_4$Cl$_{59}$Fe$_2$N$_{40}$O$_{20}$Ru$_4$ Zn$_4$	C$_{152}$H$_{172}$B$_2$FeN$_{16}$O$_6$Zn$_2$
Formula weight (g/mol)	7113.79	8247.56	2527.26
Temperature (K)	100(2)	100(2)	100(2)
Wavelength (Å)	0.700	0.700	0.71073
Crystal system	Monoclinic	Triclinic	Triclinic
Space Group	*P* 2$_1$/*n*	*P* -1	*P* -1
Unit cell dimensions	*a* = 8.525(2) Å	*a* = 19.644(4) Å	*a* = 14.058(6) Å
	b = 38.882(8) Å	*b* = 22.480(5) Å	*b* = 20.156(10) Å
	c = 41.176(8) Å	*c* = 23.784(5) Å	*c* = 24.184(5) Å
	α = 90°	α = 103.22(3)°	α = 107.66(3)°
	β = 90.85(3)°	β = 96.95(3)°	β = 99.59(3)°
	γ = 90°	γ = 112.44(3)°	γ = 103.18(3)°
Volume (Å^3)	13647(5)	9194(4)	6149(4)
Z	2	1	2
Density (calculated) (g·cm^{-3})	1.731	1.490	1.365
Absorption coefficient (mm^{-1})	1.006	0.936	0.572
F(000)	7360	4190	2680
Crystal size (mm^3)	0.02 x 0.02 x 0.01	0.05 x 0.03 x 0.01	0.27 x 0.22 x 0.09
Crystal habit	Red thin plates	Red thin plates	Purple plates

Theta range for data collection	0.71° to 19.28°	0.89° to 29.08°	1.11° to 20.00°
Resolution (Å)	1.06	0.72	1.04
Index ranges	-8 ≤ h ≤ 8 0 ≤ k ≤ 36 0 ≤ l ≤ 38	-27 ≤ h ≤ 27 -31 ≤ k ≤ 30 0 ≤ l ≤ 33	-13 ≤ h ≤ 13 -19 ≤ k ≤ 19 -23 ≤ l ≤ 23
Reflections collected	31434	143802	39572
Independent reflections (data with I>2σ(I))	11772 (6967)	50168 (38623)	11394 (6977)
Data multiplicity (max resltn)	2.60 (2.39)	2.79 (2.58)	3.45 (2.54)
I/σ(I) (max resltn)	5.33 (1.96)	11.93 (5.46)	6.14 (2.17)
R_{merge} (max resltn)	0.1162 (0.3822)	0.0367 (0.1377)	0.1197 (0.3276)
Data completeness (max resltn)	98.3% (98.6%)	97.3% (95.3%)	99.2% (97.8%)
Refinement method	Full-matrix least-squares on F^2	Full-matrix least-squares on F^2	Full-matrix least-squares on F^2
Data / restraints / parameters	11772 / 89 / 925	50168 / 192 / 2021	11394 / 2113 / 1397
Goodness-of-fit on F^2	1.037	1.029	1.058
Δ/σ_{max}	0.011	0.005	0.000
Final R indices [I>2σ(I)]	R_1 = 0.1202, wR_2 = 0.2926	R_1 = 0.0880, wR_2 = 0.2572	R_1 = 0.1036, wR_2 = 0.2681
R indices (all data)	R_1 = 0.1857, wR_2 = 0.3393	R_1 = 0.1052, wR_2 = 0.2747	R_1 = 0.1601, wR_2 = 0.3195
Largest diff. peak and hole (eÅ^{-3})	1.224 and -0.712	3.777 and -1.950	0.539 and -0.603
R.M.S. deviation from mean (eÅ^{-3})	0.143	0.144	0.131
Squeezed electrons (e/cell)	193	431	618
Squeezed Voids Volume (Å^3/cell) (%)	1081 (7.9%)	1428 (15.5%)	1762 (28.7%)
Total Solvent Voids Volume (Å^3/cell) (%)	3453 (25.3%)	3993 (43.4%)	1762 (28.7%)

$$R_1 = \Sigma \; ||F_O|-|F_C|| \; / \; \Sigma \; |F_O|; \; wR_2 = \{\Sigma \; [w(F_O^2 - F_C^2)^2] \; / \; \Sigma \; [w(F_O^2)^2]\}^{½}$$

2.5 References

[1] For reviews about metalloligands see: a) Y.-Y. Zhang, W.-X. Gao, L. Lin, G.-X. Jin *Coord. Chem. Rev.* 2017, *344*, 323; b) S. Srivastava, R. Gupta, *CrystEngComm* 2016, *18*, 9185; c) L. Ll, D. J. Fanna, N. D. Shepherd, L. F. Lindoy, F. Li, *J. Incl. Phenom. Macrocycl. Chem.* 2015, *82*, 3; d) H. Li, Z.-J. Yao, D. Liu, G.-X. Jin, *Coord. Chem. Rev.* 2015, *293-294*, 139-157; e) M. D. Wise, K. Severin, *Chimia* 2015, *69*, 191; f) G. Kumar and R. Gupta, *Chem. Soc. Rev.* 2013, *42*, 9403; g) M. C. Das, S. Xiang, Z. Zhang, B. Chen, *Angew. Chem., Int. Ed.* 2011, *50*, 10510; h) E. C. Constable, *Coord. Chem. Rev.*, 2008, 252, 842-855.

[2] E. Pardo, R. Ruiz-García, J. Cano, X. Ottenwaelder, R. Lescouëzec, Y. Journaux, F. Lloret, M. Julve, *Dalton Trans.* 2008, 2780-2805.

[3] For selected examples see: a) M. Marmier, G. Cecot, A. V. Vologzhanina, J. L. Bila, I. Zivkovoc, H. M. Ronnow, B. Nafradi, E. Solari, P. Pattison, R. Scopelliti, K. Severin, *Dalton Trans.* 2016, *45*, 15507; b) M. Marmier, M. D. Wise, J. J. Holstein, P. Pattison, K. Schenk, E. Solari, R. Scopelliti, K. Severin, *Inorg. Chem.* 2016, *55*, 4006; c) Y.-Y. Zhang, Y.-J. Lin, G.-X. Jin, *Chem. Commun.,* 2014, *50*, 2327S; d) Zhang, L. Han, L. Li, J. Cheng, D. Yian, J. Luo, *Cryst. Growth Des.* 2013, *13*, 5466; e) A.-L. Cheng, N. Liu, J.-Y. Zhang, E.-Q. Gao, *Inorg. Chem.* 2007, *46*, 1034; f) K.-T. Youm, M. G. Kim, J. Ko, M.-J. Jun, *Angew. Chem. Int. Ed.* 2006, *45*, 4003.

[4] a) S.M. Jansze, G. Cecot, K. Severin *Chem. Sci.,* 2018, *9*, 4253; b) G. Cecot, M. Marmier, S. Geremia, R. De Zorzi, A. V. Vologzhanina, P. Pattison, E. Solari, F. F. Tirani, R. Scopelliti, K. Severin, *J. Am. Chem. Soc.* 2017, *139*, 8371; c) S. M. Jansze, M. D. Wise, A. V. Vologzhanina, R. Scopelliti, K. Severin, *Chem. Sci.* 2017, *8*, 1901; d) S. Jansze, G. Cecot, M. D. Wise, K. O. Zhurov, T. K. Ronson, A. M. Castilla, A. Finelli, P. Pattison, E. Solari, R. Scopelliti, G. E. Zelinskii, A. V. Volgzhanina, Y. Z. Voloshin, J. R. Nitschke, K. Severin, *J. Am. Chem. Soc.* 2016, *138*, 2046; e) G. Cecot, B. Alameddine, S. Prior, R. De Zorzi, Silvano Geremia, R. Scopelliti, F. T. Fadaei, E. Solari, K. Severin, *Chem. Commun.* 2016, *52*, 11243; f) A. Ardavan, A. M. Bowen, A. Fernandez, A. J. Fielding, D. Kaminski, F. Moro, C. A. Muryn, M. D. Wise, A. Ruggi, E. J. L. McInnes, K. Severin, G. A. Timco, C. R. Timmel, F. Tuna, G. F. S. Whitehead, R. E. P. Winpenny, *npj Quant. Inf.* 2015, *1*, 15012; g) M. D. Wise, J. J. Holstein, P. Pattison, C. Besnard, E. Solari, R. Scopelliti, G. Bricogne, K. Severin, *Chem. Sci*. 2015, *6*, 1004-1010; h) M. D. Wise, A. Ruggi, M. Pascu, R. Scopelliti, K. Severin, *Chem. Sci.* 2013, *4*, 1658; i) S. M. Jansze, K. Severin, *Acc. Chem. Res.* 2018, *51*, 2139.

[5] For further examples see: a) G. E. Zelinskii, A. S. Chuprin, A. S. Belov, V. V. Novikov, A. V. Vologzhanina, E. G. Lebed, Y. Z. Voloshin, *Inorg. Chim. Acta* 2016, *453*, 210; b) G. E. Zelinskii, A. S. Belov, E. G. Lebed, A. V. Vologzhanina, V. V. Novikov and Y. Z. Voloshin, *Inorg. Chim. Acta* 2016, *440*, 154; c) I. G. Belaya, S. V. Svidlov, A. V. Dolganov, G. E. Zelinskii, T. V. Potapova, A. V. Vologzhanina, O. A. Varzatskii, Y. N. Bubnov, Y. Z. Voloshin, *Dalton Trans.* 2013, *42*, 13667; d) Y. Z. Voloshin, N. A. Kostromina, R. K. Krämer, *Clathrochelates. Synthesis, Structure and Properties*; Elsevier: Amsterdam, 2002.

[6] a) E. Iengo, E. Zangrado, R. Minatel, E. Alessio, *J. Am. Chem. Soc.* 2002, *124*, 1003-1013; b) E. Iengo, E. Zangrando, M.Bellini, E. Alessio, A. Prodi, C. Chiorboli, F. Scandola, *Inorg.Chem*. 2005, 44, 9752.

[7] a) E. Alessio, M. Casanova, E. Zangrando, E. Iengo, *Chem. Commun.* 2012, *48*, 5112; b) M.T. Indelli, C. Chiorboli, F. Scandola, E. Iengo. P. Osswald, F. Würthner, *J. Phys. Chem. B* 2010, *114,* 14495; c) A. Prodi, C. Chiorboli, F. Scandola, E. Iengo, E. Alessio, *ChemPhysChem* 2006, *7*, 1514.

[8] For a reviews see: a) E. Iengo, P. Cavigli, D. Milano, P. Tecilla, *Inorg. Chim. Acta* 2014, *417*, 59; b) E. Iengo, E. Zangrando, E. Alessio, *Eur. J. Inorg. Chem.* 2003, 2371.

[9] L. Avram, Y. Cohen, *Chem. Soc. Rev.* 2015, *44*, 586.

[10] A. Macchioni, G. Ciancaleoni, C. Zuccaccia, D. Zuccaccia, *Chem. Soc. Rev.* 2008, *37*, 479.

[11] A. Lausi, M. Polentarutti, S. Onesti, J. R. Plaisier, E. Busetto, G. Bais, L. Barba, A. Cassetta, G. Campi, D. Lamba, A. Pifferi, S. C. Mande, D. D. Sarma, S. M. Sharma, G. Paolucci, *The European Physical Journal Plus* 2015, *130* (43), 1.

[12] W. Kabsch, *Acta Cryst. D* 2010, *66*, 125-132.

[13] a) M. D. Winn, C. C. Ballard, K. D. Cowtan, E. J. Dodson, P. Emsley, P. R. Evans, R. M. Keegan, E. B. Krissinel, A. G. W. Leslie, A. McCoy, S. J. McNicholas, G. N. Murshudov, N. S. Pannu, E. A. Potterton, H. R. Powell, R. J. Read, A. Vagin, K. S. Wilson, *Acta Cryst. D* 2011, *67*, 235-242; b) P. R. Evans, G. N. Murshudov, *Acta Cryst. D* 2013, *69*, 1204-1214.

[14] G. M. Sheldrick, *Acta Cryst*. 2015, *A71*, 3-8.

[15] P. Emsley, B. Lohkamp, W. Scott, K. Cowtan, *Acta Cryst. D* 2010, *66*, 486-501.

[16] A. L. Spek, *Acta Cryst. D* 2009, *65*, 148-155.

[17] Diamond - Crystal and Molecular Structure Visualization, Crystal Impact - K. Brandenburg & H. Putz GbR, Rathausgasse 30, D-53111 Bonn.

[18] L. Farrugia, *Journal of Applied Crystallography* 2012, *45*, 849-854.

[19] L. Schrodinger, *The PyMOL Molecular Graphics System*, Schrodinger, 2015, LLC.

[20] E. B. Fleischer, A. M. Shachter, *Inorg. Chem.* 1991, *30*, 3763-3769.

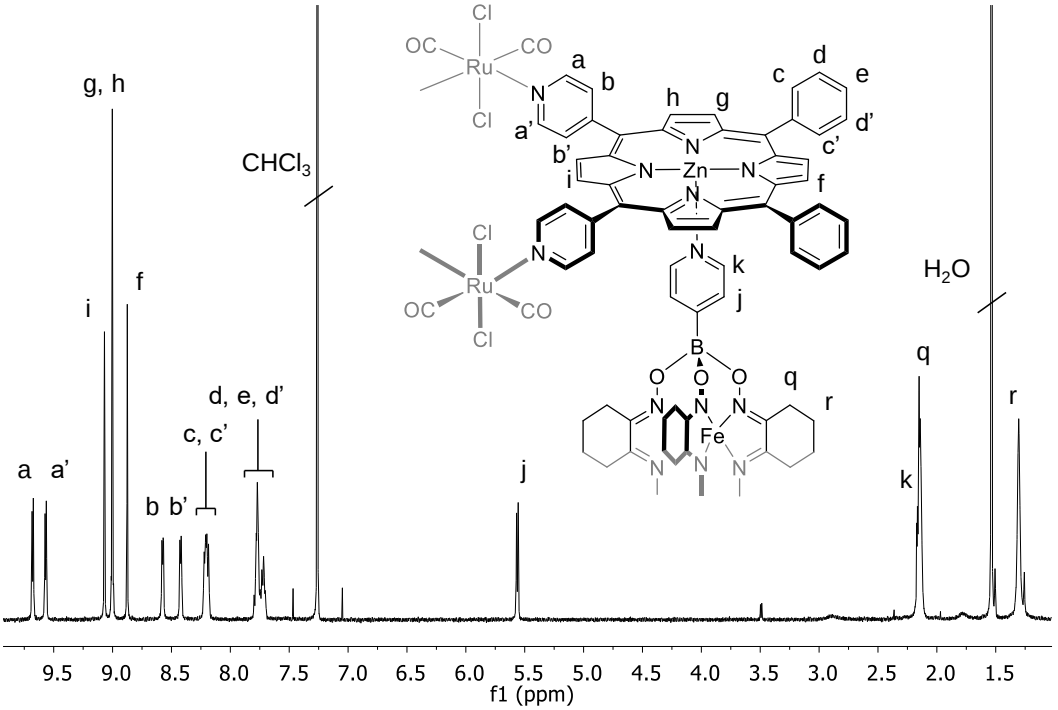

Figure A2.1. ^{1}H NMR spectrum ($CDCl_3$) of **5a**

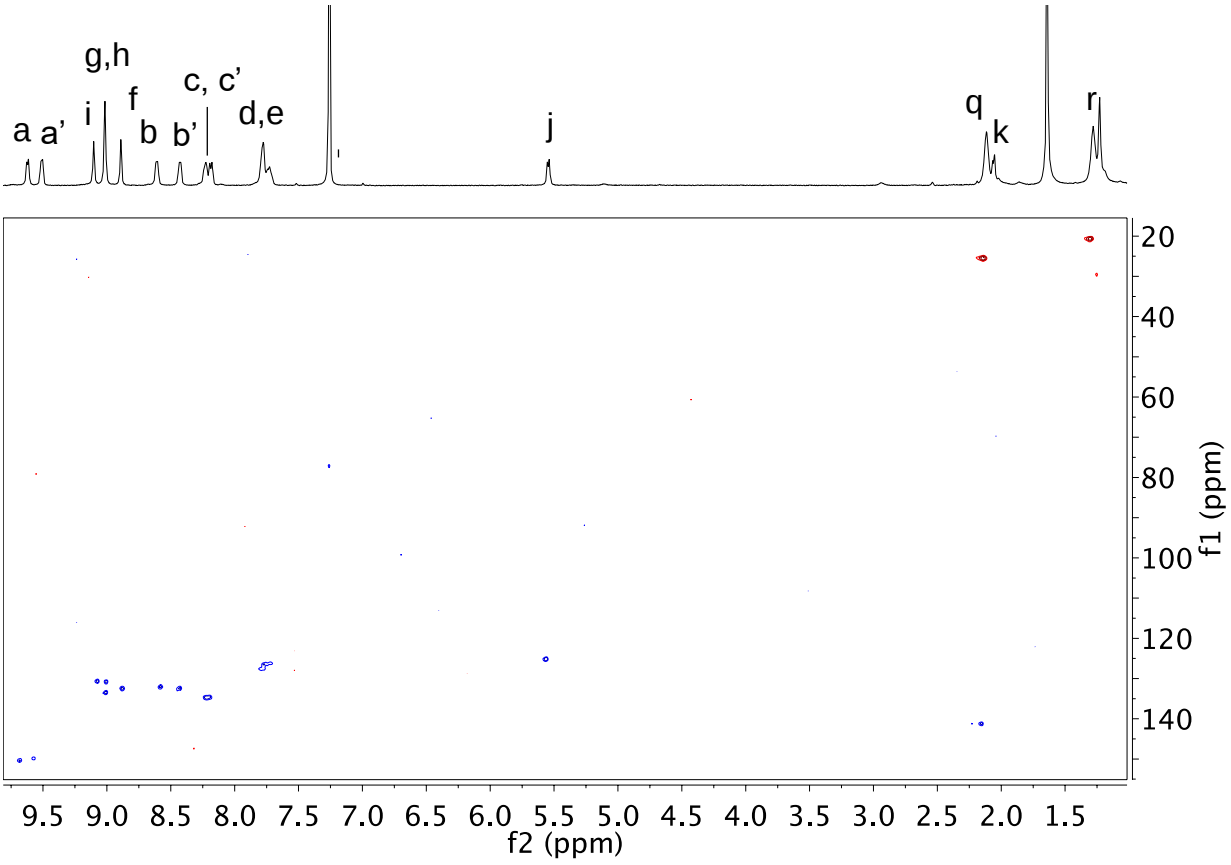

Fig Figure A2.2. H-C COSY spectrum ($CDCl_3$) of **5a**.

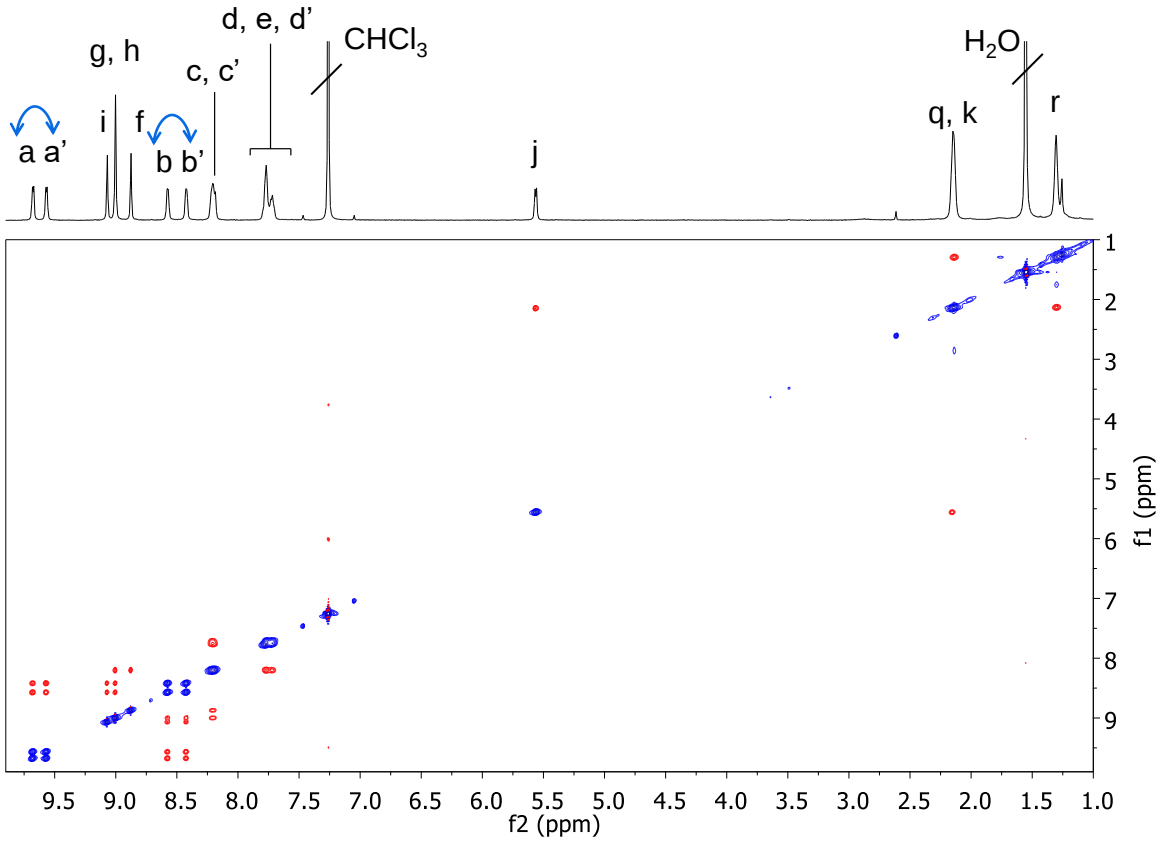

Figure A2.3. H-H ROESY spectrum ($CDCl_3$) of **5a**.

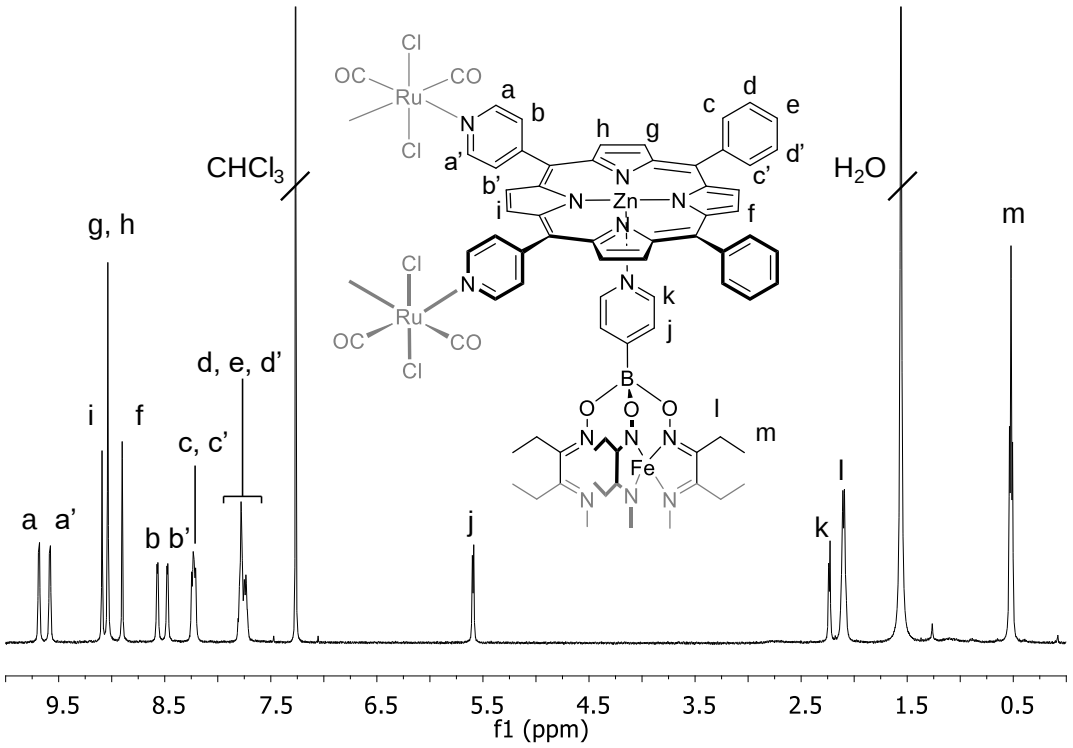

Figure A2.4. ^1H NMR spectrum ($CDCl_3$) of **5b**.

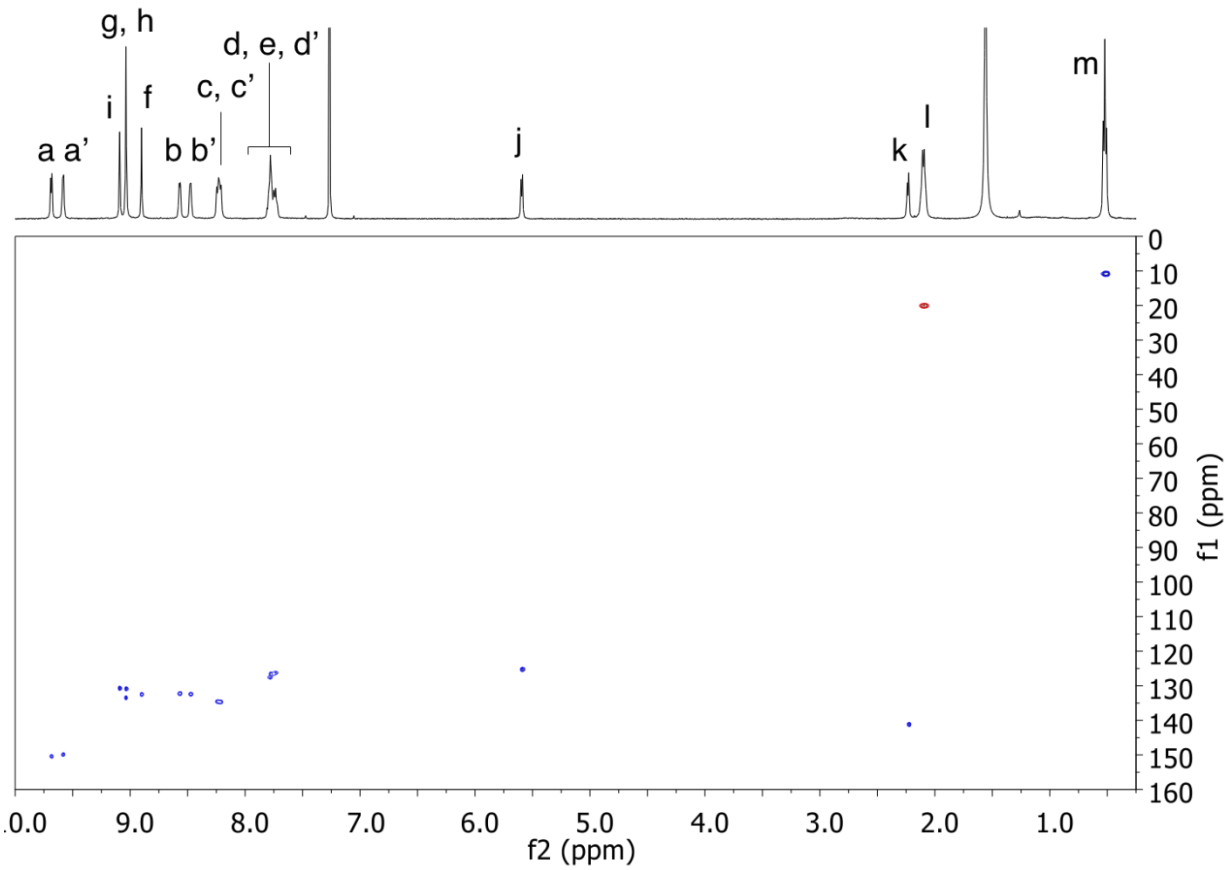

Figure A2.5. H-C COSY spectrum ($CDCl_3$) of **5b**.

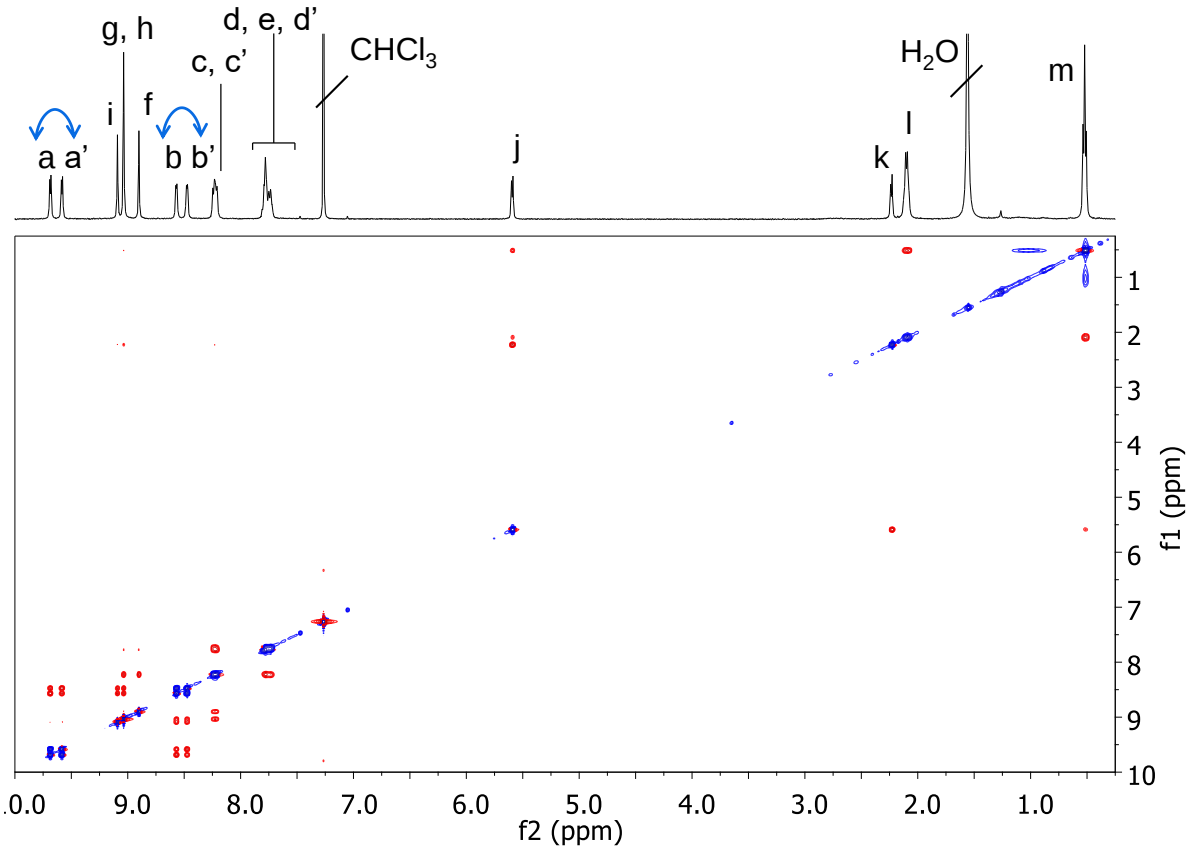

Figure A2.6. HH ROESY spectrum ($CDCl_3$) of **5b**.

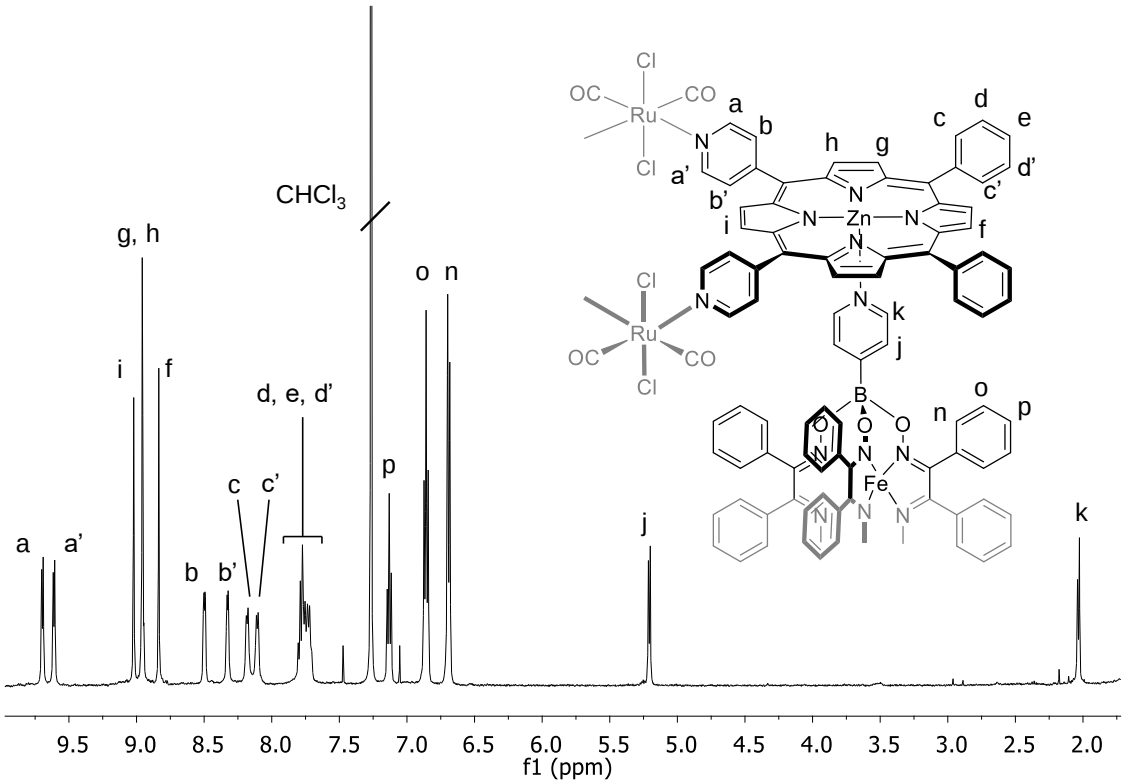

Figure A2.7. ^1H NMR spectrum ($CDCl_3$) of **5c**.

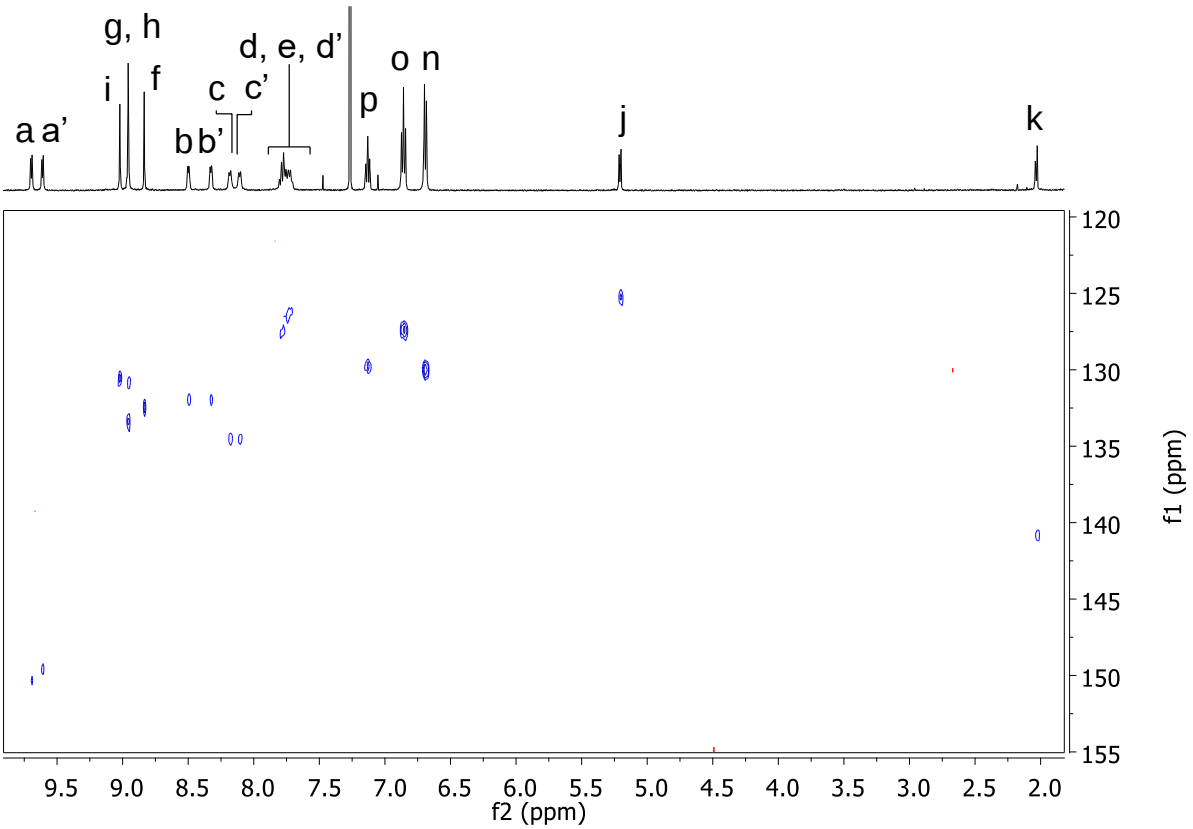

Figure A2.8. H-C COSY spectrum ($CDCl_3$) of **5c**.

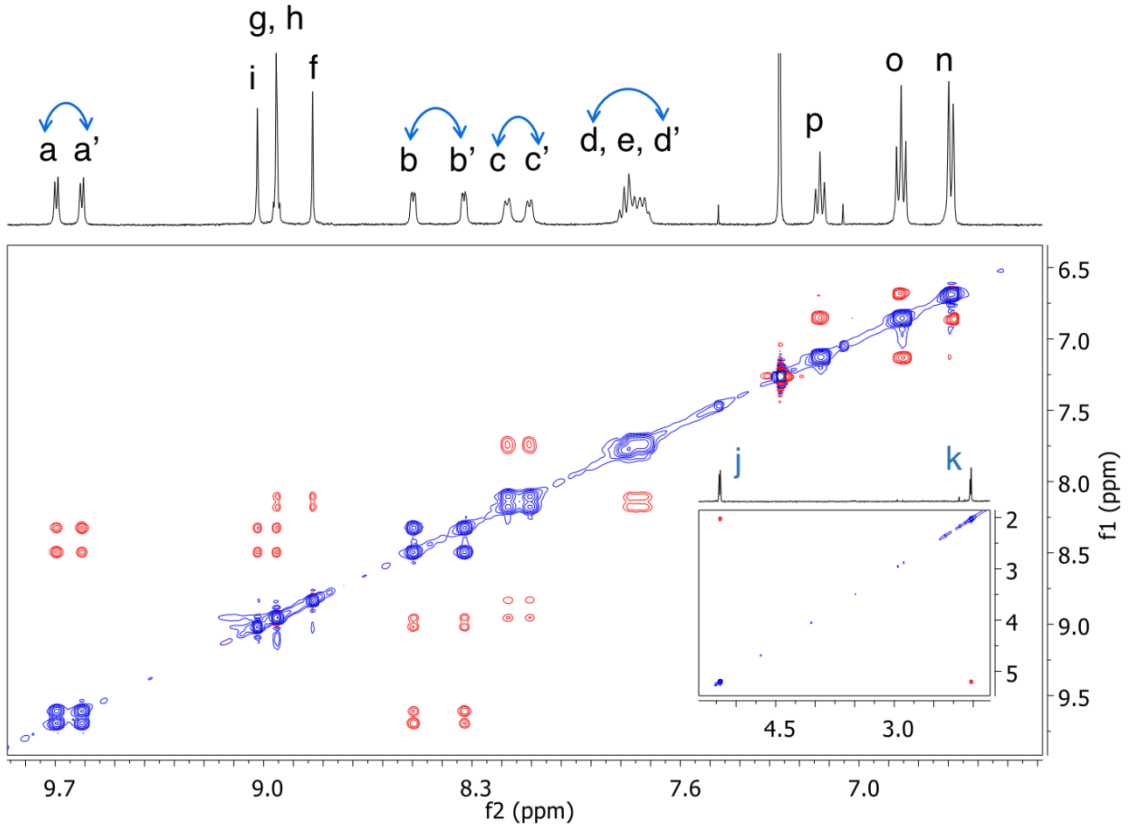

Figure A2.9. HH ROESY spectrum ($CDCl_3$) of **5c**.

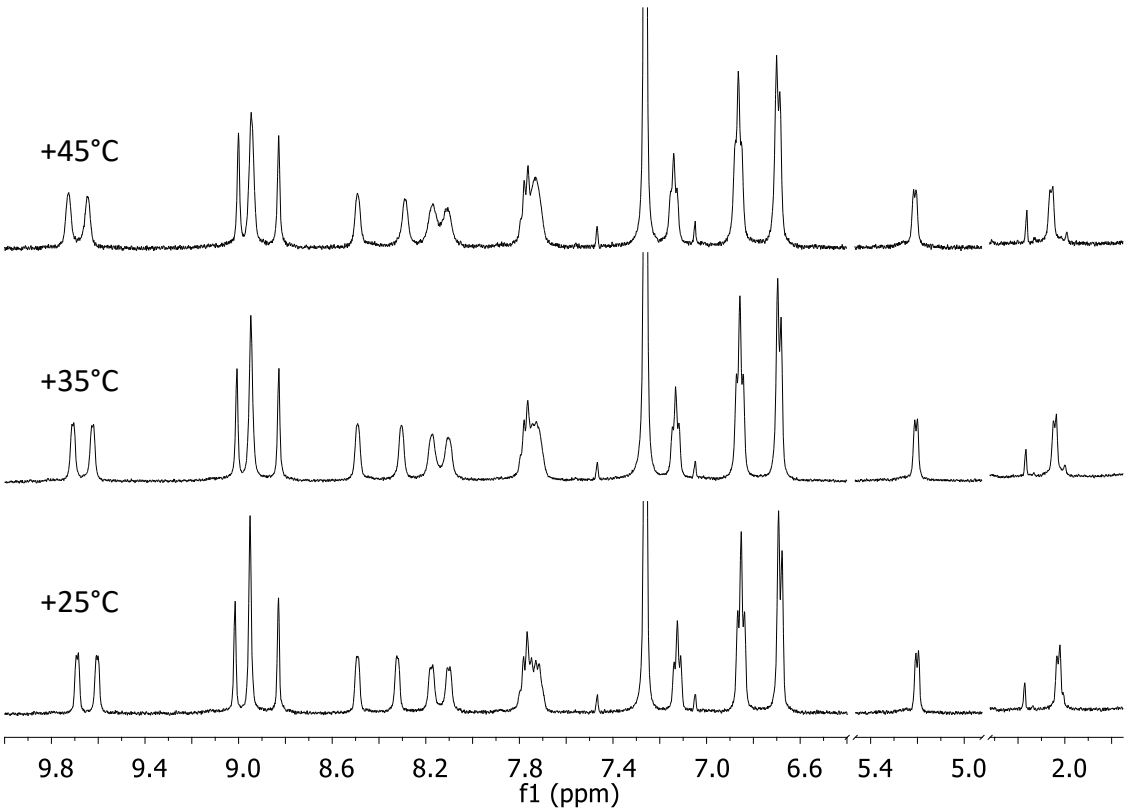

Figure A2.10. ^1H NMR spectra ($CDCl_3$) of **5c** registered at different temperatures: 25, 35 and 45°C.

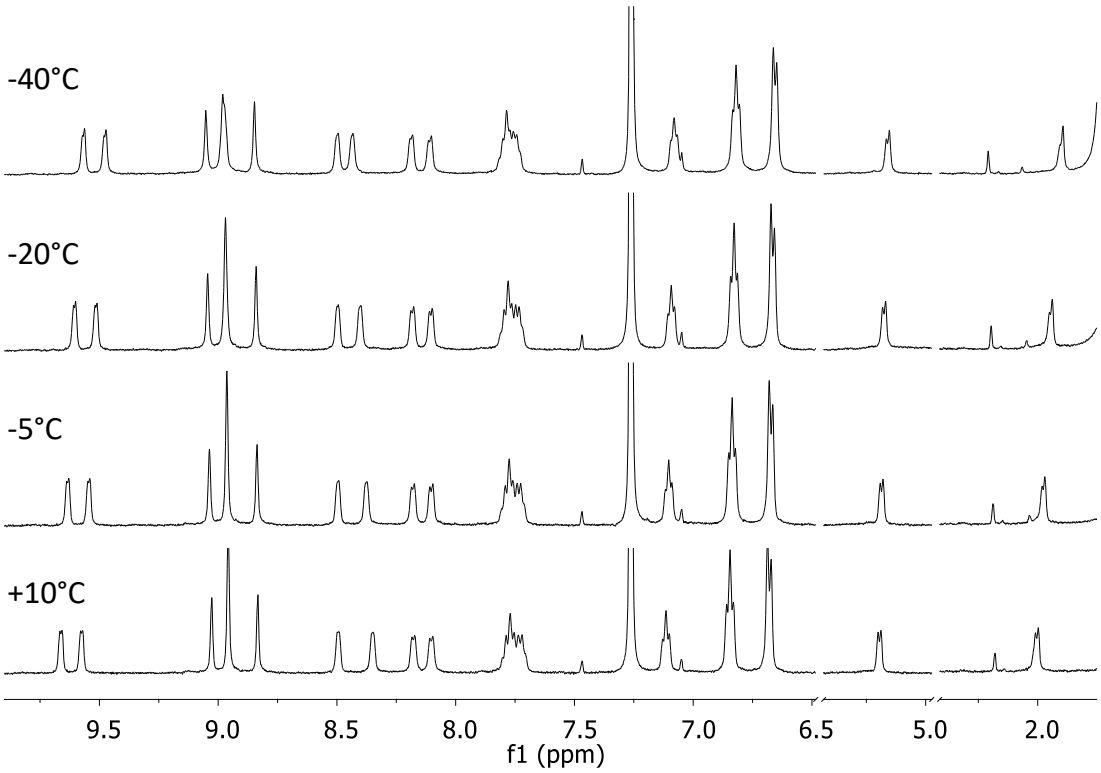

Figure A2.11. ^{1}H NMR spectra ($CDCl_3$) of **5c** registered at different temperatures.

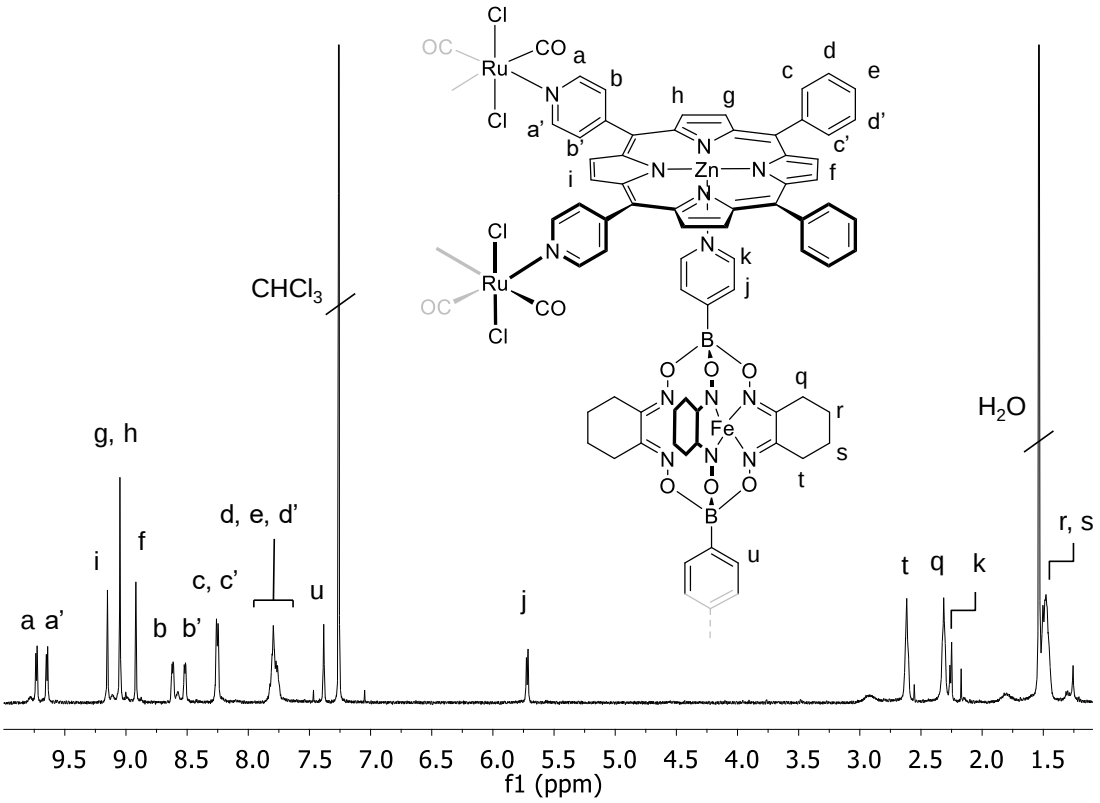

Figure A2.12. ^{1}H NMR spectrum ($CDCl_3$) of **6**.

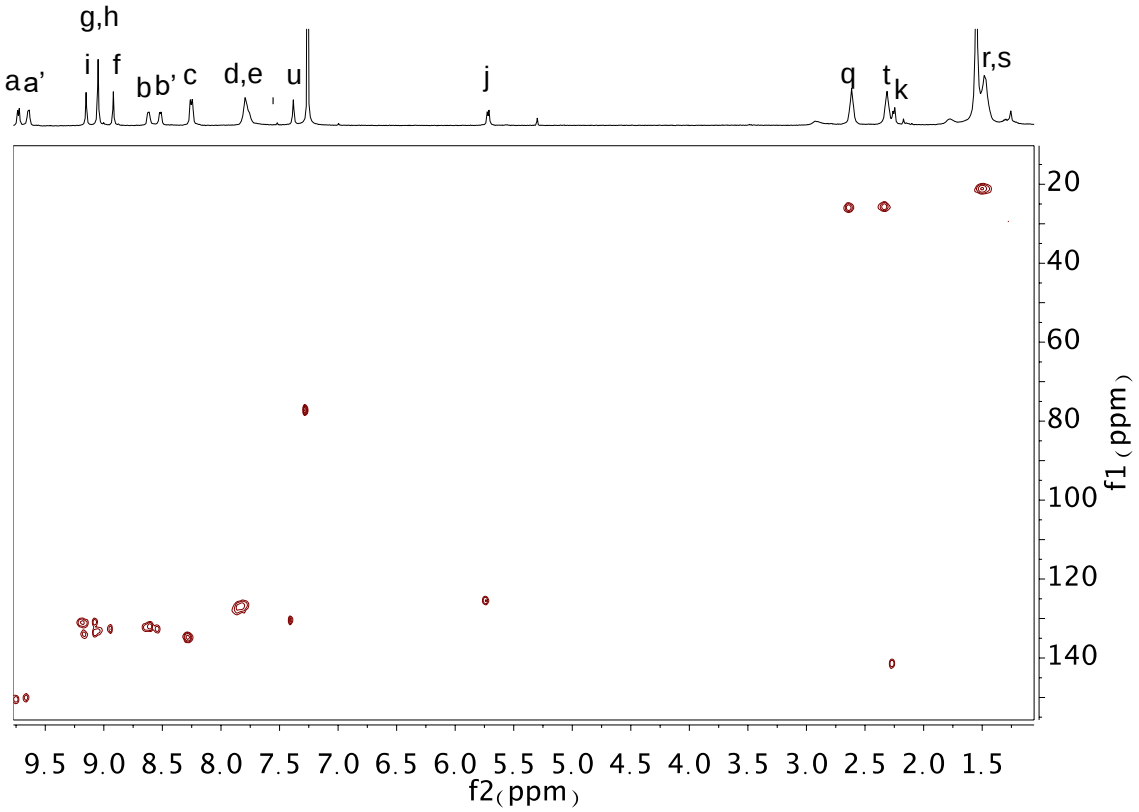

Figure A2.13. H-C COSY spectrum ($CDCl_3$) of **6**.

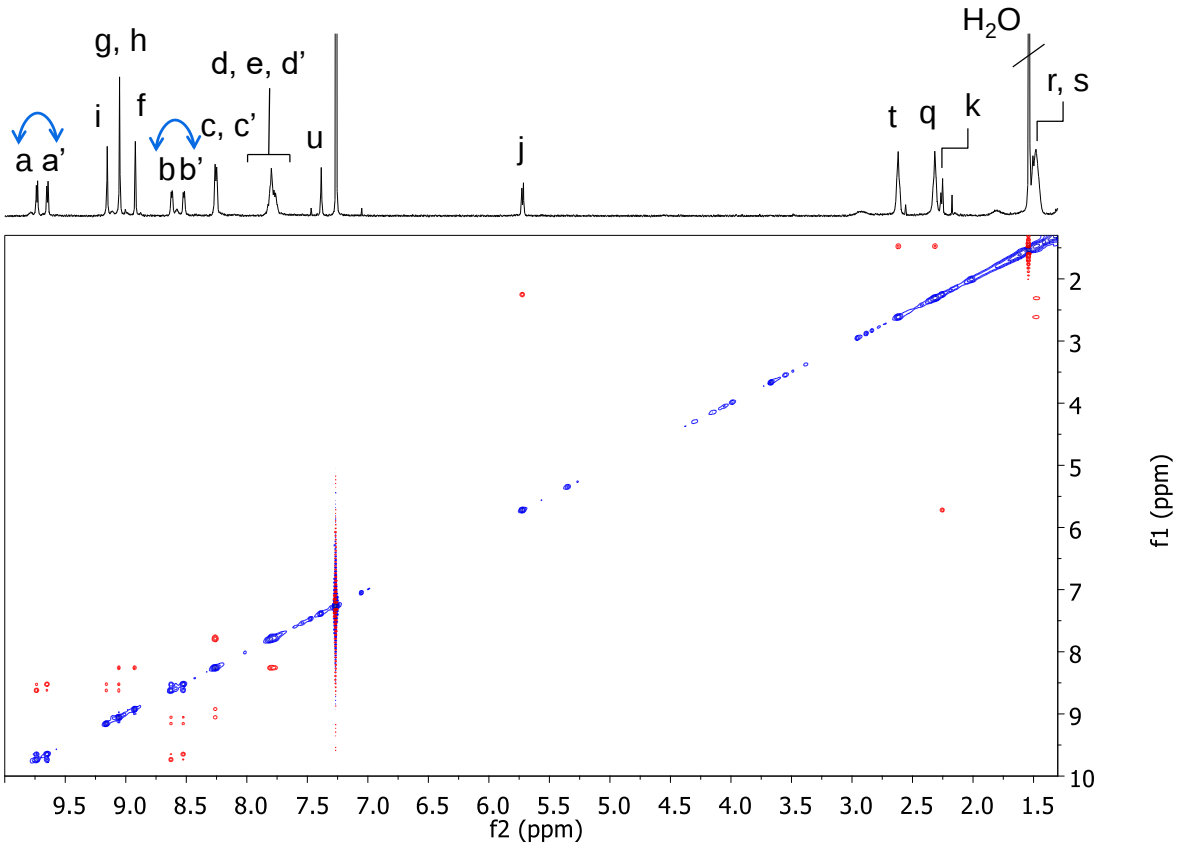

Figure A2.14. HH ROESY spectrum ($CDCl_3$) of **6**.

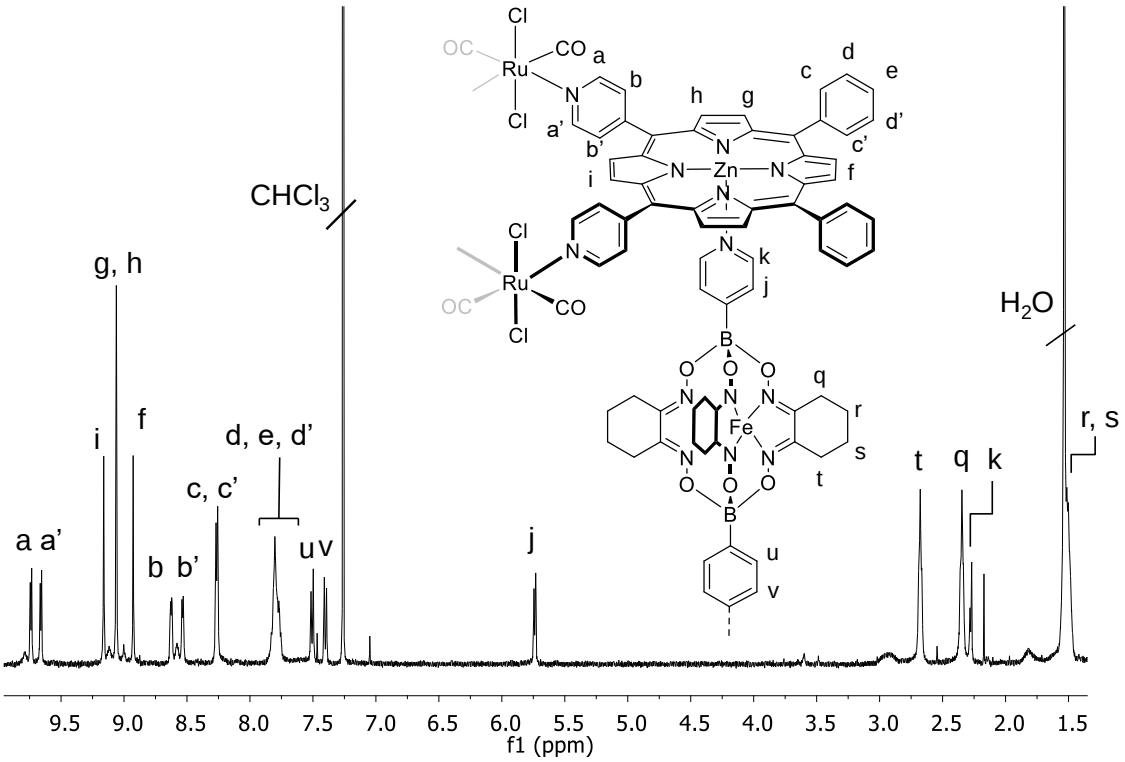

Figure A2.15. ^{1}H NMR spectrum ($CDCl_3$) of **7**.

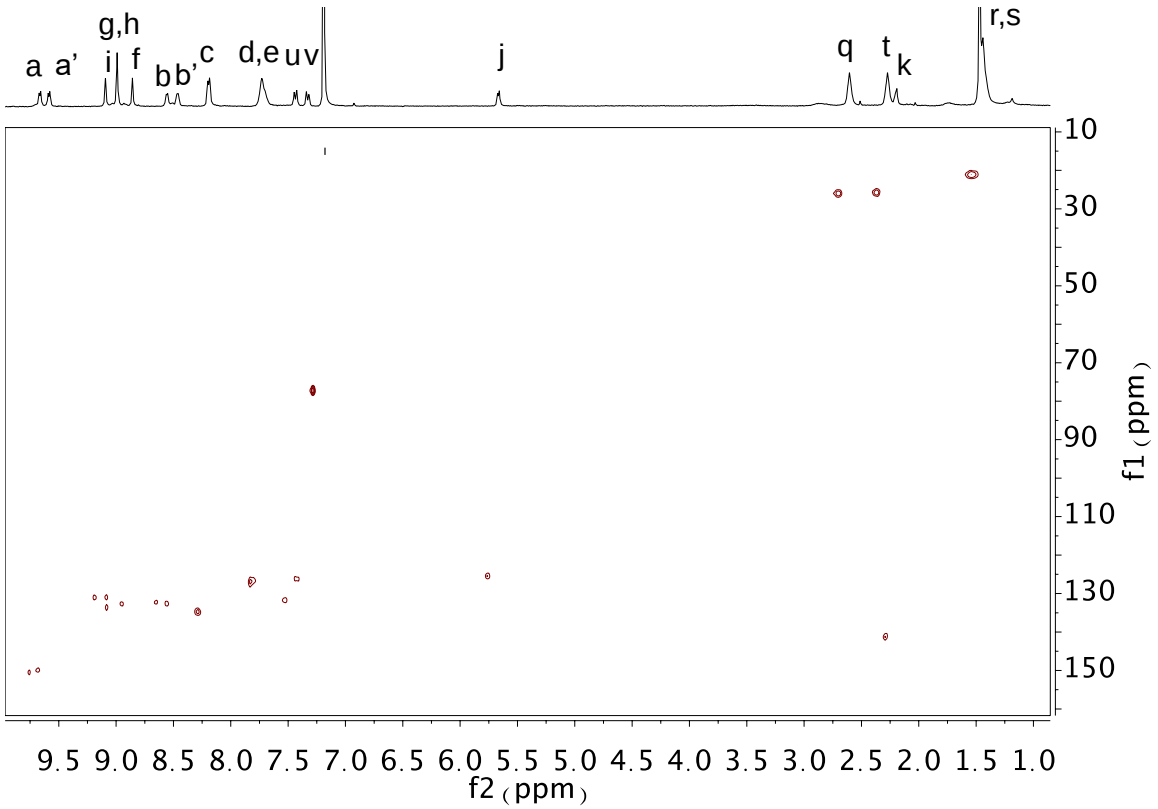

Figure A2.16. H-C COSY spectrum ($CDCl_3$) of **7**.

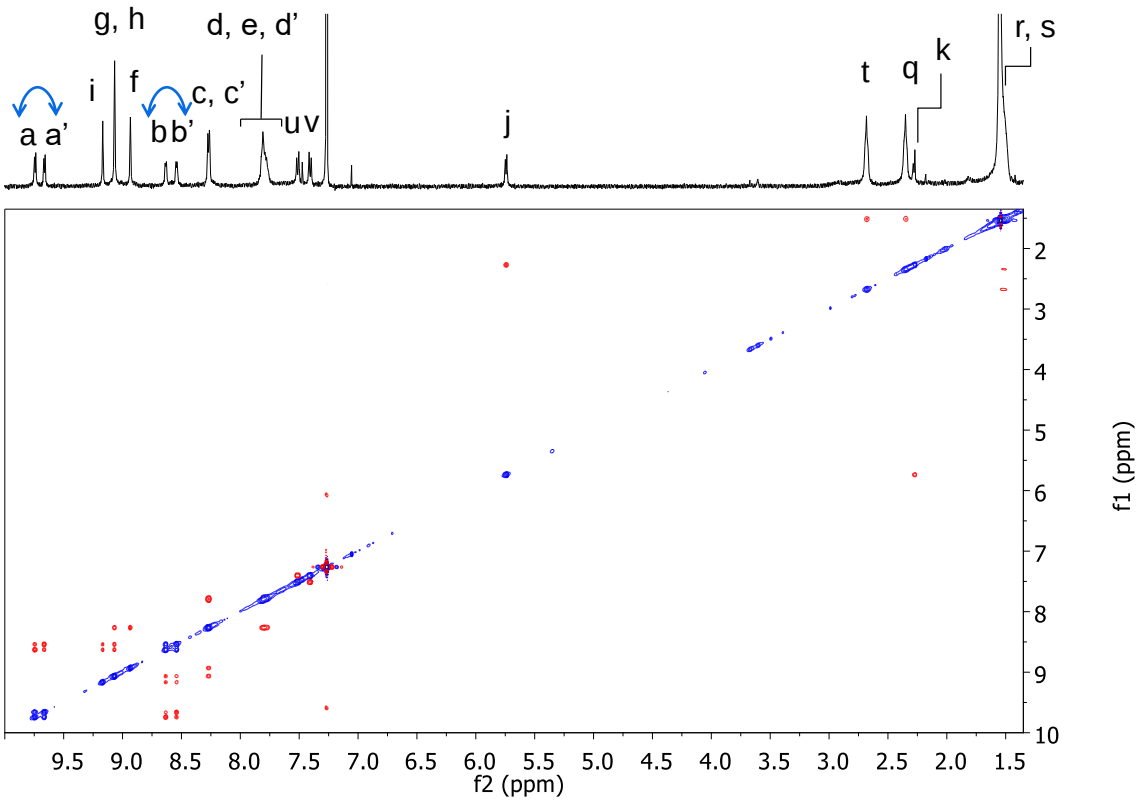

Figure A2.17. HH ROESY spectrum ($CDCl_3$) of 7.

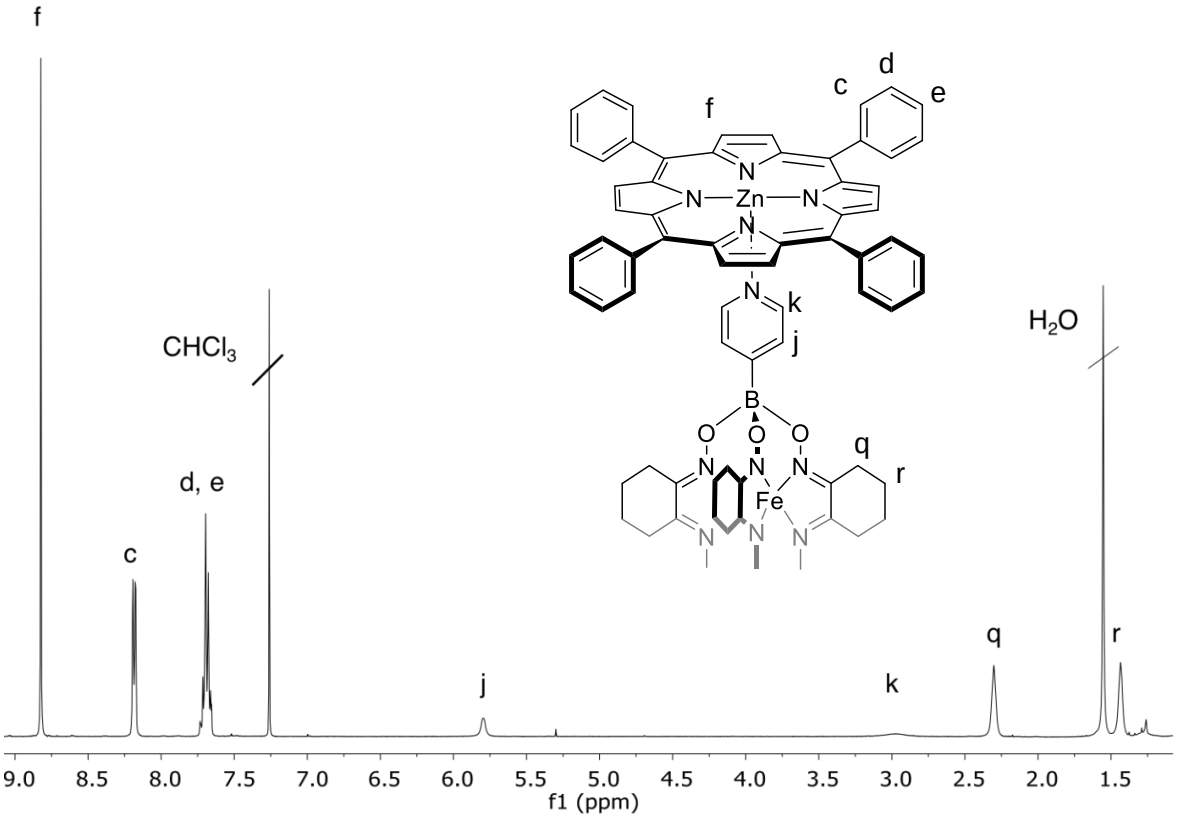

Figure A2.18. ^1H NMR spectrum ($CDCl_3$) of 8.

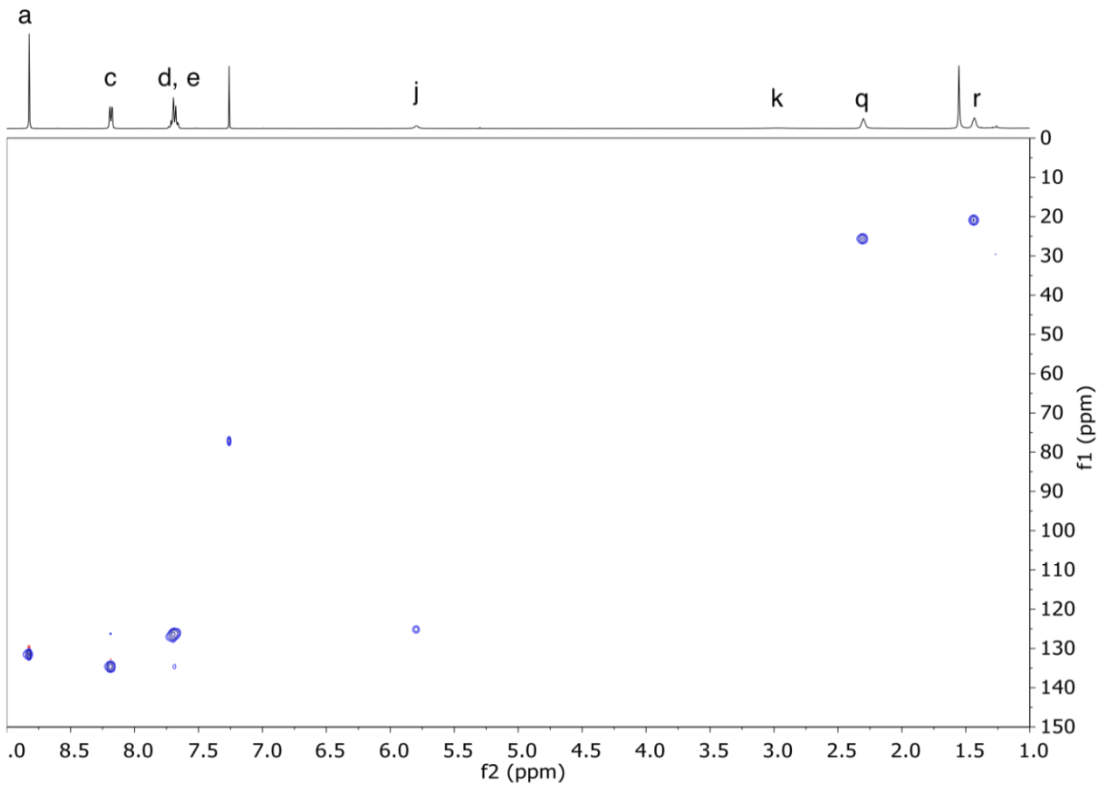

Figure A2.19. H-C COSY spectrum ($CDCl_3$) of **8**.

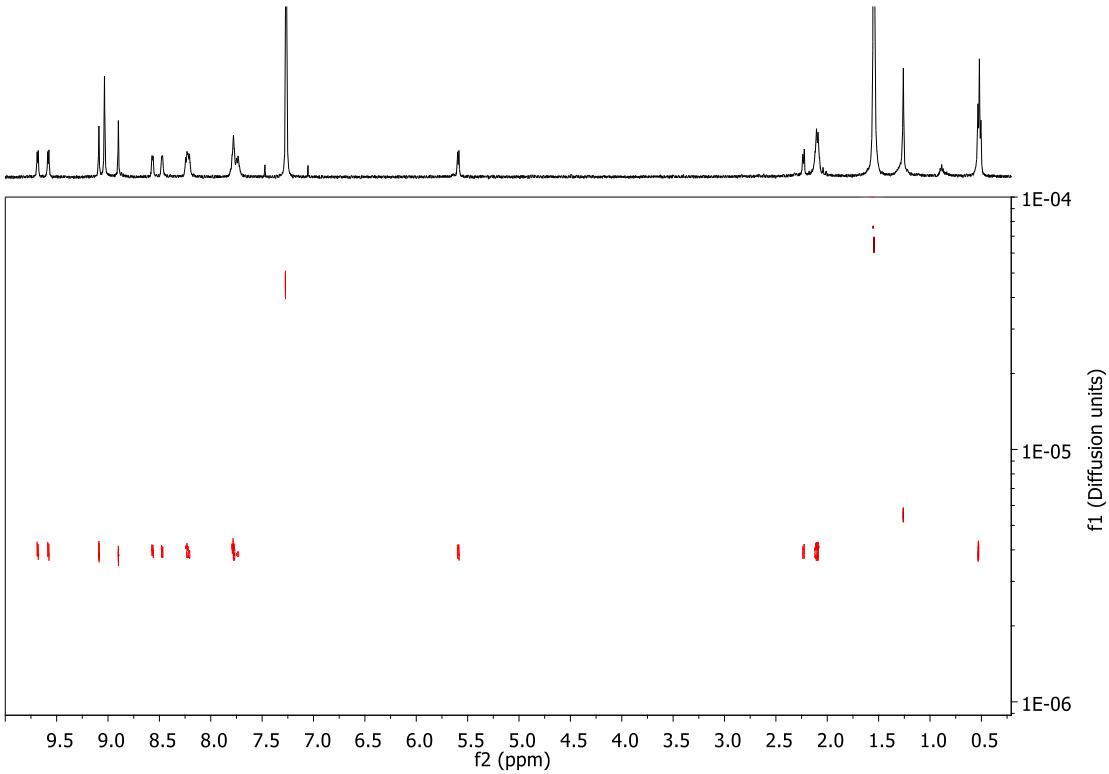

Figure A2.20. 2D ^{1}H-DOSY spectra ($CDCl_3$) of **5b**

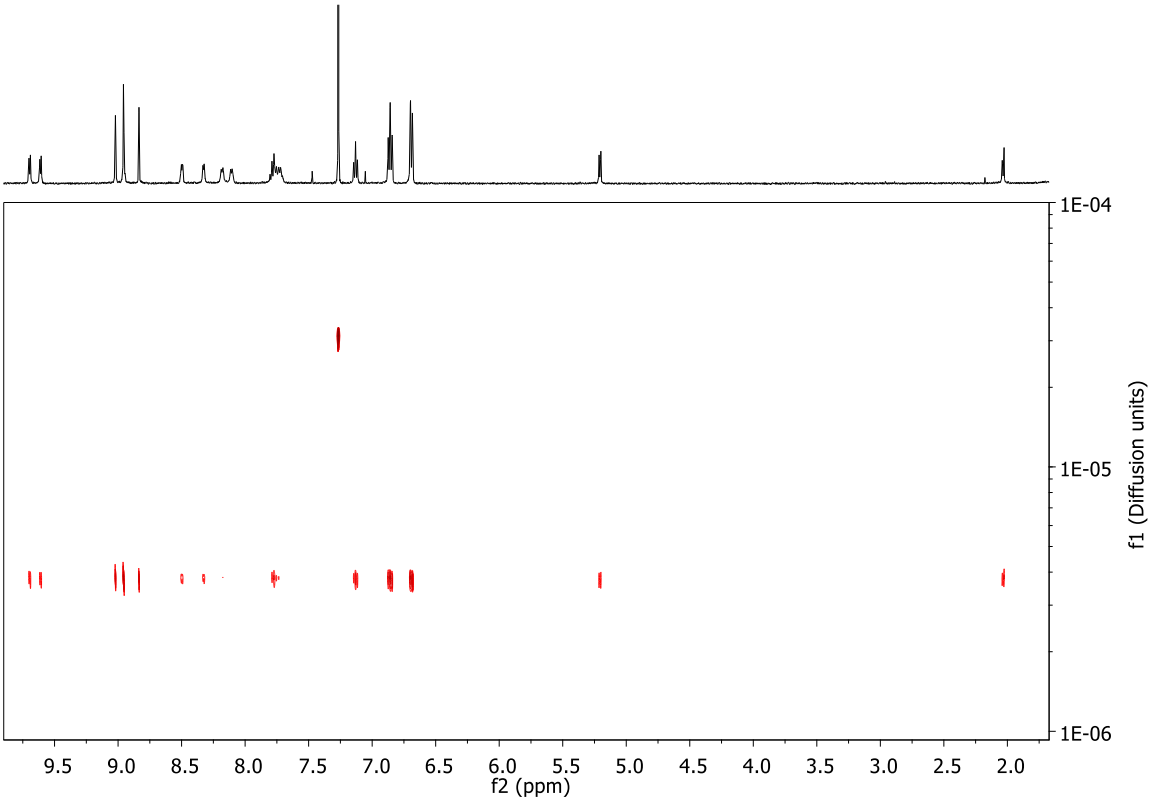

Figure A2.21. 2D ^{1}H-DOSY spectra ($CDCl_3$) of **5c**

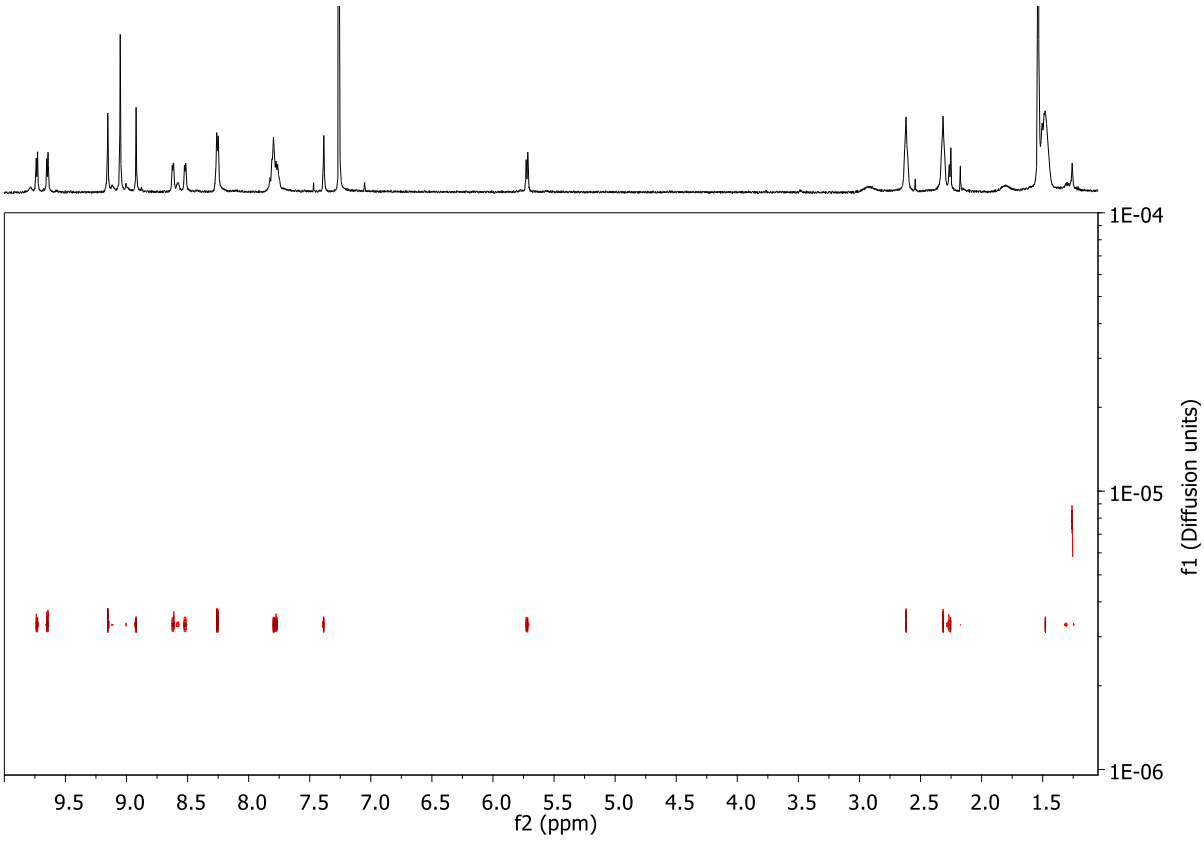

Figure A2.22. 2D ^{1}H-DOSY spectra ($CDCl_3$) of **6**

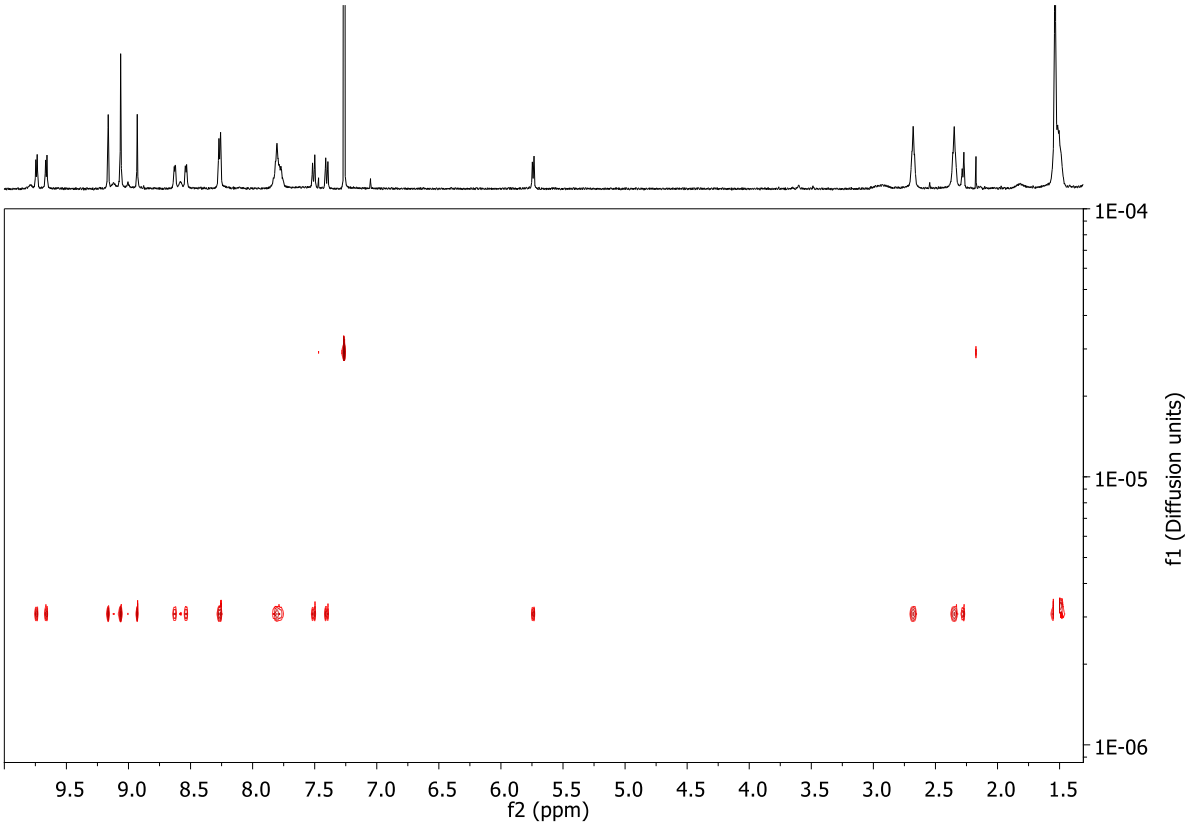

Figure A2.23. 2D ^{1}H-DOSY spectra ($CDCl_3$) of **7**.

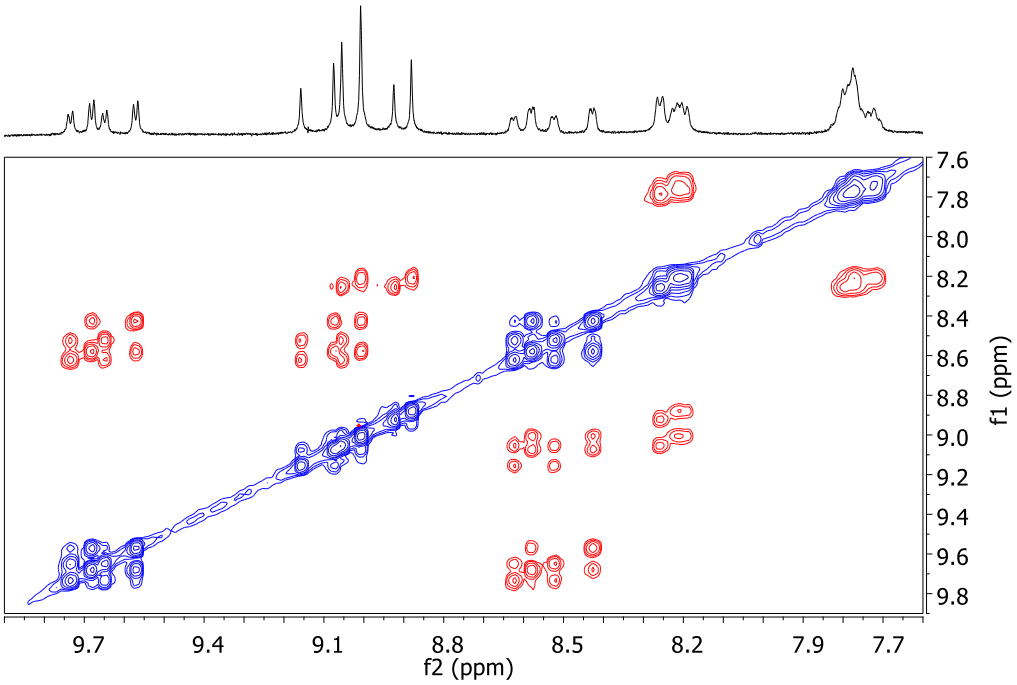

Figure A2.24. Aromatic region of H-H ROESY NMR spectrum in $CDCl_3$ of a 2:1:1 mixture of **1Zn**, **2a** and **3**.

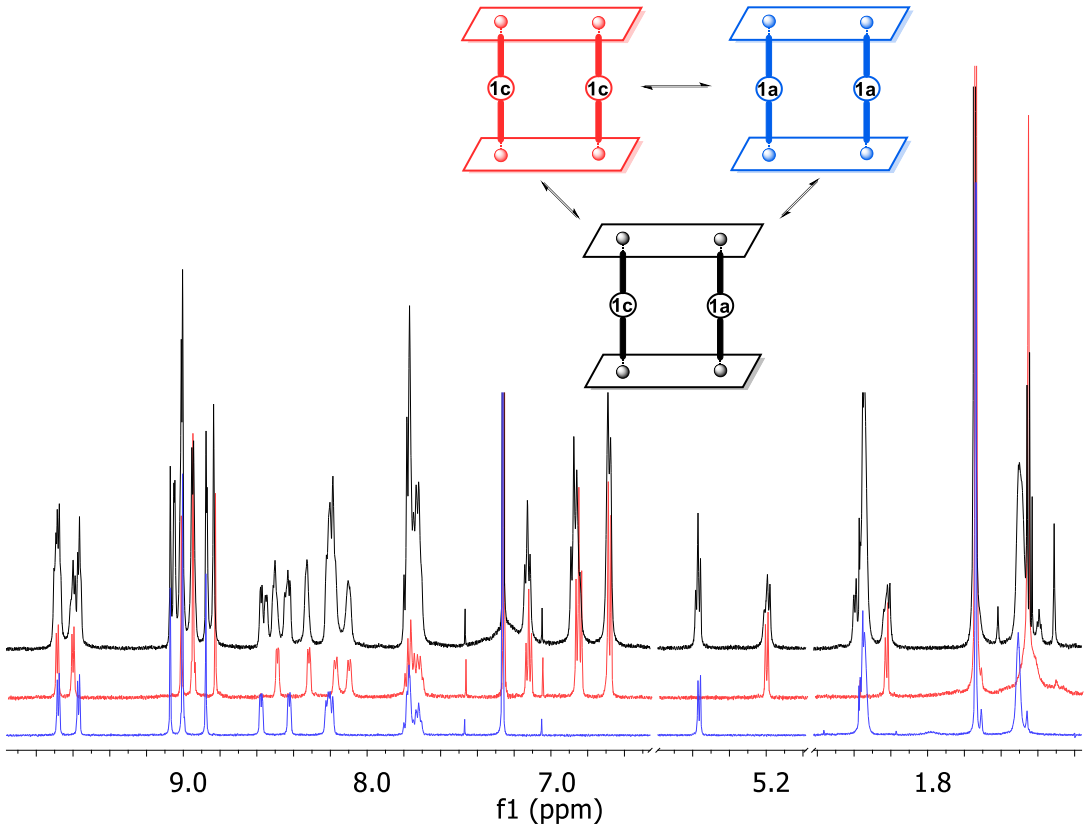

Figure A2.25. Overlay of the ^{1}H NMR spectra (selected region, $CDCl_3$) of a 2:1:1 mixture of **1Zn**, **2a** and **2c** (black), **5a** (blue), and **5c** (red). Inset: Schematic depiction of the equilibrium established by mixing in a 2:1:1 ratio **1Zn**, **2a**, and **2c** (ca. 10^{-3} M) in $CHCl_3$ at room Temperature.

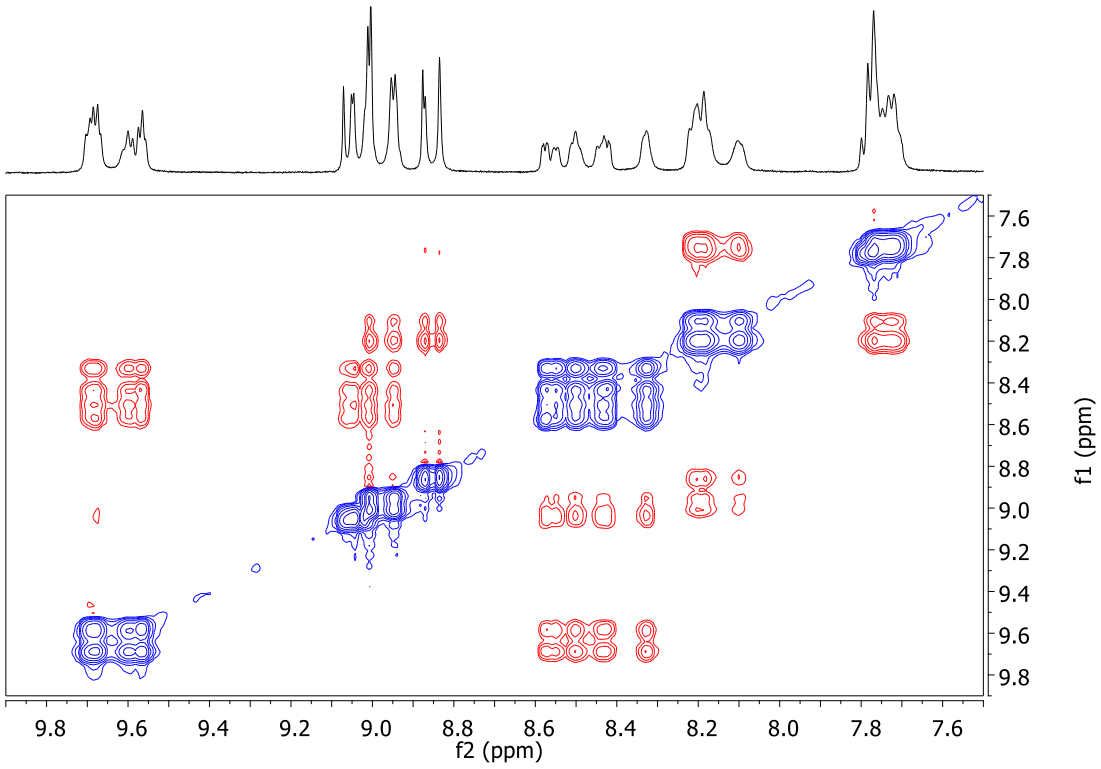

Figure A2.26. H-H ROESY spectrum ($CDCl_3$, selected region) of a 2:1:1 mixture of **1Zn**, **2c**, and **2a**.

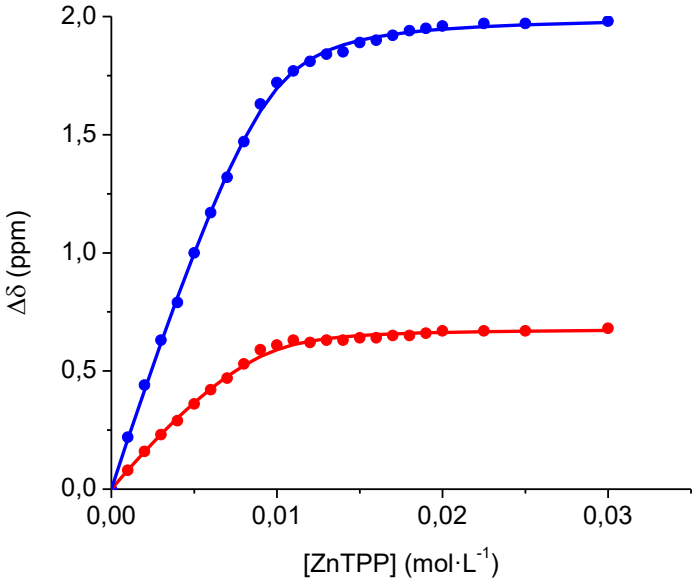

Figure A2.27. Variation of the chemical shifts of Hk (red dots) and Hq (blue dots) versus concentration of **ZnTPP** measured during the titration of **2a** to form **8**, overlapped with the corresponding calculated data fits (continuous line).

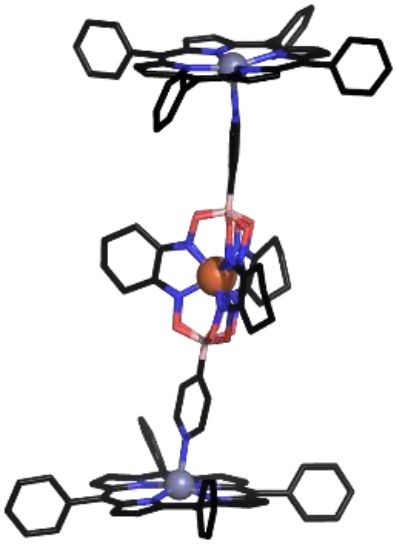

Figure A2.28. Single crystal X-ray structure of **8**. Colour code: Color coding: black sticks for C, blue for N, red for O, pink for B, orange for Fe, grey for Zn.

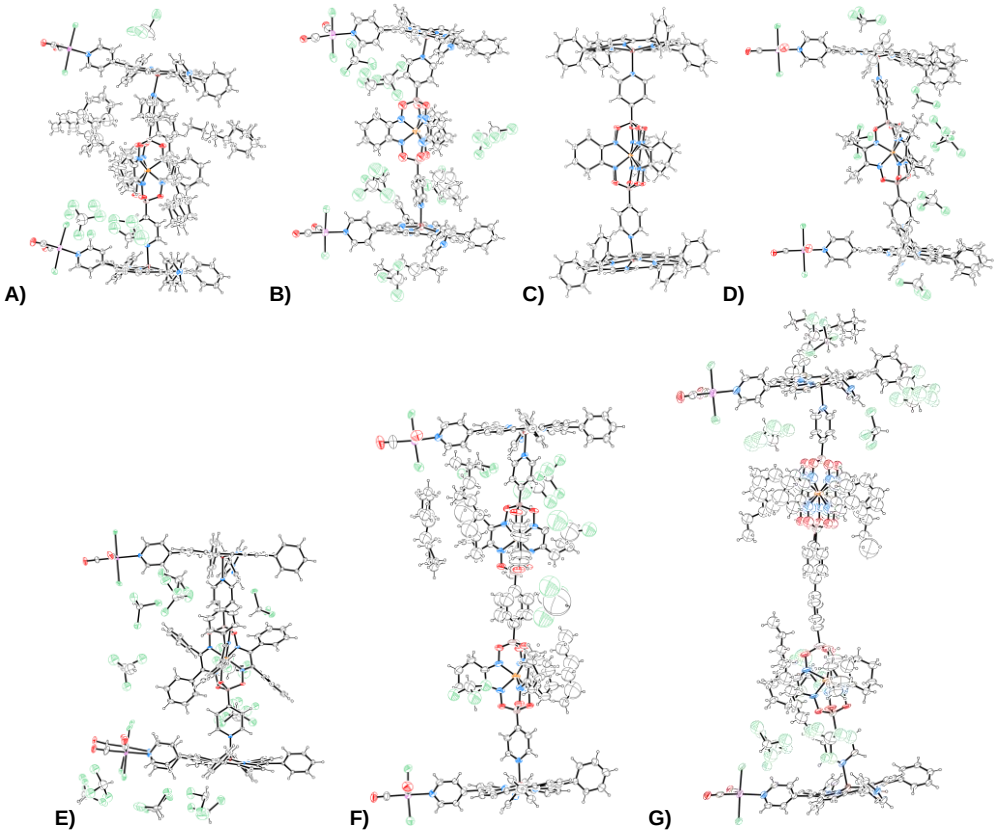

Figure A2.29. Ellipsoids representation of ASU contents (50% probability) for: A) **5a**, B) **5a'**, C) **8**, D) **5b**, E) **5c**, F) **6**, and G) **7**.

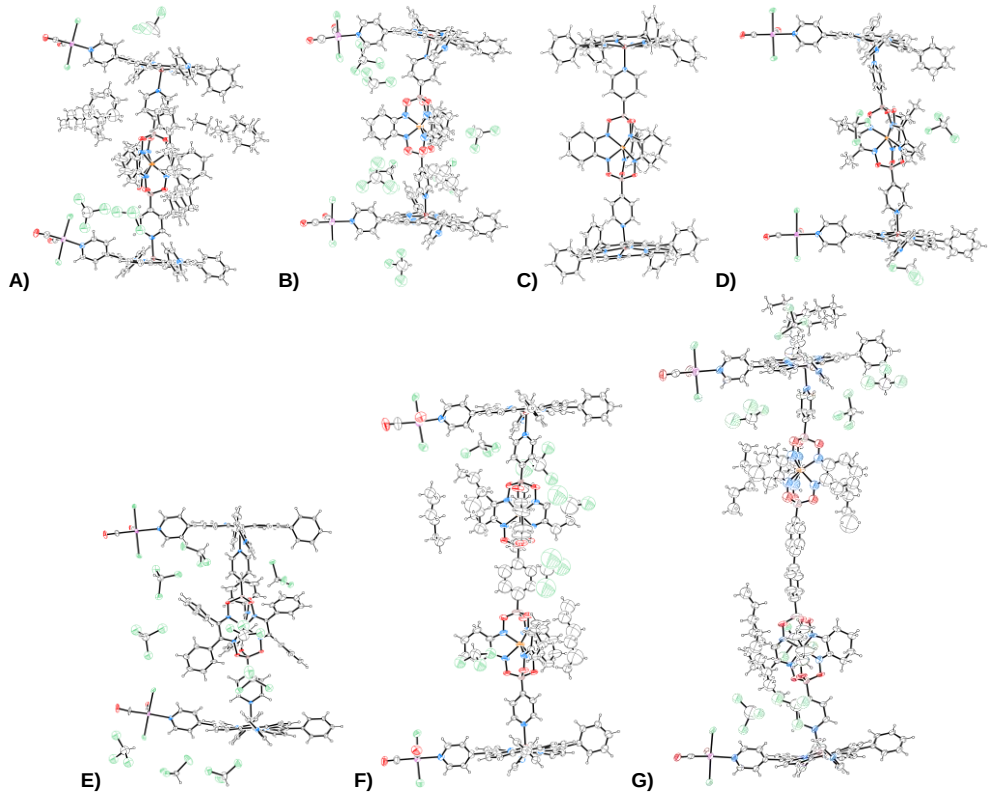

Figure A2.30. Ellipsoids representation of ASU contents (50% probability) for: A) **5a**, B) **5a'**, C) **8**, D) **5b**, E) **5c**, F) **6**, and G) **7**. Disordered conformations omitted for clarity.

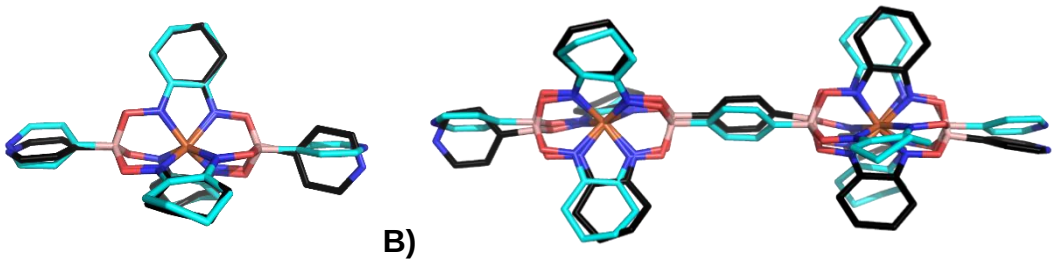

Figure A2.30. Overlapped between structures of 2a in the 5a' assembly (A), and 3 in the 6 assembly (B) (represented with black sticks), with the corresponding structures obtained from the pure metalloligands[4g] (represented with light blue sticks).

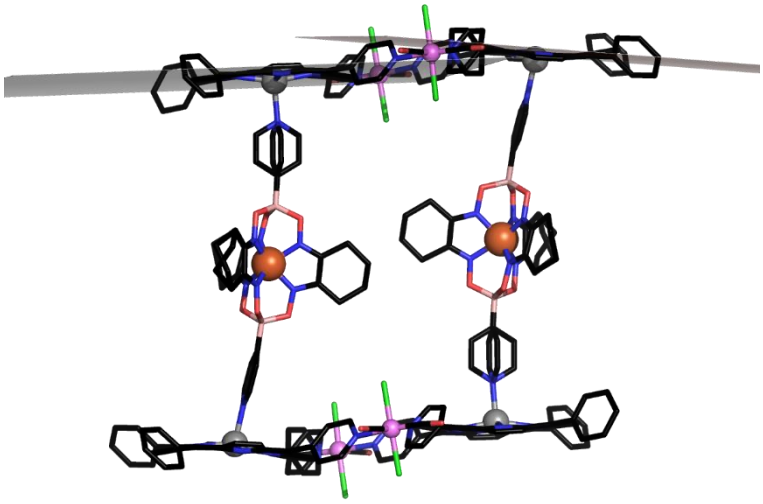

Figure A2.32. Crystal structure of the 5a assembly showing the angle between average porphyrin planes in the platform (4.72(4)°). The zinc atom displacement can be also appreciated (0.306(1) Å).

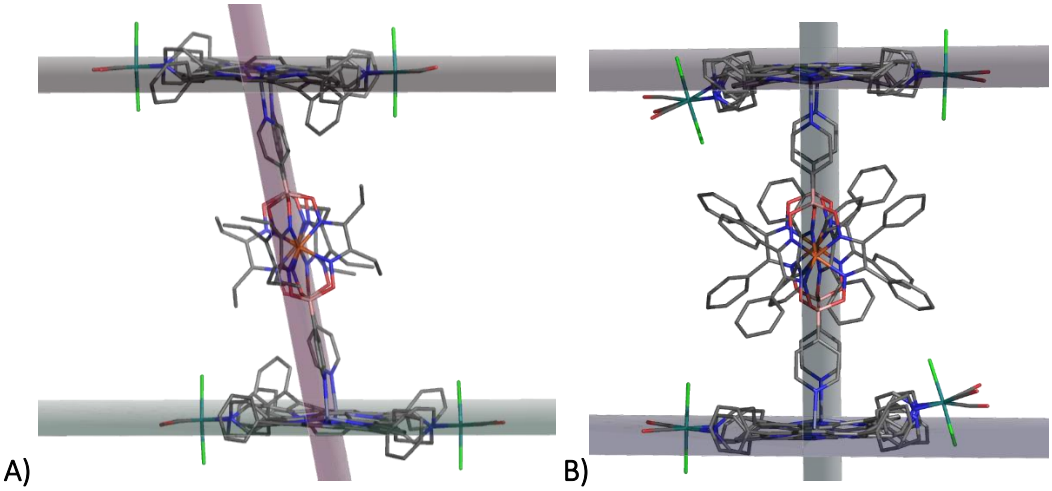

Figure A2.33. Comparison between angle involving platform planes and Zn-Fe average planes in 5b (A) and in the 5c (B) assemblies. The largest deviation from orthogonality happens in 5b, which bears the less bulky substituents to the clathrochelate iron core.

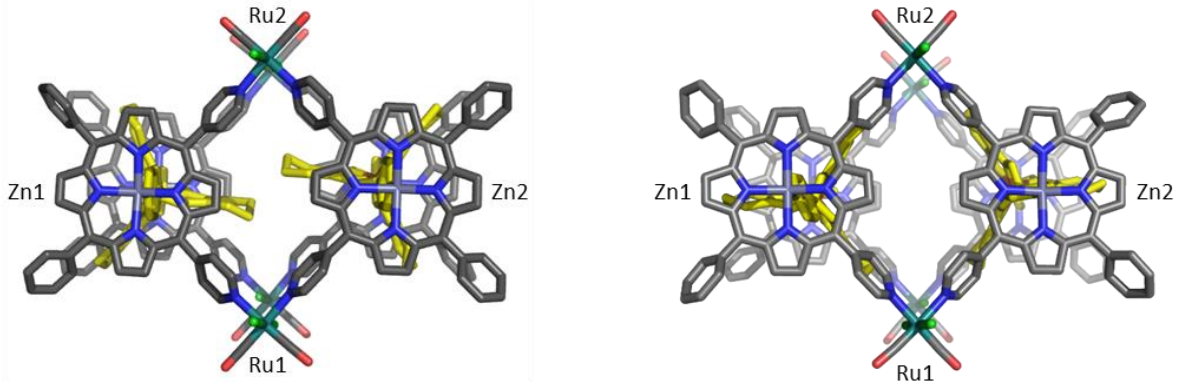

Figure A2.34. Comparison between **5a** (A) and **5a'** (B) assemblies. The yellow sticks show the different conformations for the **2a** metalloligand, found in the two triclinic polymorphs analyzed.

Table A2.1. $N_{pyridine}$-Zn bond distances calculated from the X-ray structure

Assembly	N_{py}-Zn (Å)
5a	2.130; 2.094
5a'	2.130; 2.129
5b	2.159; 2.143
5c	2.114; 2.141
6	2.140; 2.133
7	2.149; 2.137
8	2.136; 2.145
[1Zn·*trans*DPyP]$_2$	2.123[a]

(a) From reference 6a.

Chapter 3

*The work discussed in this Chapter was performed in collaboration with the groups of Prof. M. Pittelkow, University of Copenhagen (DK), and Dr. M. Natali, University of Ferrara (IT). The X-ray analysis was done in collaboration with Dr. N. Demitri, Elettra – Synchrotron Light Source, Trieste (IT), and Prof. E. Zangrando, University of Trieste (IT).

3.1 Diazadioxa[8]circulenes

[*n*]Circulenes are fully conjugated polycyclic compounds with a structure described by a central [*n*]-carbon membered ring with all edges surrounded by a band of *ortho*-fused benzene rings. Depending on the nuclearity of the central ring, [n]circulenes present different conformations ranging from bowl-shaped to planar or saddle-shaped (Figure 3.1). [8]circulenes the largest [*n*]circulenes synthesized to date, are predicted (and found in the few synthetic examples reported in the literature) to have a saddle-shape conformation and a π-extended character resulting in a strained and unstable structure.[1,2]

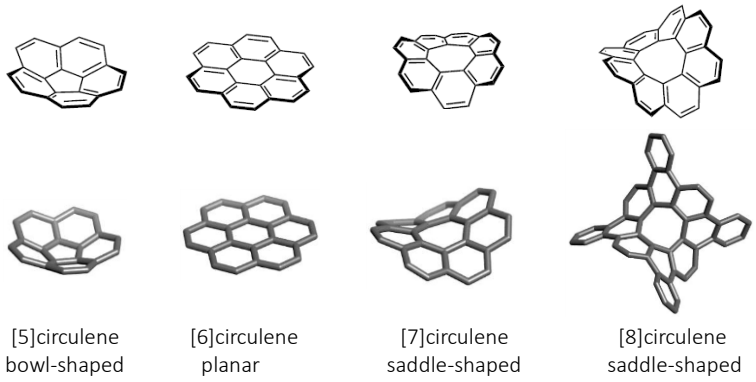

Figure 3.1. Schematic depiction (top) and crystal structure (bottom) of [*n*]circulenes with *n* = 5-8, from Ref. 2.

By contrast, hetero[8]circulenes, in which one or more etheno-bridge(s) are replaced by heteroatoms, such as oxygen, nitrogen, sulfur or selenium (*i.e*. replacement of benzene with five-membered 6π-aromatic systems) are more easily accessible and possess distinct geometrical, chemical and physical properties with respect to their hydrocarbon counterparts. In particular, highly stable (chemically and thermally) planar conformations are often reported (single crystal X-ray data or theoretical calculations).[2] Some examples of planar azatrioxa[8]circulenes, diazadioxa[8]circulenes and triazaoxa[8]circulenes are depicted in Figure 3.2.

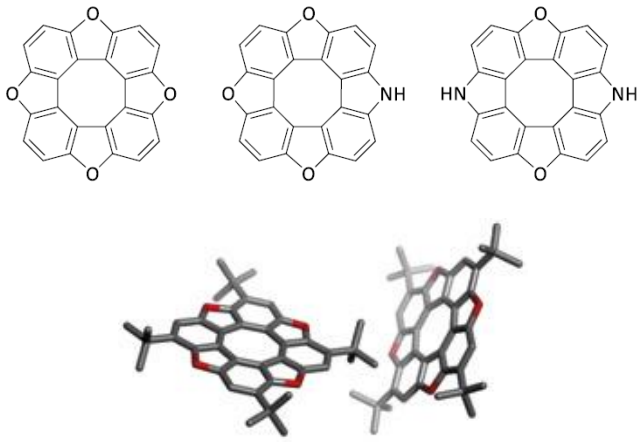

Figure 3.2. Examples of planar tetraoxa[8], azatrioxa[8] and diazadioxa[8]circulenes (above); X-ray structure of a tetra *tert*-butyl substituted tetraoxa[8]circulene, presenting a herringbone packing (below).[2]

The photophysical properties of hetero[8]circulenes have attracted a lot of attention in the recent years because of their potential applications in optoelectronic devices, such as organic light emitting diodes (OLEDs) and organic field-effect transistors (OFETs).[3] At the same time, these appealing polycyclic conjugated compounds are complex to understand in terms of aromaticity/anti-aromaticity, as the simple Hückel rules do not apply.[4] The term aromaticity is most commonly used to describe a cyclic delocalized electron system. As such, its reciprocal concept, antiaromaticity, has proven difficult to study, as compounds with cyclic 4n π-structures often assume bent conformations and localized double bonds, as opposed to the planar, delocalized structures ideal to such survey. Arriving at a definition/description of the aromatic/non-aromatic/antiaromatic character of these compounds is normally attempted by addressing four different properties – reactivity towards electrophiles, energetic state levels, bond lengths, and response to an external magnetic field – as these have distinct features when associated with aromaticity: i) low reactivity towards electrophiles; ii) low-lying energetic states (compared to non-aromatic systems), therefore larger HOMO-LUMO gaps; iii) carbon-carbon bonds of equal length and iv) an overall diatropic ring current. In practice, predictions on the actual aromatic/anti-aromatic/non-aromatic character of polycyclic 4n π-systems, based on theoretical calculations, are not as yet reliable, as the collection of experimental data (from spectroscopic experiments and X-ray analysis) is still unsatisfactory. Among all, the most frequently applied criterion is the magnetic one. From a magnetic point of view, aromatic moieties are identified with the presence of a diatropic ring current in response to an applied magnetic field, which induces a local additional field that is largely anisotropic in space and easily detectable by ^{1}H-NMR spectroscopy.[5] In general, all protons placed on the external rim of an aromatic system are down-field shifted (de-shielding effect), since the induced magnetic field (green line in Figure 3.3) is aligned and coherent to the external applied field (B_0), while protons residing on top of the aromatic plane are up-field shifted (shielding effect) due to the sum of parallel magnetic fields of opposite sign. For paratropic ring current of antiaromatic systems, the situation should be inversed (shielded region around the periphery, and de-shielded region perpendicular to the anti-aromatic plane).

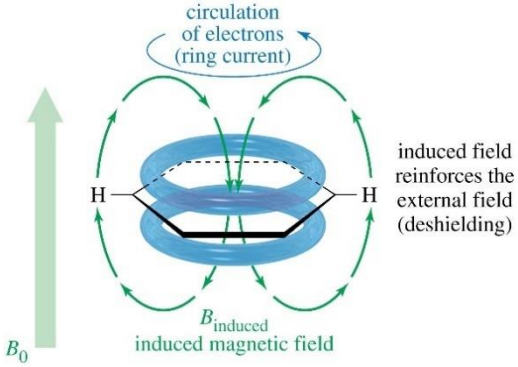

Figure 3.3. Schematic view of benzene's aromatic ring current (blue rings) and induced magnetic field (green line) with an applied external magnetic field B_0.

A widespread and apparently reliable computational method to evaluate the degree of aromaticity of a π-ring structure is the nuclear-independent chemical shift (NICS) calculation. In this computational method, a ghost atom is placed in the center of the ring (NICS(0)) or alternatively one Ångstrom above it (NICS(1)), to calculate the local increase or decrease of the magnetic effect

produced by the ring system over the ghost atom. In NICS calculations, large negative values indicate aromaticity while large positive values indicate anti-aromaticity; values around zero are likely to predict local non-aromatic properties.[6] Comparisons with experimental data (and corroboration of this method) rely mostly on the experimentally well-established diatropic ring current effects of "classical" aromatic compounds. The aromaticity/antiaromaticity character of cyclic 4n π-structures has demonstrated to be much more difficult to interpret. For instance, in hetero[8]circulenes the central eight-membered COT ring is surrounded by aromatic heterocycles, and the balance between the diatropic and paratropic ring currents determines their net aromatic, non-aromatic or anti-aromatic character, and direct observation of anisotropic effects of the central ring requires one or more protons to reside in close proximity and on top of this moiety.[7,8,9,10,11] As shown by Osuka, the NICS value at the center of the COT core decreases monotonously with increasing distance: the paratropic ring current is no longer effective for distances above 6 Å (Figure 3.4).[12] Therefore, the possibility to tailor hetero[8]circulenes with moieties that may serve as spectroscopic handles to survey the magnetic influence of their surface is of great interest. Though it is far from trivial to meet the correct structural and geometrical requirements, and experimental data are up to now limited to isolated examples.

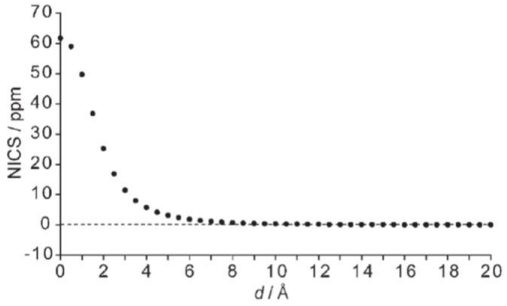

Figure 3.4. Plot of NICS values up to 20 Å from the geometric centre of COT, from Ref. 12.

To study the antiaromaticity of an annulated planar COT system, Osuka and co-workers synthesized a Zn^{II}-porphyrin tetramer (Figure 3.5) incorporating a tetraaza[8]circulene moiety.[12,13,14] The magnetic ring-current effect of the COT core and the porphyrin subunits was analyzed by coordination to the metal centers of the porphyrins of either a linear imidazolyl or a bent pyridyl fragment. The resulting complexes were studied by ^{1}H NMR spectroscopy and the data were compared to theoretical calculations. When comparing the chemical shifts of the protons residing above the COT core, with respect to the corresponding values in the free ligands, large downfield shifts (of *ca.* 3.78 ppm and of 5.29 ppm for the linear and the bent ligands, respectively) were found, clearly evidencing a strong paratropic ring current. The COT core calculated NICS values, both for the zinc-porphyrin and the free-base tetramers, were found large and positive, in line with a strong paratropic ring current, *i.e*. a net antiaromatic character, of the COT core.

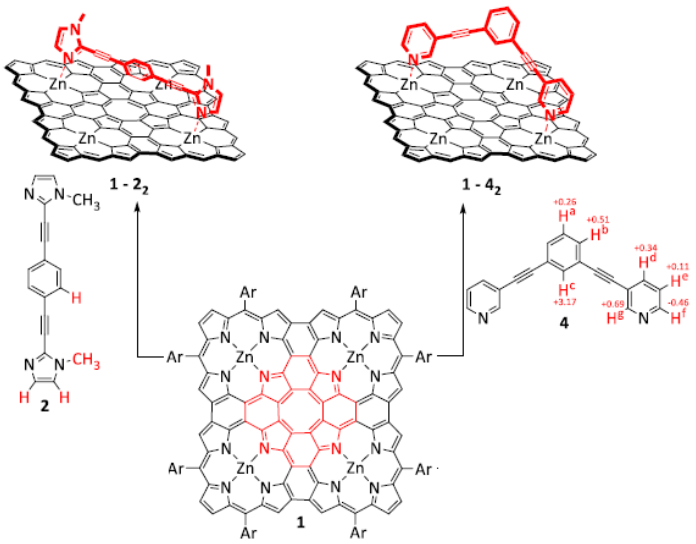

Figure 3.5. Coordination of two different ligands on a zinc-porphyrin sheet. Protons observed by ^{1}H-NMR are marked in red.[12-14]

Pittelkow and co-workers addressed the question of aromaticity and antiaromaticity of azatrioxa[8]circulenes[3,15,16] and diazadioxa[8]circulenes,[17] in the benzene, furan and COT subunits *via* geometry optimizations and nuclear-independent chemical shifts (NICS) calculations. The NICS values found suggest for all the heterocirculenes a magnetic antiaromatic character for the COT core and an aromatic character for the surrounding benzene, furan or pyrrole rings. The same group reported also on the synthesis and detailed characterization of a wide library of azaoxa[8]circulenes (one example is shown below in Chart 3.1). For these latter systems, a systematic investigation on the aromaticity/antiaromaticity of the planar COT core, along with their structural variations, was carried out.[18] NICS calculations were paralleled with comparisons of the ^{13}C-NMR chemical shifts and X-ray structure C–C bond lengths of the COT core unit. The experimental analysis was not conclusive as within single systems the chemical shift displacements were found not congruent and double/single bonds alternation was not marked. Efforts were also devoted to the possible use of *ortho* dianiline diazadioxa[8]circulene (Figure 3.6) as receptor, by means of H-bonding interactions, of different types of carboxylate substrates, aimed at gathering ^{1}H-NMR data on the COT ring current effect from the ligand chemical shift values.

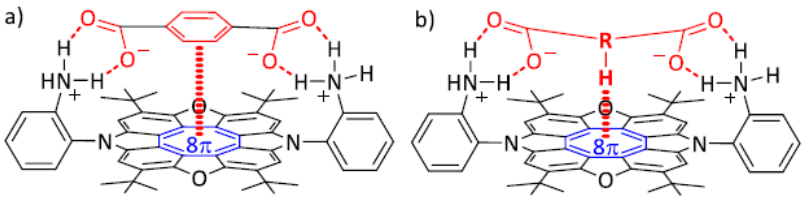

Figure 3.6. *Ortho* dianiline diazadioxa[8]circulene as possible pincer for binding of carboxylate ligands and for their positioning in proximity to the 8π COT surface, from Ref. 18.

Unfortunately, the various ideal substrates tested were scarcely soluble, or totally insoluble, in aprotic organic solvents. The limitation to the use of DMSO-*d*6, not surprisingly, was detrimental as this solvent is strongly competing for H-bonding interactions.

Among the diazadioxa[8]circulene derivatives of the library described in this work, a dipyridyl-diazadioxa[8]circulene (**Circ**, Chart 3.1) attracted our interest, as it appears particularly suited as building unit for the assembling of metal-mediated structures. As shown by the X-ray structure, this rigid molecule is perfectly planar and bears two pending pyridyl groups disposed at 180° (at a distance of 16.7 Å) and available for metal-coordination. Also for this tetra *tert*-butyl substituted circulene, a herringbone crystal packing was found (see above, Figure 3.2).

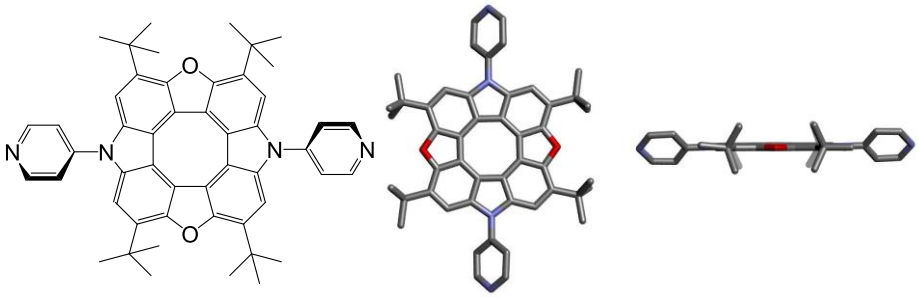

Chart 3.1. Schematic depiction and two X-ray structure views of the dipyridyl-diazadioxa[8]circulene (**Circ**) employed in the present work.[18]

The possibility to embed more than one hetero[8]circulene unit within discrete species, and in defined geometries, may be an alternative, yet unexplored, experimental possibility to validate the aromaticity/antiaromaticity characteristics of these systems. In addition, the ordering of these photo-active large surfaces in more complex closed structures may offer some new intriguing perspectives. For instance, the electronic properties of **Circ** (strong absorption spectrum, relatively intense fluorescence emission, and first oxidation potential at 1.23 V -vs SCE)[18], may find some positive expression when combined with (metallo)porphyrin partners.

The collaboration with the group of Prof. Pittelkow is based on these premises and aimed at initiating such type of investigations. In particular, given the close structural and geometrical similarities of **Circ** and ***trans*DPyP** in terms of ditopic donor ligands (i.e. rigidity, position and distance of the donor groups, surface and peripheral extension of the macrocycles), the present study was focussed at reproducing, by replacement of ***trans*DPyP** with **Circ**, two familiar metal-mediated porphyrin discrete constructs (Chart 3.2, on the top).

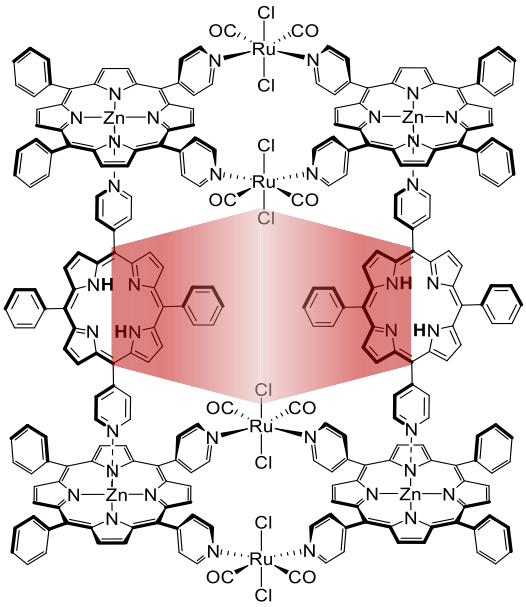

[1Zn·*trans*DPyP]$_2$

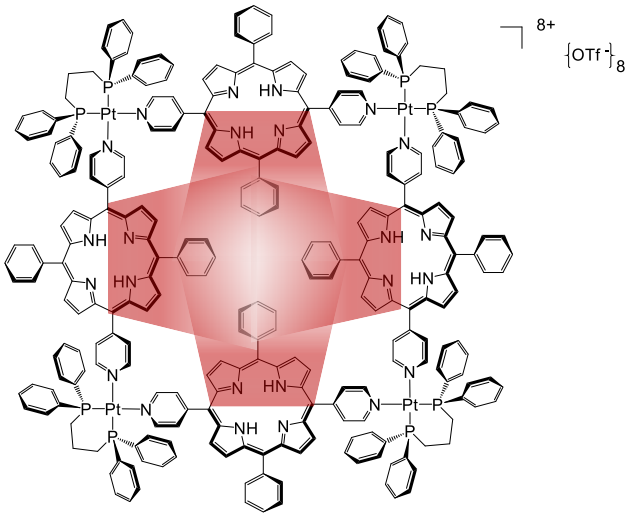

[Ptdppp(*trans*DPyP)]$_4$[OTf]$_8$

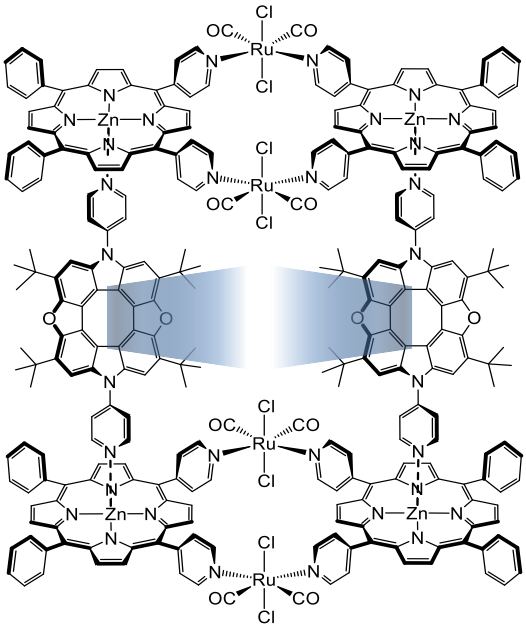

[1Zn·Circ]$_2$

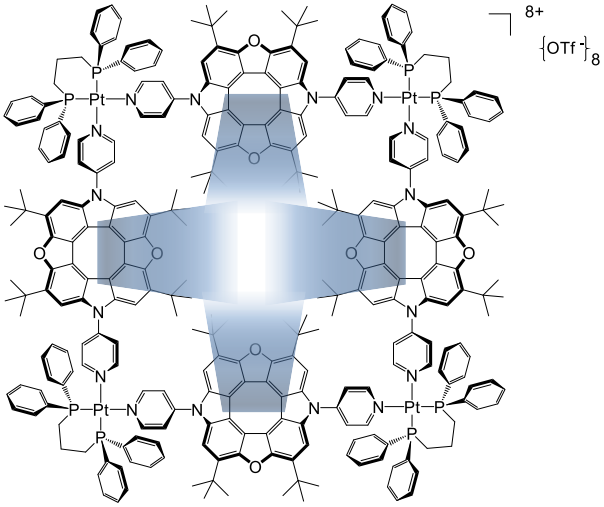

[Ptdppp(Circ)]$_4$[OTf]$_8$

Chart 3.2

The two target systems consist of a sandwich-like assembly, **[1Zn·Circ]$_2$** and the square metallacycle, [Ptdppp(Circ)]$_4$[OTf]$_8$, (Chart 3.2, on the bottom), and should in principle get formed by combination of the circulene unit with either the [*t,c,c*-RuCl$_2$(CO)$_2$(Zn·4'-*cis*DPyP)]$_2$ (**1Zn**) platform or the [Ptdppp(OTf)$_2$] metal complex. In both the parent systems (i.e., **[1Zn·*trans*DPyP]$_2$** and [Ptdppp(*trans*DPyP)]$_4$[OTf]$_8$, see also below) the presence of an ordered number of ***trans*DPyP** units (i.e. large diatropic aromatic surfaces with peripheral hydrogens) allowed to gain precious informations on the mutual disposition/motion dynamics of these units, from NMR solution data. As discussed in Chapter 1, in the sandwich-like adduct **[1Zn·*trans*DPyP]$_2$**, the two pillar dipyridyl units are disposed in a parallel fashion, at a distance of about 11 Å,[19] and are found to be in solution in relatively

free motion around the N–Zn coordination axes. In particular, the peculiar chemical shift displacement of the ***trans*DPyP** inner –NH protons provided clear evidence on that the two bridging macrocycles are, on average, facing each other. In the square metallacycle [Ptdppp(*trans*DPyP)]$_4$[OTf]$_8$, reported by Stang and co-workers,[20] the presence of neatly different magnetic environments in the inside and outside regions of the square allowed to discriminate over possible conformations of the bridging ligands, by analysis of the porphyrin ^{1}H-NMR resonance patterns. In particular, at room temperature the four porphyrin macrocycles are roughly coplanar with the plane defined by the four metal centers, and the porphyrins motion around both the pyridyl-porphyrin macrocycle and the pyridyl-Pt bonds is low on the NMR time-scale. It must be noted that alternative conformational scenarios were proposed, by similar NMR analysis, either for systems bearing different ancillary ligands on the Pt(II) and/or peripheral substituents on the porphyrin, or by changing the nature of the solvent and the temperature.[21] In all cases, the square metallacycle was reported to be the unique assembled product. Solid state X-ray data were never obtained.

Given the above-mentioned similarities between **Circ** and ***trans*DPyP**, the target systems and parent porphyrin derivatives are expected to assemble in a similar fashion and present close structural/dynamic features. Nevertheless, while for ***trans*DPyP** the diatropic induced current is extended to the whole macrocycle, in **Circ** the (presumed) paratropic current is limited to the COT core portion (Chart 3.2). Therefore, in the proposed systems, the proximity of the **Circ** units is likely not sufficient to produce the desired mutual combined effects. Also, as compared to ***trans*DPyP**, in **Circ** the peripheral substituents, that should act as NMR spectroscopic markers of these effects, are not ideally located (and most probably masked by the ring current contributions of **1Zn** in the sandwich-like derivative). Still, this premliminary investigation is valuable to: (i) promote the use of circulenes as building units for metal-mediated functional architectures; (ii) gather and validate structural analogies with the parent reference porphyrin systems by solution and X-ray data. In view of elucidating the aromatic/anti-aromatic character of circulenes, this latter aspect can serve to find more suited inspiring systems. For instance, a further elaboration into 3D constructs is certainly intriguing, as the electronic character of the circulene components may appear from unexpected host-guest recognition properties.

3.2 Results and Discussion

3.2.1 Synthesis and Characterization of the Sandwich-like Assembly [1Zn·Circ]$_2$

The reaction between **1Zn** and **Circ** occurs in mild conditions and almost immediately: stirring at room temperature for few minutes a chloroform solution containing equimolar quantities of the building units. The self-assembling process of the building blocks was qualitatively observed by an instantaneous change of the solution colour, that from the vivid red characteristic of **1Zn** turned to a dark purple. The system was isolated in microcrystalline form by slow diffusion of *n*-hexane in a chloroform solution of the assembly at room temperature. The resulting product was fully characterized in solution by NMR spectroscopy (1D ^{1}H, ^{13}C NMR, 2D HH–COSY, HSQC, HH–NOESY,

HH–ROESY, 2D ^{1}H DOSY), IR and UV–Vis absorption and emission spectroscopy. The single crystal X-ray structure of the system was also determined, by means of Synchrotron light-radiation.

The ^{1}H NMR of the collected microcrystalline solid is shown in Figure 3.7 in comparison with those of the molecular building unit **1Zn** and **Circ**. In general, all the spectroscopic features found are very alike with those reported for previous systems,[19,22] confirming unambiguously the quantitative formation of the sandwich-like assembly **[1Zn·Circ]$_2$**. Although NMR titrations with progressive addition of the bridging ligand to **1Zn** were not performed, spectra recorded on initial **1Zn** solutions followed by direct addition of stoichiometric amounts of **Circ**, indicate that this new sandwich-like adduct is formed by means of the so-called "all or nothing" assembling process, common to all the other systems previously discussed (see also Chapter 1 and 2).[19,23] In particular, the expected ^{1}H NMR resonances for the fully assembled system plus those of a very minor amount of free **1Zn** were observed, in the presence of occasional slight defects of **Circ** unit (here not shown); at room Temperature, a slow-to-fast exchange regime was found, in common with the parent porphyrin system.

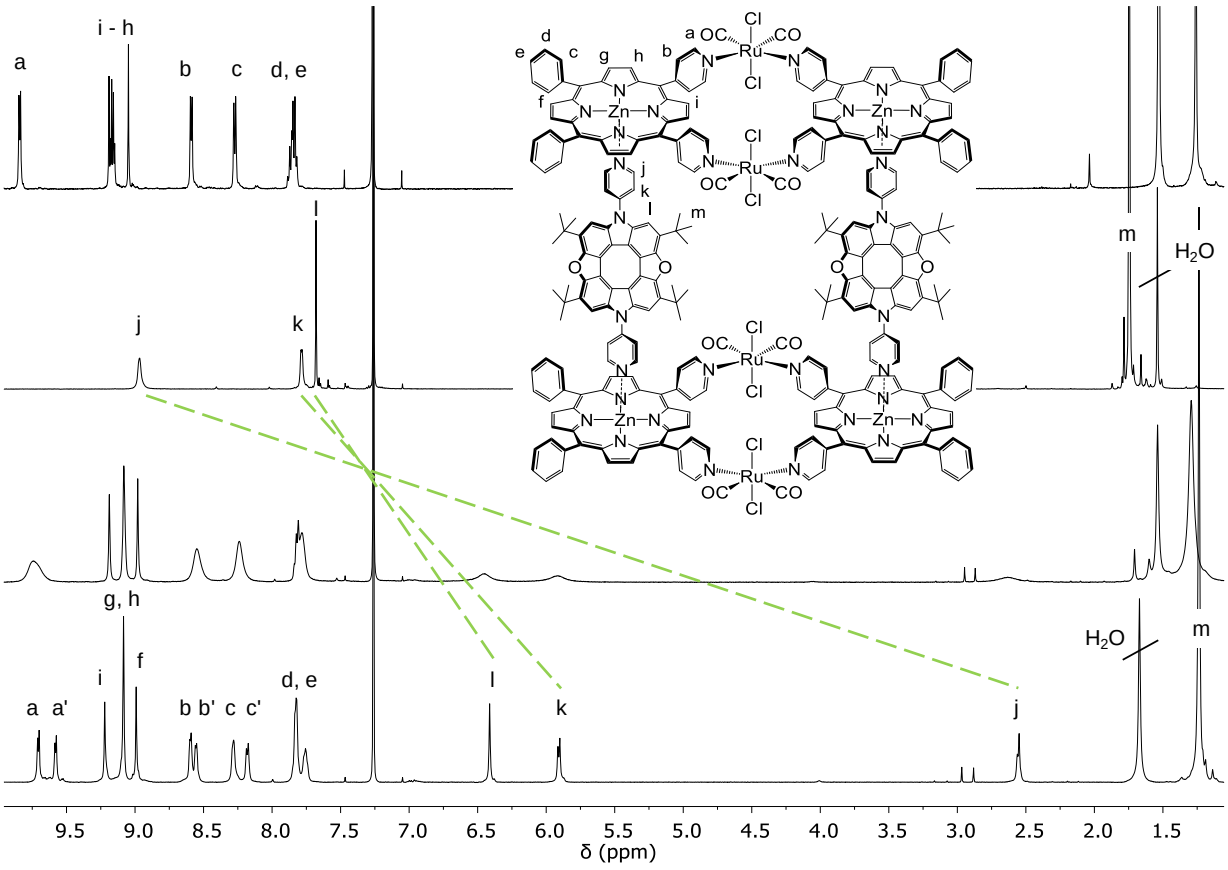

Figure 3.7. ^{1}H NMR spectra ($CDCl_3$), from the top: **1Zn**, **Circ**, **[1Zn·Circ]$_2$** (T = 25°C), and **[1Zn·Circ]$_2$** (T = – 20°C).

At room temperature, the spectrum appears as a set of broad signals that resolve and sharp upon lowering the temperature down to –20°C, as the kinetics of formation of the Zn–N bonds slows down. The complete assignment was made possible by 2D experiments (HH-, HC-COSY; HH-ROESY and -NOESY), and the corresponding resonances show the correct relative integrations. The axial

coordination of the two equivalent linkers to the zinc-porphyrins of **1Zn** is indicated by the general upfield shift experienced by all the resonances of the circulene unit. This is the consequence of the shielding effect of the combined ring currents of the zinc-porphyrins of the two facing metallacycles. This effect decreases gradually as the distance of the protons from the zinc porphyrins increases, as evidenced by the differences of the resonance chemical shifts, compared to the free circulene: Δδ = –6.42 (Hj), Δδ = –1.87 (Hk), Δδ = –1.27 (Hl), and Δδ = –0.51 ppm (Hm). Indeed, the most upfield shifted resonances arise from the protons Hj closer to the nitrogen atoms, found at 2.55 ppm (Figure 3.7). As already observed in the system discussed in the previous Chapters and confirmed by HH-ROESY and -NOESY experiments, each resonance of the *meso* aromatic rings of the Zn porphyrins in **[1Zn·Circ]$_2$** is split into two sharp signals of equal intensity (protons a-a', b-b' and c-c' in Figure 3.7). The presence of a single set of resonances for the circulene unit (pattern preserved also down to –40°C) is consistent with a symmetrical magnetic environment that may result either from a substantial degree of conformational freedom of these units or from a preferred highly symmetrical mutual disposition (see also below). Not surprisingly, the overall ^{1}H-NMR resonance pattern does not present any unusual chemical shift displacement and/or splitting, thus impeding to discriminate over the presence of local paratropic ring currents.

Interestingly, in the 2D HH–NOESY (Nuclear Overhauser Effect Spectroscopy) experiment (Figure 3.8), spatial correlations are observed between the circulene *tert*-butyl resonances and those of the porphyrin β-pyrrolic and pyridyl/phenyl a', b' and c' protons, and between the circulene pyridyl Hj resonances and those of the porphyrin β-pyrrolic and pyridyl/phenyl b' and c' protons. The simultaneous correlation of the *tert*-butyl groups with all β-pyrrolic and aryl protons of **1Zn**, is congruent with a certain degree of mobility of the ligand around the coordination axes.

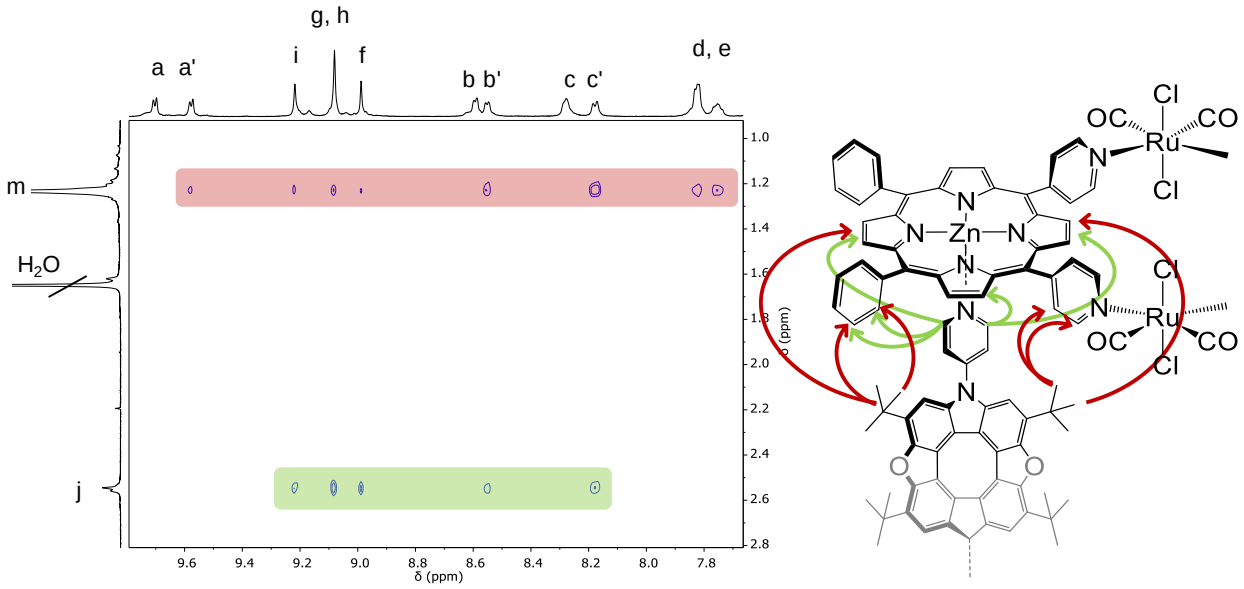

Figure 3.8. HH-NOESY spectrum ($CDCl_3$, – 20°C) of **[1Zn·Circ]$_2$**.

Systematic crystallization trials were carried out in order to obtain single crystals suitable for X-ray diffraction analysis. For **[1Zn·Circ]$_2$**, single red needle-shaped crystals were obtained by slow diffusion of *n*-hexane in a chloroform solution of the assembly kept at 4°C. Details on the crystallization and

data refinement are reported in the Experimental Section. The structural determination of compound **[1Zn·Circ]$_2$** indicates that the molecular sandwich architecture observed in solution, containing two **1Zn** macrocycles axially connected face-to-face by two circulene ligands, is maintained also in the solid state (Figure 3.9). The assembly crystallizes in the centrosymmetric spatial group *P*-1 with triclinic cells containing one **1Zn** platform and one circulene (distances and angles reported in Table 3.2 of the Experimental Section). An inversion centre is located at the assembly barycentre, that matches with the crystallographic inversion centre of *P*-1 space group, therefore only half assembly **[1Zn·Circ]$_2$** is found within the crystallographic asymmetric unit.

The two zinc-porphyrin platforms are parallel and slightly shifted, therefore they do not perfectly eclipse as was observed in previous sandwich-like structure.[19] The two bridging circulenes are yet parallel, but they do not face each other; the distance between the plans containing the two circulenes is of about 8 Å. Two *n*-hexane and three chloroform ordered molecules are found in between the **Circ** units (here not shown).

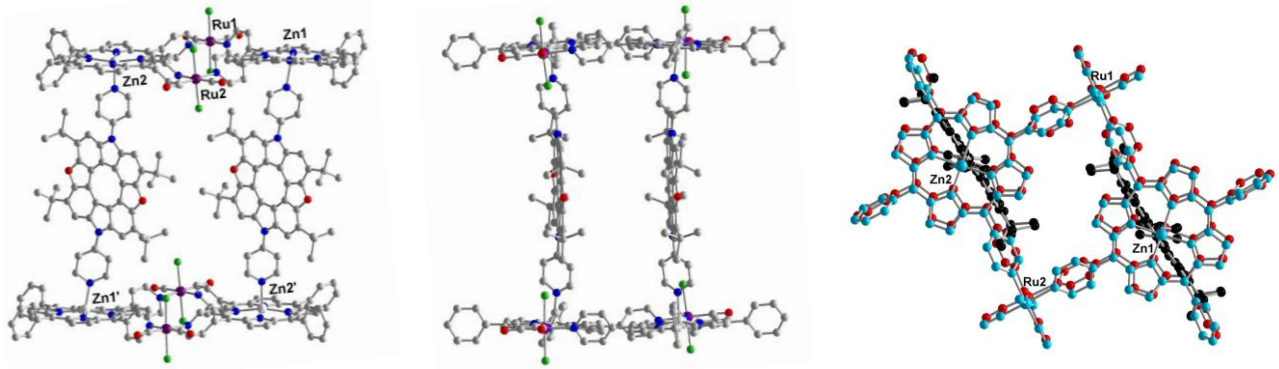

Figure 3.9. Different views of the single crystal X-ray structure of **[1Zn·Circ]$_2$**. Colour code: C, grey; N, blue; O, red; Zn, white; Ru, purple; Cl, green. On the right: the two facing **1Zn** platforms are respectively depicted in light blue and in red, while the **Circ** units are black.

The apical 4'-N(py) rings bound to the Zn ions are approximately perpendicular to the ZnN4 basal plane, and the Zn ions have a square pyramidal coordination geometry. The crystallographic analysis revealed a Zn1(II)···Zn2'(II) distance between two opposite zinc centres spanned by the same ligand unit, is of 20.3 Å. This length is related to the longitudinal dimension of the assembly and counts for the length spanned by the two pyridyl N of the bridging circulene plus the two bonds Zn – N. Considering one single platform, the distance between two zinc atoms Zn1(II)···Zn2(II) is 13.8 Å, the Ru1(II)···Ru2(II) one is 14.1 Å, indicating only minor distortion compared to what observed in the X-ray structure of the solely **1Zn** platform.[19b] The two circulenes are slightly bent towards the inside of the cavity described by the assembly: the distance between the centroids of the two COT cores is of 12.9 Å, almost one angstrom less with respect to the distance spanned by the Zn(II) cations of a single platform. The bridging ligands do not display any appreciable distorsions when compared to the X-ray structure of free molecule (see above, Chart 3.1).

The possibility to employ the supramolecular system **[1Zn·Circ]$_2$** as host receptor, by non-covalent interactions between the circulenes and large aromatic guests, has been examined. The ability of circulenes to establish π-π interactions was previously rarely evidenced and limited to the

observation of π stacking interactions between neighbouring molecules in the X-ray structure of an isolated azatrioxa[8]circulene.[15] To the best of our knowledge, investigations over possible π interactions in aromatic and anti-aromatic mixed systems were not as yet pursued. Given the rather fluxional behavior of **[1Zn·Circ]$_2$** in solution, this preliminary study was essentially done in the solid state.

To this aim, co-crystallizations between **[1Zn·Circ]$_2$** and coronene were attempted. Dark-blue single crystals were obtained by slow diffusion of *n*-hexane upon chloroform solutions of 1:2.5 equivalents of **[1Zn·Circ]$_2$** and coronene (see Experimental Section for further details). The derived X-ray structure (Figure 3.10) presents the same unit cell found for that of **[1Zn·Circ]$_2$**.

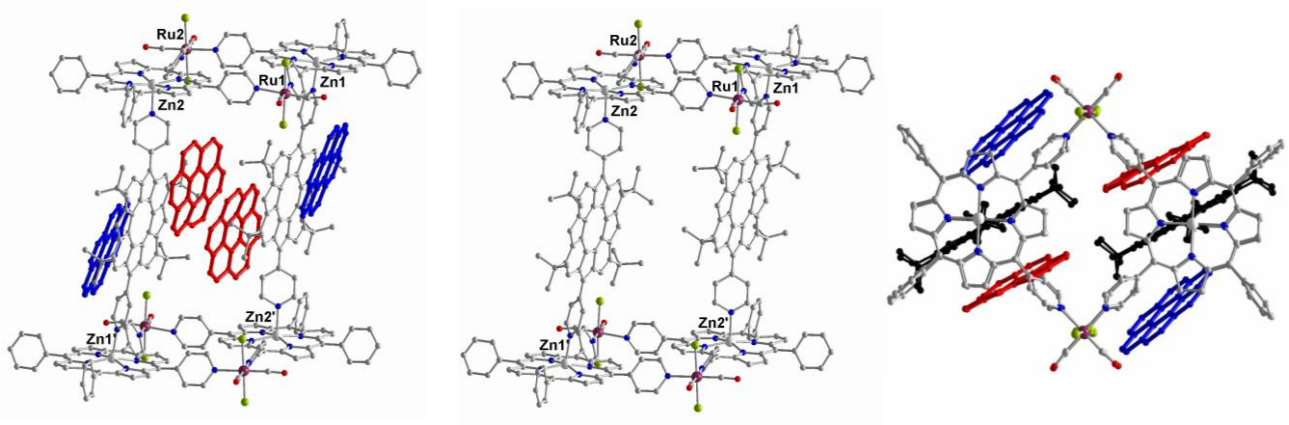

Figure 3.10. Different views of the single crystal X-ray structure of **[1Zn·Circ]$_2$·coronene**. Colour code: C, grey; N, blue; O, red; Zn, white; Ru, purple; Cl, green. Coronene molecules, omitted in the central figure, are depicted in red and blue, while, on the right, the **Circ** units are in black.

Two coronene molecules are found inside the supramolecular assembly (red in Figure 3.10) and 2 coronene outside, shared by two neighboring **[1Zn·Circ]$_2$** units (blue in Figure 3.10). The "inside" coronene molecules are disposed in the space that in the crystalline packing of the sole **[1Zn·Circ]$_2$** is occupied by solvent molecules, therefore inducing only a slight change in the mutual disposition of the circulene units. The coronene molecules inside **[1Zn·Circ]$_2$** are disordered in two different positions, indicated in red and purple in Figure 3.11, and in low occupancy (0.2/0.3), giving an overall **[1Zn·Circ]$_2$**:coronene ratio of 1:2.5.

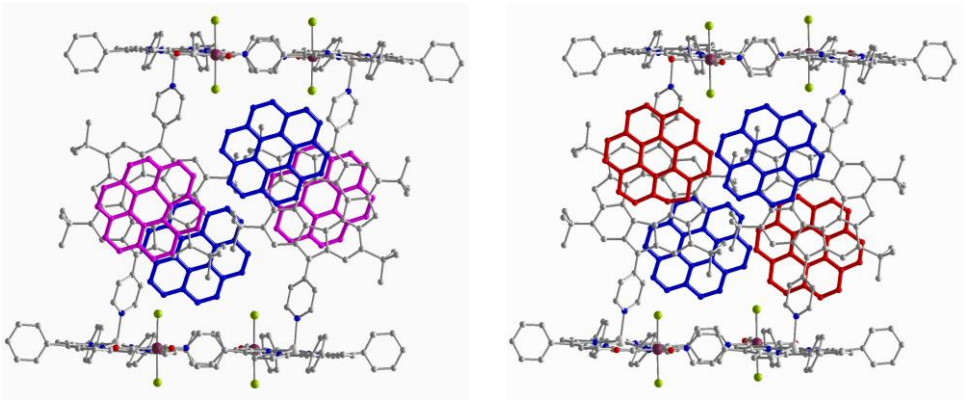

Figure 3.11. Single crystal X-ray structure of **[1Zn·Circ]$_2$·coronene**. The two disordered coronene molecules are depicted in pink and red. Colour code: C, grey; N, blue; O, red; Zn, white; Ru, purple; Cl, green.

Red (and pink) coronene molecules face the planar antiaromatic core of the circulene and the distance (3.5 Å) is consistent with a π-π stacking interaction.[24] The blue coronenes face, instead, the *tert*-butyl groups of the circulene, suggesting the occurrence of a CH-π interaction,[25] and are shared by two circulene ligands belonging to adjacent **[1Zn·Circ]$_2$** assemblies, as shown in Figure 3.12.

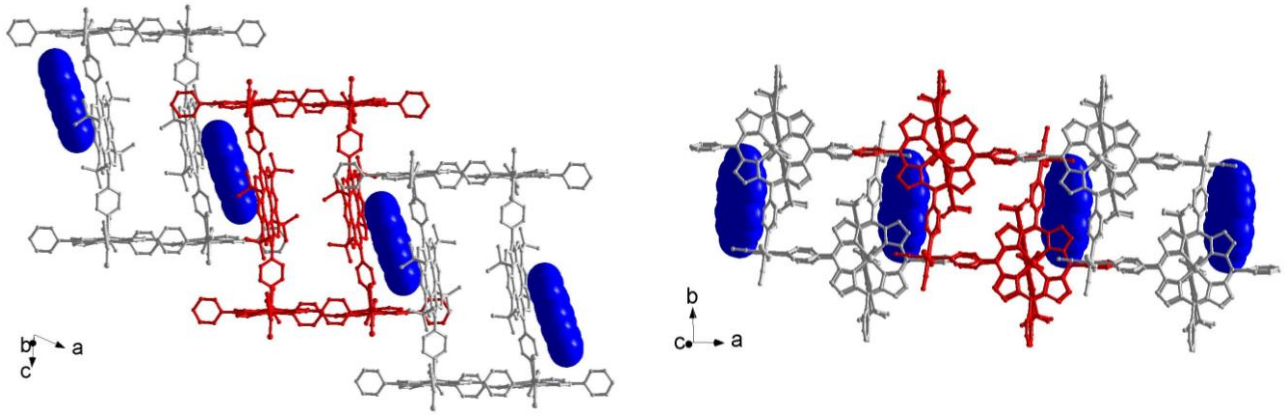

Figure 3.12. Details of the chaining of **[1Zn·Circ]$_2$** assemblies and blue coronenes (the other coronene molecules are omitted for clarity).

Table 3.1 reports a comparison between some crystal structure parameters of the **[1Zn·Circ]$_2$** assembly without (left) and with (right) coronene molecules. The presence of coronene molecules affects only to a slight extent the mutual disposition of the circulenes assumed in the original structure of **[1Zn·Circ]$_2$**. Somehow unexpectedly, a possible face-to-face conformation of the bridging ligands and consequent encapsulation of the aromatic guest is somehow impeded, or at least less effective as driving force for positive circulene-coronene interactions.

Table 3.1. Relevant distances calculated for the structures obtained for the **[1Zn·Circ]$_2$** assemblies without (left) and with (right) coronene molecules

	[1Zn·Circ]$_2$	**[1Zn·Circ]$_2$·coronene**
Zn1 - Zn2 (Å)	13.802(1)	13.852(1)
Zn1 - Zn2' (Å)	20.319(1)	20.293(1)
Ru1 - Ru2 (Å)	14.143(1)	14.075(1)
COT1 – COT2	12.9	13.03

The remaining crystals from the analyzed crystallographic batch were then collected and examined by NMR spectroscopy. In the ^{1}H NMR spectrum, no interactions between coronene and **[1Zn·Circ]$_2$** are maintained, with only the proton resonances characteristic of free coronene and **[1Zn·Circ]$_2$** being clearly detected. The same occurred upon direct addition of 3 equivalents of coronene to a **[1Zn·Circ]$_2$** $CDCl_3$ solution. These observations were quite expected, given that the coronene acts predominantly as inter-molecular connector of **[1Zn·Circ]$_2$** units, rather than as 'intra-molecular' guest for individual **[1Zn·Circ]$_2$** units.

Photophysical Characterization

In parallel to the host-guest chemistry studies, a preliminary photophysical characterization of **[1Zn·Circ]$_2$** was carried out, in collaboration with Dr. Mirco Natali from the University of Ferrara.

Circ presents, at room temperature and in chloroform solution, a strong absorption spectrum with maxima at 321, 370 and 410 nm and a relatively intense fluorescence (quantum yield, Φ = 0.11) peaking at 438, 462 and 492 nm (Figure 3.15). The lowest singlet excited state has an energy of 3.04 eV (calculated from the UV-vis spectrum) and a lifetime of 6.4 ns. It presents a first oxidation potential at 1.23 V (vs SCE).[18] All these electronic properties are a promising prerequisite for the promotion of photoinduced processes within the assembly **[1Zn·Circ]$_2$**. The absorption spectrum of a chloroform solution of **[1Zn·Circ]$_2$** is reported in Figure 3.13, in comparison with those of the model compounds. In the visible region, the light is completely absorbed by the zinc-porphyrin moiety, while in the 360-380 nm region the absorption the circulene is predominant, even though partially covered by the strong porphyrin Soret band (420 nm).

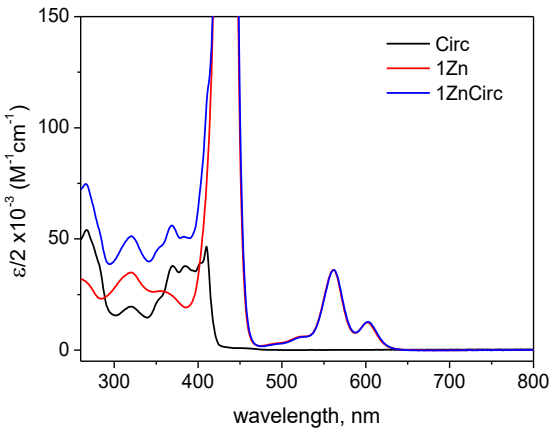

Figure 3.13. Absorption spectra ($CHCl_3$) of **Circ** (black line), **1Zn** (red line) and **[1Zn·Circ]$_2$** (blue line).

Dilution spectrofluorimetric titration experiments were performed in **[1Zn·Circ]$_2$** chloroform solution to study the stability of the assembly. The break of the pyridyl-zinc cation coordination bond causes a 5 nm blue shift in the porphyrin absorption bands, allowing to evaluate a limiting concentration, at which the structure is completely assembled in solution, that was found to be *ca.* 2 x 10^{-5} M, in agreement with what observed for analogous supramolecular systems.[19,22,26]

The absorption spectrum of the **[1Zn·Circ]$_2$** assembly results to be the almost perfect superimposition of the spectra of the molecular building blocks, proving that no electronic interaction occurs through the Zn-N coordination bond between **1Zn** and **Circ**, which maintain their electronic properties nearly unchanged (i.e. both the HOMO-LUMO gaps and the redox potentials of **[1Zn·Circ]$_2$** can be confidently approximated to those of the free constituting components, as observed in previous systems).[19,22,26] This feature, characteristic of this type of supramolecular structures, allows us to make a good prediction on the thermodynamics of the photoinduced intercomponent processes that may occur in the assembled system. More in detail we can build the energy level diagram displayed in Figure 3.14, where the excited states of the molecular building units are reported. The energy of the possible charge transfer states was estimated from the redox potentials of the free **Circ** and **1Zn** units:[18,19] since the circulene does not present any wave at negative potentials, only a charge separated state in which the circulene is oxidized, and the Zn-porphyrin reduced may be accessible.

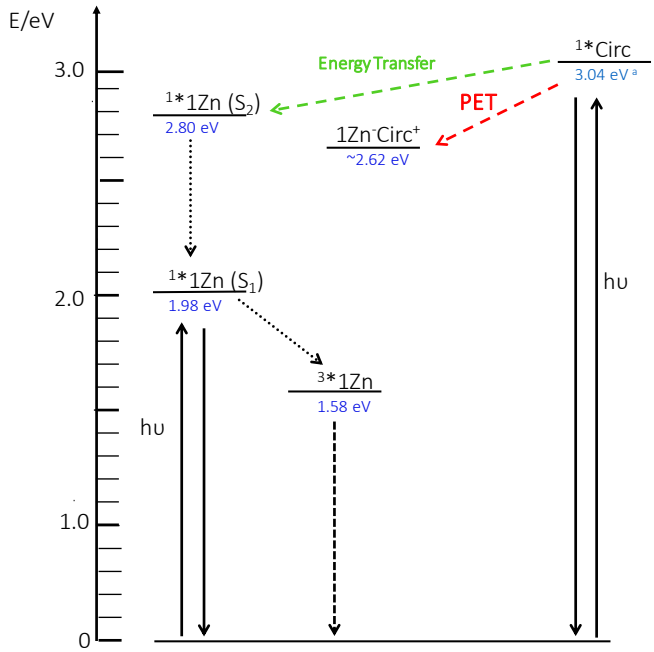

Figure 3.14. Energy level and photophysical process diagram for **[1Zn·Circ]$_2$**. The triplet excited state of the circulene is not shown, being the energy level of this state not known.

From these considerations, no intercomponent photoinduced processes are expected to occur from the Zn-porphyrin excited state. Indeed, as predicted, upon excitation at 550 nm, the emission spectrum of the zincate platform in **[1Zn·Circ]$_2$** presents the same intensity and lifetime of free **1Zn**.

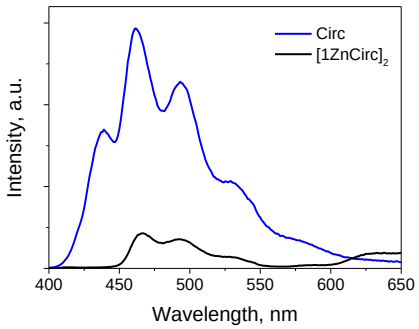

Figure 3.15. Emission spectra ($CHCl_3$, λ_{ex}= 370 nm) of iso-absorbent solutions of **Circ** (blue line) and **[1Zn·Circ]$_2$** (black line).

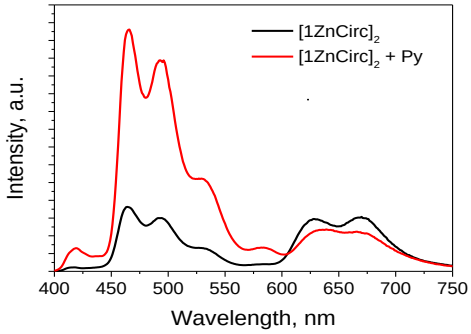

Figure 3.16. Emission spectra ($CHCl_3$, λ_{ex}= 370 nm) of a solution of **[1Zn·Circ]$_2$** before (black line) and after (red line) the addition of pyridine.

A different behavior is observed upon excitation of the circulene unit (λ_{ex}= 370 nm): fluorescence spectroscopy and lifetime measurements evidenced a quenching of the emission of *ca.* 80% (Figure 3.15) with kinetics that lies below the instrumental resolution of the TC-SPC setup (i.e., <200 ps). Addition of a slight excess of pyridine, a competitive ligand that induces disassembling of the supramolecular system, completely and immediately restored the fluorescence intensity, proving that the quenching is strictly related to the coordination of the ligand to Zn-porphyrin platform (Figure 3.16). The emission quenching could be either due to a photoinduced energy transfer process from the circulene to the Zn-porphyrin platform or a photoinduced electron transfer process leading to the formation a charge-separated state where the circulene is oxidized, and the porphyrin reduced. The decrease of the porphyrin emission intensity (600-750 nm region, Figure 3.16 on the right) observed upon addition of pyridine, suggests a contribution in the population of the Zn-porphyrin singlet excited state, coming from an energy transfer process from the circulene unit (the residual porphyrin fluorescence is due to direct excitation, as at 370 nm **1Zn** absorbs the 40% of the irradiating light). However, if the observed quenching were solely due to the energy transfer process, iso-absorbing solution of **[1Zn·Circ]$_2$**, and **1Zn** (λ_{ex} = 370 nm) should show matched porphyrin fluorescence intensities. The lower emission experimentally observed (Figure 3.17) for **[1Zn·Circ]$_2$**, therefore suggests that the contribution of a competitive photoinduced electron transfer process, in the deactivation of the circulene singlet excited state, cannot be completely ruled out.

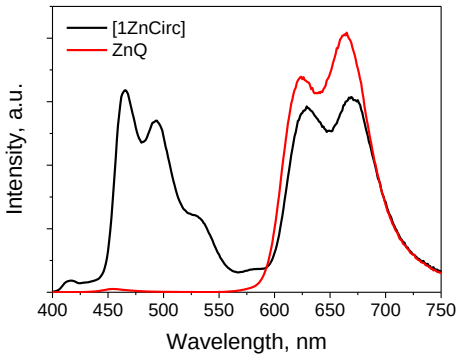

Figure 3.17. Emission spectra ($CHCl_3$, λ_{ex} = 370 nm) of iso-absorbent solutions of **[1Zn·Circ]$_2$**, and **1Zn.**

Further time-resolved transient spectroscopy experiments are required to definitively understand the nature of the quenching mechanism.

3.2.2 Synthesis and Characterization of the Square Metallacycle [Ptdppp(Circ)]$_4$[OTf]$_8$

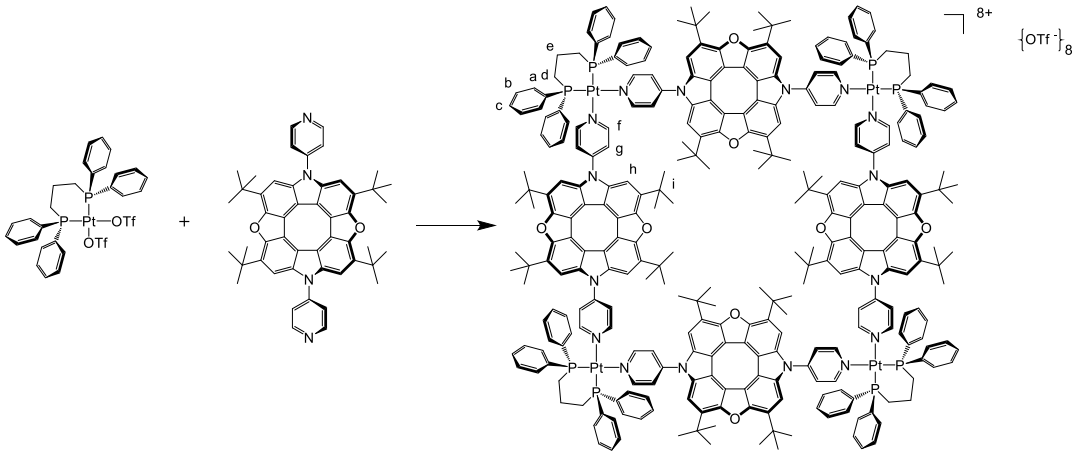

Scheme 3.1.

Initially, two parallel solution studies were performed: 1.5x10^{-3} M 1:1 mixtures of [Ptdppp(OTf)$_2$] and **Circ**, dissolved either in CD_2Cl_2 or in acetone-d_6, at room T, were monitored over time by ^{1}H and ^{31}P NMR spectroscopy. In both cases, within ten minutes the almost total consumption of the starting materials occurs, in favour of the formation of one or more new discrete systems (small contaminations from oligomeric species cannot be excluded), with features consistent with the coordination of the circulene pyridyl moieties to the [Ptdppp]$^{2+}$ (see below).[20,21] Subtle intermediate spectral changes (appreciable in the ^{31}P spectra) are no longer detected after approximately three hours, the final scenarios observed for two solutions are very alike (Figure 3.18). In general, extended signals overlap and broadening is observed, and several resonances display more complex pattern as compared to those of the parent starting materials. Assignments were done by means of 2D HH-COSY, HC-HSQC, HP-HMBC, also in reference with previously reported examples.[20,21]

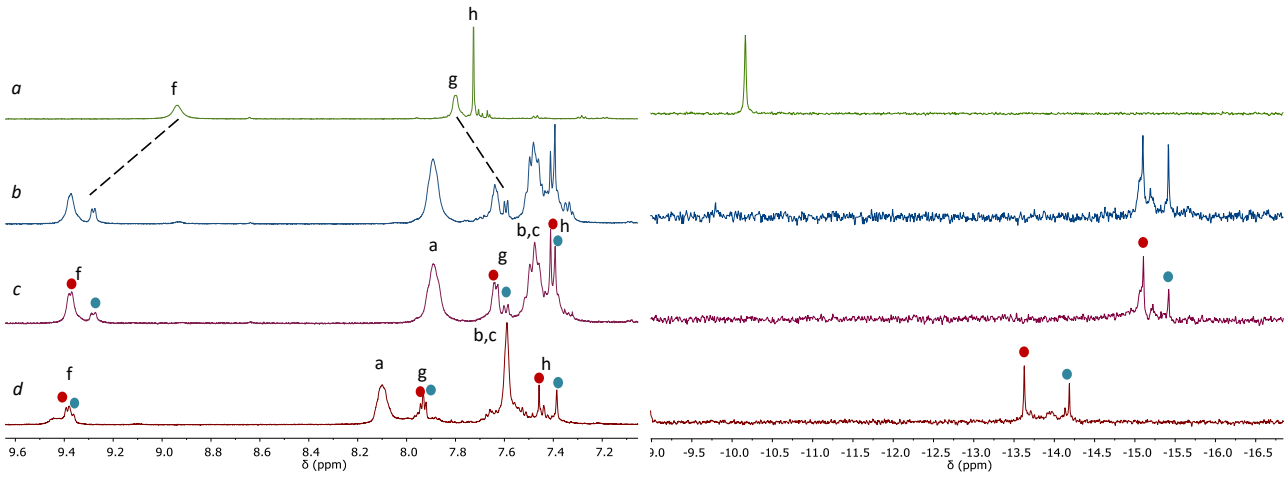

Figure 3.18. ^{1}H-NMR (down-field region) and ^{31}P-NMR spectra of: *a*) **Circ** and [Ptdppp(OTf)$_2$], CD_2Cl_2; *b*) CD_2Cl_2 equimolar mixture of **Circ** and [Ptdppp(OTf)$_2$], after approx. 10 mins from mixing; *c*) CD_2Cl_2 mixture of **Circ** and [Ptdppp(OTf)$_2$], after approx. 3 hours from mixing; *d*) acetone-d_6 mixture of **Circ** and [Ptdppp(OTf)$_2$], after approx. 3 hours from mixing.

In the proton spectra, two major sets of doublets for the Hf and Hg pyridyl protons are observed (centred at 9.4 and 7.6 ppm in CD_2Cl_2, and 9.4 and 7.9 ppm in acetone-d_6), in parallel two singlets of major intensities for the Ptdppp portion (around -15 ppm in CD_2Cl_2, and -14 ppm in acetone-d_6) appear in the ^{31}P-NMR spectra.

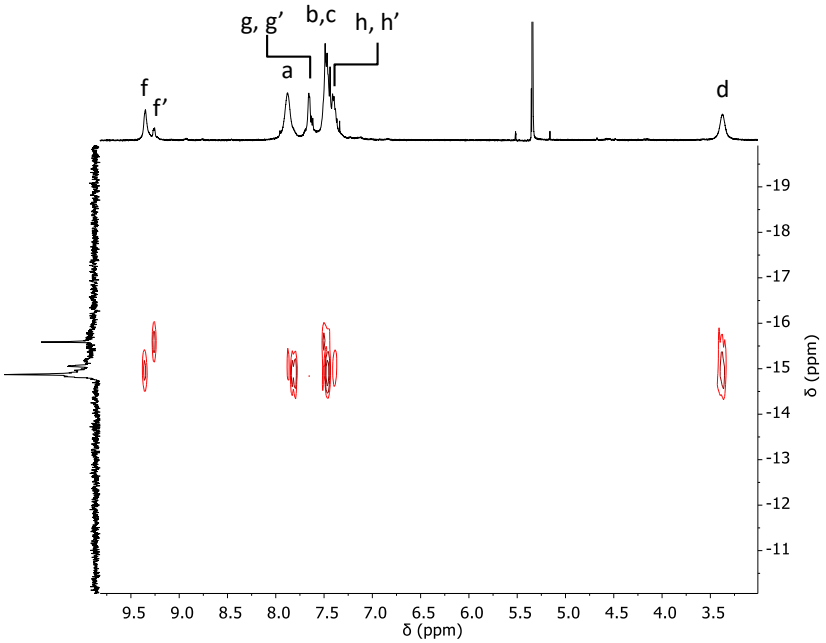

Figure 3.19. 2D H-P HMBC spectrum of a CD_2Cl_2 equimolar mixture of **Circ** and [Ptdppp(OTf)$_2$].

Separate H-P correlations between the two set of resonances are found in the 2D HP-HMBC spectra (the one in CD_2Cl_2 is shown in Figure 3.19). The **Circ** macrocycle protons (Hi and *t*Bu groups, these utter are not shown) also both resonate as two separate major singlets, while all the ^{1}H-NMR signals of the phosphine ligand are relatively broad and not resolved (aliphatic region not shown). In the 2D ROESY spectra nOe correlations are found between pyridyl protons Hf and the phosphine phenyl resonances Ha, and between the *tert*-butyl groups and protons Hb,c and Hh. A comparison with the ^{1}H and ^{31}P spectra of the parent free components indicates a downfield shift for the Hf pyridyl protons ($\Delta\delta$ of *ca.* + 0.4 ppm) and a general upfield shift for all the other relevant resonances (*e.g.*, in CD_2Cl_2, $\Delta\delta$ = – 0.4 and – 0.3 ppm for **Circ** Hh and Hi protons, respectively, and $\Delta\delta$ = – 5 ppm for the P of the ancillary dppp ligand). A longer accumulated ^{31}P spectrum (see Appendix to Chapter 3) showed Pt-correlation satellites displaying a coupling constant of 3062 Hz, congruent with the complex *cis*-configuration. In the ^{19}F-NMR spectra the resonance for the free triflate anion is found. The only distinction in the NMR analysis for the two different solvents consist in an apparently different relative intensity for the two sets of resonances (indicated with red and blue dots in Figure 3.18) and best appreciated in the comparison of the ^{31}P NMR spectra, where switching from dichloromethane to acetone the signal ratio seems to decrease from 2:1 to almost 1:1. At the same time, for both the solutions, a third minor set of signals can be partly appreciated. Even though an accurate signal integration is not feasible, a 1:1 stoichiometry of the Ptdppp fragment and the circulene ligand can be confidently assumed. In general, all the spectroscopic data are in full agreement with the formation, in both solvents, of one or more metallacyclic species bearing $[Ptdppp]^{2+}$ and **Circ** units, connected by Pt-N(pyridyl) coordination bonds, of the type $[M_nL_n][OTf]_{2n}$.[27] In fact, the increased

number of resonances with respect to the parent units may agree both with the presence of two major assemblies with different nuclearity (e.g., a molecular triangle together with the intended square) or of a single species for which the restricted motional freedom of the organic bridging ligand results in more than one possible conformation with distinct symmetry elements.

In the literature, a large number of examples concerning the assembling of metallacycles (in organic solvents at room T) from the same Pt^{II} metal complex and a variety of rigid organic di-pyridyl linkers reports the formation of: *i)* the single expected tetrameric species, with cases of restricted conformational freedom *ii)* mixtures of triangle and square products in thermodynamic equilibrium, *iii)* complex mixtures of oligomeric species, requiring high temperatures to meet equilibrating conditions and possible conversion to discrete assemblies.[27] Systems of the second class are of special interest in part for their deviation from the directional-bonding approach, but also for the insight that they may provide insights into the mechanism of self-assembly. Important stress has to be given to the difficulty of correct interpretations (and therefore previsions) that arises from a series of inherent analytical characterization difficulties. For instance, in the NMR spectra, small shift differences, signal superposition, or exchange equilibria in different rate exchange in the T_1 and T_2 and diffusion domains, plus broadening related to partial aggregations, may become problematic. As consequence, NMR exchange or DOSY experiments may lack to produce reliable information. Moreover, mass analysis, even with soft techniques, often suffers from the fragmentation because of the weak coordinative bonds frequently supported by charge repulsion existing in multiply charged ions. Thus, it is not always clear, whether, metallacyclic species appearing in the mass spectra are a true solution component or a fragment from a bigger system, and isotope peak patterns predictions may be reaching the limit of the instrumentation resolution. Cold-spray ionization is not always routinely available. In addition, unspecific aggregation during the ionization process can lead to misinterpretation in that larger aggregates seem to form which are not present in solution. In the solid state, single crystals suitable for X-ray crystal are often difficult to obtain. However, even the analysis of high-quality single crystals may mislead if one of the compounds in solution crystallizes preferentially followed by a readjustment of the solution equilibrium. Still, evaluation of these systems in solution or in crystallization processes in response to a change of certain parameters is clearly useful. In particular, concentration, temperature, solvent polarity, presence of water, and nature of the counter-anions are likely to offer useful insights.[20,27]

In light of these observations, some preliminary further investigations have been performed in the present case of study. For both samples, VT NMR experiments (in a range of + 45 ÷ – 40° C) plus progressive dilution at room T did not produce any appreciable changes. ^{1}H 2D ROESY experiments did not evidence the presence of exchange-correlation peaks between the resonances of different proton sets. Addition of excess **Circ** to the solution mixtures, resulted in the appearance of the resonances of free circulene, and no exchange correlations between bound and unbound situations were detected.[28] These data, taken with caution, seem to suggest that for the present systems a mixture of kinetic non equilibrating products are formed in solution at room Temperature. Subsequently, and with the specific aim of addressing the possibility of forcing a self-assembling regime (i.e. thermodynamic equilibration between the components in place of kinetically controlled reaction), the reaction between **Circ** and [Ptdppp$(OTf)_2$] was repeated on a larger scale and by varied

conditions: refluxing under Ar atmosphere, for three hours, a fresh-distilled dichloromethane solution ($1.5x10^{-3}$ M) of equimolar quantities of reactants. Concentration and addition of *n*-hexane afforded the precipitation of a yellow powder, that was filtered, washed with *n*-hexane and dried under vacuum. The ^{1}H-NMR spectrum (CD_2Cl_2) of the isolated compound (Figure 3.20) shows the same spectral pattern observed in the NMR-tube reaction. Quite puzzling, the same spectral pattern is observed upon leading the reaction at higher temperatures (such as in refluxing dichloroethane or at 100°C in a microwave reactor).

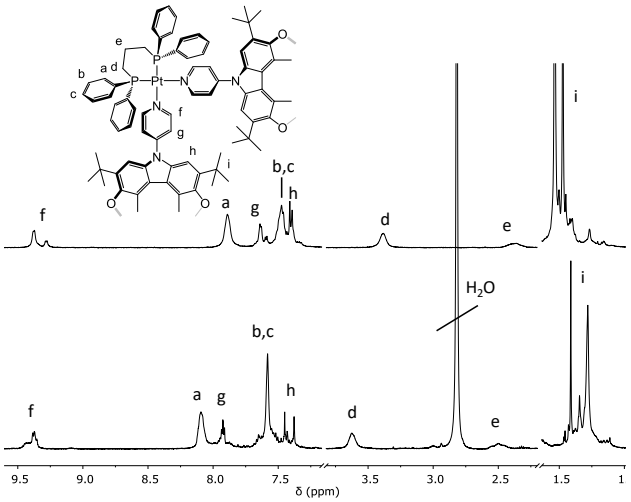

Figure 3.20. ^{1}H-NMR spectra (down-field region) of the isolated product registered in CD_2Cl_2 (top) and in acetone-d_6 (bottom).

Attempts of isolation of the possible different metallacycles by TLC resulted inefficient leading to the sole collection of free **Circ** and part of the compound stuck in the starting spot. Neither ^{1}H-DOSY NMR could afford a neat separation of the metalacyclic species (Figure 3.21). However, it is yet possible to appreciate that proton signals in the aromatic region are not perfectly aligned to a unique diffusion coefficient value, and at least two different diffusing species are found. To correctly evaluate the diffusion coefficient of each species, an accurate analysis of the signal decay is required. Analysis that we could not perform since the Bayesian DOSY method, available in the MestReNova software, is not efficient in the deconvolution of overlapping signals of systems having different diffusion coefficient.

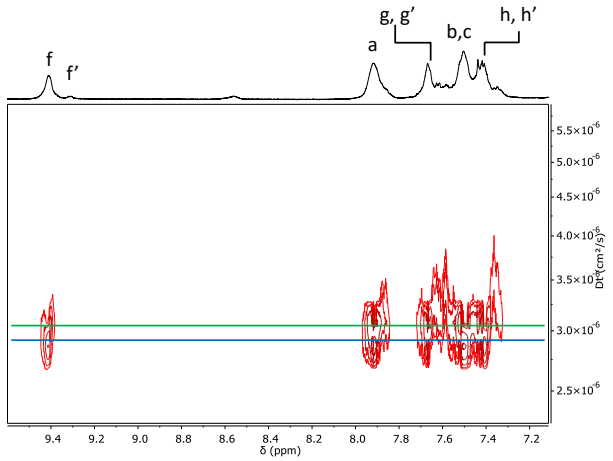

Figure 3.21. 2D ^{1}H-DOSY spectrum (CD_2Cl_2, aromatic region) of the isolated product.

Indeed, in the metallacyclic systems, the steric hindrance of the *tert*-butyl groups hampers and probably slows the free rotation of the circulene units about the Pt-N(py) coordination axes. In this way, as already mentioned, if the circulene units preferentially adopt a conformation where they are coplanar to the Pt^{II} complex plane spending sufficient time within the de-shielding cone of the neighboring circulenes, the ^{1}H-NMR resonances, facing the inside of the macrocycle, should be down-field shifted, as consequence of the mutual paratropic ring current effect of the COT cores. However, as previously described, the signal splitting observed in the ^{1}H spectrum cannot be attributed to conformational anisotropy, as also confirmed by the absence of exchange cross-peaks between the main set of signals in the 2D-ROESY spectrum. Moreover, the macrocyclic resonance Hh and the *t*-Bu group signals are generally up-field shifted and the overall NMR characterization did not evidence any de-shielding effect that could be attributed to the cyclooctatetraene core.

Mass spectrometry analysis is indeed required to reliably determine if species of different nuclearity are formed. Disappointingly, the several attempts performed with the indoor electrospray instrument were unsuccessful and only afforded spectral patterns corresponding to fragmentation in the building components. Softer ESI-MS analyses are currently under investigation in the laboratories of the University of Copenhagen.

In the UV-Vis spectrum, the formation of the macrocycle induces a slight change of the relative intensity of the absorption bands of the circulene unit (λ_{max} [Ptdppp(Circ)]$_4$[OTf]$_8$ = 410 nm), while in the emission spectrum only a 5nm redshift of the fluorescence maxima is observed.

Unambiguous and definitive proof of the formation of the molecular square [Ptdppp(Circ)]$_4$[OTf]$_8$ was achieved by single-crystal X-ray diffraction analysis (Figure 3.22). Single crystals were obtained from slow diffusion of *n*-hexane into an acetone solution of the collected product.

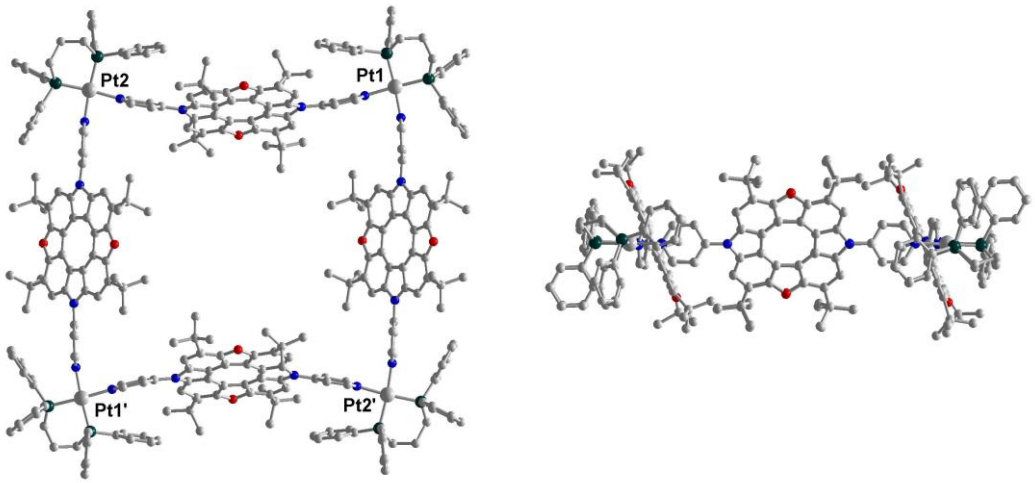

Figure 3.22. Top and side views of tan he single-crystal X-ray structure of [Ptdppp(Circ)]$_4$[OTf]$_8$. Triflate anions and hydrogen atoms are omitted for clarity. Colour code: C, grey; N, blue; O, red; P, black; Pt, white.

The assembly crystallizes in the centrosymmetric spatial group *P*-1 with triclinic cells. The coordination geometry about the cationic Pt(II) metal centres is normal square-planar, with slight

deviations of the angles (N-Pt-N angles are of 84.32 and 82.73). All Pt-P distances are normal, with a range of 2.24 - 2.26. Likewise, the Pt-N distances are normal, with a range of 2.04 - 2.08 as observed in previously reported systems, π-π stacking interaction are observed between the pyridine moieties and the phenyl of the phosphine ligand. Respect to the plane containing the Pt(II) cations all the circulene COT cores describe an angle of about 60°. As calculated from the distances between the Pt(II) metal centres, the molecular square describes a 19.9 x 20.2 Å large inner cavity which accommodates several solvent molecules (*n*-hexane and acetone), while the triflate anions are located in the proximity of the Pt(II) cations, within a 3 Å distance (see Figure A3.14). Quite interesting, in the crystalline packing the molecular squares are piled to form long porous channels, drawing a sort of MOF structure (see Figure A3.15).
The collected filtered solid, observed by microscope, evidenced the presence, together with the crystalline precipitate, of an amorphous powder. Unfortunately, neither attempting manual isolation of the remaining crystals could afford a ^{1}H NMR spectrum with the sole square $[Ptdppp(Circ)]_4[OTf]_8$ resonances.

3.3 Conclusions

In this work, the dipyridyl diazadioxa[8]circulene has been efficiently employed for the metal-mediated synthesis of new 3D systems: a sandwich-like supramolecular assembly where two platforms **1Zn** are axially connected through two bridging **Circ** ligands, and a molecular square displaying four circulene sides and four $[Ptdppp]^{2+}$ fragments as vertexes, with a total of 8 positive charges, balanced by 8 triflate counterions. The systems have been fully characterized in solution and solid-state by means of single crystal X-ray analysis. In the adducts, a precise and rigid reciprocal spatial organization of the circulene units was enforced to favour a combinatorial enhancement of the de-shielding effect of the different antiaromatic rings. Unfortunately but not unexpected, for both systems, the overall NMR characterization did not show any experimental evidence of the presence of a paratropic current. Still, this preliminary investigation is valuable to: (i) promote the use of circulenes as building units for metal-mediated functional architectures; (ii) gather and validate structural analogies with the parent reference porphyrin systems by solution and X-ray data. In view of elucidating the aromatic/anti-aromatic character of circulenes, this latter aspect can serve to find more suited inspiring systems. For instance, a further elaboration into 3D constructs is certainly intriguing, as the electronic character of the circulene components may appear from unexpected host-guest recognition properties

The **$[1Zn{\cdot}Circ]_2$** photophysical characterization evidenced the occurrence of efficient intercomponent photoinduced energy/electron transfer processes, suggesting, for the first time, the possibility to also populate a charge-separated state where the **1Zn** platform is reduced and the bridging ligand oxidized.

The preliminary host-property investigation carried out evidenced the ability of the cyclooctatetraene core to establish constructive interactions with aromatic guests. The π-π stacking of aromatic systems is well-known and documented, also in terms of positive interactions between complementary electron rich and electron poor surfaces. On the contrary, the electronic density

distribution of these antiaromatic molecules is yet an unclear issue. Further investigation over the nature of aromatic/antiaromatic surfaces interaction is indeed a key feature worth to further stress out, also to better understand - and therefore classify – the antiaromaticity of these peculiar compounds.

3.4 Experimental Section

Abbreviation

dppp = 1,3-Bis(diphenylphosphino)propane

Circ = dipyridyl-diazadioxa[8]circulene

1Zn = [*t,c,c*-$RuCl_2(CO)_2$(Zn·4'-*cis*DPyP)]$_2$

OTf **=** trifluoromethanesulfonate

Materials and Methods

Materials. All chemicals were purchased from commercial sources and used without further purification unless stated otherwise. Most of the reactions were performed under Ar atmosphere using standard Schlenk techniques, while chromatographic separations were performed in air. All solvents were degassed before being used. The following derivatives were prepared in analogy to the procedures previously reported: [*t,c,c*-$RuCl_2(CO)_2$(Zn·4'-*cis*DPyP)]$_2$ (**1Zn**),[19] [Ptdppp$(OTf)_2$].[20]

Deuterated solvents were purchased from Sigma-Aldrich and *Cambridge Isotope Laboratories* (CIL).

NMR. All spectra were recorded on a *Varian 500* or a *Varian 400* spectrometer at room temperature (if not stated otherwise). *Varian 500* operates at 500 MHz for ^{1}H, at 125 MHz for ^{13}C, at 202 MHz for ^{31}P; *Varian 400* operates at 400 MHz for ^{1}H, at 100 MHz for ^{13}C, at 161.85 MHz for ^{31}P and at 376.18 for ^{19}F. ^{1}H and ^{13}C chemical shifts were referenced to the peak of residual non-deuterated solvents: δ = 7.26 ppm and 77.16 ppm for $CDCl_3$; δ = 5.32 ppm and 54 ppm for CD_2Cl_2; δ = 2.05 ppm and 29.84 ppm for acetone-d_6, ^{31}P and ^{19}F chemical shifts were referenced, respectively, to the internal standards H_3PO_4 at 0.00 ppm and $CFCl_3$ at 0.00 ppm. ^{1}H-DOSY experiments were run at controlled temperature using the Bipolar Pulse Paired Stimulated Echo sequence[29] with convection compensation of Varian VnmrJ 3.2 software, δ = 2 ms, *G* = 1130 – 28261 G cm-1, and variable Δ. Processing was done with MestReNova© software.[30] Multiplicity of the signals is addressed as follows: s = singlet, d = doublet, t = triplet, q = quartet, qt = quintuplet, sx = sextet, sept = septuplet, m = multiplet, br = broad.

Mass Spectrometry. Electrospray Ionization (ESI) measurements were performed on a Perkin Elmer APII at 5600 eV by Dr. Fabio Hollan, Department of Chemical and Pharmaceutical Sciences, University of Trieste, Italy.

Photophysical measurements. All the solvents used in the photophysical experiments were of spectroscopic grade quality. Photophysical experiments have been performed in quartz cuvette (optical pathlength 1 cm). All absorption spectra were recorded with a UV/VIS spectrophotometer Perkin Elmer Lambda 650. Emission spectra were acquired on a Horiba-Jobin Yvon Fluoromax-2 spectrofluorimeter, equipped with a Hamamatsu R3896 tube. Fluorescence lifetimes were measured using a time-correlated single photon counting (TSPC) apparatus (PicoQuant Picoharp 300) equipped with subnanosecond LED sources (280, 380, 460, and 600 nm; 500–700 ps pulse width) powered by

a PicoQuant PDL 800-B variable (2.5−40 MHz) pulsed power supply. The decays were analyzed by means of PicoQuant FluoFit Global fluorescence decay analysis software.

X-ray Analysis. Data collections were performed at the X-ray diffraction beamline (XRD1) of the Elettra Synchrotron, Trieste (Italy).[31] Complete datasets were collected at 100 K (nitrogen stream supplied through an Oxford Cryostream 700) with a monochromatic wavelength of 0.700 Å through the rotating crystal method. Images were acquired using a Pilatus 2M image plate detector. Crystals were dipped in Nparatone, free-dried in liquid N_2 and mounted on the goniometer head with a nylon loop, under a cool stream of N_2. The diffraction data were indexed, integrated and scaled using XDS.[32] The structures were solved by direct methods using SIR2014[33] and/or the dual space algorithm implemented in the SHELXT code.[34] Fourier analysis and refinement were performed by the full-matrix least-squares methods based on F2 implemented in SHELXL-2014.[35] The Coot program was used for modeling.[36] Anisotropic thermal motion modeling was applied to atoms with occupancy greater than 40%. Restrains on bond lengths, angles and thermal motion parameters (DFIX, DANG, SIMU and DELU) have been applied on disordered and poorly defined fragments, PF6− anions and solvent molecules. Hydrogen atoms were included at calculated positions with isotropic Ufactors = 1.2 Ueq or Ufactors = 1.5 Ueq for methyl and hydroxyl groups, respectively (Ueq being the equivalent isotropic thermal factor of the bonded non hydrogen atom). Images were created using either ORTEP-3[37] or Pymol[38] software. Essential crystal and refinement data (Tables 3.2) are reported below.

[1Zn·Circ]$_2$

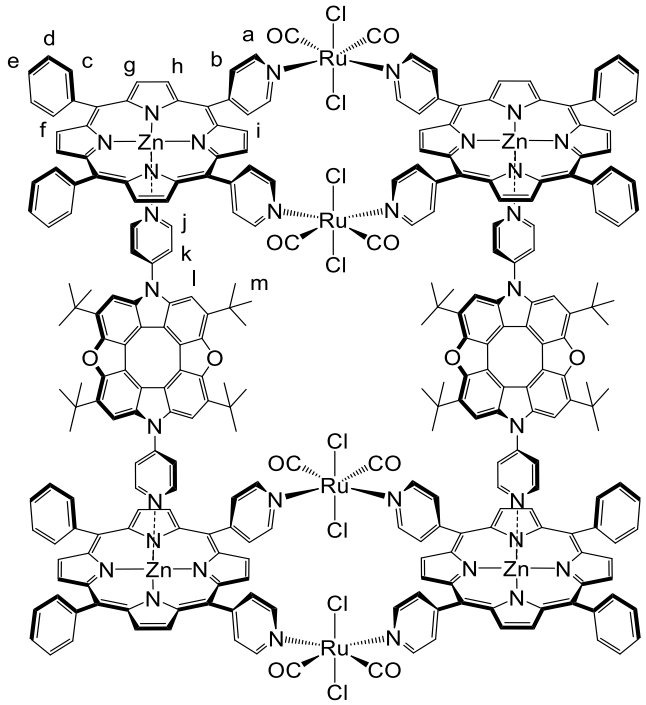

1Zn (14.6 mg, 0.00774 mmol) was dissolved in chloroform (5 mL), after few minutes **Circ** (5.8 mg, 0.00774 mmol) was added and the red solution turned violet. After stirring for 15 minutes a layer of *n*-hexane was added over the solution, and the solution was let diffuse shielded by light. Blue crystals were obtained, filtered, washed in *n*-hexane and dried in vacuum (19.2 mg, 0.00372 mmol, 96%).

^{1}H NMR (500 MHz, $CDCl_3$, T=253 K) δ (ppm): 9.70 (d, *J* = 5.5 Hz, 8H, Ha'), 9.58 (d, *J* = 5.4 Hz, 8H, Ha), 9.29 – 8.87 (m, 32H, Hf – Hi), 8.59 (d, J = 5.5 Hz, 8H, Hb'), 8.55 (d, *J* = 5.7 Hz, 8H, Hb), 8.28 (d, *J* = 5.9 Hz, 8H, Hc), 8.18 (d, *J* = 7.1 Hz, 8H, Hc'), 7.89 – 7.69 (m, 24H, Hd, He), 6.41 (s, 8H, Hl), 5.91 (d, *J* = 6.9 Hz, 8H, Hk), 2.55 (d, *J* = 6.9 Hz, 8H, Hj), 1.34 – 1.12 (m, 72H, Hm).

^{13}C NMR (125 MHz, $CDCl_3$, T=253 K, from HSQC) δ (ppm): 150.46 (Ca'), 149.86 (Ca), 144.00 (Cj), 134.38 (Cc'), 134.29 (Cc), 133.68 (Cg), 132.70 (Cf), 132.31 (Cb'), 131.99 (Cb), 131.06 (Ch), 130.80 (Ci), 127.59 (Ce), 126.62 (Cd'), 126.23 (Cd), 118.74 (Ck), 104.62 (Cl), 29.51 (Cm).

UV-vis ($CHCl_3$): λ_{max} (ε, $M^{-1}cm^{-1}$) = 265, 321, 368, 435 (532 450), 562 (36 000), 603 nm.

Single crystals were obtained by slow diffusion of *n*-hexane into a chloroform solution of **[1Zn·Circ]$_2$**.

[1Zn·Circ]$_2$·[coronene]

Single crystals were obtained by slow diffusion of *n*-hexane into a chloroform solution of **[1Zn·Circ]$_2$** (1 eq) and coronene (2.5 eq).

[Ptdppp(Circ)]$_4$[OTf]$_8$

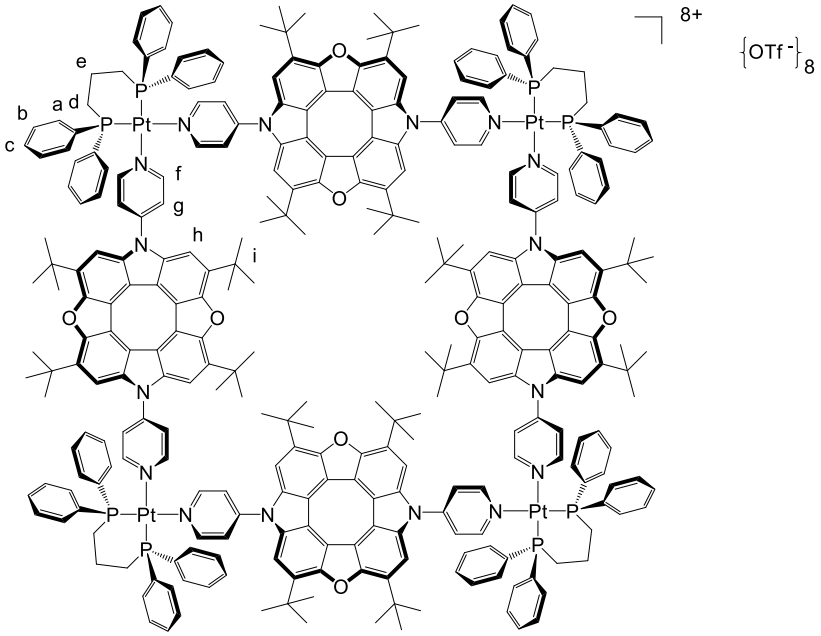

A solution in a Schlenk flask containing [Ptdppp(OTf)$_2$] (20.6 mg, 0.022 mmol) and **Circ** (17.4 mg, 0.022 mmol) in 15 mL of CH_2C1_2 was reflux for 3 h with the exclusion of light. Concentration and addition of *n*-hexane afforded the precipitation of a yellow powder, that was filtered, washed with *n*-hexane and dried under vacuum. Yield: 31 mg (85%).

^{1}H NMR (500 MHz, CD_2Cl_2) δ (ppm): 9.38 (d, *J* = 5 Hz, Hf), 7.89 (bs, Ha), 7.63 (d, *J* = 5.4 Hz, Hg), 7.54 – 7.28 (m, Hb, Hc, Hh), 3.39 (bs, Hd), 2.37 (bs, He), 1.65 – 1.35 (m, Hi).

^{1}H NMR (500 MHz, acetone-d_6) δ (ppm): 9.50 – 9.29 (m, Hf), 8.09 (bs, Ha), 7.99 – 7.83 (m, Hg), 7.71 – 7.31 (m, Hb, Hc, Hh), 3.62 (bs, Hd), 2.50 (bs, He), 1.52 – 1.00 (m, Hi).

^{13}C NMR (125 MHz, CD_2Cl_2, from HSQC) δ (ppm): 152.72, 133.57, 132.75, 129.79, 129.48, 122.61, 106.40, 30.22, 30.12, 29.87, 29.78, 21.86, 18.04.

^{13}C NMR (125 MHz, acetone-d_6, from HSQC) δ (ppm): 152.68, 152.65, 133.58, 122.85, 129.48, 132.57, 106.71, 106.36, 21.18, 29.66, 29.58, 28.69, 20.35, 38.26, 29.30, 29.18, 19.33, 38.88, 29.10, 38.14, 20.06.

^{31}P NMR (202 MHz, CD_2Cl_2) δ (ppm): -15.09 ($J_{Pt\text{-}P}$ = 3062 Hz). **^{31}P NMR** (202 MHz, acetone-d_6) δ (ppm): -13.63.

^{19}F NMR (376 MHz, CD_2Cl_2) δ (ppm): -78.46.

UV-vis (CH_2Cl_2): λ_{max} = 265, 372, 389, 410 nm.

Single crystals were obtained by slow diffusion of *n*-hexane into an acetone solution of the crude reaction mixture.

Table 3.2. Crystallographic data and refinement details for **$[1Zn{\cdot}Circ]_2$**, **$[1Zn{\cdot}Circ]_2{\cdot}[coronene]$** and **$[Ptdppp(Circ)]_4[OTf]_8$**

	$[1Zn{\cdot}Circ]_2$	$[1Zn{\cdot}Circ]_2{\cdot}[coronene]$	$[Ptdppp(Circ)]_4[OTf]_8$
Chemical Formula	$C_{294.5}H_{238.5}Cl_{18.5}N_{32}O_{12}Ru_4Zn_4$	$C_{363}H_{311}Cl_{17}N_{32}O_{12}Ru_4Zn_4$	$C_{340}H_{352}F_{24}N_{16}O_{32}P_8Pt_4S_8$
Formula weight (g/mol)	2869.62	6581.83	6914.95
Wavelength (Å)	0.700	0.700	0.700
Crystal system	Triclinic	Triclinic	Triclinic
Space Group	*P* -1	*P* -1	*P* -1
a (Å)	17.675(4)	17.542(4)	13.586(3)
b (Å)	21.695(4)	21.524(4)	28.302(6)
c (Å)	25.844(5)	25.729(5)	31.264(6)
α (°)	83.32(3)	82.17(3)	85.25(3)
β (°)	72.57(3)	71.25(3)	78.12(3)
γ (°)	85.08(3)	86.51(3)	89.05(3)
Volume (Å^3)	9378(4)	9112(4)	11724(4)
Z	1	1	1
Dcalc (g·cm^{-3})	1.016	1.199	0.979
F(000)	2936	3394	3536
μ(mm^{-1})	0.560	0.574	1.251
Θ range data collection (°)	0.82-20.49	0.83-16.85	0.66 - 20.49
Reflcts collected	58104	22648	68531
R_{merge}	0.1010	0.0552	0.0850
Data Restraints/params	19049 194 / 1624	10369 842 / 1761	23969 833 / 1939
Reflcts I>2σ(I)	10901	5808	13434
Goodness-of-fit (F^2)	1.409	1.981	1.423
Final R1, wR_2 [I>2σ(I)]	0.1351 0.3654	0.1723 0.4518	0.1001 0.2866
Largest diff. peak and hole (eÅ^{-3})	1.649, -0.605	1.047, -0.745	0.984, -0.908

3.5 References

[1] a) C.-N. Feng, M.-Y. Kuo, Y.-T. Wu, *Angew. Chem. Int. Ed.* 2013, *52*, 7791; b) R. W. Miller, A. K. Duncan, S. T. Schneebeli, D. L. Gray, A. C. Whalley, *Chem. Eur. J,* 2014, *20*, 3705.

[2] T. Hensel, N.N. Andersen, M. Plesner, M. Pittelkow, *Synlett* 2016, *27*, 498.

[3] G. V. Baryshnikov, R. R. Valiev, N. N. Karaush, V. A. Minaeva, A. N. Sinelnikov, S. K. Pedersen, M. Pittelkow, B. F. Minaev, H. Ågren, *Phys. Chem. Chem. Phys.* 2016, *18*, 28040.

[4] P. v. R. Schleyer, H. Jiao, *Pure Appl. Chem.* 1996, *68*, 209.

[5] J. A. N. F. Gomes, R. B. Mallion, *Chem. Rev.* 2001, *101*, 1349.

[6] P. v. R. Schleyer, C. Maerker, A. Dransfeld, H. Jiao, N. J. R. v. E. Hommes, *J. Am. Chem. Soc.* 1996, *118*, 6317.

[7] G. V. Baryshnikov, R. R. Valiev, N. N. Karaush, D. Sundholm, B. F. Minaev, *Phys. Chem. Chem. Phys.* 2016, *18*, 8980.

[8] G. V. Baryshnikov, R. R. Valiev, N. N. Karaush and B. F. Minaev, *Phys. Chem. Chem. Phys.* 2014, *16*, 15367.

[9] G. V. Baryshnikov, N. N. Karaush, R. R. Valiev, B. F. Minaev, *J. Mol. Model.* 2015, *21*, 136.

[10] S. Radenkovic´, I. Gutman, P. Bultinck, *J. Phys. Chem. A* 2012, *116*, 9421.

[11] G. V. Baryshnikov, B. F. Minaev, M. Pittelkow, C. B. Nielsen, R. Salcedo, *J. Mol. Model.* 2013, *19*, 847.

[12] Y. Nakamura, N. Aratani, A. Osuka, *Chem. Asian J.* 2007, *2*, 860.

[13] Y. Nakamura, N. Aratani, H. Shinokubo, A, Takagi, T. Kawai, T. Matsumoto, Z. S. Yoon, D. Y. Kim, T. K. Ahn, D. Kim, A. Muranaka, N. Kobayashi, A. Osuka, *J. Am. Chem. Soc.* 2006, *128*, 4119.

[14] Y. Nakamura, N. Aratani, K. Furukawa, A. Osuka, *Tetrahedron* 2008, *64*, 11433.

[15] C. B. Nielsen, T. Brock-Nannestad, P. Hammershøj, T. K. Reenberg, M. Schau-Magnussen, D. Trpcevski, T. Hensel, R. Salcedo, G. V. Baryshnikov, B. F. Minaev, M. Pittelkow, *Chem. Eur. J,* 2013, *19*, 3898.

[16] M. Plesner, T. Hensel, B. E. Nielsen, F. S. Kamounah, T. Brock-Nannestad, C. B. Nielsen, C. G. Tortzen, O. Hammerich, M. Pittelkow, *Org. Biomol. Chem.* 2015, *13*, 5937.

[17] T. Hensel, D. Trpcevski, C. Lind, R. Grosjean, P. Hammershøj, C. B. Nielsen, T. Brock-Nannestad, B. E. Nielsen, M. Schau-Magnussen, B. Minaev, G.V. Baryshnikov, M. Pittelkow, *Chem. Eur. J.* 2013, *19*, 17097.

[18] Dr. Thomas Hensel, Ph.D. Thesis

[19] a) E. Iengo, E. Zangrando, R. Minatel, E. Alessio, *J. Am. Chem. Soc.* 2002, *124*, 1003; b) E. Iengo, E. Zangrando, M. Bellini, E. Alessio, A. Prodi, C. Chiorboli, F. Scandola, *Inorg. Chem.* 2005, *44*, 9752.

[20] a) J. Fan, J. A. Whiteford, B. Olenyuk, M. D. Levin, P.J. Stang, E. B. Fleischer, *J. Am. Chem. Soc.* 1999, *121*, 2741; b) P. J. Stang, J. Fan, B. Olenyuk, *Chem. Commun.* 1997, 1453.

[21] E. Iengo, P. Cavigli, D. Milano, P. Tecilla, *Inorg. Chim. Acta* 2014, *417*, 59.

[22] M. T. Indelli, C. Chiorboli, F. Scandola, E. Iengo, P. Osswald, F. Würthner, *J. Phys. Chem. B* 2010, *114,* 14495.

[23] a) G. S. Wilson, H. L. Anderson, *Chem. Commun.* 1999, 1539; b) P. N. Taylor, H. L. Anderson, *J. Am. Chem. Soc.* 1999, *121,* 11538.

[24] C.R. Martinez, B.L. Iverson, *Chem. Sci.* 2012, *3*, 2191.

[25] M. Nishio, *CrystEngComm* 2004, *6*, 130.

[26] A. Prodi, C. Chiorboli, F. Scandola, E. Iengo, E. Alessio, *ChemPhysChem* 2006, *7*, 1514.

[27] a) Fujita, M.; Sasaki, O.; Mitsuhashi, T.; Fujita, T.; Yazaki, J.; Yamaguchi, K.; Ogura, K. *Chem. Commun*. 1996, 1535; b) A. Sautter, D. G. Schmid, G. Jung, F. Würthner, *J. Am. Chem. Soc*. 2001, *123*, 5424; c) M. Schweiger, S. R. Seidel, A. M. Arif, P. J. Stang, *Inorg. Chem*. 2002, *41*, 2556; d) E. Zangrando, M. Casanova, E. Alessio, *Chem. Rev.* 2008, *108,* 4979; e) T. Weilandt, R.W. Troff, H. Saxell, K. Rissanen, C.A. Schalley, *Inorg. Chem.* 2008, *47*, 7588; f) M. Ferrer, A. Pedrosa, L. Rodrìguez, O. Rossell, M. Vilaseca, *Inorg. Chem.* 2010, *49*, 9438.

[28] To further investigate the solvent dependence, a ^{1}H-NMR spectrum was recorded in dmso-d_6. The spectrum still presents broad and unresolved resonances also increased in number, hinting to the occurring of a partial decomposition of the metallacycle(s) by competitive coordination of solvent molecules to the Pt(II) centers.

[29] D. H. Wu, A. D. Chen, C. S. Johnson, *J. Magn. Reson. Ser. A* 1995, *115*, 260.

[30] *MestReNova© software, version 6.0.2, Mestrelab Res. S.L., Santiago Compost. Spain* 2016.

[31] A. Lausi, M. Polentarutti, S. Onesti, J.R. Plaisier, E. Busetto, G. Bais, L. Barba, A. Cassetta, G. Campi, D. Lamba, A. Pifferi, S.C. Mande, D.D. Sarma, S.M. Sharma, G. Paolucci, *Eur. Phys. J. Plus* 2015, *130*, 43.

[32] W. Kabsch, *Acta Crystallogr.* 2010, *66*, 125.

[33] M. C. Burla, R. Caliandro, B. Carrozzini, G.L. Cascarano, C. Cuocci, C. Giacovazzo, M. Mallamo, A. Mazzone, G. Polidori, *J. Appl. Crystallogr.* 2015, *48*, 306.

[34] G. M. Sheldrick, *Acta Crystallogr.* 2015, *71*, 3.

[35] G. M. Sheldrick, *Acta Crystallogr.* 2008, *A64*, 112.

[36] P. Emsley, K. Cowtan, *Acta Crystallogr.* 2004, *60*, 2126

[37] L. J. Farrugia, *J. Appl. Crystallogr.* 2012, *45*, 849.

[38] L. Schrodinger, *PyMOL Mol. Graph. Syst. Schrodinger, LLC.* 2015.

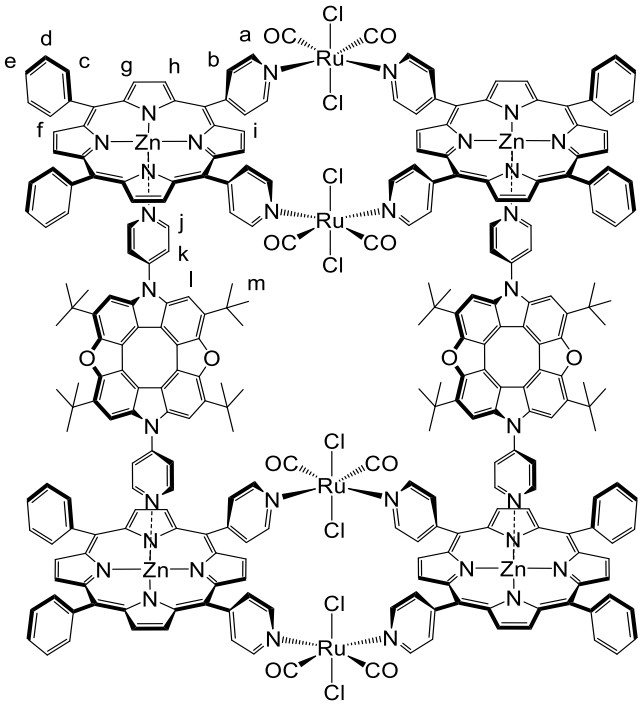

Chart A3.1. Schematic depiction of **[1Zn·Circ]$_2$** with NMR labelling.

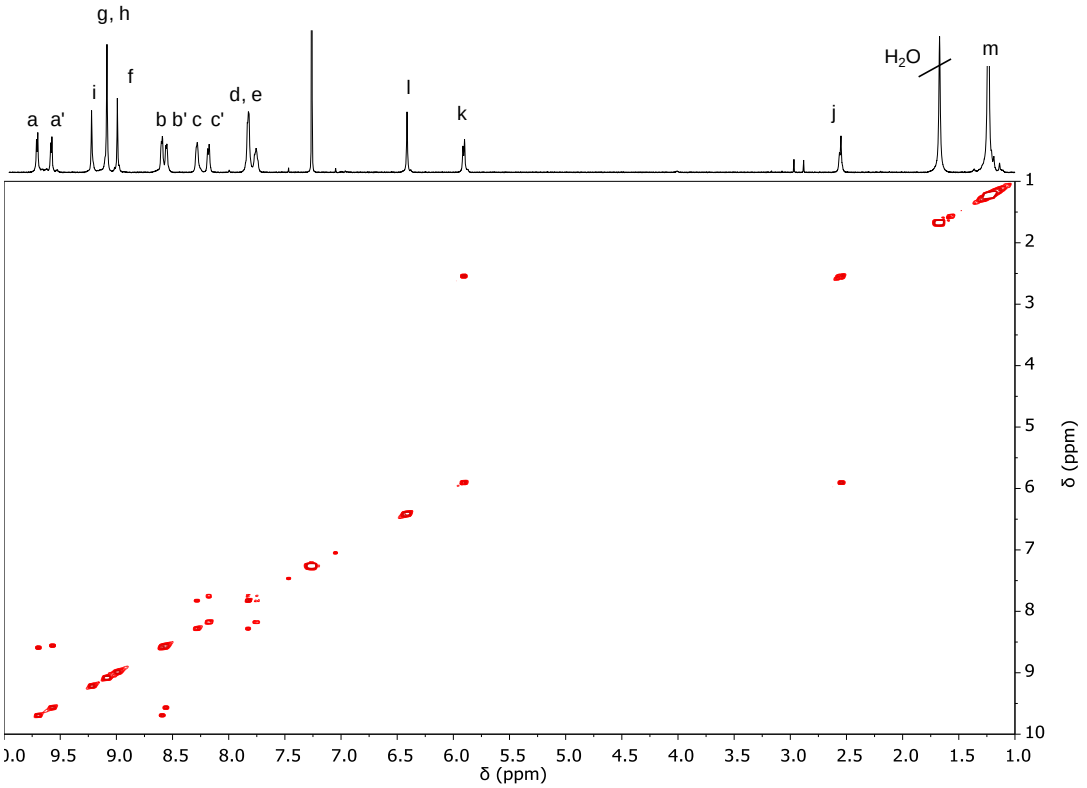

Figure A3.1. H-H COSY spectrum ($CDCl_3$) of **[1Zn·Circ]$_2$**.

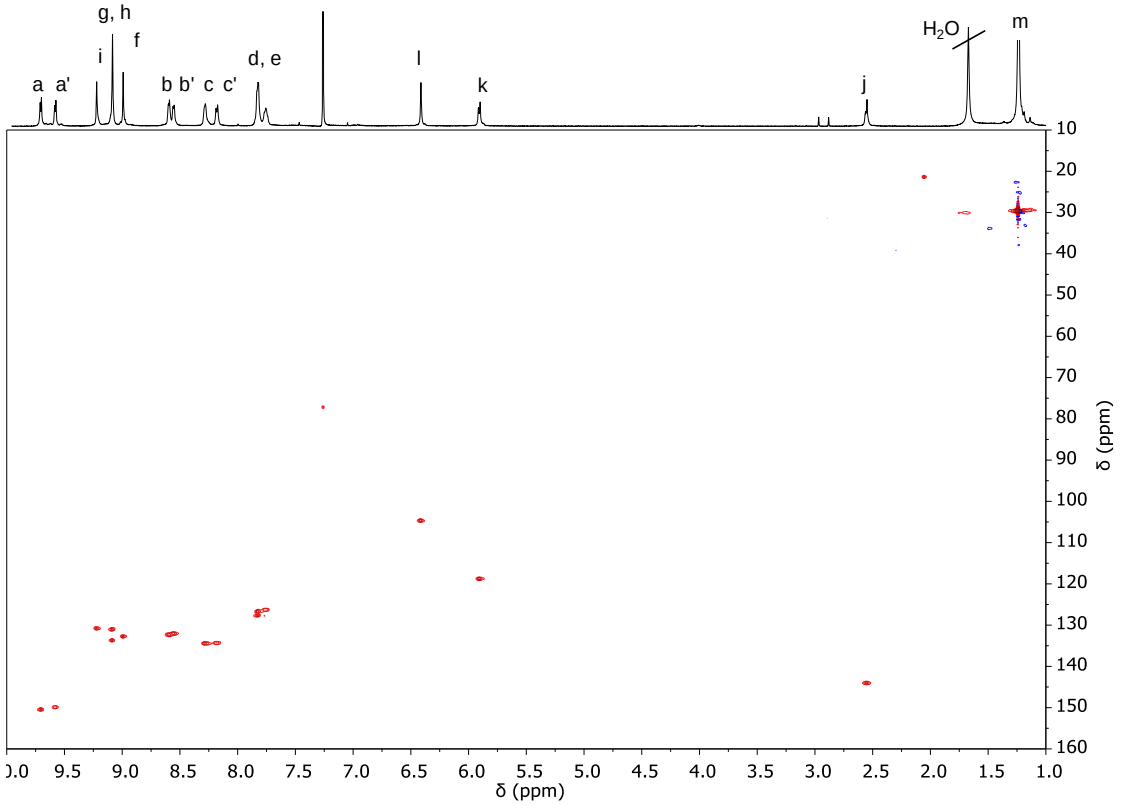

Figure A3.2. HSQC spectrum ($CDCl_3$) of **[1Zn·Circ]$_2$**.

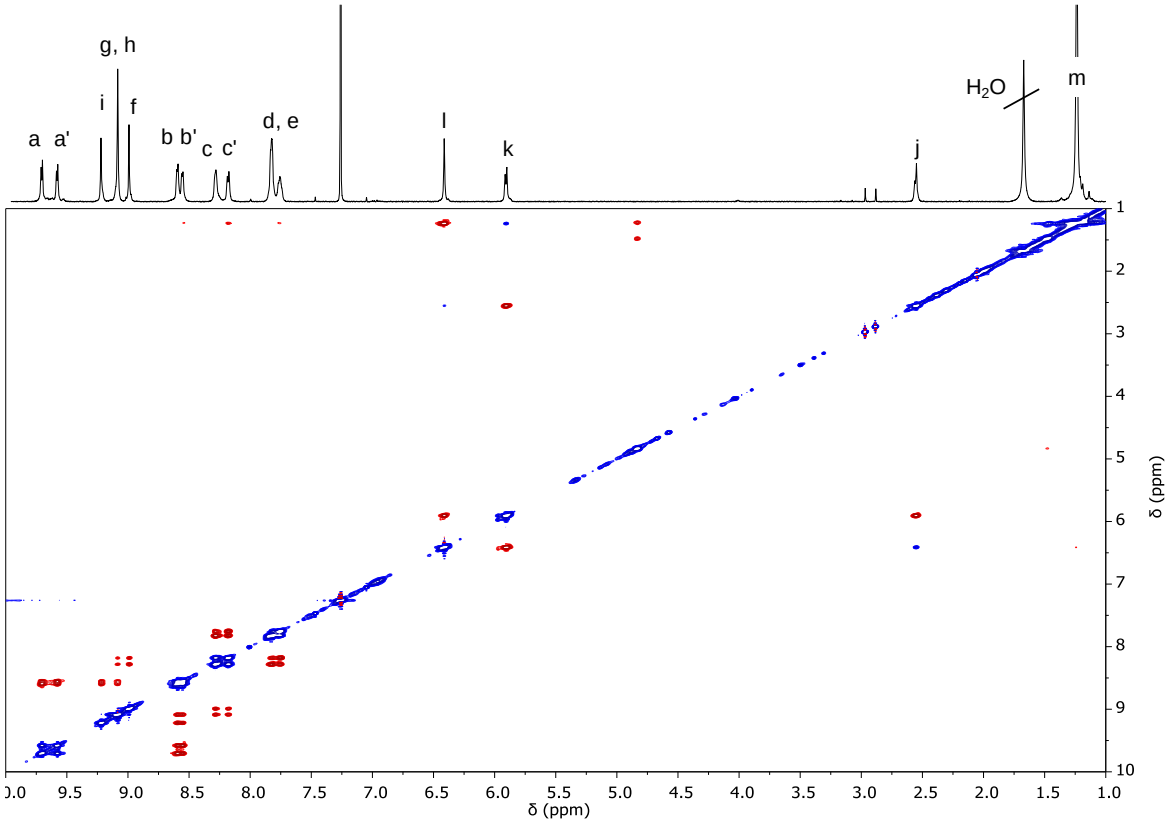

Figure A3.3. H-H ROESY spectrum ($CDCl_3$) of **[1Zn·Circ]$_2$**.

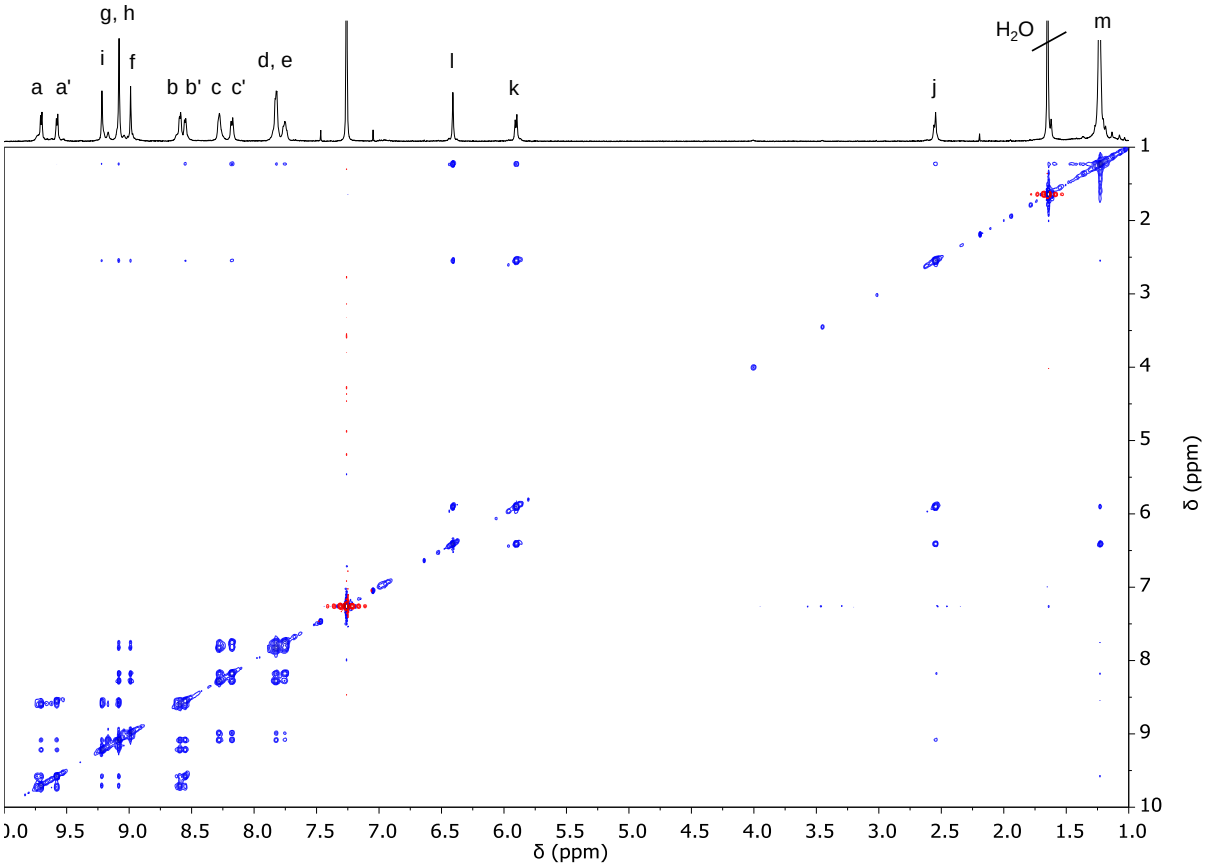

Figure A3.4. H-H NOESY spectrum ($CDCl_3$) of **[1Zn·Circ]$_2$**.

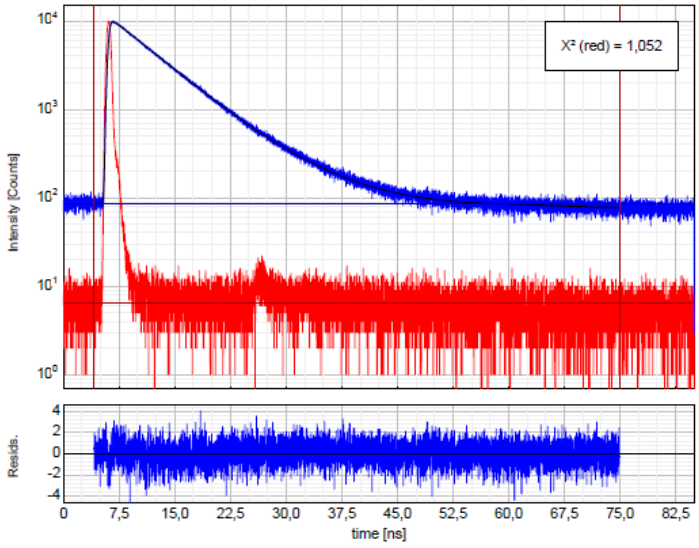

$$I(t) = \int_{-\infty}^{t} IRF(t') \sum_{i=1}^{n} A_i \, e^{-\frac{t-t'}{\tau_i}} \, dt'$$

Parameter	Value	Conf. Lower	Conf. Upper	Conf. Estimation
A_1 [Cnts]	1704,7	-9,0	+9,0	Fitting
τ_1 [ns]	6,356	-0,026	+0,026	Fitting

Figure A3.5. Lifetime measurements (Single Photon Counting) of **Circ** (λ_{ex} = 380 nm, λ_{an} = 460 nm).

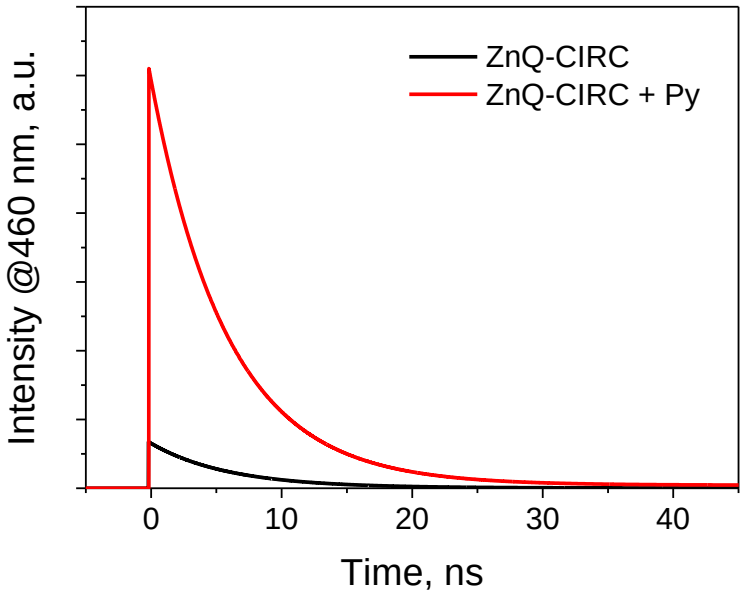

Figure A3.6. Single Photon Counting analysis of **[1Zn·Circ]$_2$** (λ_{ex} = 380 nm, λ_{an} = 460 nm) before (black) and after (red) the addition of an excess of pyridine.

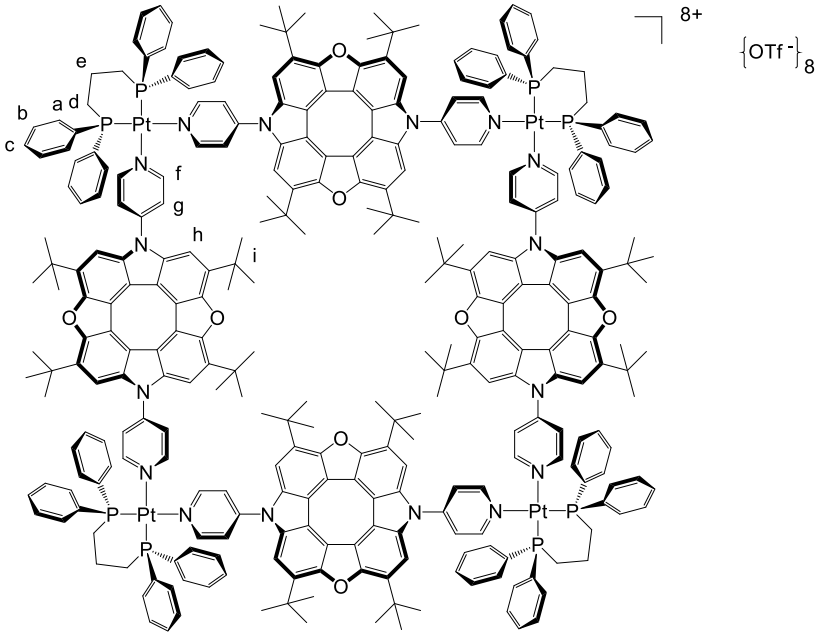

Chart A3.2. Schematic depiction of [Ptdppp(Circ)]$_4$[OTf]$_8$ with NMR labelling.

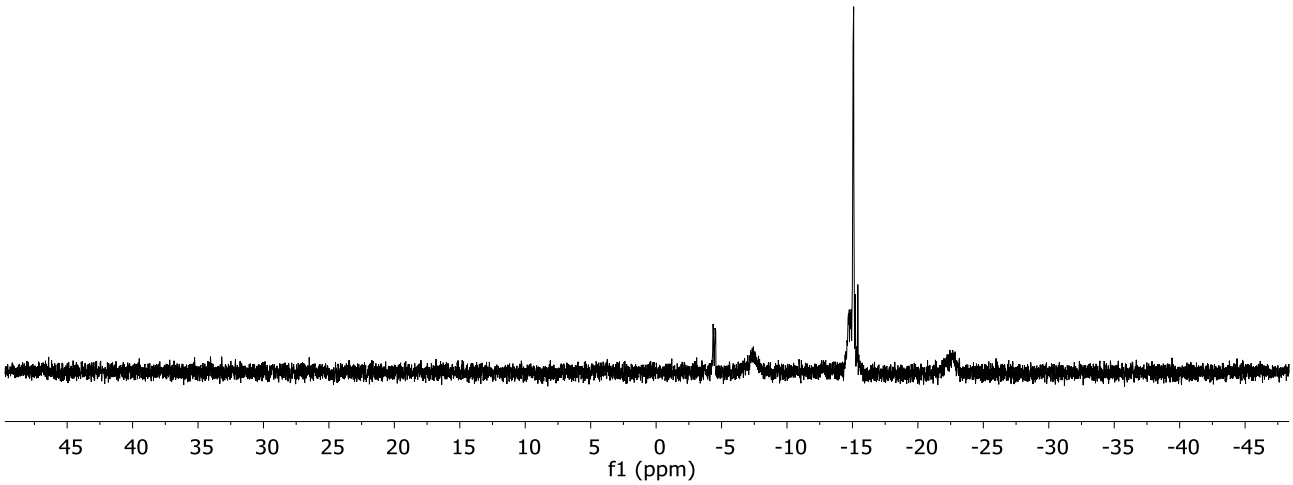

Figure A3.7. ^{31}P NMR spectrum (CD_2Cl_2) of $[Ptdppp(Circ)]_4[OTf]_8$.

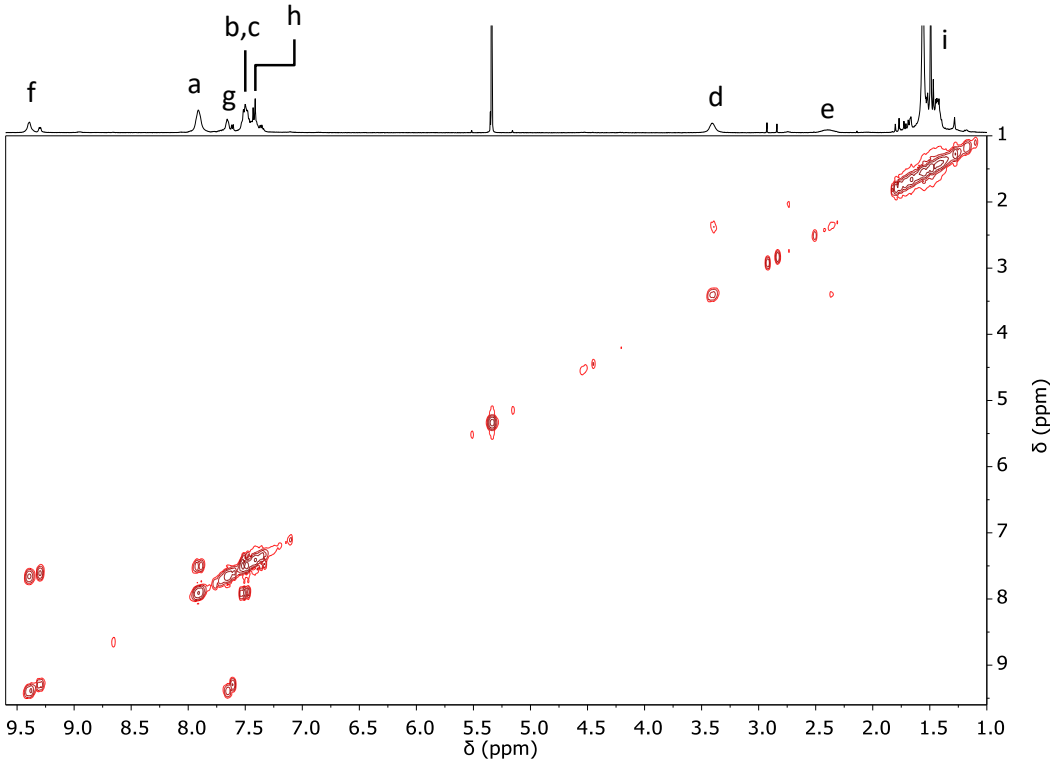

Figure A3.8. HH-COSY spectrum (CD_2Cl_2) of $[Ptdppp(Circ)]_4[OTf]_8$.

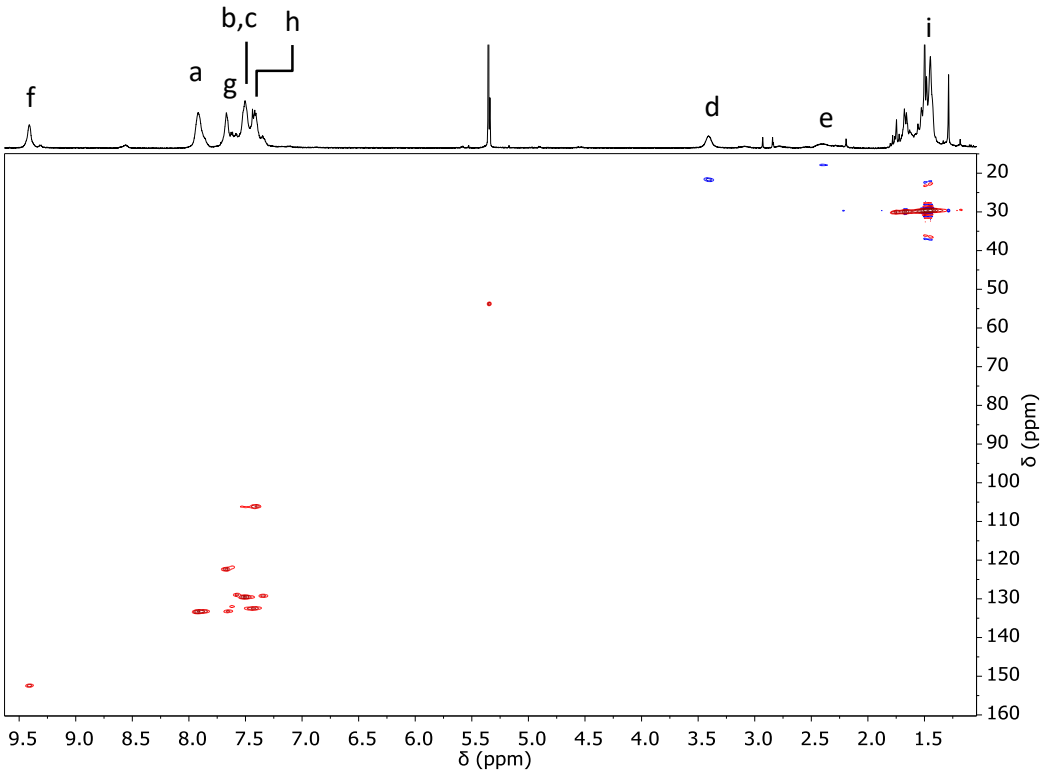

Figure A3.9. HSQC spectrum (CD_2Cl_2) of $[Ptdppp(Circ)]_4[OTf]_8$.

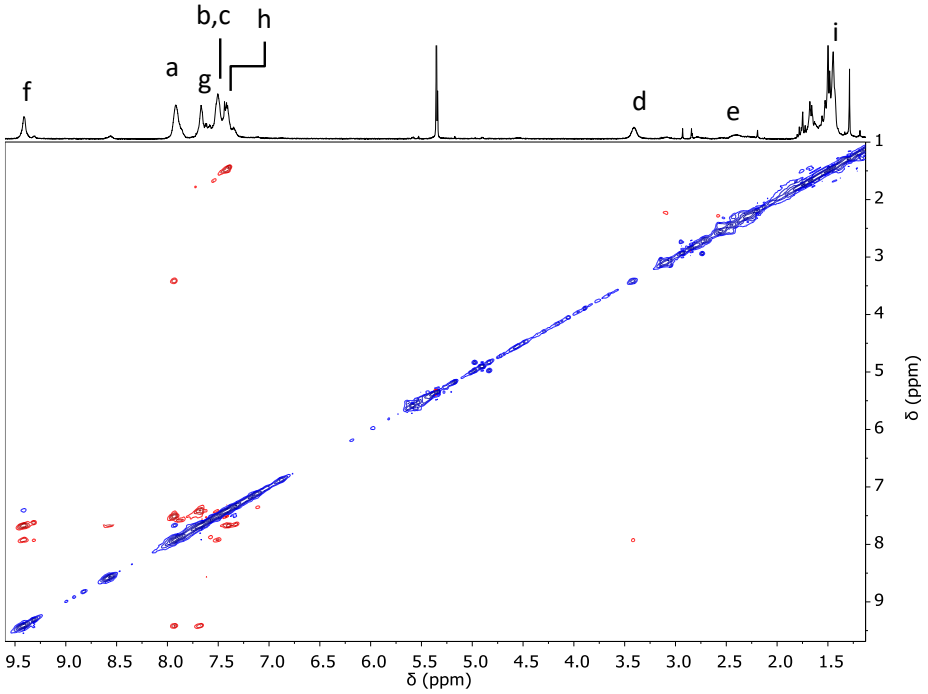

Figure A3.10. HH-ROESY spectrum (CD_2Cl_2) of $[Ptdppp(Circ)]_4[OTf]_8$.

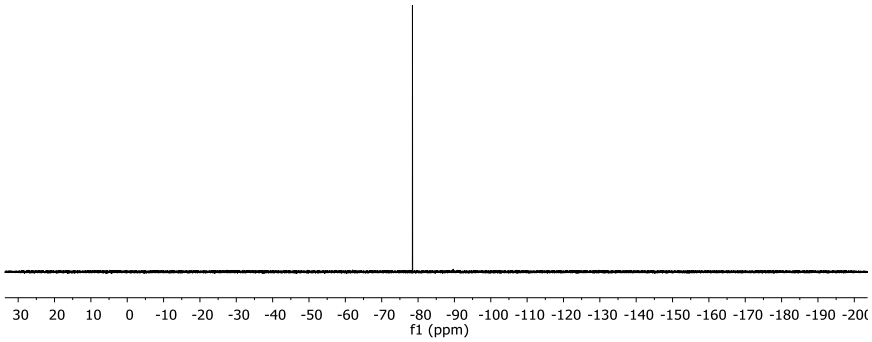

Figure A3.11. ^{19}F-NMR spectrum (CD_2Cl_2) of $[Ptdppp(Circ)]_4[OTf]_8$.

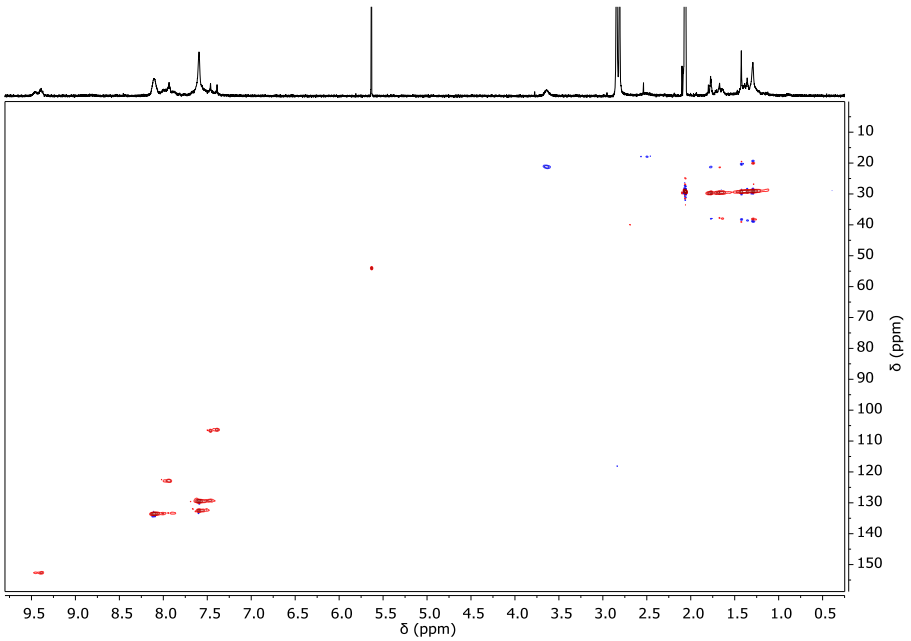

Figure A3.12. HSQC spectrum (acetone-d_6) of $[Ptdppp(Circ)]_4[OTf]_8$.

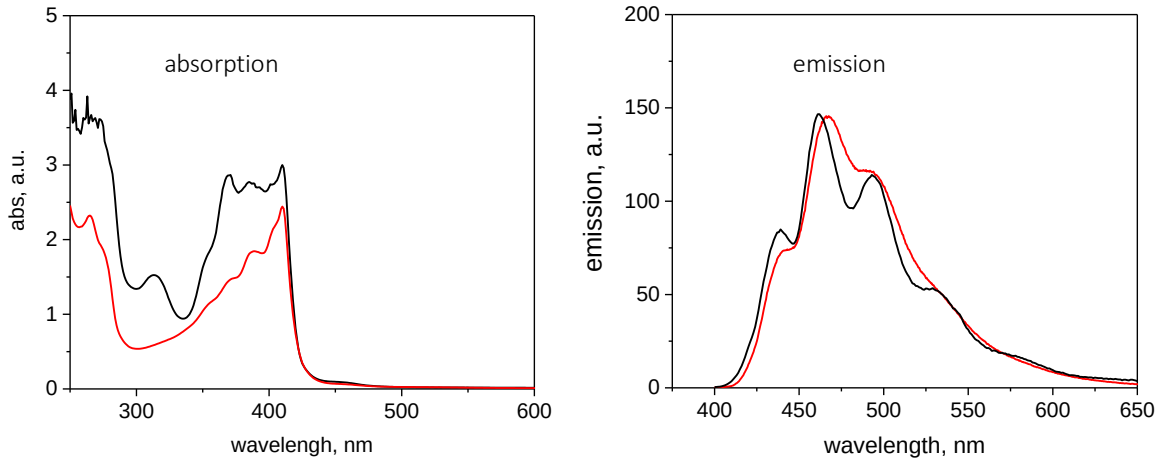

Figure A3.13. Absorption (left) and emission (right, λ_{ex} = 360 nm) spectra of dichloromethane solutions of **Circ** (black line) and $[Ptdppp(Circ)]_4[OTf]_8$ (red line).

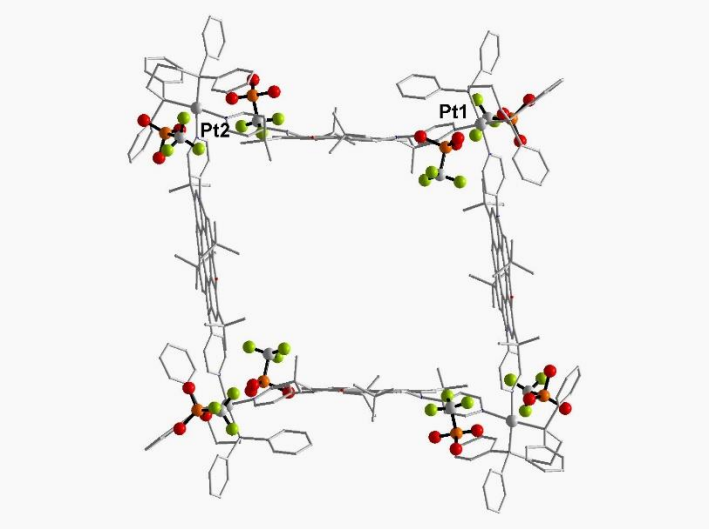

Figure A3.14. Single-crystal X-ray structure of $[Ptdppp(Circ)]_4[OTf]_8$ with triflate counterions highlighted. For clarity, the square metallacycle is depicted in grey. Colour code: C,white; O, red; S, orange; F, green.

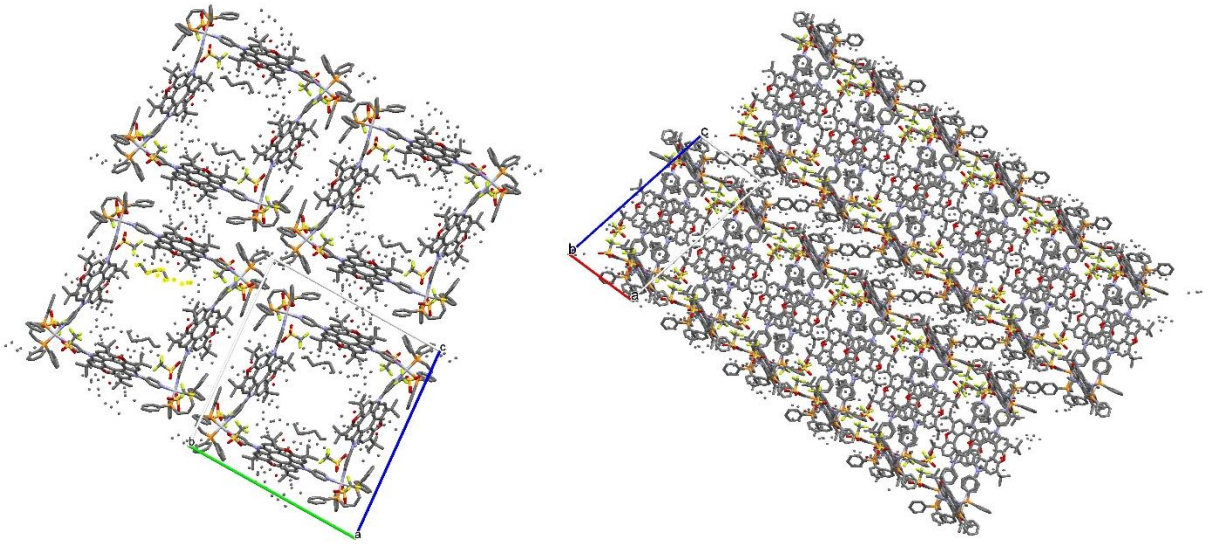

Figure A3.15. View of the crystal packing found for $[Ptdppp(Circ)]_4[OTf]_8$ along the *a* (on the left) and the *b* axis (on the right). Hydrogen atoms are omitted for clarity. Colour code: C, grey; N, blue; O, red; P, orange; S, yellow; F, green; Pt, white.

Chapter 4

Abbreviations

TPP = 5,10,15,20-(phenyl)porphyrin

***trans*DPyP =** 5,15-(4-pyridyl)-10,20-(phenyl)porphyrin

***tris*PyP =** 5,10,15-(4-pyridyl)-20-(phenyl)porphyrin

1Zn = {*t,c,c*-$RuCl_2(CO)_2$[5,10-(4-pyridyl)-15,20-(phenyl)porphyrinato]-zinc(II)}$_2$

***mono*PhCOOMePyP =** 5-(4-carboxymethylphenyl)-10,15,20-(4-pyridyl)porphyrin

***mono*PhCOOHPyP =** 5-(4-carboxyphenyl)-10,15,20-(4-pyridyl)porphyrin

***mono*PhCOOHP =** 5-(4-carboxyphenyl)-10,15,20-(phenyl)porphyrin

HBTU = N,N,N′,N′-Tetramethyl-O-(1H-benzotriazol-1-yl)uronium hexafluorophosphate

DMAP = *N*,*N*-Dimethylpyridin-4-amine

dimPh = N,N-Bis[4-[10,15,20-(phenyl)porphyrin-5-yl]-benzoyl]-1,4-benzenebis(methylamine)

dimPy = N,N-Bis[4-[10,15,20-(4-pyridyl)porphyrin-5-yl]-benzoyl]-1,4-benzenebis(methylamine)

$SnTPP(OH)_2$ = *trans*-dihydroxo[5,10,15,20-(phenyl)porphyrinato]-tin(IV)

$SnTpFP(OH)_2$ = *trans*-dihydroxo[5,10,15,20-(pentafluorophenyl)porphyrinato]-tin(IV)

$SnTPP(BA)_2$ = *trans*-dibenzoato(5,10,15,20-*tetra*phenylporphyrinato)-tin(IV)

$SnTpFP(BA)_2$ = *trans*-dibenzoato[5,10,15,20-(pentafluorophenyl)porphyrinato]-tin(IV)

4.1 Introduction

Most of the efforts spent so far in the implementation of the sandwich-like supramolecular systems described in the previous Chapters, were directed at the tuning of the inter-component photo-induced properties and/or at the introduction of new functions derived from the geometrical organization of a precise number of active-metal centers, by changing of the nature of the bridging ligands. As shown in Chapter 1 (see Paragraph 1.4) the supramolecular systems self-assembled by axial coordination of multitopic-pyridyl ligands (such as a tetra-pyridylporphyrin **TPyP**) to **1Zn**, describing more defined 3D architectures, presented very low solubility limiting their further application (such as host/guest chemistry).

In a recent Master Thesis work,[1] it was demonstrated that a combination, at millimolar concentration, of the metallacycle **1Zn** with the tri-topic porphyrin ligand *tris*(4'-pyridyl)-*mono*(phenyl)porphyrin (***tris*PyP**) , at millimolar concentration and in a 3:2 ratio, leads rapidly to the quantitative formation of the discrete supramolecular open cage-like system **[(1Zn)$_3$·(*tris*PyP)$_2$]**, featuring three **1Zn** platforms bridged by the pyridyl moieties of two freebase porphyrin ligands (Scheme 4.1). The characterization of this 3D molecular architecture is indeed not trivial: even softer mass spectrometry techniques are not useful (inevitably leading to the fragmentation of the assembly) and as expected the resulting ^{1}H-NMR spectrum is crowded with numerous resonances. The main spectroscopic features will be herein described (also in comparison with systems presented in Chapter 1), since useful for a more flowing and clear understanding of the work presented in this Chapter.

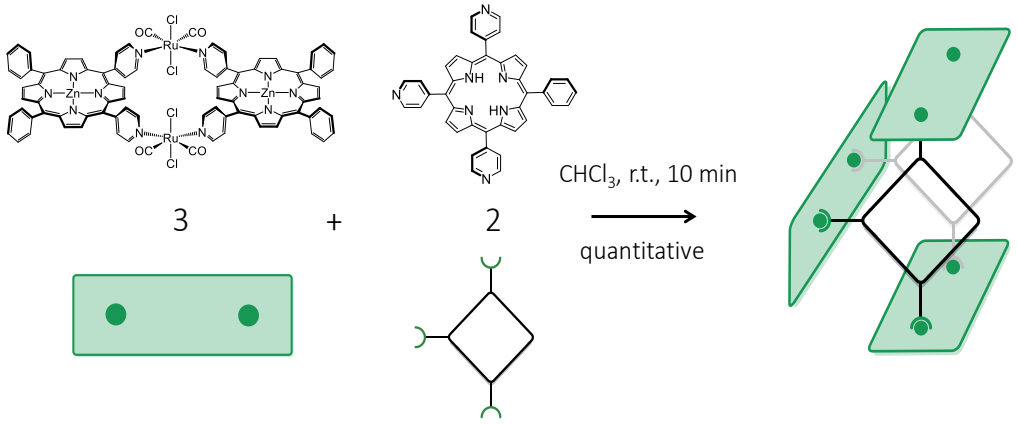

Scheme 4.1. Self-assembly between **1Zn** and ***tris*PyP** with formation of **[(1Zn)$_3$·(*tris*PyP)$_2$]**, only schematically depicted.

At room temperature, the ^{1}H-NMR spectrum of **[(1Zn)$_3$·(*tris*PyP)$_2$]** (Figure 4.1, c) presents a number of relatively broad and overlapping signals, which sharpen and partially resolve upon lowering the temperature down to -30°C. In general, the **[(1Zn)$_3$·(*tris*PyP)$_2$]** is characterized by an extensive magnetic anisotropy, due to the combined shielding cones of the eight porphyrin units. This effect is especially evident for the pyridyl signals $H_{2,6fb}$ and $H_{3,5fb}$ of ***tris*PyP** (see Figure 4.1) found, strongly upfield shifted, around 2.5 and 5.8 ppm respectively. At -30°C, the 10,20- (axial) and 15- (equatorial) pyridyl resonances of ***tris*PyP**, showing correct relative integration of 2:1, are found split into two signals of equal, according to the presence of two distinct magnetic environments in the inside or the

outside of the porphyrin cage. Furthermore, at this temperature, the tautomeric equilibrium of the internal pyrrolic protons is slowed down, and two distinct signals are observed.

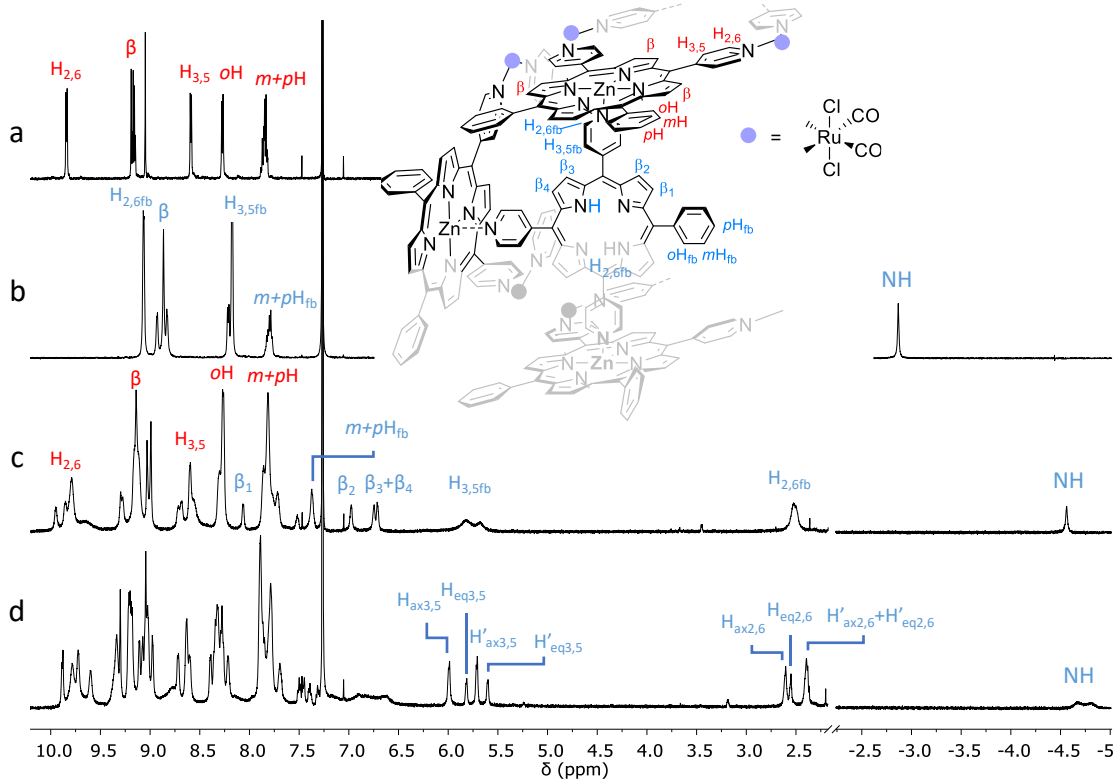

Figure 4.1 ^{1}H-NMR ($CDCl_3$) spectra of: a) **1Zn** (25°C), b) ***tris*PyP** (25°C), c) **[(1Zn)$_3$(*tris*PyP)$_2$]** (25°C) and d) **[(1Zn)$_3$(*tris*PyP)$_2$]** (-30°C).

The single crystal X-ray structure of **[(1Zn)$_3$·(*tris*PyP)$_2$]** confirmed the solution data (Figure 4.2). The **1Zn** metallacycles present minimal conformational distortions, maintaining the original coplanarity of the porphyrin units. As already proposed form solution NMR analysis of the assembly **[(1Zn)$_4$·(TPyP)$_2$]** (see Paragraph 1.4), the connecting pyridyl-porphyrins are parallel to each other at a distance of ca. 11.3 Å, but not eclipsed, defining a dihedral angle of about 29° (Figure 4.2, on the left). Indeed, the twist is needed to prevent steric clashes between carbonyl groups of adjacent **1Zn** platforms. However, the number of resonances observed in the proton NMR spectrum is consistent with two facing and eclipsed ***tris*PyP** units, hinting that, compared to **[(1Zn)$_4$·(TPyP)$_2$]** (see Chapter 1), in solution, within the temperature range explored, the system is more dynamic and possibly described by two twisted conformers in fast interconversion. From the side view it is possible to appreciate how the phenyl groups of the ***tris*PyP** units point towards the open side of the molecular cage, marking the boundary of the cavity.

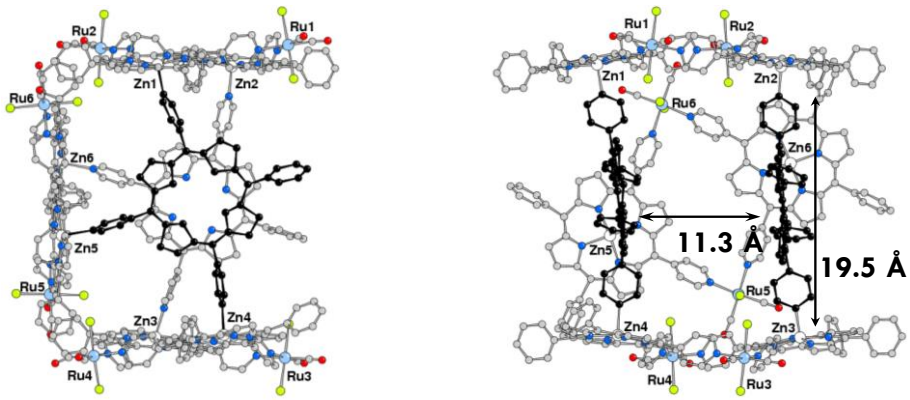

Figure 4.2. Different views of the single crystal X-ray structure of **[(1Zn)$_3$·(*tris*PyP)$_2$].** Colour code: N: blue, O: red, C: grey, Cl: yellow, Ru: light blue, Zn: white. Hydrogen atoms are omitted for clarity.

In this respect, **[(1Zn)$_3$·(*tris*PyP)$_2$]** may be viewed as a large cubic cavitand. Taking inspiration from this structural feature, the assembling was then repeated by replacement of ***tris*PyP** with a *tris*pyridyl porphyrin unit bearing a carboxylic acid function in the para position of the phenyl group (Scheme 4.2), in view of exploring the possibility to tailor the open side of the cage with functional groups.

Reaction of stoichiometry quantities of *tris*-(4-pyridyl)-*mono*(4-carboxy-phenyl)porphyrin (***mono*PhCOOHPyP**) and platform **1Zn**, yields the quantitative formation of the supramolecular cage-like system **[(1Zn)$_3$·(*mono*PhCOOHPyP)$_2$]** (Scheme 4.2).

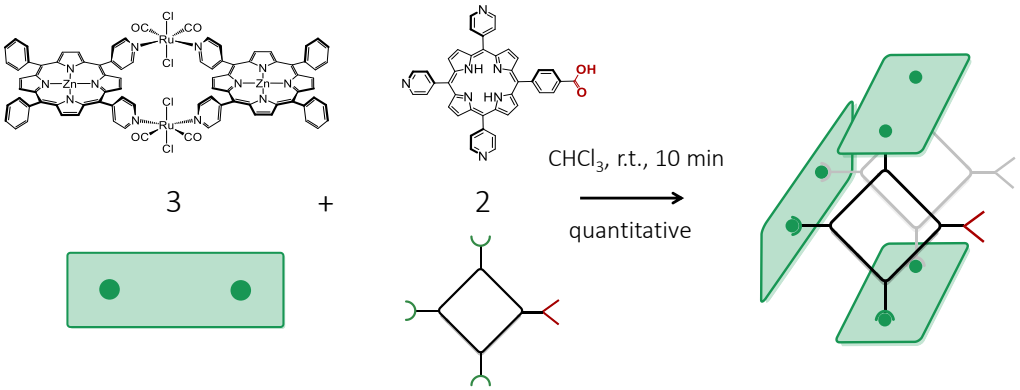

Scheme 4.2. Self-assembly between **1Zn** and ***mono*PhCOOHPyP** with formation of **[(1Zn)$_3$·(*mono*PhCOOHPyP)$_2$]**, only schematically depicted.

The X-ray structure determination evidenced the establishment of bifurcated *Acceptor-Donor* (*AD*) hydrogen bonding interaction between twin **[(1Zn)$_3$·(*mono*PhCOOHPyP)$_2$]** partner (Figure 4.3). This intermolecular hydrogen bonding network leads to the formation of a giant multi-porphyrin container comprising sixteen (metallo)porphyrin units, spanning ca. 47 Å in the longest side.

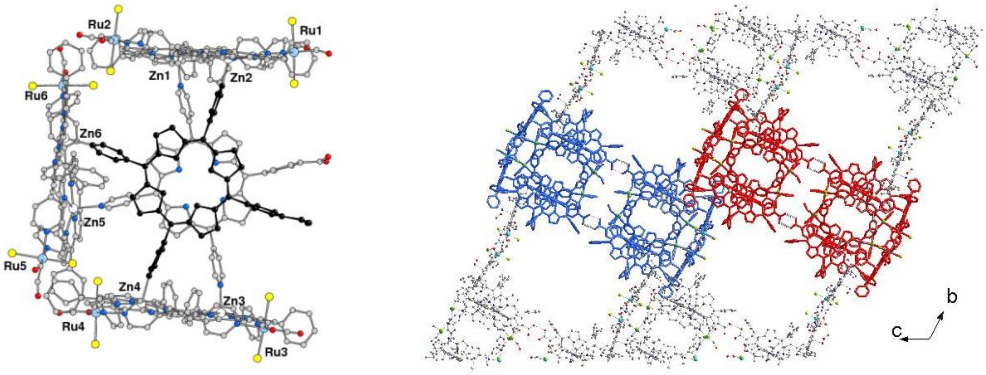

Figure 4.3. Right: single crystal X-ray structure of **[(1Zn)$_3$·(*mono*PhCOOHPyP)$_2$]**. Left: crystal packing showing the extended hydrogen bonding network, and large voids. Solvent molecules and hydrogen atoms are omitted for clarity.

[(1Zn)$_3$·(*mono*PhCOOHPyP)$_2$] presents NMR spectral feature very similar to **[(1Zn)$_3$·(*tris*PyP)$_2$]**, hinting a substantial absence of interactions between the twin cages. However, the presence of the carboxylic groups yet opens to the intriguing opportunity to further functionalize and/or de-symmetrize the final supramolecular system.

The work described in the present Chapter focused on the exploration of possible ways to exploit the established modular self-assembling approach, based on the combination of the **1Zn** platform with multi-topic porphyrin ligands for the obtainment of 3D discrete multi-porphyrin containers with extended dimensions and/or increased complexity.

To these aims, the following two different strategies were pursued (Scheme 4.3):

A. Synthesis of a hexa-topic pyridyl ligand by coupling reaction of two ***mono*PhCOOHPyP** porphyrins with an appropriate diamino spacer, followed by its use in combination with **1Zn** for the assembling of a covalently bound dimeric cage;

B. Synthesis of hexa-topic pyridyl ligands by axial coordination of two ***mono*PhCOOHPyP** porphyrins to varied Sn(IV) porphyrin scaffolds, followed by their use in combination with **1Zn** for the assembling of dimeric compartmentalized hetero-chromophore cages.

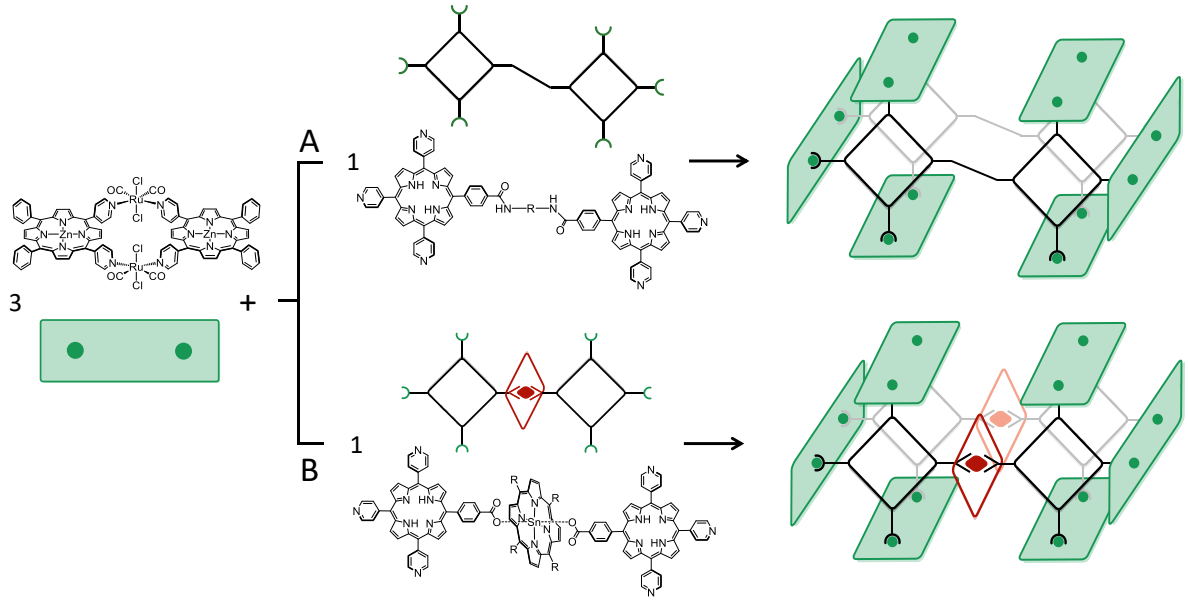

Scheme 4.3.

The two new derived systems differ not only for the nature of the connecting fragment, but also for the type and number of porphyrin units and the presence, or not, of inner compartmentation of the cavity. The synthesis of a supramolecular system via metal-mediated self-assembling of three different molecular components strictly requires selective interaction between the building units. For the present target molecule this is achieved by hard/soft discrimination of Sn(IV) and Zn(II) cations towards the *hard* (carboxylate group) and the *soft* (the pyridyl moieties) basic functions of ***mono*PhCOOHPyP**, respectively.[2,3]

As previously mentioned for **[(1Zn)$_4$·(TPyP)$_2$]**, the solubility of these multi-porphyrin assemblies is quite restricted to organic chlorinated solvents, limiting their applicability in host-guest recognition chemistry. The synthesis of larger and at the same time more confined hollow structures may lead to the enhancement of the hosting properties of the molecular containers. Finally, the well-known photophysical and electrochemical properties of the tin-porphyrin chromophore[4] may promote in the derived supramolecular architecture interesting photoinduced intercomponent properties.

4.2 Results and Discussion

4.2.1 Synthesis and Characterization of the Hexa-topic Ligand dimPy

The first synthetical strategy is based on the preparation of a hexa-topic pyridyl ligand, by covalently linking two tri-topic cruciform ***mono*PhCOOHPyP** subunits. As spacer between the two porphyrins, the *p*-xylylenediamine was selected, since it represents a relatively flexible bridge, and displays an appropriate distance between the two amine groups (Chart 4.1).

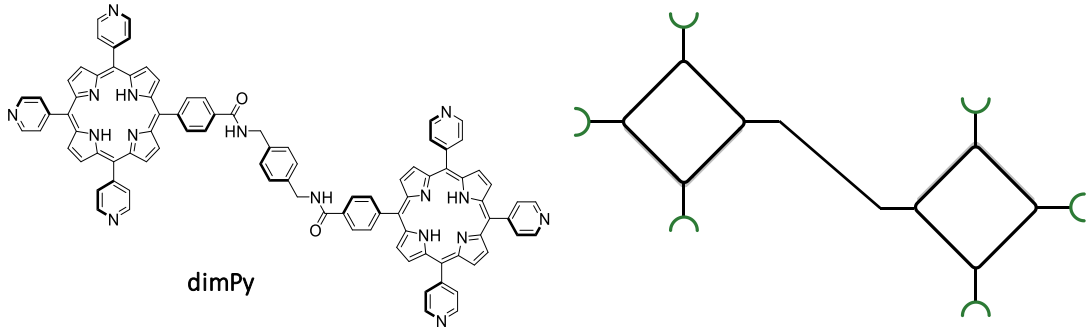

Chart 4.1.

The desired porphyrin dimer, N,N-Bis[4-[*tris*(4-pyridyl)porphyrin-5-yl]-benzoyl]-1,4-benzenebis(methylamine) (**dimPy**) is already known in the literature and reported as a reaction intermediate for the synthesis of DNA-photocleavage and singlet oxygen production agents.[5] The experimental procedure described - conversion of the carboxylic acid of ***mono*PhCOOHPyP** in acyl chloride and subsequent reaction with the diamine – presents a quite low and unsatisfactory yield (23%). For this reason, we pursued an alternative synthetic route, performing a coupling reaction between the acid function of ***mono*PhCOOHPyP** and the amino groups of the *p*-xylylenediamine.

For the optimization of the reaction conditions, the model *mono*-(4-carboxy-phenyl)-*tris*(phenyl)porphyrin (***mono*PhCOOHP**, Scheme 4.4) was initially used, as this can be obtained in larger quantities and by less demanding isolation/purification processes. After screening of the coupling agents reported in the literature for similar porphyrin substrates,[6,7] HBTU (N,N,N′,N′-Tetramethyl-O-(1H-benzotriazol-1-yl)uronium hexafluorophosphate) and DMAP (*N*,*N*-Dimethylpyridin-4-amine) were chosen.

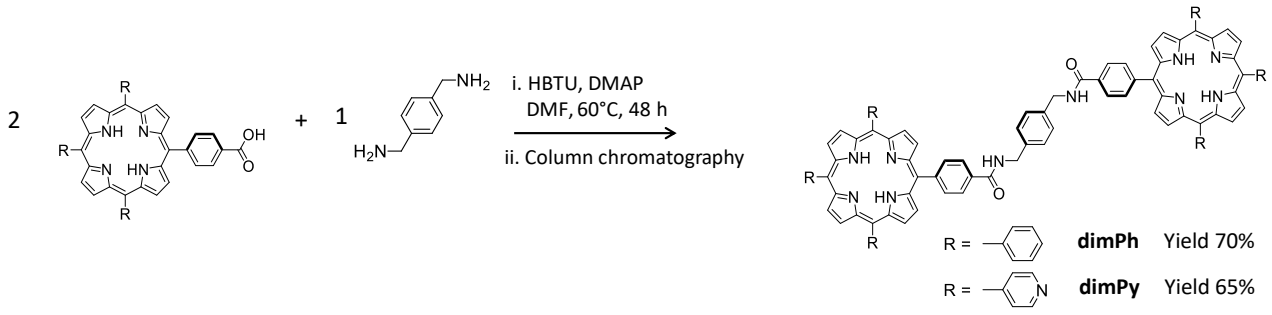

Scheme 4.4

A DMF solution of ***mono*PhCOOHPyP** and HBTU was mixed at room temperature for 30 minutes and 0.5 equivalents of *p*-xylylenediamine were then added; after stirring for additional 48 hours at 60°C.

The desired porphyrin dimer was isolated from the crude by column chromatography in 65% yield (Scheme 4.4).

In Figure 4.4 the ^{1}H NMR spectra of **dimPy** (CD_3OD 10%/$CDCl_3$) and of the precursor ***mono*PhCOOHPyP** (dmso-d_6) are reported. Only a qualitative comparison of the spectra can be done since recorded in different solvents. Formation of the amidic bonds is proved by the disappearance of carboxylic and amine resonances at 13.30 and 1.4 ppm respectively, replaced by the amidic proton signal at 7.4 ppm, resonating as a triplet and coupling with the doublet at 4.84 ppm assigned to the methylene bridge. All signals of the p-xylylene group are down-field shifted due to the conversion of the amine in amide and to the paratropic ring current effect of the peripheral porphyrins. Differently from the precursor ***mono*PhCOOHPyP**, in the spectrum of **dimPy** the resonances of the 10,20- (axial) and 15- (equatorial) pyridyl substituents, are resolved in two different set of signals with correct relative integration of 2:1. The 10% deuterated methanol required to better solubilize the porphyrin dimer causes the decrease of intensity of the inner NH signals by exchange of the inner hydrogen with deuterium. This produces (at least partial) deuterated species accompanied by a tautomerism rate decrease by kinetic isotope effect (NH/ND or ND/ND exchange, as opposed to NH/NH exchange). Consequent to this is also the observed broadening of the β-pyrrolic resonances, as the signal coalescence temperature for β-proton pertaining to distinct pyrrole rings gets markedly raised.

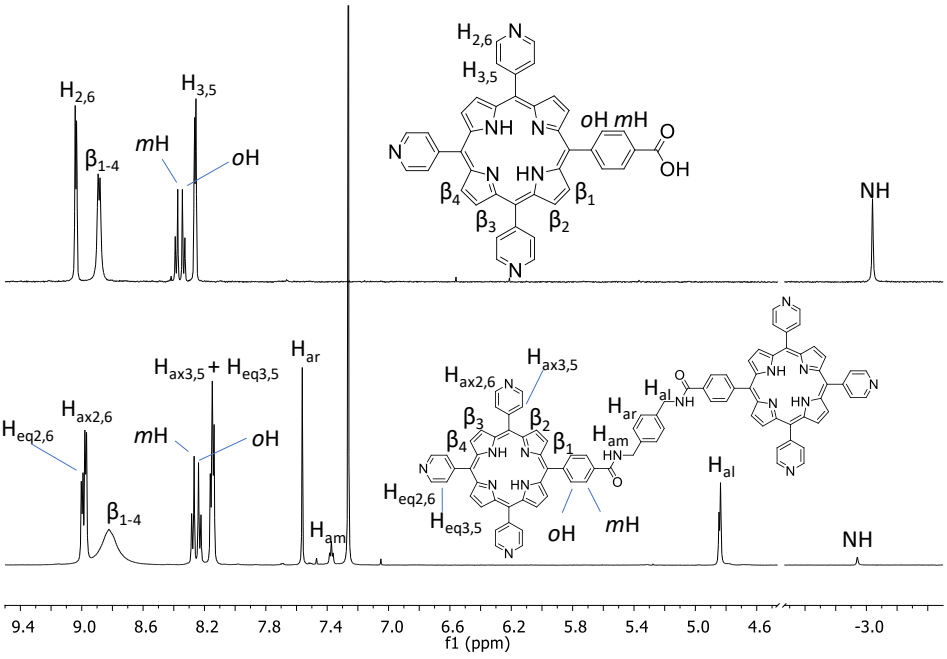

Figure 4.4. ^{1}H NMR spectra of ***mono*PhCOOHPyP** (dmso-d_6, top) and **dimPy** (CD_3OD 10%/$CDCl_3$, bottom).

The IR spectrum presents two intense bands at 1655 and 3430 cm^{-1}, respectively attributed to the stretching of the CO and of the NH of the amide groups. The UV-vis absorption spectrum of **dimPy** (CD_3OD 10%/$CDCl_3$) displays the typical spectral pattern of a freebase *meso*-aryl-porphyrin: an intense band (Soret) at 419 nm and four less intense bands (Q) between 500 and 650 nm. The molar extinction coefficient value at 514 nm, calculated with the Lambert-Beer law ($A = l \cdot \varepsilon \cdot C$), of 28670 $M^{-1}cm^{-1}$ is consistent with the presence of two porphyrin units.

Single crystals of **dimPh**, suitable for the X-ray diffraction, were obtained by slow diffusion of methanol into a chloroform solution of the porphyrin dimer (Figure 4.5). Details on the crystallization and data refinement are reported in the Experimental Section.

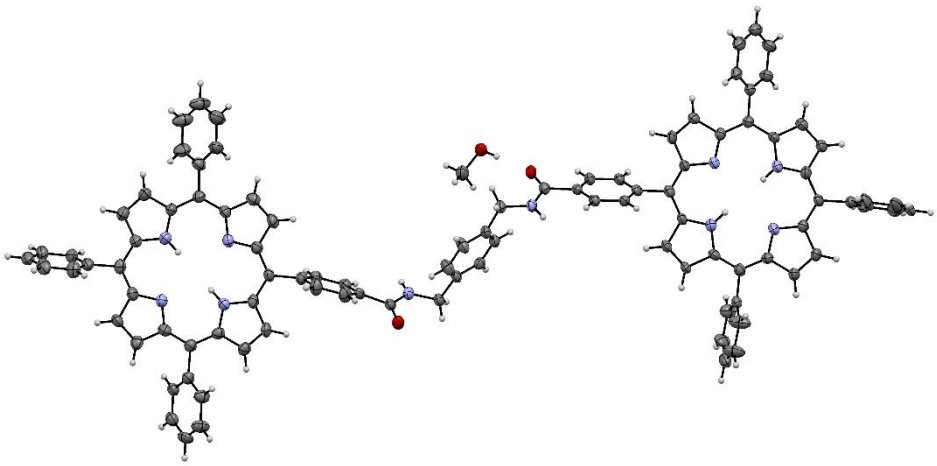

Figure 4.5. Single crystal X-ray structure of **dimPh**: ORTEP representation.

The porphyrin dimer is 40.9 Å long, length calculated as the distance between the *para*-carbons of the phenyl groups in the 15 positions of the two porphyrins, while the *para*-carbons of the phenyls in the 10 and 20 positions are spaced by ~25 Å. In the crystalline lattice, **dimPh** molecules are packed with all porphyrin planes parallel to each other. An extended hydrogen bond network iterates along all the crystalline lattice (Figure 4.6). Each **dimPh** molecule presents an ADDA sequence (acceptor-donor-donor-acceptor) establishing hydrogen bonds – through the -NH (D) and -CO (A) groups of the amide function – with another porphyrin dimer on one side, and with two methanol molecules on the other. The intermolecular measured distances are of 2.01(5) Å for N(**dimPh**$_A$)···O(**dimPh**$_B$), 1.87(3) and 2.01(5) Å for O(**dimPh**$_B$)···O(MeOH)···N(**dimPh**$_C$).

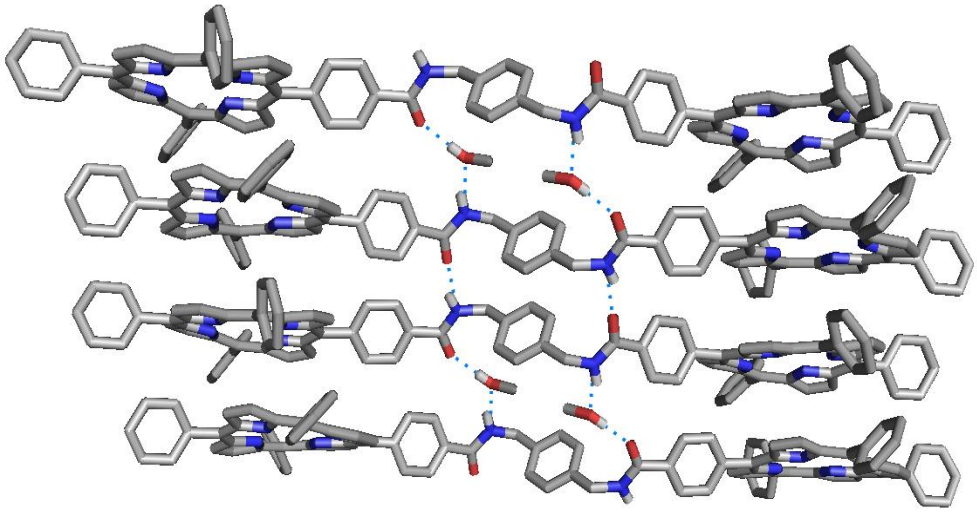

Figure 4.6. Hydrogen bond network established in the crystalline lattice of **dimPh**. Hydrogen bond distances (in Å) are referred to the nitrogen and oxygen atoms of the amide groups and the oxygen atoms of the methanol molecules. For clarity, only hydrogen atoms involved in the H-bonds are reported. Colour code: N: blue, O: red, C: grey, H: white.

The chemical shift of the amide proton (Ham in Figure A4.2 in the Appendix to Chapter 4), suggests that in solution, in the NMR concentration range, these intermolecular interactions do not persist.

4.2.2 Synthesis and Characterization of the Multi-Porphyrin Cage [(1Zn)$_6$·(dimPy)$_2$]

The reactivity of **dimPy** towards platform **1Zn** was then studied. At first, the two components were directly mixed in an NMR tube $CDCl_3$ solution, in a 3:1 ratio: as observed for the previous systems built on **1Zn** and politopic pyridyl ligands, the assembly occurs at room temperature, leading to the quantitative and almost instantaneous formation of the dimeric supramolecular cage **[(1Zn)$_6$·(dimPy)$_2$]** (Scheme 4.5). Repeating the reaction on larger scale (stirring a chloroform solution of the reactants for 10 minutes and inducing the precipitation of a dark blue powder by addition of *n*-hexane, see Experimental Section), congruent data were obtained.

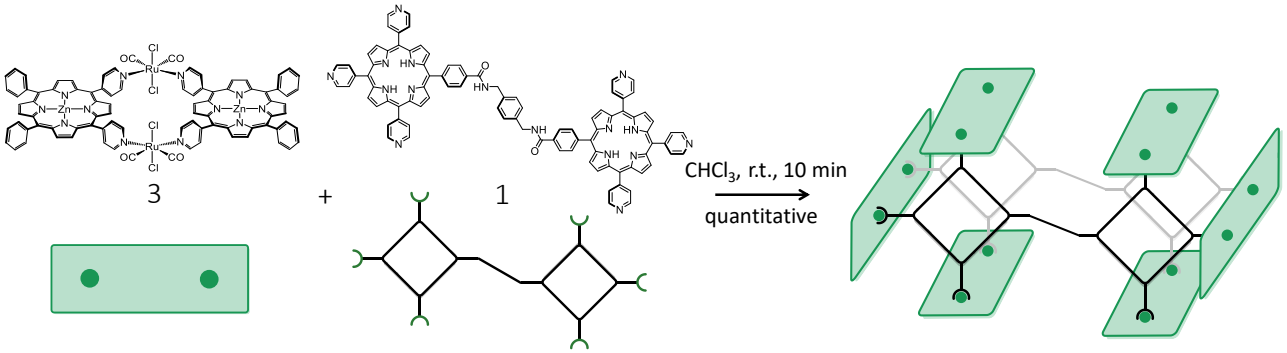

Scheme 4.5. Self-assembly between **1Zn** and **dimPy**.

Despite the intrinsic complexity of the system, the expertise and knowledge gained in the NMR characteristics of multi-porphyrin assemblies, combined with a detailed inspection through 1D- and 2D-NMR experiments, allowed us to confidently confirm the formation of the designed structure.

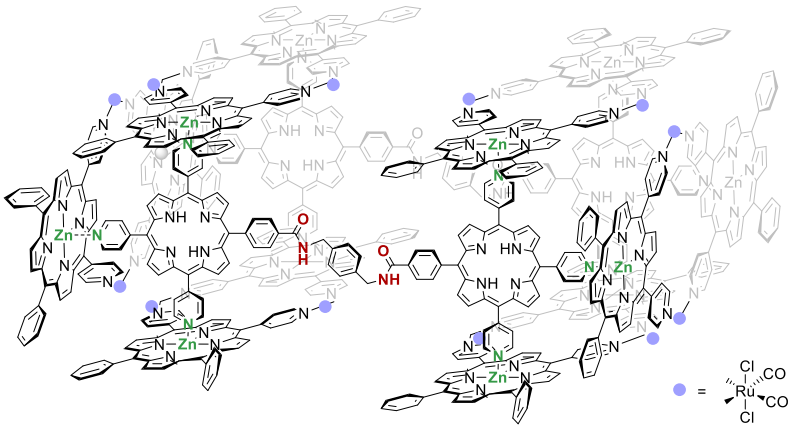

Chart 4.2. Schematic depiction of the supramolecular cage **[(1Zn)$_6$·(dimPy)$_2$]**.

Indeed, the flexibility endowed by the *p*-xylylene group intrinsically bestows **[(1Zn)$_6$·(dimPy)$_2$]** with conformational dynamicity (in principle the two facing **[(1Zn)$_3$·(*tris*PyP)$_2$]** may also be twisted of 90° one respect to the other). But, at the same time, combined with the numerous symmetry elements present in the structure, it grants that the resulting asymmetric unit does not significantly differ from

the **[(1Zn)$_3$·(*tris*PyP)$_2$]** one (Figure 4.7). Coherently to this, the spectrum of the dubbed cage (Figure 4.7, c) presents a spectral pattern similar to the **[(1Zn)$_3$·(*tris*PyP)$_2$]** one. However, in **[(1Zn)$_6$·(dimPy)$_2$]**, at room temperature, signals are generally better resolved, suggesting that the hexa-topic ligand, in comparison to the tri-topic ***tris*PyP**, endows higher stability to the assembly, both in terms of kinetics and thermodynamics.

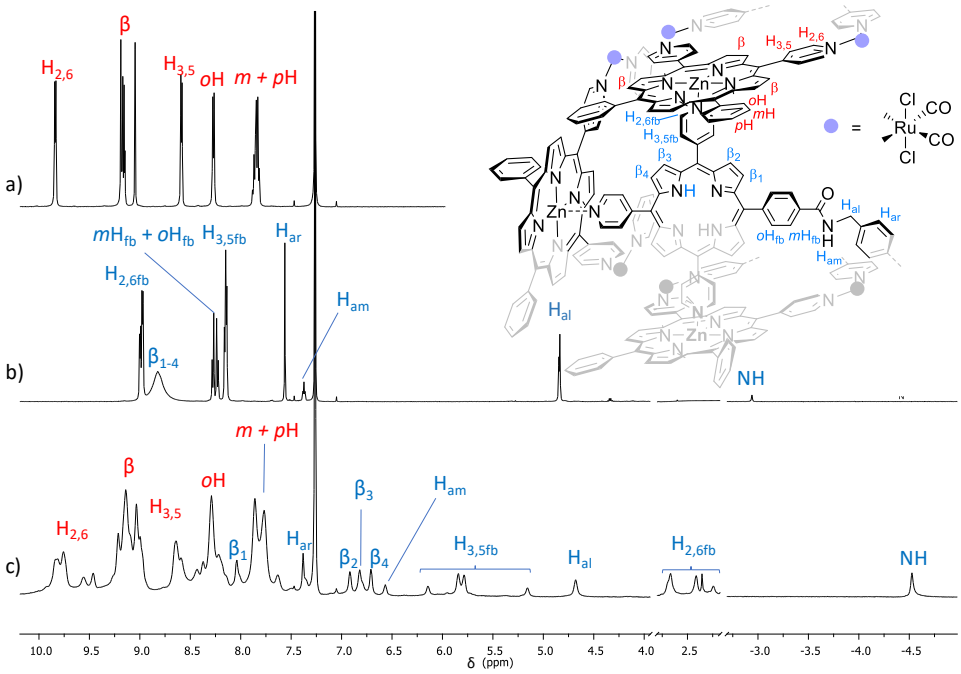

Figure 4.7. ^{1}H-NMR spectra at 25°C of a) **1Zn** ($CDCl_3$), b) **dimPy** (CD_3OD 10%/$CDCl_3$) and c) **[(1Zn)$_6$·(dimPy$_2$)]** ($CDCl_3$). Asymmetric unit of **[(1Zn)$_6$·(dimPy$_2$)]**, with NMR-proton labeling.

Despite the large number of resonances, an almost complete signal assignment was achieved by means of 2D correlation NMR techniques (HH-COSY, HC-COSY, HH-NOESY and HH-ROESY), by signals relative integration, and by comparison with the starting building blocks, and the parent.assembly (see above). Relative integration of the assigned signals is coherent with the stoichiometric ratio of 3:1 between **1Zn** and **dimPy**.

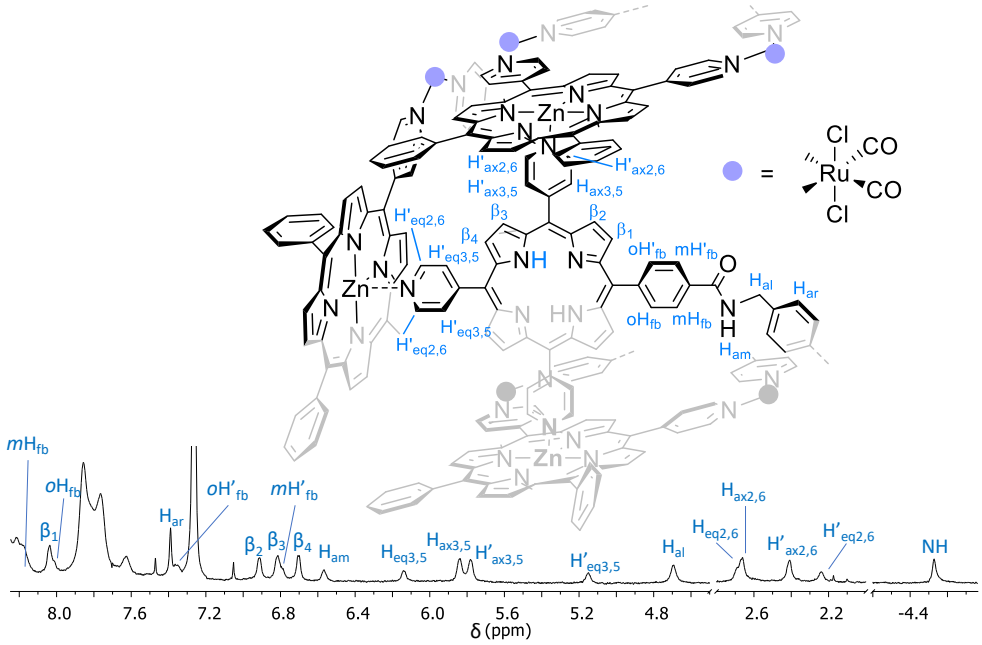

Figure 4.8. ^{1}H-NMR spectrum ($CDCl_3$, 25°C) of **[(1Zn)$_6$·(dimPy)$_2$]**: enlargement of the spectral region between 8.2 and -5.0 ppm.

The pyridyl protons of the dimPy units resonate between 2 and 6.2 ppm (Figure 4.8), strongly upfield shifted due to the coordination to zinc centres of **1Zn**. Signals $H_{eq3,5}$, $H_{ax3,5}$, $H'_{ax3,5}$, and $H'_{eq3,5}$, presenting a relative integration of 4:8:8:4, couple with the corresponding $H_{2,6}$ protons, located between 2.7 ppm and 2.2 ppm (see COSY in Figure 4.9). The methylene protons of the diamide linker resonate at 4.72 ppm, and correlate with the H_{am} amide signal, at 6.63 ppm. The β pyrrolic protons of **dimPy** present distinct signals, at around 6.8 ppm, and each of these correctly integrates for 8H. In the HH-COSY spectrum, cross-peaks between β_4 and β_3 and between β_2 and β_1 are observed, affording the identification of β_1 protons at 8.04 ppm. The benzamidic aromatic proton resonances, *o*H' (6.76 ppm, partially overlapping with β_3) correlate with *m*H' (7.33 ppm), correctly integrating for 4H each; while the external protons, *o*H (8.20 ppm) and *m*H (8.02 ppm), overlap with the **1Zn** and β_1 signals, respectively. The large magnetic anisotropy is highlighted by the pronounced chemical-shift difference ($\Delta\delta$ = 0.43) between protons $H'_{eq3,5}$ and $H_{eq3,5}$. On the contrary, the signals of the diamide linker are only slightly shifted, in line with their more distant position from the porphyrin shielding cones, and thus supporting the proposed structure.

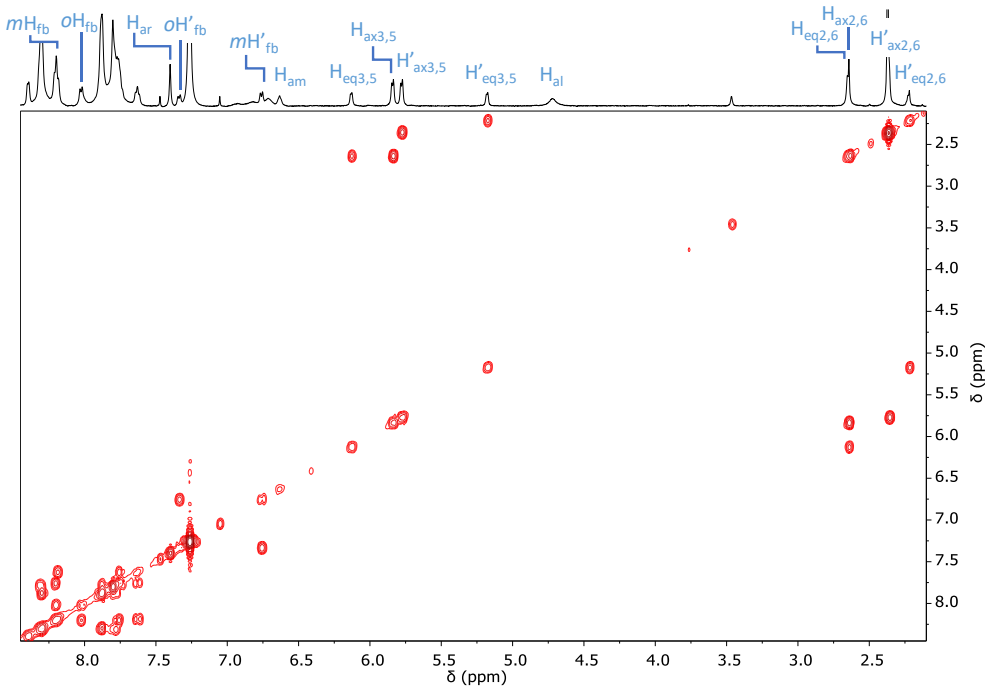

Figure 4.9. H-H COSY spectrum ($CDCl_3$, T = -10°C, 8.5 - 2.0 ppm spectral region) of **[(1Zn)$_6$·(dimPy)$_2$]**.

By lowering the temperature down to -10°C, a general sharpening of the signals, particularly marked for the **1Zn** resonances (Figure 4.10), is observed.

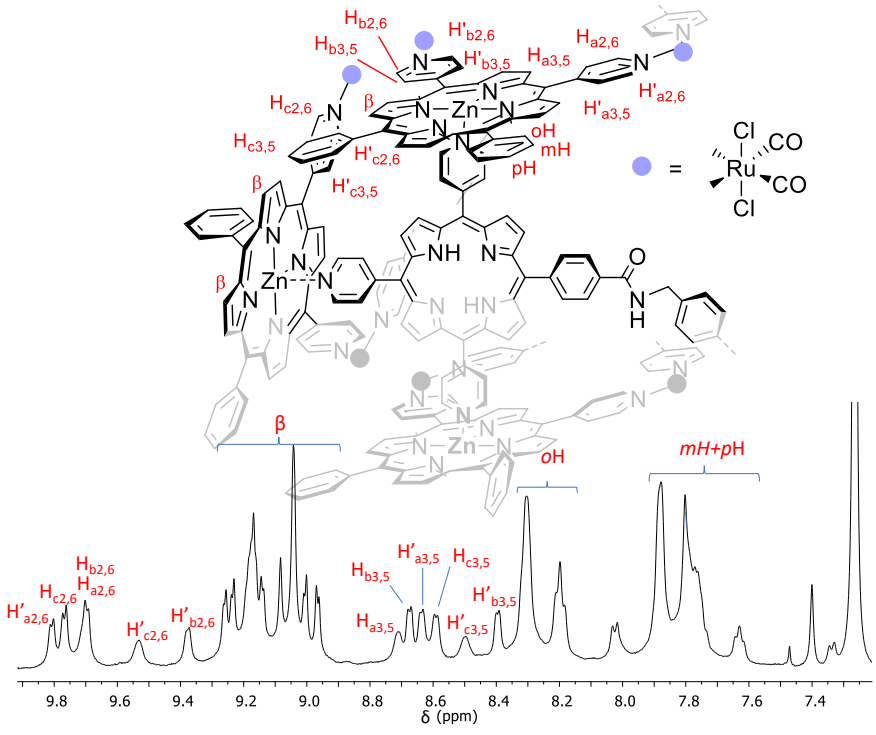

Figure 4.10. ^{1}H-NMR spectrum ($CDCl_3$, T = -10°C, aromatic region) of **[(1Zn)$_6$·(dimPy$_2$)]**.

The phenyl and beta pyrrolic proton signals of **1Zn,** are affected by an overall superimposition, making their detailed assignment unfeasible. On the contrary, the three asymmetric pyridyl groups resonances (labelled *a*, *b* or *c* in Figure 4.10) were fully assigned. As observed for the pyridyl protons

of the **dimPy** linker, each resonance of the aryl groups of **1Zn** is additionally split, depending on the proton disposition toward the inside or the outside of the cage cavity.

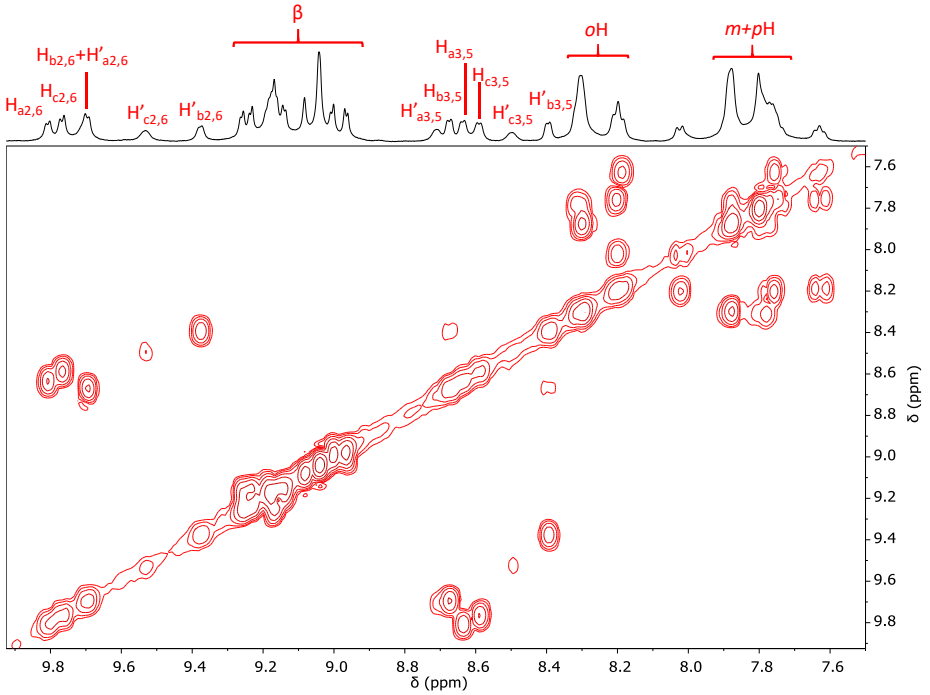

Figure 4.11. HH-COSY ($CDCl_3$, T = -10°C, aromatic region) **[(1Zn)$_6$·(dimPy)$_2$]** spectrum.

The HH-NOESY spectrum shows intercomponent spatial correlation cross-peaks between the **dimPy** pyridyl protons and **1Zn** resonances (Figure 4.12). For instance, the $H_{ax2,6}$ signal at 2.65 ppm, couples through space with phenyl *o*H, and with the β-pyrrolic protons of **1Zn**.

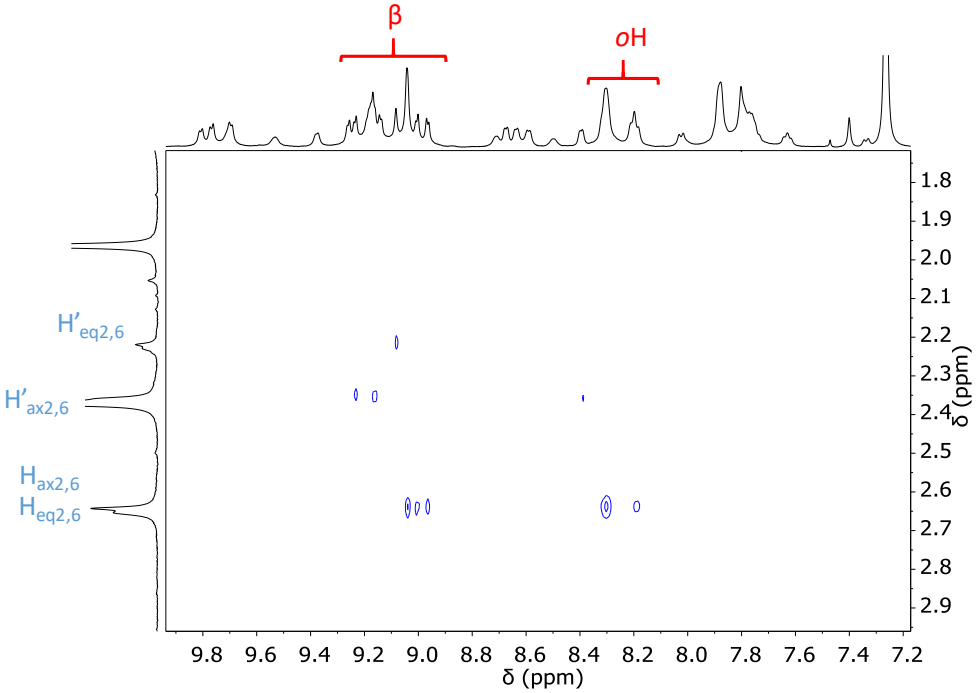

Figure 4.12. HH-NOESY ($CDCl_3$, –10°C) spectrum of **[(1Zn)$_6$·(dimPy)$_2$]**: enlargement on the intercomponent cross-peaks.

Spectra recorded at different temperatures (50 ÷ -40°C) or by progressive dilution did not show significant changes in the resonance pattern, confirming a good stability range of the adduct.

The titration of a $CDCl_3$ solution of **dimPy** (*ca.* 1.7×10^{-3} M) with increasing aliquots of **1Zn** was performed. When 2 equivalents of **1Zn** were added, the formation of the cage **[(1Zn)$_6$·(dimPy)$_2$]** was already observed, suggesting an "all or nothing" assembling mechanism.[8]

The overall NMR characterization so far described, confirms the **[(1Zn)$_6$·(dimPy)$_2$]** structure proposed (see Chart 4.2). In the IR spectrum, the correct carbonyl stretching pattern is observed: two intense bands at 2066 and 2001 cm^{-1} for the *cis*-$Ru(CO)_2$ fragments of **1Zn**, and one intense band at 1611 cm^{-1} for the –NH(CO)- amide moieties of the **dimPy** unit. Numerous attempts have been carried out to obtain single crystals of **[(1Zn)$_6$·(dimPy)$_2$]** suitable for X-ray diffraction, playing both on the solvent combination, on the concentration and the temperature. By slow diffusion of *n*-hexane into a dichloromethane solution of **[(1Zn)$_6$·(dimPy)$_2$]**, at –20°C, small purple needle crystals were grown. Disappointingly, the diffraction data collected, couldn't afford the resolution of the X-ray structure.

^{1}H NMR Diffusion-Ordered Spectroscopy (DOSY) was used to gain additional informative data over the nuclearity and size of the assembly.[9] A comparative analysis on the assemblies **[(1Zn)$_6$·(dimPy)$_2$]**, **[(1Zn)$_3$·(*tris*PyP)$_2$]**, **[1Zn·*trans*DPyP]$_2$**, and **1Zn** was performed. A superimposition of the 2D ^{1}H-DOSY maps obtained for **[(1Zn)$_6$·(dimPy)$_2$]** and **1Zn** is depicted in Figure 4.13. Notably, for **[(1Zn)$_6$·(dimPy)$_2$]** proton signals of both **1Zn** and **dimPy** units are grouped in a unique diffusion coefficient value, clearly indicating that in solution the two components diffuse together. Moreover, the diffusion coefficients of **1Zn** and **[(1Zn)$_6$·(dimPy)$_2$]** are ordered by decreasing values, which well-correlate to the relative order of increasing dimensions.

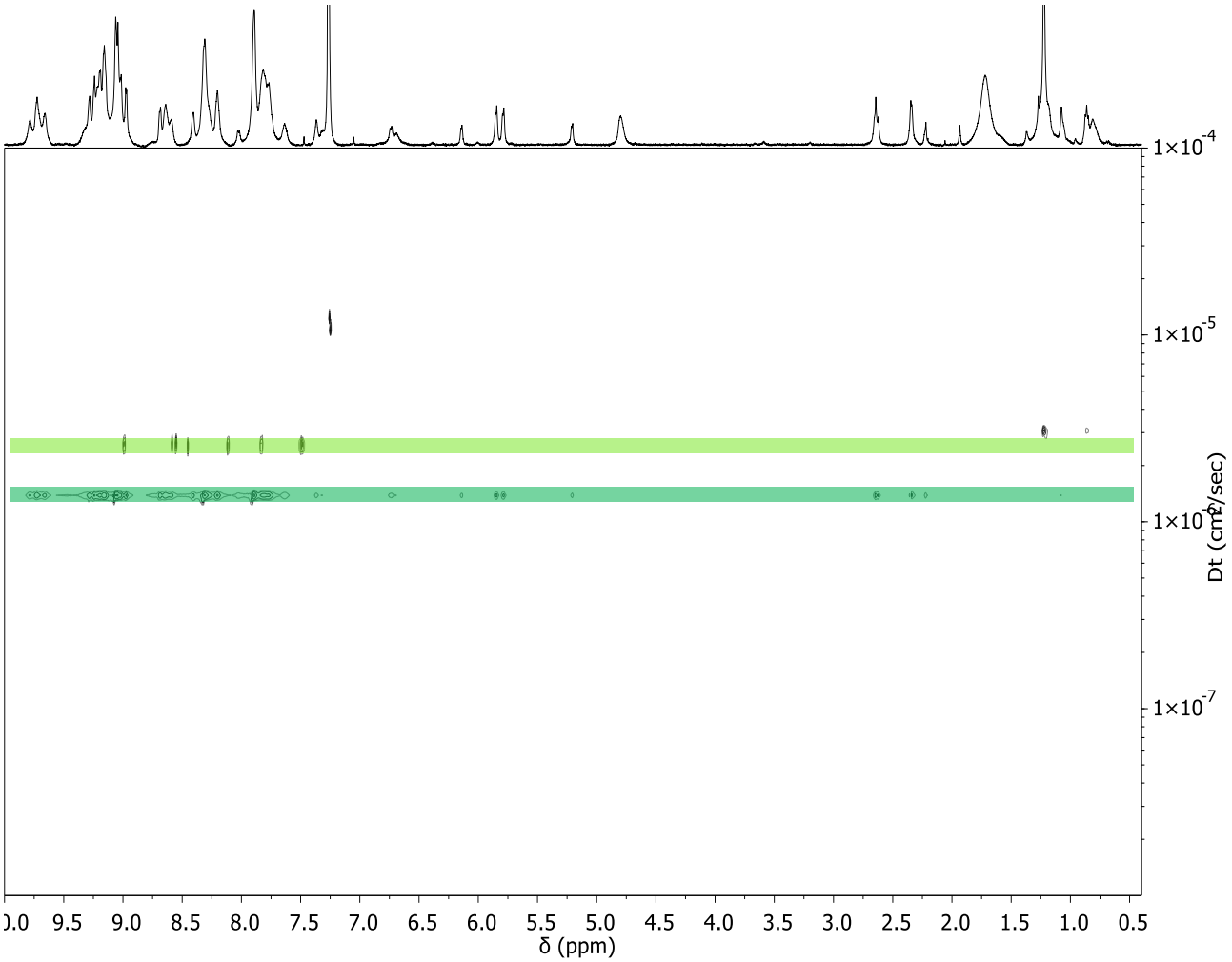

Figure 4.13. Superimposition of the 2D ^{1}H-DOSY spectra (Bayesian transform, $CDCl_3$, -30°C) of **[(1Zn)$_6$·(dimPy)$_2$]** (blue) and **1Zn** (green). On the horizontal axis, only the 1D ^{1}H trace of **[(1Zn)$_6$·(dimPy)$_2$]** is shown.

Through a detailed elaboration of the signal intensity decay (see Appendix 1), more accurate diffusion coefficients (*Dt*) values have been derived.[10] The *Dt* values are the average of at least 5 different *Dt* values calculated through the analysis of the proton signal decay of a set of 1D DOSY spectra. Diffusion coefficient, hydrodynamic radius (r_H) and hydrodynamic volume (V_H) values obtained for all the analyzed compounds are summarized in Table 4.1. The r_H values were calculated from the Stokes-Einstein equation, in the limits of the spherical approximation:

$$D_t = \frac{k_B T}{6\pi\eta r_H}$$

Table 4.1. D_t, r_H and V_H values of the examined systems.

Compound	D_t x 10^{-6} (cm^2 s^{-1})	r_H (Å)	V_H (Å^3)
1Zn	2.25 ± 0.05	8.0	2153
[(1Zn)$_2$·(*trans*DPyP)$_2$]	2.00 ± 0.05	9.0	3064

[(1Zn)$_3$·(*tris*PyP)$_2$]	1.71 ± 0.11	10.5	4849
[(1Zn)$_6$·(dimPy)$_2$]	1.38 ± 0.07	13.5	9417

All the *Dt* values well correlate with the different size of the analyzed systems. Very pleasingly, the calculated V_H value of **[(1Zn)$_6$·(dimPy)$_2$]** is approximately the double of the one calculated for **[(1Zn)$_3$·(*tris*PyP)$_2$]**: this is consistent with the fact that from a structural viewpoint, **[(1Zn)$_6$·(dimPy)$_2$]** is made of two connected **[(1Zn)$_3$·(*tris*PyP)$_2$]** subunits. It must be noted that part of the analyzed systems (e.g., **1Zn** and **[(1Zn)$_6$·(dimPy)$_2$]**) define volumes that significantly deviate from the spherical shape. More accurate and reliable hydrodynamic volume absolute values may be calculated by appropriately modifying the equation, introducing the shape factor *fs* and the size factor *c*, (the values of these factors can be calculated following the guidelines extensively discussed by A. Macchioni and coworkers) [8]:

$$D_t = \frac{k_B T}{f_s c \pi \eta r_H}$$

The absorption spectrum of **[(1Zn)$_6$·(dimPy)$_2$]** (Figure 4.14) is almost the perfect weighted sum of the absorption spectra of the building units (calculated on the basis of their stoichiometric ratio).

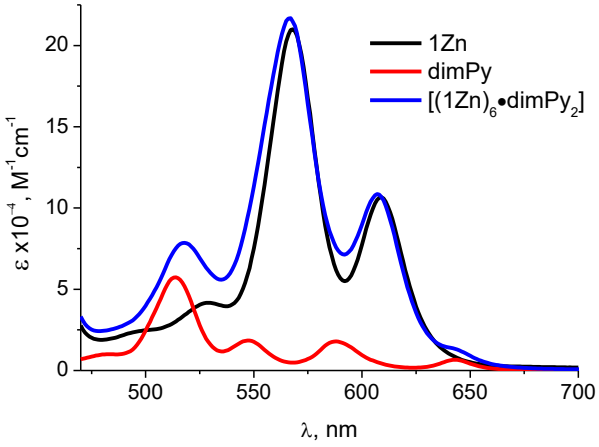

Figure 4.14. Absorption spectra ($CHCl_3$, visible region) of **[(1Zn)$_6$·(dimPy)$_2$]** (blue line) compared to those of the building blocks **1Zn** (black line) and **dimPy** (red line). As reference the **1Zn** spectrum was recorded in presence of an excess of pyridine.

The fluorescence measurements, evidenced that, as observed for systems **[1Zn·*trans*DPyP]$_2$**[11] and **[(1Zn)$_3$·(*tris*PyP)$_2$]**[1] also in **[(1Zn)$_6$·(dimPy)$_2$]** upon irradiation of the platform **1Zn**, an efficient photoinduced energy transfer process from the excited state of the zinc porphyrin to the freebase ligand, occurs. In fact, the emission spectrum recorded after selective excitation of the **1Zn** unit at 565 nm, presents the typical fluorescence pattern of the freebase-porphyrin dimer **dimPy** (Figure

4.15, on the left) with maxima at 655 and 715 nm (whereas the **1Zn** fluorescence presents two bands peaking at 608 and 651 nm).

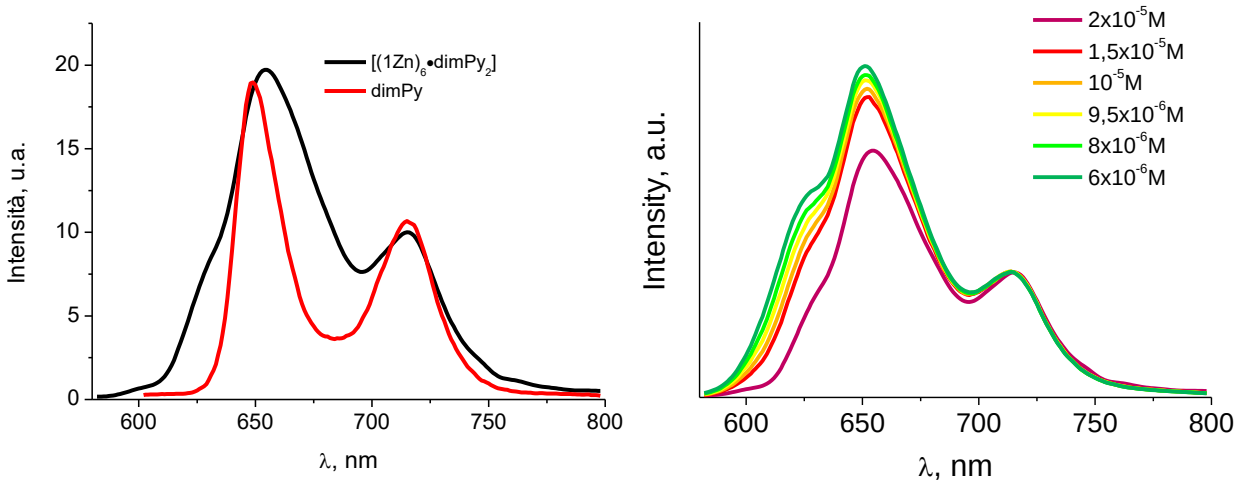

Figure 4.15. Left: emission spectra ($CHCl_3$, λ_{ex} = 565 nm) of **[(1Zn)$_6$·(dimPy)$_2$]** (black) and **dimPy** (red), registered in the same experimental conditions. Right: emission spectra ($CHCl_3$, λ_{ex} = 565 nm) of **[(1Zn)$_6$·(dimPy)$_2$]** recorded by progressive dilutions.

The occurrence of such intercomponent process, besides opening to interesting future applications, enabled to gather more detailed information about the stability of the supramolecular system and to determine the minimum concentration at which the **[(1Zn)$_6$·(dimPy)$_2$]** is found completely assembled. In fact, the coordination of the freebase ligand to the zinc-porphyrin platform is a *sine qua non* condition for the occurrence of the photoinduced energy transfer process.

A spectrofluorimetric dilution titration experiment (in chloroform solution) was therefore performed: the concentration decrease is followed by the rise of a shoulder band, peaking at 630 nm, corresponding to the emission of the **1Zn** component (Figure 4.15, on the right). For concentration lower than 10^{-5} M, system **[(1Zn)$_6$·(dimPy)$_2$]** is no longer completely assembled in solution and, therefore, the fluorescence of **1Zn** is partially restored, due to the presence of uncoordinated zinc-porphyrin platform.

In Table 4.2 the limit concentrations of stability determined for **[1Zn·*trans*DPyP]$_2$**, **[(1Zn)$_3$·(*tris*PyP)$_2$]** and **[(1Zn)$_6$·(dimPy)$_2$]** are reported.

Table 4.2. Limit concentration of stability.

Compound	Limit concentration of stability
[1Zn·transDPyP]$_2$	7 x 10^{-5} M[a]
[(1Zn)$_3$·(*tris*PyP)$_2$]	3 x 10^{-5} M[b]
[(1Zn)$_6$·(dimPy)$_2$]	1 x 10^{-5} M

[a] from reference 9; [b] from reference 1

Supramolecular system **[(1Zn)$_6$·(dimPy)$_2$]** resulted more stable than system **[(1Zn)$_3$·(*tris*PyP)$_2$]** which, in turn, is more stable than system **[1Zn·*trans*DPyP]$_2$.** Indeed, the increasing number of pyridyl-Zn(II) bonds enrolled, ensures higher stability to the supramolecular derivate. This trend well correlates with what previously observed from the ^{1}H-NMR spectra, where the higher stability endowed by the hexa-topic ligand, tangibly induced a higher spectral resolution at room temperature.

4.2.3 Synthesis and Characterization of the Hexa-topic Ligands SnP(*mono*PhCOOPyP)$_2$

The well-documented selective reactivity of Sn(IV)–di(hydroxo)-porphyrins towards hard carboxylic ligands, leading to symmetric Sn(IV)–di(carboxylate)-porphyrin complexes with total conversions, has been extensively used by several groups as scaffold to efficiently assembly elaborate multicomponent arrays.[2-4,12] Sn(IV) porphyrins are very stable and possess interesting photophysical and electrochemical properties, moreover, their diamagnetic nature allows to obtain detail structural information by NMR characterization and the Sn(IV)–carboxylate axial bonds present distinguished robustness.

Given the inertness of the Sn(IV)–carboxylate bond, initially, a two-step synthetical pathway was pursued. First, the adducts featuring two ***mono*PhCOOPyP** axially coordinated to the Sn(IV) porphyrins were prepared isolated and characterized. Secondly, each of these hexa-topic systems was combined with **1Zn** to promote the assembling of the target cage. Playing on the lateral *meso* substituents, two different Sn(IV)porphyrin have been used: one bearing normal phenyl groups, while *penta*fluoro-phenyl functions the other. The different substituents allowed to tune the photophysical and electrochemical properties of the metalloporhyrin, potentially awarding the derived supramolecular cages with distinguished photophysical characteristics (see below). Furthermore, the presence of the fluorine atoms introduced the possibility to employ ^{19}F-NMR spectroscopy, an important tool for the characterization of the final assembled cage.

SnTPP(*mono*PhCOOPyP)$_2$ and **SnTpFP(*mono*PhCOOPyP)$_2$** were synthesized and isolated in very good yields (80-90%) by refluxing a chloroform solution of the corresponding dihydroxotin(IV)porphyrins and ***mono*PhCOOHPyP**, for 7 hours, as reported in Scheme 4.6. The pure products were obtained by precipitation from chloroform:ether. A complete characterization was done by NMR (^{1}H, ^{13}C, ^{119}Sn, ^{19}F mono- and bi-dimensional experiments), IR and UV-vis absorption spectroscopy; given the close spectral features found for the two conjugates, only system**SnTpFP(*mono*PhCOOPyP)$_2$** will be discussed (for the detailed analysis of **SnTPP(*mono*PhCOOPyP)$_2$** see the Experimental Section).

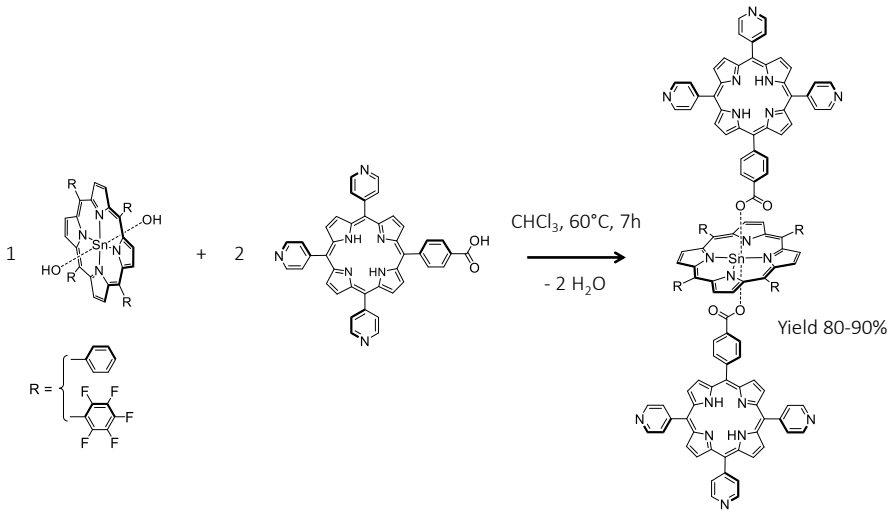

Scheme 4.6.

In Figure 4.16 the ^{1}H NMR spectra of **SnTpFP(*mono*PhCOOPyP)$_2$** ($CDCl_3$) and ***mono*PhCOOHPyP** (dmso-d_6) are reported. Full assignments were done by means of 2D H-H and H-C NMR experiments. The number and the relative integration of the resonances are in agreement with the symmetry and the stoichiometry of conjugate. As expected, the main consequence of the axial coordination to the metalloporphyrins is a remarkably up-field shift of the proton resonances of the axially bound ligand. Indeed, the benzoate protons, *o*H$_{fb}$ and *m*H$_{fb}$, are the most influenced by the porphyrin shielding effect, with a Δδ of -1.2 and -3, respectively. Moreover, a splitting of the resonances of the beta protons (β_{1-4}) is also evident, with particular regard to protons β_1 and β_2 (Δδ = -0.71 and Δδ = -0.29 respectively).

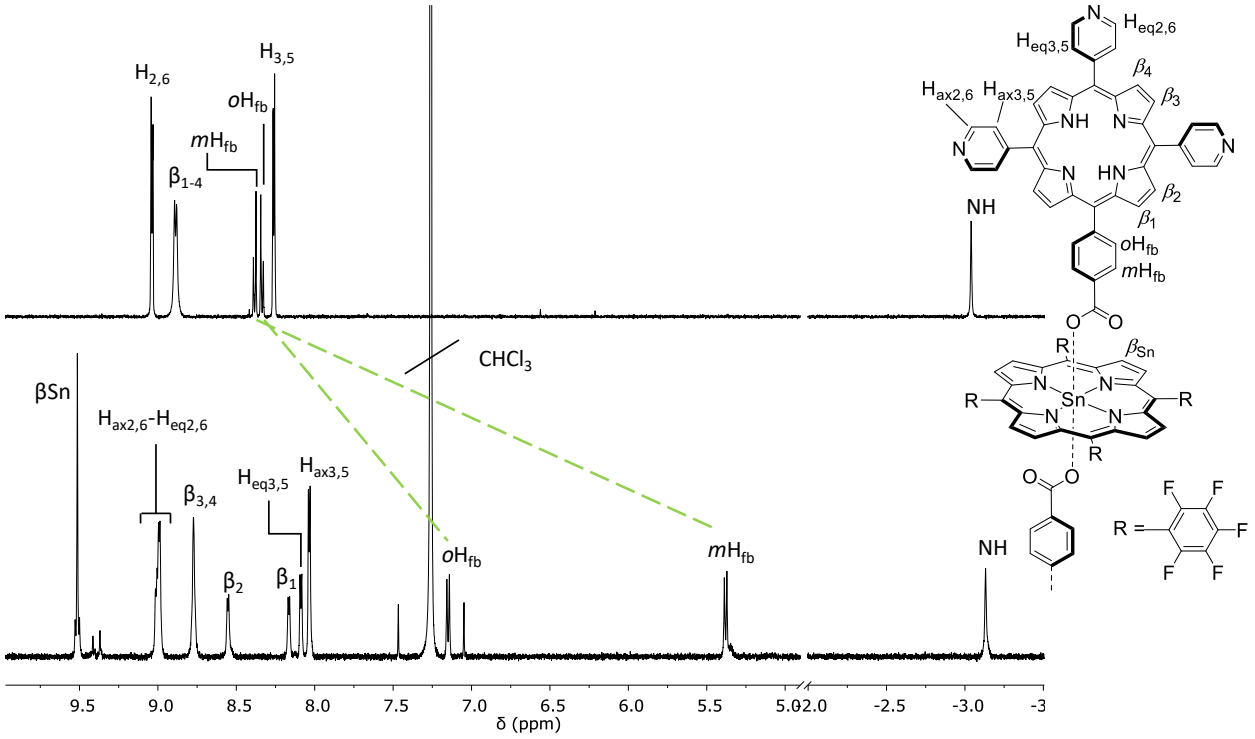

Figure 4.16. ^{1}H-NMR spectra of ***mono*PhCOOHPyP** (dmso-d_6, on the top) and **SnTpFP(*mono*PhCOOPyP)$_2$** ($CDCl_3$, on the bottom).

In the ^{19}F-NMR spectrum of **SnTpFP(*mono*PhCOOPyP)$_2$** (see below Figure 4.23) *orto-*, *meta-* and *para-*fluorine atoms resonate at 135.51, 160.15 and 149.00 ppm as a doublet, triplet and triplet signals, respectively, showing correct relative intensity ratio of 2:2:1.

At 9.51 ppm, the β-pyrrolic proton resonance of the tin-porphyrin presents satellite signals (J = 14 Hz) due to the coupling with the ^{119}Sn nucleus. Exploiting the presence of the NMR-active tin isotope, ^{1}H-^{119}Sn Heteronuclear Multiple Bond Correlation (HMBC) experiments were performed.

In 1994, Arnold and Bartley reported an accurate studio on the ^{119}Sn-NMR (relative abundance of the 8.6%, I = ½) of different tin(II/IV)-porphyrins, in dependence both of the porphyrin peripheral substituents, and of the nature of the axial ligands.[13] It was evidenced that, for the same axial anions, changing the porphyrin causes remarkably small changes in tin chemical shifts. On the contrary the δ_{Sn} is extremely sensitive to the nature of the axial ligand: in particular, for the complexes with O-bound axial ligands, stronger donors generally shift the ^{119}Sn resonance downfield, while for the carboxylates (apart from HCO_2^-) the reverse is the case.

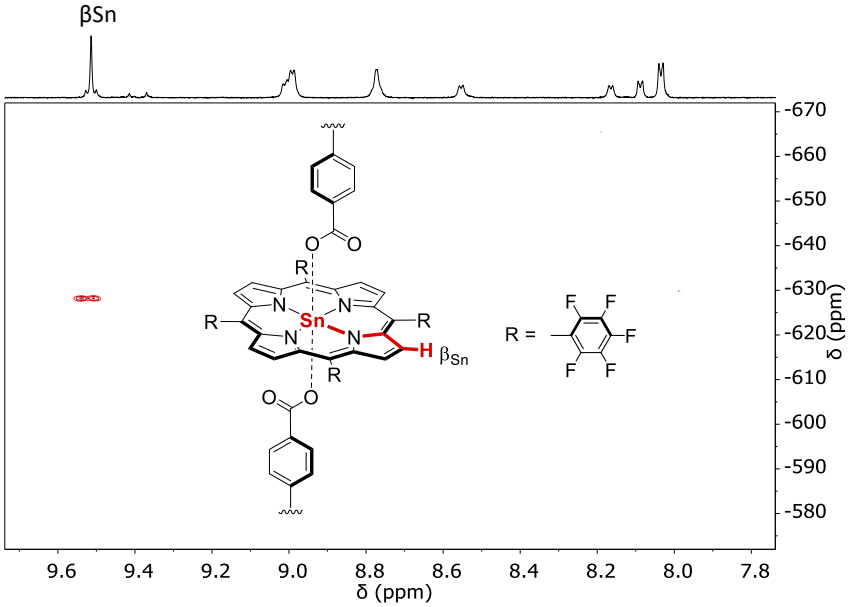

Table 4.3

Compound	δ_{Sn} (ppm)
SnTPP(Cl)$_2$*	-589.7
SnTPP(OH)$_2$*	-569.6
SnTPP(OH)$_2$	-569.2
SnTpFP(OH)$_2$	-565.8
SnTpFP(BA)(OH)	-596.5
SnTPP(BA)$_2$*	-631.1
SnTpFP(BA)$_2$	-629.6
SnTPP(monoPhCOOPyP)$_2$	-628.5
SnTpFP(monoPhCOOPyP)$_2$	-628.2
* from reference 13	

Left: **Figure 4.17.** ^{1}H-^{119}Sn HMBC spectrum ($CDCl_3$) of **SnTpFP(*mono*PhCOOPyP)$_2$**. Right: **Table 4.3.** Chemical shifts found for the different tin(IV)-porphyrin complexes synthesized, compared with those reported in the literature.

In practice, the use of 1D ^{119}Sn NMR analysis is hampered, given the low sensitivity of the tin nucleus and the dilution effect resulting from the embedding of a tin-porphyrin component into large arrays of consistent molecular weights. The use of ^{1}H-^{119}Sn 2D hetero-correlation experiments, introduced by the group of Crossley in the recent past,[14] is most certainly a, nowadays accessible, viable alternative, as these experiments permit the indirect detection of δ_{Sn} values of the sample tin-porphyrin components with short acquisition times. In the present work, we performed a comparative ^{1}H-^{119}Sn 2D HMBC analysis (limited to the detection of signal correlations between the metallo-porphyrin *beta* protons and the tin nucleus) on the series of arrays, the corresponding Sn(IV) porphyrin starting materials, selected reaction intermediates, and model compounds. The derived

^{119}Sn chemical shifts, fully congruent with literature reference systems, are reported in Table 4.3. The ^{1}H-^{119}Sn HMBC spectrum of **SnTpFP(*mono*PhCOOPyP)$_2$** (Figure 4.17) presents a cross-peak due to the J^4 correlation between the beta-pyrrolic protons and the Sn nucleus. In Table 4.3 the chemical shifts found for the different tin(IV)-porphyrin complexes synthesized, and δ_{Sn} literature values of analogous complexes, are resumed. As observed by Arnold and Bartley, δ_{Sn} values are no influenced by the nature of the lateral *meso*-substituents of the metalloporphyrin. δ_{Sn} of **SnTpFP(*mono*PhCOOPyP)$_2$** and **SnTPP(*mono*PhCOOPyP)$_2$**, found at –628.2 and –628.5 ppm respectively, are slightly different to the chemical shift value (–631.1 ppm), reported for the tin-*tetra*phenylporphyrin bearing two benzoates as axial ligands (**SnTPP(BA)$_2$**). Interestingly, replacement of both the hydroxo-ligands by the benzoate groups, causes an up-field shift of about 60 ppm, while substitution of only one hydroxide ion shifts the signal of only 30 ppm.

4.2.4 Synthesis and Characterization of the Multi-Porphyrin Cages [(1Zn)$_6$·(SnP(*mono*PhCOOPyP)$_2$)$_2$]

The coordination reaction of the hexa-pyridyl ligands to platform **1Zn** was performed directly in the NMR tubes, dissolving the building units in deuterated chloroform, in a 3:1 ratio (Scheme 4.7).

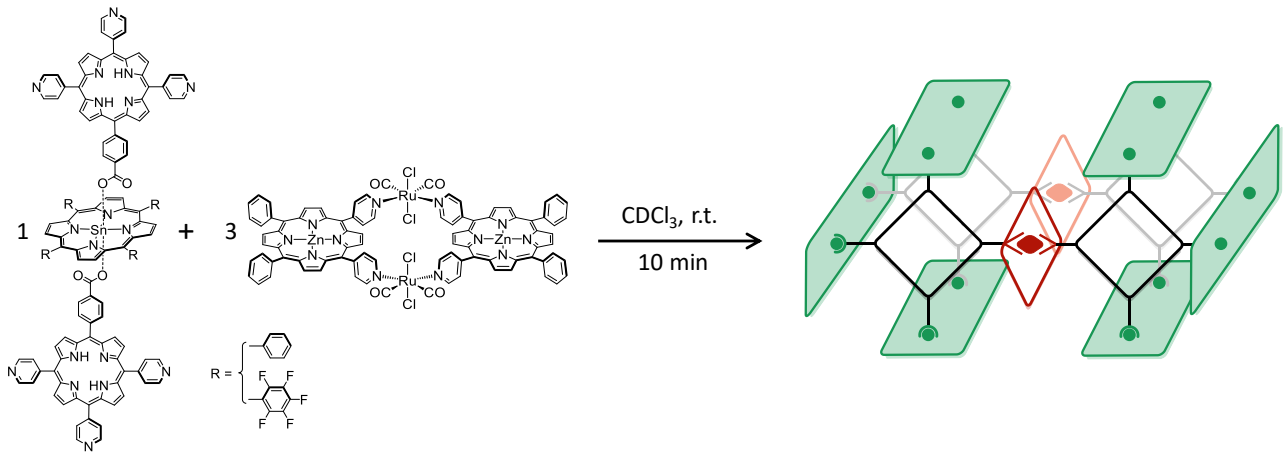

Scheme 4.7. Self-assembly between **1Zn** and the hexa-topic ligands.

The inertness of the Sn-carboxylate bonds together with the formation of selective hard/soft metal-to-ligand interactions led to the quantitative and instantaneous formation of the target supramolecular systems of formula **[(1Zn)$_6$·(SnTPP(*mono*PhCOOPyP)$_2$)$_2$]** and **[(1Zn)$_6$·(SnTpFP(*mono*PhCOOPyP)$_2$)$_2$]**. The complete NMR solution characterization (^{1}H, ^{13}C, ^{119}Sn, ^{19}F 1D and 2D experiments) confirmed the proposed structure, shown in Chart 4.3, featuring two **[(1Zn)$_3$·(*mono*PhCOOPyP)$_2$]$^{2-}$** subunits held together by two middle and likely coplanar Sn(IV)porphyrin units.

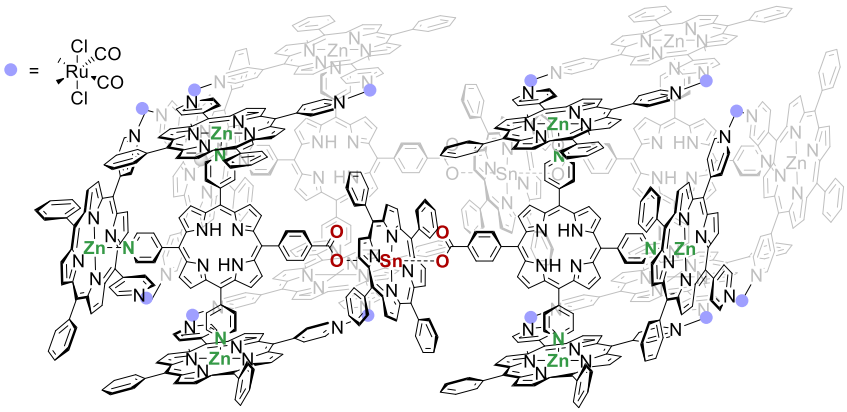

Chart 4.3. Schematic depiction of the supramolecular cage **[(1Zn)$_6$·(SnTPP(*mono*PhCOOPyP)$_2$)$_2$]**.

These dimeric cages, differently from **[(1Zn)$_6$·(dimPy)$_2$]**, present a separating "wall", constituted by the tin-porphyrin units, which creates two separate compartments. Despite the elevated complexity and the presence of a total number of 18 porphyrins, the overall symmetry elements yield the asymmetric unit shown in Chart 4.4, with the NMR-proton labelling.

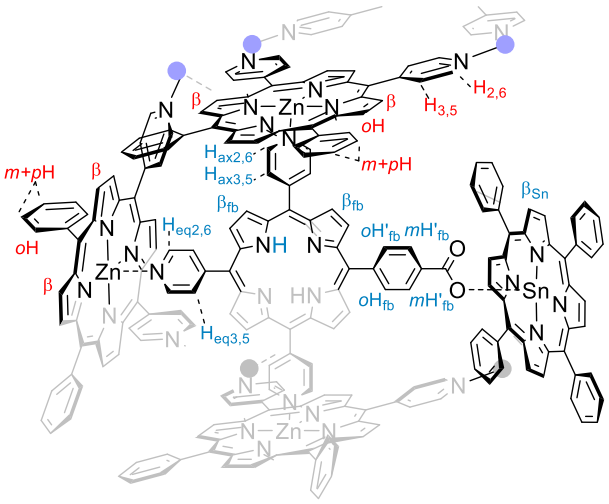

Chart 4.4

In Figure 4.18 the ^{1}H NMR spectra of the supramolecular cages **[(1Zn)$_6$·(SnTPP(*mono*PhCOOPyP)$_2$)$_2$]** and **[(1Zn)$_6$·(SnTpFP(*mono*PhCOOPyP)$_2$)$_2$]** are reported. As can be observed by a first qualitative look, changing the substituents on the Sn porphyrin ring, led to a negligible variation of the spectral pattern, suggesting only minimal chemical and conformational variation between the two structures.

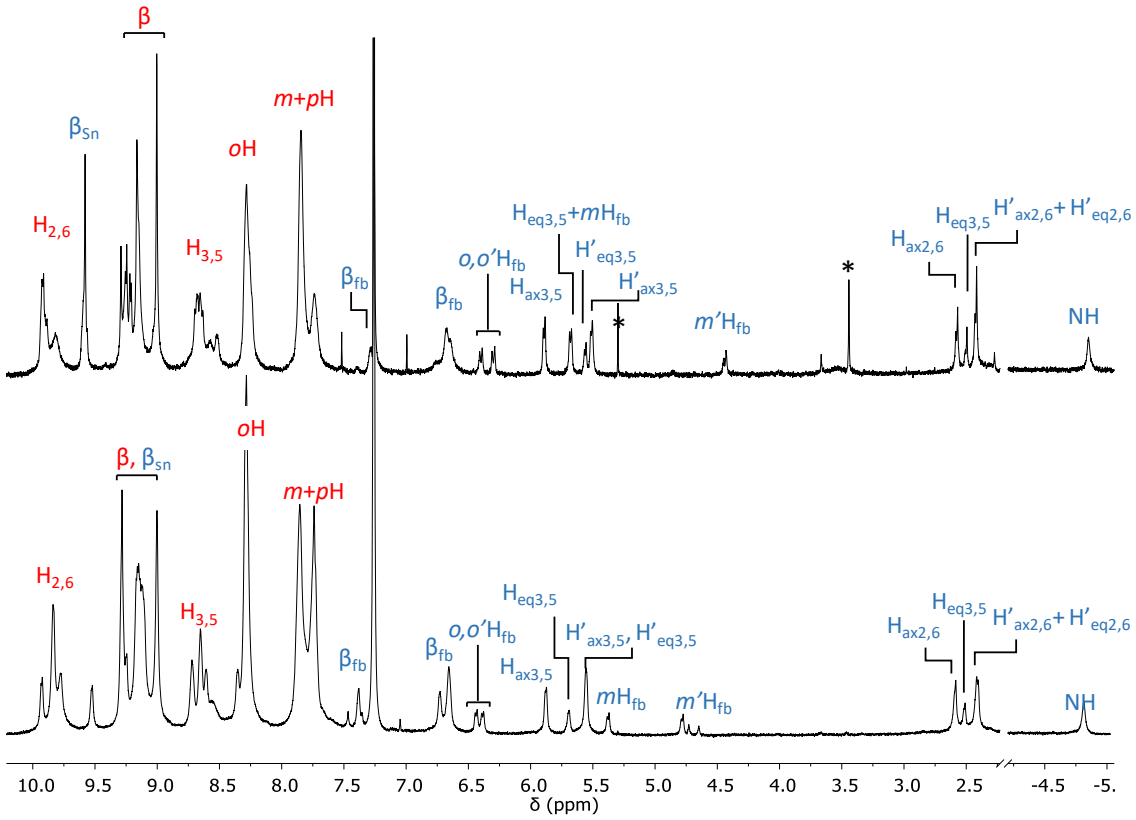

Figure 4.18. ^{1}H NMR spectra ($CDCl_3$) of **[(1Zn)$_6$·(SnTpFP(*mono*PhCOOPyP)$_2$)$_2$]** (top) and **[(1Zn)$_6$·(SnTPP(*mono*PhCOOPyP)$_2$)$_2$]** (bottom). For NMR labelling see Chart 4.4.

Given the strong similarity, only the characterization of assembly **[(1Zn)$_6$·(SnTpFP(*mono*PhCOOPyP)$_2$)$_2$]** will be described in detail, eventually pointing out the differences found between the two systems. The ^{1}H NMR spectra of **[(1Zn)$_6$·(SnTpFP(*mono*PhCOOPyP)$_2$)$_2$]** and **SnTpFP(*mono*PhCOOPyP)$_2$** are shown in Figure 4.19. As seen in the previous dimeric cage, at room temperature the proton spectrum of **[(1Zn)$_6$·(SnTpFP(*mono*PhCOOPyP)$_2$)$_2$]** presents a set of relatively well-resolved signals, hinting an increased kinetic and thermodynamic stability. Contrary to **[(1Zn)$_6$·(dimPy)$_2$]**, lowering the temperature led to a broadening of the spectrum. All the resonances were assigned by 2D NMR correlation experiments (H-H COSY, NOESY and ROESY, H-C COSY, and H-Sn HMBC, see also the Experimental Section). Indeed, some similarity with the ^{1}H spectra of the multi-porphyrin systems previously described, are observed: i) the strong upfield shift of pyridyl signals, due to coordination to **1Zn**, and ii) the splitting of all the aryl-substituent resonances due to magnetic anisotropy between proton facing the inside and the outside of the cage cavity. Protons *o*/*o'*H$_{fb}$, and *m*/*m*H'$_{fb}$, respectively at 6.42, 6.30, 5.65 and 4.44 ppm, are found at higher field compared to the corresponding signals of **[(1Zn)$_6$·(dimPy)$_2$]** (found at 8.04, 7.34, 8.2 and 6.76 ppm), confirming the persisting of the coordination to the Sn-porphyrin. All the *meso*-substituents of the ***mono*PhCOOPyP** unit (even though through different donor functions) are axially coordinated to a metalloporphyrin: the combination of the porphyrin shielding cones results in an overall minor magnetic anisotropy of the system – compared to **[(1Zn)$_6$·(dimPy)$_2$]**. This is particularly evident in the aryl resonances of the **1Zn** platforms, which, compared to the ^{1}H spectrum of **[(1Zn)$_6$·(dimPy)$_2$]** are spread in a narrower chemical-shift range.

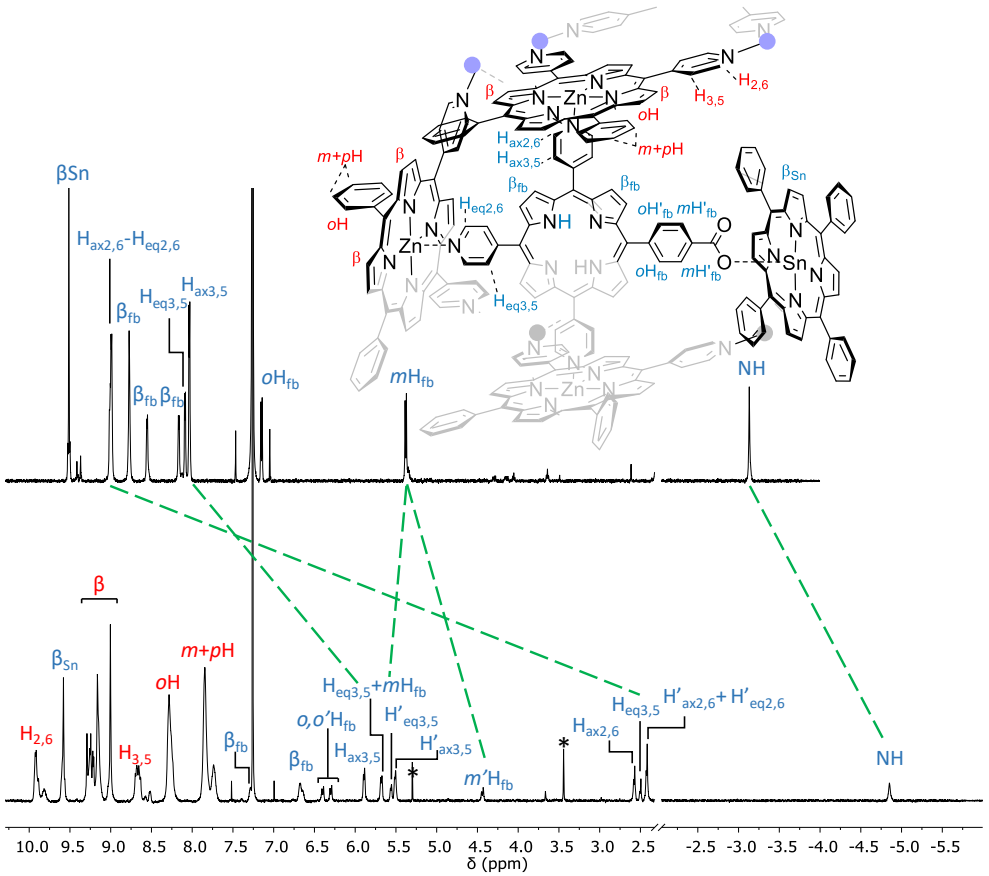

Figure 4.19. ^{1}H-NMR spectra ($CDCl_3$) of **SnTpFP(*mono*PhCOOPyP)$_2$** (top) and **[(1Zn)$_6$·(SnTpFP(*mono*PhCOOPyP)$_2$)$_2$]** (bottom). Schematic depiction of the asymmetric unit of **[(1Zn)$_6$·(SnTpFP(*mono*PhCOOPyP)$_2$)$_2$]**, with NMR labelling (fluorine atoms are omitted for clarity).

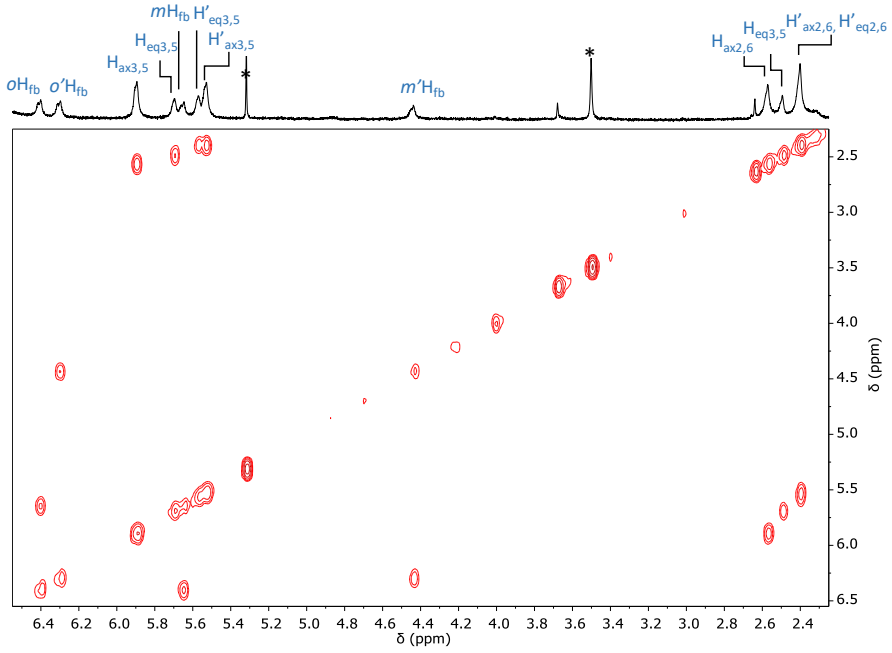

Figure 4.20. H-H COSY spectrum ($CDCl_3$) of **[(1Zn)$_6$·(SnTpFP(*mono*PhCOOPyP)$_2$)$_2$]**.

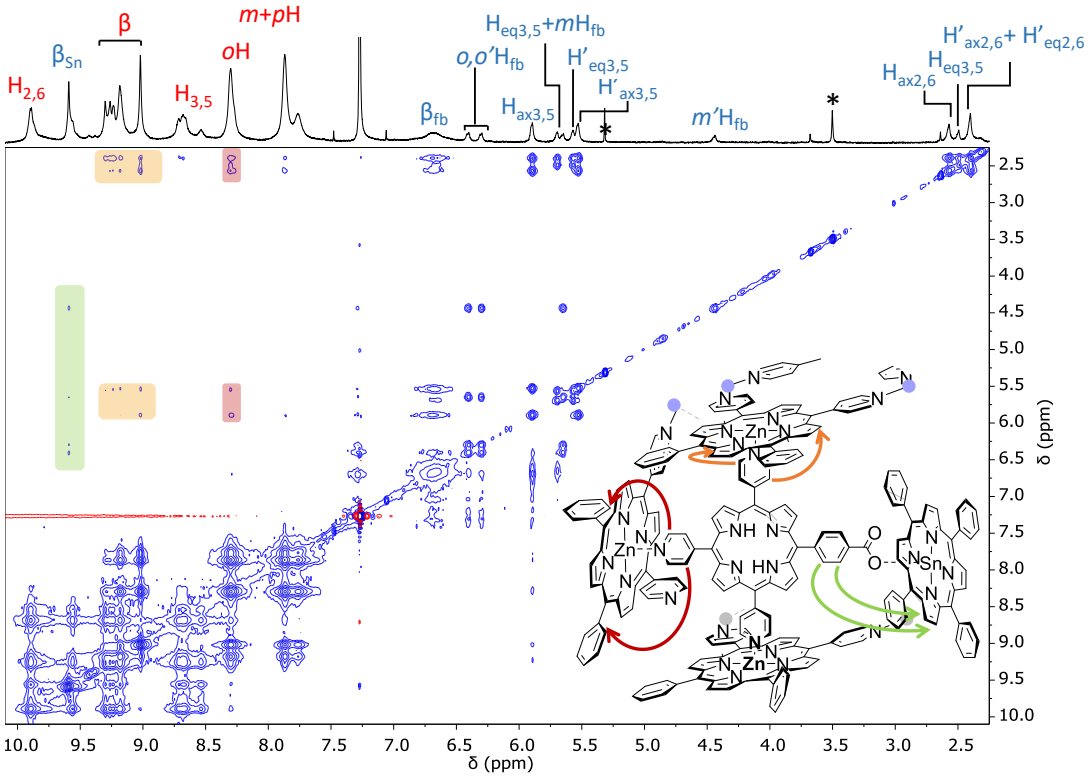

Figure 4.21. HH-NOESY spectrum ($CDCl_3$) of **[(1Zn)$_6$·(SnTpFP(*mono*PhCOOPyP)$_2$)$_2$]**.

In the HH-NOESY spectrum, intercomponent spatial correlations are also observed: in particular, cross-peaks between the benzoate resonances with the signal at 9.58 ppm (highlighted in green in Figure 4.21), allowed the individuation of the β-pyrrolic proton resonance of the Sn-porphyrin. This attribution was unambiguously confirmed by the H-Sn HMBC experiment shown in Figure 4.22, which evidenced the presence of only one ^{119}Sn resonance at –627.3 ppm correlating to the proton signal at 9.58 ppm. The tin chemical shift (a similar value of -628.1 is found for **[(1Zn)$_6$·(SnTPP(*mono*PhCOOPyP)$_2$)$_2$]**) corresponds to the δ_{Sn} value of a Sn-porphyrin with two axially coordinated benzoates (see above, Table 4.3).

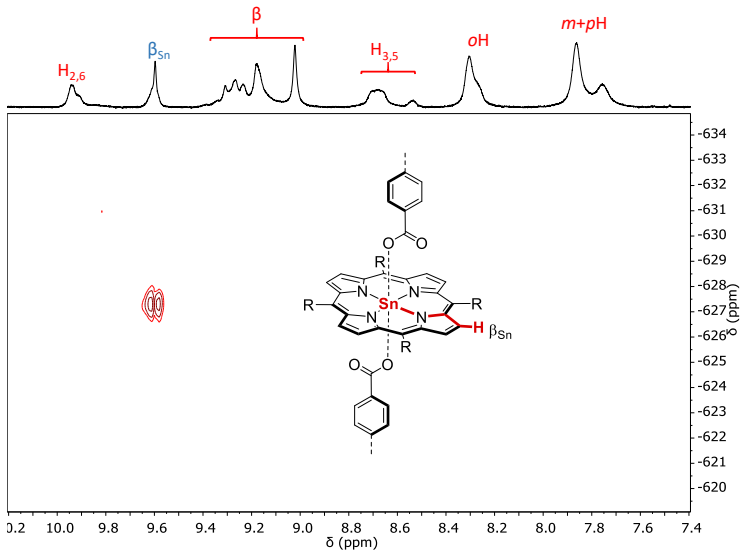

Figure 4.22. ^{1}H-^{119}Sn HMBC spectrum ($CDCl_3$) of **[(1Zn)$_6$·(SnTpFP(*mono*PhCOOPyP)$_2$)$_2$]**.

Concerning the tin-porphyrin unit, in **[(1Zn)$_6$·(SnTPP(*mono*PhCOOPyP)$_2$)$_2$]**, the sole identification of the sole β-pyrrolic singlet (by means of the H-Sn HMBC) was possible, since the phenyl resonances are inevitably overlapping and hidden below the intense **1Zn** signals. On the contrary, in **[(1Zn)$_6$·(SnTpFP(*mono*PhCOOPyP)$_2$)$_2$]**, the presence of the fluorine atoms permit to gain additional information on the connecting metalloporphyrin. The ^{19}F resonances of the *penta*-fluoro-phenyl substituents in **[(1Zn)$_6$·(SnTpFP(*mono*PhCOOPyP)$_2$)$_2$]**, compared to the free hexa-topic ligand ones, are broader and slightly up-field shifted (Figure 4.23). Indeed, the tin porphyrins are free to rotate along the axial coordination bond axis (as also indicated by the presence of only one β-pyrrolic proton resonance). However, in the assembled cage, the two Sn-porphyrins are closely located side by side: they may reciprocally sterically hinder and slow down their rotation, inducing the signal broadening. VT ^{19}F experiments are planned in order to further investigate this point.

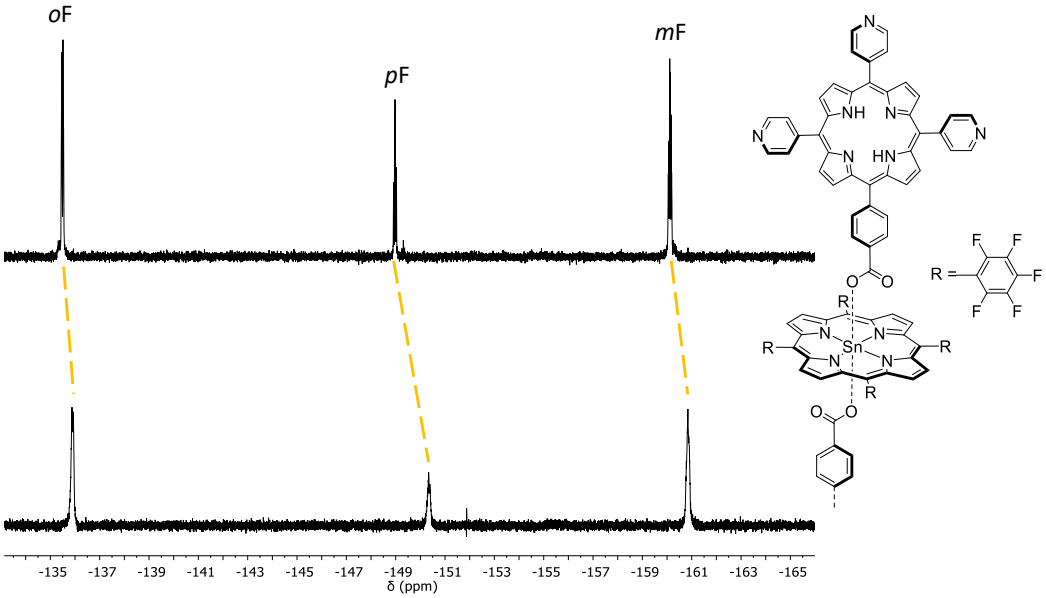

Figure 4.23. ^{19}F-NMR spectra ($CDCl_3$) of **SnTpFP(*mono*PhCOOPyP)$_2$** (top) and **[(1Zn)$_6$·(SnTpFP(*mono*PhCOOPyP)$_2$)$_2$]** (bottom).

Proton spectra recorded by progressive dilution did not show a significant change in the resonance pattern, confirming a good stability range of the adduct.

In the 2D DOSY map of **[(1Zn)$_6$·(SnTpFP(*mono*PhCOOPyP)$_2$)$_2$]** (Figure 4.24) All the resonances are found to be aligned to the same diffusion coefficient of value 2.02 x 10^{-6} cm^2s^{-1}. As expected, a similar self-diffusion coefficient was found for **[(1Zn)$_6$·(SnTPP(*mono*PhCOOPyP)$_2$)$_2$]**: the presence of phenyl groups rather than *penta*-fluoro-phenyl groups, as peripheral substituents in the tin-porphyrin unit, does not affect the overall volume of the derived assemblies.

A direct comparison with the *Dt* data collected from the DOSY analysis of **[(1Zn)$_6$·(dimPy)$_2$]** and the other assemblies is not meaningful, given the different temperatures of experimental data collections.

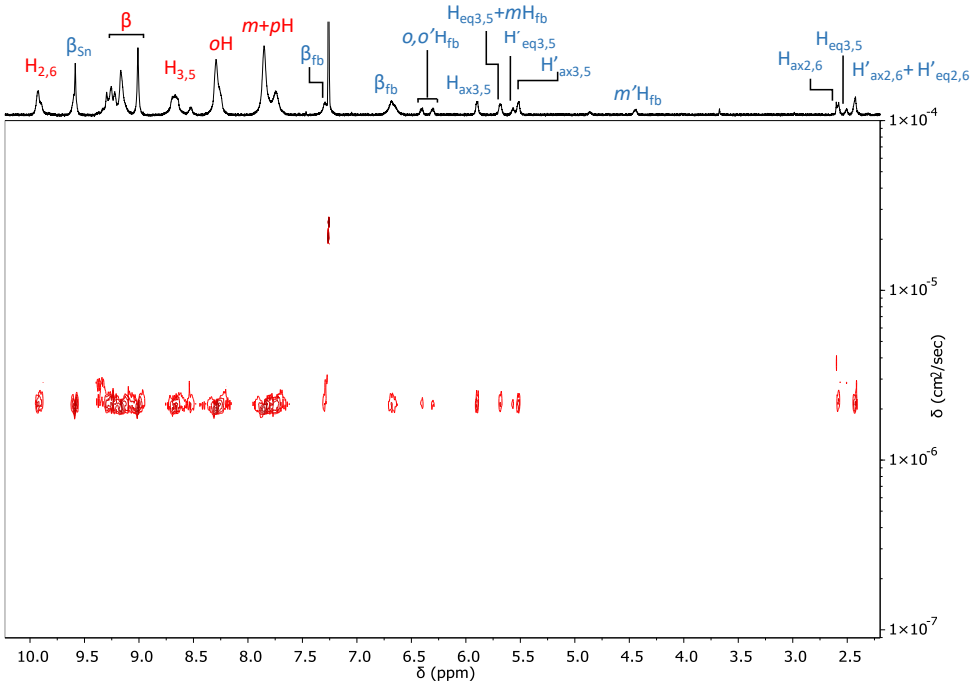

Figure 4.24. 2D ^{1}H-DOSY spectrum (Bayesian transform, $CDCl_3$) of **[(1Zn)$_6$·(SnTpFP(*mono*PhCOOPyP)$_2$)$_2$]**.

The visible absorption spectrum of **[(1Zn)$_6$·(SnTpFP(*mono*PhCOOPyP)$_2$)$_2$]**, showing maxima at 516, 565 and 607 nm, is consistent with the simultaneous presence of the three different chromophore units (the zinc-, the tin- and the freebase porphyrins), in the correct stoichiometric ratio.

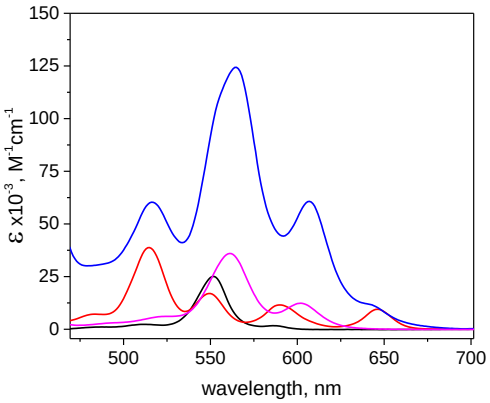

Figure 4.25. Visible absorption spectrum ($CHCl_3$) of **[(1Zn)$_6$·(SnTpFP(*mono*PhCOOPyP)$_2$)$_2$]** (blue line) in comparison with those of ***mono*PhCOOHPyP** (red line), **1Zn** (purple line) and **SnTpFP(BA)$_2$** (black line). As reference, a slight excess of pyridine was added to **1Zn**.

A one-pot reaction was performed dissolving stoichiometric quantities of the building units (**1Zn**, **SnTPP(OH)$_2$** and ***mono*PhCOOHPyP**) in $CDCl_3$, at room temperature, and monitoring the reaction over time by NMR spectroscopy (Figure 4.26). The initial ^{1}H NMR spectrum appeared rather broad and unresolved but displaying a number and position of resonances hinting the occurrence of coordinating interaction between the building units (for instance, broad coordinated pyridyl signals are observed around 2.5 and 5.6 ppm). The spectrum progressively sharpened and after 40 hours of

reaction, the same spectral pattern of the assembly **[(1Zn)$_6$·(SnTPP(*mono*PhCOOPyP)$_2$)$_2$]** was observed (see above Figure 4.18). Spectra recorded at longer reaction time showed only minimal changes. Since the formation of the Sn-carboxylate coordination bond, in virtue of the increased inertness, follows slower kinetics than the Zn-$N_{pyridyl}$ one - which is almost instantaneous - the one-pot reaction at room temperature took indeed more than one day to reach completeness.

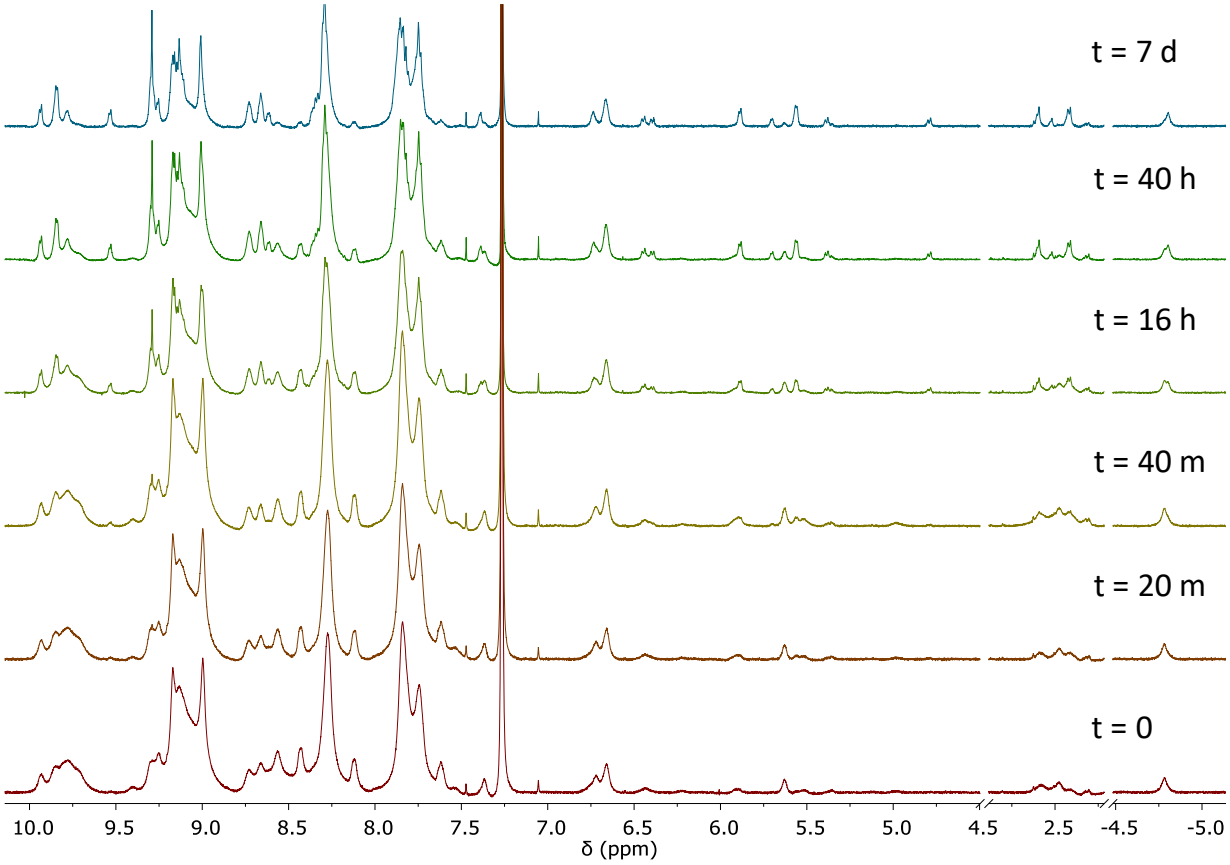

Figure 4.26. ^{1}H NMR spectra ($CDCl_3$) of a 3:2:1 mixture of **1Zn**:***mono*PhCOOHPyP**:**SnTPP(OH)$_2$** recorded at different reaction times.

4.2.5 Preliminary Photophysical Characterization of [(1Zn)$_6$·(SnP(*mono*PhCOOPyP)$_2$)$_2$].

As already described, in the assembly **[(1Zn)$_3$·(*tris*PyP)$_2$]** an efficient photoinduced energy transfer process occurs between the zinc platform and the bridging freebase. Introduction of the Sn-porphyrin unit may indeed promote additional intercomponent processes, in virtue of the well-known antenna/redox properties of this class of metalloporphyrins.[4,7,12]

View the intrinsic complexity of these multicomponent systems, composed of three different porphyrin chromophores which absorption spectra are inevitably overlapping, the detailed photophysical characterization of the supramolecular cages, resulting rather untrivial and demanding, and is yet under investigation. Nevertheless, some argumentation can be advanced.

Indeed, the supramolecular character of assemblies **[(1Zn)$_6$·(SnTPP(*mono*PhCOOPyP)$_2$)$_2$]** and **[(1Zn)$_6$·(SnTpFP(*mono*PhCOOPyP)$_2$)$_2$]**, common to other metalloporphyrin metal-mediated

derivatives, allows viable forecast of the photoinduced reactivity of the adducts, on the basis of the photophysical and electrochemical properties of the molecular building units.[2d,9,15] To simplify the photophysical studies it is useful to first understand the photophysical behavior of the separate two-component systems (i.e. **[(1Zn)$_3$·(*tris*PyP)$_2$]** and triads **SnTPP(*mono*PhCOOPyP)$_2$** and **SnTpFP(*mono*PhCOOPyP)$_2$**).

In a recent unpublished work by our group, the detailed photophysical investigation of triad systems built on freebase porphyrins axially coordinated to a tin porphyrin (via carboxylate functions) has been carried out. It was evidenced how the nature and efficiency of the photoinduced intercomponent processes occurring, can be tuned and modulated by appropriate tailoring of the substituents on both the porphyrin subunits. Among these, the photophysical characterization of two adducts, analogous to **SnTPP(*mono*PhCOOPyP)$_2$** and **SnTpFP(*mono*PhCOOPyP)$_2$**, but bearing phenyl- instead of pyridyl substituents in the freebase *meso* positions, was also performed. These systems, namely **SnTPP(*mono*PhCOOPhP)$_2$** and **SnTpFP(*mono*PhCOOPhP)$_2$** can be taken as model for **SnTPP(*mono*PhCOOPyP)$_2$** and **SnTpFP(*mono*PhCOOPyP)$_2$**, since only minor quantitative changes in the spectroscopic and photophysical behaviors of the chromophores are expected to occur as a consequence of the replacement of peripheral phenyl with pyridyl groups.[14] Without going into details, the main outstanding results will be herein pointed out.

In system **SnTPP(*mono*PhCOOPhP)$_2$** an efficient photoinduced energy transfer process occurs from the tin porphyrin excited state to the freebase one. The fluorescence spectrum, obtained upon selective excitation of the tin porphyrin (λ_{ex} = 560 nm), presents the same spectral pattern (with maxima at 650 and 660 nm) of the emission of the freebase unit (Figure 4.27, in the middle). Fluorescence excitation spectrum together with time-resolved transient spectroscopy experiments clearly indicated the occurrence of an energy transfer process as cause of the quenching (see diagram in Figure 4.27). On the contrary, upon excitation of the ***mono*PhCOOPyP** unit, no changes in the emission shape and intensity of the freebase porphyrin have been detected.

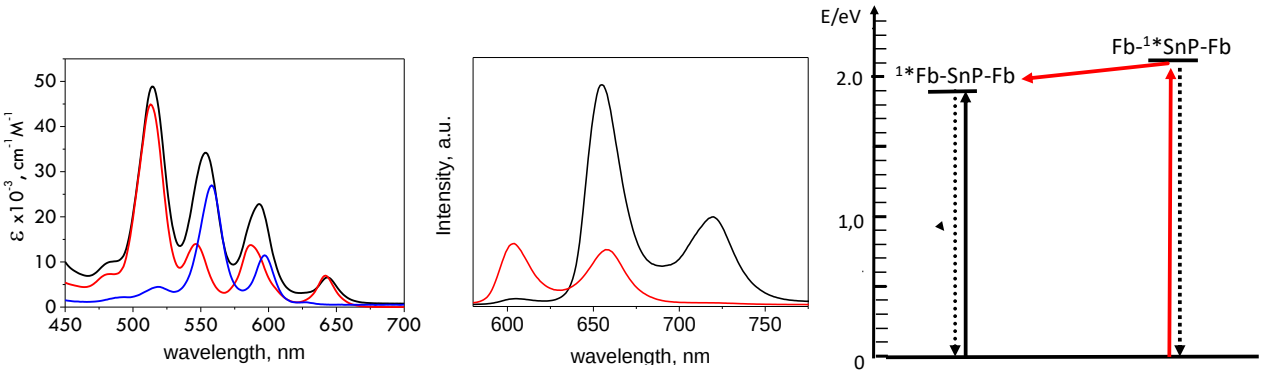

Figure 4.27. Left: absorption spectra ($CHCl_3$) of **SnTPP(*mono*PhCOOPhP)$_2$** (black), ***mono*PhCOOHPhP** (red) and **SnTPP(BA)$_2$** (blue). Middle: emission spectra ($CHCl_3$, λ_{ex} = 560 nm) of **SnTPP(*mono*PhCOOPhP)$_2$** (black) and **SnTPP(BA)$_2$** (red) recorded in the same experimental conditions. Right: energy level diagram of **SnTPP(*mono*PhCOOPhP)$_2$** with related photoinduced processes. For simplicity, triplet states are omitted and the short-hand notation ''Fb–SnP–Fb" has been employed.

A different behavior is observed in the system **SnTpFP(*mono*PhCOOPhP)$_2$**, where a strong fluorescence quenching is observed in the emission of either the Sn-porphyrin and the freebase (Figure 4.28, in the middle). The mechanistic investigation evidenced the occurrence of a photoinduced electron transfer process. The electron-withdrawing fluorine atoms significantly lower the reduction potential of the tin-porphyrin, hence the charge separated state, where the Sn-porphyrin is reduced, and the freebase oxidized, becomes energetically available from the singlet excited states of both the molecular components (Figure 4.28, on the right).

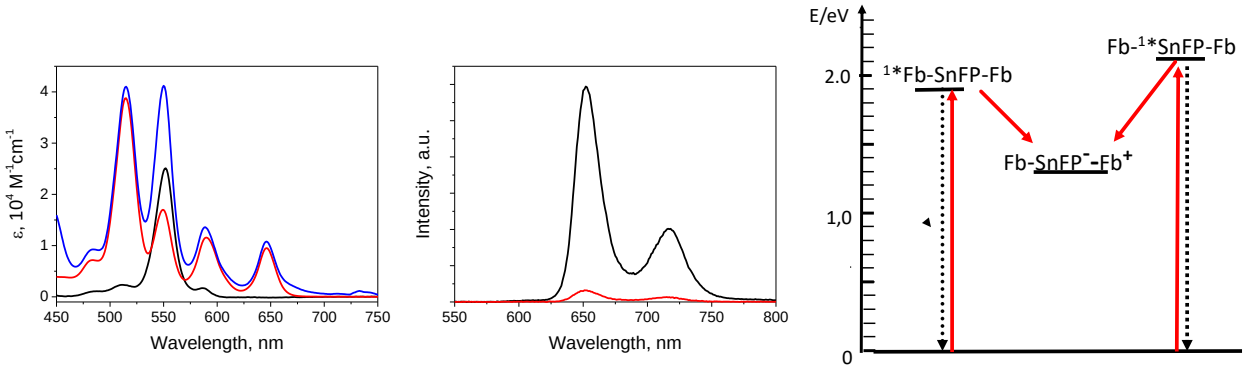

Figure 4.28. Left: absorption spectra ($CHCl_3$) of **SnTpFP(*mono*PhCOOPhP)$_2$** (black), ***mono*PhCOOHPhP** (red) and **SnTpFP(BA)$_2$** (blue). Middle: emission spectra ($CHCl_3$, λ_{ex} = 515 nm) of **SnTpFP(*mono*PhCOOPhP)$_2$** (black) and ***mono*PhCOOHPhP** (red) recorded in the same experimental conditions. Right: energy level diagram of **SnTpFP(*mono*PhCOOPhP)$_2$** with related photoinduced processes. For simplicity, triplet states are omitted and the short-hand notation ''Fb–SnFP–Fb" has been employed.

In the three-component assemblies, in addition to the photoinduced processes occurring within the two bi-component systems, intercomponent processes involving the zinc platform and the Sn porphyrin have to be considered, possibly leading to photoinduced chain energy/electron transfer processes. As anticipated, the photophysics of these systems is yet under investigation.

4.3 Conclusions

Pursuing a modular synthetic approach, a library of fascinating 3D discrete architectures, of tuned dimensions and varied number of porphyrin units, has been quantitatively obtained by simple mixing of different (metallo)porphyrin modules. By appropriate tailoring of the *meso*-4'pyridylporphyrin connectors, i.e. increasing the number of basic donor sites and/or playing on their relative disposition, larger molecular architectures become easily available. Cleverly designed molecular building units, in terms of lability/inertness and hard/soft metal-to-ligand discriminations, quantitatively self-connect by formation of mutual coordination bonds. The obtained discrete multi-porphyrin structures constitute a spatially-ordered lattice of chromophores featuring photoinduced antenna-effect and charge transfer processes.

4.5 Experimental Section

Instrumentations and experimental procedures

NMR. Mono- and bi-dimensional ^{1}H, ^{13}C and ^{119}Sn NMR spectra were recorded on a *Varian 500* while ^{19}F NMR spectra on a *Varian 400* spectrometer at room temperature, if not stated otherwise. *Varian 500* operates at 500 MHz for ^{1}H, at 125 MHz for ^{13}C, at 186 MHz for ^{119}Sn; *Varian 400* operates at 400 MHz for ^{1}H and at 376.18 for ^{19}F. ^{1}H and ^{13}C chemical shifts were referenced to the peak of residual non-deuterated solvents: δ = 7.26 ppm and 77.16 ppm for $CDCl_3$; δ = 5.32 ppm and 54 ppm for CD_2Cl_2; ^{119}Sn and ^{19}F chemical shifts were referenced, respectively, to the internal standards Me_4Sn at 0.00 ppm and $CFCl_3$ at 0.00 ppm. ^{1}H-DOSY experiments were run at controlled temperature using the Bipolar Pulse Paired Stimulated Echo sequence[16] with convection compensation of Varian VnmJ 3.2 software, δ = 2 ms, *G* = 1130 – 28261 G cm-1, and variable Δ. Processing was done with MestReNova© software.[17] Multiplicity of the signals is addressed as follows: s = singlet, d = doublet, t = triplet, q = quartet, qt = quintuplet, sx = sextet, sept = septuplet, m = multiplet, bs = broad signal.

IR. Infrared spectra were recorded on a Perkin Elmer Spectrum One Golden Gate FT/IR spectrometer in the transmission mode.

UV-Vis. Absorption spectra were recorded on an Agilent Cary 60 spectrometer in a quartz cuvette of 1 cm optic path length. Emission spectra were recorded on a Spex–Jobin Ivon Fluoromax–2 spectrofluorimeter in a quartz cuvette of 1 cm optic path length. Dilution titration experiments were performed by progressive dilution of a stock solution with noted solvent aliquots, and the concentration was check by absorption spectroscopy measurements.

Mass Spectrometry. Electrospray Ionization (ESI) measurements were performed on a Perkin Elmer APII

at 5600 eV by Dr. Fabio Hollan, Department of Chemical and Pharmaceutical Sciences, University of Trieste, Italy.

X-ray Analysis. Data collections were performed at the X-ray diffraction beamline (XRD1) of the Elettra Synchrotron of Basovizza in collaboration with Dr. Nicola Demitri (Trieste, Italy).

The crystals were dipped in an inert hydrocarbon oil (NHV Oil, Jena Biosciences) and mounted on the goniometer head with a nylon loop (average diameter 20-200 μm). Complete datasets were collected at 100 K (nitrogen stream supplied through an Oxford Cryostream 700) through the rotating crystal method.

Data were acquired using a monochromatic wavelength of 0.700 Å on a Pilatus 2M hybrid-pixel area detector. The diffraction data were indexed and integrated using XDS. Scaling have been done using CCP4-Aimless code. Complete datasets for all the molecules of interest have been obtained merging data collected from two different orientations. The structures were solved by the dual space algorithm implemented in the SHELXT code. Fourier analysis and refinement were performed by the full-matrix least-squares methods based on F^2 implemented in SHELXL-2014. The Coot program was used for modeling. Anisotropic thermal motion refinement has been used for all atoms with full

occupancy. Geometric and thermal motion parameter restrains (DFIX, DANG, SIMU or DELU) have been applied on disordered and poorly defined fragments. Hydrogen atoms were included at calculated positions with isotropic $U_{factors}$ = 1.2 U_{eq} or $U_{factors}$ = 1.5 Ueq for hydroxyl groups (Ueq being the equivalent isotropic thermal factor of the bonded non hydrogen atom). Pictures were prepared using Pymol software. Essential crystals and refinement data are reported below in Table 4.4.

Materials.

All chemicals were purchased from commercial sources and used without further purification unless stated otherwise. Deuterated solvents were purchased from Sigma-Aldrich and *Cambridge Isotope Laboratories* (CIL). 5,10,15,20-(pentafluorophenyl)porphyrin was purchased from Frontier Scientific. 5,15-(4-pyridyl)-10,20-(phenyl)porphyrin (***tris*PyP**),[18] 5-(4-carboxyphenyl)-10,15,20-(phenyl)porphyrin (***mono*PhCOOHP**),[19] 5-(4-carboxyphenyl)-10,15,20-(4-pyridyl)porphyrin (***mono*PhCOOHPyP**),[20] [*t,c,c*-$RuCl_2(CO)_2$(Zn·4'-*cis*DPyP)]$_2$ (**1Zn**),[21] **[1Zn·*trans*PyP]$_2$**,[20] *trans*-dihydroxo(5,10,15,20-phenylporphyrinato)-tin(IV) (**SnTPP(OH)$_2$**),[10] and *trans*-dihydroxo(5,10,15,20-*penta*fluorophenylporphyrinato)-tin(IV) (**SnTpFP(OH)$_2$**)[10] were synthesized and purified as described in the literature. Assemblies **[(1Zn)$_3$(*tris*PyP)$_2$]** and **[(1Zn)$_3$·*mono*PhCOOHPyP)$_2$]** were prepared following procedures reported in previous work of Thesis.

Abbreviation

TPP = 5,10,15,20-(phenyl)porphyrin

***trans*DPyP =** 5,15-(4-pyridyl)-10,20-(phenyl)porphyrin

***tris*PyP =** 5,10,15-(4-pyridyl)-20-(phenyl)porphyrin

1Zn = {*t,c,c*-$RuCl_2(CO)_2$[5,10-(4-pyridyl)-15,20-(phenyl)porphyrinato]-zinc(II)}$_2$

***mono*PhCOOMePyP =** 5-(4-carboxymethylphenyl)-10,15,20-(4-pyridyl)porphyrin

***mono*PhCOOHPyP =** 5-(4-carboxyphenyl)-10,15,20-(4-pyridyl)porphyrin

***mono*PhCOOHP =** 5-(4-carboxyphenyl)-10,15,20-(phenyl)porphyrin

HBTU = N,N,N′,N′-Tetramethyl-O-(1H-benzotriazol-1-yl)uronium hexafluorophosphate

DMAP = *N*,*N*-Dimethylpyridin-4-amine

dimPh = N,N-Bis[4-[10,15,20-(phenyl)porphyrin-5-yl]-benzoyl]-1,4-benzenebis(methylamine)

dimPy = N,N-Bis[4-[10,15,20-(4-pyridyl)porphyrin-5-yl]-benzoyl]-1,4-benzenebis(methylamine)

SnTPP(OH)$_2$ = *trans*-dihydroxo[5,10,15,20-(phenyl)porphyrinato]-tin(IV)

SnTpFP(OH)$_2$ = *trans*-dihydroxo[5,10,15,20-(pentafluorophenyl)porphyrinato]-tin(IV)

SnTPP(BA)$_2$ = *trans*-dibenzoato(5,10,15,20-*tetra*phenylporphyrinato)-tin(IV)

SnTpFP(BA)$_2$ = *trans*-dibenzoato[5,10,15,20-(pentafluorophenyl)porphyrinato]-tin(IV)

dimPh

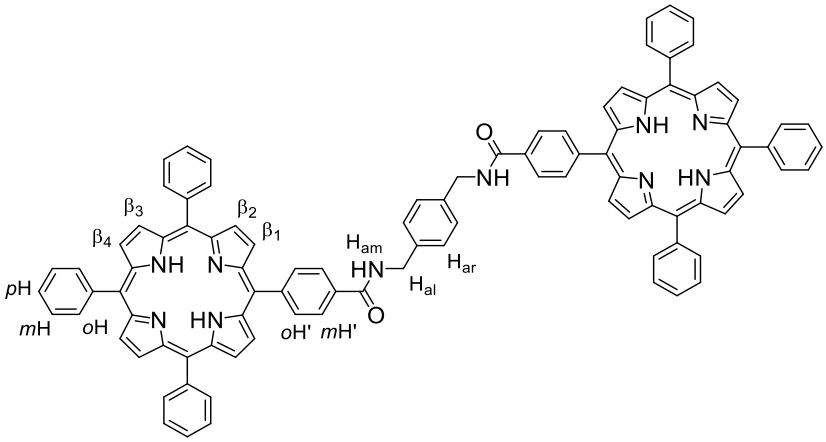

*mono*PhCOOHP (25.50 mg, 0.038 mmol) and HBTU (19.0 mg, 0.050 mmol) were dissolved in 5 mL of CH_2Cl_2 and the solution was stirred at room temperature for 30 minutes. *p*-xylylendiamine (3.00 mg, 0.022 mmol) and DMAP (5.47 mg, 0.045 mmol) were then added and the reaction mixture was stirred at room temperature, shielded by light, for 72 hours. The reaction was quenched by addition of 20 mL of distilled water. The organic phase was extracted with dichloromethane (3 × 20 mL), dried over anhydrous Na_2SO_4, filtrated and the solvent removed under reduced pressure. The residue was purified by column chromatography on silica gel and eluted with chloroform as the second band. Yield 70% (19.7 mg).

Single crystals were obtained by slow diffusion of methanol into a chloroform solution of dimPh.

^{1}H NMR (500 MHz, $CDCl_3$) δ (ppm): 8.84 (m, 12H, β_2, β_3), 8.78 (d, *J* = 4.6 Hz, 4H, β_1), 8.31 (d, *J* = 8.0 Hz, 4H, *m*H'), 8.20 (m, 16H, *o*H, *o*H'), 7.75 (m, 18H, *m*H, *p*H), 7.60 (s, 4H, H_{ar}), 6.76 (t, *J* =5.2 Hz, 4H, H_{am}), 4.89 (d, *J* = 5.6 Hz, 4H, H_{al}), -2.79 (s, 4H, NH).

^{13}C NMR (125 MHz, $CDCl_3$, from HSQC) δ (ppm): 134.79 (C'*m*), 134.45 (C'*o*), 127.70 (C*p*), 126.64 (C*m*), 125.30 (C*o*), 128.63 (C_{ar}), 44.05 (C_{al}).

ESI-MS: calculated for $C_{98}H_{69}N_{10}O_2$ ($M+H^+$) 1417.55, found 776.4.

UV-vis ($CHCl_3$): λ_{max} (ε, $M^{-1}cm^{-1}$) = 428, 516 (33 513), 550, 590, 646 nm.

IR (KBr, selected bands): ŭ = 3430(ν_{N-H} amide), 1655 cm^{-1} ($\nu_{C=O}$).

Table 4.4. Crystallographic data and refinement details for dimPh.

	dimPh
Chemical Formula	$C_{98}H_{68}N_{10}O_2 \cdot CH_4O$
Molecular Formula	$C_{198}H_{144}N_{20}O_6$
Molecular weight (Da)	1449.67
Temperature (K)	100(2)
Wavelength (Å)	0.700
Crystal system	Triclino
Space Group	*P* -1

a (Å)	11.830(2)
b (Å)	13.420(3)
c (Å)	24.801(5)
α (°)	87.19(3)
β (°)	82.70(3)
γ (°)	70.65(3)
V (Å^3)	3685(2)
Z	2
Density (calculated)	1.307 g·cm^{-3}
F(000)	1520
Absorption coefficient	0.077 mm^{-1}
θ min,max (°)	0.8, 24.8
Resolution (Å)	0.82
Reflection collected	53303
Independent reflection	13165 [R(int) = 0.0952]
Refl. Obs. [Fo>4σ(Fo)]	8198
I/σ(I) (all data)	6.54
I/σ(I) (max resltn)	2.09
Completeness (all data)	0.98
Completeness (max resltn)	0.96
Rmerge (all data)	0.103
Rmerge (max resltn,)	0.449
Data multiplicity (all data)	3.6
Data multiplicity (max	3.4
Data/restraints/parameters	13615/0/905
Goof	1.077
R_1[a] [I>2.0σ(I)], wR_2[a]	0.1055, 0.2567
R_1[a] (all data), wR_2[a] (all data)	0.1607, 0.2868

[a] $R_1 = \Sigma||Fo|-|Fc||/\Sigma|Fo|$, $wR_2 = \{\Sigma[w(Fo^2 - Fc^2)^2]/\Sigma[w(Fo^2)^2]\}^{½}$

dimPy

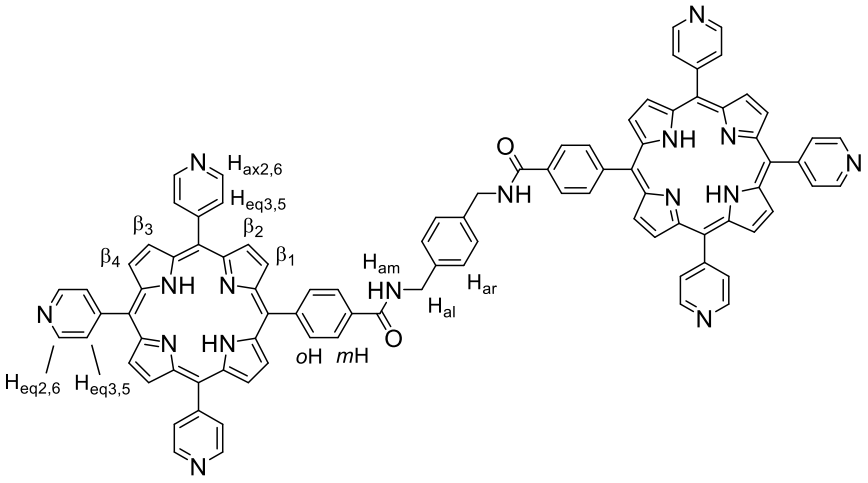

***mono*PhCOOHPyP** (25.00 mg, 0.039 mmol) and HBTU (16.12 mg, 0.042 mmol) were dissolved in 10 mL of dimethylformamide and the solution was stirred at room temperature for 30 minutes. *p*-xylylendiamine (2.31 mg, 0.017 mmol) and DMAP (4.6 mg, 0.037 mmol) were then added and the reaction mixture was stirred at 60°C, shielded by light, for 48 hours. The reaction was quenched by addition of 20 mL of distilled water leading to the formation of a purple precipitate, that was filtered, washed with distilled water and dried under *vacuo*. The residue was purified by column chromatography on silica gel and eluted with $CHCl_3$/EtOH 85:15 as the second band. Yield 65% (17.8 mg).

^{1}H NMR (500 MHz, $CDCl_3$) δ (ppm): 9.00 (d, *J* = 5.7 Hz, 4H, $H_{ax2,6}$), 8.97 (d, *J* = 5.4 Hz, 8H, $H_{eq2,6}$), 8.82 (br, 16H, $\beta_{1\text{-}4}$), 8.27 (d, *J* = 8.1 Hz, 4H, *m*H), 8.23 (d, *J* = 8.1 Hz, 4H, *o*H), 8.15 (m, 12H, $H_{ax3,5}$, $H_{eq3,5}$), 7.56 (s, 4H, H_{ar}), 7.37 (t, *J* = 5.6 Hz, 2H, H_{am}), 4.84 (d, *J* = 5.0 Hz, 4H, H_{al}), -2.84 (s, 4H, NH).

^{13}C NMR (125 MHz, $CDCl_3$, from HSQC) δ (ppm): 148.00 ($C_{ax2,6}$, $C_{eq2,6}$), 135.59 (C*m*), 129.39 ($C_{ax3,5}$, $C_{eq3,5}$), 128.40 (C_{ar}), 125.56 (C*o*), 43.85 (C_{al}).

ESI-MS: calculated for $C_{92}H_{63}N_{16}O_2$ ($M+H^+$) 1423.52, found 776.4.

Uv-Vis (CH_3OH 10%/$CHCl_3$) λ_{max} (ε, $M^{-1}cm^{-1}$) = 419, 514 (28672), 547, 588, 643 nm.

IR (KBr, selected bands): ŭ = 3430 ($\nu_{N\text{-}H}$ amide), 1655 cm^{-1} ($\nu_{C=O}$).

[(1Zn)$_3$(*tris*PyP)$_2$]

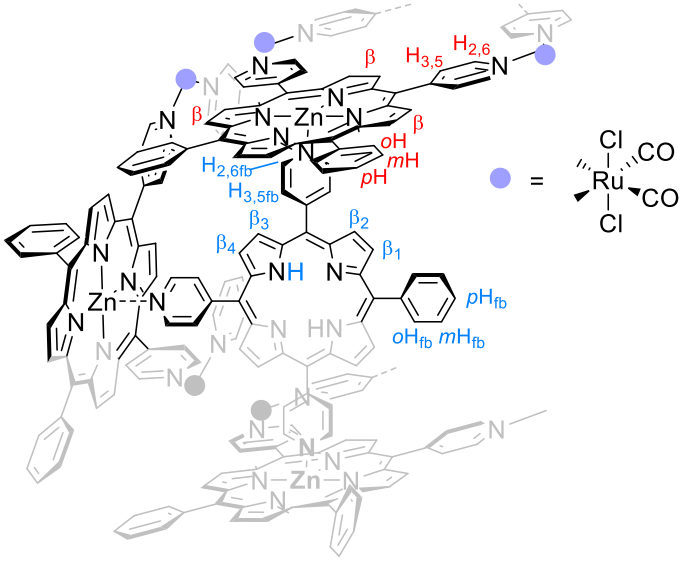

1Zn (8.5 mg, 0.0045 mmol) were dissolved in 10 mL of $CHCl_3$ and ***tris*PyP** (2 mg, 0.003 mmol) were then added. The homogeneous system was kept under stirring at room temperature for fifteen minutes. Diffusion of *n*-hexane over the deep red solution induced the precipitation of the pure product as a purple microcrystalline solid that was collected by filtration, washed with n-hexane, and vacuum-dried. Yield: quantitative.

^{1}H NMR (500 MHz, $CDCl_3$) δ (ppm): 10.04 – 9.45 (m, 24H, $H_{2,6}$), 9.39 – 8.87 (m, 48H, β), 8.80 – 8.39 (m, 24H, $H_{3,5}$), 8.38 – 8.17 (m, 24H, *o*H), 8.06 (s, 4H, β_4), 7.94 – 7.65 (m, 36H, *m*+*p*H), 7.51 (bs, 4H, *o*H_{fb}), 7.37 (bs, 6H, *m*+*p*H_{fb}), 7.01 (bs, 4H, β_3), 6.81 – 6.63 (m, 8H, β_1, β_2), 5.74 (bs, 12H, $H_{3,5fb}$), 2.52 (bs, 12H, $H_{2,6fb}$), -4.56 (s, 4H, NH).

IR (KBr, selected bands): ŭ = 2065, 1999 cm^{-1} ($\nu_{C=O}$ Ru).

Uv-Vis (CH_2Cl_2) λ_{max} = 425, 552, 590 nm.

[(1Zn)$_6$·(dimPy)$_2$]

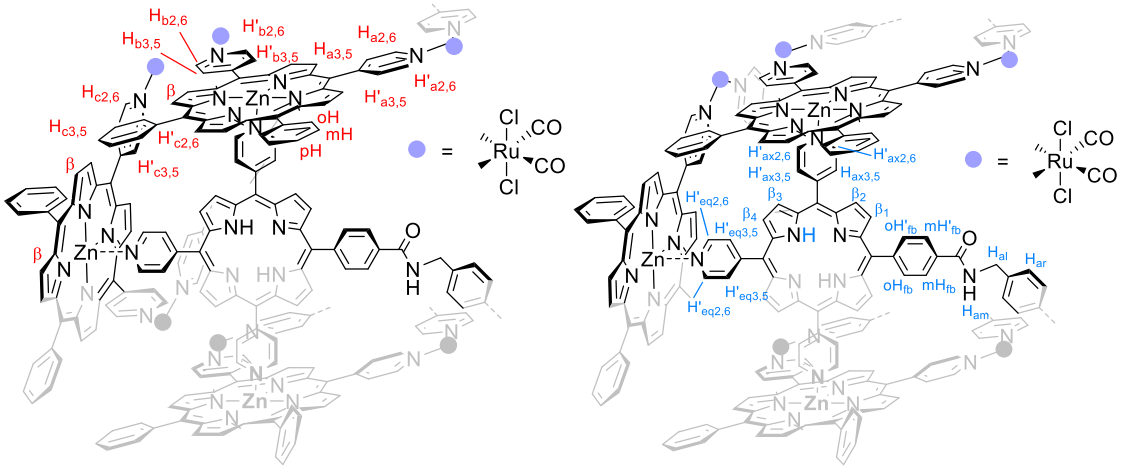

The same synthetic procedure described for **[(1Zn)$_3$(*tris*PyP)$_2$]** was followed starting from 16.0 mg of **1Zn** (8.5 µmol) and 4.1 mg of **dimPy** (2.8 µmol). Yield: 19 mg (95%).

^{1}H NMR (500 MHz, $CDCl_3$, -10°C) δ (ppm): 9.81 (d, *J* = 5.0 Hz, 8H, H'$_{a2,6}$), 9.77 (d, *J* = 5.5 Hz, 8H, H$_{c2,6}$), 9.74 – 9.66 (m, 16H, H$_{a2,6}$ + H$_{b2,6}$), 9.53 (bs, 8H, H'$_{c2,6}$), 9.38 (bs, 8H, H'$_{b2,6}$), 9.30 – 8.90 (m, 72H, β), 8.71 (bs, 8H, H$_{a3,5}$), 8.67 (d, *J* = 4.4 Hz, 8H, H$_{b3,5}$), 8.64 (d, *J* = 5.0 Hz, 8H, H'$_{a3,5}$), 8.59 (d, *J* = 4.8 Hz, 8H, H$_{c3,5}$), 8.50 (bs, 8H, H'$_{c3,5}$), 8.40 (d, *J* = 4.4 Hz, 8H, H'$_{b3,5}$), 8.39 – 8.13 (m, 48H, *o*H), 7.91 – 7.64 (m, 72H, *m*+*p*H), 8.20 (bs, 4H, *m*H$_{fb}$), 8.04 (bs, 12H, β$_1$, *o*H$_{fb}$), 7.40 (s, 8H: H$_{ar}$), 7.34 (d, *J* = 7.9 Hz, 4H, *o*H'$_{fb}$), 7 – 6.78 (bs, β$_2$, β$_3$), 6.76 (d, *J* = 7.6 Hz, 4H, *m*H'$_{fb}$), 6.71 (bs, β$_4$), 6.63 (bs, 4H, H$_{am}$), 6.13 (d, *J* = 4.3 Hz, 4H, H$_{eq3,5}$), 5.84 (d, *J* = 5.6 Hz, 8H, H$_{ax3,5}$), 5.78 (d, *J* = 5.4 Hz, 8H, H'$_{ax3,5}$), 5.18 (d, *J* = 4.0 Hz 4H, H'$_{eq3,5}$), 4.72 (bs, 8H, H$_{al}$), 2.7 – 2.6 (m, 12H, H$_{ax2,6}$, H$_{eq2,6}$), 2.36 (d, *J* = 5.2 Hz, 8H, H$_{ax2,6}$), 2.22 (d, *J* = 4.9 Hz, 4H, H'$_{eq2,6}$), -4.66 (s, 8H, NH).

^{13}C NMR (125 MHz, $CDCl_3$, -10°C, from HSQC) δ (ppm): 150.70, 150.61, 150.75, 150.35, 149.86, 141.20, 140.48, 140.41, 134.89, 134.72, 134.68, 134.13, 134.03, 133.75, 133.16, 132.98, 132.97, 132.90, 132.86, 132.75, 132.56, 132.52, 132.51, 132.48, 132.17, 131.53, 131.44, 131.23, 130.80, 130.57, 131.10, 129.33, 128.04, 127.92, 127.87, 127.86, 127.57, 127.30, 126.95, 126.89, 126.88, 126.82, 126.65, 126.53, 126.38.

Uv-Vis ($CHCl_3$) λ$_{max}$ (ε, M^{-1}cm^{-1}) **=** 517, 566 (220 000), 607.

IR (KBr, selected bands): ŭ = 2066, 2001 (ν$_{C=O}$ Ru), 1611 (ν$_{C=O}$ amide) cm^{-1}.

Tin adducts.

The preparation of the Sn(IV) porphyrin adducts were performed according to this general procedure: a concentrated $CHCl_3$ solution of 1 eq. of each tin porphyrin with 2 eq. of the axial ligand was refluxed for 6 hours in presence of Na_2SO_4 anhydrous. The solvent was partially removed under reduced pressure. The slow diffusion of *n*-hexane over the $CHCl_3$ solution induced the precipitation of the pure product as a violet powder that was collected by filtration, washed with *n*-hexane, and vacuum-dried. Yield: 80-90%

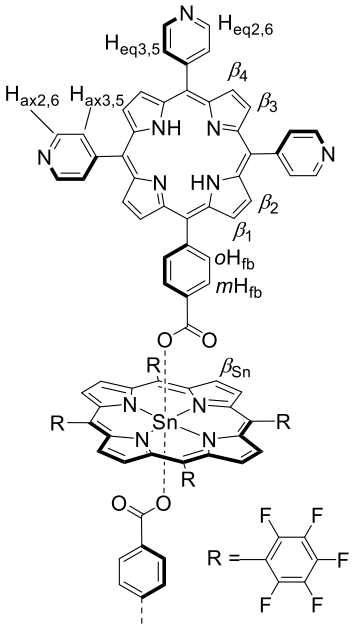

SnTpFP(*mono*PhCOOPyP)$_2$

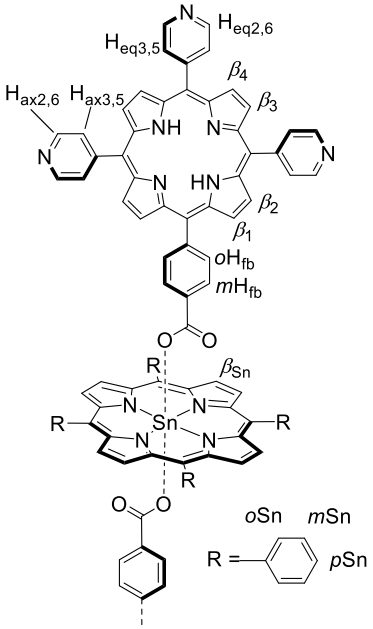

SnTPP(*mono*PhCOOPyP)$_2$

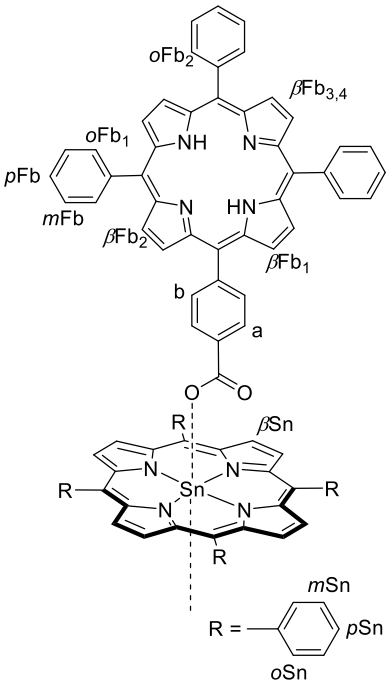

SnTPP(*mono*PhCOOPhP)$_2$

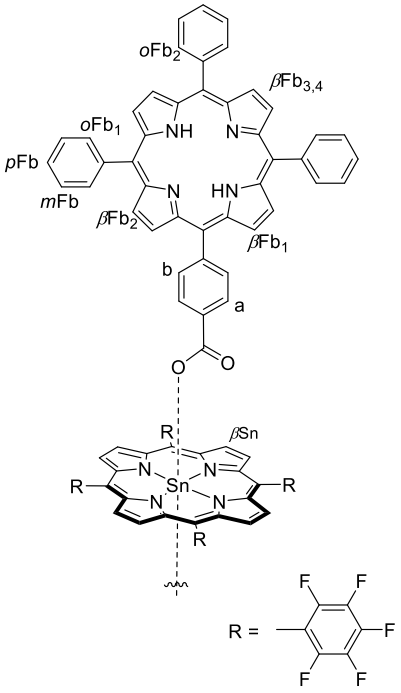

SnTpFP(*mono*PhCOOPhP)$_2$

SnTpFP(*mono*PhCOOPyP)$_2$

^{1}H NMR (500 MHz, $CDCl_3$) δ (ppm): 9.51 (s, 8H, β_{Sn}, $^4J(^{119}SnH)$ = 14.2 Hz), 9.04 – 8.94 (m, 12H, $H_{ax2,6}$, $H_{eq2,6}$), 8.77 (s, 8H, β_3, β_4), 8.55 (d, *J* = 4.8 Hz, 4H, β_2), 8.16 (d, *J* = 4.8 Hz, 4H, β_1), 8.09 (d, *J* = 4.9 Hz, 4H, $H_{eq3,5}$), 8.06 – 8.00 (d, *J* = 5.4 Hz, 8H, $H_{ax3,5}$), 7.15 (d, *J* = 8.0 Hz, 4H, *o*H_{fb}), 5.38 (d, *J* = 7.9 Hz, 4H, *m*H_{fb}), -3.13 (s, 4H, NH).

^{13}C NMR (125 MHz, $CDCl_3$, -10°C, from HSQC) δ (ppm): 148.31, 133.26, 132.64, 129.50, 129.29, 129.22, 125.64.

^{19}F NMR (376.18 MHz, $CDCl_3$) δ (ppm): -135.51 (dd, *J* = 21.6, 5.8 Hz, 8F, *o*F), -148.99 (t, *J* = 20.9 Hz, 4F, *p*F), -160.13 (dt, *J* = 21.1, 6.1 Hz, 8F, *m*F).

^{119}Sn NMR (186 MHz, $CDCl_3$, from HMBC) δ (ppm): -628.18.

Uv-Vis ($CHCl_3$) λ_{max} (ε, $M^{-1}cm^{-1}$) = 515 (41 000), 550 (41 200), 589, 646.

IR (KBr, selected bands): ŭ = 1643 ($\nu_{C=O\,ester}$)

SnTPP(*mono*PhCOOPyP)$_2$

^{1}H NMR (500 MHz, $CDCl_3$) δ (ppm): 9.38 (s, 8H, β_{Sn}, $^4J(^{119}SnH)$ = 15.1 Hz), 9.05 – 8.97 (m, 12H, $H_{ax2,6}$, $H_{eq2,6}$), 8.79 (s, 8H, β_3, β_4), 8.58 (d, *J* = 4.8 Hz, 4H, β_2), 8.44 (dd, *J* = 7.9, 1.2 Hz, 8H, *o*Sn), 8.25 (d, *J* = 4.8 Hz, 4H, β_1), 8.10 (dd, *J* = 4.4, 1.6 Hz, 4H, $H_{eq3,5}$), 8.08 (dd, *J* = 4.2, 1.5 Hz, 8H, $H_{ax3,5}$), 7.89 – 7.79 (m, 12H, *m*Sn, *p*Sn), 7.22 (d, *J* = 8.1 Hz, 4H, *o*H_{fb}), 5.37 (d, J = 8.1 Hz, 4H, *m*H_{fb}), -3.10 (s, 4H, NH).

^{13}C NMR (125 MHz, $CDCl_3$, -10°C, from HSQC) δ (ppm): 148.32, 134.85, 133.01, 132.85, 132.80, 129.29, 129.25, 128.58, 127.12, 125.68.

^{119}Sn NMR (186 MHz, $CDCl_3$, from HMBC) δ (ppm): -628.5.

Uv-Vis ($CHCl_3$) λ_{max} (ε, $M^{-1}cm^{-1}$) = 514 (48 880), 553 (34 200), 593, 643 nm.

IR (KBr, selected bands): ŭ = 1645 ($\nu_{C=O\,ester}$)

SnTpFP(*mono*PhCOOPhP)$_2$

^{1}H NMR (500 MHz, $CDCl_3$) δ (ppm): 9.50 (s, 8H, βSn, $^4J(^{119}SnH)$ = 13.9 Hz), 8.76 (d, *J* = 3.5 Hz, 8H, β$Fb_{3,4}$), 8.57 (d, *J* = 4.6 Hz, 4H, βFb_2), 8.14 (d, *J* = 6.7 Hz, 4H, *o*Fb_2), 8.09 (m, 10H, *o*Fb_{1+}βFb_1), 7.78 – 7.64 (m, 18H, *m*Fb_+*p*Fb), 7.16 (d, *J* = 8.2 Hz, 4H, b), 5.35 (d, *J* = 8.2 Hz, 4H, a), -3.02 (s, 4H, NH).

^{13}C NMR (125 MHz, $CDCl_3$, -10°C, from HSQC) δ (ppm): 134.28 (C_{oFb2}), 134.23 (C_{oFb1}), 132.95 ($C_{\beta Sn}$), 132.51 (C_b), 127.41 (C_{pFb}), 126.43 (C_{mFb}), 125.30 (C_a).

^{19}F NMR (376.18 MHz, $CDCl_3$) δ (ppm): -135.32 (d, *J* = 16.1 Hz, 8F, *o*F), -149.31 (t, *J* = 20.8 Hz, 4F, *p*F), -160.19 (t, *J* = 17.8 Hz, 8F, *m*F).

^{119}Sn NMR (186 MHz, $CDCl_3$, from HMBC) δ (ppm): -628.18.

IR (KBr, selected bands): ŭ = 1643 ($\nu_{C=O ester}$).

SnTPP(*mono*PhCOOPhP)$_2$

^{1}H NMR (500 MHz, $CDCl_3$) δ (ppm): 9.37 (s, 8H, βSn, $^{4}J(^{119}SnH)$ = 15.0 Hz), 8.77 (s, 8H, $\beta Fb_{3,4}$), 8.61 (d, *J* = 4.5 Hz, 4H, βFb_2), 8.43 (d, *J* = 6.2 Hz, 8H, *o*Sn), 8.19 (d, *J* = 4.5 Hz, 4H, βFb_1), 8.16 (d, *J* = 6.9 Hz, 8H, *o*Fb_2), 8.11 (d, *J* = 6.9 Hz, 8H, *o*Fb_1), 7.87 – 7.78 (m, 12H, *m*Sn+*p*Sn), 7.78 – 7.64 (m, 18H, *m*Fb+*p*Fb), 7.24 (d, *J* = 8.0 Hz, 4H, b), 5.32 (d, *J* = 8.0 Hz, 4H, a), -2.98 (s, 4H, NH).

^{13}C NMR (125 MHz, $CDCl_3$, -10°C, from HSQC) δ (ppm): 134.80 (C_{oSn}), 134.44 (C_{oFb2}), 134.35 (C_{oFb1}), 132.88 ($C_{\beta Sn}$), 132.70 (C_b), 127.94 (C_{pSn}), 127.52 (C_{pFb}), 127.12 (C_{mSn}), 126.58 (C_{mFb}), 125.32 (C_a).

^{119}Sn NMR (186 MHz, $CDCl_3$, from HMBC) δ (ppm): -628.18.

IR (KBr, selected bands): ŭ = 1645 ($\nu_{C=O ester}$).

[(1Zn)$_6$·(SnTPP)$_2$·(*mono*PhCOOPyP)$_4$]

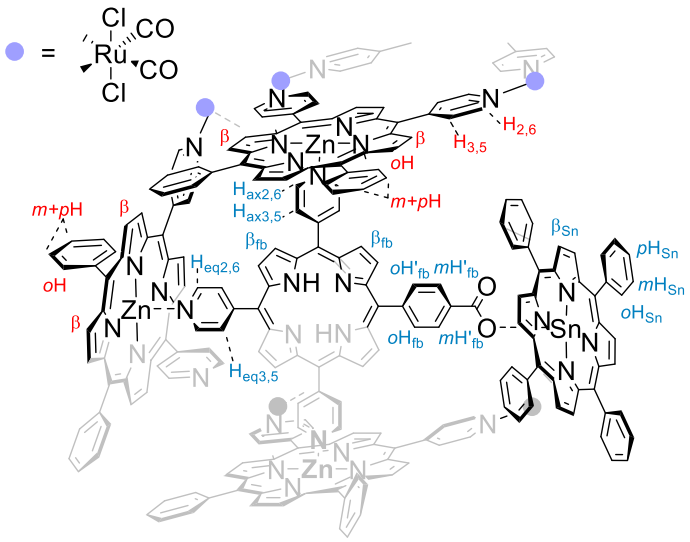

SnTPP(*mono*PhCOOPyP)$_2$ (2.84 mg, 1.38 µmol) and **1Zn** (7.8 mg, 4.14 µmol) were dissolved in 5 mL of chloroform and stirred at room temperature for 15 minutes. Addition of n-hexane induced precipitation of a dark blue precipitate that was filtered and dried under vacuum. Yield: 10.1 (95%).

^{1}H NMR (500 MHz, $CDCl_3$) δ (ppm): 9.93 (d, *J* = 6.0 Hz, 8H, $H_{2,6}$), 9.90 – 9.72 (m, 32H, $H_{2,6}$), 9.53 (d, *J* = 5.7 Hz, 8H, $H_{2,6}$), 9.33 – 8.95 (m, 112 H, β, β_{Sn}), 8.77 – 8.57 (m, 40H, $H_{3,5}$), 8.38 – 8.20 (m, *ca.* H, $H_{3,5}$, *o*H, *o*H_{Sn}), 7.95 – 7.65 (m, *ca.* 16H, *m*H, *p*H, *m*H_{Sn}, *p*H_{Sn}, β_{fb}), 7.37 (bs, 8H, β_{fb}), 6.73 (bs, 8H, β_{fb}), 6.66 (bs, 16H, β_{fb}), 6.44 (d, *J* = 7.9 Hz, 4H, *o*H_{fb}), 6.39 (d, *J* = 7.9 Hz, , 4H, *o*H'$_{fb}$), 5.88 (d, *J* = 6.1 Hz, 8H, $H_{ax3,5}$), 5.69 (s, 4H, $H_{eq3,5}$), 5.55 (d, *J* = 5.9 Hz, 12H, H'$_{ax3,5}$, H'$_{eq3,5}$), 5.38 (d, *J* = 8.0 Hz, 4H, *m*H_{fb}), 4.78 (d, *J* = 7.9 Hz, 4H, *m*H'$_{fb}$), 2.58 (s, 8H, $H_{ax2,6}$), 2.51 (s, 4H, $H_{eq2,6}$), 2.41 (d, *J* = 7.3 Hz, 12H, H'$_{ax2,6}$, H'$_{eq2,6}$), -4.8 (bs, 8H, NH).

^{13}C NMR (125 MHz, $CDCl_3$, -10°C, from HSQC) δ (ppm): 150.37, 150.39, 150.47, 150.00, 140.99, 140.78, 140.44, 134.72, 133.80, 132.81, 132.71, 132.69, 132.63, 132.52, 132.35, 131.95, 131.90, 131.50, 132.48, 132.32, 130.92, 130.85, 130.73, 130.70, 128.31, 127.77, 127.30, 127.27, 127.04, 126.97, 126.73, 126.28, 125.37.

^{119}Sn NMR (186 MHz, $CDCl_3$, from HMBC) δ (ppm): -628.5.

IR (KBr, selected bands): ŭ = 2067, 2003 ($\nu_{C=O}$ Ru), 1611 ($\nu_{C=O\,ester}$),

[(1Zn)$_6$·(SnTpFP)$_2$·(*mono*PhCOOPyP)$_4$]

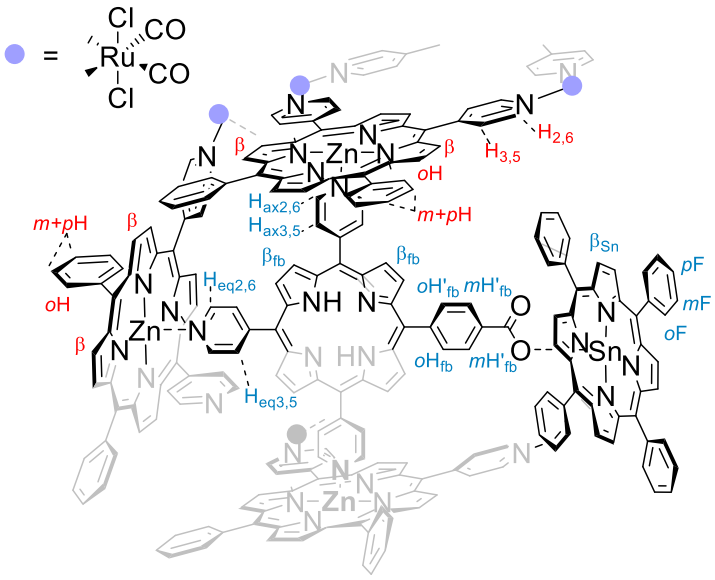

The same synthetic procedure described for **[(1Zn)$_6$·(SnTPP)$_2$·(*mono*PhCOOPyP)$_4$]** was followed starting from 19.7 mg of **1Zn** (10.5 µmol) and 8.4 mg of **SnTpFP(*mono*PhCOOPyP)$_2$** (3.5 µmol). Yield: 25 mg (90%).

^{1}H NMR (500 MHz, $CDCl_3$) δ (ppm): 9.98 – 9.74 (m, 40H, $H_{2,6}$), 9.58 (bs, 24H, $H_{2,6}$, β_{Sn}), 9.35 – 8.93 (m, *ca.* 100H, β), 8.78 – 8.48 (m, 48H), 8.28 (bs, *ca.* 48H *o*H), 7.95 – 7.61(m, ca. 80H, *m*H, *p*H, β_{fb}), 7.29 (bs, β_{fb}), 6.81 – 6.55 (bs, 16H, β_{fb}), 6.40 (d, *J* = 8.2 Hz, 4H, *o*H_{fb}), 6.30 (d, *J* = 8.1 Hz, 4H, *o*H'_{fb}), 5.89 (d, *J* = 5.9 Hz, 8H, $H_{ax3,5}$), 5.68 (d, *J* = 6.5 Hz, 8H, $H_{eq3,5}$, *m*H_{fb}), 5.56 (d, *J* = 5.0 Hz, 4H, $H'_{eq3,5}$), 5.51 (bs, *J* = 5.1 Hz, 8H, $H'_{ax3,5}$), 4.44 (d, *J* = 8.0 Hz, 4H, *m*H'_{fb}), 2.58 (d, *J* = 5.6 Hz, 8H, $H_{ax2,6}$), 2.49 (bs, 4H, $H_{eq2,6}$), 2.42 (d, *J* = 5.5 Hz, 12H, $H'_{eq2,6}$, $H'_{ax2,6}$), -4.85 (bs, NH).

^{13}C NMR (125 MHz, $CDCl_3$, -10°C, from HSQC) δ (ppm):

^{19}F NMR (376 MHz, $CDCl_3$) δ (ppm): -135.90 (bd, *J* = 23.3 Hz, 8F, *o*F), -150.34 (bs, 4F, *p*F), -160.85 (bs, 8F, *m*F).

^{119}Sn NMR (186 MHz, $CDCl_3$, from HMBC) δ (ppm): -628.18.

Uv-Vis ($CHCl_3$) λ_{max} (ε, $M^{-1}cm^{-1}$) = 516, 565, 607 nm.

IR (KBr, selected bands): ŭ = 2066, 2001 ($\nu_{C=O}$ Ru), 1643 ($\nu_{C=O}$ ester).

4.6 References

[1] Giacomo Cecot, Master Thesis A.A. 2013-2014.

[2] (a) J. C. Hawley, N. Bampos, J.K.M. Sanders, *Chem. – Eur. J.* 2003, *9*, 5211; (b) D. P. Arnold, A. Blok, *Coord. Chem. Rev.* 2004, *248*, 299

[3] G. A. Metselaar, P. Ballester, J. de Mendoza, *New J. Chem.,* 2009, *33*, 777.

[4] a) V.S. Shetti, Y. Pareek, M. Ravikanth, *Coord. Chem. Rev.* 2012, *256*, 2816; b) T. Honda, T. Nakanishi, K. Ohkubo, T. Kojima and S. Fukuzumi, *J. Phys. Chem. C*, 2010, *114*, 14290; c) G. Landrou, A.A. Panagiotopoulos, K. Ladomenou, A.G. Coutsolelos *J. Porphyrins Phthalocyanines* 2016, *20,* 1; d) M. Natali, A. Amati, N. Demitri, E. Iengo, *Chem. Commun.* 2018, *54*, 6148.

[5] Y. Ishikawa, N. Yamakawa, T. Uno, Bioorg. Med. Chem. 2007, *15*, 5230.

[6] C. Spagnul, R. Alberto, G. Gasser, S. Ferrari, V. Pierroz, A. Bergamo, T. Gianferrara, E. Alessio, *J. Inorg. Biochem.* 2013, *122*, 57.

[7] P. Cavigli, G. Balducci, E. Zangrando, N. Demitri, A. Amati, M.T. Indelli, E. Iengo, *Inorg. Chim. Acta* 2016, *439*, 61.

[8] G.S. Wilson, H.L. Anderson, *Chem. Commun.* 1999, 1539; P.N. Taylor, H.L. Anderson, *J. Am. Chem. Soc.* 1999, *121,* 11538

[9] L. Avram, Y. Cohen, *Chem. Soc. Rev.* 2015, *44*, 586.

[10] A. Macchioni, G. Ciancaleoni, C. Zuccaccia, D. Zuccaccia, *Chem. Soc. Rev.* 2008, *37* , 479.

[11] A. Prodi, C. Chiorboli, F. Scandola, E. Iengo, E. Alessio, *ChemPhysChem* 2006, *7*, 1514.

[12] a) B.G. Maiya, N. Bampos, A.A. Kumar, N. Feeder, J.K. Sanders, *New J. Chem.* 2001, *25*, 797; b) T. Lazarides, S. Kuhri, G. Charalambidis, M. K. Panda, D.M. Guldi, A.G. Coutsolelos, *Inorg. Chem.* 2012, *51*, 4193

[13] D.P. Arnold, J.P. Bartley, *Inorg. Chem.* 1994, *33*, 1486.

[14] Crossley, M. J.; Thordarson, P.; Wu, R. A.-S. Efficient Formation of Lipophilic Dihydroxotin(IV) Porphyrins and Bis-Porphyrins. *J. Chem. Soc. Perkin Trans. 1* 2001, 2294-2302.

[15] F. Scandola, C. Chiorboli, A. Prodi, E. Iengo and E. Alessio, *Coord. Chem. Rev*., 2006, *250*, 1471; E. Iengo, G. D. Pantos-, J. K. M. Sanders, M. Orlandi, C. Chiorboli, S. Fracasso, F. Scandola, *Chem. Sci*., 2011, *2*, 676.

[16] D.H. Wu, A.D. Chen, C.S. Johnson, *J. Magn. Reson. Ser. A* 1995, *115*, 260.

[17] *MestReNova© software, version 6.0.2, Mestrelab Res. S.L., Santiago Compost. Spain* 2016

[18] E.B. Fleischer, A.M. Shacter, *Inorg. Chem.* 1991, *30*, 3763.

[19] V. Bandi, H.B. Gobeze, P.A. Karr, F. D'Souza, *J. Phys. Chem. C* 2014, *118*, 18969.

[20] C. Spagnul, R. Alberto, G. Gasser, S. Ferrari, V. Pierroz, A. Bergamo, T. Gianferrara, E. Alessio, J. Inorg. Bio-chem. 2013, 122, 57.

[21] E. Iengo, E. Zangrando, R. Minatel, E. Alessio, *J. Am. Chem. Soc.* 2002, 124, 1003.

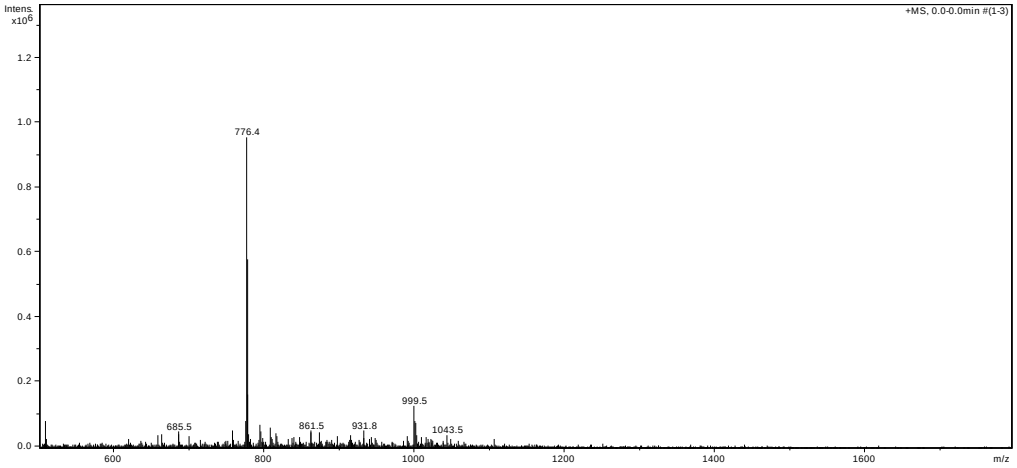

Figure A4.1. ESI-MS spectrum of of **dimPh**

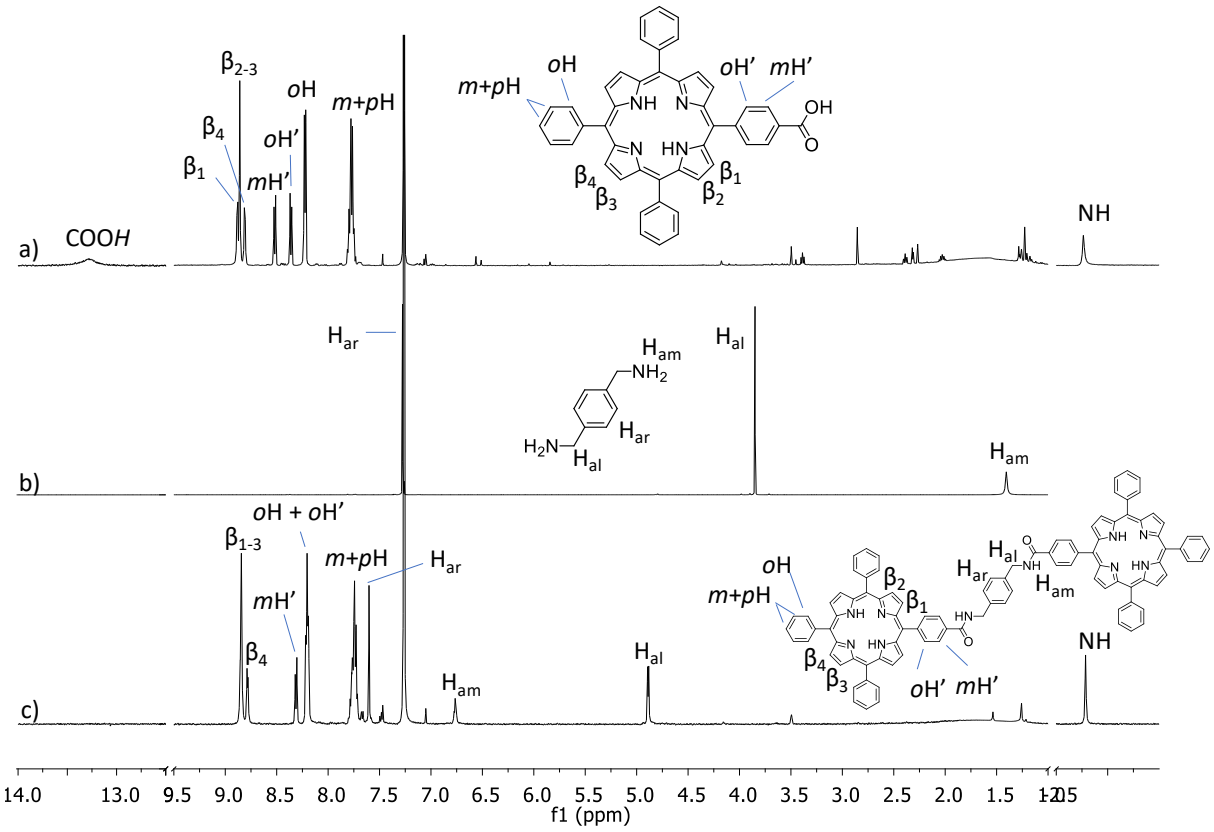

Figure A4.2. ^{1}H NMR spectra ($CDCl_3$) of a) ***mono*PhCOOHP**, b) *p*-xylylenediamine and c) **dimPh**.

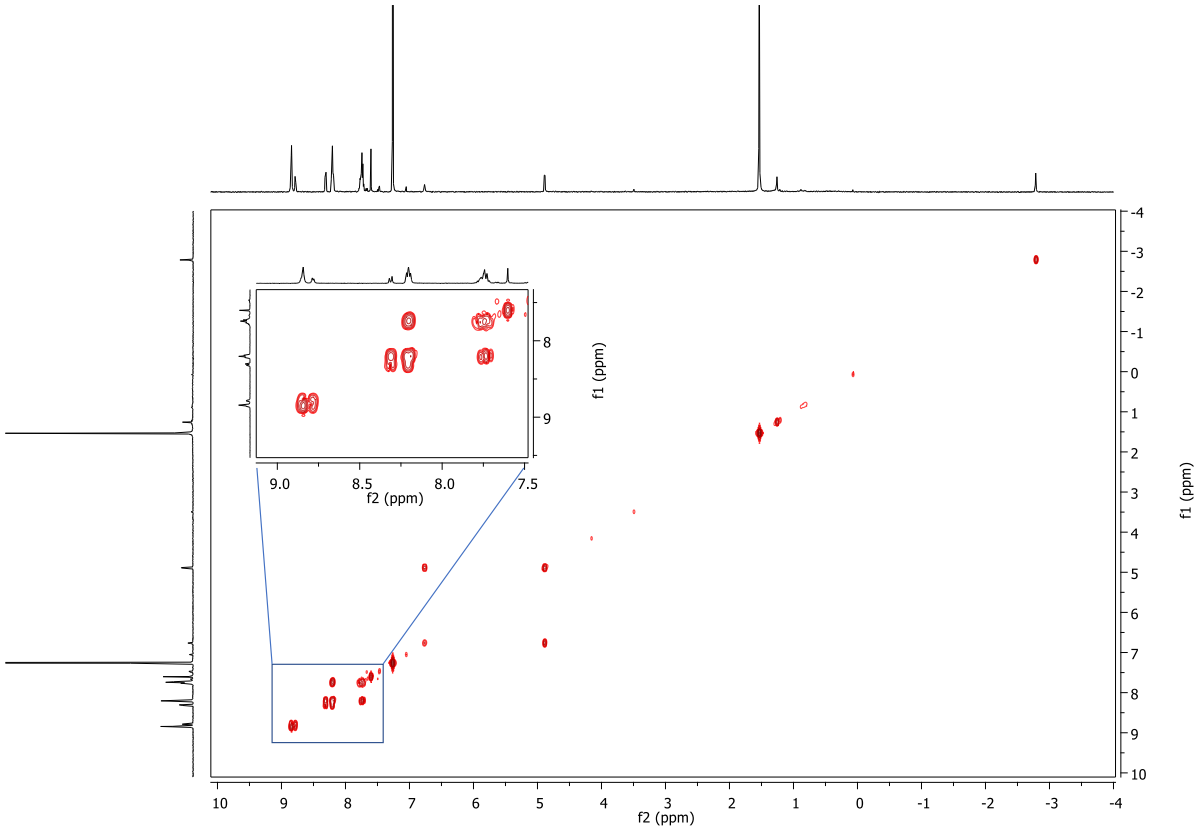

Figure A4.3. HH-COSY spectrum ($CDCl_3$) of **dimPh**

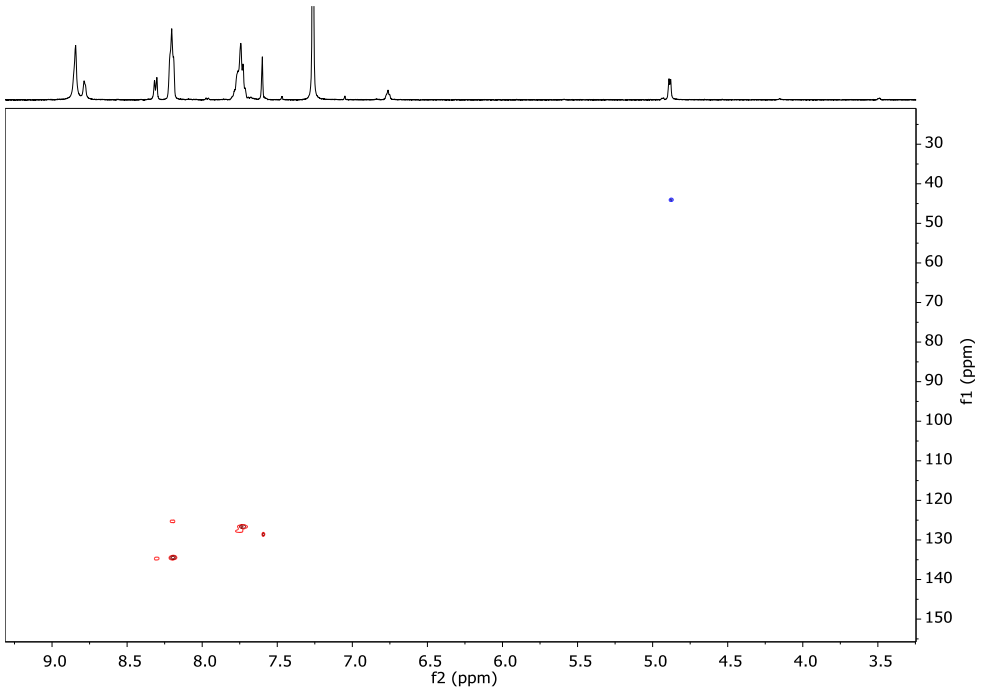

Figure A4.4. HC-COSY spectrum (HSQC, $CDCl_3$) of **dimPh**

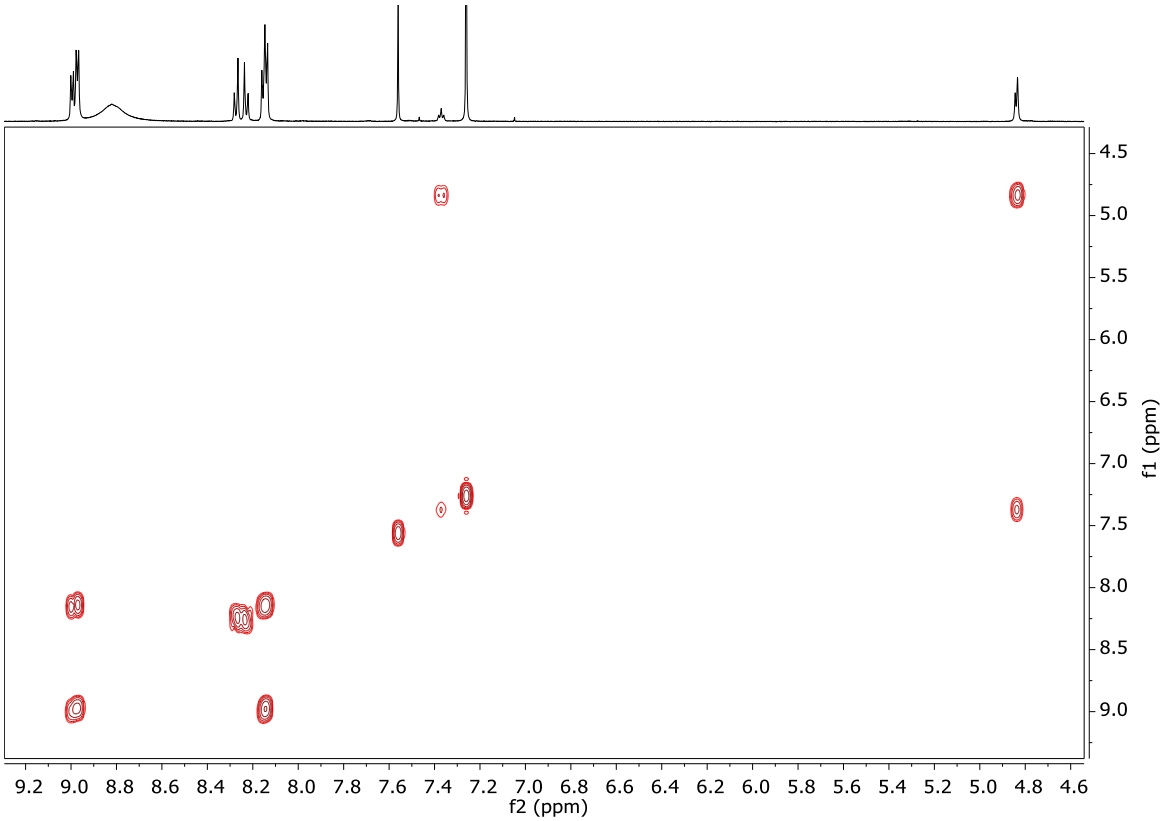

Figure A4.5. H-H COSY spectrum ($CDCl_3$) of **dimPy**

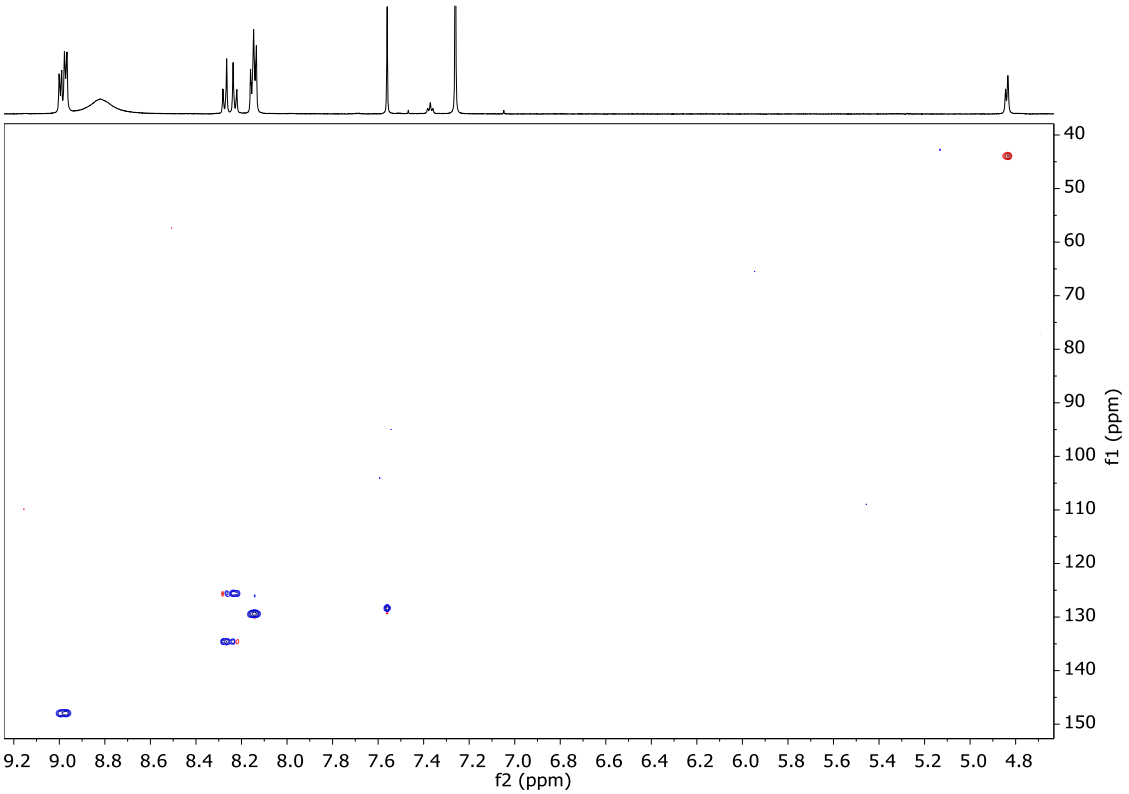

Figure A4.6. H-H COSY spectrum (HSQC, $CDCl_3$) of **dimPy**

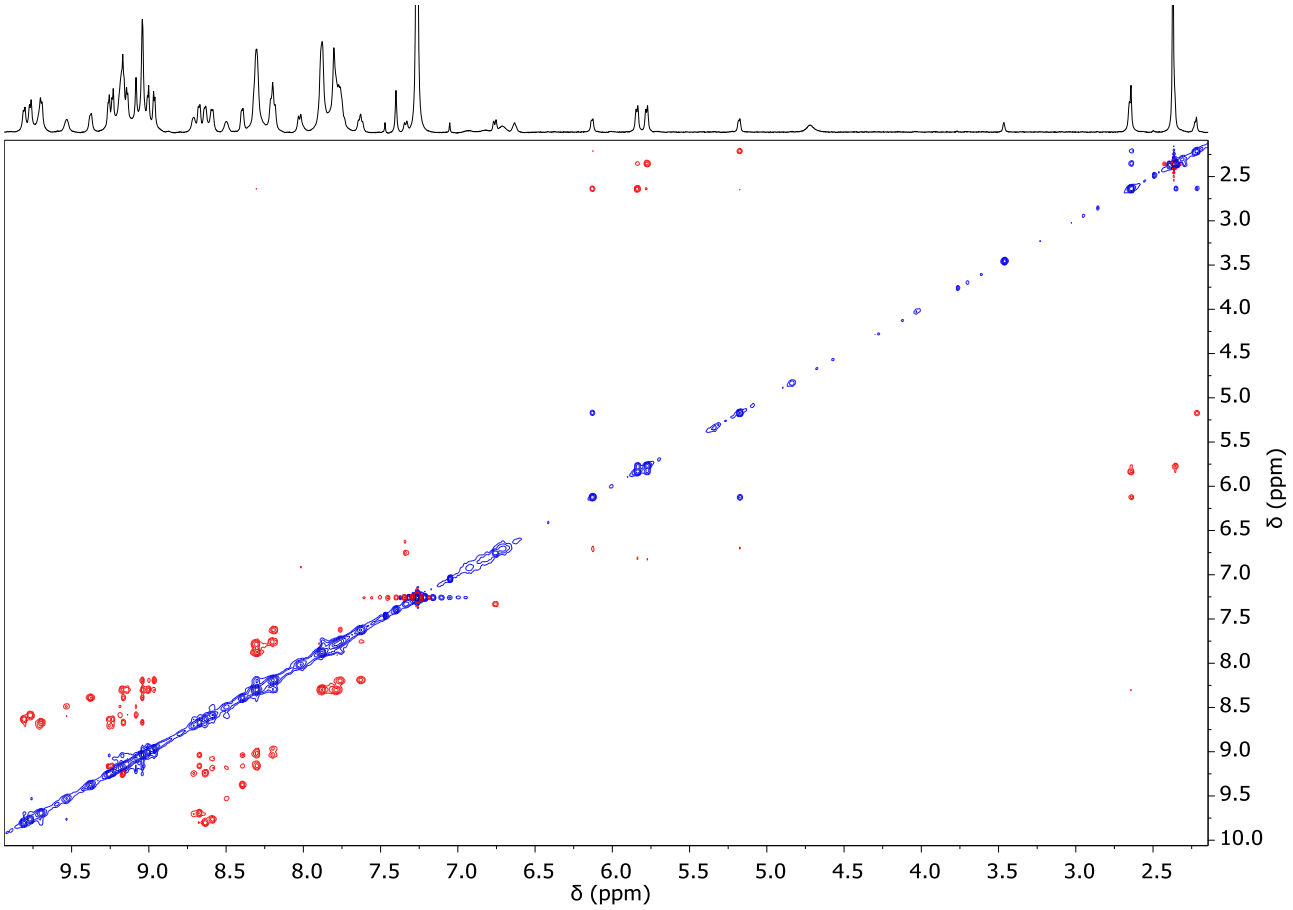

Figure A4.7. H-H ROESY spectrum ($CDCl_3$, -10°C) of **[(1Zn)$_6$·(dimPy)$_2$]**.

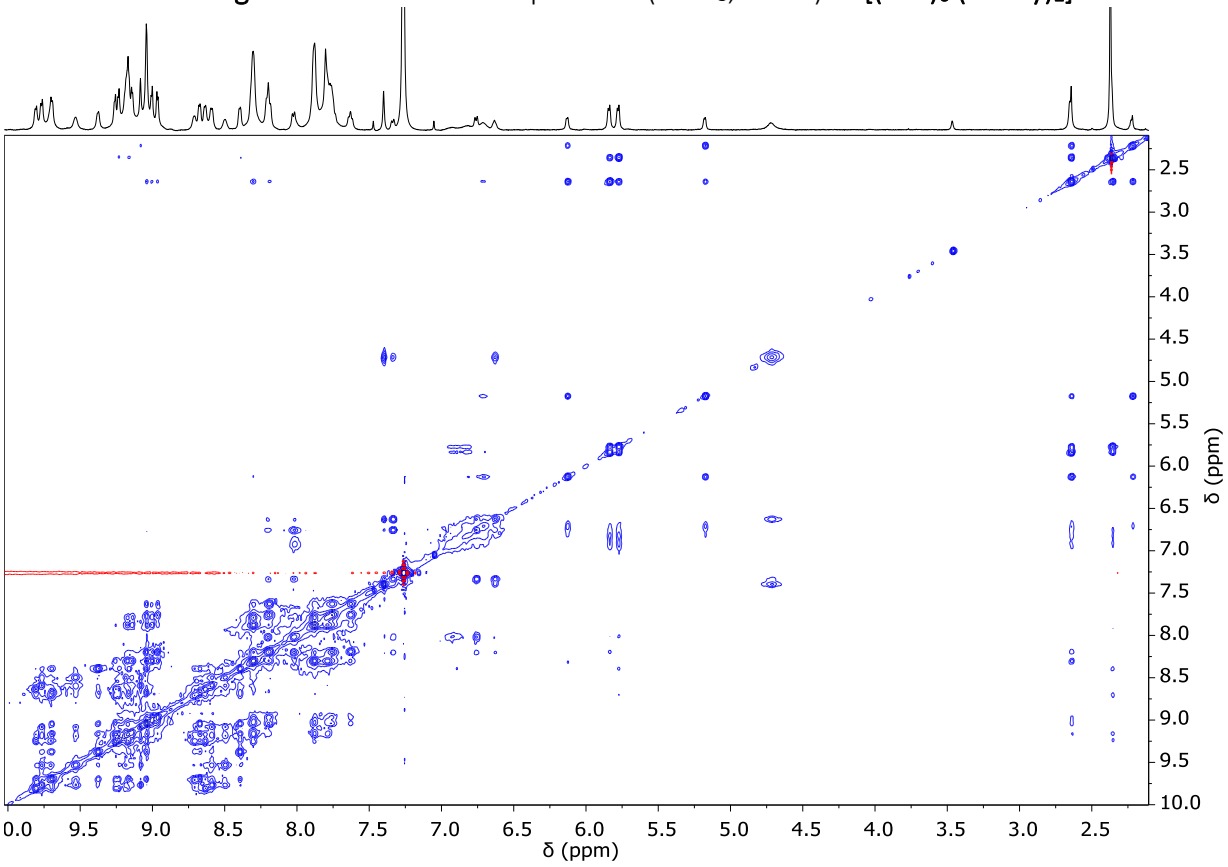

Figure A4.8. H-H NOESY spectrum ($CDCl_3$, -10°C) of **[(1Zn)$_6$·(dimPy)$_2$]**.

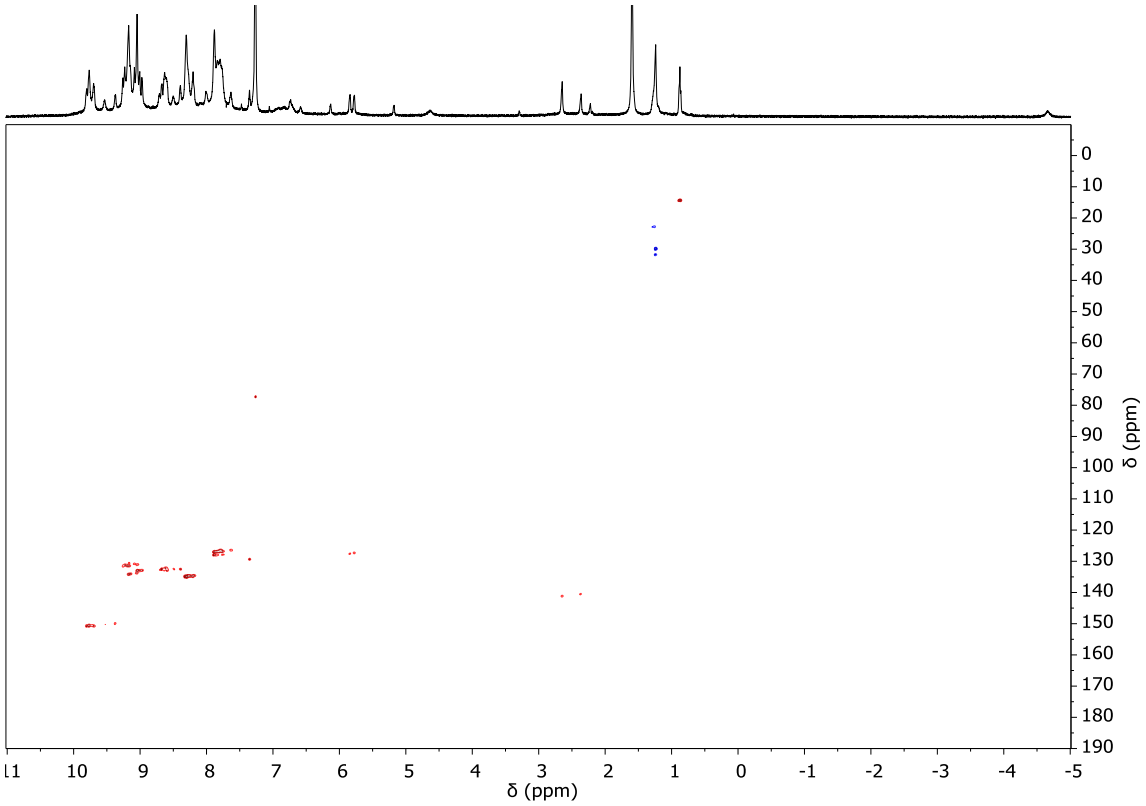

Figure A4.9. H-C COSY spectrum (HSQC, $CDCl_3$, -10°C) of **[(1Zn)$_6$·(dimPy)$_2$]**.

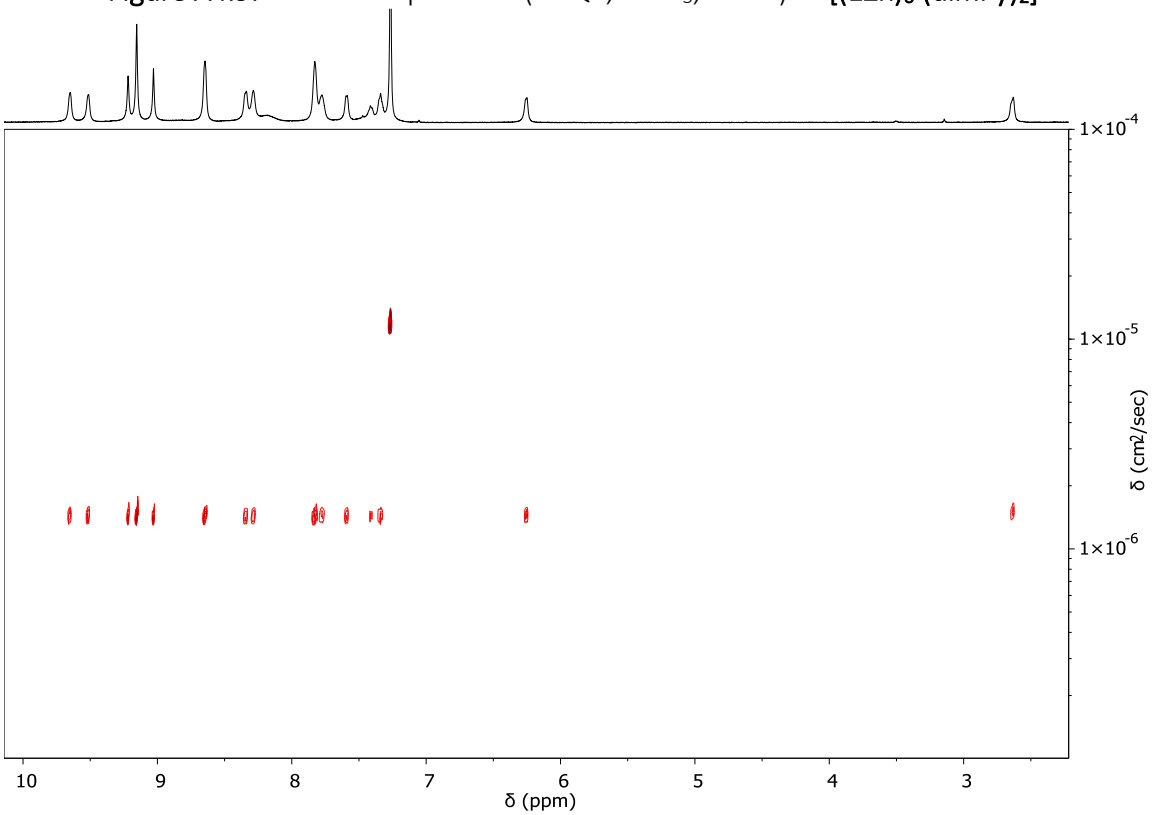

Figure A4.10. 2D ^{1}H-DOSY spectrum (Bayesian transform, $CDCl_3$, -30°C) of **[1Zn·transDPyP]$_2$**

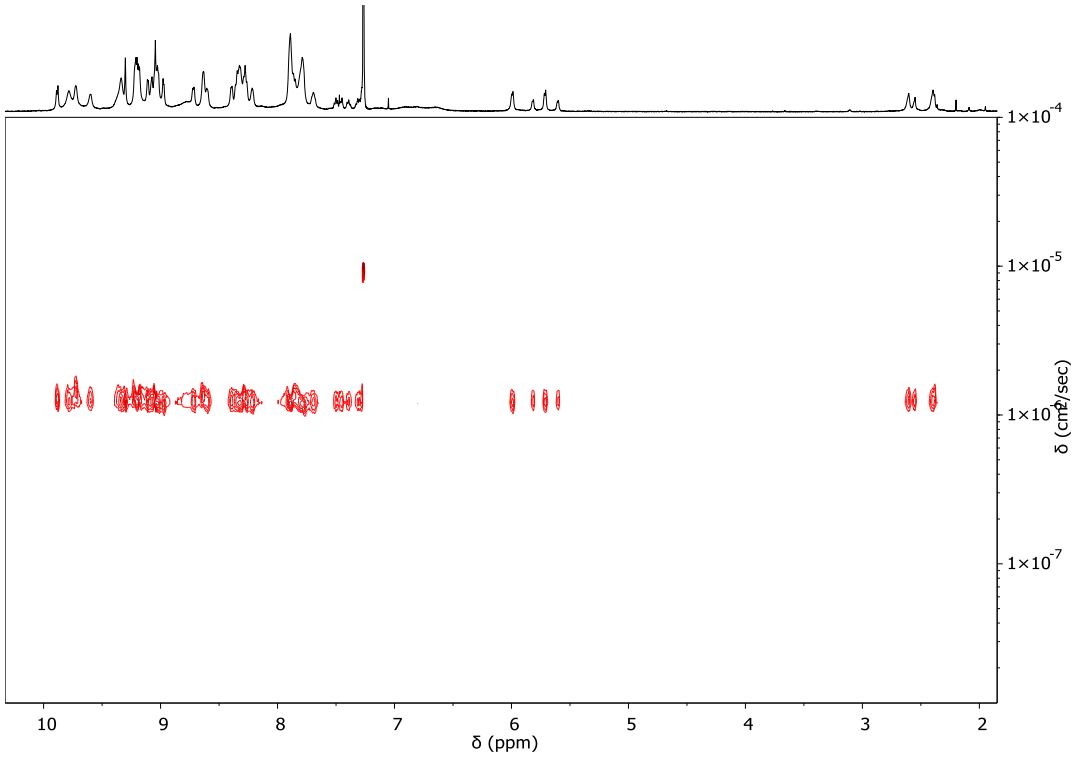

Figure A4.11. 2D ^{1}H-DOSY spectrum (Bayesian transform, $CDCl_3$, -30°C) of **[(1Zn)$_3$·(*tris*PyP)$_2$]**

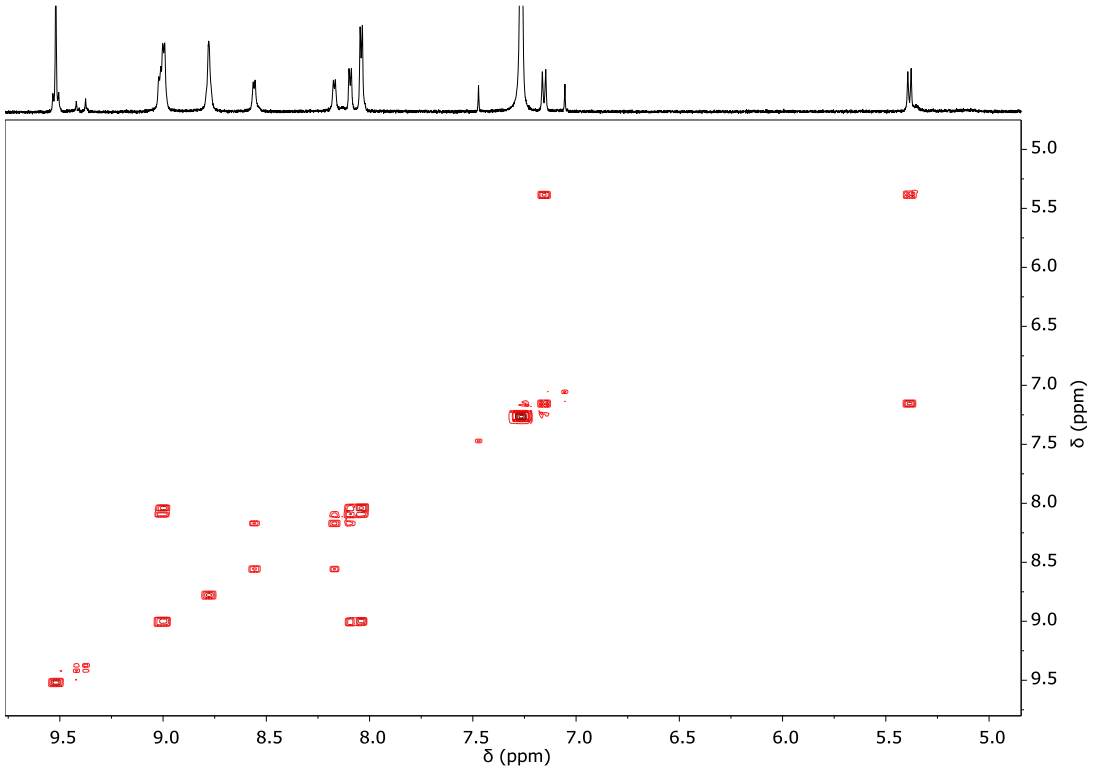

Figure A4.12. H-H COSY spectrum ($CDCl_3$) of **SnTpFP(*mono*PhCOOPyP)$_2$**.

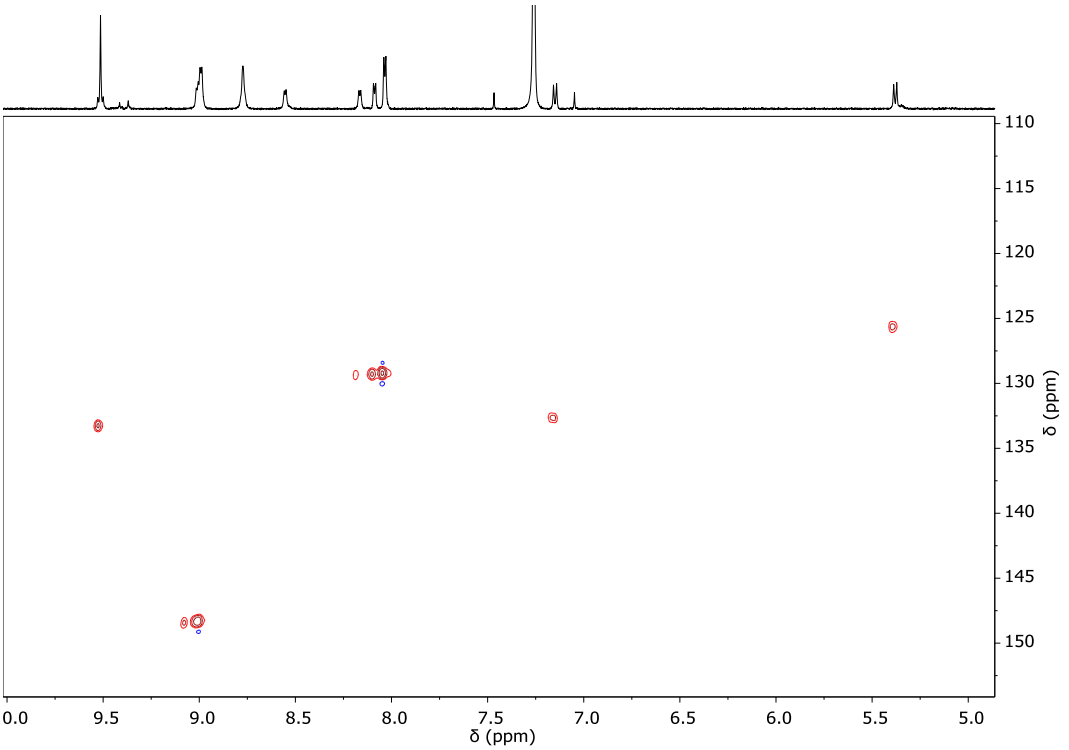

Figure A4.13. H-C COSY spectrum ($CDCl_3$) of **SnTpFP(*mono*PhCOOPyP)$_2$**.

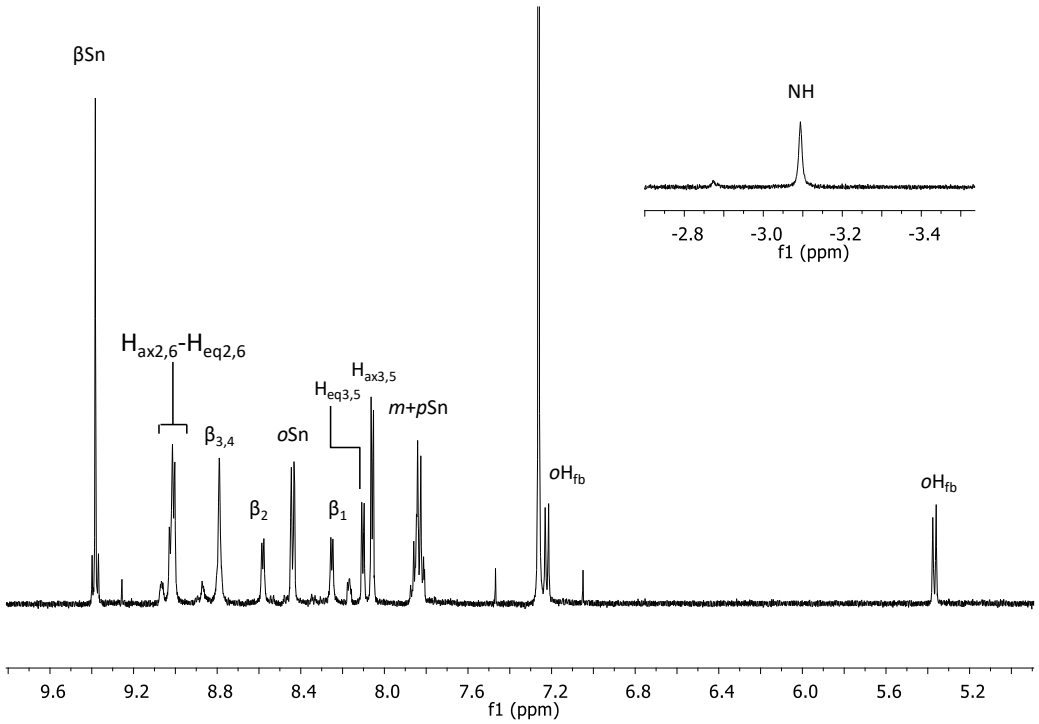

Figure A4.14. ^1H NMR spectrum ($CDCl_3$) of **SnTPP(*mono*PhCOOPyP)$_2$**.

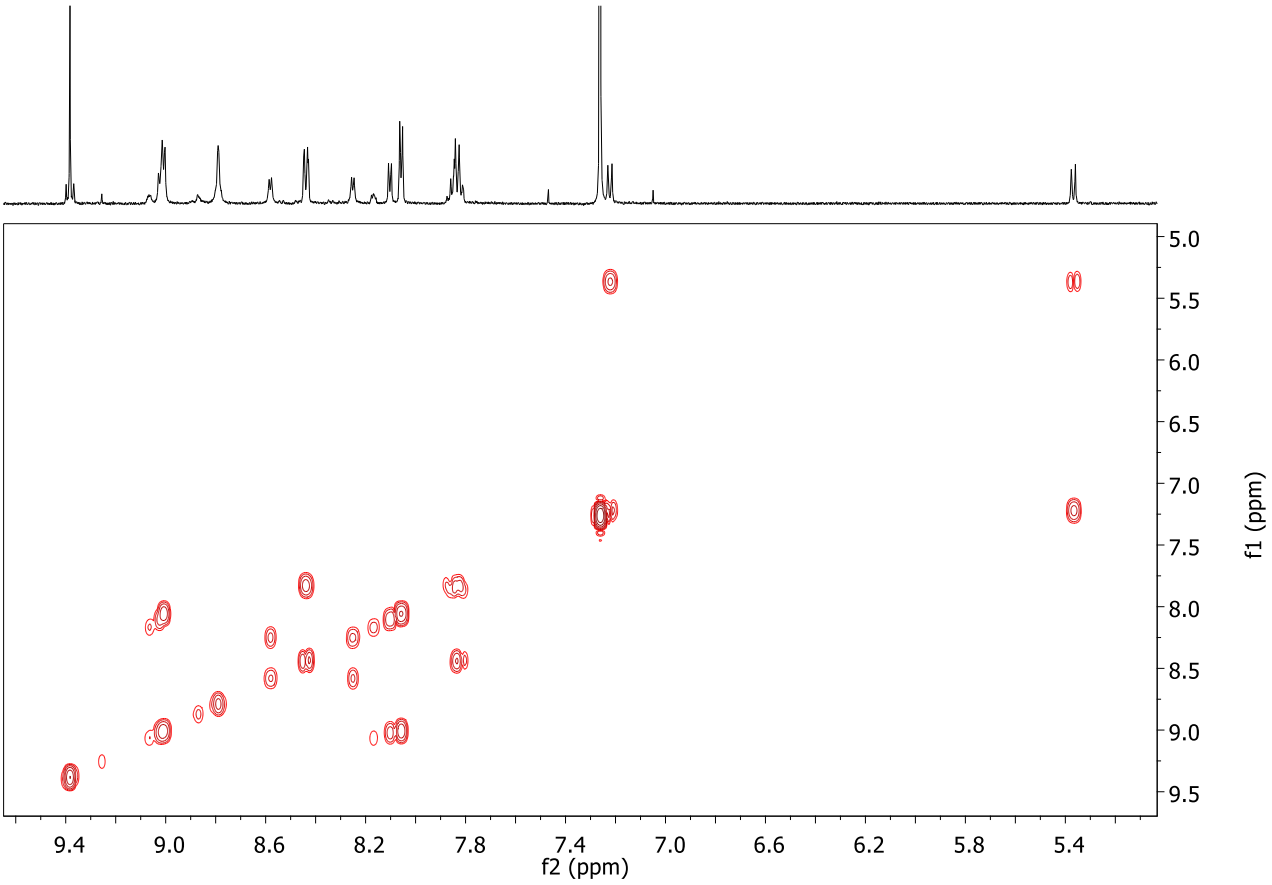

Figure A4.15. H-H COSY spectrum ($CDCl_3$) of **SnTPP(*mono*PhCOOPyP)$_2$**.

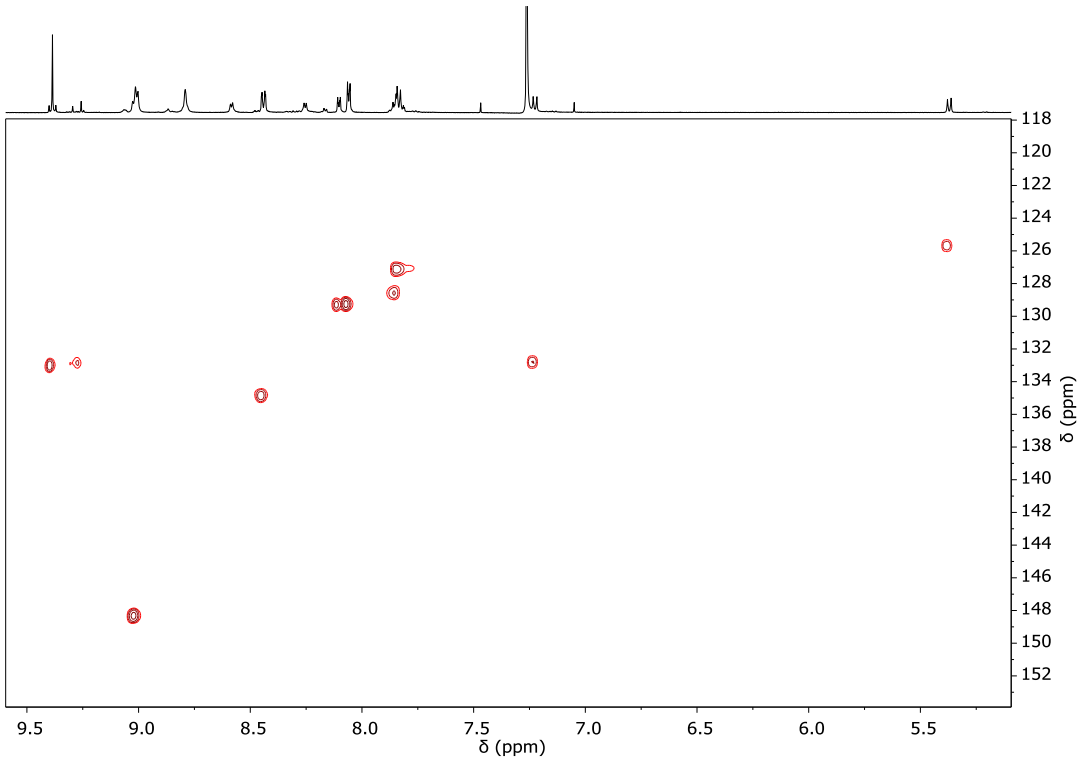

Figure A4.16. H-C COSY spectrum ($CDCl_3$) of **SnTPP(*mono*PhCOOPyP)$_2$**.

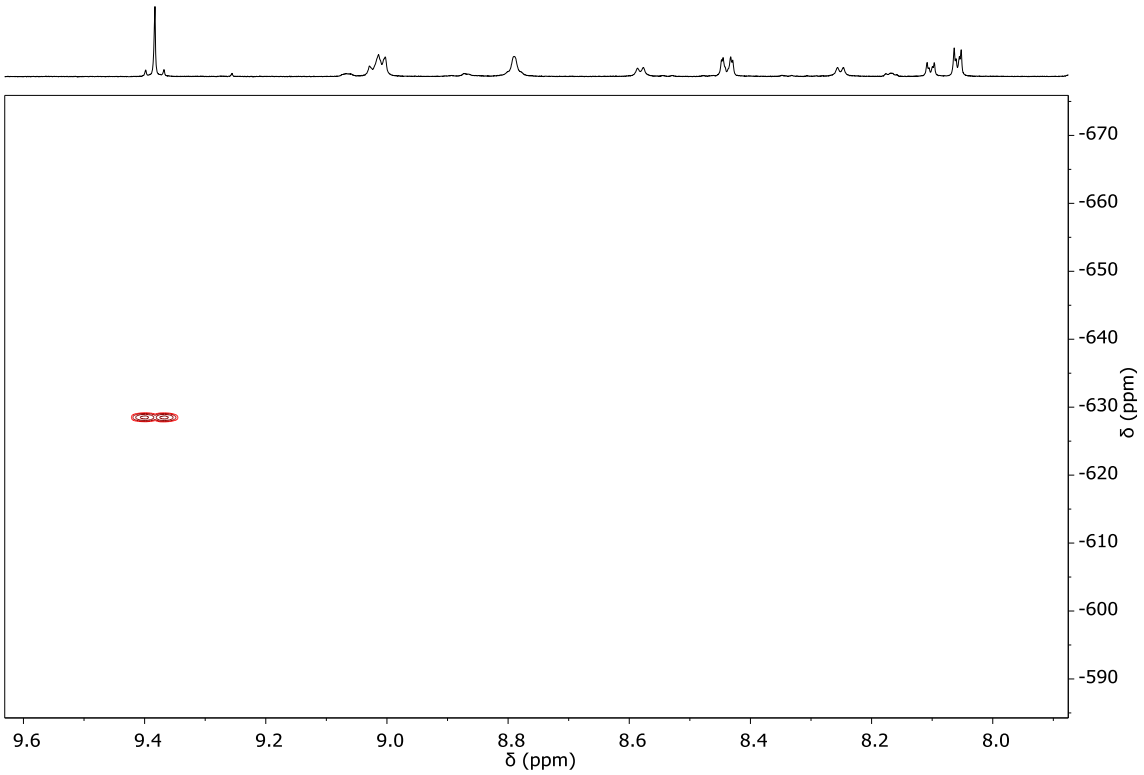

Figure A4.17. H-Sn HMBC spectrum ($CDCl_3$) of **SnTPP(*mono*PhCOOPyP)$_2$**.

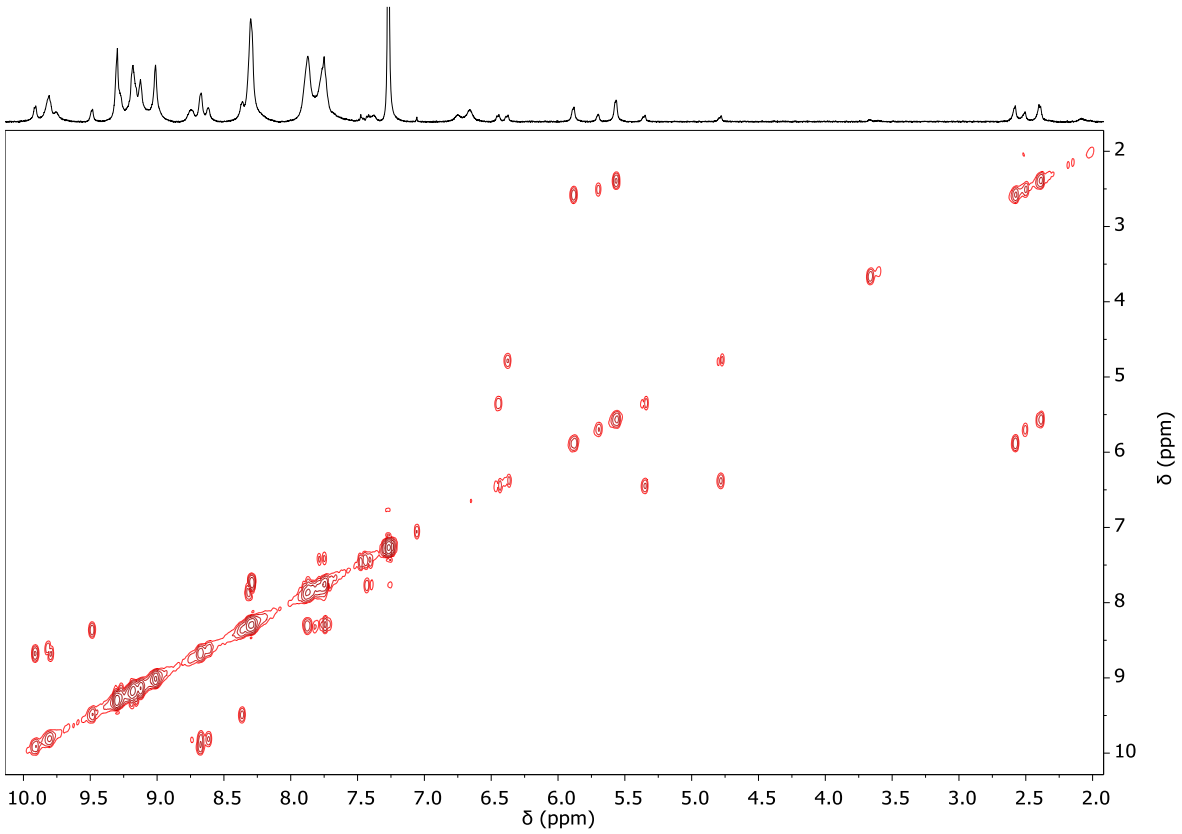

Figure A4.18. H-H COSY spectrum ($CDCl_3$) of **[(1Zn)$_6$·(SnTPP)$_2$·(*mono*PhCOOPyP)$_4$]**.

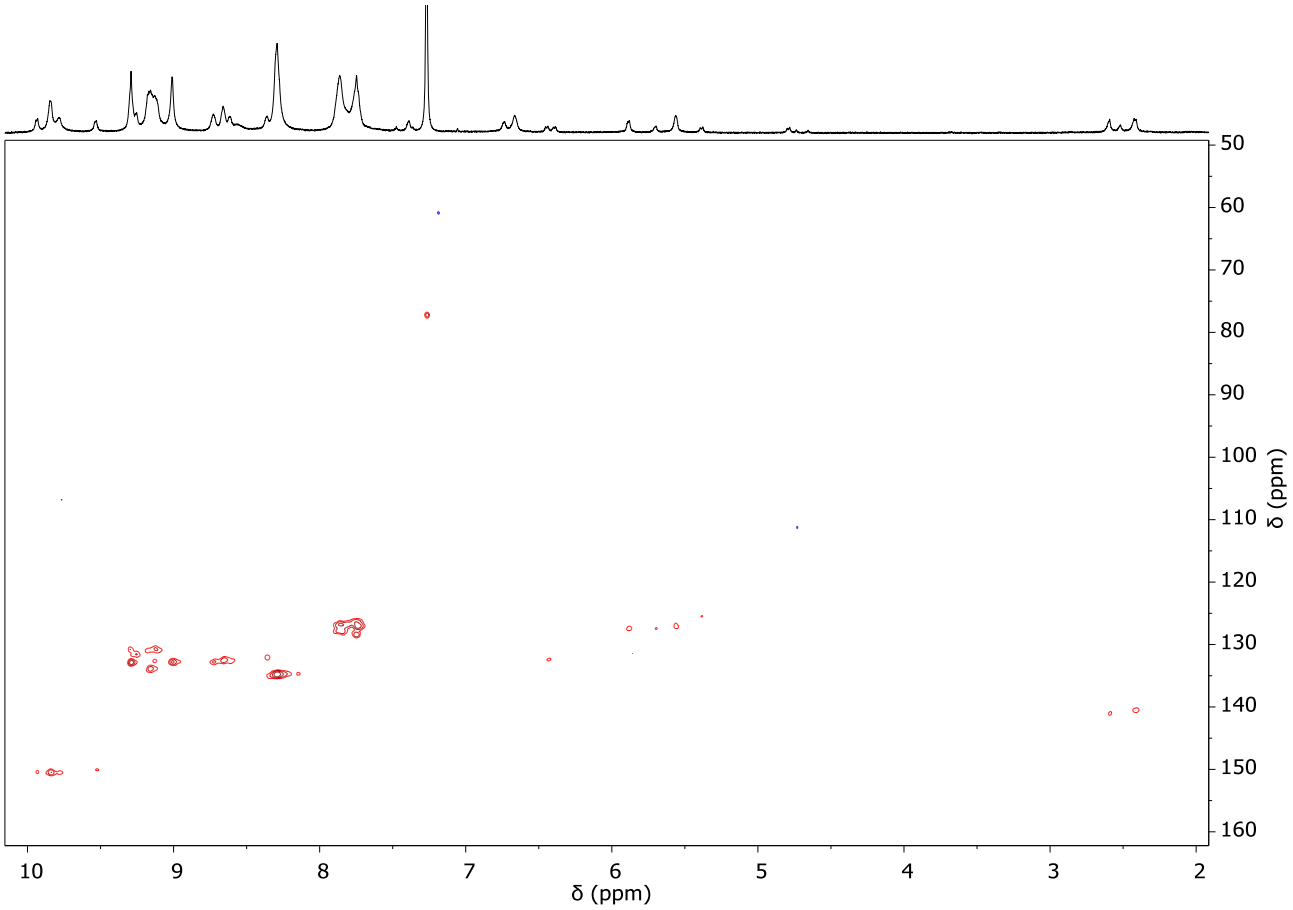

Figure A4.19. H-C COSY spectrum ($CDCl_3$) of **[(1Zn)$_6$·(SnTPP)$_2$·(*mono*PhCOOPyP)$_4$]**.

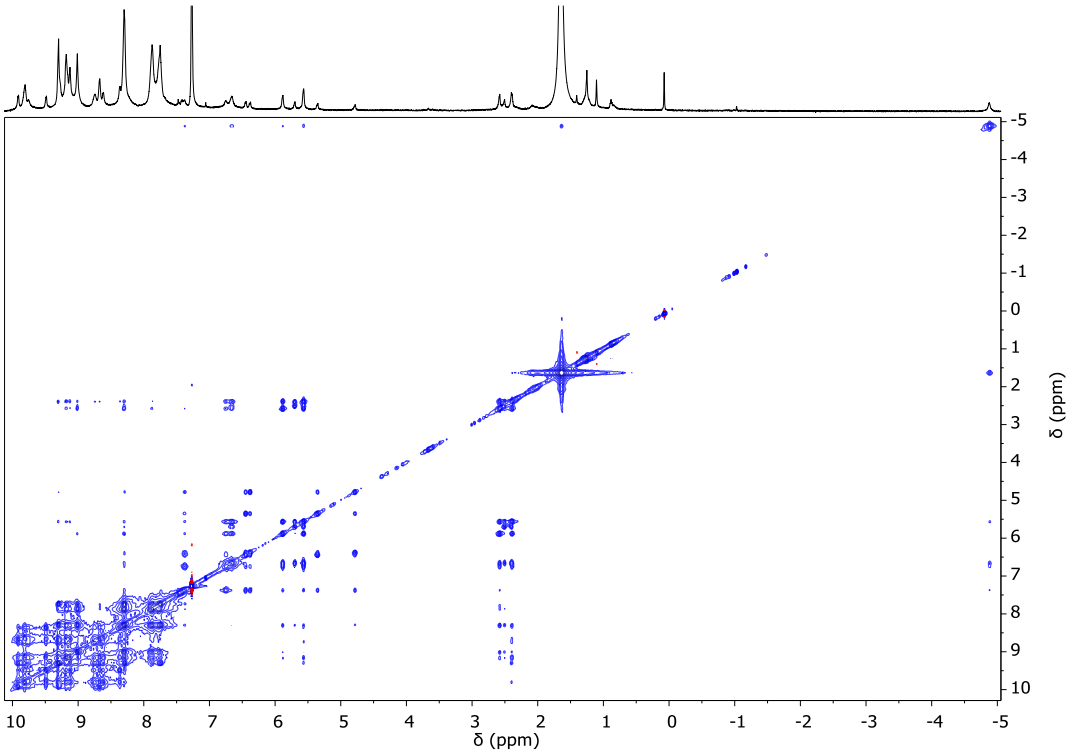

Figure A4.20. H-H NOESY spectrum ($CDCl_3$) of **[(1Zn)$_6$·(SnTPP)$_2$·(*mono*PhCOOPyP)$_4$]**.

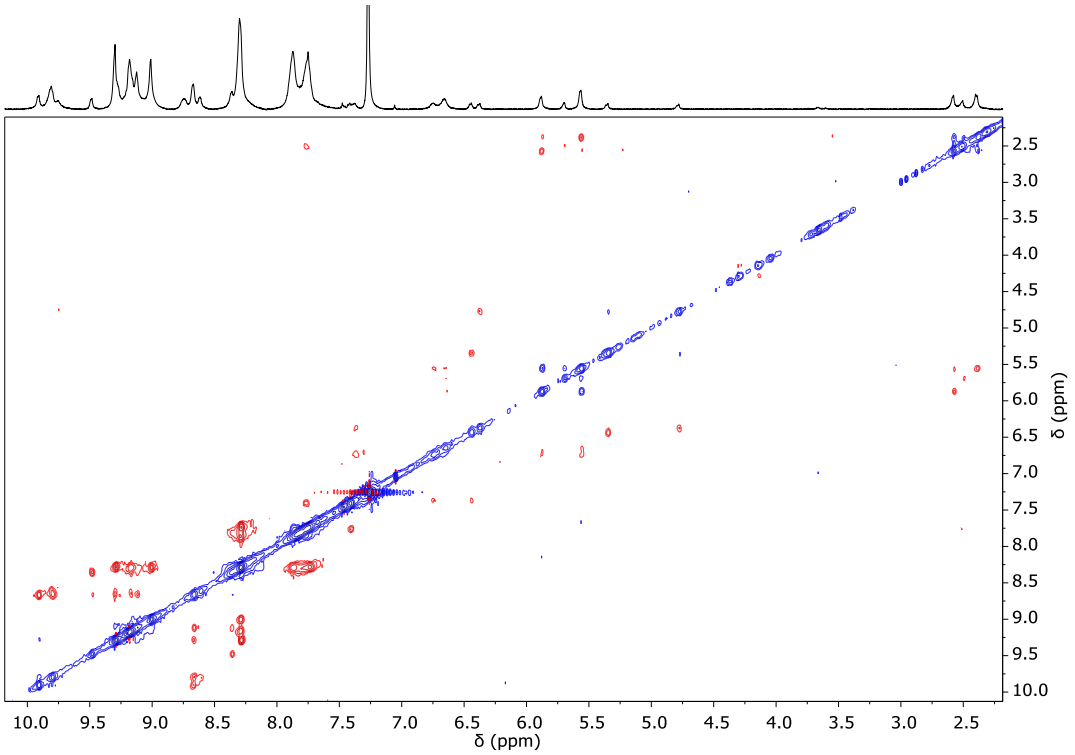

Figure A4.21.H-H ROESY spectrum ($CDCl_3$) of **[(1Zn)$_6$·(SnTPP)$_2$·(*mono*PhCOOPyP)$_4$]**.

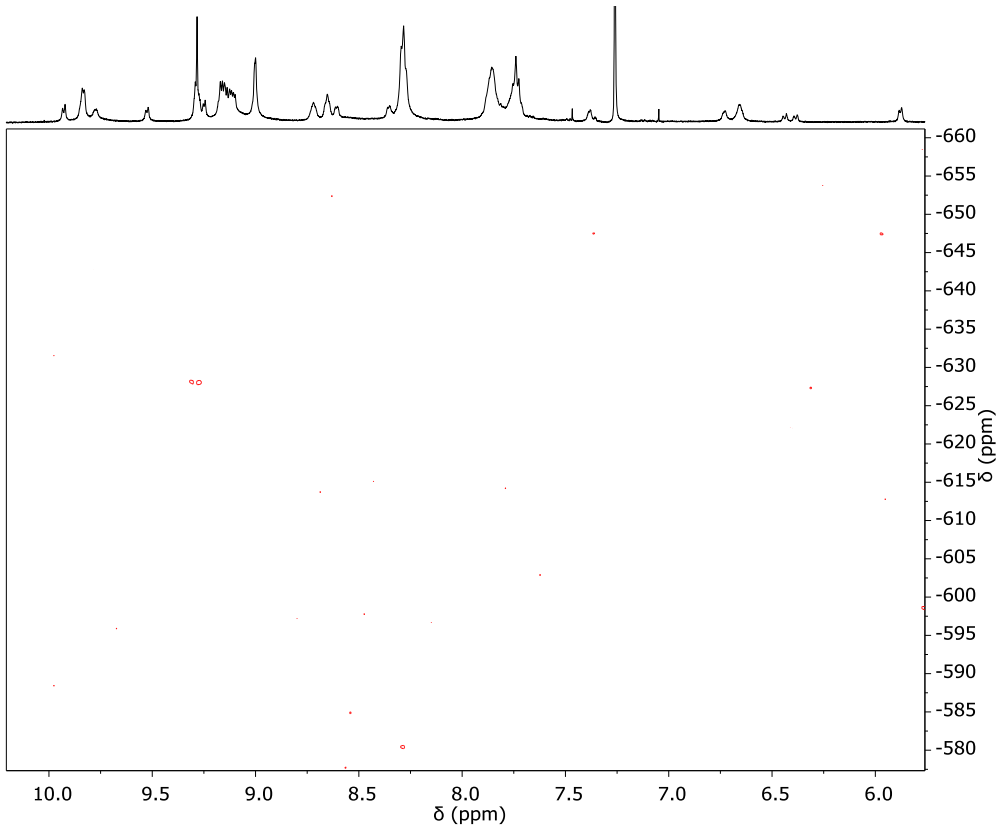

Figure A4.22.H-Sn HMBC spectrum ($CDCl_3$) of **[(1Zn)$_6$·(SnTPP)$_2$·(*mono*PhCOOPyP)$_4$]**.

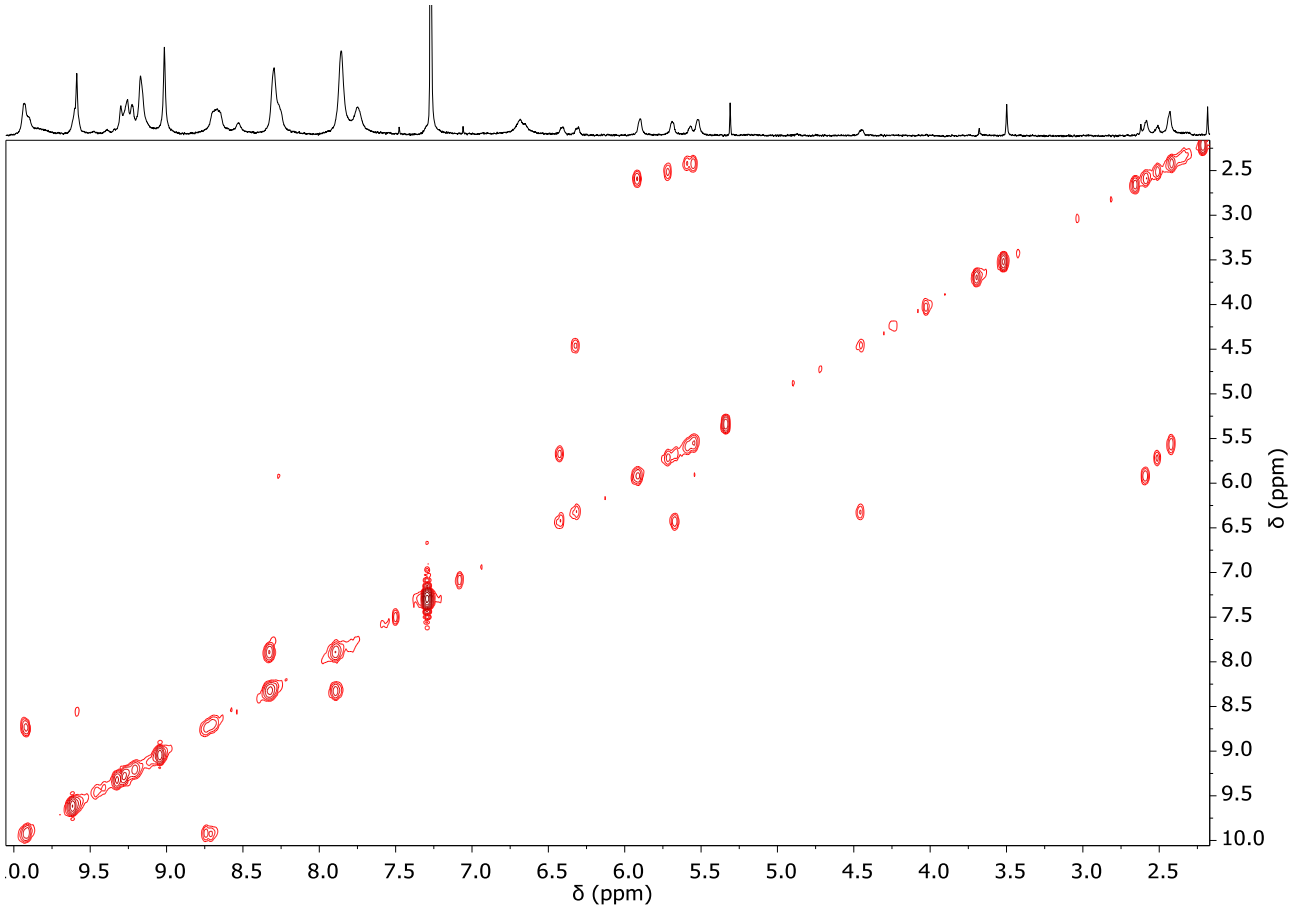

Figure A4.23. H-H COSY spectrum ($CDCl_3$) of **[(1Zn)$_6$·(SnTpFP)$_2$·(*mono*PhCOOPyP)$_4$]**.

Chapter 5

*The work discussed in this Chapter was done during a six-month stay, as Ph.D Erasmus Traineeship fellow, in the laboratories of Dr. Romain Ruppert, University of Strasbourg (FR).

5.1 Introduction

As well depicted so far, discrete supramolecular 3D architectures, self-assembled from the zinc(II)-porphyrin metallacycle **1Zn** and different linear dipyridyl connectors, possess physical properties distinct from the building components, that can be modulated by an appropriate choice of the connecting ligand. For instance, using a porphyrin (Chart 5.1, on the left), upon visible light excitation of **1Zn**, a very fast energy transfer (ET) process is observed to occur from the zinc porphyrin platform to the pillar ligand.[1] While with a perylene bisimide (Chart 5.1, on the right) the visible light promotes an efficient electron transfer (eT) process, leading to the formation of a charge-separated state.[2] Within the novel series of sandwich supramolecular structures described in the previous chapters, those obtained from the dipyridyl metallo-containing ligands connectors (see Chapter 2) represent a step forward in terms of expected properties. In fact, the resulting assembled systems contain an increased number of different (potentially photo- or magnetically-active) metal centres, with precise mutual geometrical dispositions.

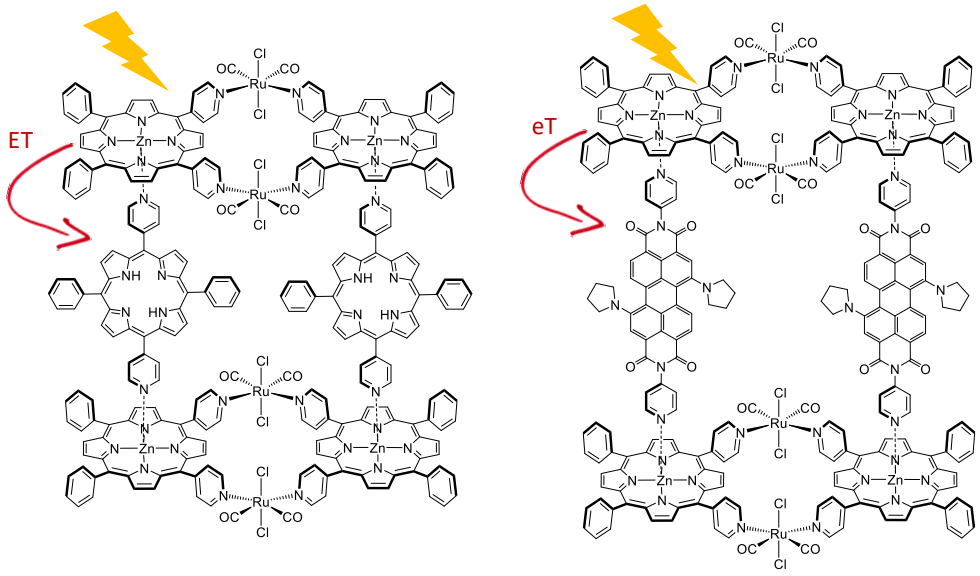

Chart 5.1.

So far, all efforts in the implementation of the 3D systems described above were directed at the tuning of the inter-component photo-induced properties and/or at the introduction of new functions derived from the geometrical organization of a precise number of active metal centres, by modulation of the nature of the bridging ligands. No attempts have yet been carried out to investigate the possibility to introduce alternative peripheral anchoring platforms in place of **1Zn**. The work illustrated in the present Chapter is devoted to explore and tackle this aspect.

In the last years, the group of Dr. Romain Ruppert (Institut de Chimie, University of Strasbourg, France), in whose laboratories the work here presented was carried out, has developed the synthesis of porphyrin homodimers connected through coordination to transition-metal cations, of peripheral chelating enaminoketone group fully conjugated with the macrocyclic π-system (Chart 5.2).[3] Contrary to **1Zn**, where the two porphyrins substantially maintain the parent isolated chromophore characteristics,[4] and the coordination to the Ru^{II} centres plays a purely structural role, in these latter

dimers a strong electronic communication between the two porphyrin macrocycles is observed to occur, mediated by the exocyclic coordination connection.[3a,3c,5]

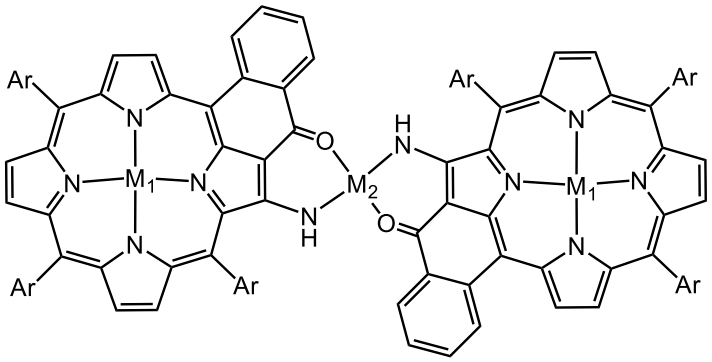

Chart 5.2. Few examples of dimers reported by Ruppert's group. In order, *meso* group (M_1-M_2-M_1): Ph (Ni-Ni-Ni); Ph (Ni/Cu/Ni); Ph (Ni/Pd/Ni); Ph (Cu/Pd/Cu); Ph (Cu/Cu/Cu); 3,5-di*tert*-butylphenyl (H2/Pd/H2); 3,5-di-*tert*-butylphenyl (Zn/Pd/Zn); 3,5-di-*tert*-butylphenyl (Zn/Pt/Zn); 3,5-di-*tert*-butylphenyl (Zn/Pt/H2).

The synthetic path, followed to prepare the chelating monomer porphyrin, is depicted in Scheme 5.1: one *meso*-aryl group was fused to the neighbouring pyrrole in a few steps,[6] and afterwards, taking advantage of the reactivity of the β-position adjacent to the carbonyl group, the corresponding enamino-ketone was obtained in good overall yields using the Katritsky reagent.[7]

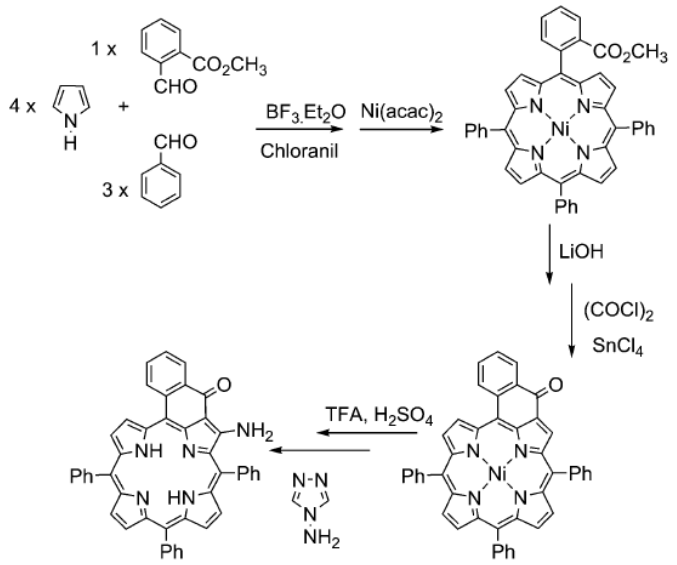

Scheme 5.1. Synthesis of the monomer enaminoketone porphyrin, from Ref. 3e.

The versatility of this approach and the use of appropriate metal salts allowed the stepwise formation of a wide library of metal-linked dimers. These compounds may differ by the nature of the coordinating heteroatom (keto or thioketone), the aryl groups at *meso* positions and/or the central metal. Generally, the steric hindrance of the aryl substituents grants a regioselective *trans* geometry to the dimers. Formation of the *cis*-enaminoketoporphyrin-dimer has been observed, only by reaction of an enaminothioketone porphyrin monomer bearing arylalkylether *meso* groups (Ph-$OC_{12}H_{25}$).[3d] Small variations in the synthetic route, afforded also the preparation of bis-chelate

porphyrin which, combined with mono-chelate building blocks, yielded longer scaffolds, such as trimers[3d,8] and tetramers.[9]

The optimized geometry, calculated for an asymmetric dimer composed of a Zn-porphyrin and a freebase coordinated to a Pt(II) cation (ZnPdFb in Figure 5.1), shows how the relatively strong coordination bonds, leads to a planarity of the PtN_2O_2 bridge.[3c] The dyad exhibits the expected non-planar structure as a result of the steric interactions between the β-pyrrolic protons and the fused benzene rings. These interactions lead to major distortions where the furthest C atoms of the fused benzenes are out of the average Zn-porphyrin and freebase porphyrin planes by 1.89 and 1.75 Å, respectively. Some expected distortions of the porphyrin macrocycles are also observed. The short Pt–ligand bonds and planarity of the PtN_2O_2 bridge suggest the presence of appropriate conditions for conjugation.

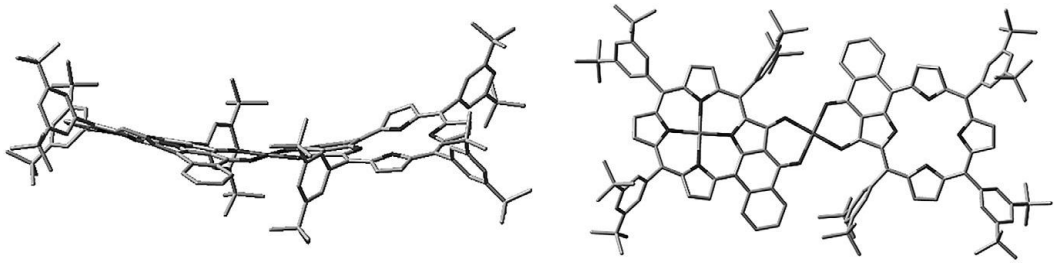

Figure 5.1. Side (left) and top (right) view of the optimized geometry of a dimer ZnPdFb, from Ref. 3c.

The electronic density map, calculated on a Pt-linked enaminothioketone-porphyrin dimer, indicates a higher concentration of density within the bridging complex, consistent with the electron-rich S, NH–, and Pt residues.[10]

The first evidence for electronic communication in the dimers was provided by electrochemical measurements that showed two characteristic features: first, a decrease of the electrochemical gap (ΔE) between the first oxidation and the first reduction potentials of the two identical monomers, and second, the splitting of the first oxidation potential of the porphyrin macrocycles. Cyclic voltammetry (CV) clearly showed that, for example, the first oxidation signal of the Ni monomer in Figure 5.2 is converted into a split signal in the voltammogram of the Ni dimer linked by Pd(II). Similar behaviour was observed for all dimers and for the building block described in Chart 5.2.

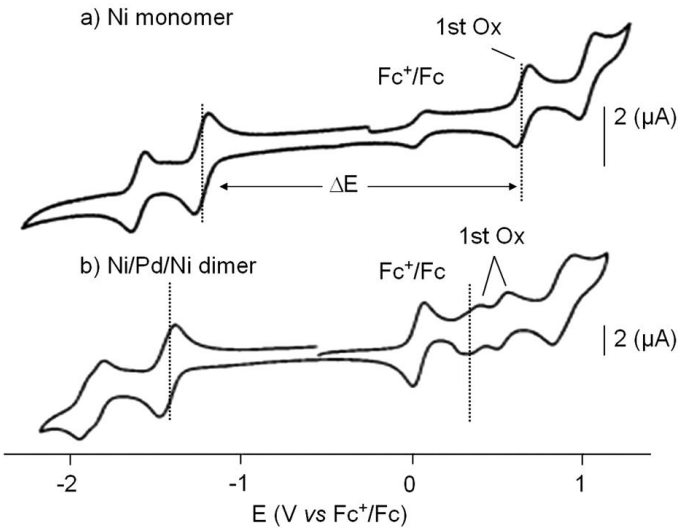

Figure 5.2. Electrochemical features of a nickel-porphyrin and its corresponding dimer assembled around palladium(II).

The extremely efficient delocalisation of the electronic density in these species led to very interesting properties of the resulting chromophores. For example, dyad composed of zinc and free base enaminoketone porphyrins linked by palladium(II) ion, exhibited an efficient ultrafast energy transfer process (660 fs).[11] Replacing the palladium(II) by platinum(II), led to a drastic increase of the photoinduced process rate (105 fs).[3c] Electronic spectroscopy, electrochemical measurements, and DFT computations clearly related this radical improvement to the significantly increased electronic communication, occurring through the Pt(II) coordinating bonds, between the energy donor (Zn porphyrin) and acceptor (freebase). Moreover, the energy transfer was even faster by introducing sulfur instead of oxygen in the chelating unit. In addition, the splitting of the first oxidation increased to values similar to those reported for covalently linked, conjugated dimers.

More recently, dimers bearing peripheral long aliphatic chains (O–$C_{12}H_{25}$), were used to self-assemble into well-ordered two-dimensional structures at a highly oriented pyrolytic graphite (HOPG)/liquid interface, as visualized by scanning tunneling microscopy (STM).[3d] Excepting this last example, so far, these dimeric systems have not been used as building units for the construction of higher order supramolecular arrays. Captivated by the overall described electronic properties of these compounds, the Pd^{II}-linked Zn(II)-porphyrin dimer (**ZnPdZn** in Scheme 5.2) bearing peripheral 4-*tert*-butyl-2,6-dimethylphenyl *meso*-substituents, was selected as candidate to be explored as valid alternative photo-active platforms for the assembling of discrete supramolecular sandwich structures (Scheme 5.2). Indeed, from a supramolecular assembling view-point, dimer **ZnPdZn**, preserves the required features already offered by **1Zn**: two Zn^{II} anchoring points, a good inertness of the exocyclic metal coordination bonds and sufficiently coplanar and rigid disposition of the zinc-porphyrin components.

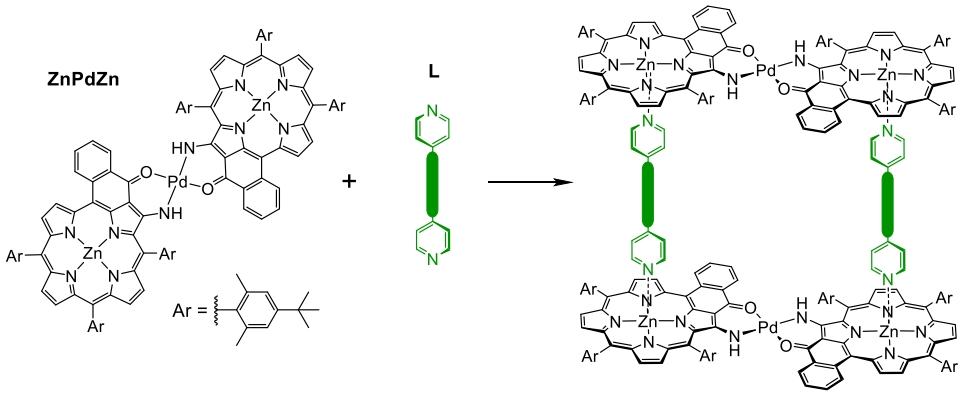

Scheme 5.2. Schematic depiction of the possible assembling of 3D *sandwich*-like structures from **ZnPdZn** and a general *trans*-dipyridyl ligand **L**.

5.2 Results and Discussion

5.2.1 Synthesis and Characterization of Dimer ZnPdZn

Monomeric compounds were the first synthetic goal: the preparation of porphyrins bearing enaminoketones as external coordination sites is well established.[3d,8] The starting porphyrin with three *meso*aryl groups and one *ortho*-carbomethoxyphenyl group was obtained *via* a classical statistical Lindsey procedure and isolated by column chromatography from the statistical mixture of esters. The choice of the 4-*tert*-butyl-2,6-dimethylphenyl *meso*-substituent was made to endow the derived dimers with higher solubility and, at the same time, grant redox activity of the porphyrin derivates (for this reason, 3,5-di-*tert*-butylphenyl substituents were ruled out, since they led to almost complete passivation of the electrodes by the derived porphyrin dimers[3c]).

Metallation of **2** with $Ni(acac)_2$, followed by hydrolysis of the ester group (LiOH in dioxane/water) and intramolecular Friedel–Crafts cyclization gave the extended nickel porphyrin **4**. Then, amination with the Katritsky reagent afforded to obtain porphyrin **5** (see Scheme 5.3).[12]

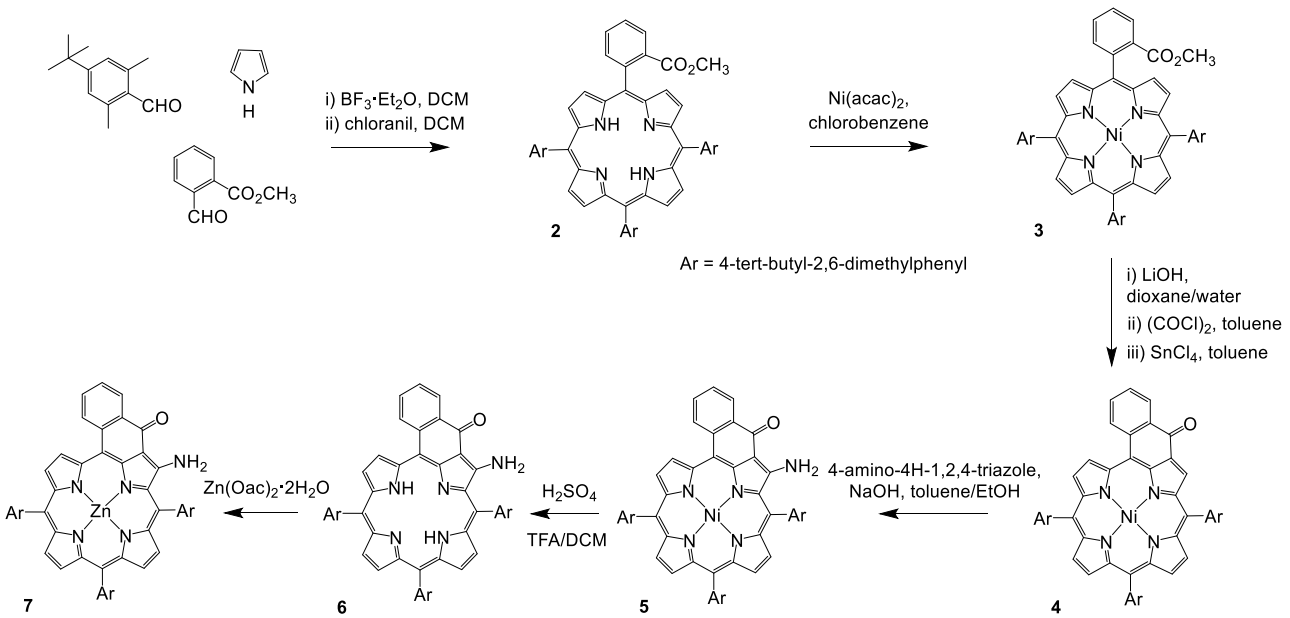

Scheme 5.3. Preparation of the starting porphyrins **2**–**7**

Demetallation with sulfuric acid and subsequent treatment of the freebase derivative with an excess of zinc acetate led to the zincate enaminoketo porphyrin **7**. Porphyrin **6** and **7**, as they were completely new compounds, were fully characterized by NMR (^{1}H and ^{13}C, 1D and 2D) and UV-vis spectroscopy, and high-resolution mass spectrometry.

The ESI-MicroTOF mass spectra of both compounds showed a peak, corresponding to the molecular ions [**6** + H]$^{+}$ and [**7**]$^{+}$, with the correct isotopic distribution. As example, the mass spectrum of **7** is reported in Figure 5.3.

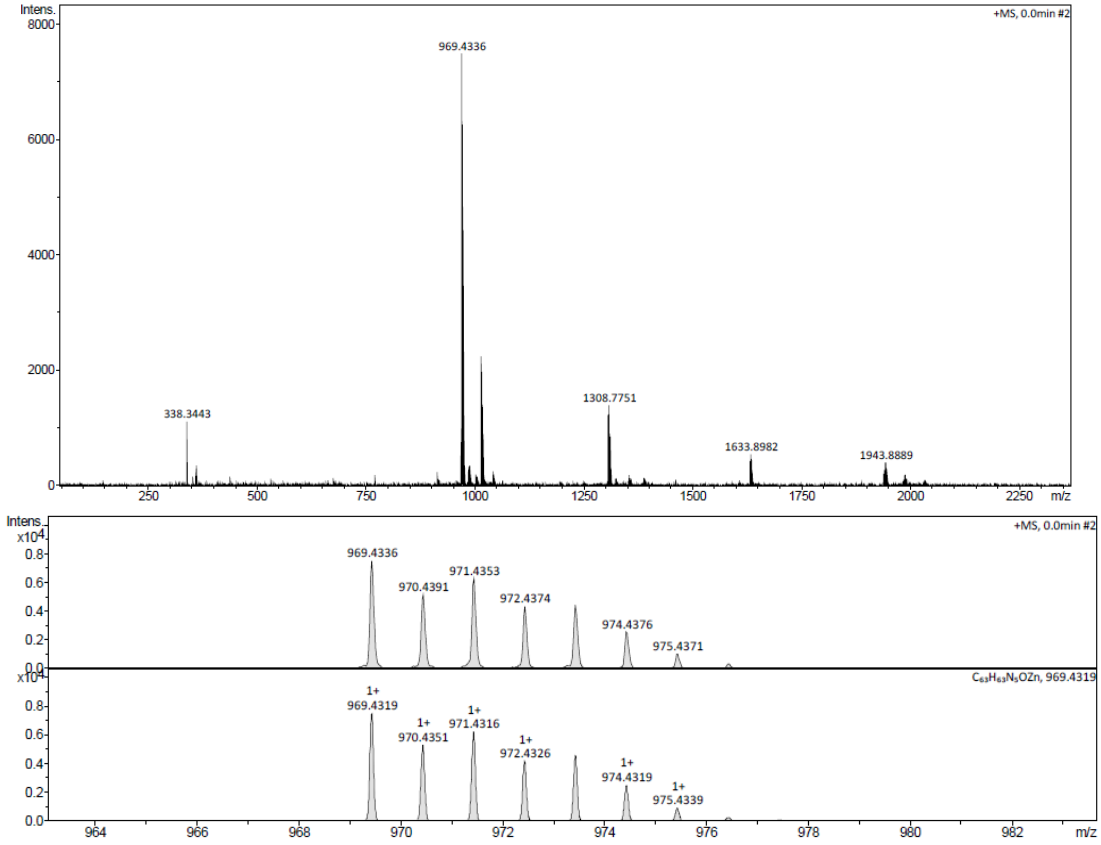

Figure 5.3. Top: ESI-MicroTOF mass spectrum of zinc-enaminoketo-porphyrin (**7**); calculated for [**7**]$^{+}$, 969.4319; found 969.4336. Bottom: experimental (top) and calculated (bottom) isotopic distribution of the molecular ion peak [**7**]$^{+}$.

No significant spectroscopic differences were found in the NMR characterization of **6** and **7**, apart for the expected disappearance, in **7**, of the internal pyrrolic proton signal. The aromatic region of the ^{1}H NMR of **7** ($CDCl_3$, 10% pyridine-d_5) is reported in Figure 5.4. All the resonances have been correctly attributed by means of 2D correlation techniques (COSY, HSQC, and NOESY) and showed the correct relative integration. Pyrrolic protons Ha resonate at 9.19 ppm, strongly deshielded by the aromatic ring current of the proximate benzene ring, an established NMR fingerprint of the cyclization reaction.[3a] The amino protons Hk and Hk' resonate at 8.72 and 5.44 ppm as two broad signals coupling to each other; the big chemical shift difference suggests that one proton (Hk) is strongly hydrogen-bonded to the carbonyl oxygen atom, while the other one is shielded by the vicinal aryl group.

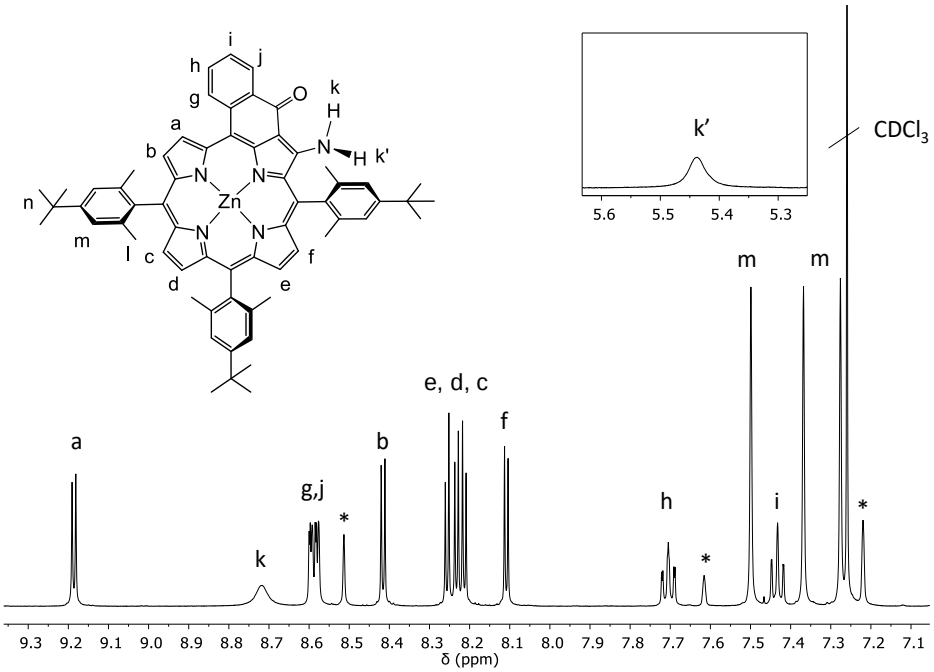

Figure 5.4. ^{1}H NMR spectrum ($CDCl_3$, 10% pyridine-d_5, aromatic region) of **7**. Pyridine signals are labeled with an asterisk.

The absorption spectrum of **6** and **7** are shown in Figure 5.5.[3a] Compared to the absorption spectrum of a *meso*-substituted porphyrin (observed in all the porphyrin derivates shown in the previous chapters), in **6** and **7** the extended delocalization of the aromatic porphyrin skeleton is reflected in the general red-shift of the absorption bands, and in the decreased intensity (with ε of *ca.* 100 000 $M^{-1}cm^{-1}$) and splitting or broadening of the Soret band.

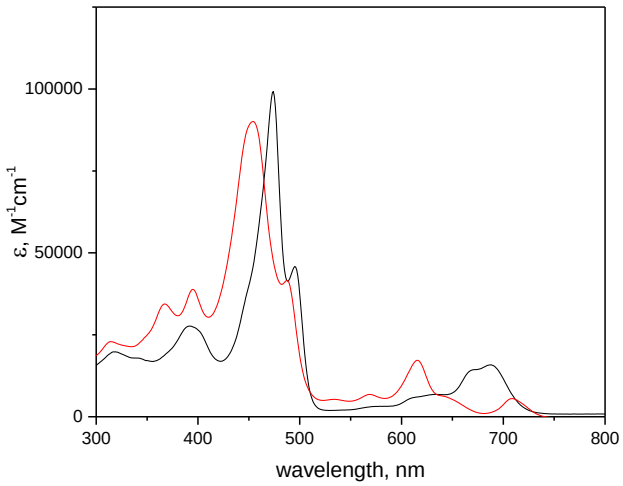

Figure 5.5. UV-visible absorption spectra (CH_2Cl_2) of enaminoketo-porphyrins **6** (red line) and **7** (black line).

Porphyrin **7** was then reacted with palladium (II) acetate to prepare the Pd^{II}-linked dimer **ZnPdZn** (Scheme 5.4). The reaction proceeds in toluene at 100°C for 12 hours, affording the desired product, upon purification by column chromatography, in good yield (85%).

Alternatively, dimer **ZnPdZn** could be prepared by first reacting the freebase enaminoketo porphyrin **6** with Pd(II) acetate, leading to the formation of the freebase Pd^{II}-linked dimer, and subsequent metallation with Zn acetate. The first procedure was more efficient: the presence of the Zn cation inside the porphyrin ring, preventing any undesired insertion of the Pd^{II} cation in the porphyrin macrocycle, allowed to increase the reaction temperature, thus leading to a faster formation of the **ZnPdZn** dimer and in higher yields.

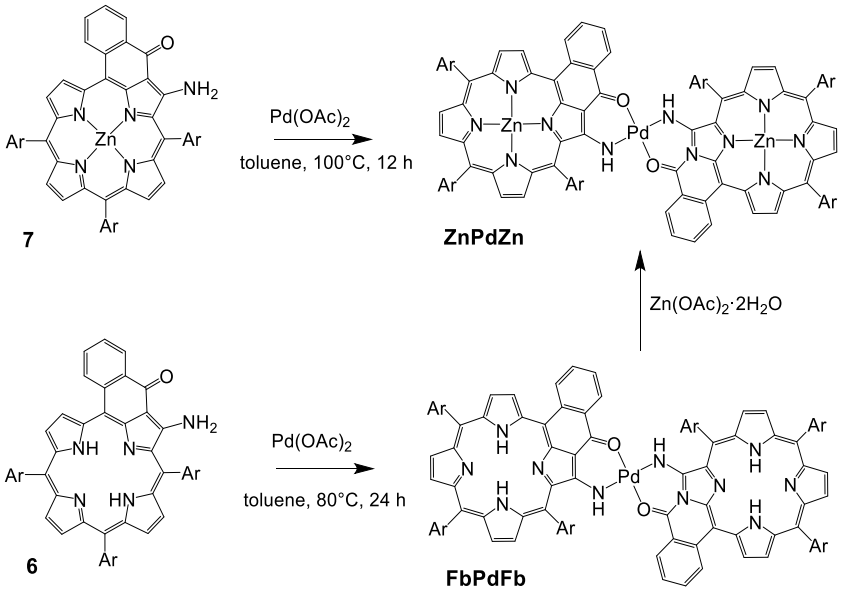

Scheme 5.4. Preparation of the Pd^{II}-linked dimer **ZnPdZn**.

Dimers **ZnPdZn** and **FbPdFb** were fully characterized by NMR (^{1}H and ^{13}C, 1D and 2D), UV-vis spectroscopy, and high-resolution MALDI-TOF mass spectrometry. As for the porphyrin monomers, the two dimers present very similar spectroscopic features, therefore only the characterization of **ZnPdZn** will be described in detail. The MALDI-TOFF mass spectrum of **ZnPdZn** (Figure 5.6) shows the molecular-ion peak ([**ZnPdZn**]$^{+}$), displaying the correct isotopic distribution, at m/z 2046.716 (calculated 2046.754).

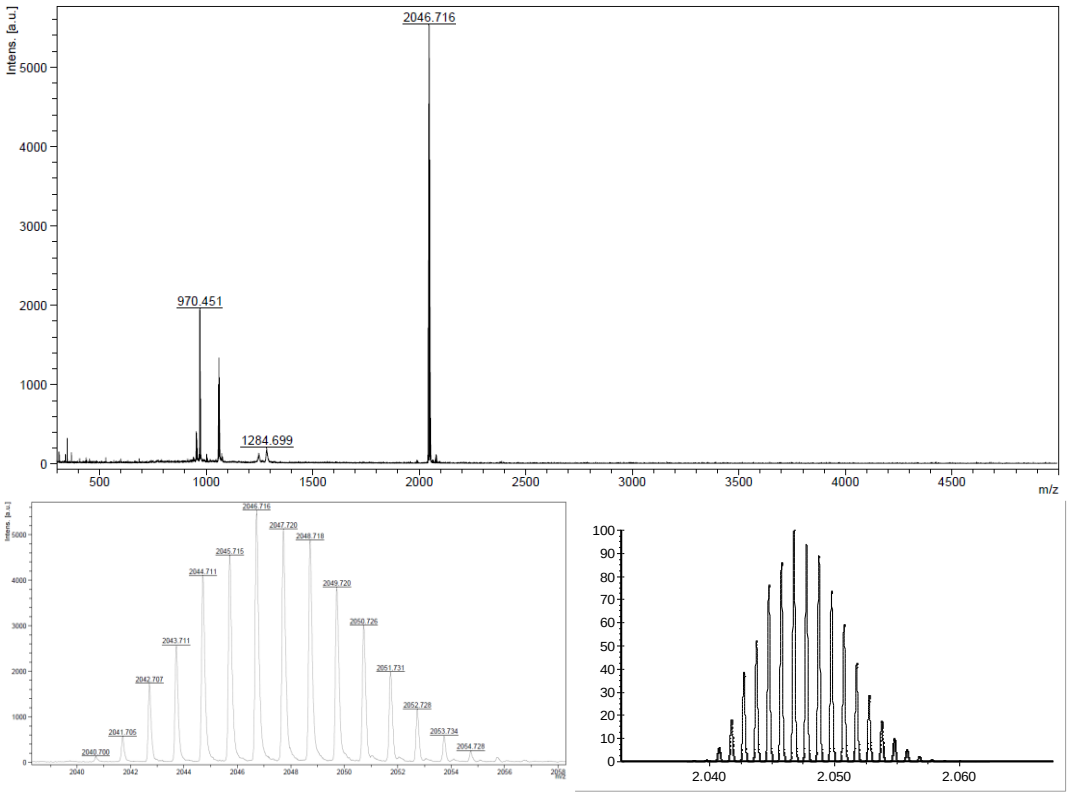

Figure 5.6. Top: MALDI-TOF (m/z) (positive mode) mass spectrum of dimer **ZnPdZn**; calculated for ([**ZnPdZn**]$^{+}$): 2046.754; found 2046.716. Bottom: experimental (left) and calculated (right) isotopic distribution of the molecular ion peak [**ZnPdZn**]$^{+}$.

As observed in the previously reported dimers,[3] the ^{1}H NMR spectrum of **ZnPdZn** presents a unique and well-resolved set of signals, consistent with the presence of two magnetically equivalent porphyrin units, confirming the formation of only one isomer (*cis* or *trans*). All the resonances, showing correct relative integration, were unambiguously attributed by means of 2D correlation experiments. Coordination to the Pd^{II} cation induces a slight up-field shift of the β-pyrrolic resonances of the Zn-porphyrin. This is particularly marked for proton Hf, exposed to the shielding cone of the adjacent aryl group (A labeled in Figure 5.7), whose rotation is now prevented by the structural rigidity entailed by the complexation of the enaminoketone. No evidence of the configurational geometry of the complex (*cis* or *trans*) could be found in the ^{1}H NMR spectrum of the dimer. ROESY experiments unambiguously allowed structural determination: HH NOE cross signals (highlighted in Figure 5.8) were observed between two proton Hj of the cyclized phenyl and protons Hm, Hl and Hn of the *meso*-aryl group A, of the adjacent porphyrin.

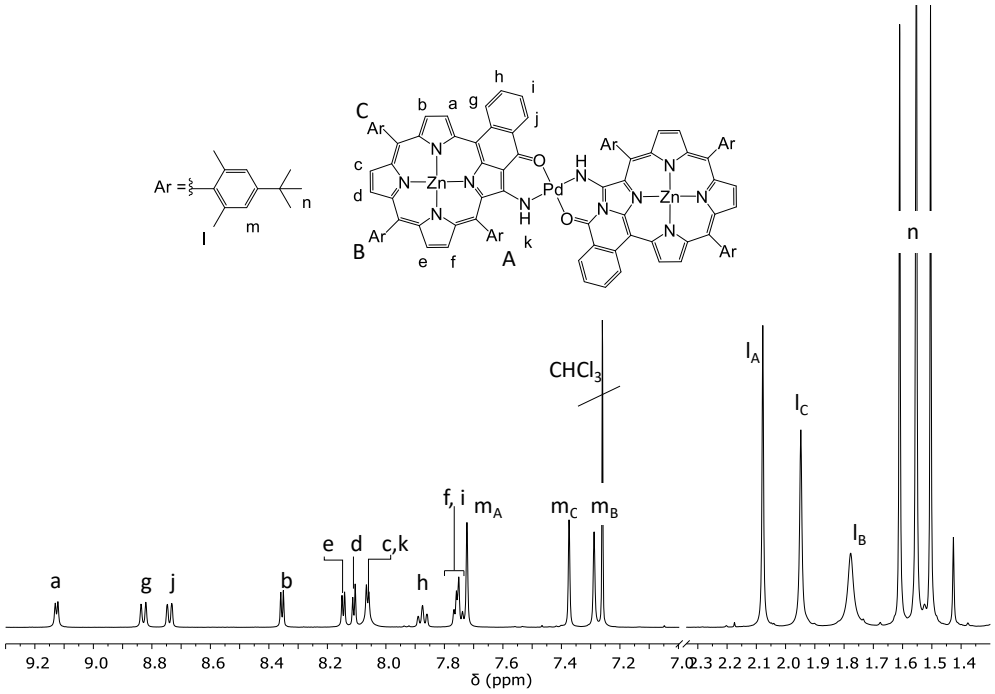

Figure 5.7. ^{1}H NMR ($CDCl_3$, 10% pyridine-d_5, aromatic region) of **ZnPdZn**.

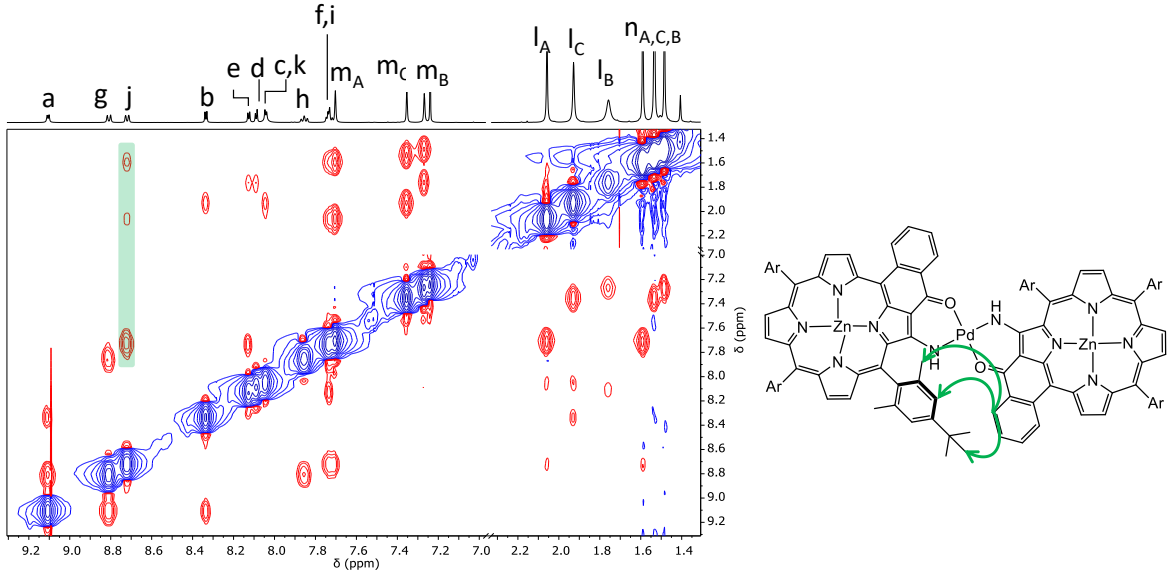

Figure 5.8. HH-ROESY spectrum ($CDCl_3$, 10% pyridine-d_5) of **ZnPdZn.**

The absorption spectrum of **ZnPdZn** (Figure 5.9) shows spectral features indicative of the interaction introduced between the two aromatic rings through the connecting metal: compared to the electronic spectrum of monomer **7**, a bathochromic shift of 10-20 nm is observed for all the absorption maxima, together with an increase of the extinction molar coefficient of the lower band. Similarly to previously reported dimers, **ZnPdZn** is not emitting at room temperature.

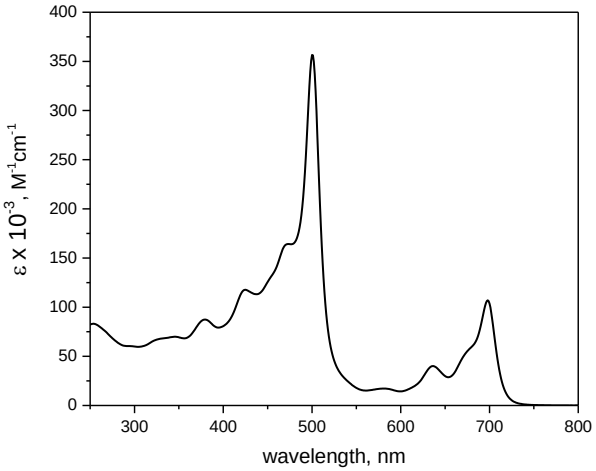

Figure 5.9. UV-visible absorption spectrum (CH_2Cl_2) of **ZnPdZn**.

5.2.2 Higher-order Supramolecular Systems

As previously observed, from a supramolecular assembling view-point, dimer **ZnPdZn** displays all the features (*i.e.*, rigid and relatively coplanar disposition of the zinc-porphyrin components, two Zn^{II} anchoring points, and sufficient inertness of the exocyclic metal coordination bonds) required to be used as building unit for the construction of higher order sandwich-like architectures. Concerning the inertness and stability of the bridging coordination bonds, few considerations could be pointed out: i) **ZnPdZn** can be purified by column chromatography without any risk of decomposition; ii) the freebase dimer was efficiently metallated by treatment with an excess of zinc acetate, confirming that the presence of Zn^{II} cations is not perturbing the coordination sphere around the Pd(II) center; and iii) upon addition of an excess of pyridine to **ZnPdZn** (a potential competitive ligand for the coordination to Pd(II)), possible undesired scrambling phenomena do not occur. All these observations confirm the possibility to use **ZnPdZn** as inert platform in the modular metal-mediated assembling of higher order supramolecular systems.

The reactivity of **ZnPdZn** toward a series of linear ditopic N-donor ligands (pyrazine, 4,4'-bipyridine (**4,4'BiPy**), and a 5,15-(4-pyridyl)-10,20-(phenyl)-porphyrin (***trans*DPyP**), see Scheme 5.5), was therefore studied and monitored by ^1H NMR spectroscopy.

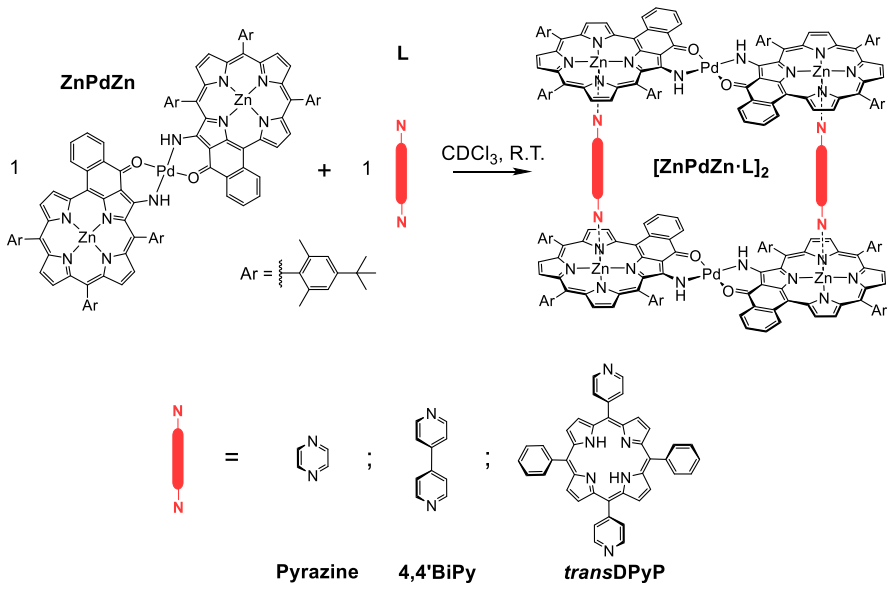

Scheme 5.5. Self-assembling reaction of **ZnPdZn** with different *trans*-dipyridyl ligands (**L**).

Addition of less than stoichiometric amounts of **4,4'BiPy** to a $3x10^{-3}$M $CDCl_3$ solution of **ZnPdZn** induces the appearance of some relatively broad signals (Figure 5.10). In particular, two new resonances are found at 5.27 and 3.72 ppm (attributed to the coordinated pyridyl ligands, see below) whose position (δ) is not affected by the stoichiometry of the reaction. When the 1:1 ratio between the zinc-porphyrin dimer and **4,4'BiPy** is reached, only one set of quite sharp resonances is observed, suggesting the complete formation of the intended system.

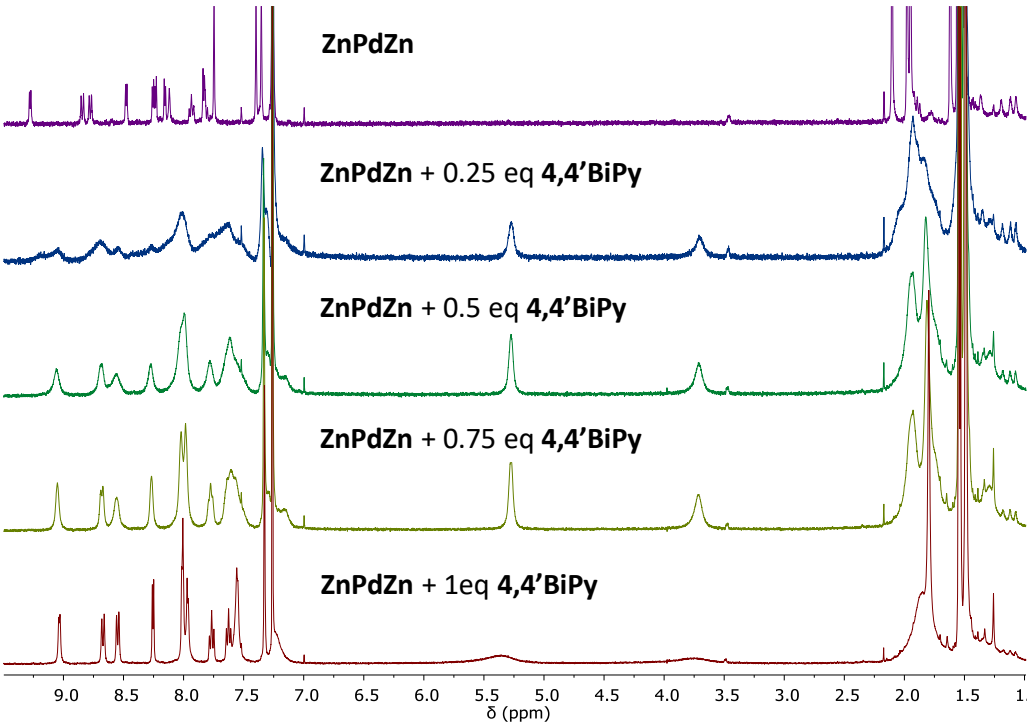

Figure 5.10. ^{1}H NMR ($CDCl_3$) titration of **ZnPdZn** with 4,4'-bipyridine (**4,4'BiPy**).

The final spectrum with the complete signal assignment (done by means of combined 2D NMR experiments) is shown in Figure 5.11.

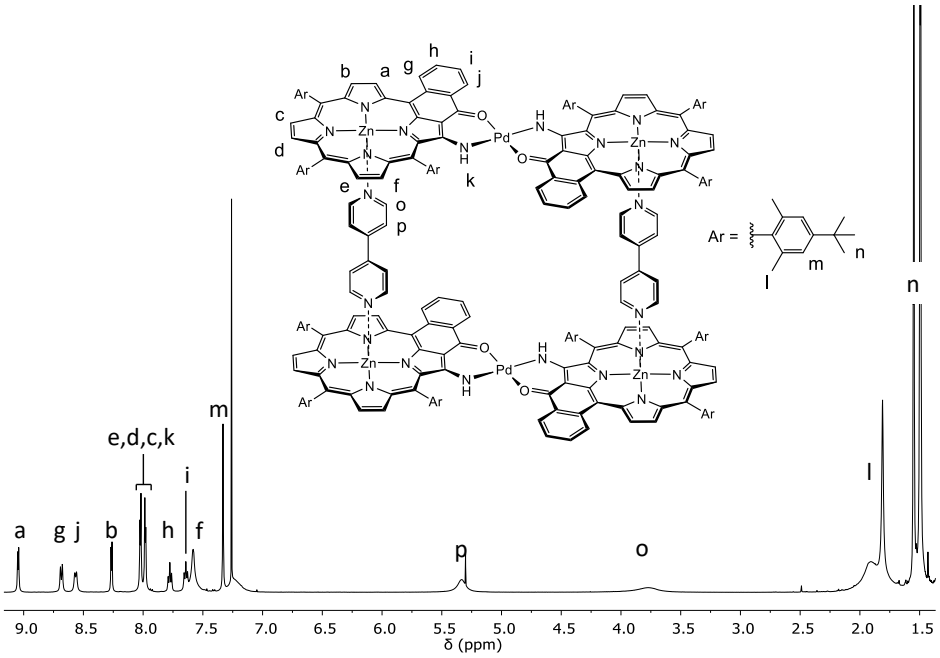

Figure 5.11. ^{1}H NMR ($CDCl_3$) spectrum of **[ZnPdZn·4,4'BiPy]$_2$**.

Complete NMR characterization (^{1}H and ^{13}C, 1D and 2D NMR experiments), clearly suggest the formation of the sandwich-like supramolecular adduct **[ZnPdZn·4,4'BiPy]$_2$**, consisting of two **ZnPdZn** dimers connected face-to-face by two **BiPy** ligands, by axial coordination to the zinc-porphyrins (Scheme 5.5). At room temperature, most of the resonances are sharp and well-resolved, except for the signals of the bridging bipyridine ligands and the aryl substituents of the zinc-porphyrin platforms. Axial coordination of the bipyridine is unequivocally indicated by the large upfield shift of Ho and Hp resonances (found at 3.7 and 5.3 ppm, respectively) due to the combined ring currents of both porphyrin dimers. A single set of signals for **ZnPdZn** is detected (slightly upfield shifted as compared to free **ZnPdZn**), in agreement with the proposed cofacial disposition of the two metalloporphyrin dimers. The overall NMR features, also in line with what observed for the previously discussed sandwich-like supramolecular assemblies, indicate that at ambient temperature, the equilibrium between **ZnPdZn** and **4,4'BiPy** to yield **[ZnPdZn·4,4'BiPy]$_2$** is totally shifted toward the 2:2 product (with an "all or nothing" process[4a,13]), suggesting that there must be considerable cooperativity between the coordination of the first and the second bridging ligands. By combination of a *trans*-dipyridyl ligand with the **ZnPdZn** dimer, two structural isomers could form, as depicted in Scheme 5.6.

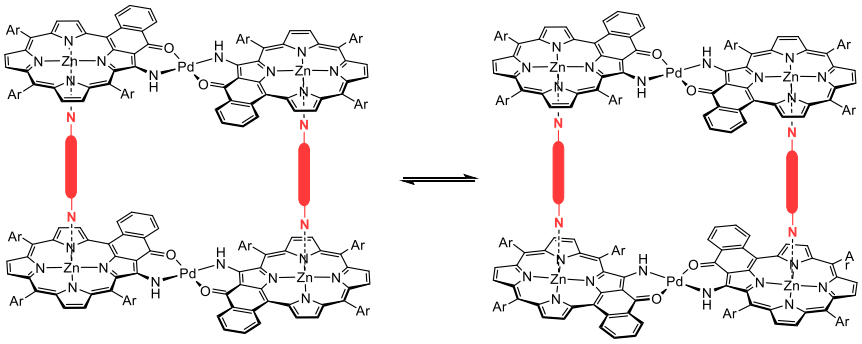

Scheme 5.6.

The NMR characterization of **[ZnPdZn·4,4'BiPy]$_2$** revealed the presence of only one set of signals and no experimental evidence (from ROESY or NOESY correlation experiments) of stereoselective formation of one of the isomers was found. Lowering the temperature down to -50° C, produced a general broadening and complication of the resonance patterns (see Figure A5.15 in the Appendix to Chapter 5). Most likely, both the stereoisomers get formed and undergo a fast interconversion process. For simplicity, in all the chapter, only one structural isomer is shown in the depiction of the supramolecular assemblies.

Analogous results were obtained by combination of **ZnPdZn** with pyrazine or *trans-di*pyridyl-porphyrin ***trans*DPyP**, thus assessing the formation of the corresponding sandwich-like assemblies **[ZnPdZn·Pyrazine]$_2$** and **[ZnPdZn·*trans*DPyP]$_2$** (Figure 5.12). Given the short N-N distance spanned by the pyrazine ligand, concomitant to the presence of relatively bulky *meso* aryl substituents on the metallo-porphyrin platforms, the sole formation of a sandwich-like discrete assembly, was indeed not granted.

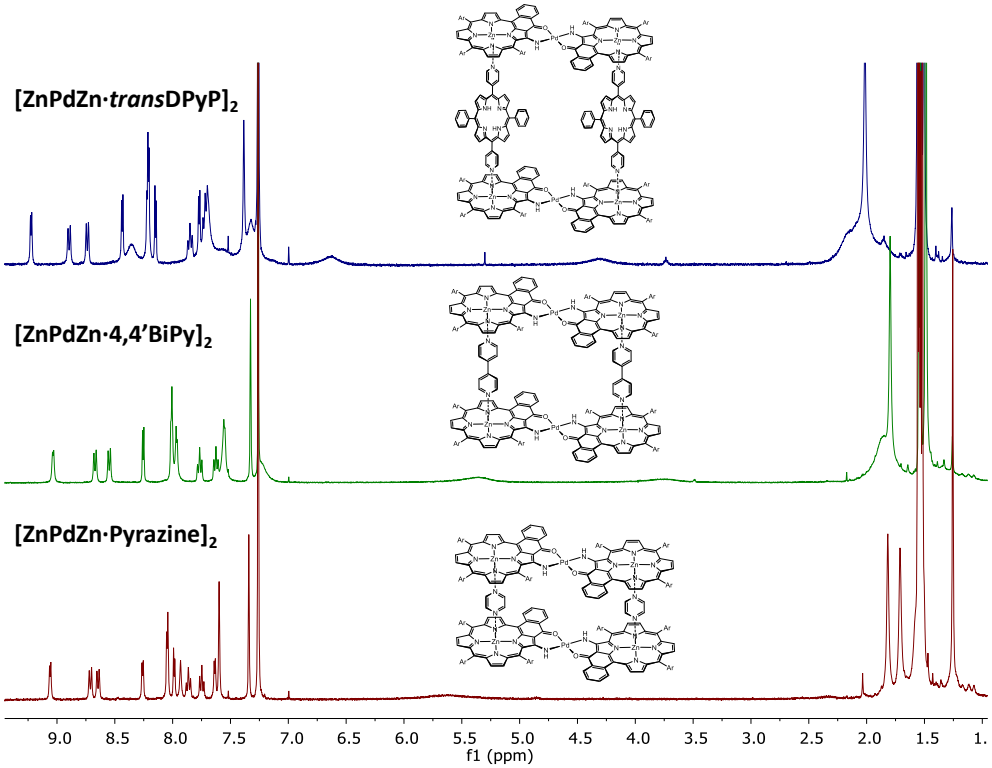

Figure 5.12. ^{1}H NMR ($CDCl_3$) spectra of **[ZnPdZn·*trans*DPyP]$_2$** (top), **[ZnPdZn·4,4'BiPy]$_2$** (middle), and **[ZnPdZn·Pyrazine]$_2$** (bottom).

Efforts are currently being done in order to grow single crystals suitable for X-ray analysis.

^{1}H-NMR Diffusion-Ordered Spectroscopy (DOSY) was used to gain additional information on the size of the assemblies. In Figure 5.13 the overaly of the 2D DOSY maps of the assemblies and the free **ZnPdZn** dimer is reported. For all the systems studied, only one diffusing species was found in solution (in addition to the faster diffusing small solvent molecules). In particular, for the assemblies, signals belonging to the dimer and to the bridging ligand are aligned to a unique self-diffusion coefficient. Just by a qualitative look, it is possible to appreciate how from top to bottom the analyzed compounds

are aligned to decreasing self-diffusion coefficient, consistently with their different molecular dimension.

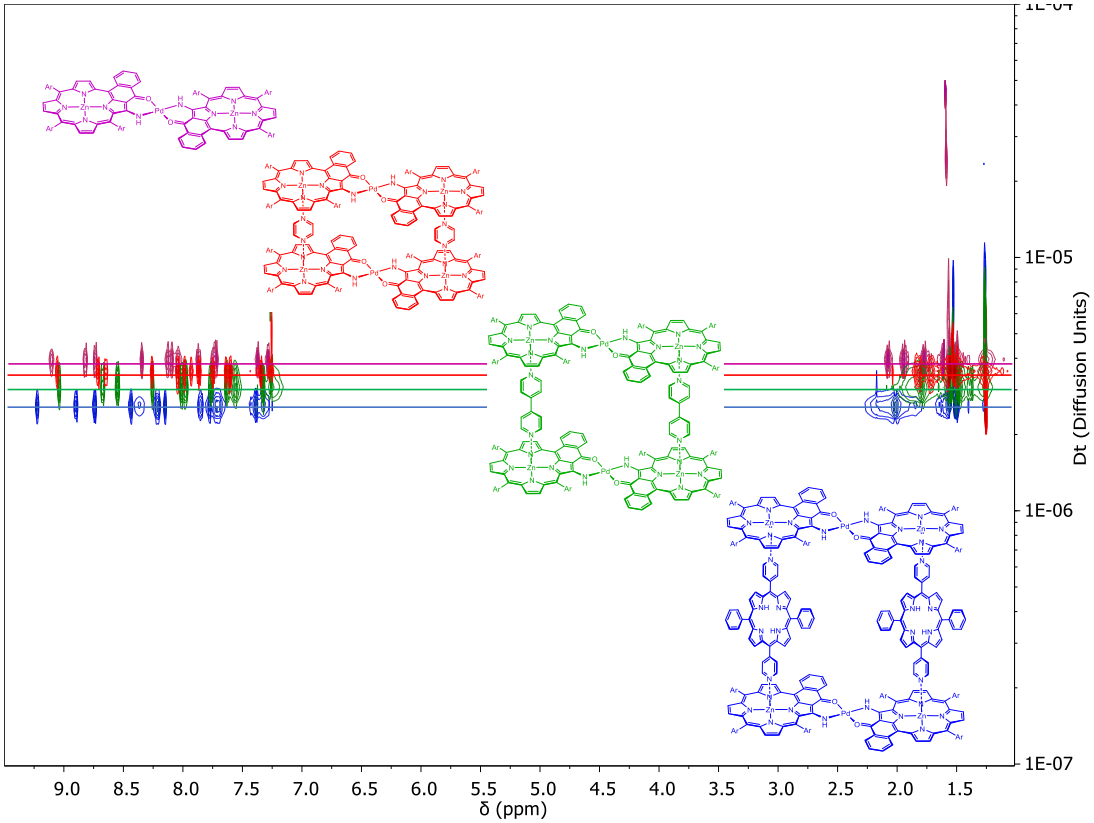

Figure 5.13. Overaly of the 2D ^{1}H-DOSY maps (Bayesian transform, $CDCl_3$) of **ZnPdZn** (purple), **[ZnPdZn·Pyrazine]$_2$** (red), **[ZnPdZn·4,4'BiPy]$_2$** (green) and **[ZnPdZn·*trans*DPyP]$_2$** (blue).

A summary of the diffusion coefficient values, D_t (see Appendix 1), obtained for the various compounds, is listed in Table 5.1, along with the hydrodynamic radii and volumes, calculated from the Stokes-Einstein equation within the spherical approximation ($D_t = \frac{k_B T}{6\pi\eta r_H}$).

Table 5.1. Experimental diffusion coefficient values, D_t, derived from the ^{1}H-NMR DOSY experiments; hydrodynamic radii, r_H, and hydrodynamic volumes, V_H, calculated from the Stokes-Einstein equation.

Compound	D_t (cm^2s^{-1})[a]	r_H (Å)[b]	V_H (Å^3)[c]
ZnPdZn	3.84 x 10^{-6}	10.6	4970
[ZnPdZn·pyrazine]$_2$	3.45 x 10^{-6}	11.8	6860
[ZnPdZn·4,4'BiPy]$_2$	3.08 x 10^{-6}	13.2	9630
[ZnPdZn·*trans*DPyP]$_2$	2.56 x 10^{-6}	15.9	16800

[a] $D_t/10^{-10}$ m^2 s^{-1}. [b] calculated from Stokes-Einstein ($\eta_{chloroform}$ = 5.37 x10^{-4} N m^{-2} s, at 25 °C). [c] $V_H = {}^{4}/_{3}\pi r_H^3$.

A comparison between the D_t values can be done on the basis of the volume defined by each system, as qualitative depicted in Chart 5.3. Going from the free dimer **ZnPdZn** – smaller and thus faster diffusing – to **[ZnPdZn·*trans*DPyP]$_2$**, larger and slower diffusing – a decreasing trend of the diffusion coefficient value is observed, in agreement with what expected. The difference in the hydrodynamic volumes of **[ZnPdZn·Pyrazine]$_2$** and **[ZnPdZn·4,4'BiPy]$_2$** is smaller than what may be expected by considering the N-N relative distances featured by the series of bridging ligands. The same consideration arises when comparing the V_H values calculated for of **ZnPdZn** and **[ZnPdZn·Pyrazine]$_2$**. This may be explained by the fact that in all of the three systems, the **ZnPdZn** unit has the predominant influence on the overall dimensions attained by the assemblies, thus contributing mostly at defining the diffusing spherical volume. Differently, system **[ZnPdZn·*trans*DPyP]$_2$**, for which the length spanned by the ***trans*DPyP** pillar ligand is more comparable to that defined by the **ZnPdZn** lateral extension, a significant increase of the hydrodynamic volume is observed. These data quite confidently confirm the formation of the proposed supramolecular structures.

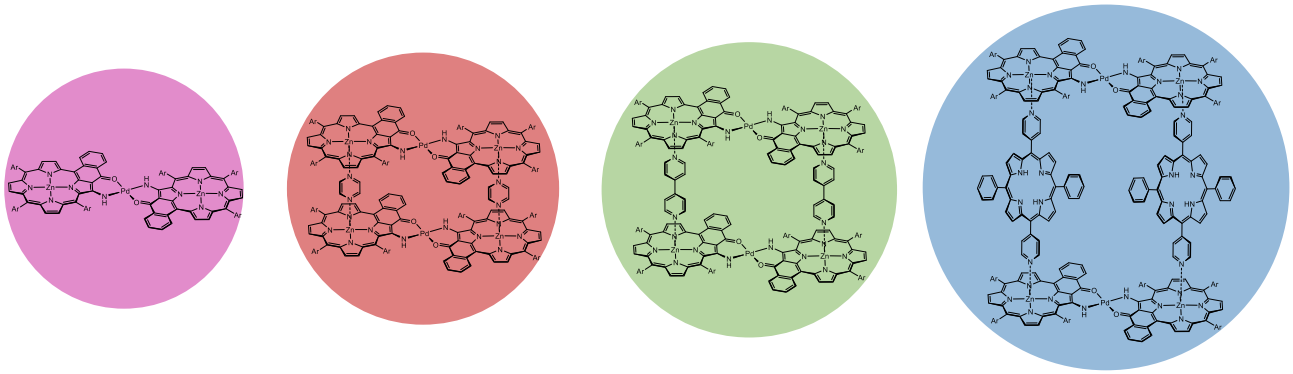

Chart 5.3.

A preliminary photophysical characterization of the system **[ZnPdZn·*trans*DPyP]$_2$** was also performed, to investigate whether new intercomponent properties occur in the assembly. The study was carried out by comparison with model compounds, representative of the individual components, **ZnPdZn** and ***trans*DPyP**. As reference for the dimer, a solution of **ZnPdZn** with an excess of pyridine (**ZnPdZn·Py**) was used. Coordination of pyridine induces, in the absorption spectrum, a decrease of the intensity and a 4 nm red shift, of the band at 500 nm, together with the disappearance of a shoulder absorption around 670 nm, and a slight increase of the absorption at 700 nm. These spectral features can be considered as experimental proof of the coordination of a pyridyl ligand to the Zn-porphyrin dimer and allowed to evaluate the stability of the assembly **[ZnPdZn·*trans*DPyP]$_2$** (see below).

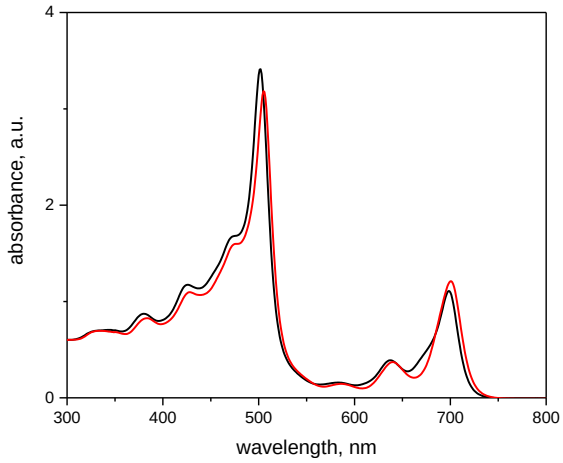

Figure 5.14. Absorption spectra of CH_2Cl_2 solution of **ZnPdZn** before (black) and after (red) the addition of an excess of pyridine.

The absorption spectrum of the assembly **[ZnPdZn·*trans*DPyP]$_2$** is, in good approximation, the superimposition of the spectra of the building units **ZnPdZn·Py** and ***trans*DPyP** (Figure 5.15). In almost the whole spectral window, the contribution of the Zn-porphyrin dimer is predominant; however, selective excitation of the freebase unit is feasible at 420 nm, thanks to the strong absorption of the Soret band. Upon dilution of a **[ZnPdZn·*trans*DPyP]$_2$** solution, spectral changes, consistent with the break of the pyridyl-Zn coordination bond, are observed: i) the rise of a shoulder band at 671 nm, and ii) the blue shift and increased intensity of the band at 505 nm. The system is hence completely assembled in solution for concentration higher than $5x10^{-5}$ M, hinting a stability similar to the analogous assembly built on **1Zn** (shown in Chart 5.1).[1] To confirm this, more informative association-constant measurements of ***trans*DPyP** with **ZnPdZn** (or a reference mono-coordinating compound), should be performed.

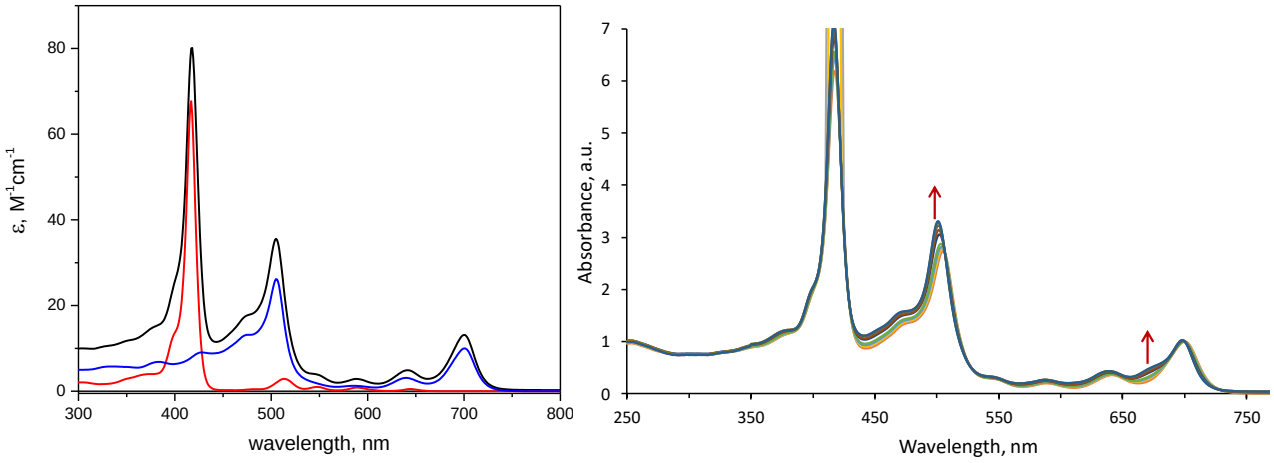

Figure 5.15. Left: Absorption spectra (CH_2Cl_2) of **[ZnPdZn·*trans*DPyP]$_2$** (black), **ZnPdZn·Py** (blue) and ***t*DPyP** (red). Right: absorption spectra (CH_2Cl_2) of **[ZnPdZn·*trans*DPyP]$_2$**, recorded in progressive diluted solutions.

As anticipated dimer **ZnPdZn** is not emitting at room temperature, while the freebase ***trans*DPyP** shows an intense fluorescence peaking at 652 and 722 nm, with a lifetime of 7.3 ns.[1] In **[ZnPdZn·*trans*DPyP]$_2$**, upon excitation of the freebase unit, a strong quenching (~ 90%) of the fluorescence is observed. Addition of an excess of pyridine, a competitive ligand that induces disassembling of the supramolecular system, completely and immediately restored the original emission intensity, suggesting that the quenching is strictly related to the coordination of the ligand to Zn-porphyrin dimer (Figure 5.16.a). As reference, the same experiment was performed on free ***trans*DPyP** (Figure 5.16.b) and a solution of **[ZnPdZn·*trans*DPyP]$_2$** 5x10^{-7} M (Figure5.16.c), concentration at which the system is mostly disassembled. In both cases, no significant variation of the emission spectrum was observed before and after the addition of pyridine.

These data unambiguously confirm that the quenching is correlated to the coordination of the *trans* dipyridyl porphyrin to the **ZnPdZn** dimer.

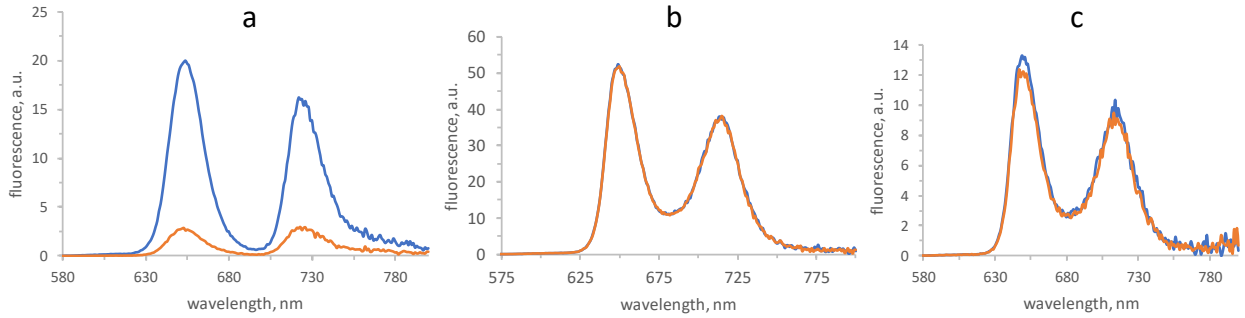

Figure 5.16. Comparison between the emission spectra (DCM) before (orange line) and after (blue line) the addition of a slight excess of pyridine in a solution of: a) **[ZnPdZn·*trans*DPyP]$_2$** 8x10^{-5} M; b) ***trans*DPyP**; c) **[ZnPdZn·*trans*DPyP]$_2$** 5x10^{-7} M.

Single photon counting experiments demonstrated that, in **[ZnPdZn·*trans*DPyP]$_2$**, the lifetime of the residual fluorescence lies below the instrumental resolution of the TC-SPC technique (i.e., < 250 ps) (see the Appendix) clearly indicating that, in the assembly, the emission lifetime is dramatically quenched compared with the ***trans*DPyP** model. A relatively long-lived component (lifetime, 1–7 ns), probably arising from impurities of unquenched ***trans*DPyP** porphyrin species, is observed, suggesting that the quenching is even stronger than what estimated by the emission spectra.

In order to visualize the thermodynamically favored photoinduced processes involved in the quenching mechanism of **[ZnPdZn·*trans*DPyP]$_2$**, it is useful to construct a simplified energy level diagram (Figure 5.17). Given the supramolecular nature of **[ZnPdZn·*trans*DPyP]$_2$**, its energy levels can be approximated as a simple superposition of those of the constituent Zn–porphyrin dimer and free-base chromophores.[14] The energy of the excited states of ***trans*DPyP** was taken from literature data,[1] while the energy of the singlet excited state of the **ZnPdZn** dimer was calculated from the absorption spectrum (the triplet excited state of **ZnPdZn** is omitted since for the moment we have no information about its energy). To this simple picture, a possible charge separated state (**ZnPdZn$^+$*t*DPyP$^-$**), where the Zn-porphyrin dimer is oxidized and the freebase reduced, must be considered. The energy of this state (~ 1.5 eV) in CH_2Cl_2 solution can be calculated from the measured redox potentials (Table 5.2).

Table 5.2. Electrochemical Data

	$E_{½}^{ox1}$	$E_{½}^{ox2}$	$E_{½}^{red1}$	$E_{½}^{red2}$
[ZnPdZn·*trans*DPyP]$_2$	0.64	0.75	-1.05	-1.21
ZnPdZn	0.57	0.71	-1.16	-1.27
*trans*DPyP			-1.13*	

All measurements were made in argon deaerated CH_2Cl_2 solutions at 298 K, 0.1 M TBA(PF_6) as supporting electrolyte, scan rate 200 mV/s, SCE as the reference electrode, ferrocene (0,46 V vs SCE) as the internal standard, and glassy carbon as the working electrode. $E_{½}$=(Epc+Epa)/2, where Epc and Epa correspond to the cathodic and anodic peak potentials, respectively. * from Ref. 1.

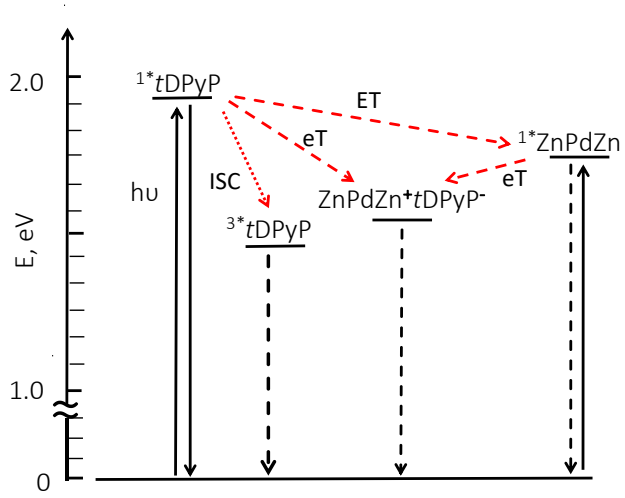

Figure 5.17. Energy-level diagram and photophysical processes for [ZnPdZn·*trans*DPyP]$_2$. For simplicity, the shorthand notation *t*DPyP and ZnPdZn are used to designate the energy levels and oxidation states of the free-base and Zn–dimer units. Energetically allowed energy transfer (ET) and electron transfer (eT) quenching pathways are indicated by dashed red arrows.

As shown in the diagram, three possible quenching mechanisms are available from the singlet excited state of the freebase unit: i) a photoinduced energy transfer process to the Zn-porphyrin unit, ii) an electron transfer process leading to the formation of the charge-separated state ZnPdZn^{+}*t*DPyP^{-}, or iii) an enhancement of the inter-system crossing (ISC) process induced by heavy atom effect of the Pd^{II} centres. As we can see, the charge separated state is accessible also from the singlet excited state of the Zn-porphyrin dimer. Time-resolved transient experiments are under investigation in order to understand the quenching mechanism, and clearly elucidate the overall photophysical behavior of the system.

5.3 Conclusions

The Pd-linked dimer **ZnPdZn** was successfully applied for the assembly of discrete sandwich-like supramolecular systems, obtained by axial coordination of different dipyridyl ligands to the Zn-porphyrin units. As demonstrated by the NMR-titration experiments, the assembling reaction is quantitative and follows the all-or-nothing process already observed in analogous supramolecular systems. DOSY experiments proved the formation of the designed structures, yielding diffusion coefficient in agreement with the different dimension of the assemblies. Changing the bridging ligand afforded to tune and control the dimensions of the cavity delimited by the cofacial porphyrin dimers and, in one case, to promote the occurrence of a fast intercomponent photoinduced process.

Indeed, these results demonstrate that the modular synthetic approach, validated for the assembling of supramolecular systems from the **1Zn** platform, can be also efficiently applied to dimer **ZnPdZn**. Given the peculiar electronic property these porphyrin dimer, this result, if combined with the versatility offered by the dimer synthesis, opens numerous interesting possibilities (such as tuning the photophysical properties by cleverly tailoring the dimer substituents and/or the connecting metal cation; extending the lateral dimension of the assembly by substituting the dimer with a trimer; or exploiting the electron density, strongly localized around the linking Pd^{II}-complex, for the selective uptake of electron deficient aromatic guests).

5.4 Experimental Section

Materials and Methods

^{1}H and ^{13}C NMR spectra were recorded on Bruker Avance 400, 500, or 600 MHz using $CDCl_3$ as solvent. ^{1}H and ^{13}C chemical shifts were referenced to the peak of residual non-deuterated solvents: δ = 7.26 ppm and 77.16 ppm, respectively. Multiplicity of the signals is addressed as follows: s = singlet, d = doublet, t = triplet, q = quartet, m = multiplet, br = broad. ESI-TOF MS experiments were performed with a Bruker daltonics microTOF spectrometer. MALDI-TOF mass spectra were obtained using dithranol as matrix with a Bruker Autoflex II equipped with a 337 nm laser. Elemental analyses were performed on a « Flash 2000 » apparatus from ThermoFisher Scientific for the simultaneous analysis of the C, H and N elements on about 1 mg (typical mass) of solid or liquid samples. UV–visible spectra were recorded on a CARY 5000 UV–vis–NIR spectrometer. Measurement of self-diffusion coefficients was performed on a BRUKER 600 MHz spectrometer-Avance III, equipped with a Bruker BBI probe developing a pulsed field gradient of 5.1 G/cm/A. Diffusion NMR data were acquired at 298 K using a Stimulated Echo pulse sequence with smoothed square bipolar z gradients in 34 increments. The duration of half gradients was of 1 ms while the diffusion time was optimized for each sample. A recycle delay of at least 4 s was respected between each scan. Processing was done with the automatic Bayesian transform processing of the MestReNova© software.[15] Steady-state and lifetime fluorescence measurements were recorded on a "Fluorolog FL3-22" spectrometer from HORIBA JobinYvon, using as excitation sources: a) a Xe lamp 450 W, continuous spectrum from 240 to 600 nm, for steady state measurements; b) a light-emitting diodes (NanoLED) for excitation at 370 nm (pulse: width 15-20 nm, pulse duration: 1 ns, repetition rate to be fixed between 10 kHz and 1 MHz), for lifetime measurements. Cyclic voltammetry measurements were carried out at room temperature in Argon purged CH_2Cl_2 containing 0.1 TBA(PF_6) in a classical three-electrode cell. The working electrode was a glassy carbon disk (GC, 3-mm diameter). The auxiliary and the pseudoreference electrode were Pt wires. All potentials were referenced to the ferricinium/ferrocene (Fc+/Fc) couple used as an internal standard.

The starting benzaldehyde derivatives 2-Bromo-5-*tert*-butyl-1,3-dimethylbenzene[16] and 4-*tert*-Butyl-2,6-dimethylbenzaldehyde[17] were synthesized following the published procedures. Porphyrin **2-5** were synthesized following procedures reported in a previous Ph.D Thesis.[12] Dichloromethane was distilled from calcium hydride and toluene from sodium/ benzophenone ketyl. Chromatographic separations were performed with Merck TLC silica gel 60 F254 and Kieselgel Si 60 (40–63 µm) and gel permeation with Bio-Beads S-X1 from Bio-Rad.

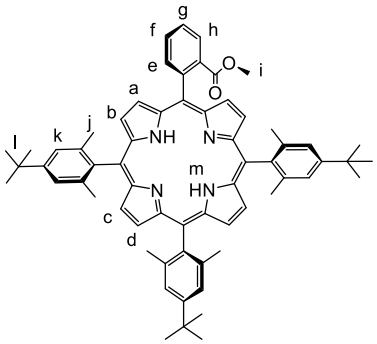

Porphyrin 2

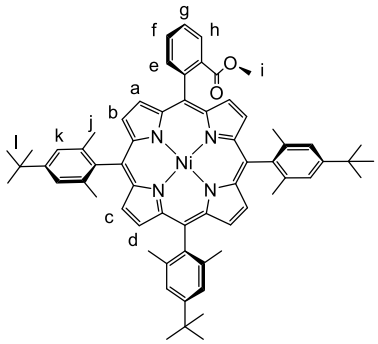

Porphyrin 3

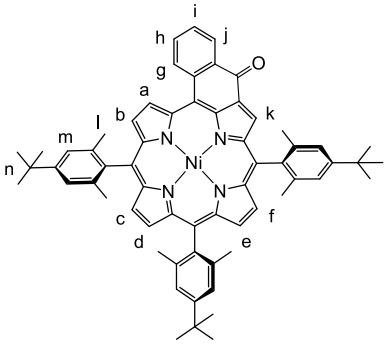

Porphyrin 4

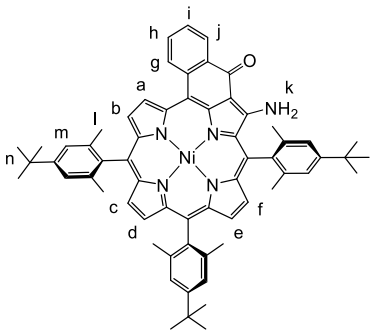

Porphyrin 5

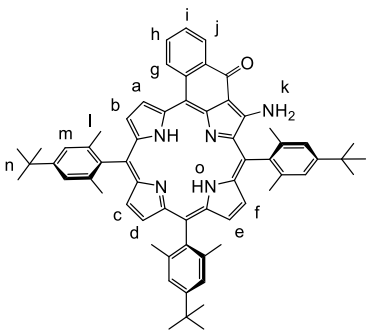

Porphyrin 6

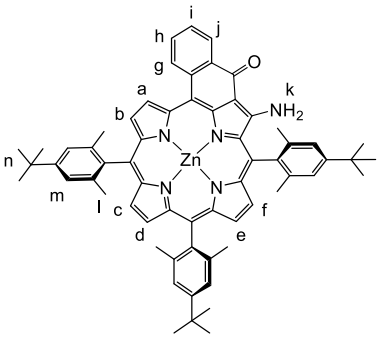

Porphyrin 7

5,10,15-Tris(4-*tert*-butyl-2,6-dimethylphenyl)-20-(2-carboxymethylphenyl)porphyrin [Porphyrin 2]

A chloroform solution (600 mL) of pyrrole (1.07 g, 16 mmol), 4-*tert*-butyl-2,6-dimethylbenzaldehyde (2.28 g, 12 mmol) and methyl 2-formylbenzoate (655 mg, 4 mmol) was purged with argon for 30 min. BF3OEt2 (5.7 mM) was added and the solution stirred at room temperature shielded from light for 2 h. p-chloranil (2.9 g, xx mmol) was added and the resulting solution was refluxed for 30 min. Once cooled down, the reaction mixture was filtered through a pad of alumina and solvent was removed under reduced pressure. Thin-layer chromatography of the crude product (cyclohexane/dichloromethane) showed it to be a mixture of the possible porphyrin isomers that were separated by silica-gel column chromatography (cyclohexane/dichloromethane). Yield: 21%.

^{1}H NMR (400 MHz, $CDCl_3$) δ (ppm): 8.69 – 8.54 (m, 8H, Ha-Hd), 8.37 (dd, *J* = 7.8, 1.5 Hz, 1H, He), 8.08 (dd, *J* = 7.5, 1.4 Hz, 1H, Hh), 7.90 – 7.73 (m, 2H, Hf, Hg), 7.47 – 7.39 (m, 6H, Hk), 2.80 (s, 3H, Hi), 1.99 (s, 3H, Hj), 1.89 (s, 6H, Hj), 1.87 (s, 6H, Hj), 1.81 (s, 3H, Hj), 1.58 (s, 27H, Hl), -2.45 (s, 2H, Hm).

(5,10,15-Tris(4-*tert*-butyl-2,6-dimethylphenyl)-20-(2-carboxymethylphenyl)porphyrinato)Nickel(II) [Porphyrin 3]

Porphyrin **2** (380 mg, 0.41 mmol) was dissolved in chlorobenzene (100 mL) and refluxed with an excess of nickel acetate (180 mg, 0.74 mmol) for 3 hours under argon atmosphere. After cooling the solution was filtered through a short alumina column and the solvent removed under reduced pressure. The pure compound was obtained as a red powder by precipitation with methanol from a dichloromethane solution. Yield: 382 mg (95 %).

^{1}H NMR (500 MHz, $CDCl_3$) δ (ppm): 8.55 – 8.46 (m, 8H, Ha-Hd), 8.30 – 8.27 (m, 1H, Hf), 8.09 – 8.04 (m, 1H, Hg), 7.81 – 7.75 (m, 2H, He, Hh), 7.40 – 7.31 (m, 6H, Hk), 2.83 (s,3H, Hi), 1.90 – 1.84 (m, 12H, Hj), 1.81 (s, 6H, Hj), 1.53 (s, 27H, Hl).

Ni- ketoporphyrin [Porphyrin 4]

A solution of porphyrin **3** (720 mg, 0.73 mmol) and lithium hydroxide (4.23 mg, 176 mmol) in a dioxane/water mixture (150 mL, 8/2) was heated to reflux for 6 hours under argon. After cooling, dichloromethane (50 mL) was added to the mixture, the aqueous phase was removed and the remaining organic solvents were evaporated. The residue was purified by column chromatography (silica gel, dichloromethane, 1% acetic acid). To a solution of the crude acid (290 mg, 0.3 mmol) in dry toluene (100 mL) oxalyl chloride (~400 eq) was added and this mixture was stirred for 2 hours at room temperature. The solution was partially evaporated to remove the excess of oxalyl chloride. $SnCl_4$ (1 mL, 8.54 mmol, 28 eq) was then added and the solution stirred at room temperature for 30 minutes. The solution was diluted with dichloromethane (200 mL) and the excess of Lewis acid was neutralized with a sufficient amount of aqueous NaOH. The organic phase was washed several times with water, dried with anhydrous sodium sulfate and the solvent removed under reduced pressure. Precipitation from dichloromethane/methanol of the crude compound, filtration and drying under vacuum afforded pure product as a green powder. Yield: 592 mg (85%).

^{1}H NMR (400 MHz, $CDCl_3$) δ (ppm): 9.21 (d, *J* = 5.1 Hz, 1H, Ha), 8.97 (s, 1H, Hk), 8.47 – 8.42 (m, 2H), 8.27 (dd, *J* = 5.0, 1.6 Hz, 2H), 8.21 (d, *J* = 4.9 Hz, 1H), 8.17 (d, *J* = 4.9 Hz, 1H), 8.00 (d, *J* = 7.9 Hz, 1H), 7.69 (t, *J* = 7.5 Hz, 1H, Hh), 7.44 (t, *J* = 7.5 Hz, 1H, Hi), 7.36 (s, 2H, Hm), 7.32 (s, 4H, Hm), 1.94 (s, 6H, Hl), 1.90 (s, 12H, Hl), 1.52 (s, 18H, Hn), 1.49 (s, 9H, Hn).

Ni-enaminoketoporphyrin [Porphyrin 5]

A solution of porphyrin **4** (260 mg, 0.27 mmol), 4-amino-4H-1,2,4-triazole (277 mg, 3.3 mmol, 12 eq) and sodium hydroxide (1.36 g, 34 mmol, 125 eq) in a toluene/ethanol mixture (90 mL, 5/1) was heated to reflux for 1.5 hours. After cooling, the mixture was diluted with dichloromethane (70 mL) and washed twice with water (2 x 40 mL). The organic phase was then dried over Na_2SO_4 and solvent evaporated under reduced pressure. The residue was purified by column chromatography (silica gel, dichloromethane) and the pure product was isolated by recrystallization from dichloromethane/methanol. Yield 240 mg (92 %).

^{1}H NMR (500 MHz, $CDCl_3$) δ (ppm): 9.18 (d, *J* = 5.0 Hz, 1H, Ha), 8.58 (dd, *J* = 7.8, 1.4 Hz, 1H, Hj), 8.51 (s, 1H, Hk), 8.50 (d, *J* = 5.0 Hz, 1H, Hb), 8.28 (d, *J* = 4.8 Hz, 1H, Hd), 8.24 (d, *J* = 4.8 Hz, 1H, He), 8.21 – 8.17 (m, 2H, Hc, Hg), 8.14 (d, *J* = 4.7 Hz, 1H, Hf), 7.74 (ddd, *J* = 8.3, 7.1, 1.5 Hz, 1H, Hh), 7.52 (td, *J* = 7.5, 1.0 Hz, 1H, Hi), 7.49 (s, 2H, Hm), 7.36 (s, 2H,Hm), 7.32 (s, 2H, Hm), 5.42 (s, 1H, Hk'), 1.97 (s, 6H, Hl), 1.95 (s, 6H, Hl), 1.92 (s, 6H, Hl), 1.54 – 1.52 (m, 18H, Hn), 1.50 (s, 9H, Hn).

Freebase enaminoketoporphyrin [Porphyrin 6]

Porphyrin **5** (210 mg, 0.22 mmol) was dissolved in 70 mL of trifluoroacetic acid/dichloromethane (7/1) and after the addition of 30 mL of H_2SO_4 the reaction mixture was stirred at room temperature for 7 hours. The solution was then diluted with dichloromethane (100 mL) and the acid neutralized with a sufficient amount of aqueous NaOH solution. The organic phase was washed several times with water and then solvent removed under reduced pressure. The residue was purified by column chromatography (silica gel, dichloromethane/cyclohexane). Reprecipitation from dichloromethane/methanol and drying under vacuum afforded pure product as a green powder. Yield: 140 mg (70 %).

^{1}H NMR (500 MHz, $CDCl_3$) δ (ppm): 9.39 (d, *J* = 4.9 Hz, 1H, Ha), 8.92 (d, *J* = 5.0 Hz, 1H, Hk), 8.66 (d, *J* = 7.6 Hz, 2H, Hg, Hj), 8.58 (d, *J* = 4.9 Hz, 1H, Hb), 8.40 (d, *J* = 4.6 Hz, 1H, He), 8.31 (d, *J* = 4.5 Hz, 1H, Hd), 8.29 – 8.22 (m, 2H, Hc, Hf), 7.82 (t, *J* = 7.5 Hz, 1H, Hh), 7.62 – 7.54 (m, 3H, Hi, Hm), 7.43 (s, 2H, Hm), 7.39 (s, 2H, Hm), 5.59 (d, *J* = 4.8 Hz, 1H, Hk'), 1.96 (s, 6H, Hl), 1.95 – 1.92 (m, 12H, Hl), 1.58 (s, 18H, Hn), 1.55 (s, 9H, Hn), -0.67 (s, 2H, Ho).

^{13}C NMR (125 MHz, $CDCl_3$) δ (ppm): 181.43, 152.97, 151.18, 141.21, 138.84, 138.65, 138.27, 137.82, 137.52, 135.93, 134.81, 134.02, 131.70, 127.42, 126.55, 126.29, 124.15, 122.48, 119.84, 117.16, 112.10, 105.61, 35.03, 34.83, 34.81, 31.83, 31.80, 31.75, 22.13, 22.04, 21.54.

UV-vis (CH_2Cl_2): λ_{max} (ε, $M^{-1}cm^{-1}$) = 367 (34 650), 395 (39 100), 454 (90 100), 616 (17 540), 709 (5 950) nm.

ESI-MicroTOF (m/z) (positive mode) Exact mass calculated for $C_{63}H_{66}N_5O$ ([**6** + H]$^+$): 908.5262; found 908.5289.

Zinc (II)-enaminoketoporphyrin [Porphyrin 7]

A zinc(II) acetate (30 mg, 132µmol) ethanol solution (5 mL) was added to a chloroform solution (20 mL) of Porphyrin **6** (60 mg, 66 µmol) and stirred at room temperature for 2 hours. The reaction mixture was then filtered through a short alumina column and the pure product isolated by precipitation from dichloromethane/methanol. Yield: 62 mg (97 %).

^{1}H NMR (500 MHz, $CDCl_3$, 1% pyridine-d_5) δ (ppm): 9.19 (d, *J* = 4.7 Hz, 1H, Ha), 8.72 (s, 1H, Hk), 8.61 – 8.57 (m, 2H, Hg, Hj), 8.42 (d, *J* = 4.6 Hz, 1H, Hb), 8.26 (d, *J* = 4.4 Hz, 1H, He), 8.23 (d, *J* = 4.4 Hz, 1H, Hd), 8.21 (d, *J* = 4.4 Hz, 1H, Hc), 8.11 (d, *J* = 4.4 Hz, 1H, Hf), 7.71 (ddd, *J* = 8.3, 7.0, 1.6 Hz, 1H, Hh), 7.50 (s, 2H, Hm), 7.43 (ddd, *J* = 8.2, 7.1, 1.0 Hz, 1H, Hi), 7.37 (s, 2H, Hm), 7.28 (s, 2H, Hm), 5.44 (s, 1H, Hk'), 1.90 (s, 6H, Hl), 1.88 (s, 6H, Hl), 1.70 (s, 6H, Hl), 1.53 (s, 9H, Hn), 1.52 (s, 9H, Hn), 1.47 (s, 9H, Hn).

^{13}C NMR (125 MHz, $CDCl_3$, 1% pyridine-d_5) δ (ppm): 182.02, 159.73, 152.22, 151.20, 150.82, 150.48, 150.45, 150.20, 149.78, 149.21, 148.26, 148.08, 142.34, 139.06, 138.71, 138.48, 138.13, 137.88, 136.69, 136.39, 136.28, 133.61, 131.25, 131.14, 131.01, 130.63, 129.52, 129.47, 128.26, 127.15,

125.82, 125.09, 123.82, 123.68, 123.50, 120.82, 118.59, 111.46, 104.72, 34.85, 34.68, 34.61, 31.76, 31.69, 31.67, 22.02, 21.69, 21.51.

UV-vis (CH_2Cl_2): λ_{max} (ε, $M^{-1}cm^{-1}$) = 392 (27 000), 474 (99 200), 495 (45 600), 688 (15 200) nm.

ESI-MicroTOF (m/z) (positive mode) Exact mass calculated for $C_{63}H_{63}N_5OZn$ ([**7**]$^+$): 969.4319; found 969.4336.

Dimer FbPdFb

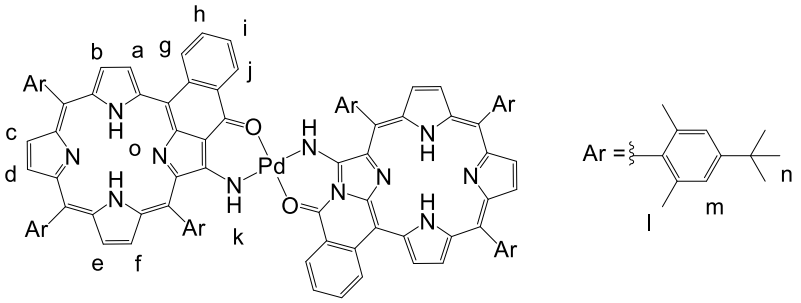

A solution of Porphyrin **5** (50 mg, 55 µmol) in toluene (30 mL) was heated at 80°C in the presence of $Pd(acac)_2$ (6.2 mg, 27 µmol, 0.5 eq) under argon for 24 hours. The solvent was evaporated, and the product was purified by column chromatography (silica gel, dichloromethane/cyclohexane). The palladium(II) dimer **FbPdFb** was obtained after recrystallization from dichloromethane/methanol. Yeld: 39 mg (37 %).

^{1}H NMR (500 MHz, $CDCl_3$) δ (ppm): 9.35 (d, *J* = 5.0 Hz, 2H, Ha), 8.91 (d, *J* = 8.0 Hz, 2H, Hg), 8.75 (dd, *J* = 7.7, 1.6 Hz, 2H, Hj), 8.53 (d, *J* = 4.9 Hz, 2H, Hb), 8.34 (d, *J* = 4.8 Hz, 2H, He), 8.23 (s, 2H, Hk), 8.21 (d, *J* = 4.4 Hz, 2H, Hd), 8.18 (d, *J* = 4.4 Hz, 2H, Hc), 7.99 – 7.91 (m, 4H, Hf, Hh), 7.86 (t, *J* = 7.1 Hz, 2H, Hi), 7.77 (s, 4H, Hm), 7.41 (s, 4H, Hm), 7.37 (s, 4H, Hm), 2.10 (s, 12H, Hl), 1.97 (s, 12H, Hl), 1.94 (s, 12H, Hl), 1.64 (s, 18H, Hn), 1.56 (s, 18H, Hn), 1.54 (s, 18H, Hn), – 0.26 (s, 4H, Ho).

^{13}C NMR (125 MHz, CDCl3) δ (ppm): 181.31, 152.85, 151.04, 141.09, 138.72, 138.53, 138.15, 137.70, 137.40, 135.81, 134.69, 133.90, 131.58, 127.30, 126.43, 126.17, 124.03, 123.95, 122.36, 119.72, 117.04, 111.99, 105.49, 34.91, 34.71, 34.69, 31.71, 31.68, 31.63, 22.01, 21.92, 21.42.

Elemental analysis Calculated for $C_{126}H_{132}N_{10}O_6PdZn_2$ (FbPdFb + CH_3OH + 4 H_2O): C, 75.33; H, 6.97; N, 6.92; found: C, 75.60; H, 6.76; N, 6.87.

MALDI-TOF (m/z) (positive mode) Mass calculated for $C_{126}H_{128}N_{10}O_2Pd$ ([**FbPdFb**]$^+$): 1920.892; found 1920.769.

Dimer ZnPdZn

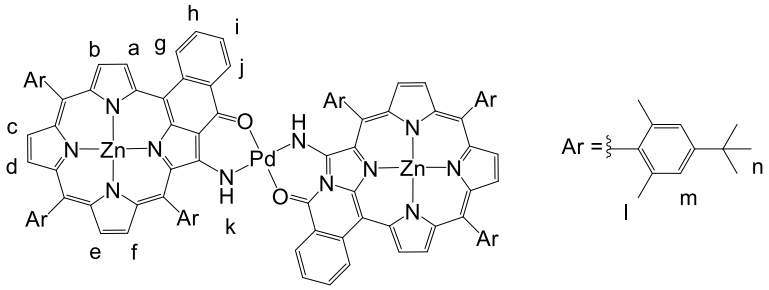

A solution of Porphyrin **6** (62 mg, 64 µmol) in toluene (20 mL) was heated at 100°C in the presence of $Pd(acac)_2$ (7.2 mg, 32 µmol, 0.5 eq) under argon for 12 hours. The solvent was evaporated, and the product was purified by column chromatography (silica gel, dichloromethane/cyclohexane). The palladium(II) dimer was obtained after recrystallization from dichloromethane/methanol. Yield: 55.3 mg (85 %).

^{1}H NMR (500 MHz, $CDCl_3$) δ (ppm): 9.27 (d, *J* = 4.7 Hz, 2H, Ha), 8.84 (d, *J* = 8.1 Hz, 2H, Hg), 8.76 (d, *J* = 7.7 Hz, 2H, Hj), 8.48 (d, *J* = 4.6 Hz, 2H, Hb), 8.25 (d, *J* = 4.5 Hz, 2H, He), 8.23 (d, *J* = 4.3 Hz, 2H, Hd), 8.16 (d, *J* = 4.3 Hz, 2H, Hc), 8.11 (s, 2H, Hk), 7.93 (t, *J* = 7.5 Hz, 2H, Hh), 7.85 – 7.78 (m, 4H, Hf, Hi), 7.74 (s, 4H, Hm), 7.39 (s, 4H, Hm), 7.35 (s, 4H, Hm), 2.10 (s, 12H, Hl), 1.97 (s, 12H, Hl), 1.95 (s, 12H, Hl), 1.62 (s, 18H, Hn), 1.56 (s, 18H, Hn), 1.53 (s, 18H, Hn).

^{1}H NMR (500 MHz, $CDCl_3$ 1% pyridine-d_5) δ (ppm): 9.13 (d, *J* = 4.6 Hz, 2H, Ha), 8.83 (d, *J* = 8.1 Hz, 2H, Hg), 8.74 (dd, *J* = 7.8, 1.5 Hz, 2H, Hj), 8.35 (d, *J* = 4.5 Hz, 2H, Hb), 8.15 (d, *J* = 4.4 Hz, 2H, He), 8.11 (d, *J* = 4.3 Hz, 2H, Hd), 8.06 (d, *J* = 4.3 Hz, 2H, Hc), 7.87 (t, *J* = 7.3, 2H, Hh), 7.79 – 7.74 (m, 4H, Hf, Hi), 7.72 (s, 4H, Hm), 7.37 (s, 4H, Hm), 7.29 (s, 4H, Hm), 2.08 (s, 12H, Hl), 1.95 (s, 12H, Hl), 1.78 (s, 12H, Hl), 1.61 (s, 18H, Hn), 1.55 (s, 18H, Hn), 1.50 (s, 18H, Hn).

^{13}C NMR (125 MHz, $CDCl_3$ 1% pyridine-d_6) δ (ppm): 166.58, 164.68, 152.94, 152.53, 152.13, 151.53, 150.44, 150.41, 149.37, 147.68, 147.40, 147.11, 144.69, 144.48, 144.26, 140.63, 139.95, 139.12, 138.82, 138.76, 138.39, 138.09, 136.57, 135.61, 131.26, 131.22, 130.37, 129.64, 129.19, 129.03, 128.76, 128.43, 127.22, 126.94, 125.80, 125.03, 124.24, 123.85, 123.71, 123.33, 122.43, 122.23, 122.03, 115.85, 113.62, 102.27, 77.41, 77.36, 77.16, 76.91, 35.03, 34.76, 34.70, 32.08, 31.94, 31.86, 31.80, 21.91, 21.79, 21.64.

UV-vis (CH_2Cl_2): λ_{max} (ε, $M^{-1}cm^{-1}$) = 380 (88 260), 425 (118 270), 501 (356 150), 636 (40 250), 700 (104 300) nm.

Elemental analysis Calculated for $C_{126}H_{132}N_{10}O_6PdZn_2$ (ZnPdZn + 4 H_2O): C, 71.40; H, 6.28; N, 6.61; found: C, 71.52; H, 6.25; N, 6.55.

MALDI-TOF (m/z) (positive mode) Mass calculated for $C_{126}H_{124}N_{10}O_2PdZn_2$ ([**ZnPdZn**]$^+$): 2046.754; found 2046.716.

[ZnPdZn·Pyrazine]$_2$

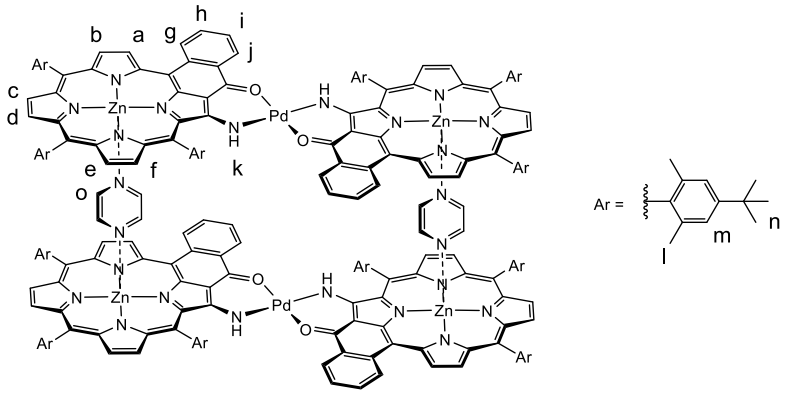

System **[ZnPdZn·Pyrazine]$_2$** was obtained by NMR titration, performed by progressive addition of aliquots of a pyrazine stock solution (25 mM, $CDCl_3$) to a ca. 10^{-3} M $CDCl_3$ solution of **ZnPdZn** in a 5 mm NMR tube; ^{1}H NMR spectra were recorded after each addition. When 1 equivalent of ligand was added and formation of **[ZnPdZn·Pyrazine]$_2$** was complete, the product was isolated upon removal of the solvent.

^{1}H NMR (500 MHz, $CDCl_3$) δ (ppm): 9.02 (d, *J* = 4.5 Hz, 4H, Ha), 8.67 (d, *J* = 8.0 Hz, 4H, Hg), 8.61 (d, *J* = 7.6 Hz, 4H, Hj), 8.21 (d, *J* = 4.4 Hz, 4H, Hb), 8.04 – 7.98 (m, 8H, Hd, He), 7.95 (d, *J* = 4.2 Hz, 4H, Hc), 7.91 – 7.80 (m, 8H, Hk, Hh), 7.74 (t, *J* = 7.3 Hz, 4H, Hi), 7.59 (d, *J* = 4.3 Hz, 4H, Hf), 7.55 (s, 8H, Hm), 7.33 (s, 8H, Hm), 7.24 (s, 8H, Hm), 5.65 (br, Ho), 1.74 (br, 24H, Hl), 1.64 (bs, 24H, Hl), 1.56 (s, 36H, Hn), 1.56 (s, 41H), 1.54 – 1.47 (m, 72H, Hn).

^{13}C NMR (125 MHz, $CDCl_3$, from HSQC) δ (ppm): 135.31 (Cg), 131.10 (Cb), 130.99 (Ce), 129.58 (Cd), 129.18 (Ch), 128.75 (Ca), 128.43 (Cc), 127.07 (Cf), 126.86 (Cj), 125.69 (Cm), 124.42 (Ci), 123.95 (Cm), 123.60 (Cm), 31.72 (Cn), 31.60 (Cn), 21.41 (Cl), 21.37 (Cl).

UV-vis (CH_2Cl_2): λ_{max} = 383, 428, 475, 505, 586, 640, 701 nm.

[ZnPdZn·4'4'BiPy]$_2$

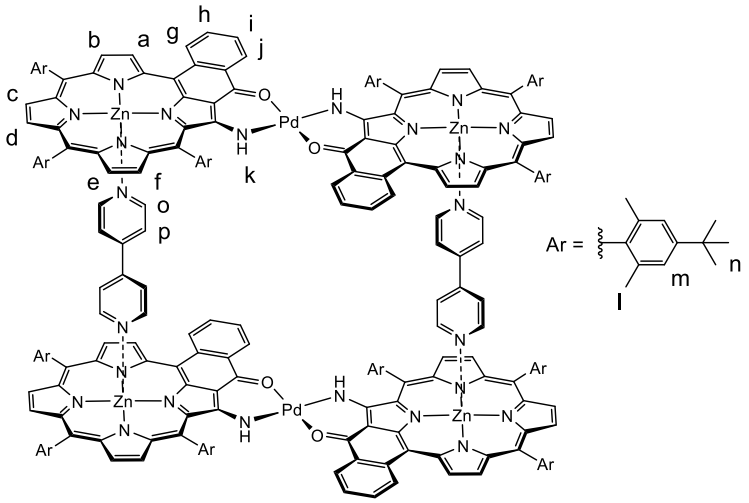

System **[ZnPdZn·4'4'BiPy]$_2$** was obtained either by NMR titration (analogously to **[ZnPdZn·Pyrazine]$_2$**) and, on larger scale, by addition of 4,4'-Bipyridine (1.3 mg, 8 µmol) to a dichloromethane solution (10 mL) of **ZnPdZn** (17 mg, 8 µmol), stirring for 15 minutes and removing the solvent under reduced pressure.

^{1}H NMR (500 MHz, $CDCl_3$) δ (ppm) 9.05 (d, *J* = 4.5 Hz, 4H, Ha), 8.68 (d, *J* = 8.0 Hz, 4H, Hg), 8.56 (d, *J* = 7.6 Hz, 4H, Hj), 8.26 (d, *J* = 4.4 Hz, 4H, Hb), 8.05 – 7.95 (m, 16H, He, Hd, Hc, Hk), 7.78 (t, *J* = 7.2 Hz, 4H, Hh), 7.64 (t, *J* = 7.3 Hz, 4H, Hi), 7.60 – 7.54 (br, 12H, Hf, Hm), 7.33 (s, 8H, Hm), 7.30 – 7.10 (br, Hm) 5.49 – 5.18 (br, Hp), 4.01 – 3.52 (br, Ho), 2.05 – 1.74 (br, Hl), 1.81 (s, 24H, Hl), 1.55 (s, 36H, Hn), 1.51 – 1.48 (m, 72H, Hn).

^{13}C NMR (125 MHz, $CDCl_3$) δ (ppm): 166.46, 164.69, 152.81, 152.41, 152.13, 151.37, 150.48, 149.12, 147.48, 147.25, 146.90, 144.90, 144.26, 140.46, 139.74, 138.93, 138.63, 138.22, 137.85, 136.20, 135.60 (Cg), 131.20, 131.12 (Cb), 130.36, 129.58 (Cd), 129.05, 128.94 (Ch), 128.73 (Ca), 128.39 (Cc), 127.25 (Cf), 126.99 (Cj), 124.88, 124.22 (Ci), 123.83 (Cm), 123.15, 119.86 (Cp), 115.54, 113.54, 102.24, 77.41, 34.94, 34.75, 34.68, 31.85 (Cn), 31.83 (Cn), 31.78 (Cn), 21.79 (Cl), 21.54 (Cl).

UV-vis ($CHCl_3$): λ_{max} = 380, 427, 473, 503, 638, 700 nm.

[ZnPdZn·*trans*DPyP]$_2$

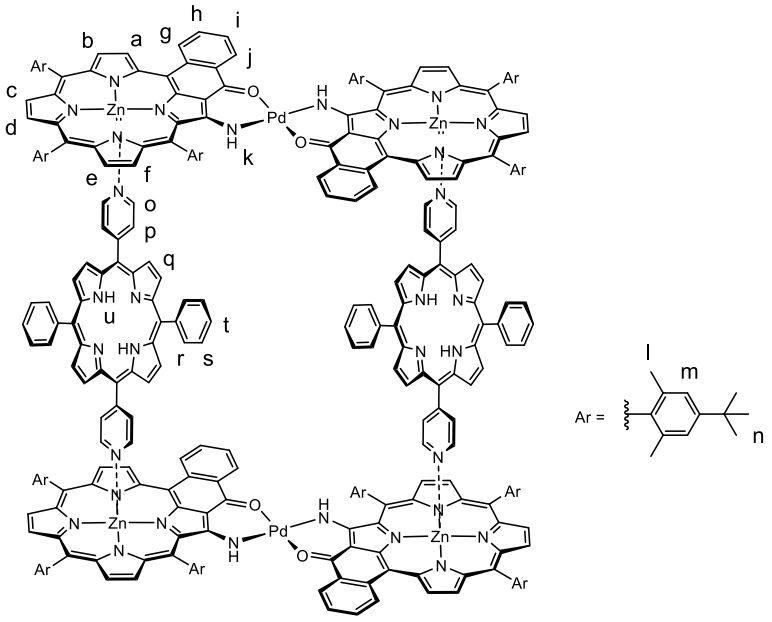

Dimer **ZnPdZn** (16.10 mg, 7.8 μmol) and ***trans*DPyP** (4.85 mg, 7.8 μmol) were dissolved in 10 mL of dichloromethane and the solution stirred at room temperature for 15 minutes. Precipitation by addition of *n*-hexane afforded pure product as a black powder. Yield: 17.5 mg (83%).

^{1}H NMR (500 MHz, $CDCl_3$) selected resonances, δ (ppm): 9.22 (d, *J* = 4.5 Hz, 4H, Ha), 8.89 (d, *J* = 8.0 Hz, 4H, Hg), 8.73 (d, *J* = 7.7 Hz, 4H, Hj), 8.43 (d, *J* = 4.4 Hz, 4H, Hb), 8.40 – 8.14 (br), 8.25 – 8.16 (m, 8H, Hd, He), 8.14 (d, *J* = 4.2 Hz, 4H, Hc), 7.85 (t, *J* = 7.4 Hz, 4H, Hh), 7.76 (d, *J* = 4.4 Hz, 4H, Hf), 7.80 – 7.45 (br), 7.72 (t, *J* = 7.3 Hz, Hi), 7.38 (br, Hm), 7.14 (br), 6.57 (br, Hp), 4.27 (br, Ho), 2.35 – 1.69 (m, 72H, Hl), 1.60 – 1.44 (m, 108H, Hn), -3.66 (br, 4H, Hu).

UV-vis ($CHCl_3$): λ_{max} (ε, $M^{-1}cm^{-1}$) = 423, 506 (278 800), 588, 641, 701 (114 250) nm.

5.5 References

[1] A. Prodi, C. Chiorboli, F. Scandola, E. Iengo, E. Alessio, *ChemPhysChem* 2006, *7*, 1514.

[2] M. T. Indelli, C. Chiorboli, F. Scandola, E. Iengo, P. Osswald, F. Würthner, *J. Phys. Chem. B* 2010, *114*, 14495.

[3] a) S. Richeter, C. Jeandon, J.-P. Gisselbrecht, R. Ruppert, H. J. Callot, *J. Am. Chem. Soc.* 2002, *124*, 6168; b) S. Richeter, C. Jeandon, J.-P. Gisselbrecht, R. Graff, R. Ruppert, H.J. Callot, *Inorg Chem*, 2004, *43*, 251; c) H. Dekkiche, A. Buisson, A. Langlois, P.L. Karsenti, L. Ruhlmann, R. Ruppert, P. Harvey, *Chem. Eur. J*. 2016, *22*, 10484; d) M.A. Carvalho, H. Dekkiche, L. Karmazin, F. Sanchez, B. Vincent, M. Kanesato, Y. Kikkawa, R. Ruppert, *Inorg. Chem.* 2017, *56*, 15081; e) J.A. Wytko, R. Ruppert, C. Jeandon, J. Weiss, *Chem. Commun*. 2018, *54*, 1550.

[4] a) E. Iengo, E. Zangrado, R. Minatel, E. Alessio, *J. Am. Chem. Soc.* 2002, *124*, 1003-1013; b) E. Iengo, E. Zangrando, M.Bellini, E. Alessio, A. Prodi, C. Chiorboli, F. Scandola, *Inorg.Chem*. 2005, 44, 9752.

[5] S. Richeter, C. Jeandon, J.-P. Gisselbrecht, R. Ruppert, H. J. Callot, *Inorg. Chem.* 2007, *46*, 10241.

[6] S. Richeter, C. Jeandon, C. Sauber, J.-P. Gisselbrecht, R. Ruppert, H. J. Callot, *J. Porphyrins Phthalocyanines,* 2002, *6*, 423.

[7] A.R. Katritzky, K. S. Laurenzo, *J. Org. Chem.* 1988, *53*, 3978.

[8] S. Richeter, C. Jeandon, R. Ruppe, H. J. Callot, *Chem. Commun.* 2002, 266.

[9] H. J. Callot, R. Ruppert, C. Jeandon, S. Richeter, *J. Porphyrins Phthalocyanines* 2004, *8*, 111.

[10] H. Dekkiche, A. Buisson, A. Langlois, P.-L. Karsenti, L. Ruhlmann, P. D. Harvey, R. Ruppert, *Inorg. Chem.* 2016, *55*, 10329.

[11] M. Abdelhameed, A. Langlois, P.-L. Karsenti, S. Richeter, R. Ruppert, P. D. Harvey, *Chem. Commun.* 2014, *50*, 14609.

[12] Dr. Hervé Dekkiche, PhD Thesys, 2017.

[13] P.N. Taylor, H.L. Anderson, *J. Am. Chem. Soc.* 1999, *121,* 11538.

[14] A. Prodi, M. T. Indelli, C. J. Kleverlaan, F. Scandola, E. Alessio, T. Gianferrara, L. G. Marzilli, *Chem. Eur. J.* 1999, *5*, 2668.

[15] *MestReNova© software, version 6.0.2, Mestrelab Res. S.L., Santiago Compost. Spain* 2016.

[16] J. E. Field, T. J. Hill, D. Venkataraman*, J. Org. Chem.* 2003, *68*, 6071.

[17] S. Ito, S. Hiroto, S. Lee, M. Son, I. Hisaki, T. Yoshida, D. Kim, N. Kobayashi, H. Shinokubo, *J. Am. Chem. Soc.* 2015, *137*, 142.

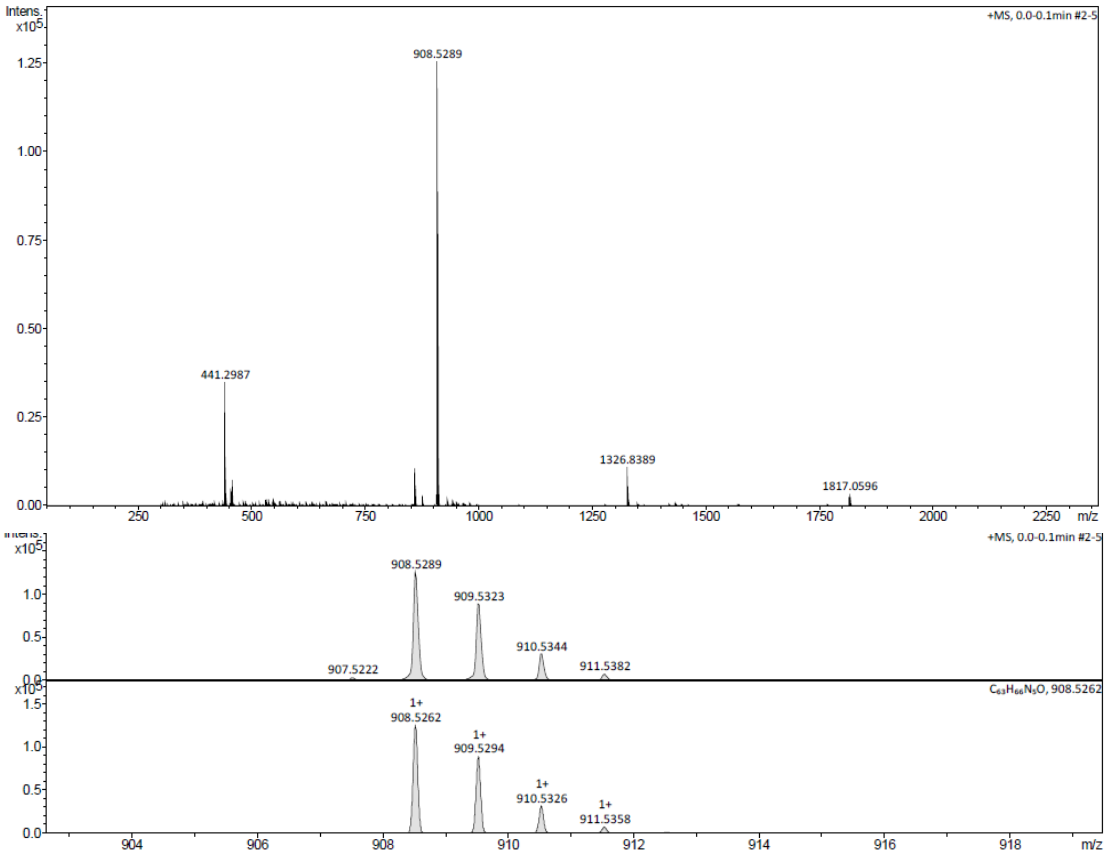

Figure A5.1. Top: ESI-MicroTOF mass spectrum of porphyrin (**6**); calculated for [**6** + H]$^+$, 908.5262; found 908.5289. Bottom: experimental (top) and calculated (bottom) isotopic distribution of the molecular ion peak [**6** + H]$^+$.

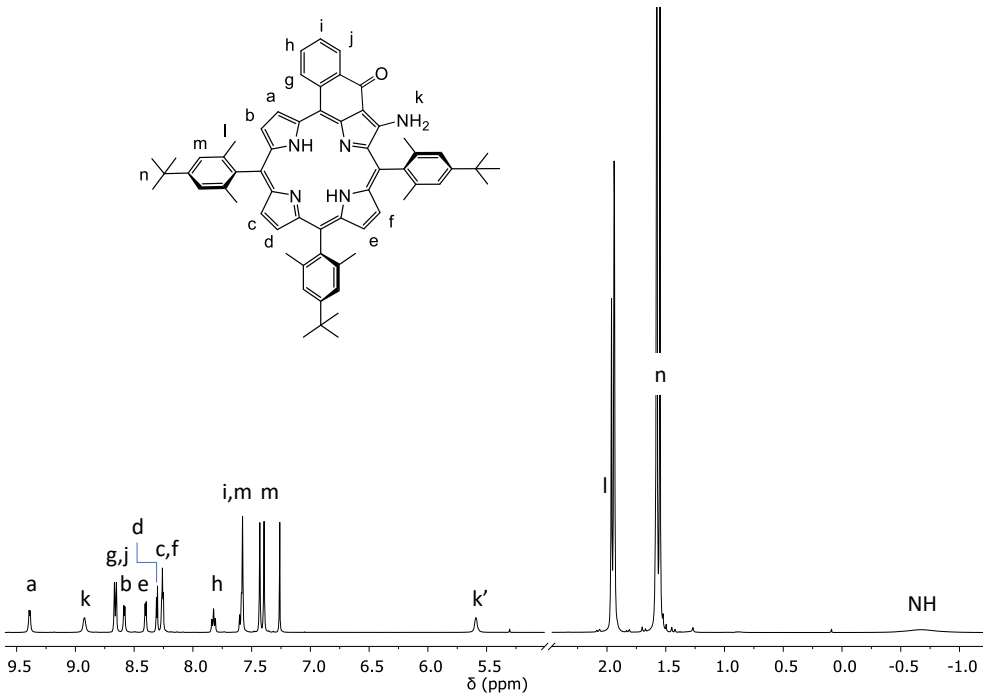

Figure A5.2. ^{1}H NMR spectrum ($CDCl_3$) of porphyrin **6**.

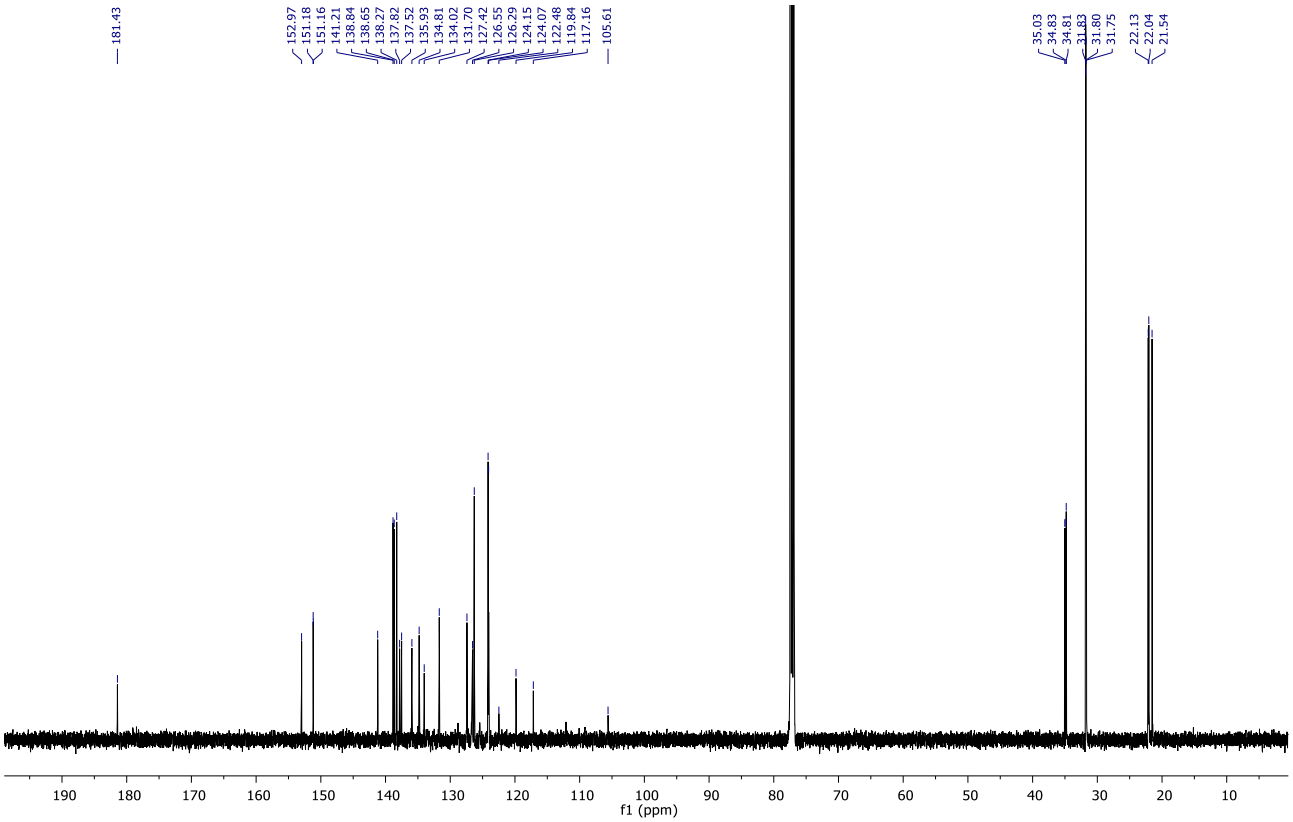

Figure A5.3. ^{13}C NMR spectrum ($CDCl_3$) of porphyrin **6**.

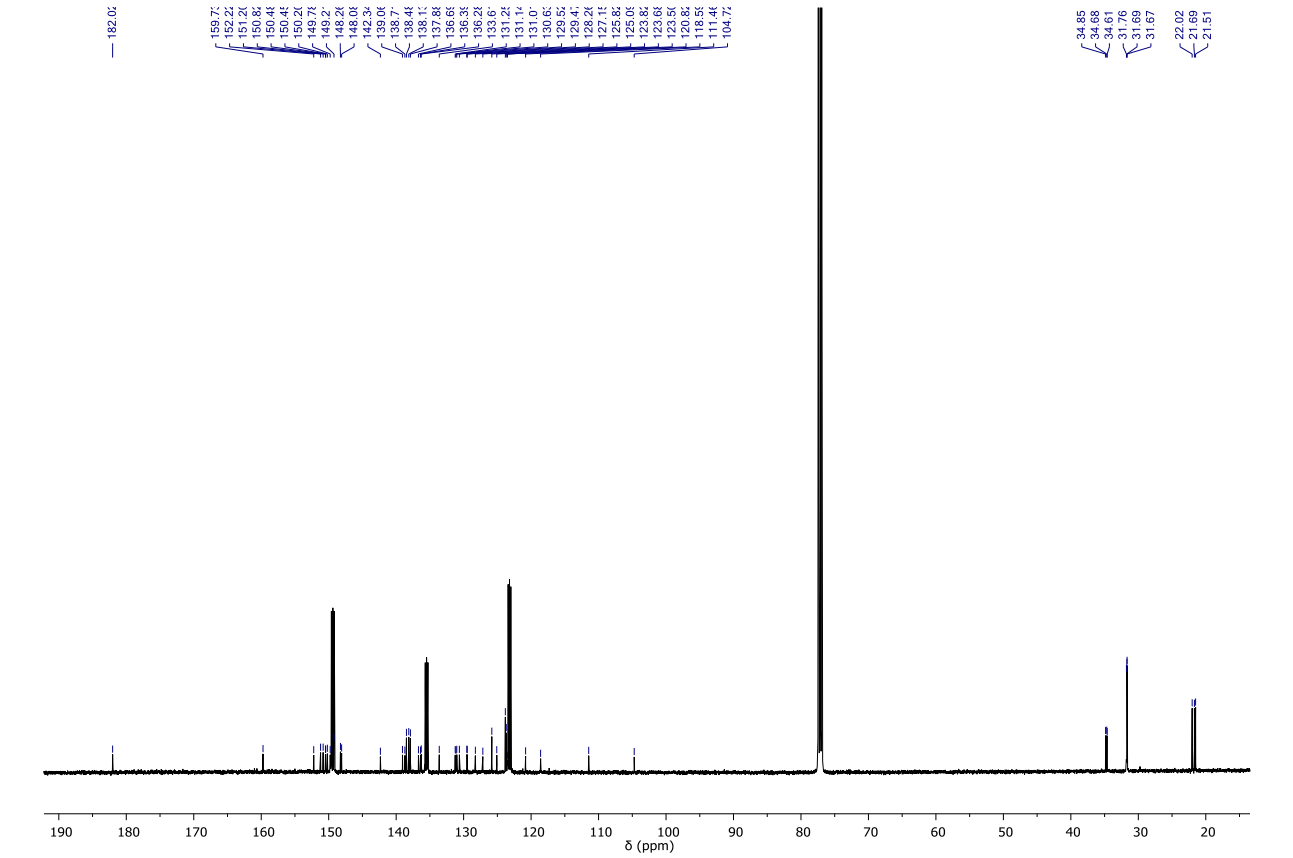

Figure A5.4. ^{13}C NMR spectrum ($CDCl_3$, 1% pyridine-d_5) of porphyrin **7**.

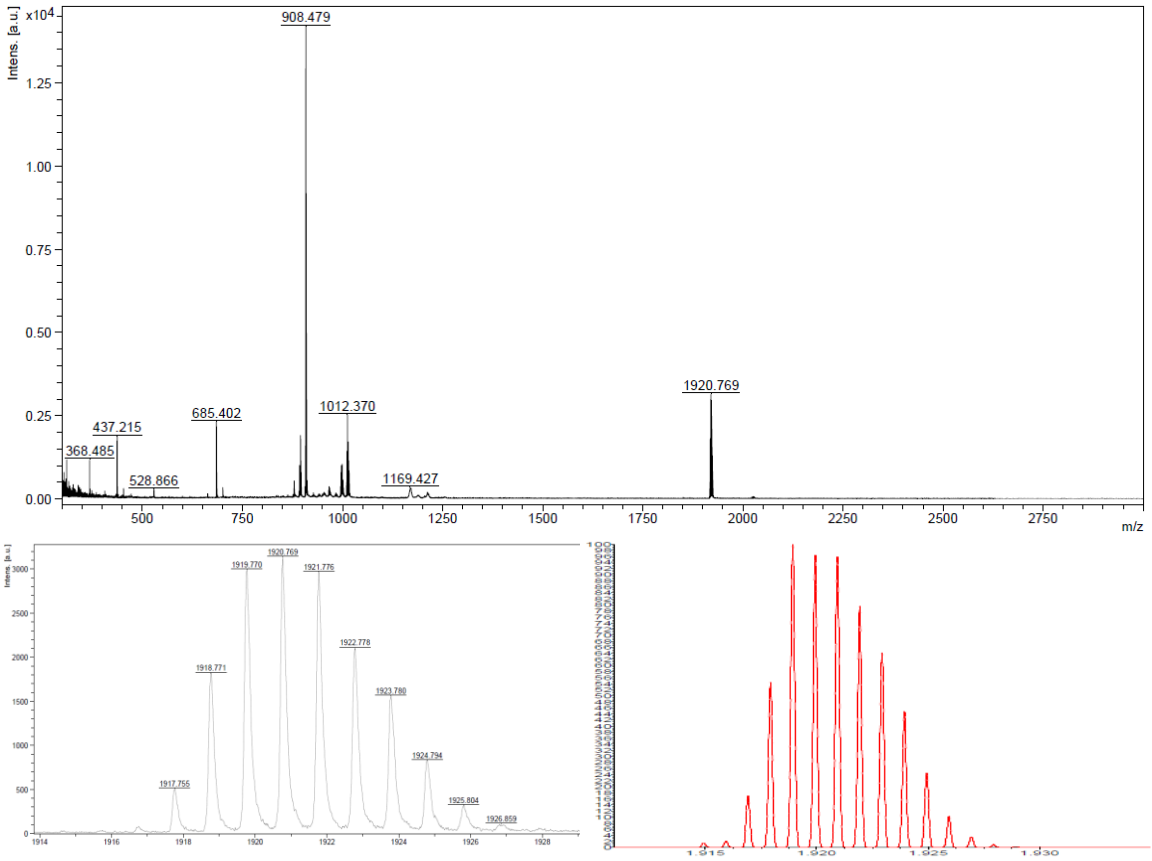

Figure A5.5. Top: MALDI-TOF (m/z) (positive mode) mass spectrum of dimer **FbPdFb**; calculated for ([**FbPdFb**]$^+$): 1920.892; found 1920.769. Bottom: experimental (left) and calculated (right) isotopic distribution of the molecular ion peak [**FbPdFb**]$^+$.

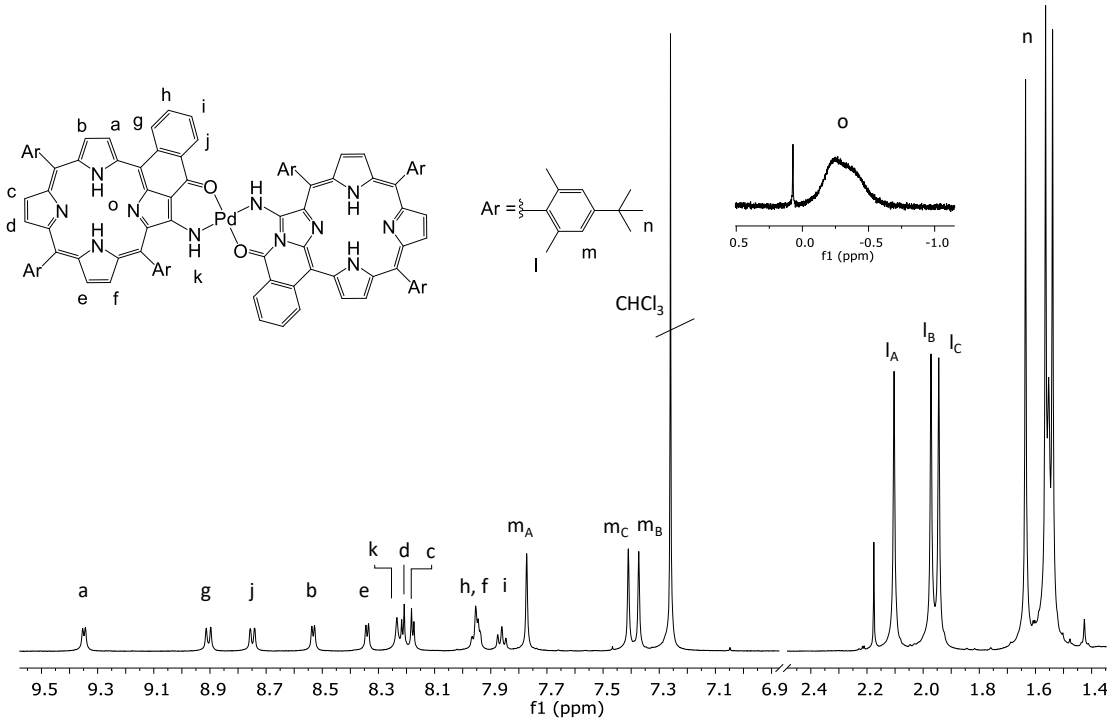

Figure A5.6. ^{1}H NMR spectrum ($CDCl_3$) of dimer **FbPdFb**.

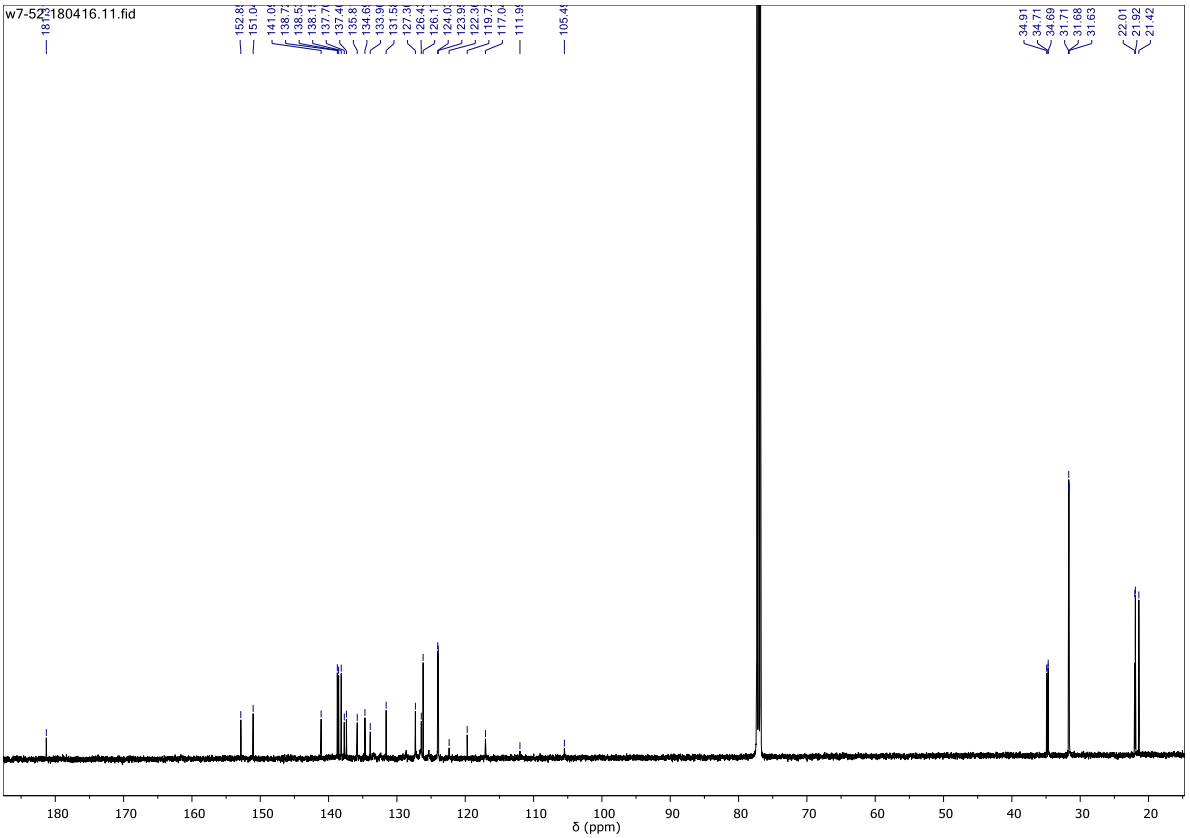

Figure A5.7. ^{13}C NMR spectrum ($CDCl_3$) of dimer **FbPdFb**.

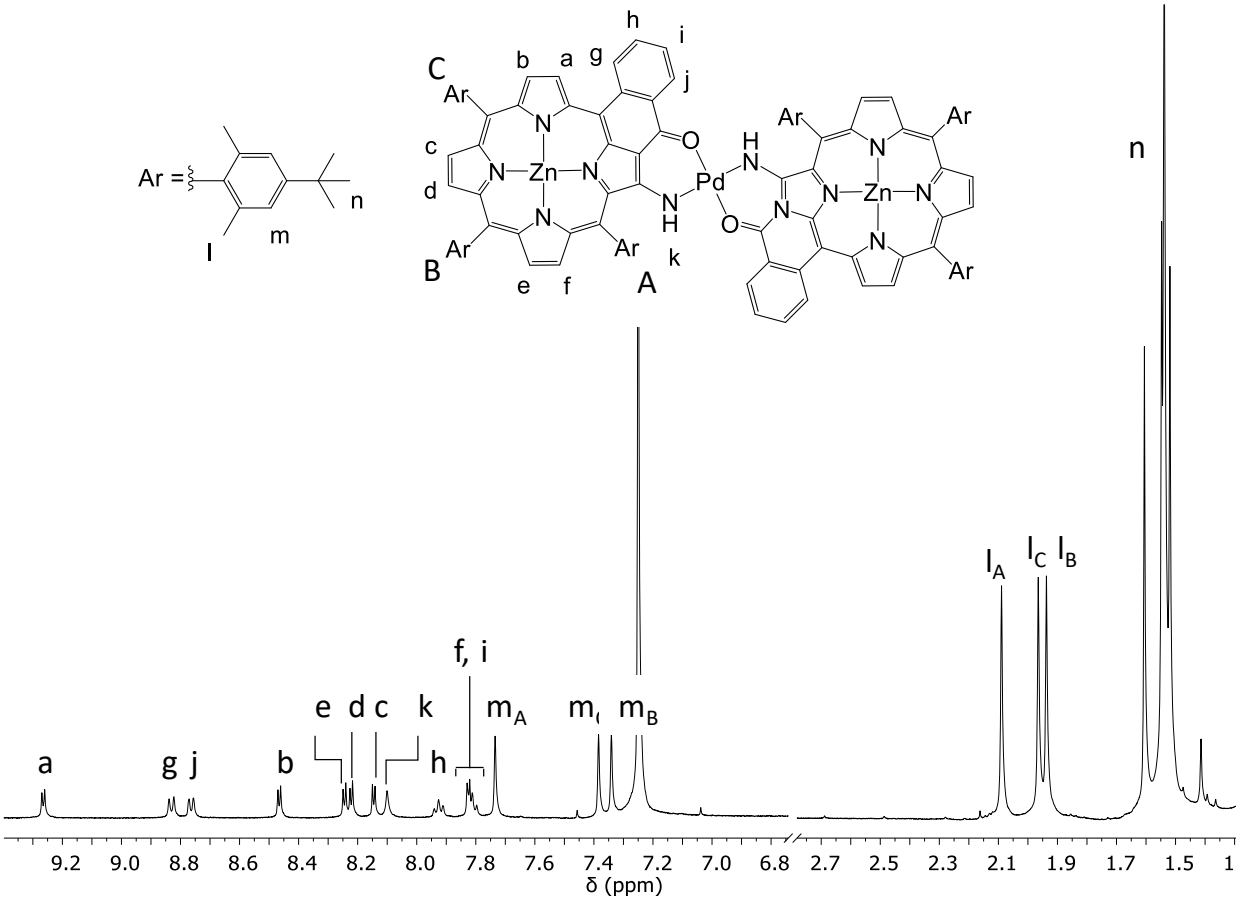

Figure A5.8. ^{1}H NMR spectrum ($CDCl_3$) of dimer **ZnPdZn**.

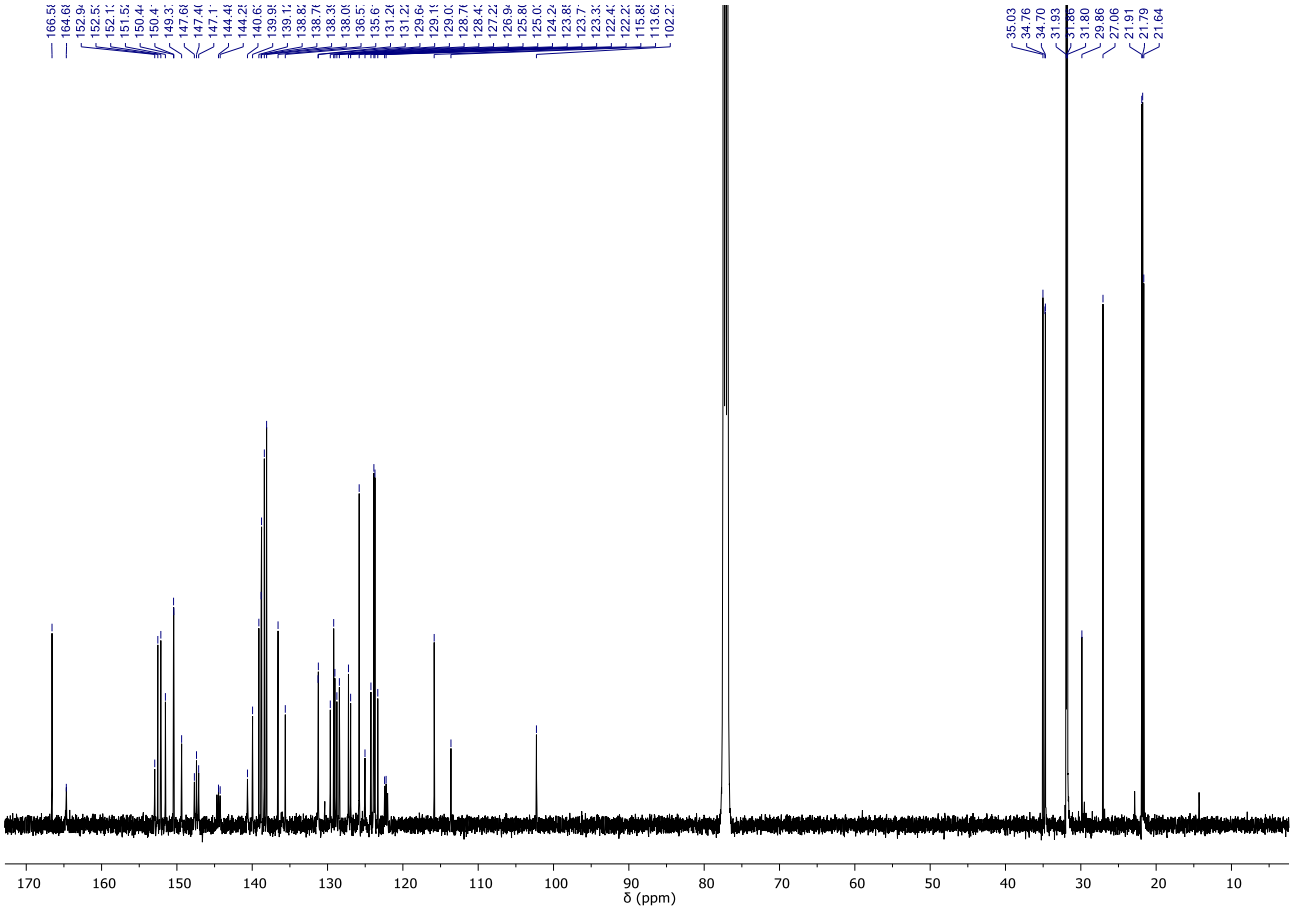

Figure A5.9. ^{13}C NMR spectrum ($CDCl_3$, 1% pyridine-d_5) of dimer **ZnPdZn**.

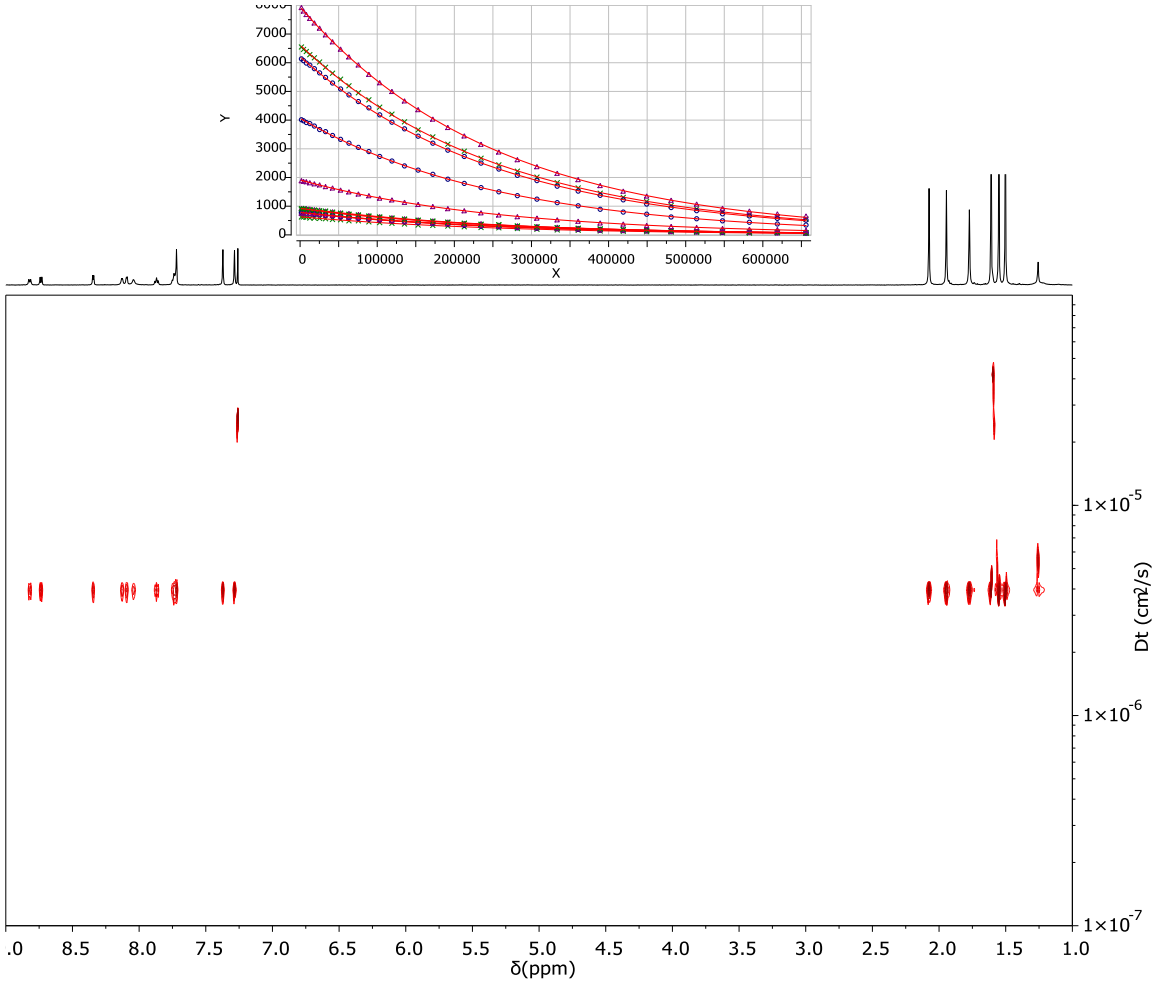

Figure A5.10. 2D ^{1}H-DOSY spectrum (Bayesian transform, $CDCl_3$, 600 MHz,) of **ZnPdZn** (bottom); signal decay with monoexponential fitting, analysis performed on each proton resonance (top).

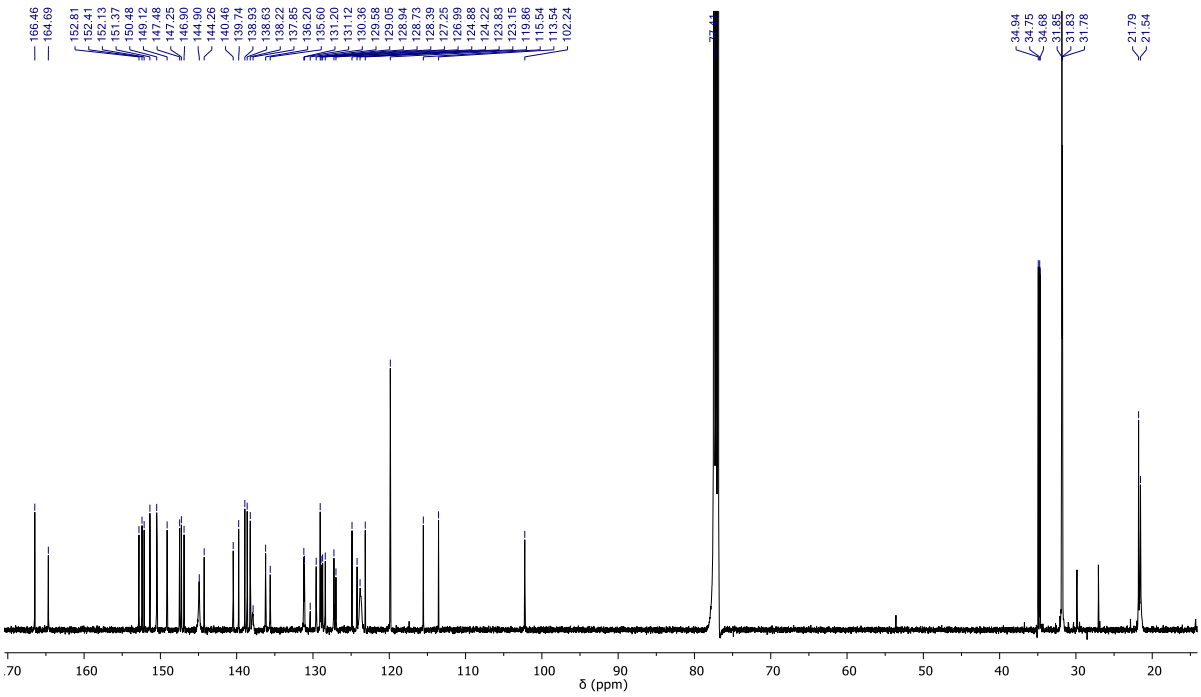

Figure A5.11. ^{13}C NMR spectrum ($CDCl_3$) of **[ZnPdZn·4,4'BiPy]$_2$**.

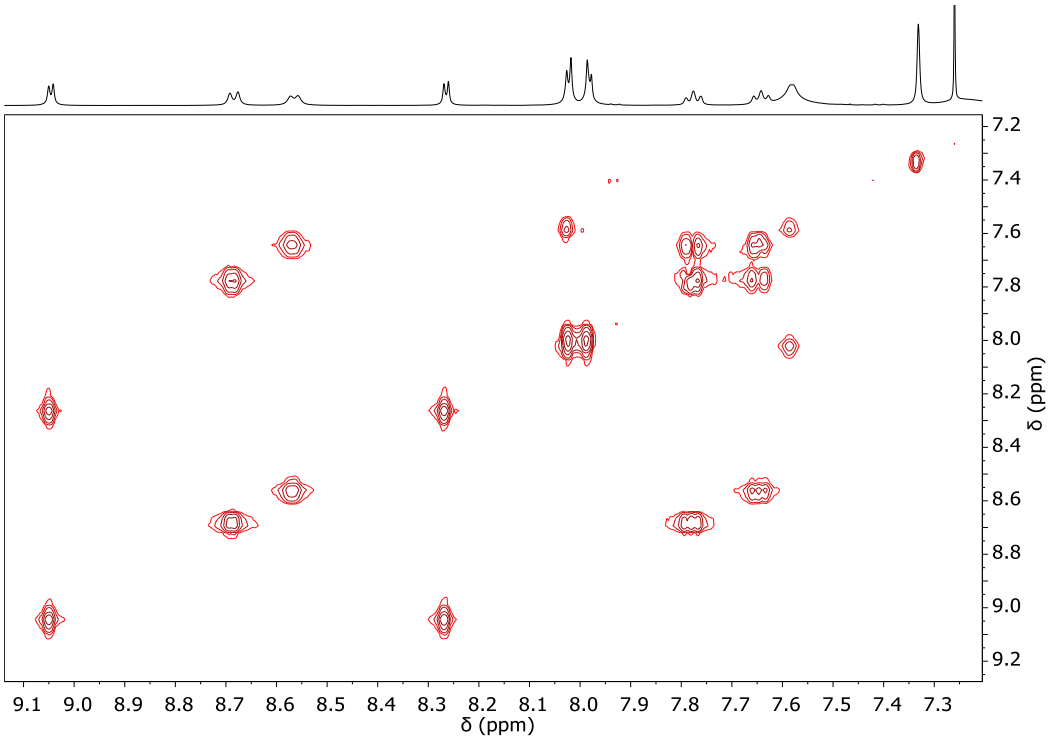

Figure A5.12. H-H COSY spectrum ($CDCl_3$) of **[ZnPdZn·4,4'BiPy]$_2$**.

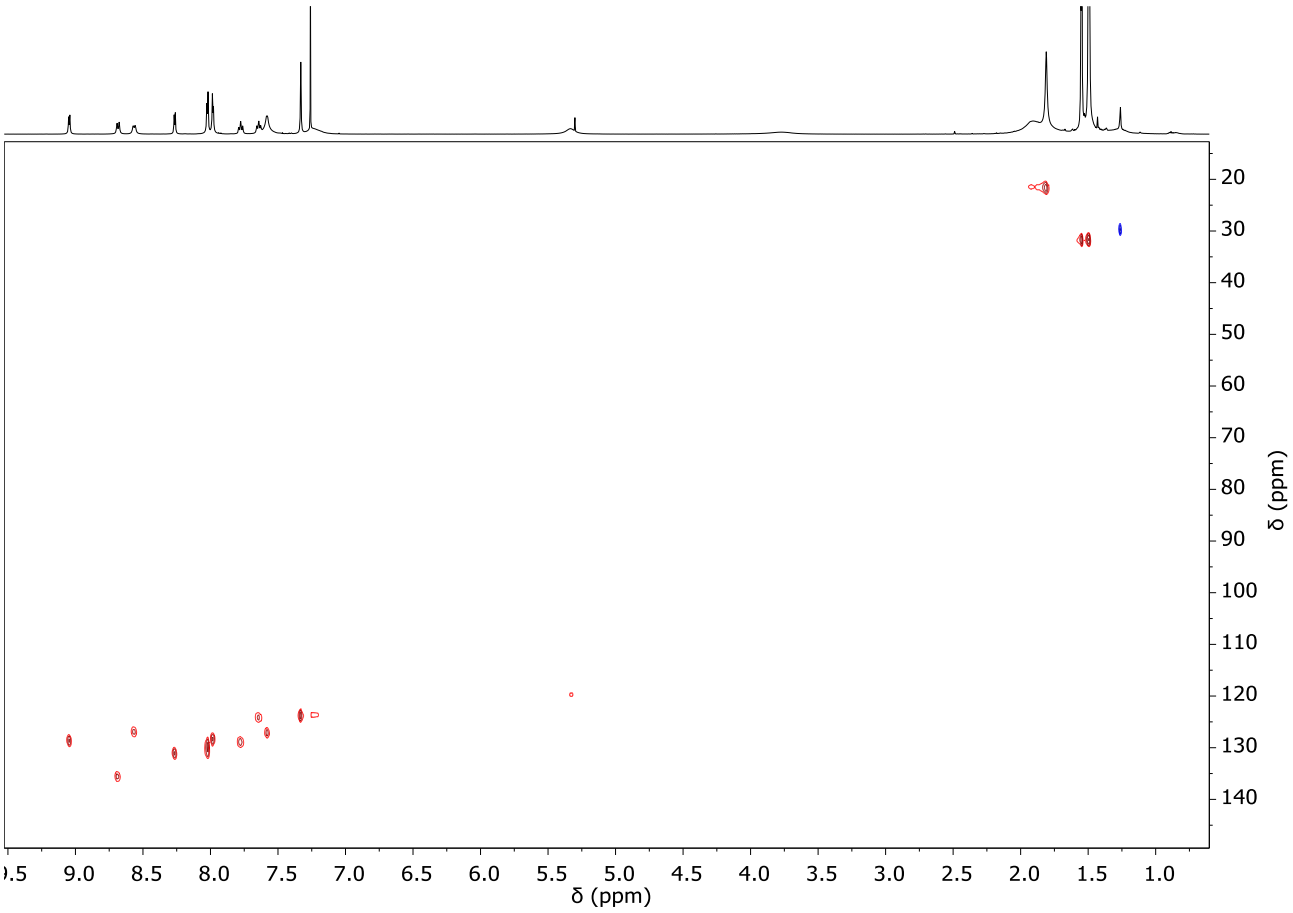

Figure A5.13. HSQC spectrum ($CDCl_3$) of **[ZnPdZn·4,4'BiPy]$_2$**.

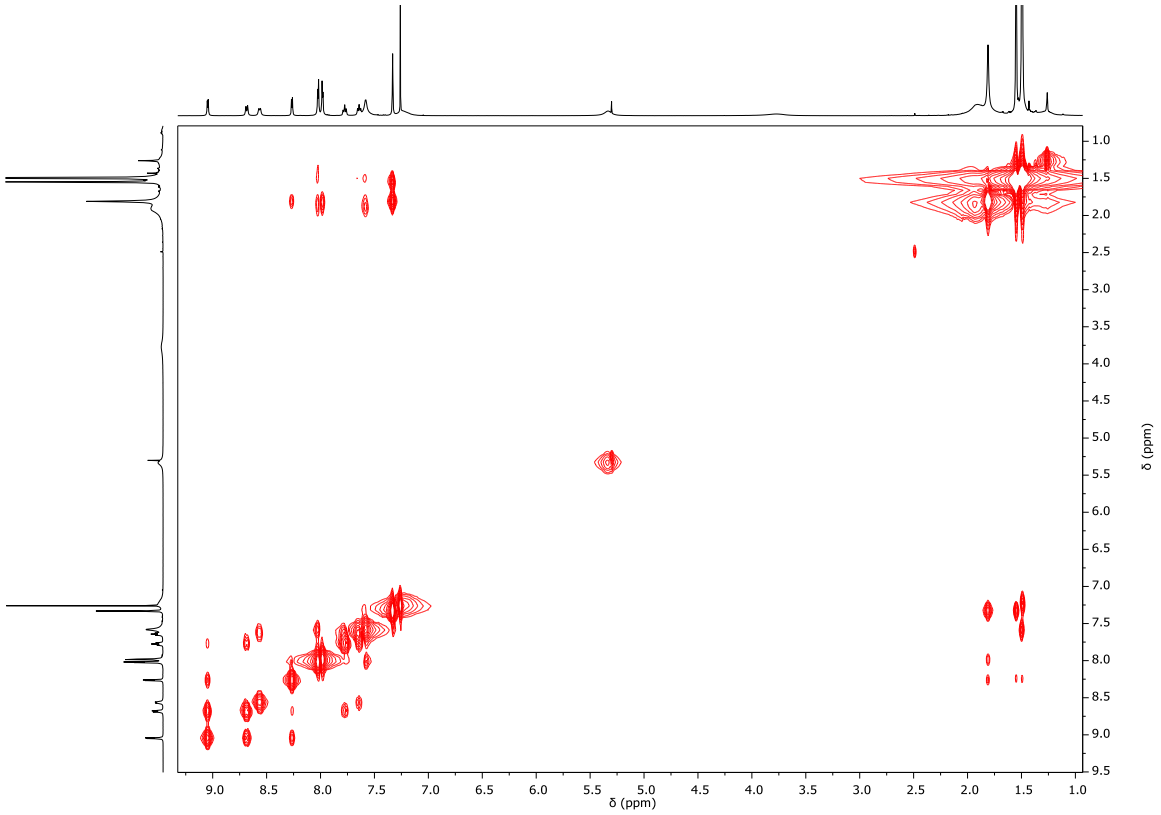

Figure A5.14. H-H NOESY spectrum ($CDCl_3$) of **[ZnPdZn·4,4'BiPy]$_2$**.

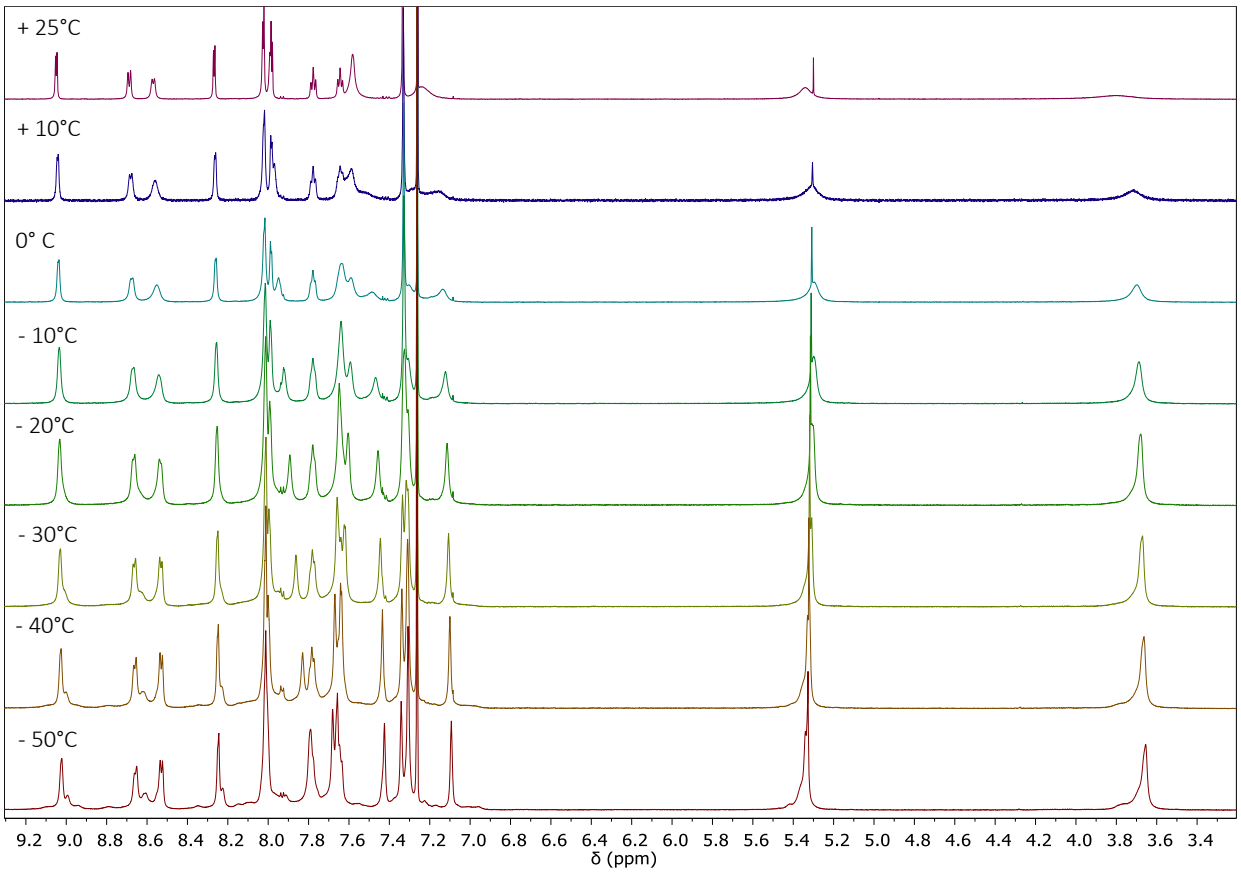

Figure A5.15. VT (-50 ÷ +25°C) ^{1}H NMR spectra ($CDCl_3$) of **[ZnPdZn·4,4'BiPy]$_2$**.

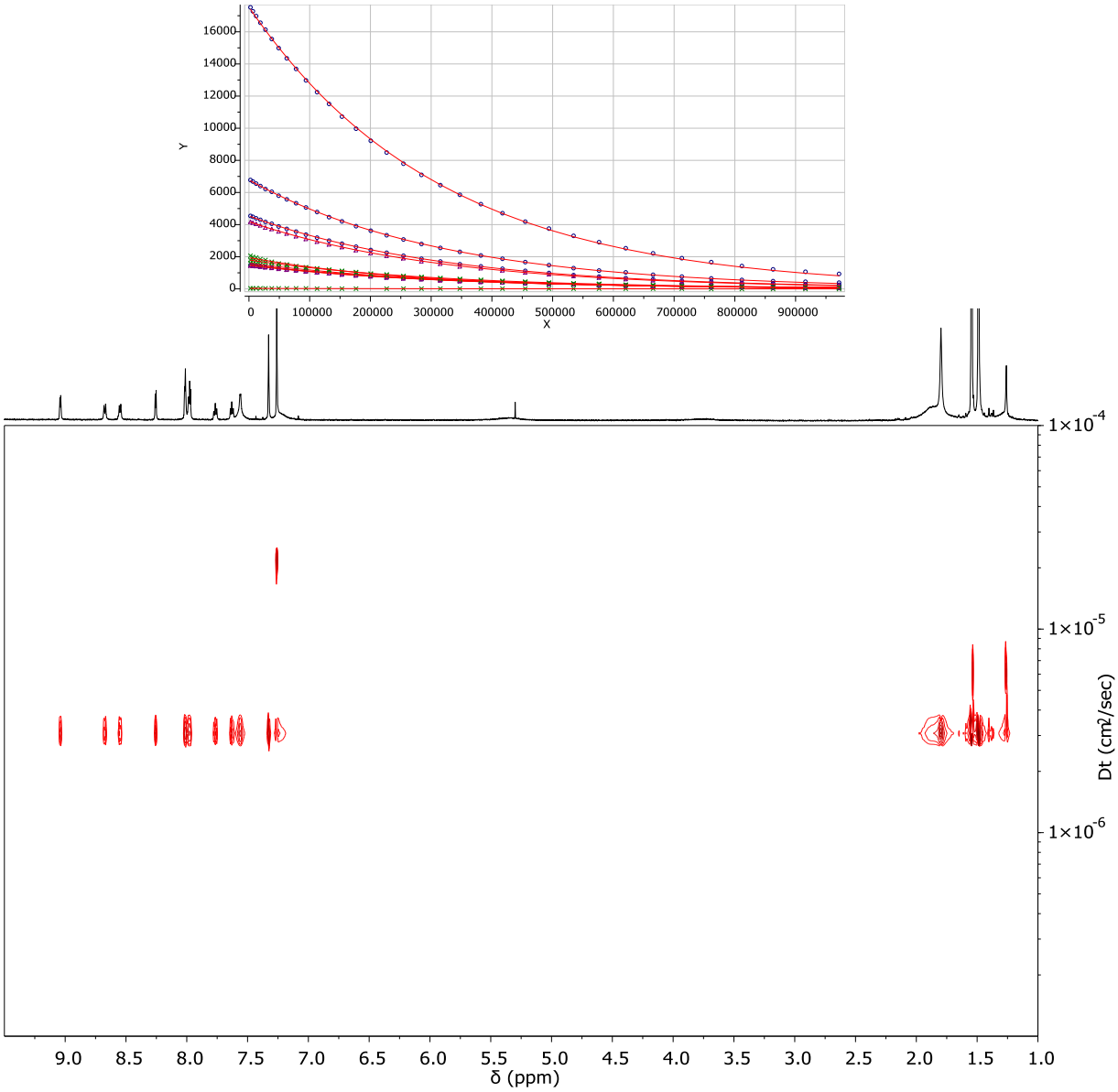

Figure A5.16. 2D ^{1}H-DOSY spectrum (Bayesian transform, $CDCl_3$, 600 MHz,) of **[ZnPdZn·4,4'BiPy]$_2$** (bottom); signal decay with monoexponential fitting, analysis performed on each proton resonance (top).

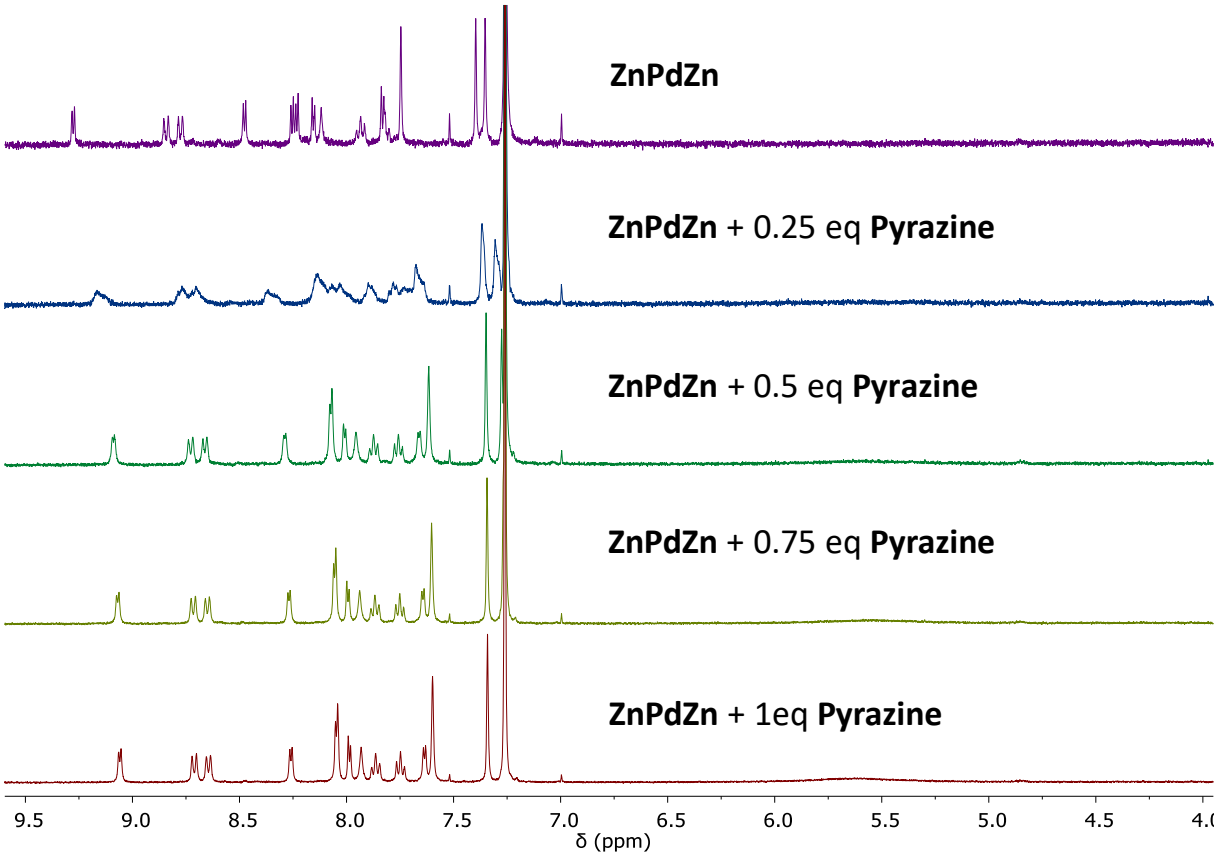

Figure A5.17. ^{1}H NMR ($CDCl_3$, 400 MHz) titration of **ZnPdZn** with **Pyrazine.**

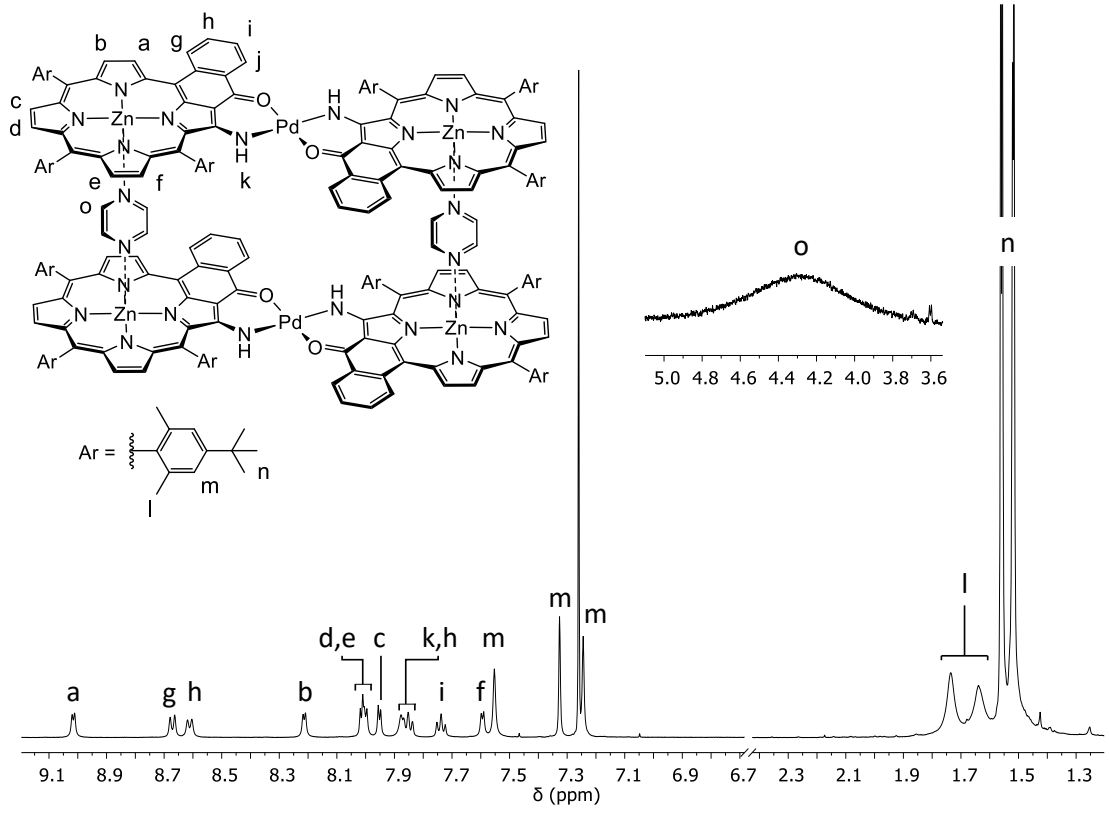

Figure A5.18. ^{1}H NMR spectrum ($CDCl_3$) of **[ZnPdZn·Pyrazine]$_2$**.

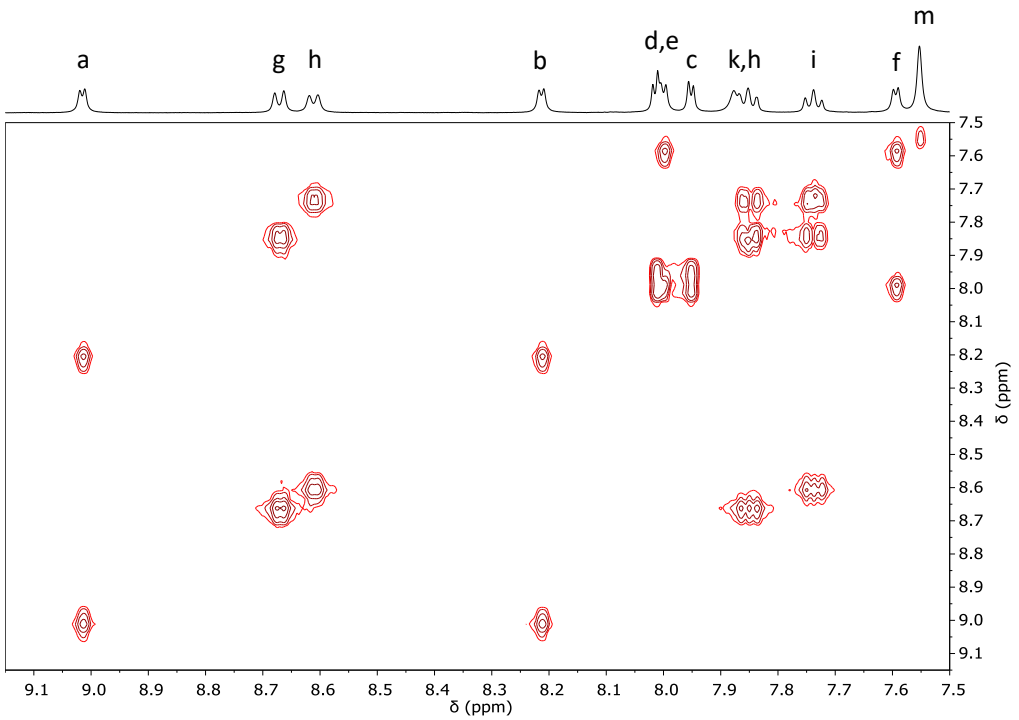

Figure A5.19. H-H COSY spectrum ($CDCl_3$) of **[ZnPdZn·Pyrazine]$_2$**.

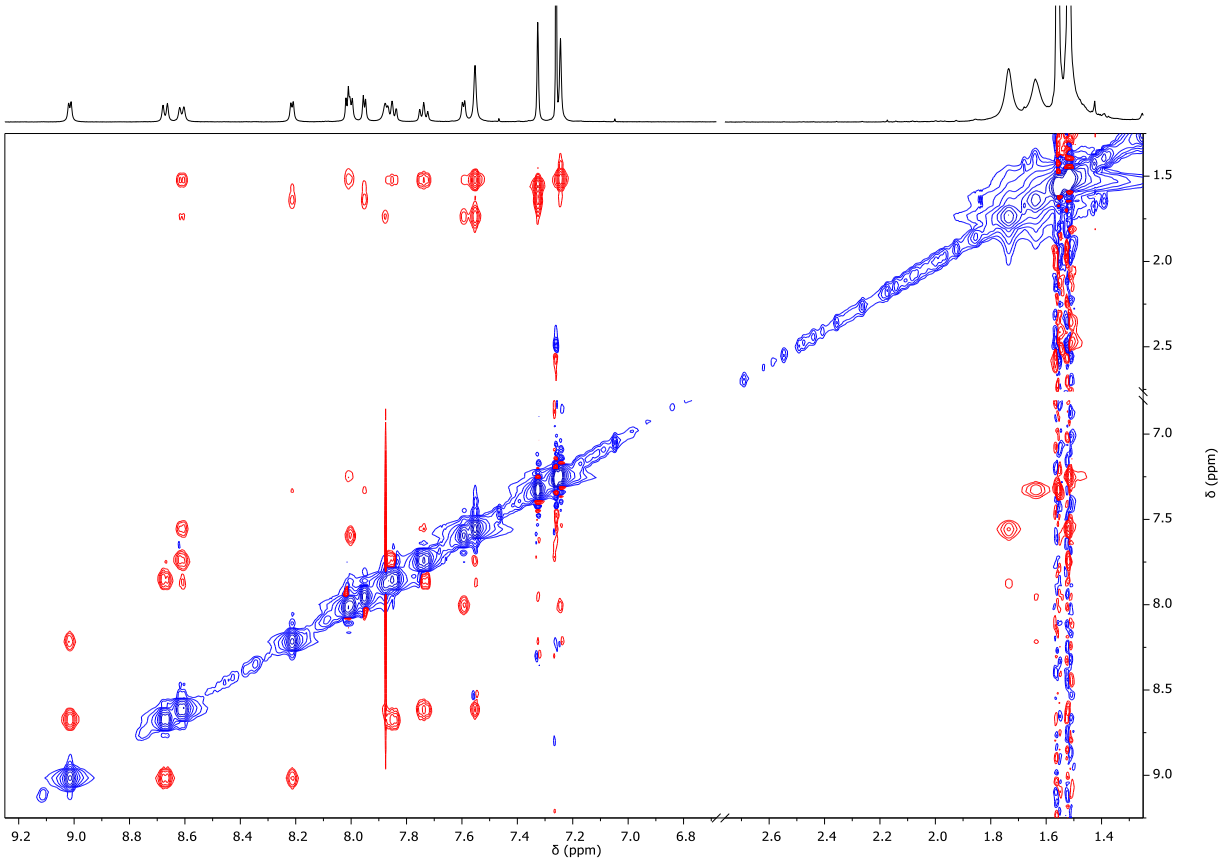

Figure A5.20. H-H ROESY spectrum ($CDCl_3$) of **[ZnPdZn·Pyrazine]$_2$**.

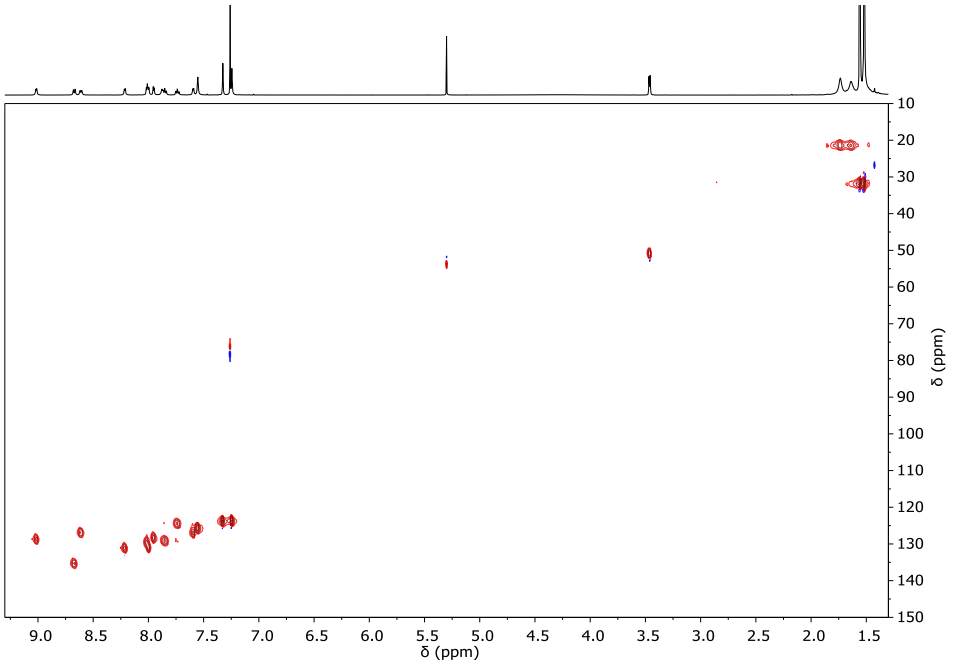

Figure A5.21. HSQC spectrum ($CDCl_3$) of **[ZnPdZn·Pyrazine]$_2$**.

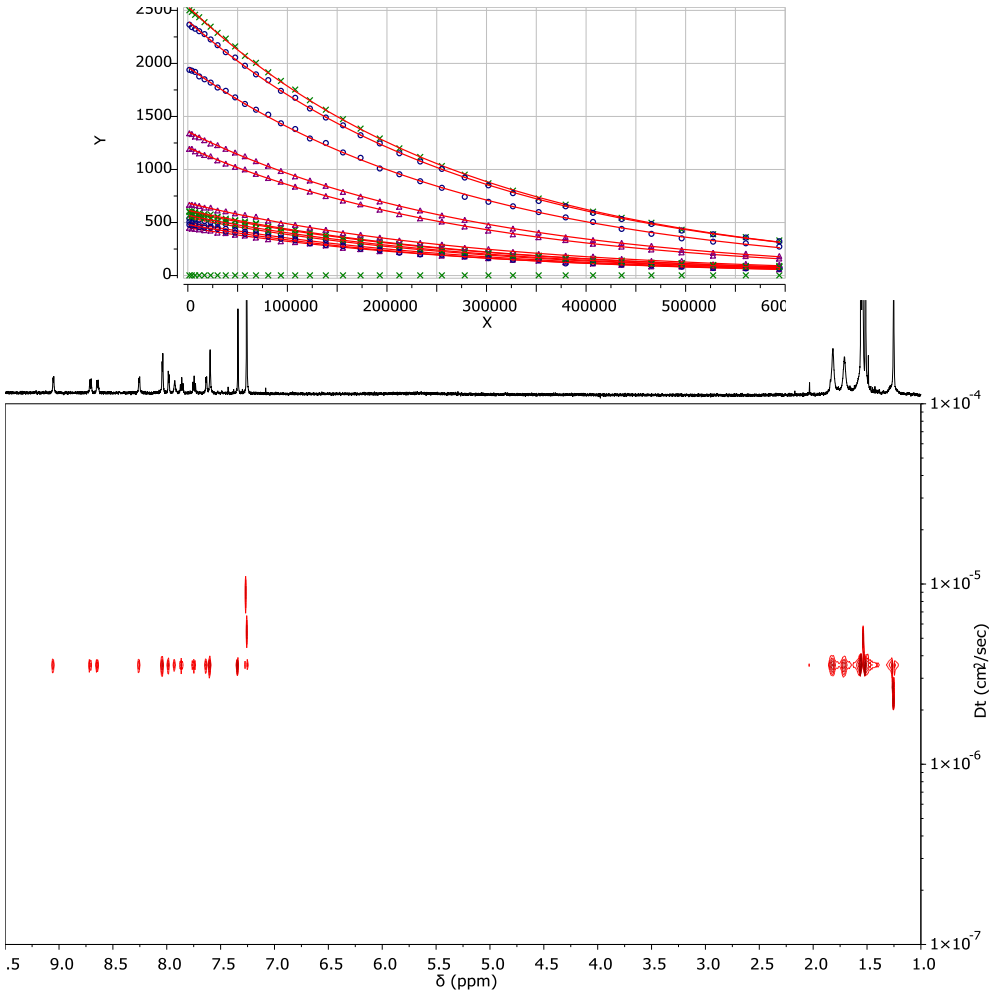

Figure A5.22. 2D ^{1}H-DOSY spectrum (Bayesian transform, $CDCl_3$, 600 MHz,) of **[ZnPdZn·Pyrazine]$_2$** (bottom); signal decay with monoexponential fitting, analysis performed on each proton resonance (top).

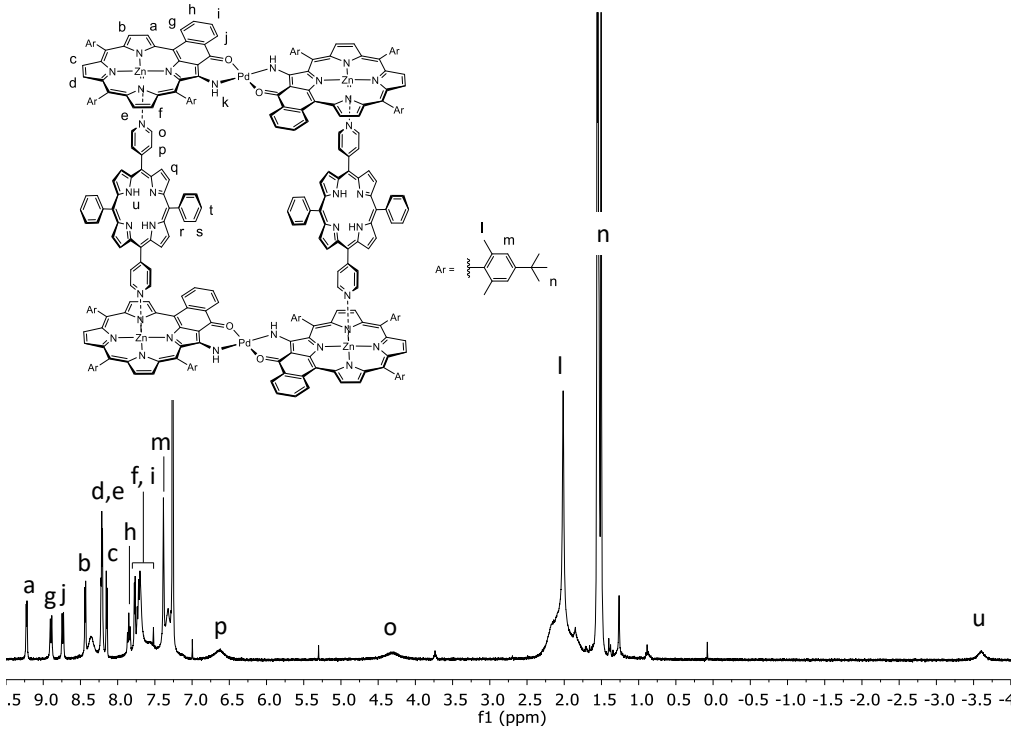

Figure A5.23. ^{1}H NMR spectrum ($CDCl_3$) of **[ZnPdZn·*t*DPyP]$_2$**

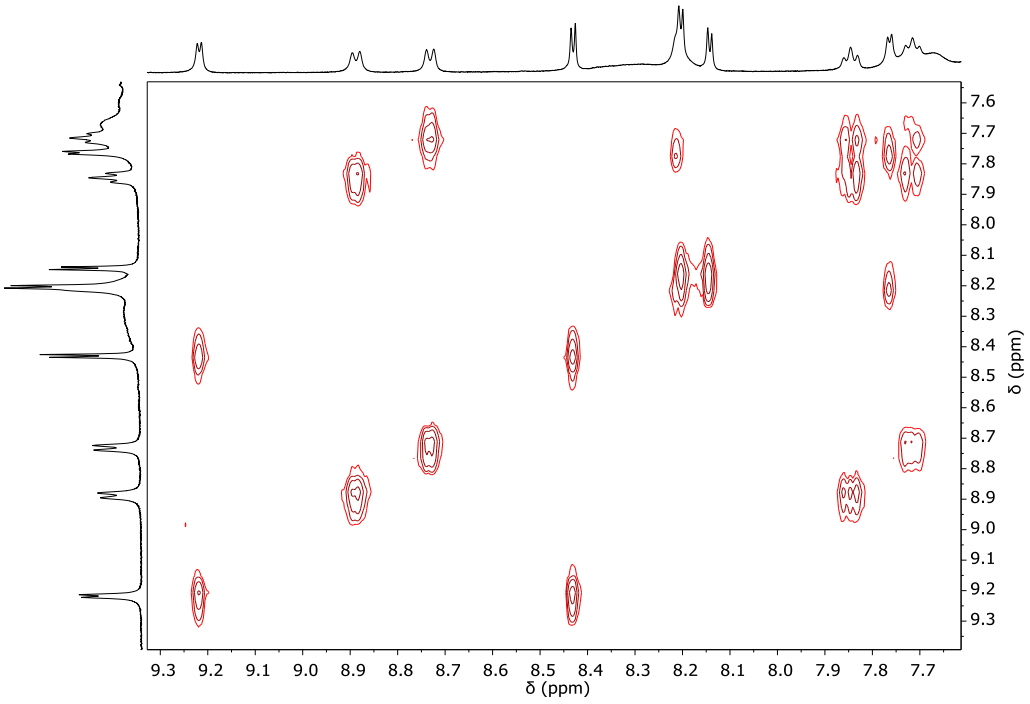

Figure A5.24. H-H COSY spectrum ($CDCl_3$) of **[ZnPdZn·*t*DPyP]$_2$**

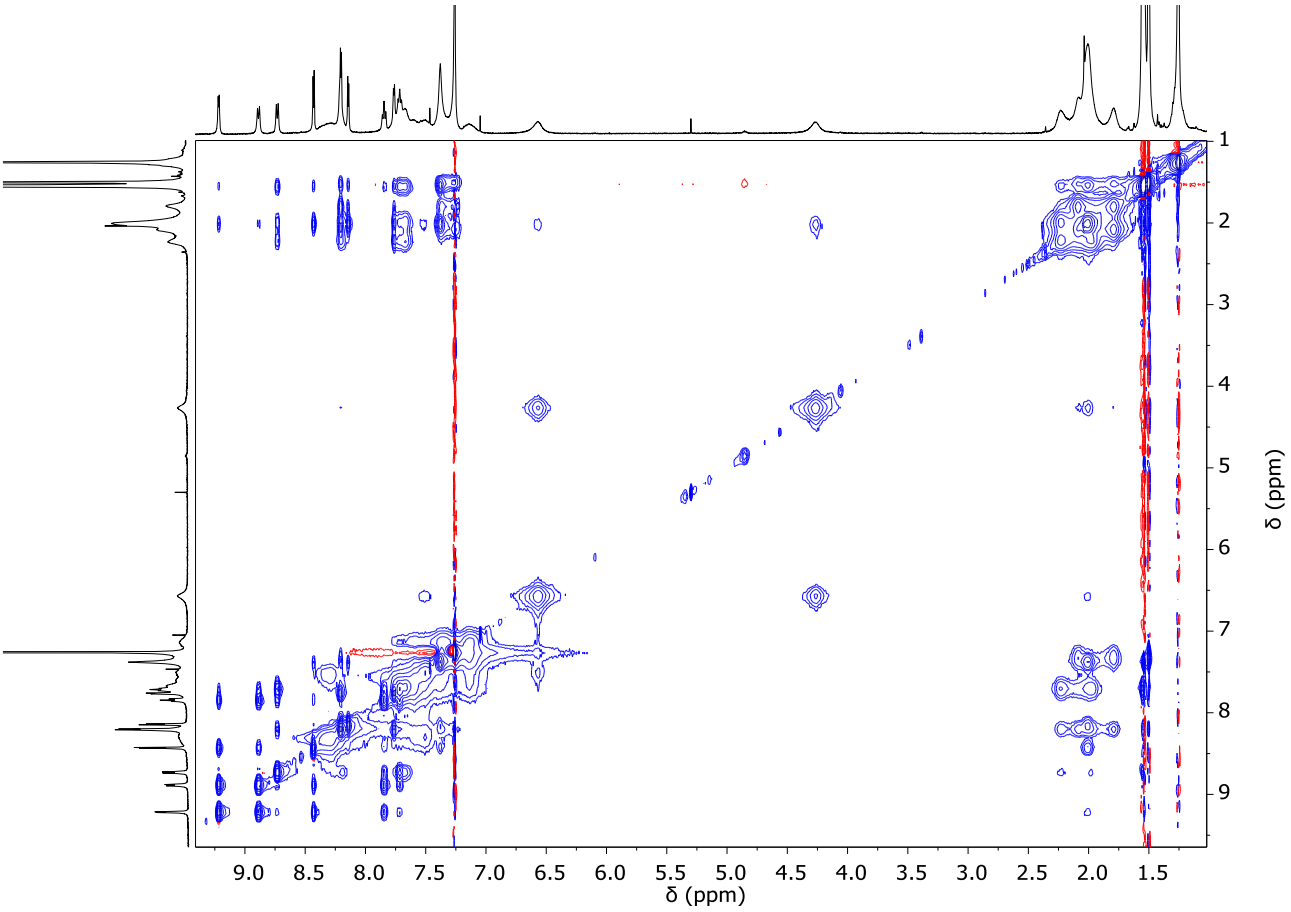

Figure A5.25. H-H NOESY spectrum ($CDCl_3$) of **[ZnPdZn·*t*DPyP]$_2$**

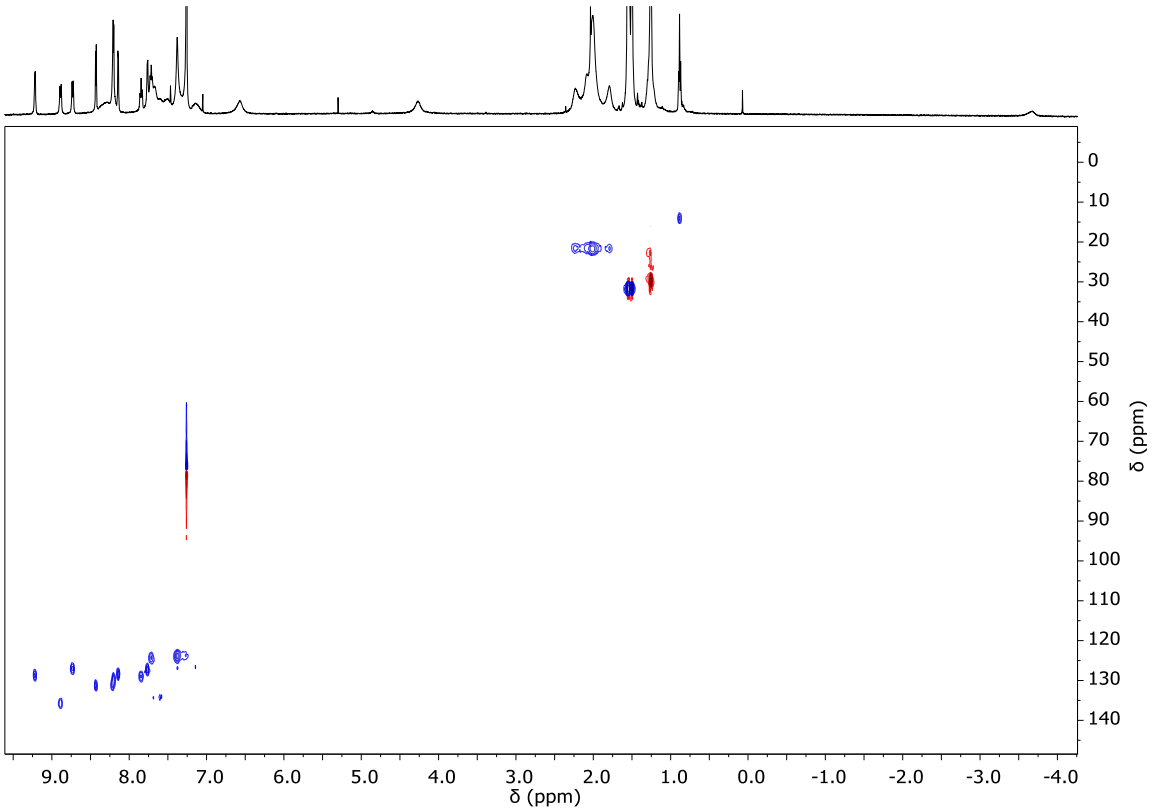

Figure A5.26. HSQC spectrum ($CDCl_3$) of **[ZnPdZn·*t*DPyP]$_2$**

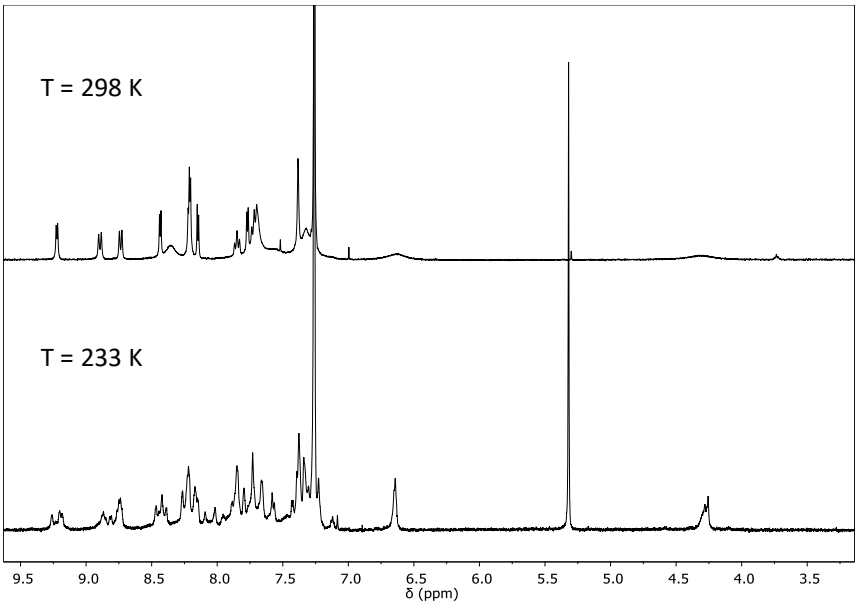

Figure A5.27. ^{1}H NMR spectra ($CDCl_3$) of **[ZnPdZn·*t*DPyP]$_2$** recorded at 298 K (top) and 233K (bottom).

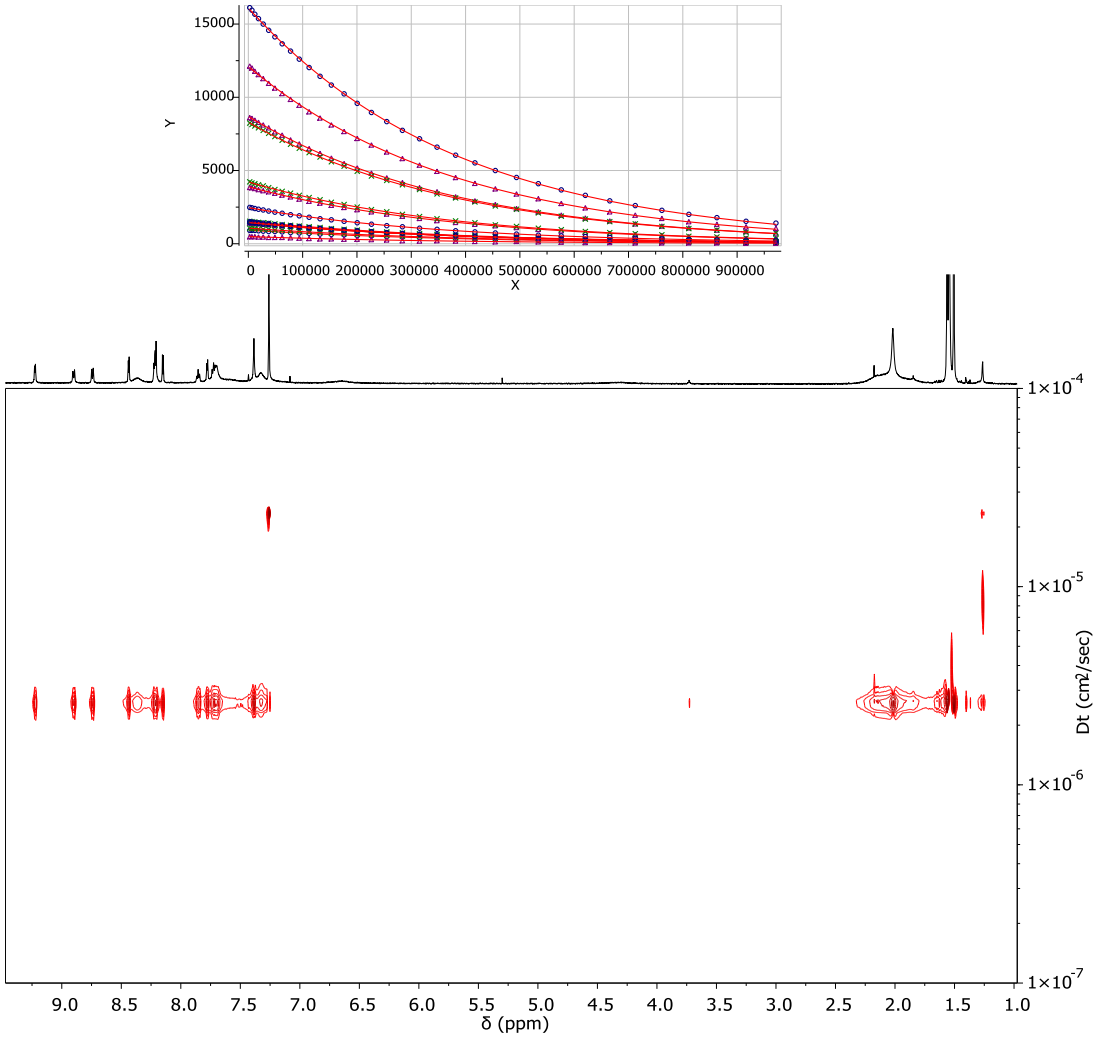

Figure A5.28. 2D ^{1}H-DOSY spectrum (Bayesian transform, $CDCl_3$, 600 MHz,) of **[ZnPdZn·*t*DPyP]$_2$** (bottom); signal decay with monoexponential fitting, analysis performed on each proton resonance (top).

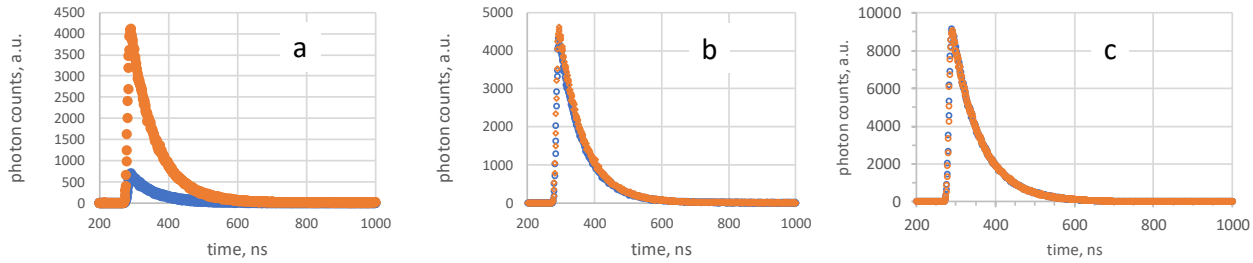

Figure A5.29. Single photon counting experiments monitored at 650 nm carried out before (blue) and after (orange) the addition of a slight excess of pyridine to DCM solutions of: a) **[ZnPdZn·*t*DPyP]$_2$** 8x10^{-5} M; b) ***t*DPyP**; c) **[ZnPdZn·*t*DPyP]$_2$** 5x10^{-7} M

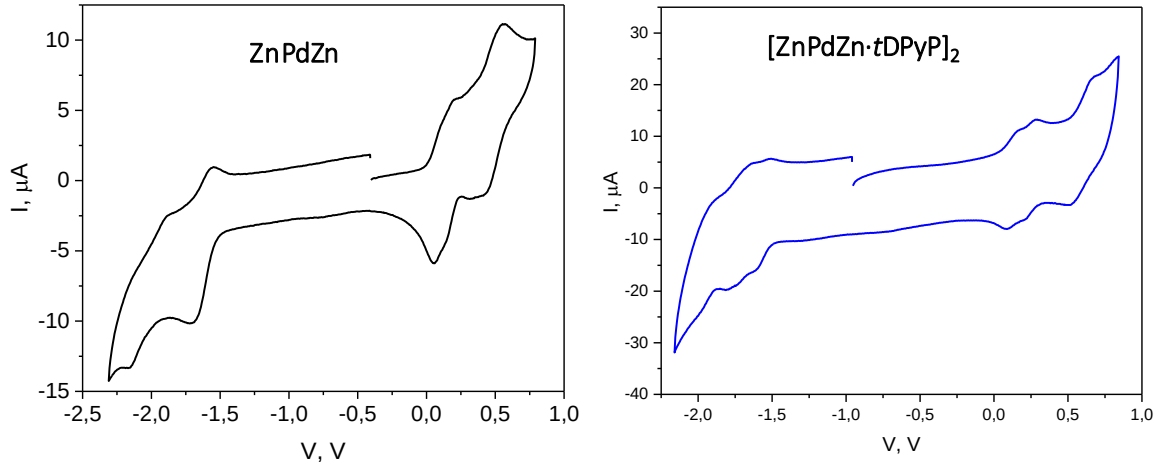

Figure A5.30. Cyclic voltammogram (DCM) of the **ZnPdZn** (left) and **[ZnPdZn·*t*DPyP]$_2$** (right). All measurements were made in argon purged CH_2Cl_2 solutions at 298 K, 0.1 M TBA(PF_6) as supporting electrolyte, scan rate 200 mV/s, SCE as reference electrode, ferrocene (0,46V *vs* SCE) as internal standard and glassy carbon as working electrode.

Appendix 1

General procedure followed for the elaboration of the DOSY experiments

The values reported in Tables 2.1, 4.1 and 5.1 for the diffusion coefficients (*Dt*) are the average of at least 5 different Dt values calculated through the analysis of a set of 1D DOSY spectra. Each *Dt* has been determined by a mono-exponential fit (Figure A1.1, left) of the proton signal decay through the Stejskal-Tanner equation (1),

$$\frac{I}{I_0} = \exp(-D_t\gamma^2\delta^2G^2\Delta), \qquad (1)$$

where I/I_0 is the intensity of the considered signal, D_t is the self-diffusion coefficient of the species which generate the signal, γ^2 is the gyromagnetic ratio, δ^2 and G^2 are respectively the duration and the amplitude of the gradient and Δ is the separation between two pulsed gradients. By applying the linearization $-\ln I/I_0$ *versus* the constant term $\gamma^2\delta^2G^2\Delta$, the *Dt* is obtained as the slope of the data regression line (Figure A1.1, right). All plots of echo amplitudes showing correlation coefficient (R) lower than 0.99 were discarded for the calculation of the average D_t value. The final average values agree with those observed for the different species from the 2D-DOSY spectra obtained with the *Bayesian DOSY transform* of the MestReNova software.

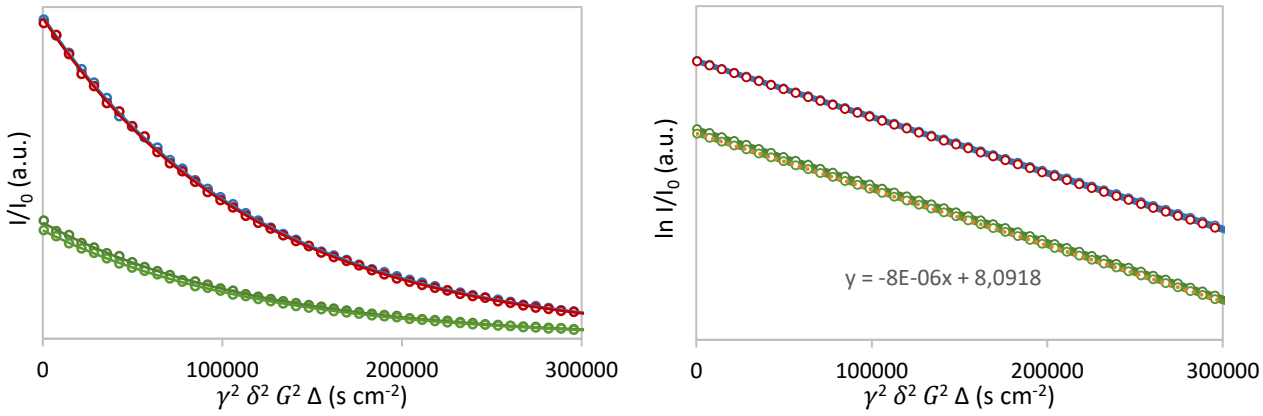

Figure A1.1. ^{1}H DOSY experiments of **5a** (Chapter 2): monoexponential fit of the proton signal decays (left), and linearization of the decay (right).

The hydrodynamic radius data (r_H) reported in Tables 2.1, 4.1 and 5.1 have been calculated by the Stokes-Einstein equation (2),

$$D_t = \frac{k_BT}{6\pi\eta r_H} \qquad (2)$$

using the average D_t values obtained, T = 298 K and $\eta_{chloroform}$ = 5.37x10^{-4} Pa·s;[1] or T = 243 K and $\eta_{chloroform}$ = 9.88x10^{-4} Pa·s.[1]

[1] Handbook of Chemistry and Physics 90th edition, David R. Lide. Ed., CRC Press, 2009, 6, 209.

Aknowledgements

I want to greatly acknowledge the groups of Prof. Kay Severin, École Polytechnique Fédérale de Lausanne (EPFL), and of Prof. Michael Pittelkow, University of Copenhagen, for the fruitful collaboration.

A special acknowledgement goes to Dr. Nicola Demitri (Elettra Synchrotron Trieste, Italy) and the staff of the XRD1 beamline are also appraised for the crystal data collection, reduction and final determination of the X-Ray structures.

The photophysical results illustrated in Chapters 3 and the work carried out as side project were obtained thanks to the longstanding collaboration with Dr. Mirco Natali (University of Ferrara, Italy).

Prof. Ennio Zangrando (University of Trieste) for the help with the last-minute graphical rendering of the X-ray structures reported in Chapter 3.

I would like to especially thank Dr. Romain Ruppert and Prof. Jean Weiss (University of Strasbourg) for giving me the chance to work in their group and supervising my research during my Erasmus period in Strasbourg.

I sincerely thank my supervisor, Prof. Elisabetta Iengo, for teaching me so much during the past three years, alongside Prof. Enzo Alessio and Prof. Barbara Milani and all the present and former members of the Alessio-Milani-Iengo group, who have accompanied me during this scientific adventure, in particular Irene Regeni, Erica Giraldi and Lorenzo Metilli for the great contribution given during their Master Thesis internship.

ChemComm

COMMUNICATION

View Article Online
View Journal

Cite this: DOI: 10.1039/c8cc03441a

Received 27th April 2018,
Accepted 18th May 2018

DOI: 10.1039/c8cc03441a

rsc.li/chemcomm

Formation of a long-lived radical pair in a Sn(IV) porphyrin–di(L-tyrosinato) conjugate driven by proton-coupled electron-transfer†

Mirco Natali, *[a] Agnese Amati,[b] Nicola Demitri[c] and Elisabetta Iengo*[b]

The novel conjugate 1, featuring two L-tyrosinato residues axially coordinated to the tin centre of a Sn(IV)-tetraphenylporphyrin, is reported as the first example of a supramolecular dyad for photochemical PCET. It is noteworthy that the excitation of 1 in the presence of a suitable base is followed by photoinduced PCET leading to a radical pair state with a surprisingly long lifetime.

Artificial photosynthesis (AP), that is conversion of solar energy into chemical fuels, represents a viable, yet challenging solution in response to the global energy issue.[1] In a biomimetic approach, any artificial photosynthetic scheme must envision a charge-separating system wherein light-absorption triggers a series of electron transfer (ET) processes eventually leading to a spatial separation of an electron and a hole (radical pair).[2] The achievement of a long-lived charge separation is essential in order to couple the photoinduced one-electron transfer processes with the dark multi-electron catalytic steps, namely conversion of substrates (*e.g.*, H_2O, CO_2, *etc.*) into fuels (*e.g.*, H_2, CO, CH_3OH, *etc.*).[2,3] In the electron transport chain of natural photosystem II (PSII) oxidation of the tyrosine donor (Y_Z) and reduction of the quinone acceptor (Q_B), after light absorption by chlorophyll P680, are both coupled to the transfer of protons (proton-coupled electron-transfer, PCET) that help in stabilizing the radical pair state from both thermodynamic and kinetic standpoints.[4,5] Hence, in a biomimetic fashion, several artificial systems have been recently investigated based on PCET.[6–8] However, the systems reported so far are all covalent in nature, thus requiring demanding synthetic protocols and impeding the use of simple and reliable comparative models.

On the other hand, the well-documented selective reactivity of Sn(IV)–di(hydroxo)-porphyrins towards the carboxylic functional group, leading to symmetric Sn(IV)–di(carboxylate)-porphyrin complexes with total conversions,[9] has been pursued by us and others as a metal-mediated strategy to target photoactive dyads (or pseudo-triads).[10] The supramolecular character of these conjugates, common to other metallo-porphyrin metal-mediated derivatives,[11] combined with the distinguished robustness of the Sn(IV)–carboxylate axial bonds and the antenna/redox properties of tin-porphyrins forecast the possibility of accessing valuable photoinduced charge separated states by exploiting combinatorial screening of different chromophore/carboxylate partners.[10] In fact, the combinatorial flexibility offered by these conjugates joined with the large databases on the opto-electronic properties of structural alternative components may allow for viable predictions of the photoinduced reactivity, as well as the design and facile preparation of multiple photochemical systems. However, the kinetic limitations, namely fast charge recombination, have been, so far, difficult to overcome. In this regard, we present here the first pioneering system based on the successful merging of Sn(IV)-porphyrin metal-mediation with proton-coupled electron-transfer by exploiting the well-established PCET reactivity of the phenol group.[12] Quite unexpectedly, **1** is only the third reported example of derivatives in which chiral amino acid residues are connected to a tin-porphyrin chromophore by metal mediation,[13] and their use as synthons in the supramolecular realm, while intriguing, is yet unexplored.

SnP-TyrOH (**1**, Scheme 1) was easily prepared from readily available starting materials by a method recently reported by us and adapted from literature procedures.[9,10] A 1 : 2 mixture of *trans*-dihydroxo(5,10,15,20-tetraphenylporphyrinato)-tin(IV) and *N*-acetyl-L-tyrosine was kept under refluxing conditions, in $CHCl_3$, for 12 hours. Solvent evaporation followed by recrystallization of the crude with a $CHCl_3$/acetone/*n*-hexane mixture afforded the desired product as a pure microcrystalline material, in quantitative yield. **1** was unambiguously characterized with a

[a] *Department of Chemical and Pharmaceutical Sciences, University of Ferrara and Centro Interuniversitario per la Conversione Chimica dell'Energia Solare (SOLARCHEM), Via L. Borsari 46, 44121 Ferrara, Italy. E-mail: mirco.natali@unife.it*

[b] *Department of Chemical and Pharmaceutical Sciences, University of Trieste, Via L. Giorgieri 1, 34127 Trieste, Italy. E-mail: eiengo@units.it*

[c] *Elettra–Sincrotrone Trieste, S.S. 14 Km 163.5 in Area Science Park, 34149 Basovizza, Trieste, Italy*

† Electronic supplementary information (ESI) available: Experimental section, synthesis and characterization, detailed crystallographic data, electrochemistry, and detailed photophysical characterization. CCDC 1813181. For ESI and crystallographic data in CIF or other electronic format see DOI: 10.1039/c8cc03441a

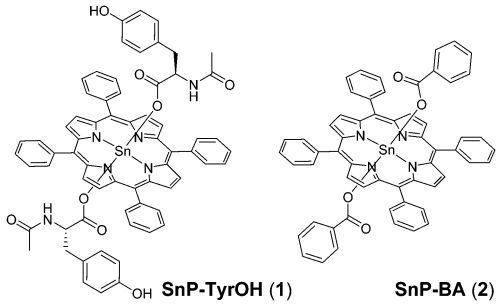

Scheme 1 Molecular structures of conjugate **1** and model compound **2**.

variety of techniques, with all the data confirming the presence of two amino acid residues axially bound to the metal centre of one tin-porphyrin *via* the carboxylate groups (see the ESI† for full details). A distinguishing feature of **1** is that of being chiral, as nicely evidenced by the induced CD signal observed in the absorption region (Soret-band) of the metallo-porphyrin (Fig. S5, ESI†). This fingerprint is observed under diluted conditions (25 μM of **1** in CH_2Cl_2), thus confirming the stability in the solution of **1**, as already documented for related tin-porphyrin adducts,[9,10] and ensuring the integrity of the conjugate in the photophysical studies (see below). Single crystals were obtained by slow diffusion of *n*-hexane into a $CHCl_3$/acetone solution of **1**, the resulting X-ray structure (Fig. 1 and Fig. S6–S8, ESI†) confirms the expected C_α stereocenter (S) configurations and evidences ordered patterns of intermolecular H-bonds.

Comparison of the optical and cyclic voltammetry data in CH_2Cl_2 for **1**, SnP-BA (**2**) (Scheme 1), and *N*-acetyl-L-tyrosine (see absorption and emission spectra in Fig. S9–S11, ESI,† and Table 1) evidences the absence of relevant ground state electronic interactions between the amino acid and the tin-porphyrin components in **1**. This supramolecular feature, well documented in previous reports by us and others,[10,11] legitimates the use of **2** and the free amino acid as reliable comparative models. In particular, from these data it is possible to confidently anticipate that, on simple thermodynamic grounds, both singlet and triplet excited states of the tin-porphyrin are not sufficiently high in energy to promote oxidation of the attached tyrosine in pure CH_2Cl_2 (see the ESI†). Indeed, comparable emission profiles, in terms of spectral shape and intensities (Fig. S11, ESI†), are found upon excitation of optically matched solutions of **1** and **2**. Also, similar fluorescence lifetimes ($\tau \approx 1.15$ ns, Fig. S12, ESI†) are measured in both cases. Similarly, the triplet excited state of

Table 1 Electrochemical data[a]

	E_{ox} (V)	E_{red} (V)
1	+0.89[b,c]	−1.40
2	+0.91	−1.37
N-Acetyl-L-tyrosine	+0.83[b]	—

[a] Obtained by cyclic voltammetry (CV) in N_2-purged CH_2Cl_2 (0.1 M $TBAPF_6$) at 298 K, scan rate v = 100 mV s^{-1}, using GC as a WE, Pt as a CE, and SCE as a reference, potentials are referred to Fc/Fc^+ used as an internal standard (Fig. S14 and S15, ESI). [b] Irreversible wave, peak potential given. [c] Process attributed to tyrosine for intensity reasons, SnP oxidation is likely buried under this intense wave.

the Sn(IV) porphyrin in **1**, as detected by flash photolysis (Fig. S13, ESI†), is also comparable in both absorbance and lifetime ($\tau \approx 2.2$ and $\tau \approx 35$ μs under air-equilibrated and oxygen-free conditions, respectively) with that of **2**. All these observations confirm negligible quenching of both singlet and triplet excited states of the chromophore and therefore the impossibility for **1** to exhibit inter-component photoinduced processes in pure CH_2Cl_2.

The photophysics of **1** changes dramatically in the presence of an organic base. Addition of pyrrolidine in the range of 0–0.084 M brings about a severe quenching of the SnP fluorescence (Fig. 2) with an efficiency that is dependent on the pyrrolidine concentration and almost saturates above *ca.* 0.05 M base reaching a value of *ca.* 60% (Table S4, ESI†). The fluorescence lifetime decreases along with the emission intensity (Fig. 2b). The observed behaviour can be attributed to the occurrence of a photoinduced PCET from the singlet excited state of the chromophore involving reduction of the porphyrin and oxidation of the tyrosine with a concomitant proton shift from the phenol of the amino acid to the base, according to eqn (1), and presumably taking place *via* a concerted mechanism (CPET).

$$^1\text{*SnP-TyrOH}\cdots\text{Pyr} \rightarrow \text{SnP}^-\text{-TyrO}^\bullet\cdots{}^+\text{HPyr} \qquad (1)$$

This process is indeed expected to be exergonic by *ca.* 1.1 eV, as estimated from the electrochemical data in Table 1, the energy of the ^{1}*SnP excited state, and the energy stabilization arising from the deprotonation of the oxidized tyrosine by the base (see the ESI† for details). Most importantly, the hypothesis of a CPET quenching mechanism is strongly supported by the following considerations.‡ (i) Addition of pyrrolidine to a solution of **2** in CH_2Cl_2 has almost negligible effects on the SnP fluorescence intensity and lifetime (Fig. S16, ESI†), thus ruling out any alternative ET quenching by the base. (ii) Pyrrolidine

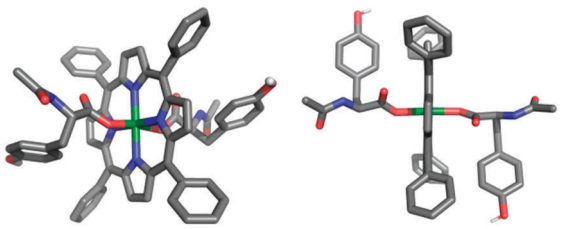

Fig. 1 Two views of the single crystal X-ray structure of **1**, solvent molecules and hydrogens, except for those of the OH groups, are omitted for clarity. Color code: H, white; C, gray; N, blue; O, red; Sn, green.

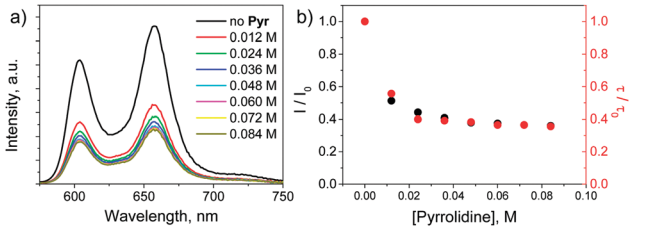

Fig. 2 (a) Emission spectra (λ_{exc} = 532 nm) in CH_2Cl_2 solutions containing 25 μM **1** and 0–0.084 M pyrrolidine; (b) trend of I/I_0 and τ/τ_0 ratios *vs.* pyrrolidine concentration.

does not deprotonate the tyrosine hydroxyl moiety as confirmed by absorption measurements (Fig. S17, ESI†), thus excluding a simple ET pathway to a putative phenolate. Conversely, the latter observations clearly support the presence of a pre-association equilibrium between the amino acid and the base *via* hydrogen bonding, a fundamental requirement for the occurrence of PCET.[5,7,14] (iii) The kinetic treatment of the quenching data of Fig. 2b, by considering the above-mentioned SnP-TyrOH···Pyr interaction,[6,15] results in an accurate fitting for a chosen value of association constant of $K_A = 45(\pm 5)\ M^{-1}$, in line with the literature data,[15] and a rate constant of $k_{CPET} = 2.1(\pm 0.03) \times 10^9\ s^{-1}$ (see the ESI† for detailed analysis). Importantly, the K_A value so obtained is fully compatible with the value of $K_A = 47(\pm 7)\ M^{-1}$ independently determined for the hydrogen-bonding association between tyrosine and pyrrolidine in CH_2Cl_2 (Fig. S23, ESI†).[16] (iv) The prompt transient spectrum detected by laser flash photolysis of **1** with 0.06 M base (Fig. S18, ESI†) can be reasonably represented by a combination of differential spectra of the triplet excited state and a fraction of the radical pair state (see the ESI†). Indeed, the presence of a more pronounced shoulder at *ca.* 450 nm with respect to the transient spectrum of the triplet only, as measured in **2**, can be possibly attributed to the presence of some SnP radical anion (*i.e.*, one product expected after the process in eqn 1 has occurred, Fig. S18 and S19, ESI†).

The fraction of triplet state formed *via* intersystem crossing from the singlet, in competition with the PCET, displays pyrrolidine-dependent deactivation profiles. Progressive additions of the base cause indeed faster decays, as monitored at the transient absorption maximum (Fig. 3a). This evidence is consistent with the occurrence of a quenching process also at the triplet level. Similarly to what was observed for the singlet excited state (Fig. 2b), the pyrrolidine concentration has a remarkable effect on the quenching efficiency (Fig. 3b). Accordingly, this process can be attributed to a parallel CPET originating from the triplet excited state level (eqn (2)).

$$^3\text{*SnP-TyrOH}\cdots\text{Pyr} \rightarrow \text{SnP}^-\text{-TyrO}^\bullet\cdots{}^+\text{HPyr} \qquad (2)$$

On the basis of thermodynamic considerations, this process is indeed expected to be exergonic by *ca.* 0.7 eV and can be substantiated by the following arguments.‡ (i) Bimolecular quenching of the triplet excited state by pyrrolidine, as observed using model **2** (Fig. S20, ESI†), is considerably less efficient than

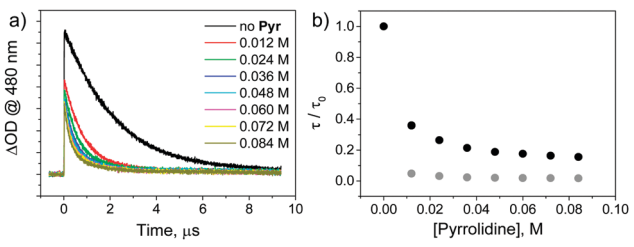

Fig. 3 (a) Kinetic traces at 480 nm obtained by laser flash photolysis (λ_{exc} = 532 nm) in air-equilibrated CH_2Cl_2 solutions containing 25 μM **1** and 0–0.084 M pyrrolidine; (b) trend of τ/τ_0 ratio *vs.* pyrrolidine concentration under air-equilibrated (black dots) and oxygen-free conditions (grey dots).

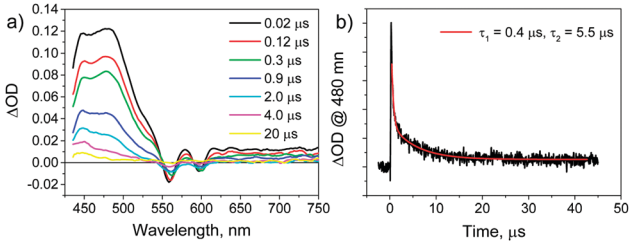

Fig. 4 (a) Spectral evolution of the transient absorption and (b) kinetic trace at 480 nm with related biexponential fitting obtained by laser flash photolysis (λ_{exc} = 532 nm) in oxygen-free CH_2Cl_2 with 25 μM **1** and 0.06 M pyrrolidine.

the quenching process measured in **1**, thus ruling out a direct ET from the pyrrolidine. (ii) Fitting of the kinetic data in Fig. 3b, using the same procedure[6,15] employed for the singlet excited state (see the ESI†), is found satisfactory with the same association constant ($K_A = 45(\pm 5)\ M^{-1}$) and a rate of $k_{CPET} = 3.4(\pm 0.08) \times 10^6\ s^{-1}$.§ (iii) The spectral evolution of the transient absorption of **1** in the presence of 0.06 M pyrrolidine, as measured by laser flash photolysis under oxygen-free conditions, displays a biphasic behaviour (Fig. 4). In the first process, *ca.* 1 μs (τ_1 = 0.4 μs, Fig. 4b), the prompt transient signal, mainly attributable to the triplet excited state (maximum at 480 nm), progressively decays and changes in shape yielding a new transient signal featuring a maximum at 450 nm, attributable to the presence of the SnP radical anion only (Fig. S18b, ESI†). In the second process (τ_2 = 5.5 μs, Fig. 4b), the latter spectrum decays to the baseline. The first spectral evolution can be safely attributed to the formation of the SnP$^-$-TyrO$^\bullet\cdots{}^+$HPyr state (the tyrosyl radical is spectroscopically silent in this wavelength range),[7] while the second process corresponds to the ground-state repopulation from the above-mentioned radical pair state (see below). A quantum yield of $\Phi = \sim 0.3$ can be estimated for the formation of such a PCET photoproduct which definitely points towards a sole triplet contribution (see the ESI†). Most importantly, the SnP$^-$-TyrO$^\bullet\cdots{}^+$HPyr state is considerably long-lived, with a lifetime reaching the μs time-scale (*ca.* 6 μs). Notably, this result is rather impressive when compared to both dyad systems displaying photoinduced ET processes, wherein only few exceptions can be found,[18,19] and related two-component systems involving light-driven PCET.[6,7] Interestingly, a comparable, albeit shorter, lifetime has been achieved only in a more complex (covalent) triad system featuring related molecular components.[8]

In summary, upon visible-light excitation of **1** in the presence of pyrrolidine, two radical pair states of the type SnP$^-$-TyrO$^\bullet\cdots{}^+$HPyr can be populated that differ in terms of spin multiplicity: the first one is formed in the sub-ns regime by singlet quenching and undergoes an extremely fast decay ($k > 10^8\ s^{-1}$), and the second one has triplet spin multiplicity and is long-lived, as experimentally detected by transient absorption in both its formation and deactivation (Fig. 4).

The overall set of photochemical processes occurring in **1** in CH_2Cl_2 in the presence of pyrrolidine is summarized in Fig. 5. Two alternative mechanisms may be available for the ground-state decay from both radical pair states (singlet and triplet):

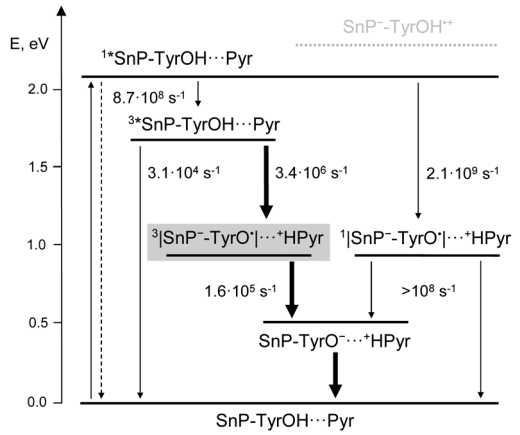

Fig. 5 Energy level diagram in **1** with related photoinduced processes and rates in CH_2Cl_2 in the presence of pyrrolidine (see the ESI† for details on the energy levels; for simplicity the same energy is assigned to both singlet and triplet charge transfer states); formation and decay of the long-lived charge separated state are highlighted for guiding the reader.

(i) stepwise ET-PT (eqn (3) and (4)) or (ii) concerted PCET (CPET, eqn (5)).

$$SnP^{-}\text{-}TyrO^{\bullet}\cdots{}^{+}HPyr \rightarrow SnP\text{-}TyrO^{-}\cdots{}^{+}HPyr \quad (3)$$

$$SnP\text{-}TyrO^{-}\cdots{}^{+}HPyr \rightarrow SnP\text{-}TyrOH\cdots Pyr \quad (4)$$

$$SnP^{-}\text{-}TyrO^{\bullet}\cdots{}^{+}HPyr \rightarrow SnP\text{-}TyrOH\cdots Pyr \quad (5)$$

As for the long-lived triplet radical pair state,¶ the spectral changes do not allow to unambiguously establish the actual mechanism (the phenolate anion potentially formed *via* eqn (3) has indeed no fingerprint in the visible region, Fig. S17, ESI†). However, the observation of appreciably pyrrolidine-independent kinetics (Table S4 and Fig. S24, ESI†) favours the stepwise ET-PT (eqn (3) and (4)) over the CPET pathway (eqn (5)). Interestingly, this behaviour is similar to that observed in related polypyridine Re(I)/Ru(II)–phenol dyads[6] where efficient charge separation *via* CPET was actually followed by intramolecular reverse electron transfer. It is noteworthy that, with respect to those systems,[6] the reverse backward ET process (eqn (3)) is herein considerably slower. This evidence can be confidently attributed to the absence of relevant spin–orbit coupling in conjugate **1**, with respect to the ruthenium/rhenium cases,[6] which makes the spin-forbidden, backward reaction substantially slower.[20]

In conclusion, we have reported on the first example of a supramolecular dyad, based on a tin-porphyrin antenna/electron-acceptor and a tyrosine amino acid electron-/proton-donor, that displays a surprisingly long-lived radical pair state when excited in the presence of pyrrolidine. Its formation follows a CPET mechanism mediated by H-bonding between the tyrosyl residues and the base. The present work thus elects the combination of the simple metal-mediated conjugates with the PCET reactivity as an effective turning point within artificial photosynthetic schemes. Also, the symmetric, disubstituted characteristic of Sn(IV) porphyrins (pseudo-triad structural motif) may also potentially lead to light-induced accumulation of multiple redox equivalents *via* PCET.[21] Hence, this novel interpretation of the supramolecular combinatorial flexibility[11] will offer a unique opportunity for the development of an extended library of new photochemical systems aimed at a better understanding of the fundamental rules governing PCET. Research towards this direction is currently being planned in our labs.

Financial support from the University of Ferrara (FAR 2017) and the University of Trieste (FRA 2016) is gratefully acknowledged.

Conflicts of interest

There are no conflicts to declare.

Notes and references

‡ Determination of the H/D kinetic isotope effect may be useful to additionally confirm the CPET mechanism. However, the difficulties in the preparation of the deuterated analogue of **1** by standard literature methods[6] due to the oxophilicity of **1** hampered this type of study at this stage. This issue will be addressed in the near future.
§ The almost 1000-fold difference in rates between singlet and triplet PCET can be mainly imparted to the different ΔG° values. Such a difference in rates would be indeed compatible, in a classical Marcus-type treatment assuming comparable pre-exponential factors, with a total reorganization energy of $\lambda \approx 1.2$ eV (see the ESI†). This value is much larger than that measured, *e.g.*, in a SnP–carboxylate adduct displaying ET only[17] and may further support the PCET nature of both singlet and triplet quenching processes.[5]
¶ The very short lifetime of the singlet radical pair state (see the ESI†) makes a detailed mechanistic analysis not much relevant at this stage and will be discussed elsewhere.

1 N. Armaroli and V. Balzani, *Angew. Chem., Int. Ed.*, 2007, **46**, 52.
2 B. D. Sherman, M. D. Vaughn, J. J. Bergkamp, D. Gust, A. L. Moore and T. A. Moore, *Photosynth. Res.*, 2014, **120**, 59.
3 L. Hammarström, *Acc. Chem. Res.*, 2015, **48**, 840.
4 J. L. Dempsey, J. R. Winkler and H. B. Gray, *Chem. Rev.*, 2010, **10**, 7024.
5 (*a*) D. R. Weinberg, C. J. Gagliardi, J. F. Hull, C. F. Murphy, C. A. Kent, B. C. Westlake, A. Paul, D. H. Ess, D. G. McCafferty and T. J. Meyer, *Chem. Rev.*, 2012, **112**, 4016; (*b*) J. C. Lennox, D. A. Kurz, T. Huang and J. L. Dempsey, *ACS Energy Lett.*, 2017, **2**, 1246.
6 (*a*) M. Kuss-Petermann, H. Wolf, D. Stalke and O. S. Wenger, *J. Am. Chem. Soc.*, 2012, **134**, 12844; (*b*) M. Kuss-Petermann and O. S. Wenger, *J. Phys. Chem. A*, 2013, **117**, 5726; (*c*) J. Chen, M. Kuss-Petermann and O. S. Wenger, *Chem. – Eur. J.*, 2014, **20**, 4098; (*d*) A. Pannwitz and O. S. Wenger, *J. Am. Chem. Soc.*, 2017, **139**, 13308.
7 (*a*) T. Irebo, S. Y. Reece, M. Sjödin, D. G. Nocera and L. Hammarström, *J. Am. Chem. Soc.*, 2007, **129**, 15462; (*b*) T. Irebo, M.-T. Zhang, T. F. Markle, A. M. Scott and L. Hammarström, *J. Am. Chem. Soc.*, 2012, **134**, 16247; (*c*) A. A. Pizano, J. L. Yang and D. G. Nocera, *Chem. Sci.*, 2012, **3**, 2457.
8 (*a*) G. F. Moore, M. Hambourger, M. Gervaldo, O. G. Poluektov, T. Rajh, D. Gust, T. A. Moore and A. L. Moore, *J. Am. Chem. Soc.*, 2008, **130**, 10466; (*b*) J. D. Megiatto, A. Antoniuk-Pablant, B. D. Sherman, G. Kodis, M. Gervaldo, T. A. Moore, A. L. Moore and D. Gust, *Proc. Natl. Acad. Sci. U. S. A.*, 2012, **109**, 15578; (*c*) S. J. Mora, E. Odella, G. F. Moore, D. Gust, T. A. Moore and A. L. Moore, *Acc. Chem. Res.*, 2018, **51**, 445.
9 (*a*) J. C. Hawley, N. Bampos and J. K. M. Sanders, *Chem. – Eur. J.*, 2003, **9**, 5211; (*b*) D. P. Arnold and A. Blok, *Coord. Chem. Rev.*, 2004, **248**, 299; (*c*) V. S. Shetti, Y. Pareek and M. Ravikanth, *Coord. Chem. Rev.*, 2012, **256**, 2816.
10 (*a*) T. Honda, T. Nakanishi, K. Ohkubo, T. Kojima and S. Fukuzumi, *J. Phys. Chem. C*, 2010, **114**, 14290; (*b*) T. Lazarides, S. Kuhri, G. Charalambidis, M. K. Panda, D. M. Guldi and A. G. Coutsolelos, *Inorg. Chem.*, 2012, **51**, 4193; (*c*) P. Cavigli, G. Balducci, E. Zangrando, N. Demitri, A. Amati, M. T. Indelli and E. Iengo, *Inorg. Chim. Acta*, 2016, **439**, 61.

11 (*a*) F. Scandola, C. Chiorboli, A. Prodi, E. Iengo and E. Alessio, *Coord. Chem. Rev.*, 2006, **250**, 1471; (*b*) E. Iengo, G. D. Pantoş, J. K. M. Sanders, M. Orlandi, C. Chiorboli, S. Fracasso and F. Scandola, *Chem. Sci.*, 2011, **2**, 676; (*c*) M. Natali, R. Argazzi, C. Chiorboli, E. Iengo and F. Scandola, *Chem. – Eur. J.*, 2013, **19**, 9261; (*d*) A. Amati, P. Cavigli, A. Kahnt, M. T. Indelli and E. Iengo, *J. Phys. Chem. A*, 2017, **121**, 4242.
12 (*a*) J. J. Warren, T. A. Tronic and J. M. Mayer, *Chem. Rev.*, 2010, **110**, 6961; (*b*) C. Constentin, M. Robert and J.-M. Savéant, *Acc. Chem. Res.*, 2010, **43**, 1019.
13 (*a*) S. H. Kim, H. Kim, K. K. Kim and H. J. Kim, *J. Porphyrins Phthalocyanines*, 2009, **13**, 806; (*b*) K. Karikis, E. Georgilis, G. Charalambidis, A. Petrou, O. Vakuliuk, T. Chatziioannou, I. Raptaki, S. Tsovola, I. Papakyriacou, A. Mitraki, D. T. Gryko and A. G. Coutsolelos, *Chem. – Eur. J.*, 2016, **22**, 11245.
14 S. Hammes-Schiffer and A. A. Stuchebrukhov, *Chem. Rev.*, 2010, **110**, 6939.
15 L. Biczòk, N. Gupta and H. Linschitz, *J. Am. Chem. Soc.*, 1997, **119**, 12601.
16 P. Dongare, A. G. Bonn, S. Maji and L. Hammarström, *J. Phys. Chem. C*, 2017, **121**, 12569.
17 T. Kojima, K. Hanabusa, K. Okhubo, M. Shiro and S. Fukuzumi, *Chem. – Eur. J.*, 2010, **16**, 3646.
18 S. Fukuzumi, K. Ohkubo and T. Suenobu, *Acc. Chem. Res.*, 2014, **47**, 1455.
19 (*a*) D. Gust, T. A. Moore and A. L. Moore, *Acc. Chem. Res.*, 2001, **34**, 40; (*b*) F. Wessendorf, B. Grimm, D. M. Guldi and A. Hirsch, *J. Am. Chem. Soc.*, 2010, **132**, 10786; (*c*) M. Natali, S. Campagna and F. Scandola, *Chem. Soc. Rev.*, 2014, **43**, 4005.
20 J. W. Verhoeven, *J. Photochem. Photobiol., C*, 2006, **7**, 40.
21 M. Kuss-Petermann, M. Orazietti, M. Neuburger, P. Hamm and O. S. Wenger, *J. Am. Chem. Soc.*, 2017, **139**, 5225.